Department of
Civil & Environmental Engineering
Massachusetts Institute of Technology

Experimental and Analytical Research on Fracture Processes in Rock

Final Report

on

Project: DE-FG3606 GO16061

Principal Investigator: Herbert H. Einstein

Team Members: Jay Miller; Bruno Silva

February 24, 2009

Experimental and Analytical Research on Fracture Processes in Rock

Project: DE-FG3606 GO16061

Executive Summary

Background

The research, which was conducted in the period June 2006 – August 2007, addressed the interest areas: "Fracture Formation and Growth" and "Fracture Evolution", in the context of Enhanced Geothermal Systems (EGS) Technology Development. As is well known, water flow through fractures is used as the major process to extract heat in EGS. Since natural fracturing is often insufficient, creating new fractures is essential in EGS development, which in turn necessitates a thorough understanding of the fracture process. Specifically, work on the following tasks was proposed:

1. Testing of different rock types and fracture geometries under ambient temperature.

2. Similar to task 1 but at elevated temperatures.

3. Extension of crack (fracture) initiation -, propagation - and coalescence criteria and incorporation in numerical model.

4. Initial steps toward modeling of larger/smaller fractures.

5. Reporting and suggestions for further research.

As can be seen, Tasks 1 and 2 are experimental, while Tasks 3 and 4 are analytical/numerical. Based on feedback, received mostly at the PI meeting on July 13 and 14, 2006, in Golden, CO, but also based on discussions with researchers and practitioners active in enhanced (engineered) geothermal systems, the actual work was slightly different than what is listed above:

- A detailed study on the use of acoustic emissions to trace crack/fracture propagation was added. The reason is as follows: While the usual (highspeed camera) observations in our tests are entirely sufficient for research purposes, one cannot do such direct observations in the field. Relating acoustic (seismic) emissions to the visual observations would, therefore, be an important addition, making the research results more applicable in practice.

- Initial tests, in which the cracks were pressurized with water were conducted. This corresponds to the situation in the field where the fractures are water filled and where water pressurization is used to create additional fractures.

Work Performed and Results

This will be in sequence of the report chapters.

After Chapter 1 (Introduction) a brief review on theoretical fracture mechanics and experimental fracture mechanics is provided in Chapter 2. The emphasis in the experimental fracture mechanics reviews are on experiments that have been conducted on a variety of model materials (plexiglass, gypsum) and real rock (mostly marble but also granite) with different flaw geometries. Flaws are artificially created cracks (fractures) and the experiments investigate how cracks propagate from these flaws and, if applicable, how the cracks coalesce from multiple flaws! This preceding work made it possible to identify different crack types (Fig. E1) and different coalescence patterns (Figure E2).

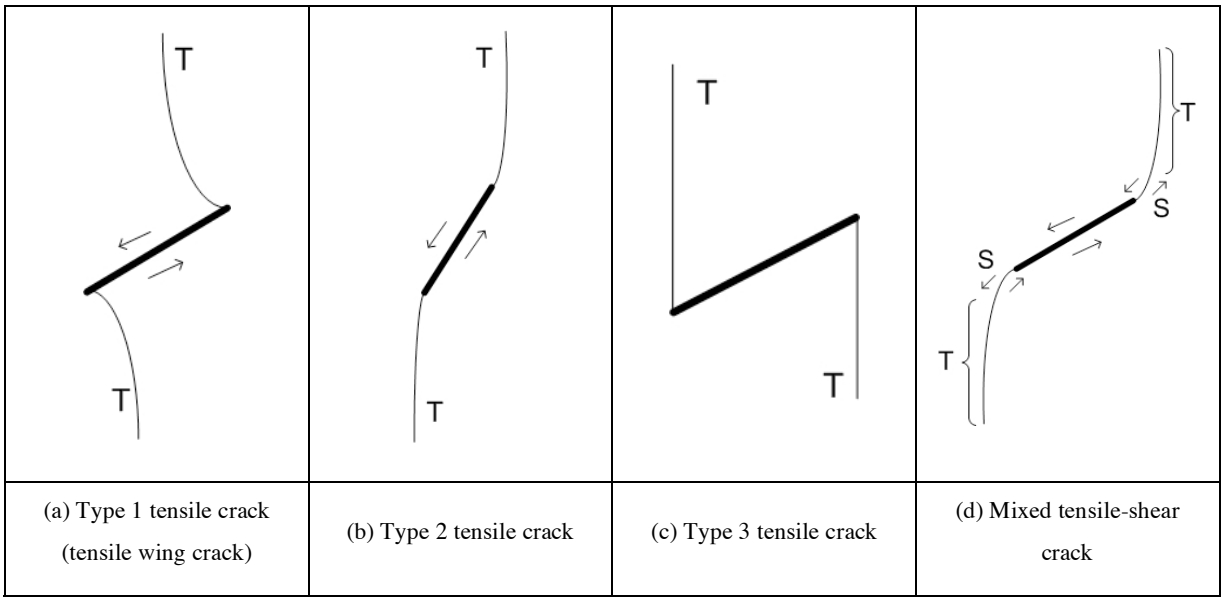

(a) Type 1 tensile crack (tensile wing crack)	(b) Type 2 tensile crack	(c) Type 3 tensile crack	(d) Mixed tensile-shear crack

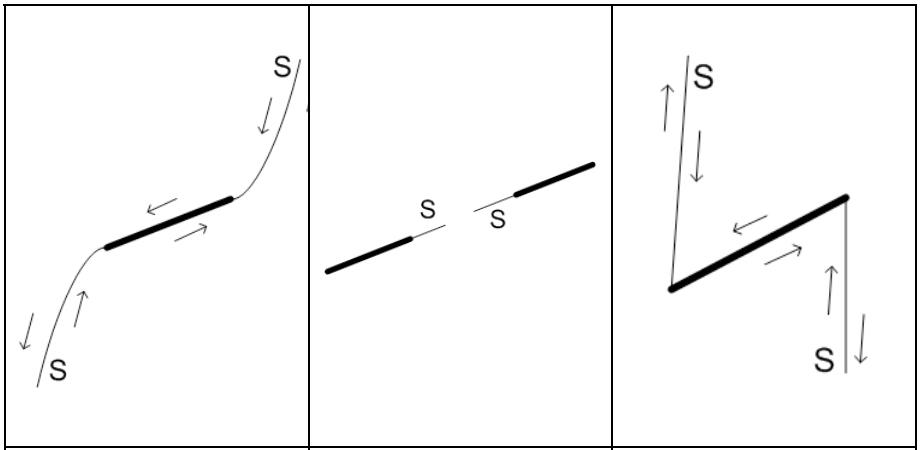

(e) Type 1 shear crack	(f) Type 2 shear crack	(g) Type 3 shear crack

Figure E1. Seven crack types identified by Wong (2008) in his single-flaw experiments in gypsum and marble

Category	Coalescence patterns	Crack types involved
1	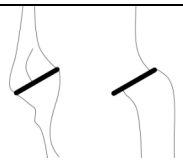	**No** coalescence
2	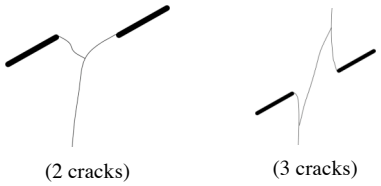	**Indirect** coalescence by two or multiple cracks (crack types vary)
3	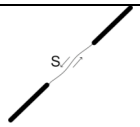	Type 2 **S** crack(s)
4	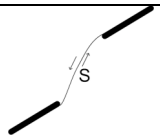	Type 1 **S** crack(s)
5	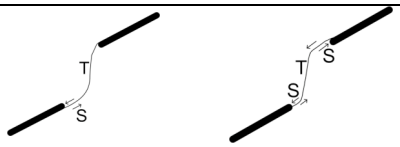	One or more type 2 **S** crack(s) and type 2 **T** crack segments between inner flaw tips
6	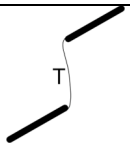	Type 2 **T** crack(s). There may be occasional short **S** segments present along the coalescence crack.
7		Type 1 **T** crack(s)
8	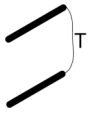	Flaw tips of the same side linked up by **T** crack(s) not displaying wing appearance (crack type not classified). There may be occasional short **S** segments present along the coalescence crack.
9	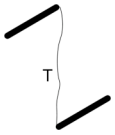	Type 3 **T** crack(s) linking right tip of the top flaw and left tip of the bottom flaw. There may be occasional short **S** segments present along the coalescence crack.

Figure E2 Nine coalescence patterns observed by Wong (2008).
The Crack Types are those Described in E1.

Chapter 3 describes the specimen preparation and setup for conducting uniaxial compression tests on granite. The study presented here concentrated on granite since, as mentioned above, model material and marble had been tested before at MIT while only a limited set of tests had been run on granite (a specific list of papers and other publications on the MIT work is given at the end of this Executive Summary – in addition to being included in the reference list (Appendix A). Tests were conducted on prismatic specimens containing two flaws in a feedback controlled loading machine. The basic flaw components are shown in Figure E3.

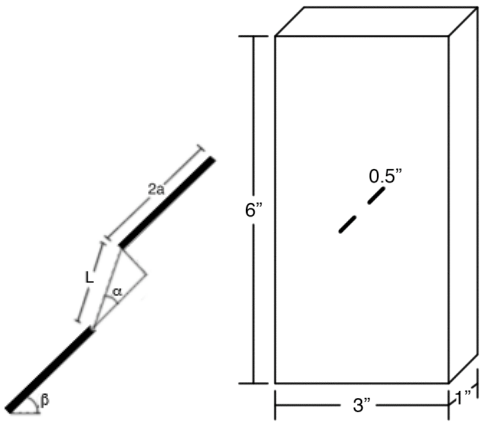

a)

	β = 0°	β = 30°	β = 45°	β = 60°	β = 0°
Coplanar (α = 0°)					
Stepped (α = 60°)					

b)

Figure E3. a) Basic Flaw Pair Geometry and Definitions (L = Ligament Length, β = Flaw Inclination Angle, α = Bridging Angle)

b) Tested Geometries (shown for Ligament Length L = 2a = Flaw Length; the same basic geometries were also tested with Ligament Length L = a)

The load displacement (stress-strain) behavior was recorded and the cracking process was visually observed with two video systems (Sony, Phantom). The Sony records the entire process, the Phantom is a high speed camera which observes the details of the crack coalescence. All this is schematically shown in Figure E4.

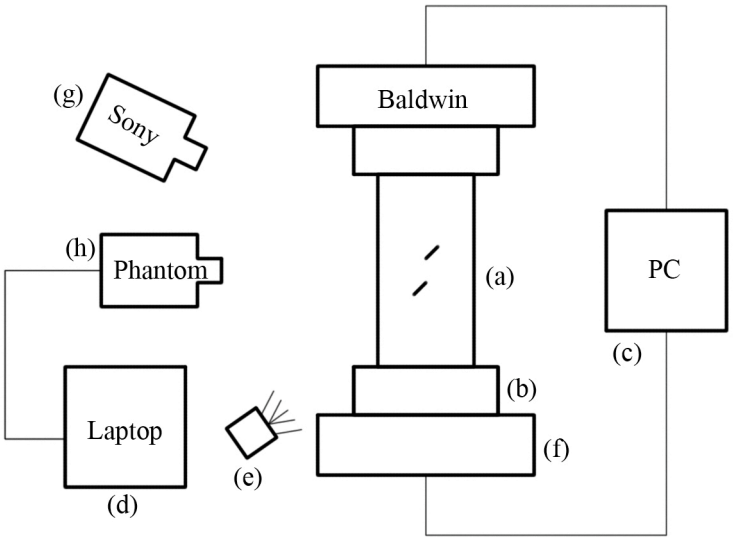

Figure E4. Schematic representation of a typical experimental set up: (a) specimen, (b) platen, (c) loading machine control and data logger, (d) high-speed camera laptop, (e) lighting source for high-speed camera, (f) loading machine, (g) Sony camcorder, and (h) Phantom high-speed camera.

The recording and observation processes are synchronized allowing one to relate the cracking details to the stress-strain behavior. This is done in the so called analysis, in which the observed video pictures are painstakingly related to the cracking and loading process. An example of this analysis is shown in Chapter 2 while the analyses for all the experiments are reported in Appendices D through J.

It is important to note that the text setup had to be changed somewhat during this research. The platens ('b') in Figure E4) in previous tests at MIT and usually in this test series consisted of so called brush platens, which reduce the confining effect of these platens. However, the steel sheets making up these platens deform excessively under the high loads required in the granite tests. A redesign with stiffer sheets did not work and we eventually

ran the tests with solid platens. All this and the resulting confining effect is documented in Chapter 3 and Appendices C and D respectively.

In Chapter 4 the results of unconfined compression tests on granite with the different flaw geometries shown earlier (Figure E3). The cracking process showed similar phenomena as earlier tests on marble and to some extent on gypsum: So called white patches (process zones) developed! Tensile cracks often but not always developed in the zones of the white patches while shear cracks developed usually unrelated to the white patch.

Two categories of white patches were observed in this study: Diffuse and linear. This is different from marble where only linear patches were observed. Linear white patches could be further subdivided into boundary-following and through-going features. The white patches were observed to initiate prior to, concurrent with, or after crack initiation. Boundary-following linear white patches were the most prevalent of all the white patches. Given the different surface appearance of granite, it is not easy to distinguish the white patches. This was helped using the image processing toolbox in Matlab. The use of this approach, its limitations and how to overcome them are described in Appendix E.

Tensile cracks grew and propagated very quickly. They often initiated in zones having some white patches, although this was not always the case. Tensile cracks normally followed grain boundaries as they propagated. Tensile wing cracks did not always initiate at the tips of flaws, but rather in zones of white patching above or below flaw tips These small tensile cracks then extended and connected with the nearest tip of the other flaw.

Shear cracks generally initiated in conjunction with surface spalling, probably indicating a compressive state of stress. Diffuse grain lightening often preceded longer shear cracks. In observable shear cracks, it was seen that they generally initiate and propagate along grain boundaries, although some grain breakage was observed.

The coalescence patterns proposed by Wong (2008) shown in Figure E2, were also appropriate for describing most patterns observed in this study. One pattern of indirect coalescence, however, has not been previously described. It involved an initial development

of tensile cracks above and below the bridge region before further cracking led to initial coalescence (see Figure 4.8 and 4.9 in Chapter 4.)

In geometries with L = 2a and L = a, stepped flaws resulted in more cases of direct coalescence than did coplanar flaws. More shear cracking was seen in specimens with L = a than those with L = 2a, although this trend might not only be attributed to a change in ligament length, as the boundary conditions between the two series were also changed (solid platens and brush platens, respectively).

Crack initiation in specimens with coplanar flaws and L = 2a was always very close to specimen failure. Specimens with stepped flaws with L = 2a showed a greater variation of crack initiation with β (varying from 95% of failure stress for β= 0 ° to 80% of failure stress for β = 45°). For specimens with L =a, the crack initiation stress ratio for coplanar and stepped flaws exhibited similar variation in crack initiation stress ratio with β.

The variation in coalescence patterns seen for coplanar flaws with L = a does not agree with the observations of Martinez (1999) on granite at MIT. He observed direct coalescence for all coplanar flaws. Also the observation in this study that tensile wing cracks initiated at locations away from flaw tips is different from Martinez' observations where wing cracks always initiated at flaw tip. Overall though, the cracking processes observed in the two studies (Martinez' and this one) were similar, with cracks propagating mostly along grain boundaries and fracturing being a very rapid process. Martinez (1999) also noted white patches, although he did not distinguish different types of white patches or comment on their temporal relationship with cracking (other than to say that they appeared before coalescence).

Specimens with coplanar flaws and L = 2a allow one to compare the three materials: gypsum, marble, and granite. This is, so far, the only comparable series for all three materials. Similar to gypsum, granite cracks propagate in a brittle manner. Failure is often sudden and cracks propagate quickly. Similar to marble, granite often forms white patches. The white patches in granite, however, can be subdivided into linear white patches and diffuse white patches (whereas only linear white patches were observed in marble). Also unlike marble, the white patch initiation stress ratio for granite does not follow the same trend as the crack

initiation stress ratio for gypsum. (The stress ratio relates the stress at white patch initiation or crack initiation to the failure stress. The white patch initiation stress ratio in marble and the crack initiation stress ratio in gypsum were very similar.) Finally, tensile coalescence cracks become more common from gypsum to marble to granite (See Figure 4.26 in Chapter 4.)

Chapters 5 and 6 introduce the equipment design and evaluation (Chapter 5) and describe the tests run with flaws under water pressure. The equipment had to ensure application and maintenance of water pressure as well as the visibility of the crack propagation process in order to use the video imaging observations. The device satisfying these criteria is shown in Figure E5 and the control system in Figure E6.

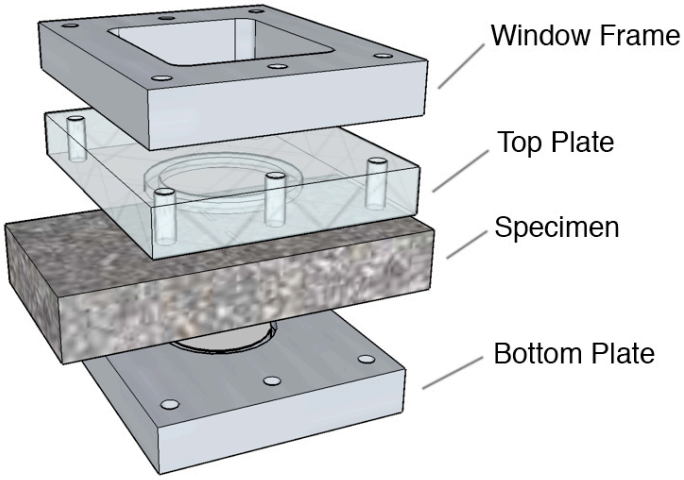

Figure E5. Water Pressure Device

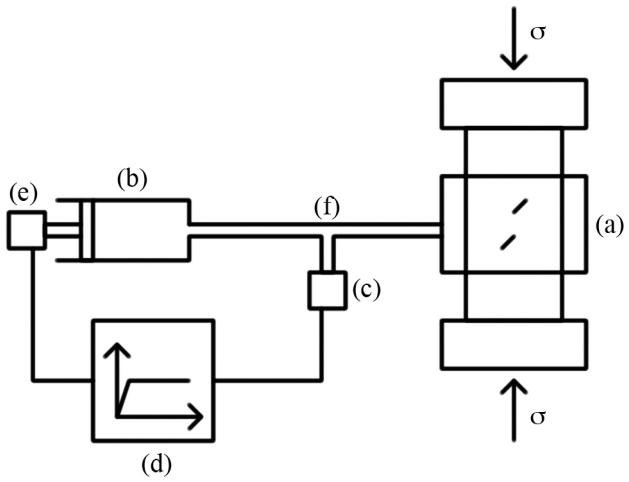

Figure E6. Pressure volume controller (PVC) consists of the following components: (a) pressure plates (see Figure E5) (b) cylinder and piston (c) pressure transducer (d) data acquisition and motor control (e) piston motor (f) copper pipe connected pressure plates and piston.

The pressure-volume controller shown in Figure E6 is essential for maintaining a constant pressure during the test. Nevertheless, as cracks become pervasive, the water volume loss makes it impossible to maintain water pressure. In order to have constant pressure during most of the test, the loading rate was increased to 1.0008 inches/sec (please see Table 3.2 or 5.1 in Chapters 3 and 5 respectively, for normal loading rate information.)

Chapter 6 starts with preliminary investigations to check if the faster loading rate and the confinement produced by the pressure device per se have an effect. The loading has an effect on the white patch-cracking process but not on the maximum stress. Confinement, as to be expected, affects the maximum stress.

The main test series consisted of tests with 0, 100, 200 and 400 psi waterpressure in the flaws. The pressurization had a marked effect on the stress at failure (maximum stress), which was also the stress at which coalescence occurred; this changed from ~150 MPa for zero waterpressure to 125 MPa for 100, 200 psi and to 30 MPa for 400 psi. Also the types of coalescence changed (shear crack at low pressure, tensile at higher pressure). As mentioned

at the beginning, the purpose of these tests was to investigate if tests with pressurized flaws can be run and if they show an effect of water pressure. Both objectives were achieved. Future tests will have to include a larger variety of flaw geometries and running of additional tests under the same loading rate and with the device under unpressurized conditions (confinement) for comparison purposes.

In Chapter 7 the modeling work is reported. The rock mechanics group at MIT has developed over the years on crack initiation-, propagation - and coalescence model and computer code FROCK (Fractures ROCK), which is based on a hybridized boundary element technique. Most but not all experiments can be duplicated numerically with FROCK. In order to make this model more comprehensively applicable, some basic work was done in the context of this research. Specifically, it was investigated if the stress field based approach used so far could be improved by also considering the strain field in the area between two eventually coalescing flaws. This was done using the finite element code ABAQUS and double checked with Mohr stress and strain diagram. The results show that for crack (both shear and tension) initiation and propagation both the stress-and strain field approach produce suitable results. However, coalescence is better modeled with the strain field approach. This provides the basis for further work on the FROCK failure criterion and model.

A detailed study on the use of acoustic emission in laboratory experiments on crack initiation, propagation reparation and coalescence was conducted and is reported in Appendix B (with a separate specific set of literature references). Using acoustic emission together with the visual and stress-strain observations is per se interesting. It would provide additional information on cracking processes particularly also on those that are not visible at the surface. In addition, this technique is interesting because of its analogy with seismic signals in the field. If properly scaled and related, a step toward relating the cracking processes in the laboratory to the fracturing processes in the field could be made.

The investigation on acoustic emission techniques in Appendix B briefly explains the principle and then looks at applications in rock testing in the laboratory. Possible observation range from first arrival and event records (using root mean square-RMS-records)

to full wave form recordings. The event recordings can be done with resonant sensors while full wave form recording requires broadband transducers (which can also be used for event observations). While resonant sensors are commercially available also at the required small size, broadband transducer would have to be custom made including each having its own pre-amplifier. Either sensor can be used with standard data acquisition systems (required sampling rate above 2 MHz, 8 to 12 channels). The study showed, however, that there are quite a few open questions and limitations: While cumulative RMS values are well suited for well sequenced events, it is not clear how this will work with many overlapping events. The usual resonant transducers "ring", which means that events at short intervals are not distinguishable. Broadband transducers, in addition to the fabrication issue mentioned above, require calibration, which is very time consuming. Most importantly, the initial calibration may be invalidated by the effect of newly created cracks. Finally there is the issue of coordinating the acoustic, visual and stress-strain observations.

So it seems that, at the present time, observing acoustic emissions would come at the cost of significantly reducing the number of experiments, particularly given that the stage of technological development is not where it should be.

The main body of the report concludes with Chapter 8, Conclusions and Recommendations. Since the conclusions are essentially repeated in an extended way in this Executive Summary, only the recommendations are summarized here:

Further tests on granite should be conducted to consider a wider range of flaw geometries. This will make a full comparison to tests on other materials possible. Part of these experiments should be detailed investigations on the microscopic level to determine the microcracking process similar to what has been done for other materials.

The water pressure equipment works well and the initial experiments show significant effects of water pressure. This series of experiments should be expanded by conducting tests with zero and elevated water pressure but using the same boundary conditions. Also an extension to other geometries is necessary.

The modeling effort should be expanded by making the crack initiation-, propagation- and coalescence criteria more broadly representative. This means considering normal stress effects and possibly consideration of additional material properties. Additional calibration/validation against laboratory experiments is also necessary.

References on Preceding MIT Work on Crack Initiation, Propagation and Coalescence. (Note these references are also included in Appendix A.)

Bobet, A. 1997. Fracture coalescence in rock materials: experimental observations and numerical predictions, Sc.D. Thesis, Massachusetts Institute of Technology, 824p.

Bobet, A. Einstein, H.H. 1998. Fracture Coalescence in Rock-type Materials under Uniaxial and Biaxial Compression. Int'l. J. Rock Mech. Min. Sci., Vol. 35, No. 7, pp. 863-888.

Chan, H.C.M. 1986. Automatic Two-dimensional Multi-Fracture Propagation Modelling of Brittle Solids with Particular Application to Rock, Ph.D. Thesis, MIT.

Chan, H.C.M. 1991. Equivalent Crack Formation by Propagating Cracks Under Tension, Engineering Fracture Mechanics, Vol. 39, No. 2, pp. 433-441.

Chan, H.C.M.; Li, V.; Einstein, H.H. 1990. A Hybridized Displacement Discontinuity and Indirect Boundary Element Method to Model Fracture Propagation. Int'l. Journal of Fracture, Vol. 45, pp. 263-282.

Einstein, H.H.; Hirschfeld, R.C. 1973. Model studies on mechanics of jointed rocks, ASCE Journal of the Geotechnical Division, Vol. 99, SM3.

Ko, T.Y. .2005. Crack coalescence in rock-like material under cyclic loading, Civ. Eng. Thesis, Massachusetts Institute of Technology, 184 p.

Ko, T.Y.; Einstein, H.H.; Kemeny, J. 2006. Crack coalescence in brittle material under cyclic loading. Golden Rocks 2006, Proc. of the 41st U.S. Symposium on Rock Mechanics

(USRMS): “50 Years of Rock Mechanics – Landmarks and Future Challenges.”, Golden, Colorado, June 17-21. ARMA/USRMS 06-930.

Martinez, A. 1999. Fracture coalescence in natural rocks, M.Sc. Thesis, Massachusetts Institute of Technology, 341 p.

Miller, J. 2008. Crack Coalescence in Granite, M.Sc. Thesis, Massachusetts Institute of Technology, 474 p.

Miller, J.; Einstein, H. H. 2008. Crack Coalescence Tests on Granite. 42nd U.S. Rock Mechanics Symposium, Proc. 2nd U.S.-Canada Rock Mechanics Symposium, San Francisco.

Reyes, O. 1987. Experimental study and analytical modeling of compressive fracture in brittle materials, Ph.D. Thesis, Massachusetts Institute of Technology, 212 p.

Reyes, O.; Einstein, H. H. 1991. Failure mechanism of fractured rock – a fracture coalescence model. In W. Wittke (ed) Proc. of the 7th International Congress of Rock Mechanics 1991, Aachen, Germany, 1, pp.333-340. Rotterdam: Balkema.

Wong, L.N.Y.; Einstein, H. H. 2008. Crack Coalescence in Molded Gypsum and Carrara Marble: Part 1. Macroscopic Observations and Interpretation. Rock Mech. and Rock Eng.

Wong, L.N.Y.; Einstein, H. H. Crack Coalescence in Molded Gypsum and Carrara Marble: Part 2. Microscopic Observations and Interpretation. Rock Mech. and Rock Eng.

Wong, L.N.Y.; Einstein, H. H. 2006. Fracturing behavior of prismatic specimens containing single flaws. Proc. Golden Rocks 2006, The 41st U.S. Symposium on Rock Mechanics (USRMS): “50 Years of Rock mechanics – Landmarks and Future Challenges.”, Golden, Colorado, June 17-21, 2006, ARMA/USRMS 06-899.

Wong, L.N.Y.; Einstein, H. H. 2008. Using high speed video images in the study of cracking process in rock. Accepted for publication in Geotechnical Testing Journal.

Wong, L.N.Y. 2008. Crack coalescence in molded gypsum and Carrara Marble, Ph.D. Thesis, Massachusetts Institute of Technology, 876 p.

Wong, R.H.C.; Chau, K.T. 1998. Crack coalescence in rock-like material containing two cracks. Int. J. Rock Mech. Min. Sci., 35 (2), pp 147-164.

Chapter 1. Introduction

1.1 The Project

This report documents the research done for the U.S. Department of Energy. The research was conducted in the period June 2006 to August 208 to address the interest areas: "Fracture Formation and Growth" and "Fracture Evolution" specified in the RFP, Enhanced Geothermal Systems Technology Development DE-PS36-05GO95002. In the context of Enhanced (Engineered) Geothermal Systems water flow through fractures is used to extract heat. Natural fractures and fracturing processes and, particularly artificial fracturing process are of major importance in this domain. The research intended to increase the fundamental understanding of fracturing processes through experimentation and theoretical and numerical modeling with the following specific tasks:

1. Testing of different rock types and fracture geometries under ambient temperature.

2. Similar to task 1 but at elevated temperatures.

3. Extension of crack (fracture) initiation -, propagation - and coalescence criteria and incorporation in numerical model.

4. Initial steps toward modeling of larger/smaller fractures.

5. Reporting and suggestions for further research.

When conducting the research, the tasks were somewhat modified. It was shown that elevated temperature in the range of 110°C did not have a significant effect on the fracturing/cracking processes. For this reason and based on input received from the sponsor and scientists and engineers working in the EGS domain (mostly at the meeting July 13/14, 2006, in Golden) additional experimental work was conducted through an investigation of flaws pressurized with water. This involved conceptualization, design and building of equipment and control systems as well as running a series of initial tests to examine the

feasibiity of the equipment and procedure. Also, while the visual recording of the cracking processes together with stress/strain behavior is satisfactory, we wanted to know if recording of acoustic emissions would enhance the experimental output. For this reason, a detailed study on the suitability of acoustic emissions was undertaken.

1.2 Approach

As discussed above, the research had an experimental and modeling components. Specificlaly this consisted of:

- Conduct experiments on Barre granite with the same specimen and flaw dimensions as previous tests on molded gypsum and Carrara marble. Also use the same experimental set-up to ensure consistency.
- Conduct experiments on Barre granite with new flaw geometries expected to help understand crack initiation, propagation, and coalescence.
- Observe the fracturing processes with a high-speed camera to determine crack nature (shear/tensile) of new cracks and overall crack sequence.
- Attempt to explain the influence of flaw geometry parameters on coalescence patterns.
- Develop equipment and conduct an initial series of tests to investigate the effect on the final coalescence pattern of pressurizing the pre-cut flaws with water.
- Apply the crack initiation, propagation and coalescence criteria of the computer code FROCK to see if all physical experiments can be modeled correctly.
- Examine how the crack initiation, propagation and coalescence criteria can be improved by modeling the stress and strain fields in the coalescence area.
- Review usage of acoustic emissions in rock testing and evaluate if it should be used in the context of this or follow-up research.

1.3 Organization of the Report

- Chapter 2 provides a background of previous studies
- Chapter 3 describes specimen preparation and experimental methodology of the unconfined, uniaxial compression tests performed in this study.
- Chapter 4 summarizes the results of the unconfined, uniaxial compression tests.

- Chapter 5 describes the experimental methodology of the uniaxial compression tests performed on specimens with water pressurized flaws
- Chapter 6 summarizes the results of the water pressurized flaws tests.
- Chapter 7 summarizes the modeling work.
- Chapter 8 offers conclusions of the present study as well as recommendations for future research.
- Appendix reviews acoustic emission technology in the context of rock testing.

Chapter 2 . Background

2.1 Introduction

This section provides a background of past research in fracture mechanics. A brief introduction to the theory of fracture mechanics will be followed by review of experimental work. There will be an emphasis on fracture interaction and coalescence. The work done by Martinez (1999) and Wong (2008) is especially relevant to this study, so a more thorough summary of their work will be included.

2.2 Theoretical Fracture Mechanics

Why are cracks important? Brittle materials are not as strong as their interparticle forces predict they should be. Griffith (1920) showed that the presence of very small cracks (flaws) led to this decrease in measured tensile strength in brittle materials. Inglis (1913) had already provided a solution for the stress distribution around an elliptical hole embedded in an infinite plate with an applied tension perpendicular to the major axis of the hole. This arrangement is illustrated in Figure 2.1.

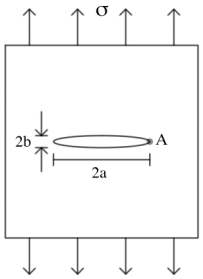

Figure 2.1. An elliptical hole embedded in an infinite plate with an applied far field tensile stress. Point "A" indicates the tip of the flaw for which σ_A is calculated (see text).

Based on Inglis' stress distribution, Griffith (1927) found that the stress at the tip of a sharp flaw (a flaw that is much longer than it is wide) increases with flaw length. He showed that the stress at the tip of a sharp flaw (σ_A) could be approximated by

$$\sigma_A = 2\sigma\sqrt{\frac{a}{\rho}} \tag{2.1}$$

where σ is the applied far field stress and ρ is the radius of curvature of the flaw tip (equal to b^2/a). This expression concludes that longer flaws have greater stresses at their flaw tips than shorter flaws with the same tip curvature. When the local stress exceeds the strength of the material surrounding the flaw, cracks propagate from the flaw.

Prior to the stress based theory, Griffith (1920) derived a fracture theory based on the conservation of energy. Consider the situation depicted in a sharp, elliptical flaw (length 2a) is in an infinitely wide plate of thickness B. In the far field, a tensile stress σ is applied perpendicular to the major axis of the flaw. As the flaw increases in length, the increased surface energy of the material surrounding the flaw must be equal to an increase in potential energy. For an incremental increase in flaw area, dA, this can be stated as:

$$\frac{dE}{dA} = \frac{d\Pi}{dA} + \frac{dW_s}{dA} = 0 \tag{2.2}$$

or

$$-\frac{d\Pi}{dA} = \frac{dW_s}{dA} \tag{2.3}$$

where E is the total energy, Π is the potential energy supplied by external forces and the internal strain energy, and W_s is the work required to create new surfaces. W_s can be expressed as

$$W_s = 4aB\gamma_s \tag{2.4}$$

where γ_s is the surface energy of the material. This surface energy arises because particle forces are not in equilibrium at a surface. Potential energy, Π, can be expressed as

$$\Pi = \Pi_0 - \frac{\pi\sigma^2 a^2 B}{E} \tag{2.5}$$

where Π_0 is the potential energy of the plate without the flaw.

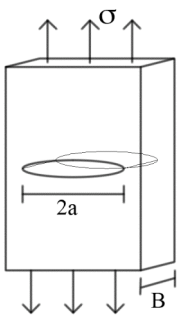

Figure 2.2. An elliptical hole in an infinitely wide plate subjected to a far field stress σ.

To find the stress to force crack propagation (σ_f), Griffith differentiated equations (2.4) and (2.5) with respect to A and substituted the expressions into equation (1.3). Griffith found that this stress was

$$\sigma_f = \sqrt{\frac{2E\gamma_s}{\pi a}}. \tag{2.6}$$

The work by Inglis (1913) and Griffith (1920) created the theoretical basis to determine when cracks propagate in a tensile stress state. Griffith (1920), however, also observed that cracks propagate from a flaw in a compressive stress field. This observation is most often explained with the sliding wing crack model in brittle materials (Brace and Bombolakis, 1963; Gramberg, 1965; Hoek and Bieniawski, 1965; Moss and Gupta, 1982; Horii and Nemat-Nasser, 1986; Ashby and Sammis, 1990; Kemeny and Cook, 1991; Germanovich and Dyskin, 2000). This model describes the process by which curvilinear tensile cracks initiate

from the tips of an inclined flaw in a compressive stress field. The appearance of these cracks led to them being called "tensile wing cracks." The faces of the flaw usually slide in opposite directions from one another, hence the model's name.

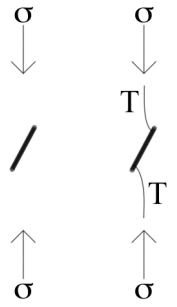

Figure 2.3. Formation of tensile wing cracks for an inclined flaw in a compressive stress field.

At this point, a distinction between fracture initiation and propagation should be made. Bienawski (1967) defined fracture initiation as the process by which a pre-existing crack (flaw) starts to extend (grow). Fracture initiation, obviously, is then restricted to the material immediately surrounding the crack tips. Bienawksi (1967) defined fracture propagation as the continuation of crack growth after initiation. He also considered fracture propagation to be a failure process, as cracks eventually extend to the boundaries of the stressed material.

Fractures processes (whether initiating or propagating) can also be subdivided into three different modes:

1. **Mode I**: Tensile fracturing. The fracture simply opens. There are no shear components (Figure 2.4 (a)).
2. **Modes II and III**: In-plane shear fracturing. The two faces of the crack move in the plane of the crack (Figure 2.4 (b) and (c)).

Irwin (1956) extended Griffith's energy balance concept to the energy release rate concept. Irwin (1957) also introduced the stress-intensity factor K, which relates the stresses and displacements around a flaw tip to the energy released as a crack grows infinitesimally.

Further criteria have been developed since that time (Erdogan and Sih, 1963, Hussain et al., 1974, and Sih, 1973,1974) to better model the behavior of fractures with mixed-mode loading (combination of modes I and II – see Figure 2.4).

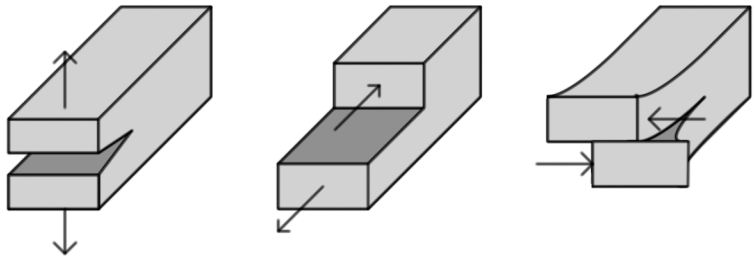

(a) (b) (c)

Figure 2.4. The three modes of fracturing and the associated loading modes. Mode I (a) is tensile and Modes II and III ((b) and (c)) are shear.

Linear elastic fracture mechanics was normally deemed appropriate for application to rocks and rock-like materials because of their brittle behavior. The region just ahead of flaw tips has been observed to behave inelastically. This inelastic behavior in rocks (and concrete) is caused by microcracks (Anderson, 2005) and is called the process zone. The term process zone was actually introduced for metals (e.g. – Argon and Safoglu, 1975). Maji and Wang (1992) speculated that this inelastic zone could also be in part caused by a phenomenon known as bridging, wherein individual grains still transmit across both faces of a crack (see Section 0 for a discussion of this phenomenon, also known as "aggregate interlock"). Several researchers have investigated the process zone (e.g. – Friedman et al., 1972; Segall and Pollard, 1983). Other researchers have successfully modeled the effect of a process zone ahead of a flaw in concrete (Hillerborg et al., 1976; Hillerborg, 1991) and rock (Reyes, 1987; Bobet, 1997) by using the cohesive zone model (Dugdale, 1960, Barenblatt, 1962).

Up to this point, the discussion has focused on models for cracks that do not interact with other cracks. Several researchers have proposed models to study crack interaction. Costin (1985) and Kachanov (1985) both proposed methods for calculating the way in which cracks intensify the stress at flaw tips of neighboring cracks. The method of Costin (1985) requires the solution of many subproblems of single cracks in an infinite medium with a far-field stress applied and the effect of these cracks on other cracks. Kachanov's (1985) method is

more applicable to calculating crack interaction before crack propagation, while Costin's (1985) allows one to calculate the interaction of propagating cracks.

Ashby and Hallam (1986) and Hallam and Ashby (1990) assumed tensile wing cracks initiated from pre-existing cracks and propagated parallel to the direction of maximum loading. Tensile wing cracks from pre-existing flaws that passed close to one another would form effective beams that would lengthen as the cracks propagated. Bending deflections in these beams would increase the stress intensity at the tips of the pre-existing cracks. Kemeny and Cook (1987) extended this model to include the curved initial portion of tensile wing cracks.

2.6 Experimental Fracture Mechanics

The other side to research in fracture mechanics is experimental. Griffith (1920) discovered that tensile strength reduction was caused by microcracks while he was conducting experiments with glass specimens. Later, researchers have become interested in experimentally investigating pre-cracked materials under compression. In the context of this study, these investigations can be divided into those that have conducted experiments in rock-like materials and those in natural rock:

Rock-like materials (brittle/semi-brittle)

- **Columbia Resin 39:** Bombolakis, 1963; Brace and Bombolakis, 1963; Nemat-Nasser and Horii, 1982; Horii and Nemat-Nasser, 1985.
- **Glass:** Hoek and Bieniawski, 1965; Bieniawski, 1967.
- **Plaster of Paris:** Lajtai, 1971; Nesetova and Lajtai, 1973;
- **Polymethylmethacrilate (PMMA):** Petit and Barquins, 1988; Chaker and Barquins, 1996.
- **Molded Gypsum:** Einstein et al., 1969; Reyes, 1987; Reyes and Einstein, 1991; Shen et al., 1995; Bobet, 1997; Bobet and Einstein, 1998; Sagong, 2001; Sagong and Bobet, 2002; Wong and Einstein, 2006; Wong, 2008.
- **Sandstone-like Molded Barite**: Wong and Chau, 1998.
- **Sandstone-like Concrete Mix:** Mughieda and Alzo'ubi, 2004.

Natural rocks

- **Sandstone:** Petit and Barquins, 1988.
- **Granodiorite:** Ingraffea and Heuze, 1980.
- **Limestone:** Ingraffea and Heuze, 1980.
- **Granite:** Martinez, 1999.
- **Marble:** Huang et al., 1990; Chen et al., 1995; Martinez, 1999; Li et al., 2005; Wong, 2008.
- **Ice:** Wang and Shrive, 1995.

With the number of different researchers named in the above list (which is most likely incomplete), it is hardly surprising that specimen size and flaw geometry was varied. Specimens ranged from small (50 mm × 32 mm × 5 mm; Petit and Barquins, 1988) to large (635 mm × 279 × 203; Mughieda and Alzo'ubi, 2004). Flaw length and aperture were also not held constant.

2.6.1 Specimens with a Single Flaw

Table 2.1 summarizes selected experiments performed on specimens with one flaw. Emphasis has been placed on tests in rock and rock-like material under compression. The particular references were chosen to illustrate fracture processes in a variety of materials.

Table 2.1 demonstrates that some generalized observations can be made about fracturing from a pre-existing flaw under compression. In all the experiments, tensile cracks were the first cracks to appear. In rock, shear cracks were usually observed afterward (although sometimes the crack type was not specified, and the subsequent cracks were only called "secondary" cracks). This was not seen in other brittle materials, such as glass and plastic. Li et al. (2005) observed white patches form where tensile cracks would eventually form. Chen et al. (1995) observed an X-shaped band that they speculated was composed of microcracks, although no proof was given to confirm this fact. A more detailed summary of all experiments can be found in Wong (2008).

Table 2.1 – Selected summary of experiments with one pre-existing flaw. The sequence of observed events is given for each experiment. All experiments were uniaxial compression tests with the exception of Chen, et al. (1995), who also conducted biaxial tests as well.

Researchers	Material	Sequence
Lajtai (1974)	Plaster of Paris	1. Tensile wing cracks 2. Normal shear fractures 3. Inclined shear cracks
Ingraffea and Heuze (1980) Literature Review	Glass, PMMa, CR39 (plastic polymer)	1. Tensile wing cracks
	Rock	1. Tensile wing cracks 2. Shear cracks
Ingraffea and Heuze (1980) Experiments	Limestone	1. Tensile wing cracks 2. Secondary cracks (unspecified nature)
Petit and Barquins (1988)	Sandstone (low and high porosity)	1. Tensile wing cracks 2. Shear cracks
Huang et al. (1990)	Fangshan Marble	1. Tensile wing cracks 2. Secondary Tensile cracks 3. Shear belts 4. Tensile cracks
Chen et al. (1995)	Marble	1. Tensile wing cracks 2. Secondary cracks (unspecified nature) 3. X-shaped black band – speculated to be microcracks
Li et al. (2005)	Huangshi Marble	1. White patches 2. Tensile wing cracks 3. Shear cracks

Wong (2008) also conducted a study on fracture propagation from a single flaw in molded gypsum and Carrara Marble specimens under uniaxial compression. By recording experiments with a high-speed camera, he was able to determine the nature (tensile/shear) of cracks throughout the tests. In both gypsum and marble, he observed tensile cracks were the

first cracks to appear. Subsequent cracks, he found, could be categorized into seven crack types, as shown in Figure 2.5.

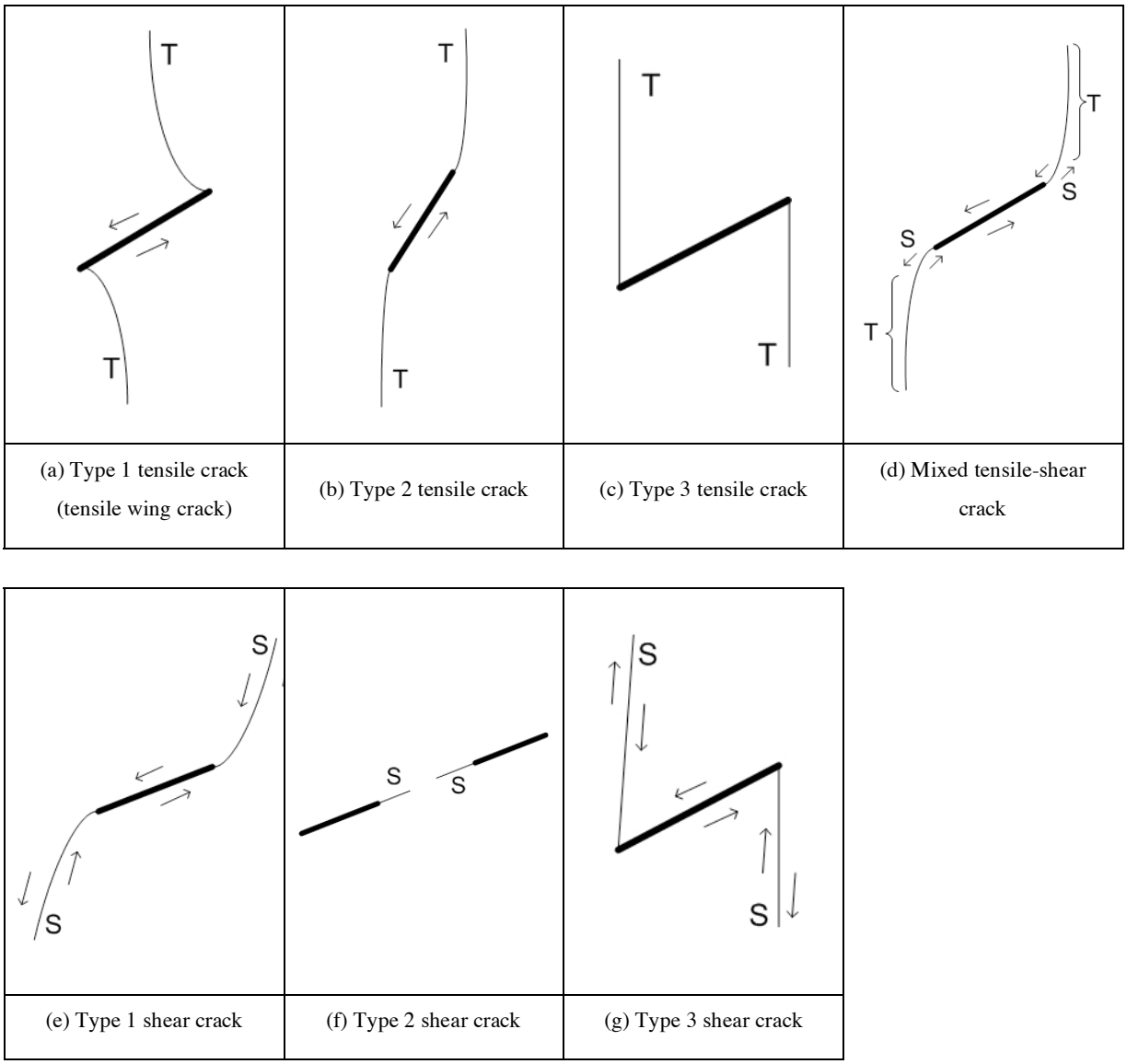

(a) Type 1 tensile crack (tensile wing crack) | (b) Type 2 tensile crack | (c) Type 3 tensile crack | (d) Mixed tensile-shear crack

(e) Type 1 shear crack | (f) Type 2 shear crack | (g) Type 3 shear crack

Figure 2.5. Seven crack types identified by Wong (2008) in his single-flaw experiments in gypsum and marble.

2.6.2 Specimens with Multiple Flaws

Experiments with a single flaw help understand fracture initiation and propagation, but do not allow one to observe fracture interaction and coalescence. Several researchers have performed experiments with specimens with more than one pre-existing flaw to better understand these latter two phenomena. The following review gives a glimpse of experiments

performed to investigate fracture coalescence. Emphasis is placed on showing the wide variety of coalescence patterns observed. A more in-depth review can again be found in Wong (2008).

To parametrically study the coalescence of cracks, a method to describe the geometry of flaw pairs had to be adopted. Two methods emerged: "ligament length – flaw inclination angle – bridging angle" and "flaw inclination angle – spacing – continuity." Both of these methods are illustrated in Figure 2.6. Ligament length (L), it should be noted, is generally defined in terms of the half-flaw length, a.

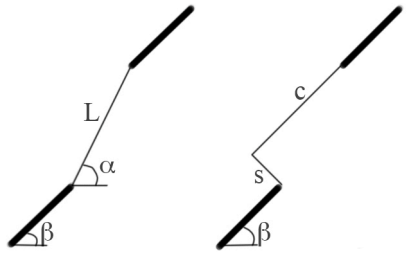

Figure 2.6. Flaw pair geometry defined by (a) ligament length (L), flaw inclination angle (β), and bridging angle (α) and (b) flaw inclination angle (β), spacing (s), and continuity (c).

In general, flaws can either be overlapping or non-overlapping. The distinction is illustrated in Figure 2.7. Overlapping flaws can be defined as those flaws with a negative continuity (c) value or those with a bridging angle α greater than 90°.

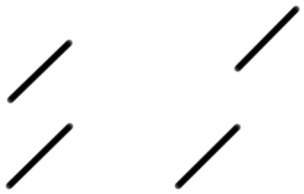

(a) (b)

Figure 2.7. (a) Overlapping and (b) non-overlapping flaws.

Brace and Bombolakis (1963) performed one of the earliest multiple-flaw studies. They ran uniaxial compression tests on plexiglass specimens with en-echelon flaws. They observed tensile wing crack initiation, but did not see secondary cracks or coalescing cracks. See Figure 2.8. for an illustration of their observations. Note that tensile wing cracks, after initiating, propagated in the vertical direction; parallel to the direction of loading.

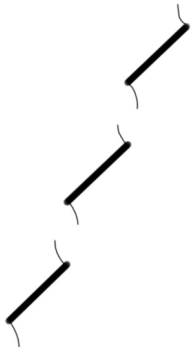

Figure 2.8. En-echelon flaws in plexiglass were tested by Brace and Bombolakis (1963). Tensile wing cracks initiated at the tips of pre-existing flaws and propagated along the vertical loading direction.

Horii and Nemat-Nasser (1985) conducted loading tests on Columbia Resin CR 39. They used two different configurations of flaws: a single row of short flaws flanked by several long flaws and multiple rows of short flaws flanked by several long flaws, as illustrated in Figure 2.9.

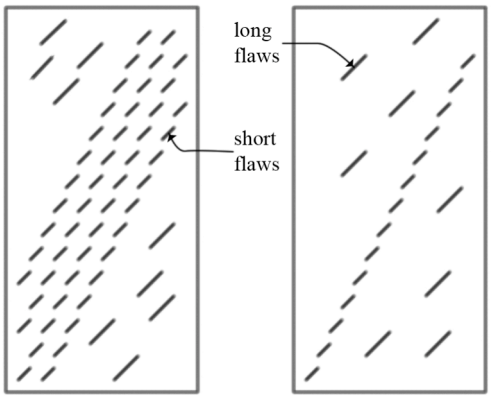

Figure 2.9. Two specimen configurations used by Horii and Nemat-Nasser (1985): long flaws flank either several rows of short flaws (left) or a single row of short flaws (right).

When Wong (2008) reviewed the results of the experiments performed by Horii and Nemat-Nasser (1985), he distinguished five different types of coalescence, as depicted in Table 2.2. Each pattern was identified from the coalescence of two long flaws (see Figure 2.9). Coalescence was achieved with at least two cracks in the case of flaw pairs A and D (see Table 2.2 for flaw pair identification) and either one or two cracks in the remaining flaw pairs. Crack types and numbers of cracks were not identified in the original study (Horii and Nemat-Nasser, 1985) but identified by Wong (2008) using crack trajectories.

Table 2.2. Coalescence patterns identified by Wong (2008) in experiments by Horii and Nemat-Nasser (1985).

Flaw pair number	Geometry parameters					Coalescence pattern*
	β (°)	s	c	α (°)	L	
A	45	a	a	45	1.4a	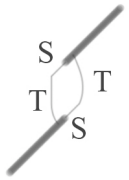
B	45	3a	a	72	3.2a	
C	45	a	0.5a	63	1.2a	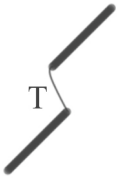
D	45	3a	a	72	3.2a	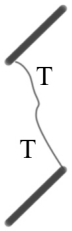
E	45	0.7a	0	90	0.7a	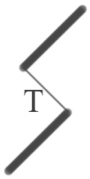

* - T indicates a tensile crack and S indicates a shear crack.

Chen et al. (1995) also performed loading tests on marble specimens with multiple flaws. Once again, crack types were not identified. The first cracks to appear ("primary" cracks, as labeled by the authors) were likely tensile cracks based on trajectory and proximity to flaw tips. "Secondary" cracks appeared after these primary cracks. The authors did summarize the sequence of events in their tests:

1. **Crack initiation stage:** primary cracks appeared and initiated normal to flaw faces. Secondary cracks appeared later and initiated from the flaw tips.
2. **Coalescence stage:** the flaws were connected either by the primary or secondary cracks. Generally, primary crack coalescence was more likely for overlapping flaws and secondary crack coalescence was more likely for non-overlapping flaws (see Figure 2.7 for a definition of overlapping and non-overlapping flaws).
3. **Specimen failure:** similar to the single flaw cases, an X-shaped band developed from the tips of the outermost flaws.

Reyes (1991) conducted uniaxial compression tests on molded gypsum specimens with two flaws. The geometries tested are listed in Table 2.3. Reyes observed that for overlapping flaws (see Table 2.3), coalescence was achieved by tensile wing cracks. If, however, the flaws did not overlap, then coalescence was achieved by cracks appearing after tensile wing cracks (see Figure 2.10). There was evidence (surface spalling and crushing – both indicative of a compressive stress state) that some of these secondary cracks were shear cracks while others were tensile.

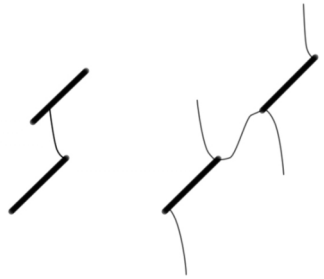

(a) (b)

Figure 2.10. Reyes (1991) observed that overlapping flaws (a) coalesced with a tensile wing crack. Non-overlapping flaws (b) coalesced with a secondary crack that initiated after tensile wing crack formation.

Table 2.3. Geometry parameters for the specimens tested by Reyes (1991).

β (°)	α (°)	L	Overlapping flaws?
30	0	2a	No
30	15	2a	No
30	30	2a	No
30	45	2a	No
30	60	2a	No
30	90	2a	Yes
30	105	2a	No
45	0	2a	No
45	15	2a	No
45	30	2a	No
45	45	2a	No
45	90	2a	Yes
60	-15	2a	No
60	0	2a	No
60	15	2a	No
60	30	2a	No
60	45	2a	Yes
60	75	2a	Yes
60	90	2a	Yes

Shen et al. (1995) also performed tests on specimens of molded gypsum with two flaws. Unlike Reyes (1991), Shen et al. (1995) tested both open and closed flaws. Cracks were identified as either wing cracks or secondary cracks. Coalescence patterns observed are summarized in Figure 2.11 and Figure 2.12.

Shen et al. (1995) observed coalescence pattern was influenced by varying bridging angle. He found three distinct coalescence patterns based on this variation:

- **Coalescence by shear crack**: for small positive and negative bridging angles, coalescence was the result of shear cracks linking the inner flaw tips (numbers 1, 2, 3, 8, 9, and 13 in Figure 2.11 and Figure 2.12).
- **Coalescence by shear and tensile cracks**: for intermediate bridging angles, coalescence was the result of shear and tensile cracks linking the inner flaw tips (numbers 4, 5, 10, and 11 in Figure 2.11 and Figure 2.12).
- **Coalescence by tensile cracks**: for large bridging angle, coalescence was the result of tensile cracks. These tensile cracks mostly linked inner flaw tips (numbers 6, 7, and 12 in Figure 2.11 and Figure 2.12).

Bobet (1997) tested gypsum specimens (specimen dimensions identical to those tested by Reyes, 1991) with two flaws. Like Shen et al. (1995), Bobet tested both open and closed flaws. As with previous studies, Bobet (1997) noted that tensile wing cracks were the first cracks to appear followed by secondary cracks. Secondary cracks were determined to be shear cracks. In both Reyes' (1991) and Bobet's (1997) work, the distinction between tensile cracks and shear cracks was made on the basis of fractography (plumose structure on tensile cracks, rough surfaces and powder on shear crack surfaces). Also, surface spalling indicates compressive stresses and was taken to be indicative of shear. Fractography has the disadvantage that crack surfaces can only observed after an entire compression test. A crack surface with evidence of shearing does not allow one to distinguish between a crack that initiated as shear crack and a crack initiating as a tensile crack and later shearing. This problem was solved by Martinez (1999) who used a high-speed camera, which made is possible to observe the cracking process (see below). Bobet (1997) distinguished five different types of coalescence, as shown in Figure 2.13.

Specimen α/β	Critical Load at Coalescence, MPa	Schematic Path of Coalescence (a) frictional (b) nonfrictional	Description of Coalescence	Mode of Coalescence
30°/45° (2 specimens with friction fractures + 1 specimen with nonfrictional fractures)	No coalescence (frictional fractures) 17.2 MPa (nonfrictional fractures)	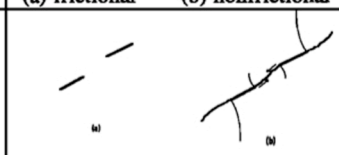	Type of coalescing fracture: secondary fracture. Initiation position: preexisting fracture tips. Surface characterization: rough, with many small kink steps; containing crushed gypsum.	Shearing
45°/45° (2 + 2)	21.9, 22.2 MPa (frictional fractures) 19.4, 17.9 MPa (nonfrictional fractures)	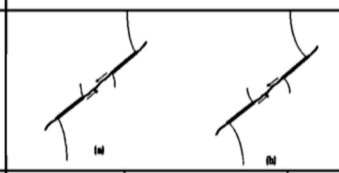	Type of coalescing fracture: secondary fracture. Initiation position: preexisting fracture tips. Surface characterization: rough, with many small kink steps; containing crushed gypsum.	Shearing
45°/60° (1 + 1)§	17.8 MPa (frictional fractures) 14.1 MPa (nonfrictional fractures)	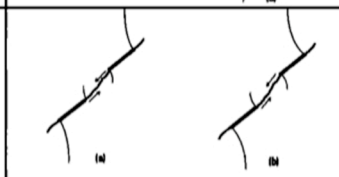	Type of coalescing fracture: secondary fracture. Initiation position: preexisting fracture tips. Surface characterization: rough, with several large kink steps. Noticeable crushed gypsum presented.	Shearing
45°/75° (1 + 1)§	19.2 MPa (frictional fractures) 14.1 MPa (nonfrictional fractures)		Type of coalescing fracture: secondary fracture. Initiation position: unclear. Surface characterization: rough, with two big kink steps. No noticeable crushed gypsum.	Shearing +tension
45°/90° (2 + 1)	(a) 17.8, MPa (a') 16.8* MPa (frictional fractures) (b) 16.4 MPa (nonfrictional fractures)	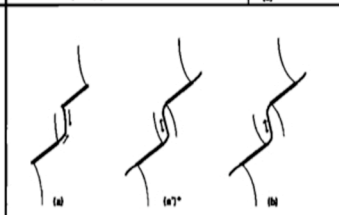	Type of coalescing fracture: (a) wing fracture + secondary fracture; (a') and (b) secondary fracture. Initiation position: (a) preexisting fracture tips; (a') and (b) intact material. Surface characterization: some parts are clean and smooth while other parts are rough with crushed gypsum.	Shearing +tension
45°/105° (2 + 1)	17.8, 16.8 MPa (frictional fractures) 16.4 MPa (nonfrictional fractures)		Type of coalescing fracture: wing fracture. Initiation position: preexisting fracture tips. Surface characterization: smooth and clean. Note: additional secondary fractures occur from the outer tips in case (b).	Tension
45°/120° (2 + 1)	(a) 21.0 MPa (a') 23.1 MPa (frictional fractures) (b) 17.6 MPa (nonfrictional fractures)	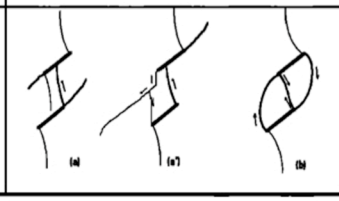	Type of coalescing fracture: wing fracture. Initiation position: preexisting fracture tips. Surface characterization: smooth and clean. Note additional coalescence by secondary fractures occurs in case (b).	Tension

Figure 2.11. Coalescence patterns observed by Shen et al. (1995) (continued in Figure 2.12).

Specimen α/β	Critical Load at Coalescence MPa	Schematic Path of Coalescence (a) frictional (b) nonfrictional	Description of Coalescence	Mode of Coalescence
60°/45° (2 + 1)	22.4, 21.4 MPa (frictional fractures) 17.8 MPa (nonfrictional fractures)	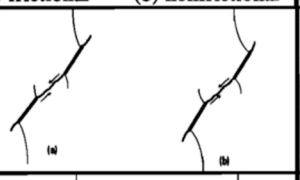	Type of coalescing fracture: secondary fracture. Initiation position: preexisting fracture tips. Surface characterization: rough, with many small kink steps; containing crushed gypsum.	Shearing
60°/60° (4+ 1)	20.5, 17.8, 20.3, 20.9 MPa (frictional fractures) 15.2 MPa (nonfrictional fractures)	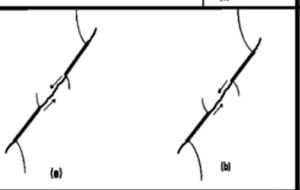	Type of coalescing fracture: secondary fracture. Initiation position: preexisting fracture tips. Surface characterization: rough, with several large kink steps. Noticeable crushed gypsum presented.	Shearing
60°/75° (1 + 1)§	18.5 MPa (frictional fractures) 13.7 MPa (nonfrictional fractures)		Type of coalescing fracture: (a) secondary fracture ; (b) secondary fracture + wing fracture. Initiation position: pre-existing fracture tips. Surface characterization: rough, with a few kink steps. No noticeable crushed gypsum.	Shearing +tension
60°/90° (1 + 1)§	19.2 MPa (frictional fractures) 14.2 MPa (nonfrictional fractures)	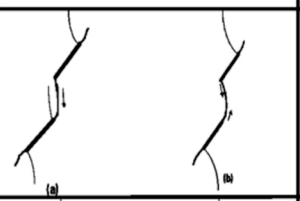	Type of coalescing fracture: (a) wing fracture ; (b) wing fracture + secondary fracture. Initiation position: preexisting fracture tips; Surface characterization: most parts are clean and smooth.	Tension +shearing
60°/105° (2 + 1)	19.9, 22.2 MPa (frictional fractures) 18.0 MPa (nonfrictional fractures)	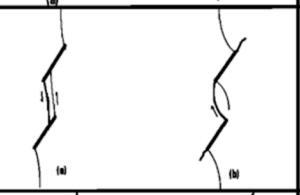	Type of coalescing fracture: wing fracture. Initiation position: preexisting fracture tips. Surface characterization: smooth and clean.	Tension
60°/120° (1 + 1)§	23.5 MPa (frictional fractures) 21.0 MPa (nonfrictional fractures)		Type of coalescing fracture: secondary fracture. Initiation position: preexisting fracture tips. Surface characterization: very rough, coated with a lot of crushed gypsum.	Shearing

§ Only two of the three specimens produced useful results, the other specimen failed due to mismanipulation of the loading machine.

* The frictional fractures in this specimen have weaker contact than other frictional fractures. The polyethylene sheets were left longer (45 min) by mistake before they were pulled out. As a result, the created fractures did not close firmly.

Figure 2.12. Coalescence patterns observed by Shen et al. (1995) (continued from Figure 2.11).

Type	Schematic path of Coalescence	Description of Coalescence	Mode of Coalescence
I	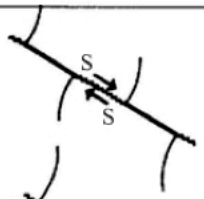	Type of coalescing fracture: secondary shear crack. Initiation position: preexisting flaw tips. Crack surface characterization: rough, with many small kink steps; contains crushed gypsum	Shearing
II	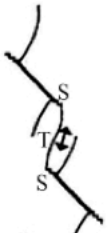	Type of coalescing fracture: secondary shear and tensile cracks. Initiation position: preexisting flaw tips. Crack surface characterization: some parts are clean and smooth while other parts are rough with crushed gypsum	Shearing + tension
III	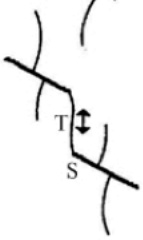	Type of coalescing fracture: secondary shear crack and wing crack. Initiation position: preexisting flaw tips. Crack surface characterization: some parts are clean and smooth while other parts are rough with crushed gypsum	Shearing + tension
IV		Type of coalescing fracture: wing crack. Initiation position: preexisting flaw tips. Crack surface characterization: smooth and clean.	Tension
V	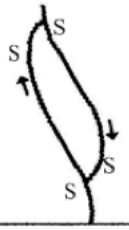	Type of coalescing fracture: secondary crack. Initiation position: preexisting flaw tips. Crack surface characterization: very rough, coated with a lot of crushed gypsum	Shearing?

Figure 2.13. Coalescence patterns observed by Bobet (1997), taken from Bobet and Einstein (1998).

Martinez (1999) continued the work of Bobet (1997). He tested specimens with identical dimensions in two natural rock types: marble (Vermont White Marble) and granite (Barre Granite). As just mentioned, Martinez (1999) was able to determine the crack sequence and nature by observing the loading tests with a high-speed camera. The introduction of this technology also allowed him to continuously load the specimens (unlike Reyes, 1988 and Bobet, 1997, who used incremental loading – see Section 3.4.3 for a comparison of the two loading methods). In his experiments, Martinez (1999) noted five different types of

coalescence, shown in Figure 2.14. Table 2.4 summarizes the geometries tested and coalescence patterns observed.

TYPE I	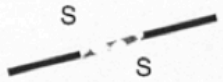	Produced by the linkage of two internal shear cracks
TYPE II	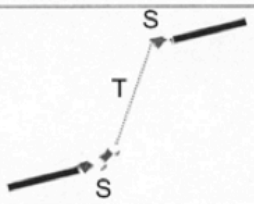	Produced by the linkage of two internal shear cracks by a vertical tensile crack (not a wing crack)
TYPE III	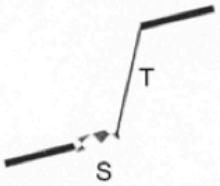	Produced by the propagation of the internal shear crack from one of the flaws until it reaches the internal wing crack of the other flaw
TYPE IV	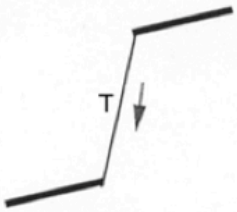	Produced by the propagation of an internal wing crack from one flaw until it reaches the other flaw. Observed only for granite, but not for marble.
TYPE IVB	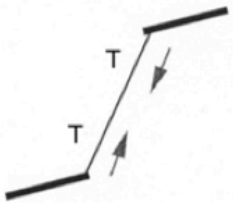	Produced by the linkage of two internal wing cracks that propagate until they join each other half-way. Observed only for granite, but not for marble.

Figure 2.14. Coalescence types observed by Martinez (1999) in marble and granite. Figure taken from Martinez (1999).

Table 2.4. Coalescence type observed for each geometry tested by Martinez (1999).

Geometry*	Coalescence type in granite	Coalescence type in marble
30-0-a	I	No
30-0-2a	I	No
30-2a-2a	II / some III	II
30-a-a	II	II
30-a-2a	II	II / III
45-0-a	I	I
45-0-2a	I	I
45-2a-2a	II / some III	II / some III
45-a-2a	II	III / some II
45-a-a	II/ some IV/ some IVB	II / III
60-0-a	I	I
60-0-2a	I	I
60-0-3a	No	N/A
60-a-2a	II / some no	II

* - Geometry was defined as flaw inclination – spacing – continuity (see **Error! Reference source not found.**)

Martinez (1999) made the following general observations (valid for both material types):

- The most common coalescence pattern for coplanar flaws was type I. The most common coalescence pattern for non-coplanar flaws was type II. The other types of coalescence were not common and never the dominant type of coalescence.
- Cracks could transition in nature from shear to tensile (as seen in type II and type III coalescence).

Observations for granite specimens were the following:

- Failure of intact specimens was violent and sudden. Failure of specimens with flaws was caused by the propagation of wing cracks to the specimen boundaries.
- Tensile wing cracks initiated at the flaw tips.

- Coalescence and failure stresses did not coincide.
- A “brighter area” was visible in the rock bridge between the two flaws when the stress level approached the coalescence stress. It was difficult to clearly identify this detail due to material color.
- On the observed surface, cracks generally propagated along grain boundaries. Inspection of the crack surfaces also supported this conclusion throughout the thickness of specimens.

Observations specific to marble included:

- Intact specimens failed by shearing and were not as violent as granite. Failure of specimens with flaws was caused by the propagation of wing cracks or shear cracks to the specimen boundaries.
- Some wing cracks (in roughly 25% of tested specimens) initiated about ¼ of the flaw length away from the flaw tips.
- A “brighter area” was visible in the rock bridge between the two flaws when the stress level was near the coalescence stress.

Martinez (1999) also compared his results to those of Bobet (1997) in gypsum and found that:

- Both granite and gypsum specimens with ligament length equal to or larger than 3a have minimal flaw interaction/no coalescence.
- In all three materials, the coalescence mode can be related to the spacing to continuity ratio (s/c). This relationship is shown in Table 2.5 (proposed by Bobet, 1997):

Table 2.5. Relationship between spacing to continuity ratio (s/c) and coalescence type as originally proposed by Bobet (1997) and confirmed by Martinez (1999). Martinez (1999) claimed that the relationship is valid for gypsum, marble, and granite.

s/c ratio	Type of coalescence
s/c < 1/3	I
1/3 < s/c < 1	II
s/c > 1	III

Wong (2008) expanded the work of Bobet (1997) and Martinez (1999). He performed uniaxial compression tests on gypsum and marble (Carrara Marble) specimens with two flaws (in addition to his tests on specimens with one flaw). He performed eight distinct test series (four in gypsum and four in marble), as summarized in Table 2.6. His tests were categorized as either coplanar (bridging angle equal to zero) or stepped (non-zero bridging angle).

Table 2.6. The geometry parameters (see Figure 2.6) for the four test series run in gypsum and marble by Wong (2008)

Series	General flaw pair relationship	Ligament Length L	Bridging angle α (°)	Flaw inclination β (°)
1	Coplanar	2a	0	0, 30, 45, 60, 75
2	Stepped	2a	-60, -30, 0, 30, 60, 90, 120	30
3	Coplanar	4a	0	0, 30, 45, 60, 75
4	Stepped	4a	-60, -30, 0, 30, 60, 90, 120	30

After these eight series, Wong (2008) distinguished nine coalescence categories, eight of which were describable with his seven crack types (see Figure 2.5). The coalescence categories are shown in Figure 2.15. A more thorough description of these nine coalescence categories can be found in Section 4.3.1.

Category	Coalescence patterns	Crack types involved
1	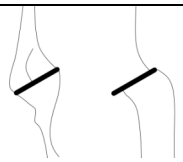	**No** coalescence
2	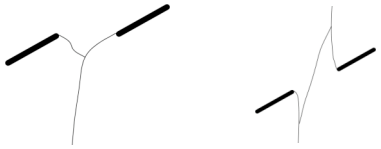	**Indirect** coalescence by two or multiple cracks (crack types vary)
3	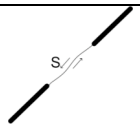	Type 2 **S** crack(s)
4	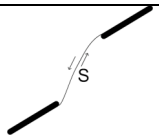	Type 1 **S** crack(s)
5	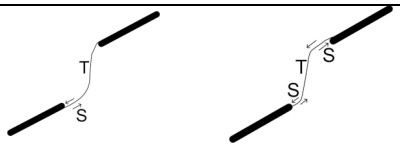	One or more type 2 **S** crack(s) and type 2 **T** crack segments between inner flaw tips
6	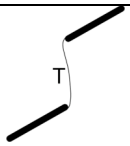	Type 2 **T** crack(s). There may be occasional short **S** segments present along the coalescence crack.
7		Type 1 **T** crack(s)
8	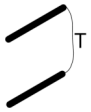	Flaw tips of the same side linked up by **T** crack(s) not displaying wing appearance (crack type not classified). There may be occasional short **S** segments present along the coalescence crack.
9	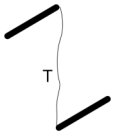	Type 3 **T** crack(s) linking right tip of the top flaw and left tip of the bottom flaw. There may be occasional short **S** segments present along the coalescence crack.

Figure 2.15. Nine coalescence patterns observed by Wong (2008). For crack type description, refer to Figure 2.5.

Wong (2008) also commented on the influence on coalescence of material type and all three flaw pair geometry parameters:

- **Ligament length:** larger ligament length leads to reduced interaction between flaws. This effect is more pronounced in coplanar flaws than in stepped flaws.
- **Flaw inclination angle β (coplanar flaws only):** in general, coalescence trends from no coalescence to shear coalescence to tensile coalescence with increasing flaw inclination angle β.
- **Bridging angle α (stepped flaws only):** There is a general trend from no coalescence to indirect coalescence to direct coalescence as bridging angle α increases from negative values. Within cases of direct coalescence, there is a trend from shear to mixed shear-tensile to tensile coalescence as bridging angle α increases.
- **Material (coplanar flaws):** For all values of flaw inclination β tested, tensile cracks are more likely to occur in marble than in gypsum.
- **Material (stepped flaws):** tensile cracking is more likely to occur in marble than in gypsum, and each material has some categories unique to itself.

Wong (2008) noticed areas of brighter material in marble specimens (as was also noted by Martinez, 1999). He referred to these zones of brighter material as "white patches". No such white patches were observed in gypsum. Further study by scanning electron microscope (SEM) revealed these white patches were, in fact, process zones composed of microcracks:

- Preceding a tensile crack in marble, these microcracks flank a central crack and decrease in density with distance from this central crack.
- Preceding a shear crack in marble, en-echelon arrays of microcracking zones develop preferentially near the flaw tips and are near parallel to the applied load direction.
- Hairline tensile crack segments flanked by much shorter microcracks preceded tensile cracks in gypsum.
- Shear cracks in gypsum were preceded by surface spalling only.

2.6.3 Experimental Observation in Fracture Mechanics

As should be obvious from the previous sections, results and conclusions from experiments are only as good as the observations made during tests. Several methods exist to garner as much useful information as possible from tests:

- Incremental loading increases the time to observe a specimen.
- Inspecting fracture surfaces after tests allows one to gain insight into the history of each fracture.
- Using a high-speed video system enables one to observe crack initiation and propagation at the surface of a specimen.
- Scanning electron microscopy is used to investigate microscopic details regarding cracks and process zones.
- Transparent testing material gives observers visual access to any point in the specimen.

A compromise is often necessary, however. Researchers often must make sacrifices to get more information. Ideally, information can be quickly obtained in real time on relevant materials without disrupting testing protocol (in regards to loading rate, boundary conditions, etc.). These goals are shared by those working in the field of non-destructive testing (NDT). A literature review was performed to evaluate the feasibility of applying one of these NDT methods – acoustic emission – to the research performed by the MIT rock mechanics group in fracture coalescence. While it was found to have some interesting possible applications, it is not a practical technology at this time. See Appendix A for this review.

Chapter 3. Uniaxial Compression Tests

3.1 Introduction

Unconfined uniaxial compression tests were performed on prismatic specimens of granite. Stress-strain data were recorded as well as video footage of the entire experiment and high-speed video footage of crack coalescence processes. This chapter describes the experimental details ranging from the specimen geometry and material to the processing of recorded data.

3.2 Specimen Geometries

Prismatic specimens of Barre granite with dimensions 6" × 3" × 1" (~152 mm × ~76 mm × ~25 mm) were used. Each specimen included two pre-cut flaws. The relationship between flaws is referred to as specimen geometry. Specimen geometries are defined by three parameters: ligament length (L), flaw inclination angle (β), and bridging angle (α). These parameters are shown in Figure 3.1, as is an example specimen. All flaws were 0.5" (12.7 mm) long.

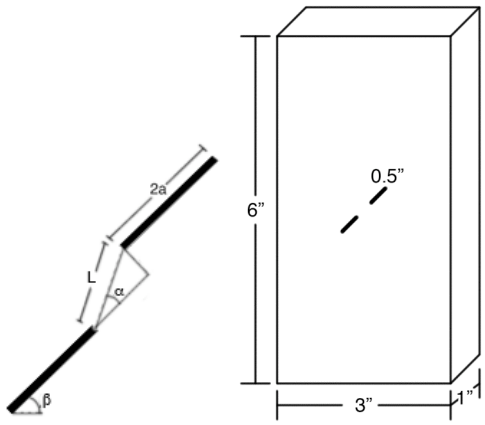

(a) (b)

Figure 3.1. (a) Flaw pair geometry defined by ligament length (L), flaw inclination angle (β), and bridging angle (α). (b) Specimen dimensions.

In the tests, all three geometric parameters were varied: ligament length was set at either a or 2a (0.25" or 0.5"), α was set at either 0º (coplanar) or 60º (stepped), and β was varied over

five values (0º, 30º, 45º, 60º, and 75º). This led to 20 unique geometries. For illustrative purposes, all the geometries tested with ligament length equal to flaw length (0.5") are shown in Figure 3.2.

	β = 0º	β = 30º	β = 45º	β = 60º	β = 0º
Coplanar (α = 0º)		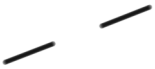			
Stepped (α = 60º)	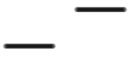				

Figure 3.2. Geometries tested with ligament length equal to flaw length. A comparable set of geometries with ligament length equal to half the flaw length was also tested.

These geometries were selected for two reasons:

1. To make comparisons with results obtained by Wong (2008) for Carrara Marble and molded gypsum with coplanar flaws and L = 2a (in the tests by Wong (2008) it was shown that for L > 2a the interaction between the two flaws lessens and hence the effect on coalescence diminishes).
2. The value L = a was chosen, in contrast to what was done earlier in the gypsum and marble materials when L was usually 2a and 4a. This was done to ensure interaction in the coalescence process. Note, however, that Martinez (1999) did test three geometries with L = a, so comparisons with his results are possible.

3.3. Specimen Preparation and Material Properties

3.3.1 Introduction

As mentioned in Section 3.2, prismatic specimens were created with Barre Granite. These specimens were prepared in a similar manner to the Carrara Marble specimens with a diamond saw and waterjet as Wong (2008) used. The granite specimens had dimensions of 6" (height) × 3" (width) × 1" (thickness) (~152 mm × ~76 mm × ~25 mm).

2.3.2 Specimen preparation

Barre Granite (in this study referred to as granite) was selected since it had been used previously within the MIT rock mechanics group (Martinez, 1999) and has been investigated by many other researchers (Sano et al., 1992, Nasseri and Mohanty, 2008, and Xia et al., 2008). It is also a part of a standard rock suite as designated by the U.S. Bureau of Mines (Krech et al., 1974). It was ordered from North Barre Granite, Inc., a quarry in Vermont specializing in granite memorials. A piece, which was roughly 36" × 12" × 4" was then cut into four 1" thick slices using a diamond saw at the quarry. Each slab was then taken to the Gelb Laboratory in the Department of Aeronautics and Astronautics at MIT and cut into 3" × 6" bricks with an OMAX waterjet. This same waterjet was also used to cut 0.5" long flaws into the granite specimens. The use of the waterjet for cutting flaws was first introduced within the MIT rock mechanics group by Martinez (1999).

In order to cut flaws into granite bricks, the waterjet had to first pierce through the thickness of the specimen before traversing the 0.5" length of the flaw. While piercing, the waterjet creates a slightly wider opening than while traversing, so the flaws do not have a uniform width over their entire length, as shown in Figure 3.3.

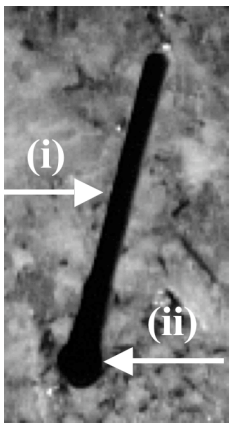

Figure 3.3. Artificial flaw created in Barre Granite using an OMAX waterjet. Note that at location (ii), where the jet pierced first, the flaw is wider than over the remainder (i).

This wider opening was always located on the left tip of each flaw. This was done to make any effects consistent throughout all tests. No obvious effect, however, was observed. For more details regarding the waterjet, refer to Wong (2008).

3.3.3 Material Properties

Barre Granite comes from North Barre Granite, Inc. near the town of Barre, Vermont (Rock of Ages also owns a quarry in the same formation). The formation is very uniform, does not have fault or fracture zones along its contacts with surrounding materials, and has not reacted significantly with the surrounding material nor with inclusions. This indicates that the formation was put into place as magma embedded by gentle intrusion (Krech et al., 1974). Barre Granite has an average grain size of 2.54 mm (0.1”). Its mineral content is 36.5% plagioclase, 31.9% quartz, 17.8% potash feldspar, 8% biotite, 3% muscovite, and 2.8% granophyre (Goldsmith et al., 1976). A more extensive description of Barre Granite is available in Chayes (1952).

Granitic rocks are known to have three orthogonal splitting planes (often used in quarrying). These planes are – in order of increasing resistance to rock cleavage – the rift, grain, and hardway planes (Chen et al., 1999). The rift and grain planes are also generally the preferred orientation of microcracks, with the rift plane being the primary orientation (Dale, 1923,

Osborne, 1935, Isnard and Leymarie, 1964, Peng and Johnson, 1972, Simmons et al., 1975). These microcracks, in turn, can cause anisotropy (Nur and Simmons, 1969, Anderson et al., 1974, Hoenig, 1979, Hudson, 1981, Crampin, 1984).

A summary of relevant material properties is shown in Table 3.1.

Table 3.1. Relevant mechanical properties of Barre Granite. Values marked with an "*" are from Kessler et al. (1940) and those marked with an "+" are from Goldsmith et al. (1976). Those marked "N/A" are not available. Modulus values calculated by Martinez (1999) and in the present study were measured on intact specimens oriented (as discussed below) identically to specimens with flaws.

Property	**Value from Sources**	**Value from Martinez (1999)**	**Values measured in the present study**
Density [g/cm^3]	2.61*	N/A	N/A
Porosity [%]	1.51 – 1.62*	N/A	N/A
Compressive Strength [MPa]	170 (perpendicular to rift)* 192.5 (parallel to rift)*	140	151
Modulus of Elasticity [GPa]	11.9 Minimum* 23.1 Maximum*	17.5 Average	19.2
Tensile Fracture Stress [MPa]	5.08 Minimum+ 10.65 Maximum+	N/A	N/A

See Appendix B for calculations of compressive strength and modulus of elasticity.

Table 3.1 shows that the mechanical properties of a specimen are influenced by its orientation (e.g. – compressive strength is a function of splitting plane orientation). When the granite is shipped from North Barre Granite, Inc., the splitting planes are not indicated on the slabs. An understanding of the quarrying process (Wood, 2006), however, can aid in understanding of how specimen faces relate to these planes.

Granite is typically quarried from benches twenty feet deep by twenty feet tall and hundreds of feet wide. Twenty-foot cubes are removed, with the splitting planes oriented as shown in Figure 3.4.

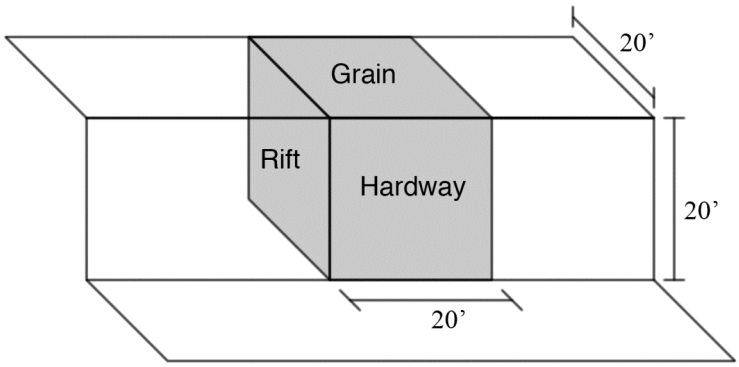

Figure 3.4. Typical orientation of splitting planes for a block removed from a bench.

The granite is cut by first drilling vertical holes (called deep holes) – 1 ¼” diameter on 6” centers – and then removing material between the drilled holes or by using a high-pressure jet flame that causes granite to spall due to differential heating. The bottom face (parallel to the grain plane) is cut by drilling horizontal holes (called lift holes). The large 20’ × 20’ × 20’ block is split into four slabs by cutting three vertical planes parallel to the hardway. Each of these slabs is then tipped forward out of the bench and split further. Holes are drilled perpendicular to the hardway direction to produce 5’ × 5’ x 10’ blocks (with the 5’ × 10’ face being parallel to the hardway direction). These smaller blocks are known as saw blocks. By drilling plug holes (6” deep holes on 3” centers) perpendicular to the hardway plane, one can then split the saw block into the desired size before using a diamond saw to cut these smaller pieces parallel to the hardway direction.

Some of the slabs that arrived from North Barre Granite, Inc. had drill holes along one of their edges, as seen in Figure 3.5.

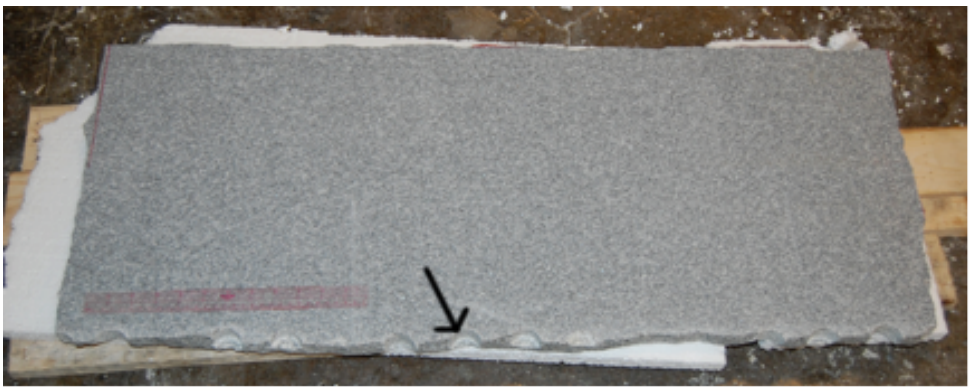

Figure 3.5. One of the slabs from North Barre Granite, Inc., showing drill holes (one of which is indicated by an arrow) along one edge and split along the other three. The largest face was cut with a diamond saw.

These holes are interpreted to be the plug holes perpendicular to the hardway direction. As only one plane was split using these holes, the plane parallel the edge with the holes is taken to be the grain plane. Our 6" × 3" × 1" bricks were cut with sides parallel with these planes, so the assumed relationship between splitting planes and specimens is shown in Figure 3.6.

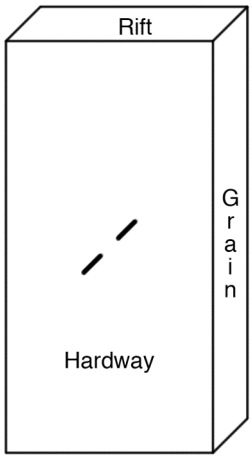

Figure 3.6. Assumed orientations of splitting planes for test specimens.

It should be emphasized that the relationship shown in Figure 3.6 is an assumption and not known for certain. If the assumption is valid, compression was applied in the direction perpendicular to the rift plane.

3.4 Testing

3.4.1 Introduction

A typical experimental set up is shown in Figure 3.7 and is schematically represented in Figure 3.8. There were at least five components to each test (and more for heated and pressurized tests see Chapter 5): specimen, platens, loading machine, camcorder, and high-speed video system (composed of camera, lights, and a laptop). Specimen preparation was described in the previous section. The other components will be described in further detail below.

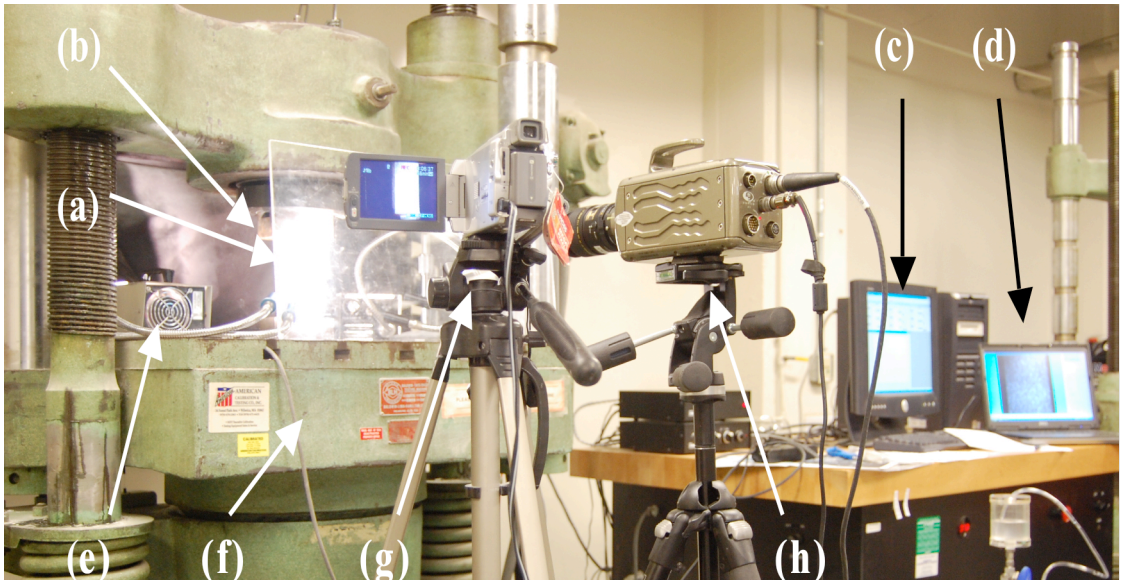

Figure 3.7. Typical experimental set-up with the following components labeled: (a) specimen, (b) platen, (c) loading machine control and data logger, (d) high-speed camera laptop, (e) lighting source for high-speed camera, (f) loading machine, (g) camcorder, and (h) high-speed camera.

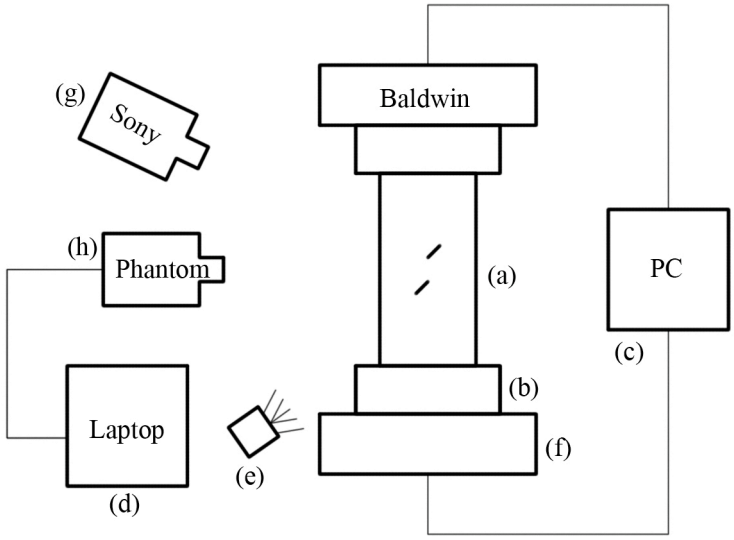

Figure 3.8. Schematic representation of a typical experimental set up. The following components are labeled: (a) specimen, (b) platen, (c) loading machine control and data logger, (d) high-speed camera laptop, (e) lighting source for high-speed camera, (f) loading machine, (g) camcorder, and (h) high-speed camera.

3.4.2 Platens

Specimens were held in place with steel end pieces (platens). For granite specimens with ligament length '2a', the same platens as those used by Wong (2008) were used (Figure 3.9). However, specimens with ligament length 'a' used a different type of platens. This change was made due to the increased loads required to fail granite in comparison to gypsum and marble specimens.

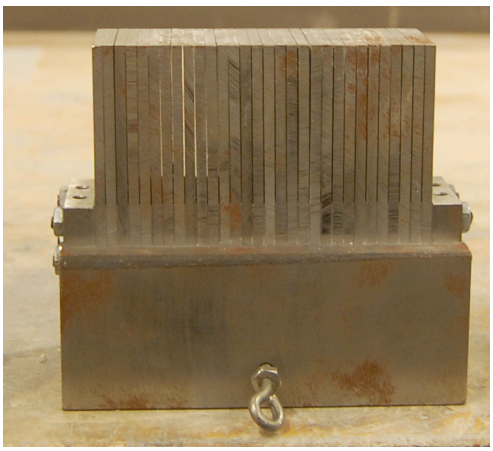

Figure 3.9. Brush platens as those used by Wong (2008) for gypsum and marble specimens. Note the individual vertical brushes.

Note the vertical teeth of the brush platens in Figure 3.9. These teeth provide end conditions which minimize lateral confinement. Refer to Bobet (1997) for details regarding the dimensioning of these brushes. The increased loads applied to granite, however, led to buckling of individual teeth, as shown in Figure 3.10. Pieces of granite specimens became wedged between two teeth, and were then forced down at the time of failure. This caused buckling of individual teeth.

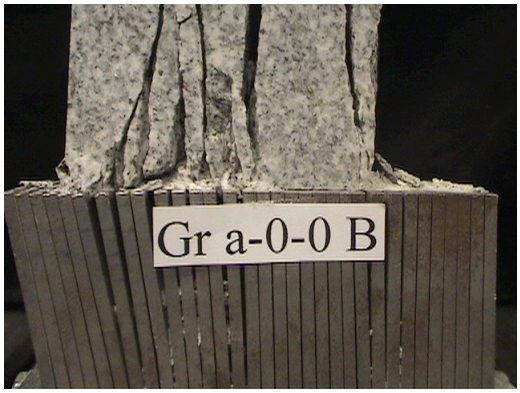

Figure 3.10. Increased loads for granite specimens caused buckling of the teeth in the brush platens. Many of the teeth in the left third of the platen shown have buckled.

At first, teeth were removed from the platens and bent back to their original, straight, shape. After having failed, however, these teeth were more likely to buckle again. Subsequently new platens were designed with the same dimensions but using a new, stiffer steel (see Appendix D for the design of these platens). Once again, however, the teeth buckled while loading granite specimens. This problem had been avoided by Martinez (1999) who used solid platens. Similar solid platens (Figure 3.11) were then chosen for the remaining test series on granite specimens with ligament length a. Time constraints prevented retesting specimens with ligament length 2a with these solid platens. Figure 3.11 shows the three different types of platens discussed above.

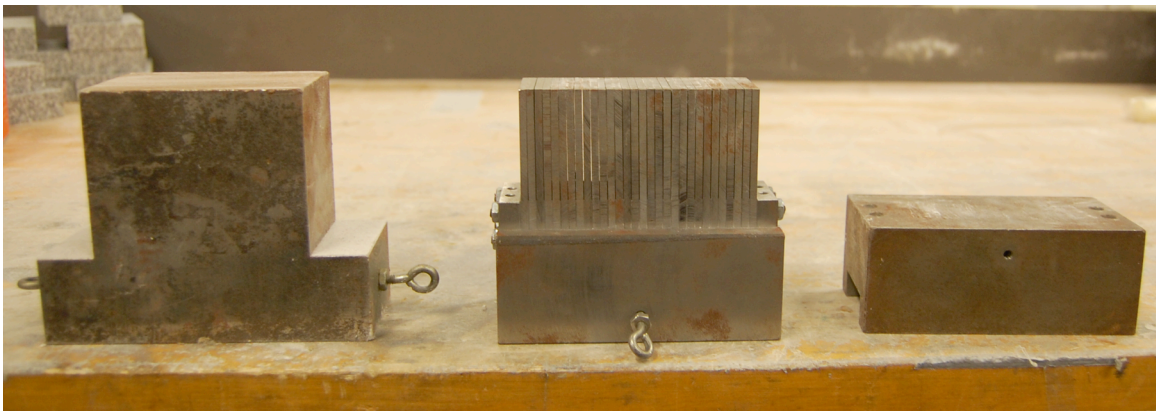

Figure 3.11. The three types of platens discussed above: solid platens used by Martinez (1999) (left), brush platens used by Wong (2008) and Bobet (1997) (middle), and solid platens used for specimens with ligament length a in this test series.

Due to the fact that solid platens restrict lateral ("Poisson") expansion, tests run using these platens were not truly unconfined. Calculations shown in Appendix D show how much confining stress can be expected for different uniaxial loads. Section 4.5 also discusses the effect of the change in platens.

3.4.3 Uniaxial Compression with Stress-Strain Recording

A Baldwin 200 Kips Loading Machine (f in Figure 3.7) was used to conduct uniaxial compression tests. The machine was feedback controlled using a computer program named

MTESTWindows^{TM}. Load and displacement were recorded at a rate of 1800 samples per minute. Bobet (1997) and Ko (2005) include more details regarding the loading machine.

Previous research at MIT used two different loading techniques. The first was to incrementally load the specimen with pauses for crack inspection (Reyes, 1988, Bobet 1997). The second was to continuously load the specimen and record data from the experiment to review at a later time (Martinez, 1999, Ko, 2005, and Wong, 2008). Continuous loading was used for this study to maximize the advantages of the high-speed camera as video footage can be synchronized with stress-strain data more accurately. It was also selected to be analogous with experiments performed on gypsum and marble by Wong (2008). The "loading profile" was the same as that described by Wong (2008) and is shown in Table 3.2.

Table 3.3. Loading profile used for gypsum, marble and granite specimens.

	Loading Rate	**Range**
Stage 1	0.0017 in/sec	0 – 1000 lbs.
Stage 2	0.0003 in/sec	1000 – 2500 lbs.
Stage 3	38.3333 lb/sec	2500 lbs – failure
Stage 4	5.0 in/min	Failure – starting position

Differently from Wong (2008), the "home rate" (stage 4) for the profile was changed to five in/min in order to reduce problems in the hardware/software interface during testing. The home rate is the rate at which the machine returns to its original position. After a software upgrade, a bleed valve often did freeze after each test and require a hard reset of the software. Changing the home rate corrected this issue.

3.4.4 Camcorder Observation

A Sony Camcorder (DCR-HC65) was used to videotape the entire front face of specimens during testing. The camcorder recorded the complete experiment at approximately 30 frames per second. Tape recordings were converted to digital videos (Windows Media Video format) with Windows Movie Maker. While finer details were difficult to distinguish on the camcorder video, having a video record of an entire test is valuable for synchronization purposes.

3.4.5 High-Speed Camera Observation

A Phantom v7.1 high-speed camera was used to record in detail one short segment of each test. The high-speed camera is capable of recording at up to 30,000 frames per second. Due to memory constraints, however, typical frames rates were between 5,000 and 10,000 frames per second. The faster the frame rate, the shorter the recorded duration could be. As the camera was human-triggered, typical durations needed to be on the order of one second at the shortest. For more details regarding the high-speed camera and recording methods, refer to Wong and Einstein (2008).

Unique to tests in granite, regular still pictures were also taken with the high-speed camera prior to the high-speed video recording. They were taken near the start of each test, every 10,000 pounds of load for the first 40,000 pounds of load, and then every 1,000 to 5,000 pounds until failure. These pictures were taken for two reasons:

1. Images captured with the high-speed camera were of higher resolution than those captured by the camcorder.
2. Images captured with the high-speed camera were directly comparable with those captured later in the high-speed recording.

These images were used to identify white patches (see Section 4.2.1) and sometimes crack initiation. While the synchronization of these individual high-speed images was not as accurate as for the high-speed series (see Section 3.5.2), they were often extremely helpful in determining white patch formation as well as early crack sequencing. Synchronization was not as accurate because pictures were triggered by hand as the corresponding approximate load was recorded. Typically, the load value for each picture is accurate to plus or minus fifty pounds of load (approximately plus or minus 110 kPa).

3.5 Data Analysis and Interpretation

3.5.1 Introduction

Each test consisted of three types of observations: load-displacement, camcorder video, and high-speed video. By combining these three sets of data, a reasonably complete picture of each test was created summarizing the cracking sequence and nature as well as the stress-strain behavior. The following describes the interpretation process in detail.

3.5.2 Synchronization

As mentioned by Wong (2008), all three observations were taken independently of one another, and therefore not automatically synchronized. The first step, therefore, was to correlate all three with a single experimental timeline. This was accomplished by correlating events observed in both videos with their corresponding point on the stress-strain curve (obtained by combining load-displacement data with specimen dimensions). Two different events were used to achieve this correlation:

1. Specimen failure. Maximum stress was defined as failure and failure could usually be seen in both video recordings.
2. The sudden initiation of a new crack. These events were visible in both video recordings, often audible on the camcorder recording (the high-speed system did not record sound), and did sometimes correspond to a sudden drop or change in slope of the stress-strain curve. However, this sudden change in the stress-strain curve was not as common in granite as it was in gypsum (Wong, 2008).

Figure 3.12 illustrates a typical synchronization (images and data taken from specimen Gr 2a-30-60 C). The bottom timeline in Figure 3.12 is the stress-strain timeline. The middle timeline is of the camcorder video. Note how the camcorder starts recording after stress-strain data begins being logged. Specimen failure could be observed on the camcorder video. This point corresponded to the point of maximum stress on the stress-strain timeline (connection (a) in Figure 3.12). This made it possible to synchronize the camcorder and stress-strain recordings. The next step was to synchronize the high-speed video with the other

two recordings. Note the short duration of the high-speed video. Coalescence was captured on both video recordings, making synchronization possible (connection (b) in Figure 3.12). Now all three sources were synchronized, so coalescence could be placed on the stress-strain record.

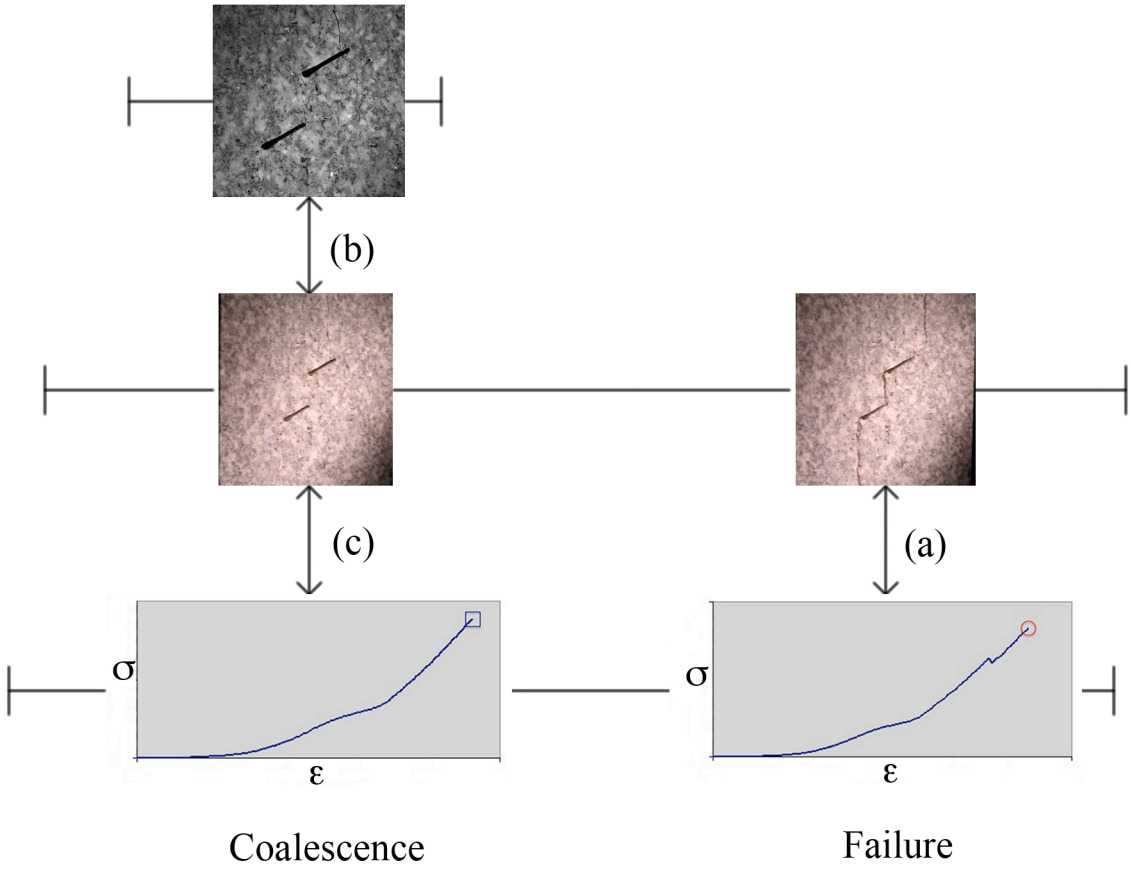

Figure 3.12. Simplified process to synchronize high-speed video (top), camcorder (middle), and stress-strain (bottom) timelines. (a) Failure is used to synchronize camcorder and stress-strain timelines. (b) Coalescence is used to synchronize camcorder and high-speed video timelines. (c) Coalescence on camcorder is then used to place coalescence on stress-strain data.

The regular images captured with the high-speed camera before the video (see Section 3.4.5) were approximately synchronized with the stress-strain record. As mentioned, the approximate load (later converted to stress) at which the pictures were taken was recorded.

By using these recorded loads, the point along the stress-strain record at which the pictures were captured could be found.

Unlike the example given in Figure 3.12, failure was often captured in the high-speed recordings (in addition to coalescence). As a result, the high-speed video could be synchronized with the stress-strain data directly.

3.5.3 Video Analysis

After both video recordings were synchronized with the σ-ε record, the recorded pictures were analyzed using Adobe Photoshop by performing four tasks simultaneously:

1. Identify the type of white patches (will be explained in Chapter 5) that were present
2. Establish the sequence in which these patches appeared
3. Identify the mode of initiation and propagation (shear or tensile) of new and existing cracks
4. Establish the sequence in which these cracks appeared

As Wong (2008) noted, extreme care had to be taken to differentiate between cracks initiating as tensile cracks that subsequently sheared and true shear cracks. The sequence of white patch and crack development (see Section 4.2 for a more general discussion) of a Barre Granite specimen is illustrated in Figure 3.13. A second example is provided in Figure 3.14, which gives a better illustration of diffuse white patching. The process is similar to that in marble specimens as described by Wong (2008).

In Figure 3.13 and Figure 3.14, the original flaws are the large black straight lines with rounded tips. Black lines indicate a crack, thin gray lines indicate a linear white patch that follows grain-boundaries (see below), thick (bold) gray lines indicate a linear white patch that appears to go through grain-boundaries, and gray patches indicate groups of grains that have lightened. Each linear feature is given an identifier. These identifiers first indicate the feature type with a letter. **L** refers to a single or group of linear white patches, **T** refers to a crack, which initiated in a tensile mode, and **S** refers to one that initiated in a shear mode (where possible, the direction of shear is indicated as well). After this letter, there is a

number in the subscript. This number differentiates a particular feature from other features of the same type. It is not associated with the crack initiation sequence. Finally, for cracks (or groups of related cracks) that are not initially connected to a flaw but later become connected, the identifier (letter and number) is put inside parentheses. Each image is labeled with a time (either test time or in relation to coalescence) and corresponding stress state.

<table>
<tr>
<td>(1) Time: 0.098s before coalescence
σ: 44.33MPa
 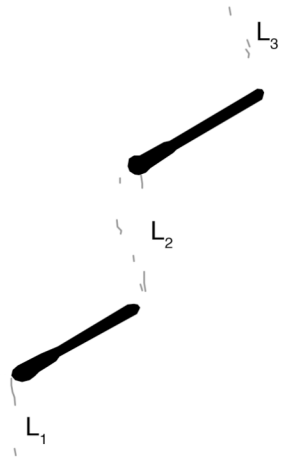
</td>
<td>(2) Time: 0.0228s before coalescence
σ: 44.33 MPa
 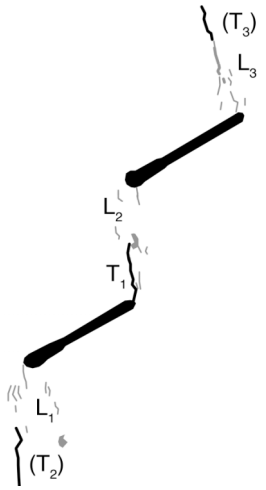
</td>
</tr>
<tr>
<td>(3) Time: 8m42.45s; σ: 44.42 MPa
 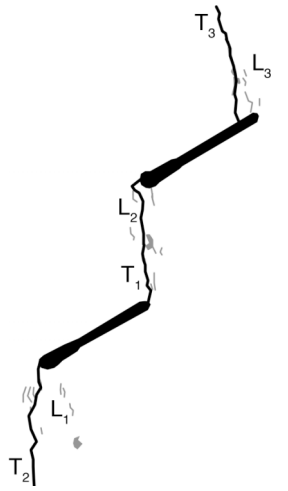
</td>
<td>(4) Time: 11m42.45s; σ: 57.86 MPa
 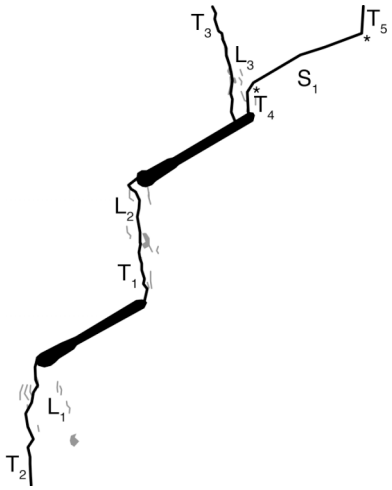
</td>
</tr>
<tr>
<td colspan="2">1. Linear white patches L_1, L_2, and L_3 appear near the flaw tips. All are boundary-following linear features.
2. L_1 – L_3 grow. L_1 and L_2 have grains lighten while L_3 develops some through-going linear white patches. Tensile wing crack T_1 appears. (T_2) and (T_3) grow into the camera's field of view.
3. (T_2) and (T_3) extend and connect with outer flaw tips, becoming T_2 and T_3, respectively. T_1 extends upward and connects with the right flaw's inner tip, causing crack coalescence.
4. Specimen failure occurs with a new wing crack T_4. T_4 extends from the outside tip of the right flaw. It transitions to S_1 at the '*' on. At the next '*' the crack transitions to T_5.</td>
</tr>
</table>

Figure 3.13. White patch development and cracking process of a granite specimen (specimen Gr 2a-30-60 C). See text above for explanation.

(1) Time: ~9m14s; σ: ~47.3 MPa	(2) Time: ~15m00s; σ: ~74.7 MPa
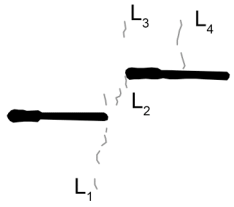	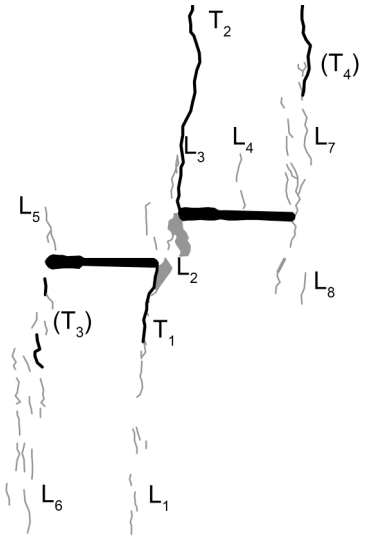
(3) Time: ~16m13s; σ: ~81.6 MPa	(4) Time: 18m37.32s; σ = 93.43 MPa
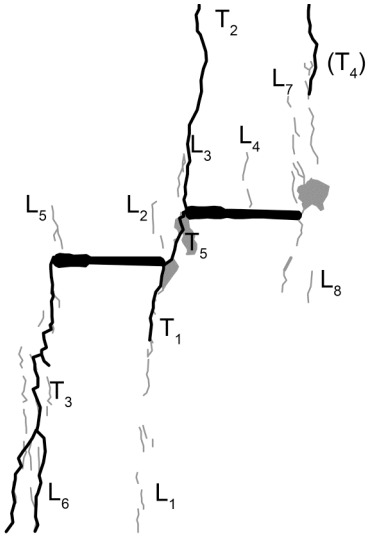	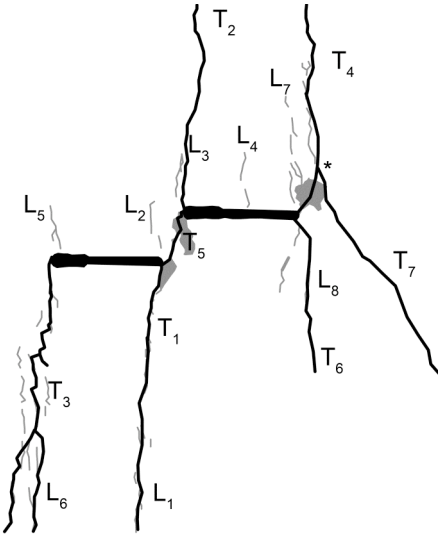

1. Linear white patches L_1 through L_4 appear. All are boundary-following linear features.
2. L_5 through L_8 appear with boundary-following linear features (L_8 has one through-going feature. Diffuse white patches appear in the L_2 region. Tensile wing crack T_1 and T_2 appear. Tensile cracks (T_3) and (T_4) also appear.
3. Some diffuse white patching appears in the L_7 region.
4. (T_4) becomes tensile wing crack T_4 and specimen failure occurs with the simultaneous appearance of tensile cracks T_6 and T_7.

Figure 3.14. White patch development and cracking process of a granite specimen (specimen Gr a-0-60 D). See text above for explanation.

3.5.4. Stress-Strain Analysis

After the video analysis was complete, the stress-strain curve (see Figure 3.15) was used to show the entire stress-strain history of the test as well as to indicate the maximum stress (uniaxial compressive strength) of the specimen, the crack initiation stress, and the coalescence stress. The stress-strain plot for the specimen visually analyzed in Figure 3.13 is shown in Figure 3.15.

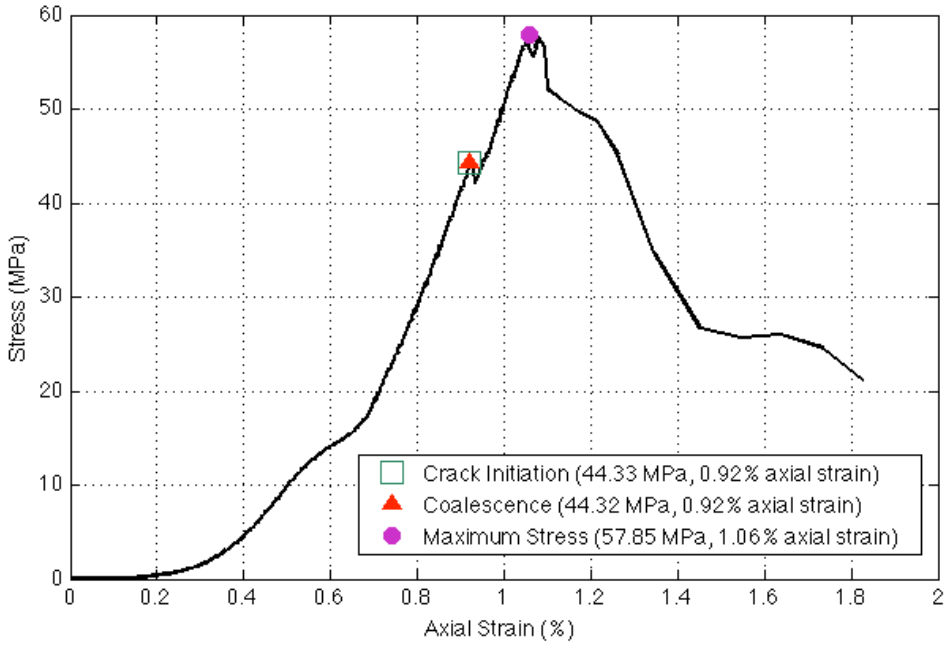

Figure 3.15. Stress-strain curve of the granite specimen shown in Figure 3.13.

Chapter 4. Results on Uniaxial Compression Tests

4.1 Introduction

In Chapter 2, the fracturing and coalescence behavior of flaws in gypsum and marble were reviewed. In this chapter, results obtained in this experimental study on Barre Granite are described and discussed. The effects on coalescence of the three parameters associated with specimen geometry are investigated and a comparison of these results with those in the other two materials is made. For a description of geometries tested and testing procedures for granite, refer to Chapter 4.

4.2 Crack Initiation and Propagation

4.2.1 White Patches

Granite behaved similarly to marble in that white patches appeared before or simultaneously with the first crack. Unlike marble, however, there were two general categories of white patches in granite: diffuse white patches and linear white patches. In marble only linear white patches were noted by Wong (2008). Linear white patches in granite could then be further subdivided into two categories, as will be discussed shortly. Figure 4.1 shows the distinction between linear and diffuse white patches. It should be noted that Martinez (1999) also noted white patches in marble and granite.

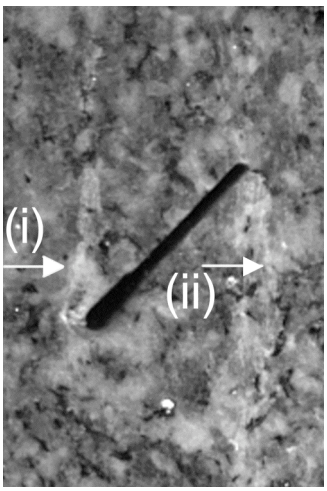

Figure 4.1. Illustration of the two categories of white patching in granite: (i) diffuse white patch and (ii) linear white patch.

Diffuse patches occurred when a group of mineral grains became more reflective (brighter) while linear white patches were very narrow zones becoming brighter. Linear white patches often ran parallel to one another (also generally parallel with the direction of maximum stress) giving the impression of a broad linear white patch. This can be seen in Figure 4.1 (ii). Several linear white patches extend downward from the right tip of the flaw shown. All forms of white patch initiation in granite were different from that in marble because they did not always start at or near the tips of flaws. Another difference between marble and granite was the timing of white patch initiation. In marble, white patches formed before a crack. In granite, white patches formed before, during, or after the appearance of a crack. In both materials, cracks did not always form where there was white patching.

As indicated at the start of this section, a further distinction could be made between two types of linear white patches in granite: some appeared to follow grain boundaries (boundary-following) while others appeared to go through grains (through-going). The two linear white patches are illustrated in Figure 4.2 (a). Through-going white patches were observed to go across whole grains, and were generally straight features. The distinction between boundary-following and through-going features could only be made after magnifying the images extensively. Such a magnification is shown in Figure 4.2 (b). Even after magnification, it was difficult to distinguish between a true through-going white patch and a boundary-following

white patch going between two grains of the same mineral. Boundary-following linear white patches were much more common than through-going ones.

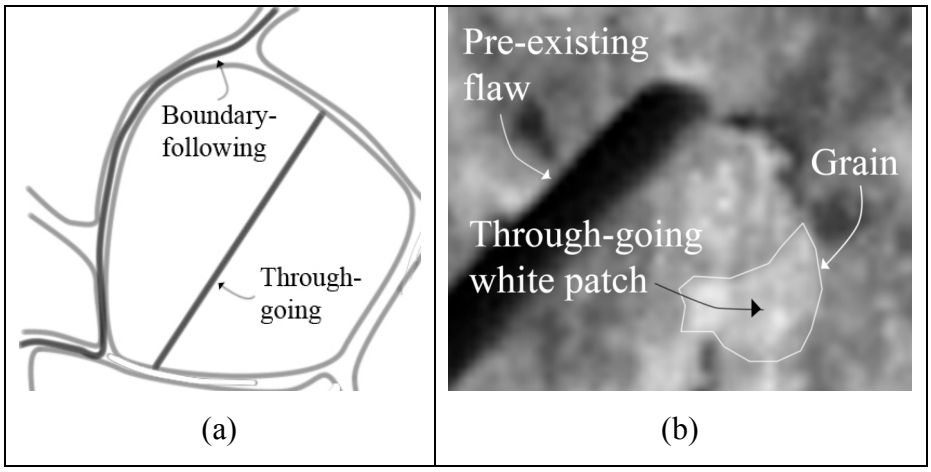

Figure 4.2. (a) illustration of boundary-following and through-going linear white patches. (b) magnified image near a flaw tip showing a linear white patch going through a single grain.

The visual complexity of granite made finding and tracing white patches very difficult. Typically images were overlaid and compared in Adobe Photoshop. In some cases, however, MATLAB was used to aid in the task. By comparing images on a pixel-by-pixel basis, one could find regions of white patching. The original images still needed to be consulted to classify linear white patches, however. Figure 4.3 shows one of these comparisons.

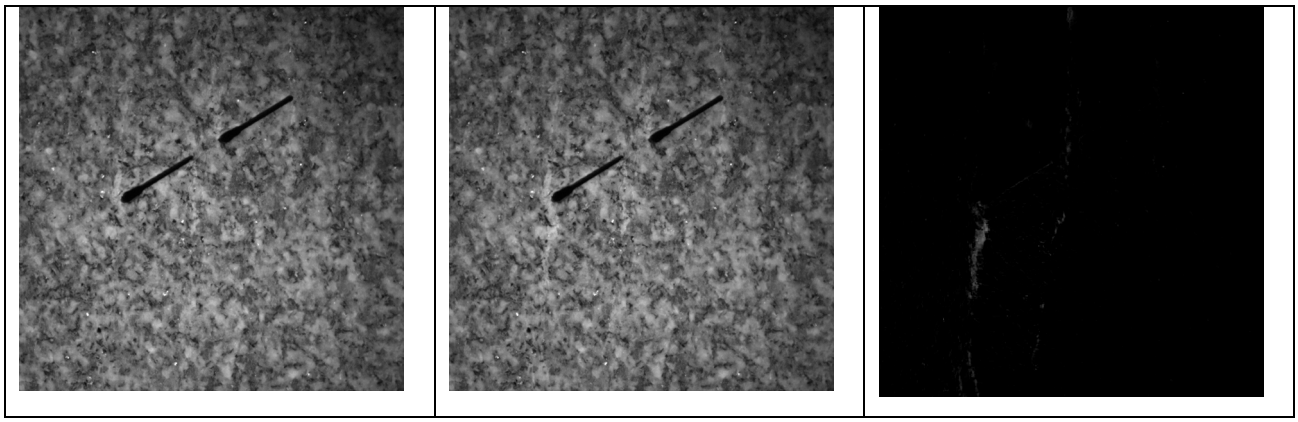

(i) (ii) (iii)

Figure 4.3. Two frames taken during a compression test (specimen Gr a-30-0 A) and their difference. Frame (i) was taken at a load of approximately 45,000 pounds while frame (ii) was taken at a load of approximately 46,000 pounds. Image (iii) is the difference between the two images. Zones of brightening become apparent.

Refer to Appendix E for a longer discussion of advantages and disadvantages regarding the use of this MATLAB technique as well as a more thorough description of the procedure.

4.2.2 Crack Processes

Unlike both molded gypsum and marble (as observed by Wong, 2008), tensile wing cracks in granite did not always originate at or near flaw tips. Small tensile cracks often appeared above or below flaw tips in zones of white patching, then extended and connected with flaw tips. This is illustrated in Figure 4.4. It should also be mentioned that this phenomenon was not observed by Martinez (1999), who noted that tensile wing cracks in Barre Granite always started at flaw tips. Wong (2008) also observed tensile wing cracks initiating only from flaw tips in gypsum and marble. Also of note is the section of tensile crack labeled "*" in Figure 4.4 (b). Small tensile cracks such as this one often appeared ahead of tensile wing cracks in zones of white patching. Both the wing crack and smaller crack then extended and connected with one another.

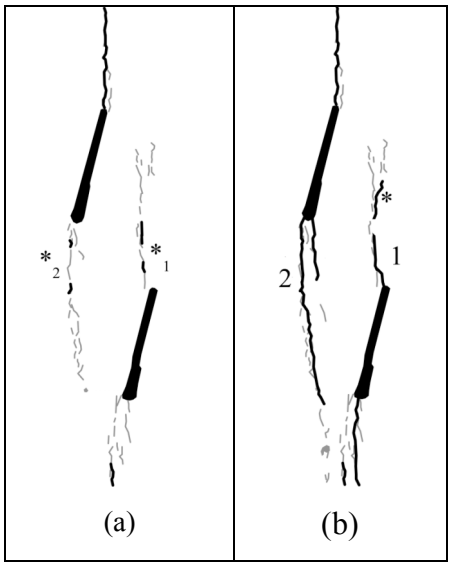

Figure 4.4. Tensile wing crack formation in granite showing small tensile cracks away from flaw tips growing into tensile wing cracks ($*_1$ and $_2$ in (a) growing into 1 and 2 in (b), respectively). Also note the second segment of tensile crack 1 (labeled "*") appearing unconnected to the tensile wing crack.

Tensile cracks in general grew and propagated very quickly in granite. Tensile cracks often started in or near zones having some white patches, although this was not always the case. Tensile cracks could also form either simultaneously with or prior to white patching. This variation in the sequence between white patching and tensile cracking represents a major difference between granite and marble. In marble white patches always preceded the tensile cracks. In granite, tensile cracks opening in zones of white patches often followed an individual linear white patch for a short distance before then following another, nearby white patch. Tensile cracks, like most white patches, most commonly followed grain boundaries.

Shear cracks in granite initiated in a similar manner as those observed in molded gypsum and marble. This initiation was generally seen in conjunction with surface spalling, probably indicating a compressive state of stress (see Figure 4.5 (a)). After the spalled material fell from the specimen's surface, the shear crack's trace could be seen (see Figure 4.5 (b)). Relative motion between material on both sides of the crack track established the direction of shear. Due to this spalling, it was sometimes difficult to determine if shear cracks initiated

and propagated along grain boundaries. When spalling was not present, shearing was observed to generally follow grain boundaries. Shearing of individual grains was also observed, but this was rare. Diffuse grain lightening often preceded longer shear cracks.

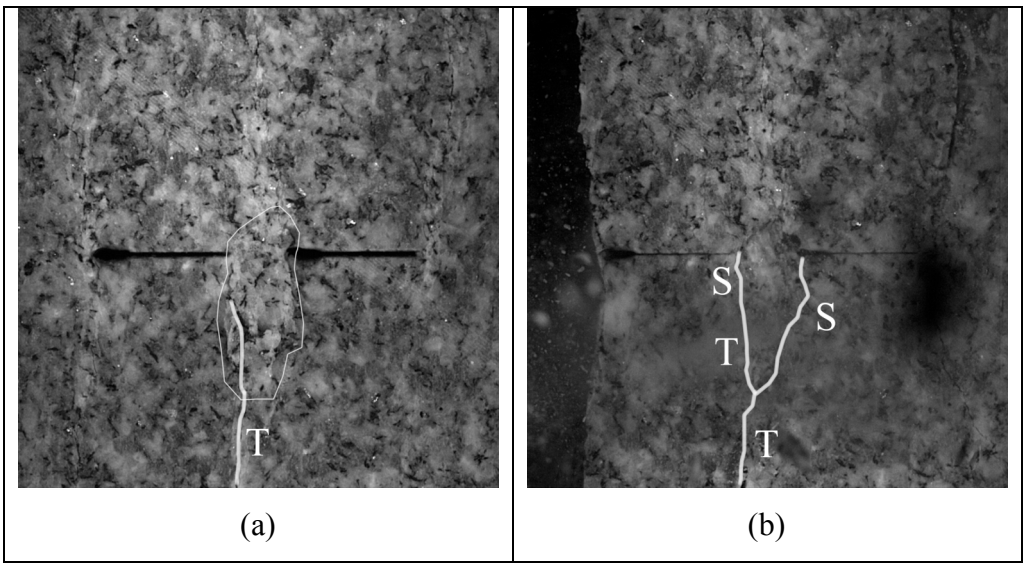

Figure 4.5. Two high-speed images from specimen Gr a-0-0 C showing shear cracks preceded by spalling. (a) spalling (inside the white boundary) in the bridging zone indicates possible shear crack formation. (b) crack traces are revealed and traced after spalled material falls from face of specimen 0.3412 seconds later.

Figure 4.6 shows the seven crack types classified by Wong (2008). These classifications were made after observing uniaxial compression tests on marble specimens performed by Martinez (1999). No new crack types were observed in Barre Granite. It should be emphasized that this indicates that these crack types can cover all the materials so far investigated by the MIT rock mechanics group.

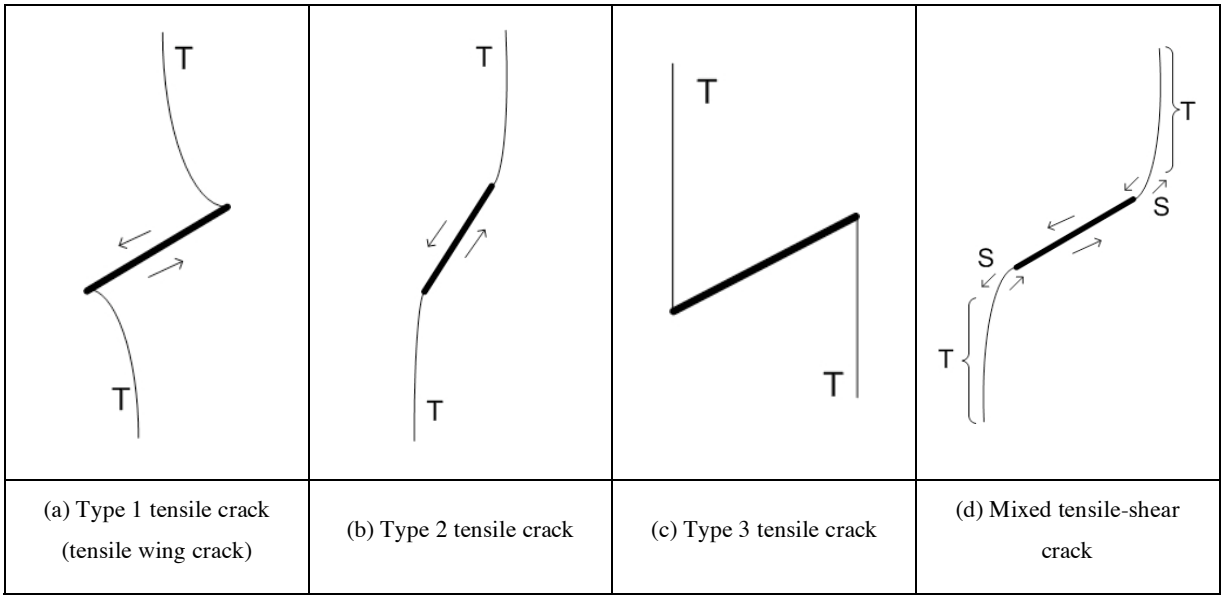

(a) Type 1 tensile crack (tensile wing crack)	(b) Type 2 tensile crack	(c) Type 3 tensile crack	(d) Mixed tensile-shear crack

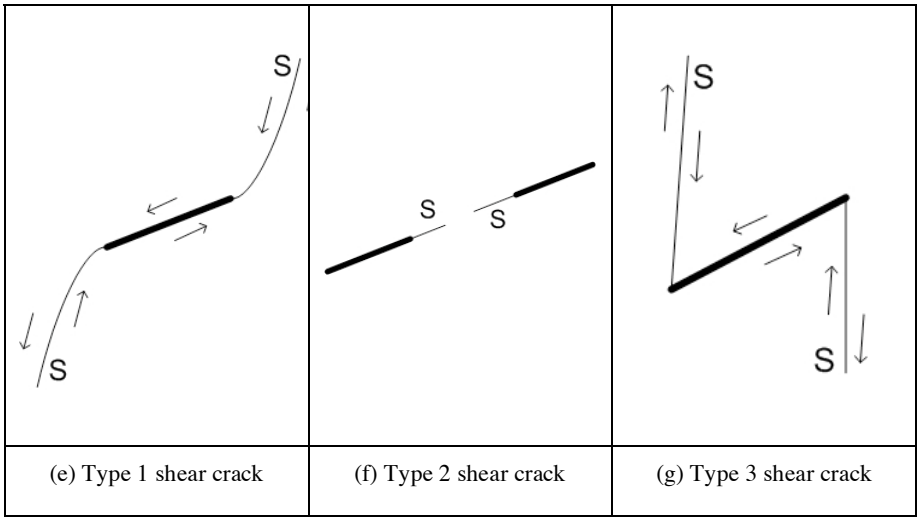

(e) Type 1 shear crack	(f) Type 2 shear crack	(g) Type 3 shear crack

Figure 4.6. The seven crack types observed by Wong (from Wong, 2008).

4.3 Coalescence Behavior

4.3.1 Coalescence Categories

Figure 4.7 shows the nine categories of coalescence proposed by Wong (2008). These categories were used to classify coalescence in granite in this study.

Category	Coalescence patterns	Crack types involved
1	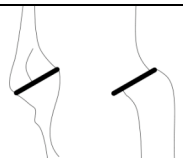	**No** coalescence
2	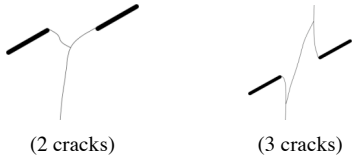	**Indirect** coalescence by two or multiple cracks (crack types vary)
3	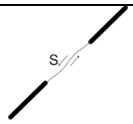	Type 2 **S** crack(s)
4	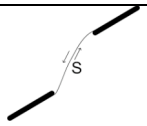	Type 1 **S** crack(s)
5	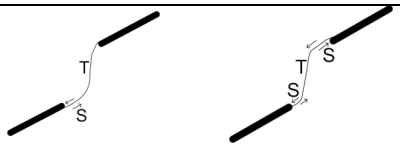	One or more type 2 **S** crack(s) and type 2 **T** crack segments between inner flaw tips
6	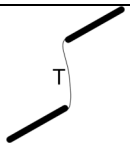	Type 2 **T** crack(s). There may be occasional short **S** segments present along the coalescence crack.
7		Type 1 **T** crack(s)
8	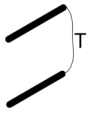	Flaw tips of the same side linked up by **T** crack(s) not displaying wing appearance (crack type not classified). There may be occasional short **S** segments present along the coalescence crack.
9	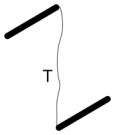	Type 3 **T** crack(s) linking right tip of the top flaw and left tip of the bottom flaw. There may be occasional short **S** segments present along the coalescence crack.

Figure 4.7. Crack coalescence categories as defined by Wong (2008). "S" and "T" in the images indicate shear and tensile cracks, respectively. Image taken from Wong (2008)

A brief description of the nine categories shown in Figure 4.7 is appropriate at this point:

- **Category 1**: No coalescence occurs, despite the presence of tensile wing cracks and secondary cracks.
- **Category 2**: Indirect coalescence occurs when two or more cracks are involved in coalescence. In category 2 coalescence, it is impossible to follow a single coalescence crack from one flaw to the other.
- **Category 3**: The inner flaw tips are linked by one or two type 2 shear cracks. In this category, the coalescence cracks are coplanar with the flaws.
- **Category 4**: The inner flaw tips are linked by one or two type 1 shear cracks. In this category, the coalescence cracks are generally not coplanar with the flaws.
- **Category 5**: The inner flaw tips are linked by a combination of type 2 shear cracks and a type 2 tensile crack segment. The category is exemplified by an "S" shaped coalescence crack.
- **Category 6**: The inner flaw tips are linked by one or two type 2 tensile cracks.
- **Category 7**: The two flaws are linked by one type 1 tensile crack. The crack can either propagate from the tip of one flaw to the face of the other flaw or vice versa.
- **Category 8**: The flaw tips on the same side of both flaws are connected by a tensile crack. This crack is not considered a tensile wing crack because it curves opposite the direction of a normal tensile wing crack. Some short segments along the crack may be shear in nature.
- **Category 9**: The right tip of the left flaw and the left tip of the right flaw are connected by a type 3 tensile crack. Some short segments along the crack may be shear in nature.

Most coalescence patterns observed in granite also fit into this framework. In low-angle (β = 0° and 30°) coplanar flaw geometries with L = 2a, however, some of the coalescence patterns observed did not seem to fit into any previously defined coalescence category. The pattern observed most closely resembles category 2 (indirect) coalescence. The new pattern was different, however, in the type of cracks involved in coalescence. Tensile cracks extending down the center of the specimen were involved in this new category. Two examples will serve to illustrate this coalescence pattern.

For each example, a simplified sketch of the test progress is shown. Only cracks (and not white patches) are displayed because they are the relevant features for this discussion. In each case, a crack is given a letter identifier followed first by the opening type (T for tensile or S for shear) and then by a number indicating the relative order that crack has opened in. In some cases a crack opened with both shear and tensile portions. When this is the case, the opening type is listed as TS.

The first example is test Gr 2a-0-0 B and is shown in Figure 4.8. In step one, tensile crack A opened downward from above the bridge area. After this, tensile crack B opened upward from below the bridge area and tensile wing cracks C and D opened. In step two, tensile crack E connected cracks B and C. Step three saw the development of tensile wing cracks F, G, and H. Finally, in step four, tensile crack I connected cracks A and F and the tensile/shear crack J connected cracks A and E. Coalescence in this example involves 6 cracks (from left to right in step four of Figure 4.8: F, I, A, J, E, and C). This would normally be classified as category 2 coalescence, but the strong influence from secondary cracks coming into the bridge area from above and below makes this case abnormal.

Figure 4.9 illustrates the crack development for specimen Gr 2a-0-0 C. In this example, the final sketch could easily be interpreted as a traditional category 2 coalescence, but knowing the history of the specimen shows another mechanism in action. In step one, tensile crack A came down from above the bridge area, tensile wing cracks B and C developed on the right flaw, tensile crack D opened upward from below the bridge area, and tensile wing cracks E and F opened on the left flaw. In step two, tensile crack F connected tensile crack D to the junction of tensile crack E and the left flaw. At the same time, tensile crack A connected to the right flaw with shear crack G. Finally, tensile cracks A and F were connected by tensile crack H. The final pattern appears as if both inner flaw tips have two tensile wing cracks with the inner wing cracks connected by a secondary tensile crack. However, these inner cracks originated from above and below the bridge area before becoming involved in coalescence.

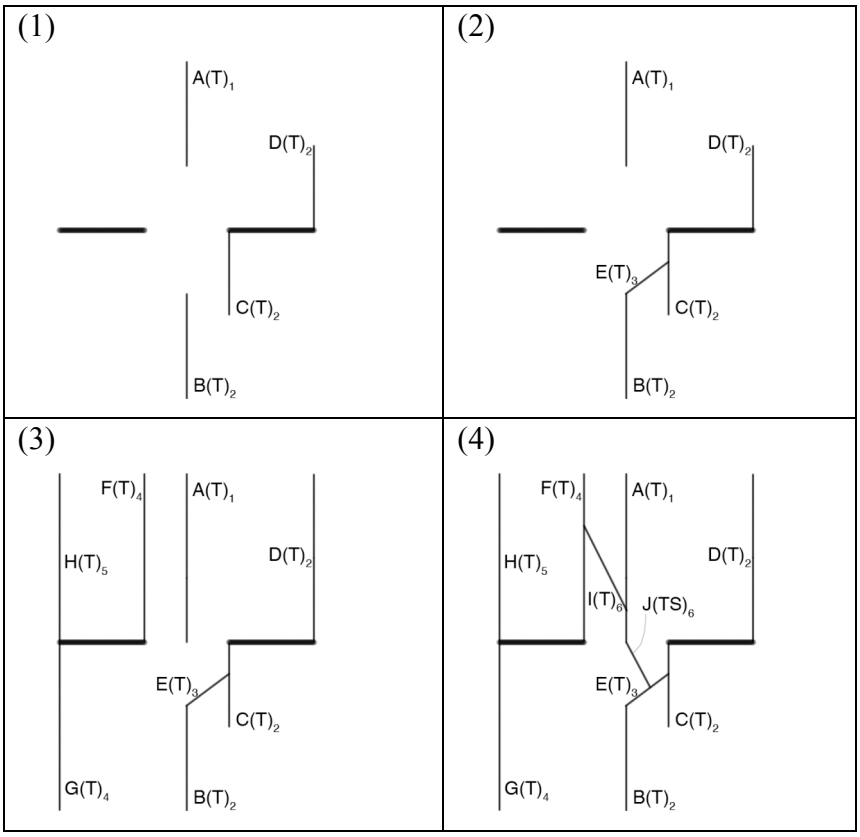

Figure 4.8. Development of cracks in specimen Gr 2a-0-0 B. Refer to text for notation explanation.

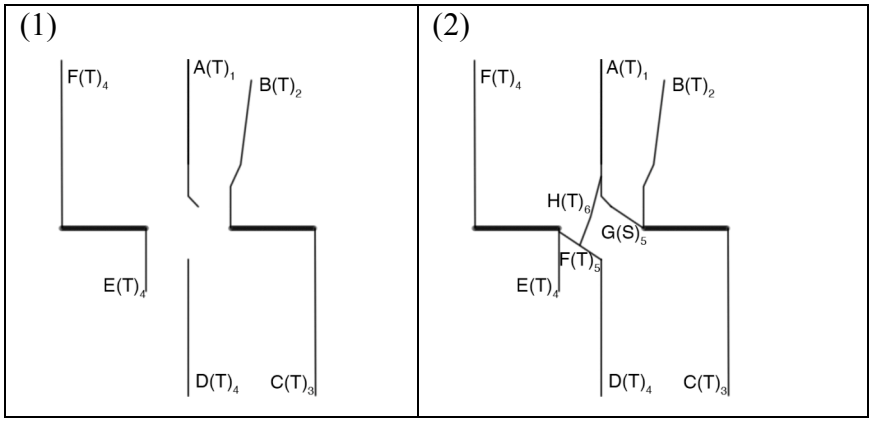

Figure 4.9. Development of cracks in specimen. Refer to text for notation explanation.

This new coalescence pattern was called "2*". It was not given a new category number because – while it was a new pattern – it is still a type of indirect coalescence.

4.3.2 Coplanar Flaws Separated by "2a"

Detailed interpretations of each experiment involving coplanar flaws separated by "2a" are presented in Appendix G. All experiments were conducted with end pieces having vertical teeth as mentioned in the platen discussion in Section 3.4.2. Figure 4.10 summarizes the coalescence categories observed.

	β = 0°	**β = 30°**	**β = 45°**	**β = 60°**	**β = 75°**
α = 0°	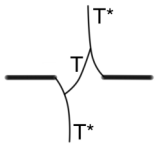 2* (1)	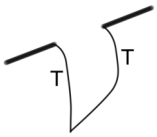 2 (1)	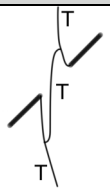 2 (1)	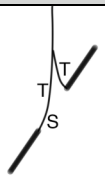 2 (1)	 5 (3)
	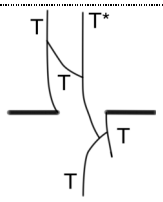 2* (2)	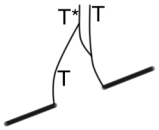 2* (1)	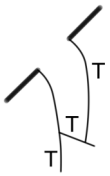 2 (1)	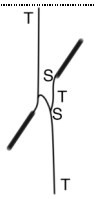 2 (1)	

Figure 4.10. Coalescence patterns observed in granite for coplanar flaws separated by ligament length 2a. The numbers below the sketches indicate first the category of coalescence and then (in parentheses) the number of specimens exhibiting that behavior. "T*" indicates a central tensile crack involved in coalescence. Refer to Section 4.3.1 for an explanation of coalescence categories.

Coalescence behavior varied with flaw inclination angle β. Horizontal flaw pairs (β = 0°) exhibited indirect coalescence with the involvement of vertical cracks extending into the bridging area (category 2*, see Section 4.3.1). In two out of three of the tested specimens, vertical tensile cracks appeared first. Tensile wing cracks then appeared. Coalescence followed with the wing cracks and vertical cracks connecting with tensile or shear cracks. In the third tested specimen, the order of crack formation was slightly different, while the end result was the same. The vertical tensile cracks connected to the flaw tips instead of the

tensile wing cracks. Coalescence then occurred when a tensile crack connected these two vertical cracks.

When β increased to 30°, two different coalescence categories were observed. One specimen coalesced indirectly with two tensile wing cracks connecting below the bridging zone. In the second specimen, indirect coalescence was observed, but with a vertical tensile crack extending down toward the bridging area. Different from the horizontal flaws, the tensile wing cracks were the first cracks to appear. The vertical tensile crack then appeared and specimen coalescence followed when tensile wing cracks from both flaws extended and connected with the vertical crack.

For intermediate flaw inclination angles (β = 45° and 60°), coalescence was indirect (category 2). Tensile wing cracks either connected directly with one another or with a third crack connecting the two tensile wing cracks.

Specimens with steeply inclined flaws (β = 75°) were the only ones to exhibit direct coalescence. In all three tested specimens, the two flaws were linked by a single, S-shaped crack consisting of a short shear portion adjacent to both inner flaw tips and a central tensile crack connecting these two shear cracks (see Figure 4.10). This mode of coalescence is category 5. In two of the three tested specimens, the coalescing crack could be seen as extending from one flaw tip to the other. In the third specimen, however, shear cracks initiated at both flaw tips at the same time as small tensile cracks in the bridging zone.

4.3.3 Stepped Flaws Separated by "2a"

As mentioned in Section 3.2, stepped flaws refer to geometries with a 60° bridging angle. Detailed interpretations of each experiment involving stepped flaws separated by "2a" are presented in Appendix G. All experiments were conducted with end pieces having vertical teeth as mentioned in the platen discussion in Section 3.4.2, Figure 4.11 summarizes the coalescence categories observed.

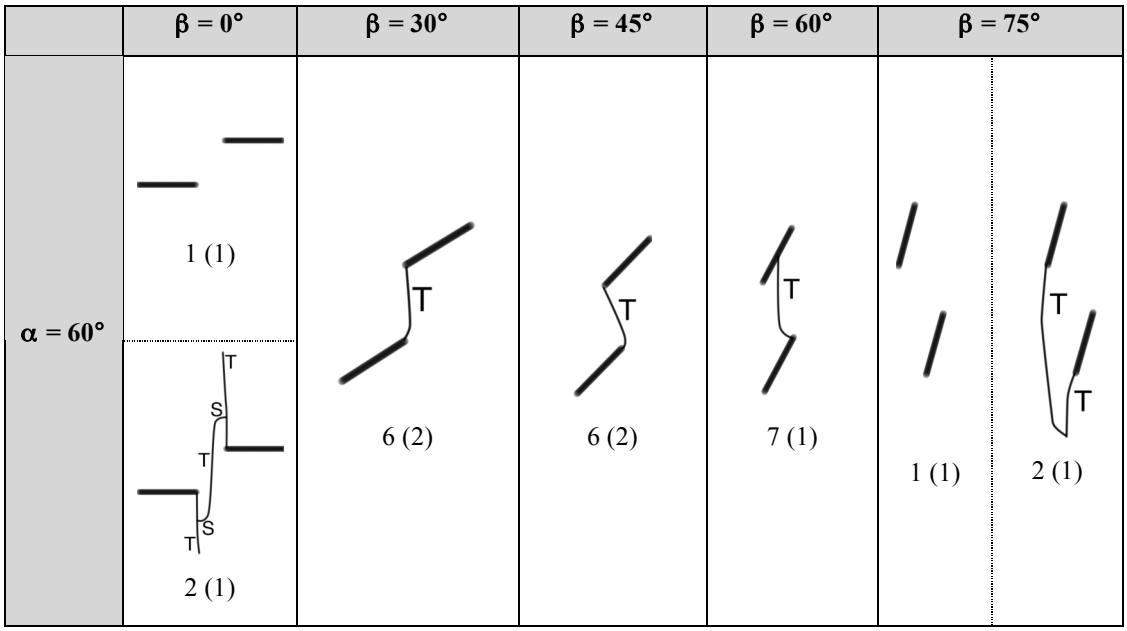

Figure 4.11. Coalescence patterns observed in granite for stepped flaws separated by ligament length 2a. The numbers below the sketches indicate first the category of coalescence and then (in parentheses) the number of specimens exhibiting that behavior. Refer to Section 4.3.1 for an explanation of coalescence categories.

Unlike coplanar flaws for L = 2a, indirect coalescence was the exception rather than the rule. For both horizontal (β = 0°) and steeply inclined flaws (β = 75°), one of the tested specimens coalesced indirectly while the other did not coalesce at all. In the specimens that did not coalesce, tensile wing cracks appeared on both flaws before eventual specimen failure. In the case of the specimen with horizontal flaws that did coalesce, the S-shaped coalescing crack consisted of short shear portions and one large tensile portion connecting two tensile wing cracks. This was the only specimen with any shear cracks involved in coalescence. The specimen with flaws inclined at 75° coalesced with two tensile wing cracks connecting with one another below the left flaw tips.

For all specimens with intermediate flaw inclinations (β = 30°, 45°, and 60°), coalescence was direct. For β = 30° and 45°, coalescence occurred with type 2 tensile wing cracks (refer to Figure 4.6 for crack types). For β = 60°, only one specimen was successfully tested and

coalescence occurred with a type 1 tensile wing crack extending from one flaw to the face of the other flaw.

4.3.4 Coplanar Flaws Separated by "a"

Detailed interpretations of each experiment involving coplanar flaws separated by "a" are presented in Appendix I. All experiments were conducted with solid end pieces as mentioned in the platen discussion in Section 3.4.2. Figure 4.12 summarizes the coalescence categories observed.

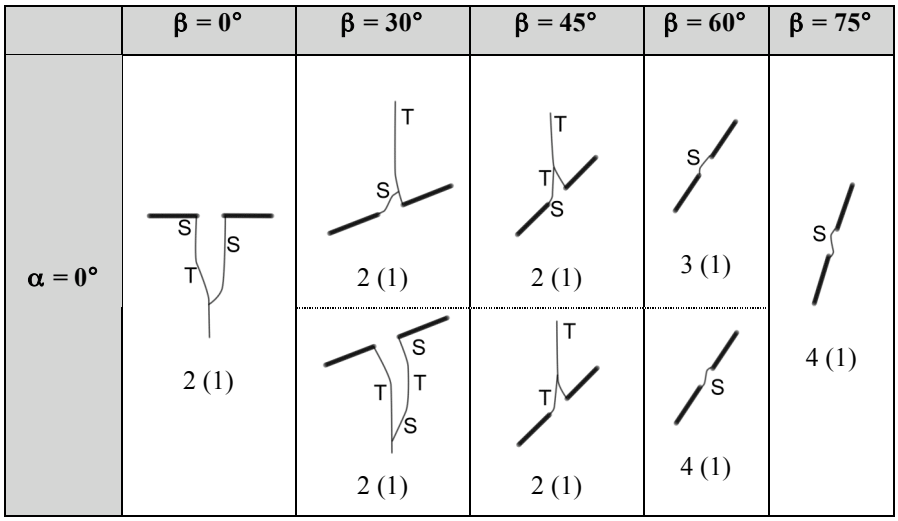

Figure 4.12. Coalescence patterns observed in granite for coplanar flaws separated by ligament length a. The numbers below the sketches indicate first the category of coalescence and then (in parentheses) the number of specimens exhibiting that behavior. Refer to Section 4.3.1 for an explanation of coalescence categories.

Indirect coalescence is the only mode of coalescence for low and intermediate flaw inclinations (β = 0°, 30°, and 45°). For these geometries shear cracks were involved in coalescence in all but one of the tested specimens. Shear cracks involved in indirect coalescence were often very long. This was different from shear cracks involved in indirect coalescence for geometries with L = 2a, which were often very short (if they existed at all).

For the two steep flaw inclinations (β = 60° and 75°), direct coalescence was observed. The coalescing crack in all three tested specimens was a shear crack. In two out of the three tested specimens, the shear crack was a type 1 shear crack (refer to Figure 4.6 for a description of crack types), while the remaining specimen coalesced with a type 2 shear crack.

4.3.5 Stepped Flaws Separated by "a"

Detailed interpretations of each experiment involving coplanar flaws separated by "a" are presented in Appendix I. All experiments were conducted with solid end pieces as mentioned in the platen discussion in Section 3.4.2. Figure 4.13 summarizes the coalescence categories observed.

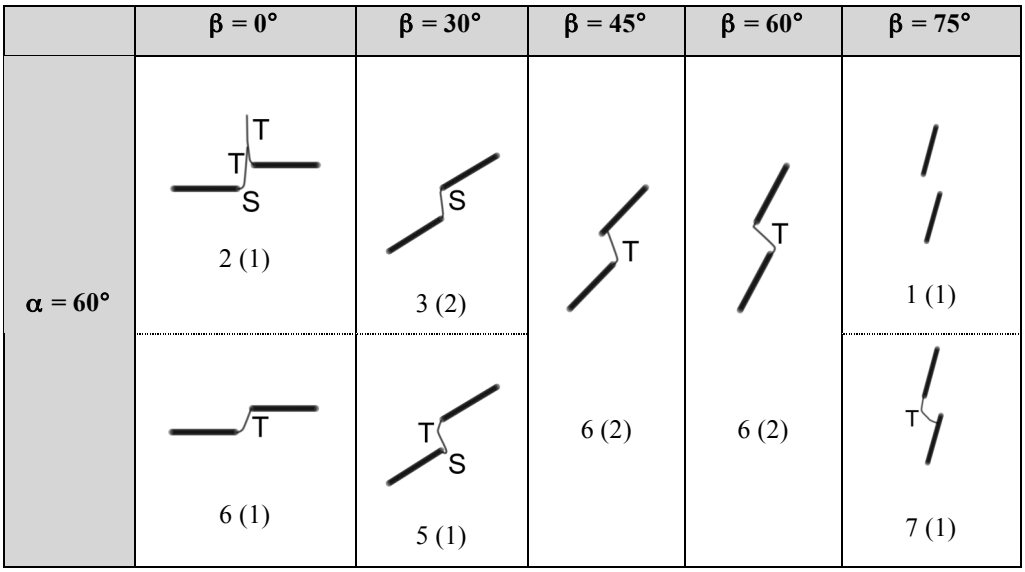

Figure 4.13. Coalescence patterns observed in granite for stepped flaws separated by ligament length a. The numbers below the sketches indicate first the category of coalescence and then (in parentheses) the number of specimens exhibiting that behavior. Refer to Section 4.3.1 for an explanation of coalescence categories.

Indirect coalescence was only observed in one of the tested specimens for stepped flaws with L = a. This specimen had horizontal flaws (β = 0°). Coalescence was achieved with a short shear wing crack transitioning to a tensile crack that connected to a tensile wing crack from

the other flaw. The other horizontal specimen tested coalesced directly with a single type 2 tensile crack.

Direct coalescence by type 2 shear crack was observed in two out of the three tested specimens with flaws inclined at 30°. In the third tested specimen, a tensile wing crack extended from the upper flaw's inner tip toward the lower flaw's inner tip. It then transitioned to a shear crack before connecting to the lower flaw's inner tip.

Intermediate flaw inclinations ($\beta = 45°$ and 60°) exhibited exclusively category six coalescence. In all four tested specimens, a type 2 tensile crack connected the two inner flaw tips.

For steeply inclined flaw pairs ($\beta = 75°$), one specimen did not coalesce while the other coalesced with a type 1 tensile crack connecting the inner tip of one flaw with the face of another.

4.4 Effect of Bridging Angle

As can be seen by comparing Figure 4.10 with Figure 4.11 (as done in figure 4.14) and Figure 4.12 with Figure 4.13 (as done in Figure 4.15), changing the bridging angle from coplanar to stepped has one major effect: increasing the likelihood of direct coalescence. Neither Figure 4.14 nor Figure 4.15 show all the coalescence patterns observed for each geometry. Rather, they both show the distinction between geometries with specimens that coalesced directly and geometries with no specimens that coalesced directly.

L = 2a	β = 0°	β = 30°	β = 45°	β = 60°	β = 75°
α = 0°	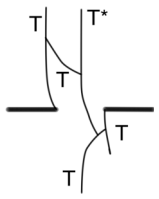	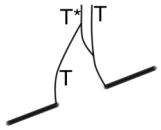	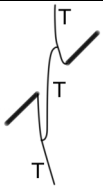	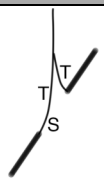	
α = 60°	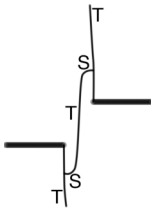	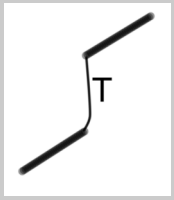			

Figure 4.14. Comparison of Figure 4.10 and Figure 4.11 showing the effect of bridging angle α on coalescence pattern for tested geometries with L = 2a. Highlighted geometries coalesced directly while those that are not highlighted coalesced indirectly.

As can be seen in Figure 4.14 only one out of the five tested coplanar geometries for L = 2a had at least one specimen coalesce directly (25% of the tested specimens coalesced directly). When the flaws were stepped, three out of the five tested geometries had at least one specimen that coalesced directly (56% of the tested specimens coalesced directly).

L = a	β = 0°	β = 30°	β = 45°	β = 60°	β = 75°
α = 0°	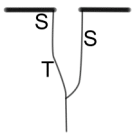	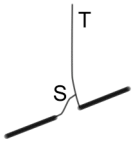	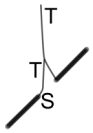	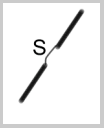	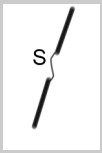
α = 60°	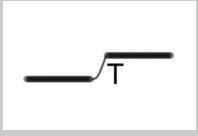	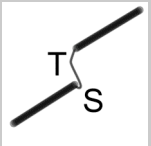	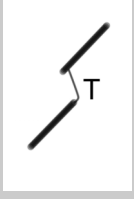	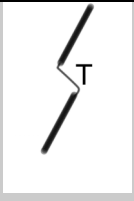	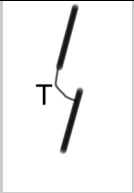

Figure 4.15. Comparison of Figure 4.12 and Figure 4.13 showing the effect of bridging angle on coalescence pattern for tested geometries with L = a. Highlighted geometries coalesced directly while those that are not highlighted coalesced indirectly.

A similar trend is seen for L = a. Figure 4.15 shows that only two out of the five tested coplanar geometries for L = a had at least one specimen coalesce directly (37% of the tested specimens coalesced directly). When the flaws were stepped, all five tested geometries had at least one specimen that coalesced directly (82% of the tested specimens coalesced directly).

For coplanar flaws (for both L = a and L = 2a) inclined at 30° and 45°, coalescence was always observed to be indirect. For stepped flaws at the same inclination, however, coalescence was always observed to be direct. This trend is reversed for steeply inclined flaws (β = 75°). In this case, direct coalescence was always observed for coplanar flaws while coalescence was always either nonexistent or indirect for stepped flaws at the same inclination.

4.5 Effect of Boundary Conditions

As mentioned in Section 3.4.2, the platens used for geometries with L = 2a were different than those used for geometries with L = a (brush platens for L = 2a, solid platens for L = a). Before changing platen type, however, two tests in the L = a series were run with brush platens (horizontal flaws, both coplanar and stepped). The data and observations made during these tests can be seen in Appendix J but are not included in any other section of this study.

For the coplanar horizontal flaws, maximum stress was comparable. The specimen tested with solid platens had a maximum stress ~10 MPa lower than the specimen tested with brush platens. In both cases, coalescence was indirect. Crack initiation occurred at 90% of maximum stress in the solid platen test while it occurred at 97% of the maximum stress in the brush platen test. Coalescence occurred nearly concurrent with failure in both tests.

For stepped horizontal flaws, maximum stress for the tests using solid platens was significantly greater than the maximum stress for the test using brush platens with (~35 Mpa higher on average). All three major events (crack initiation, coalescence, and maximum stress) were clustered in the test using brush platens. In tests using solid platens, however, the events were spread out.

4.6 Stress Analysis

4.6.1 Introduction

The previous sections of this chapter have focused on the fracturing behavior and coalescence behavior in Barre Granite. This section deals with observations made regarding the stress data recorded during tests.

4.6.2 Maximum Stresses

All specimens were loaded to failure, which was defined as the maximum stress. These peak stresses for granite specimens with L = 2a are shown in Figure 4.16 and for L = a in Figure 4.17.

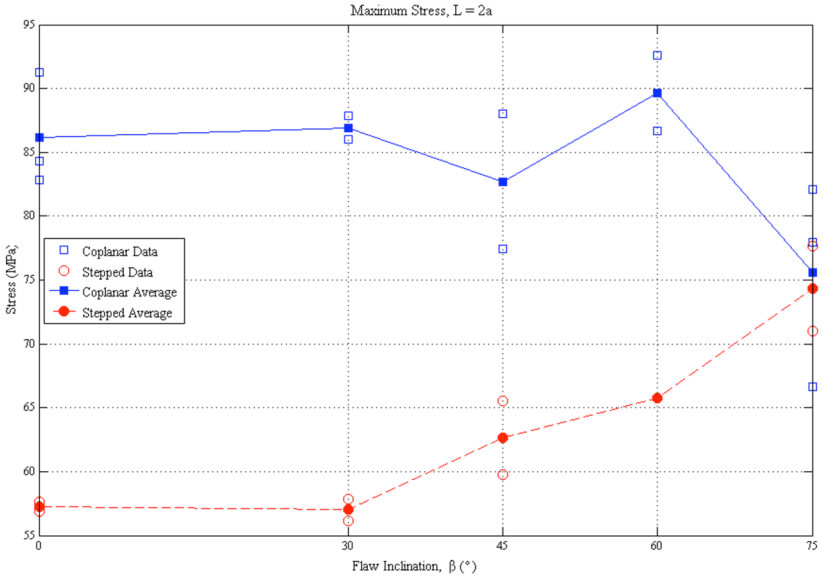

Figure 4.16. Maximum stresses for specimens with L = 2a. Hollow points represent actual data points while filled points and lines represent averages.

As can be seen in Figure 4.16, coplanar flaws had a higher maximum stress than stepped flaws for all flaw inclinations except β = 75°. Notable is the fact that the maximum stress for both coplanar and stepped geometries does not change significantly when flaw inclination increases from β = 0° to 30°. The general shape of the two curves is different beyond β = 30°. One can tell that a complex relationship exists between flaw pair geometry and

maximum stress: for stepped flaws, there is a general increase in maximum stress with increase in β. For coplanar flaws, however, no such relationship appears to exist, with the average maximum stress increasing and decreasing as β increases.

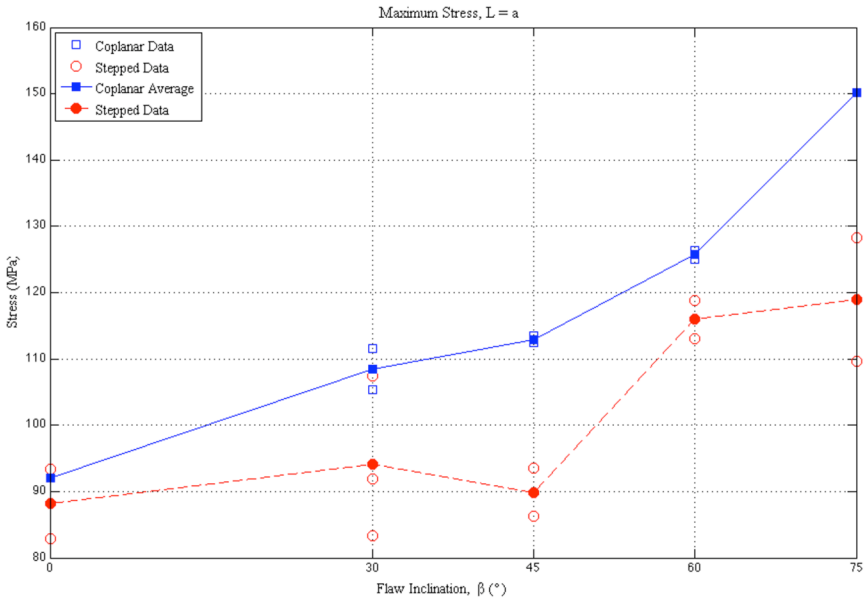

Figure 4.17. Maximum stresses for specimens with L = a. Hollow points represent actual data points while filled points and lines represent averages.

For L = a, coplanar flaws generally also had a higher average maximum stresses than stepped flaws. However, unlike the L = 2a geometries, the two averages shown in Figure 4.17 appear to follow a similar upward trend with increasing flaw inclination (the stepped flaw pair with β = 45° is the sole exception to this trend).

4.6.3 Crack Initiation Stress and Stress Ratio

Figure 4.18 shows the stress at which cracks first appear in specimens with L = 2a.

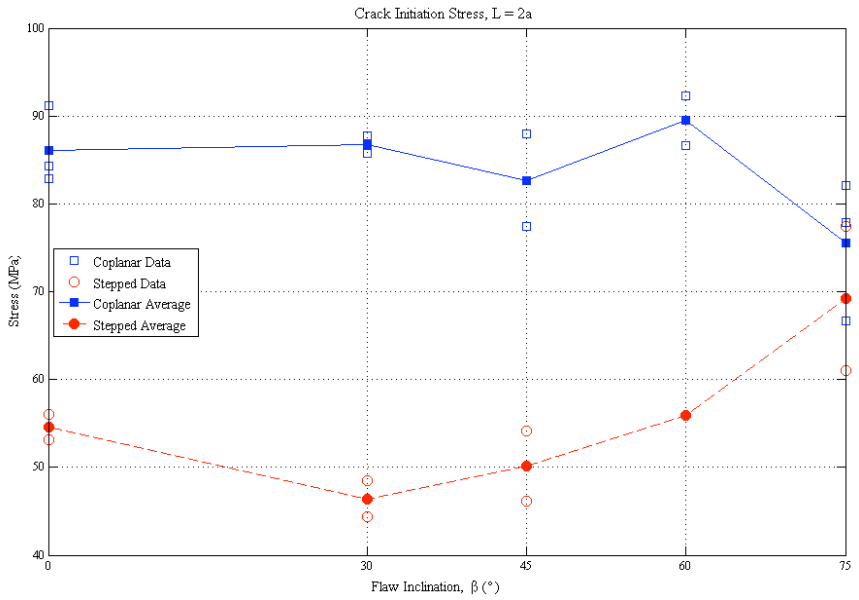

Figure 4.18. Crack initiation stress for specimens with L = 2a. Hollow points represent actual data points while filled points and lines represent averages.

Comparing Figure 4.16 with Figure 4.18, one can see that the shape of the curves and values of the crack initiation and maximum stresses are very similar for coplanar flaws with L = 2a. Stepped flaws with L = 2a have slightly different curve shapes and the crack initiation stress is lower than the maximum stress for most flaw inclinations. One can get a better idea by normalizing the crack initiation stress in the form of the crack initiation stress ratio, which is the ratio of the crack initiation stress to the maximum stress. This normalization is shown in Figure 4.19.

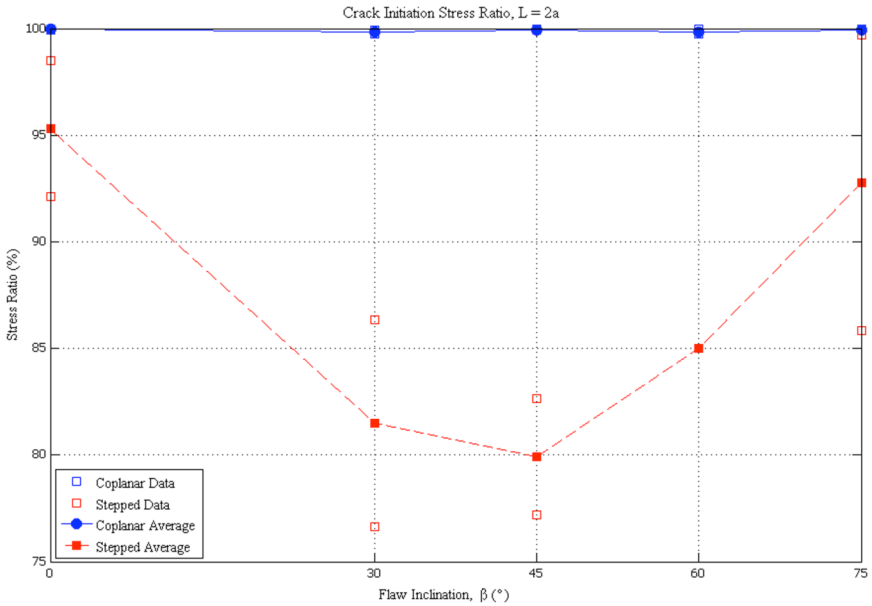

Figure 4.19. Crack initiation stress ratio for coplanar and stepped specimens with L = 2a. Hollow points represent actual data points while filled points and lines represent averages.

As can be seen in Figure 4.19, crack initiation in coplanar geometries occurred very close to failure while stepped flaw pairs have significantly different crack initiation stress ratios for all values of β tested for L = 2a.

A similar analysis can be made for L = a geometries, and this is shown in Figure 4.20 and Figure 4.21. . The curves shown in Figure 4.20 have similar shapes. The average crack initiation stress for coplanar flaws was higher than that for stepped flaws. The coplanar curve shows a small increase as β increases from 0° to 30° and continues to increase with larger values of β. The stepped data, however, does not show this same continuous increase. Once again, insight can be gained from examining the crack initiation stress ratio. Figure 4.21 shows the variation of the crack initiation stress ratio with β for coplanar and stepped specimens with L = a.

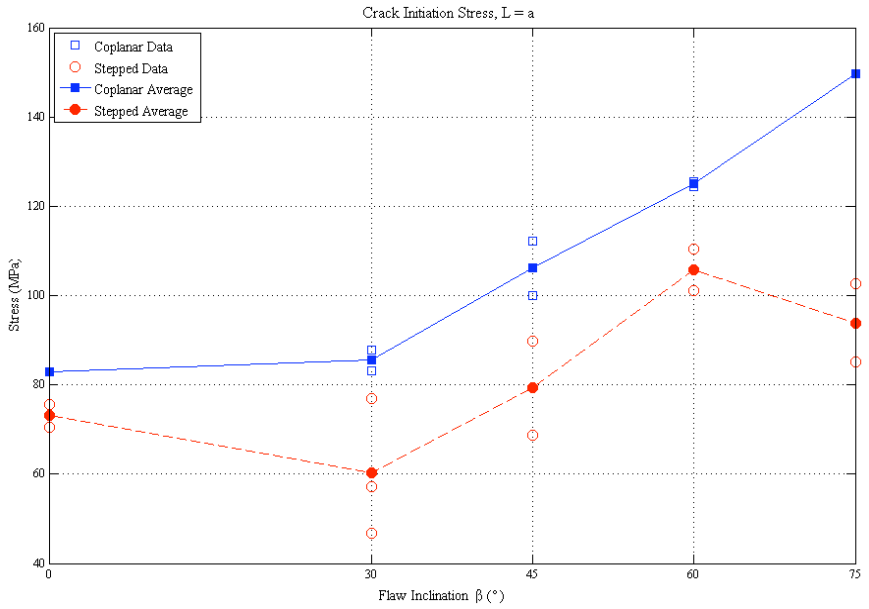

Figure 4.20. Crack initiation stress for coplanar and stepped specimens with L = a. Hollow points represent actual data points while filled points and lines represent averages.

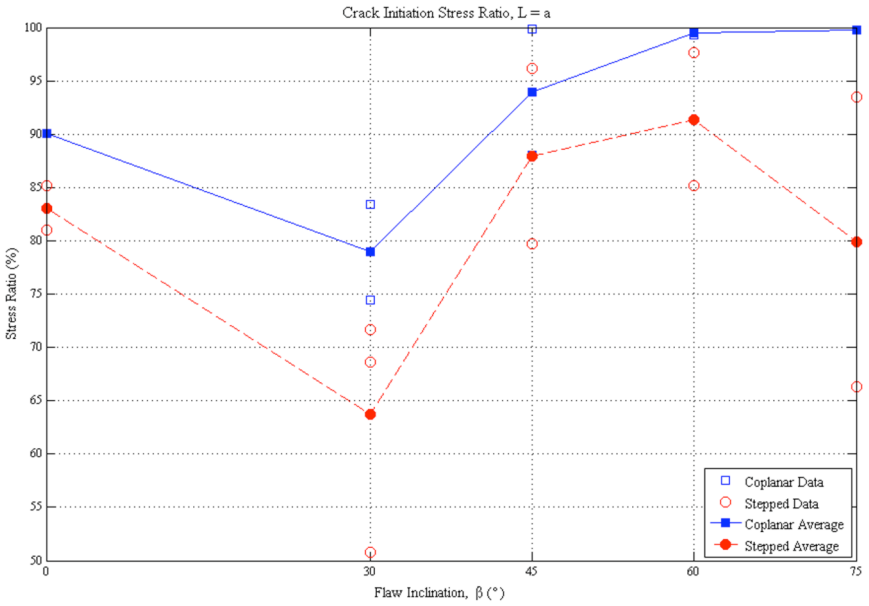

Figure 4.21. Crack initiation stress ratio for coplanar and stepped specimens with L = a. Hollow points represent actual data points while filled points and lines represent averages.

Figure 4.21shows that the crack initiation stress ratio for coplanar specimens with L = a is greater than that for specimens with stepped flaws. It also shows that both averages behaved similarly. However, the stepped flaws exhibited opposite behavior as β increased from 60° to 75°. With the exception of β = 60° and 75°, the crack initiation stress ratios for coplanar geometries with L = a were lower than corresponding coplanar flaws with L = 2a. For stepped flaws, the crack initiation stress ratio was higher for geometries with L = a only when β = 45° and 60° (see Table 4.1). When comparing the shapes of the curves for the two different ligament lengths, neither coplanar nor stepped flaws had shapes similar to their counterpart.

Table 4.1. Average crack initiation ratio for specimen geometries tested.

	β = 0°	**β = 30°**	**β = 45°**	**β = 60°**	**β = 75°**
L = 2a, α = 0°	100.0%	99.8%	99.9%	99.8%	100.0%
L = a, α = 0°	93.8%	78.9%	94.0%	99.4%	99.8%
L = 2a, α = 60°	95.3%	81.5%	79.9%	85.0%	92.8%
L = a, α = 60°	83.0%	63.7%	87.9%	91.4%	79.9%

4.7 Comparison with Martinez's Results

As mentioned previously, Martinez (1999) also performed uniaxial compression tests on Barre Granite specimens. Many of his geometries did not match the geometries tested in this study, but six coplanar geometries were identical (coplanar flaws with β = 30°, 45°, and 60°, L = 2a and a). Of these six geometries, those with L = 2a were tested with different boundary conditions than those used in this study; Martinez used solid platens as opposed to the platens with vertical teeth used here. Martinez observed different coalescence patterns than those shown in Section 4.3.4 for the most part. Table 4.2 provides a comparison of the two sets of observations with identical boundary conditions and Table 4.3 compares observations with different boundary conditions.

Table 4.2. Comparison of Martinez's observations and those made in this study with identical boundary conditions. Only for $\beta = 60°$ do the two sets of observations agree.

L = a, $\alpha = 0°$	$\beta = 30°$	$\beta = 45°$	$\beta = 60°$
Miller	Indirect	Indirect	Direct, Shear
Martinez (1999)	Direct, Shear	Direct, Shear	Direct, Shear

Table 4.3. Comparison of Martinez's observations and those made in this study for different boundary conditions. The two observations do not match for any of the flaw inclinations

L = 2a, $\alpha = 0°$	$\beta = 30°$	$\beta = 45°$	$\beta = 60°$
Miller	Indirect	Indirect	Indirect
Martinez (1999)	Direct, Shear	Direct, Shear	Direct, Shear

Martinez (1999) observed direct coalescence for all coplanar geometries. This does not agree with the observations presented in Section 4.3.4, where indirect coalescence was the most common coalescence pattern. For $\beta = 60°$, the observations do agree.

Martinez (1999) made broad observations that can also be compared with the observations made in this study. Similar to this study, Martinez noted that failure of granite specimens was sudden, cracks normally follow grain boundaries (but with some grain breakage occurring), and that horizontal cracks sometimes appear in tests. Martinez did observe a "brighter area"

between the inner flaw tips near coalescence in granite. He did not make further observations, however, due to difficulty seeing these areas. Different from this study, Martinez observed that tensile wing cracks always initiated from flaw tips (could be explained by poorer image resolution). Possible sources for disagreements between the two studies include:

- Both studies used Barre Granite but were ordered from different quarries and nearly a decade apart.
- Specimens may have been tested with the rift oriented differently.
- Fractographic observations after tests are often misleading, showing shear-indicative surfaces when a crack originally opened in tension (see Martinez, 1999 for a very good discussion of this problem).
- Hairline tensile cracks in granite are extremely hard to distinguish and generally require post-processing of images to become visible.

4.8 Comparison with Wong's Results

4.8.1 Cracking Processes

Section 4.2.2 describes how the nature of tensile and shear cracks differ between gypsum, marble and granite. Previously, Wong (2008) noted that tensile cracks were more common in marble than in gypsum. In other words, for identical flaw geometries, the crack pattern changed between materials. This change reflected an increasing likelihood for tensile crack formation in marble when compared with gypsum. Wong (2008) suggested that tensile cracking increased with grain size (see Table 4.4 for a grain size comparison of gypsum, marble, and granite). In granite, this proposed trend was also observed. It should be noted, however, that comparisons are only possible between all three materials for specimens with coplanar specimens with L = 2a. Wong did not test specimens with L = a. A comparison of coalescence patterns in all three materials can be seen in Section 4.8.3..

Table 4.4. Grain sizes of the tested materials

Material	Grain Size
Molded Gypsum*	50 μm long and 2 μm wide
Carrara Marble*	50 μm – 200 μm average
Barre Granite	0.87 mm^{+} – 2.54 mm^{++} average

*- from Wong (2008) SEM investigation, + - from Iqbal and Mohanty (2006),
++ - from Goldsmith et al. (1976)

A possible explanation for increased tensile cracking with grain size is as follows: larger grains increase the shearing resistance of a material as explained below. This increased shearing resistance makes it less likely for a shear crack to initiate. It has no effect on the stress needed to initiate a tensile crack. As a specimen is loaded, both compressive and tensile stresses exist. As shear cracks are less likely to initiate due to increased shearing resistance, tensile cracks become more likely to initiate. Wong (2008) also observed this effect when performing parametric studies in his numerical modeling section.

The question as to why shearing resistance increases with grain size needs to be discussed. As described in Section 4.2.2, tensile cracks commonly appear to initiate along grain boundaries. Shear cracks that were not obscured by surface spalling were observed to do the same. As a result, the larger the grain size, the more surface roughness a shear crack will have, increasing its shearing resistance. This concept is illustrated in Figure 4.22.

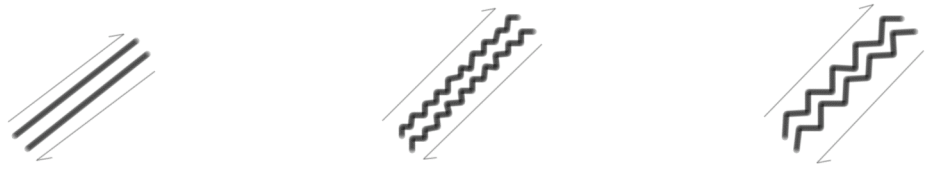

(a) (b) (c)

Figure 4.22. Illustration of increased shearing resistance with increasing grain size. As the grain size increases from gypsum (a) to marble (b) to granite (c), the size of asperities grows as well, making shearing more difficult.

Figure 4.22 shows a concept known as aggregate interlock in the concrete literature (MacGregor, 1964; Fenwick and Paulay, 1968; Taylor, 1970; Kani et. al, 1979; Sherwood et. al, 2007). Through the presence of aggregates, both shear and compression stresses can be transmitted across a crack. As such, larger maximum aggregate size has been found to yield a higher failure shear stress (Sherwood et. al, 2007).

As mentioned in Sectin 4.2.2, surface spalling obscured initiation of some shear cracks. Other shear cracks, however, were visible and observed to mostly propagate along grain boundaries. Occasionally single grains were observed to shear, although this was rare. Martinez (1999) also observed that cracks (both shear and tensile) initiated and propagated along grain boundaries. He did note some grain breakage in his fractography studies. He reasoned that most of this grain breakage was not from shear crack initiation and propagation. Rather, after a crack had initiated as a tensile crack, the grain breakage was from material sliding along the crack face at a later point in the test. Grain breakage at fracture initiation was never observed during his experiments. Martinez also noted that cracks propagate next to biotite grains most commonly.

4.8.2 White Patches

While gypsum did not display any observable white patching during unconfined compression tests (Wong, 2008), both marble and granite specimens did. As previously noted in Section 4.2.1, however, white patches in granite were different than those observed in marble by Wong (2008). Figure 4.23 shows typical white patches for both granite (a) and marble (b).

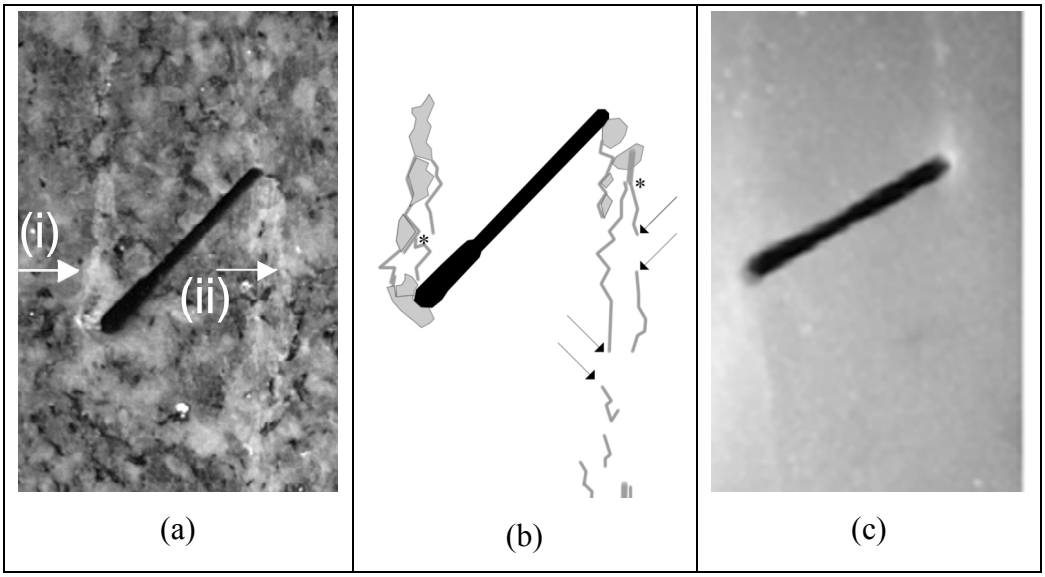

Figure 4.23. White patching in granite (a). As in Figure 4.1, (i) indicates a diffuse white patch while (ii) indicates a linear portion. Analysis sketch of same white patching in granite (b), where "*" indicates branching and the arrows point to a linear feature stopping and starting (see text). In marble (c), the two white patches extending from the flaw tips are linear features.

While granite included an additional type of white patch (diffuse), the linear white patches were also different in nature, as can be see when comparing Figure 4.23 (a) and (c). Linear white patches in granite often branched, as can be see in Figure 4.23 (b). One linear feature branches below the right tip and another branches above the left tip. Following the white patches under the right tip, one sees that they typically do not follow smooth, straight lines, but weave from side to side. As indicated by the arrows in Figure 4.23 (b), the linear white patches also are often not continuous, but stop and start. In comparison, the linear white patches shown in marble in Figure 4.23 (c) are easy to follow and do not branch. It is important to emphasize that these differences are noted at the macroscopic level.

Wong (2008) investigated the nature of the white patches observed in marble with a scanning electron microscope (SEM). For white patches preceding tensile cracks (as is the white patch shown for marble in Figure 4.24), he found the white patches were the consequence of both inter-granular and intra-granular microcracks (similar to the boundary-following and through-going features identified in this study, see both Figure 4.2 and Figure 4.25). Within

these zones of microcracking (process zones), a dominant microcrack (with both inter-granular and intra-granular microcracks) was flanked by shorter orthogonal intra-granular microcracks in white patches preceding a tensile crack. For white patches preceding a shear crack, microcracking zones developed in an en echelon manner. Microcracks in these zones are oriented nearly vertically and then link to form the coalescing crack. Wong (2008) also observed some spalling features in white patches preceding a shear crack.

No SEM investigations were performed in this study. Some comparisons can, however, be made. Wong (2008) noted that at the microscopic level, the microcracks that composed white patches in marble followed tortuous paths. These paths were not dissimilar to those followed by boundary-following linear white patches in granite. When comparing the sketches in Figure 4.24, more, smaller secondary microcracks (compared to the main, long microcrack) exist in marble than smaller linear features in granite. Marble appeared to have a more even ratio of intra-granular features to inter-granular features than granite's ratio of boundary-following features to through-going features. Note, and this is important to remember, that the comparisons made in this paragraph and Figure 4.24 are made on quite different scales. To confirm what has been stated, it will be necessary to conduct a SEM investigation similar to that performed by Wong (2008).

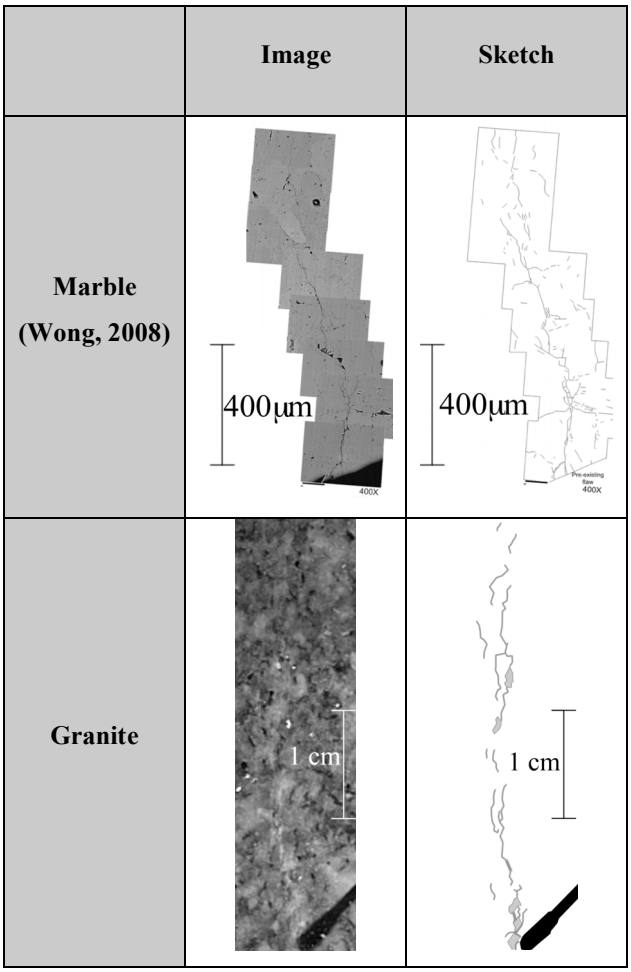

Figure 4.24. Comparison of SEM image composite in marble (from Wong, 2008) and linear white patch in granite. For ease of viewing, sketches are also provided.

Chen et al. (1999) investigated the relationship between microcracking and splitting planes (the same planes as described Section 3.3.3) in Inada Granite – a granite from Japan (splitting planes are the three planes used in quarrying). In order of increasing resistance to rock cleavage, they are: the rift, grain and hardway planes. The rift and grain planes are generally the preferred orientation of microcracks, with the rift plane being the primary orientation (Dale, 1923; Osborne, 1935; Isnard and Leymarie, 1964; Peng and Johnson, 1972; Simmons et al., 1975). Chen et al. (1999) used the fluorescent technique to visualize microcracks with an optical microscope (see Nishiyama and Kusuda, 1994 for a better description of the fluorescent technique). In their investigation, they first traced each microcrack present (with

software, not by hand). They then identified three different kinds of microcracks (by hand): intra-crystalline (lying completely within a grain), inter-crystalline (extending from a grain boundary into a grain), and those lying completely along grain boundaries. These three types of microcracks are illustrated in Figure 4.25 (a) – (c). Parts (d) and (e) of Figure 4.25 show the two types of linear white patches identified in this study.

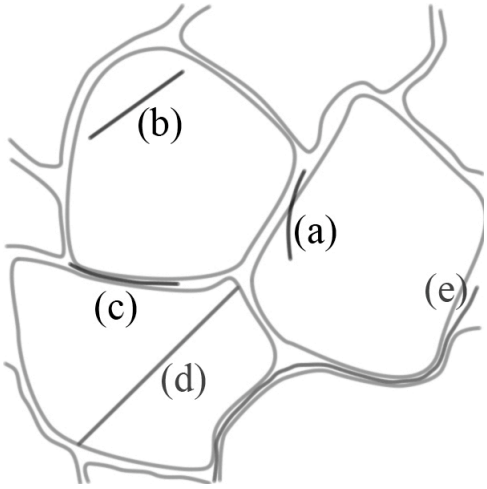

Figure 4.25. Illustration of the three types of microcracks identified by Chen et al. (1999): (a) inter-crystalline, (b) intra-crystalline, and (c) microcracks lying completely along grain boundaries. The two types of white patches identified in this study are illustrated as well: (d) through-going and (e) boundary-following.

Note that intra-crystalline microcracks (Figure 4.25 (b)) and through-going linear white patches (detail (d)) as well as microcracks lying along grain boundaries (detail (c)) and boundary-following linear white patches (detail (e)) are similar to one another. The difference between the two pairs is that they are features of different scales (microcracks not being visible to the naked eye, while linear white patches are). One additional difference exists between intra-crystalline microcracks (b) and through-going linear white patches (d): the microcracks do not necessarily span entire grains while the linear white patches were always observed to do so. Inter-crystalline cracks (Figure 4.25 (a)) are a hybrid of the other two types of microcracks.

Chen et al. (1999) found that intra-crystalline microcracks (Figure 4.25 (b)) were oriented predominantly along the grain plane and inter-crystalline microcracks (Figure 4.25 (a)) were oriented preferentially along the rift plane. Microcracks lying completely along grain boundaries (Figure 4.25 (c)) were found to have no preferred orientation. Overall, they found intra-crystalline microcracks dominated when compared to inter-crystalline microcracks or boundary-following microcracks. Both of the preferred planes for the granular microcracks (both intra- and inter-granular) according to Chen et al. (1999) correspond to faces not observed during testing in this study (the face observed in this study is thought to be parallel to the hardway plane – see Section 3.3.3).

The observations of Chen et al. (1999) do not match with the observations made in this study. In the hardway plane (the observed face in this study), boundary-following linear white patches were dominant in all cases. This discrepancy can be for several reasons:

- **Specimen orientation:** observations in this study were made on the hardway plane, which Chen et al. (1999) claimed was not the preferred orientation for either type of granular microcrack.
- **Material type:** microcrack orientations in Barre Granite may differ from those in Inada Granite.
- **Effect of load:** Chen et al. (1999) examined specimens that had not been loaded while linear white patches only appeared after specimens were loaded.
- **Mechanism:** white patches in granite have so far not been proven to be the result of microcracking. It is also not known if some microcracks cause a more visible effect at the macroscopic scale than others do.
- **Visual bias:** White patches were identified by eye in this study. It is possible boundary-following linear white patches are more likely to be identified by eye. Portions of white patches only partially entering grains (making them more similar to intra-crystalline microcracks) may not be identified.

To address these possible explanations, a microcrack investigation (either SEM or fluorescent technique) should be undertaken to understand the original microcrack

distribution as well as the evolution of microcrack type inside white patches (assuming microcracks cause white patches).

4.8.3 Coalescence

As discussed in Section 4.8.1, tensile cracks appear to be more prevalent as grain size increases from gypsum to marble to granite. Figure 4.26 shows the coalescence patterns for coplanar specimens with L = 2a made of gypsum, marble, and granite. This is the only comparable geometry series between this study and the experiments performed by Wong (2008). In the gypsum series, shear cracks were present in all (100%) tested specimens. In marble, shear cracks were present in five out of the seven (71%) coalescence patterns. In granite, only three out of the nine (33%) observed coalescence patterns contained shear cracks. It is interesting to note, however, that at high flaw inclinations ($\beta = 60°$ and $75°$), shear cracks are involved in coalescence in gypsum and granite specimens, but not in marble specimens.

Another interesting pattern emerging from Figure 4.26 is the effect of material on direct versus indirect coalescence (grey geometries are those with an indirect coalescence pattern). In four out of the five tested flaw inclinations for gypsum, direct coalescence was observed. In marble, direct coalescence was observed in only three flaw inclinations. In granite, it was only observed in one flaw inclination.

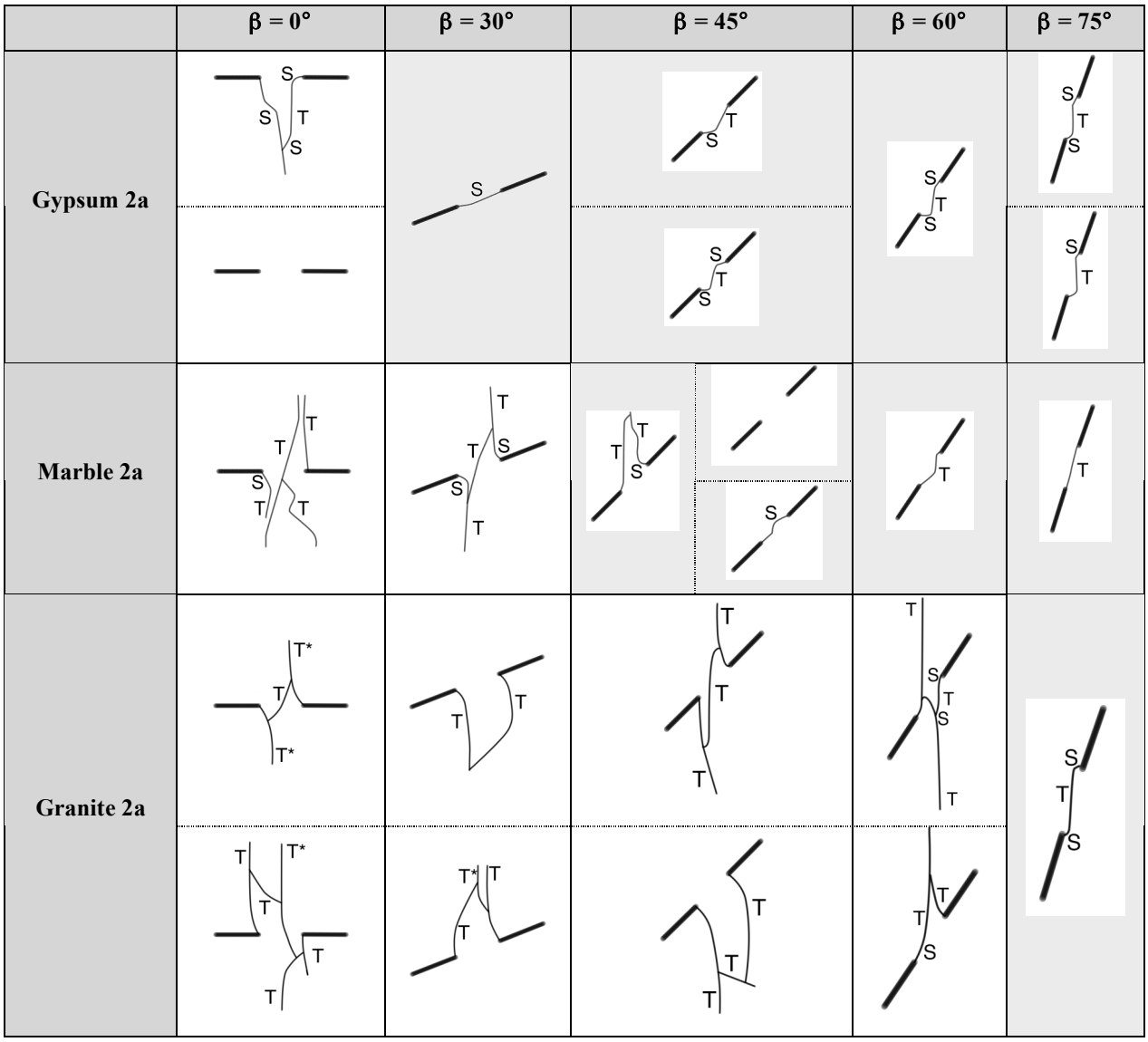

Figure 4.26. Summary of coalescence patterns for coplanar specimens with L = 2a for three different materials. Results for gypsum and marble are summarized from Wong (2008). Geometries with at least one direct coalescence pattern are highlighted with grey.

4.8.4 Stress Analysis

One major difference between marble and gypsum observed by Wong (2008) was the crack initiation stress ratio (the ratio between the stress of the first crack appearing and the maximum stress for a particular specimen). In marble, these cracks appeared much later (closer to maximum stress) in the test than in gypsum. This was also the case with granite, as can be seen in Figure 4.27. As was shown in Section 4.6.3, crack initiation in coplanar granite specimens with L = 2a occurs nearly coincident with failure. The crack initiation stress ratio for both marble and granite is consistently higher than in gypsum, with the exception of β = 75°. Once again, a comparison of all three materials is only possible for coplanar geometries with L = 2a.

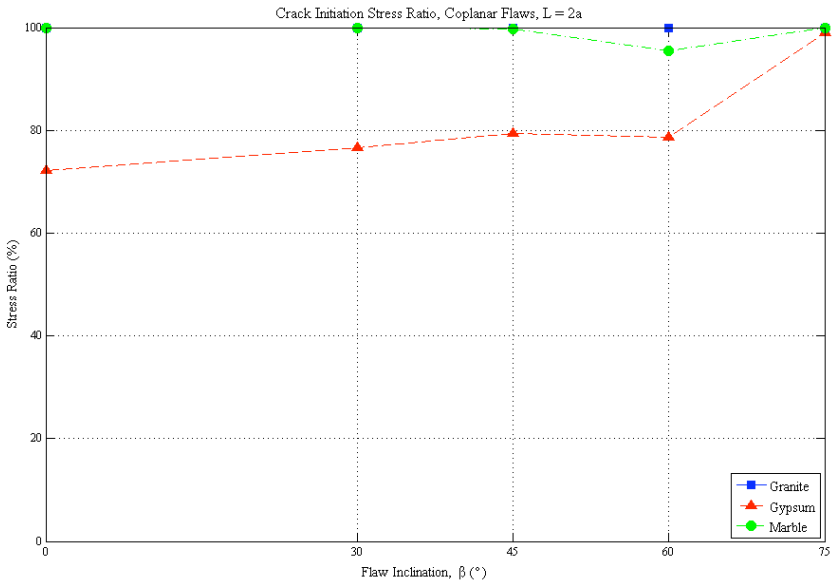

Figure 4.27. Comparison of average crack initiation stress ratio between granite, marble, and gypsum for coplanar specimens with L = 2a. Marble and gypsum results taken from Wong (2008).

Instead of comparing crack initiation stress ratios, Wong (2008) recommended comparing crack initiation in gypsum with white patch initiation in marble. Similar to the crack initiation stress ratio, the white patch initiation ratio is defined as the ratio of the stress level of white patch initiation to the maximum stress for a particular specimen. He found the crack initiation stress ratio of gypsum to be similar to the white patch initiation stress ratio in

marble in both magnitude and trend. Figure 4.28 shows this comparison as well as the average white patch initiation stress ratio observed in granite specimens with coplanar flaws and L = 2a. Here we see that granite did not follow the same trend as observed in marble. The magnitude, however, for all three materials is often similar.

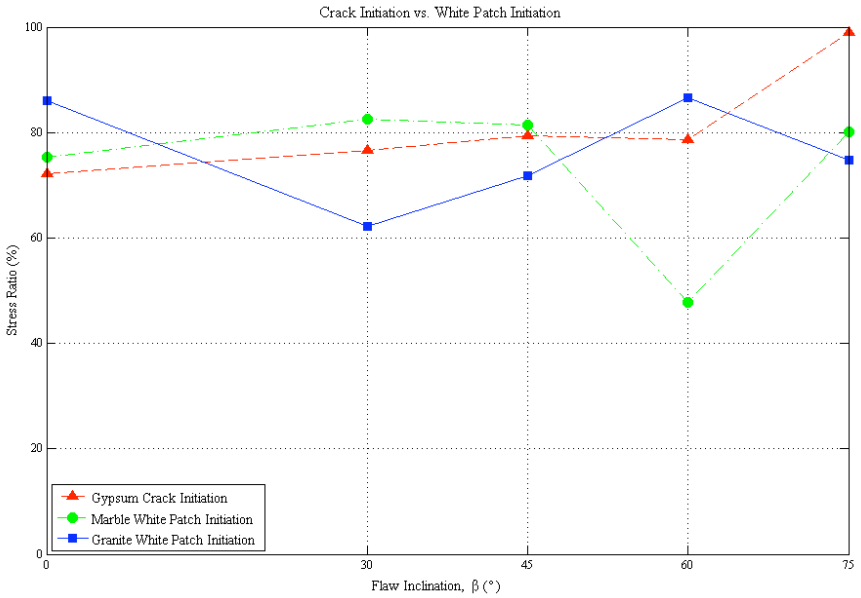

Figure 4.28. Comparison of average white patch initiation stress ratio in marble and granite with average crack initiation stress ratio in gypsum. Marble and gypsum results taken from Wong (2008).

4.9 Summary

Unconfined uniaxial compression tests were performed on prismatic specimens of granite with two artificial flaws. This chapter presented observations made regarding white patches, crack processes, coalescence patterns, and stress levels of different relevant events.

Two categories of white patches were observed in this study: diffuse and linear. Linear white patches could be further subdivided into boundary-following and though-going features. The white patches were observed to initiate prior to, concurrent with, or after crack initiation. Boundary-following linear white patches were the most prevalent of all the white patches by far.

Tensile cracks grew and propagated very quickly. They often initiated in zones having some white patches, although this was not always the case. Tensile cracks normally followed grain boundaries as they propagated. Tensile wing cracks did not always initiate at the tips of flaws, but rather in zones of white patching above or below flaw tips. These small tensile cracks then extended and connected with the nearest flaw tip.

Shear cracks generally initiated in conjunction with surface spalling, probably indicating a compressive state of stress. Diffuse grain lightening often preceded longer shear cracks. In observable shear cracks, it was seen that they generally initiate and propagate along grain boundaries, although some grain breakage was observed.

The coalescence patterns proposed by Wong (2008) were also appropriate for describing most patterns observed in this study. One pattern of indirect coalescence, however, had not been previously described (see Section 4.3.1) – In geometries with L = 2a and L = a, stepped flaws resulted in more cases of direct coalescence than did coplanar flaws. More shear cracking was seen in specimens with L = a than those with L = 2a, although this trend might not only be attributed to a change in ligament length, as the boundary conditions between the two series were also changed (solid platens and brush platens, respectively).

Crack initiation in specimens with coplanar flaws and L = 2a was always very close to specimen failure. Specimens with stepped flaws with L = 2a showed a greater variation in crack initiation with β (varying from 95% of failure stress for β = 0° to 80% of failure stress for β = 45°). For specimens with L = a, the crack initiation stress ratio for coplanar and stepped flaws exhibited similar variation in crack initiation stress ratio with β.

The variation in coalescence patterns seen for coplanar flaws with L = a does not agree with the observations of Martinez (1999). He observed direct coalescence for all coplanar flaws. Also the observation in this study that tensile wing cracks initiated away from flaw tips is different from Martinez' observation that wing cracks always initiate at flaw tip. Overall though, the cracking processes observed in the two studies were similar, with cracks propagating mostly along grain boundaries and fracturing being a very rapid process. Martinez (1999) also noted white patches, although he did not distinguish different types of

white patches or comment on their temporal relationship with cracking (other than to say that they appeared before coalescence).

Specimens with coplanar flaws and L = 2a allow one to compare the three materials: gypsum, marble, and granite. This is the only comparable series for all three materials. Wong (2008) tested gypsum and marble. Similar to gypsum, granite cracks propagate in a brittle manner. Failure is often sudden and cracks propagate quickly. Similar to marble, granite often forms white patches. The white patches in granite, however, can be subdivided into linear white patches and diffuse white patches (whereas only linear white patches were observed in marble). Also unlike marble, the white patch initiation stress ratio for granite does not follow the same trend as the crack initiation stress ratio for gypsum. It is, however, close to the same magnitude for most values of β. Finally, tensile coalescence cracks become more common from gypsum to marble to granite (see Figure 4.26), i.e. with increasing grain size.

Chapter 5. Pressurized Flaw Tests

5.1 Introduction

Crack coalescence in different types of rocks and different flaw geometries is of great interest in understanding failure processes. The tests in this study reported so far and in preceding studies on "dry" rock are essential first steps. However, natural rock masses are usually water saturated and, important in the context of this research, fractures can be artificially created by water pressure. Hydraulic fracturing (see, e.g. Gedly et al., 1989; Yew, 1997) is used extensively in petroleum applications and is of primary importance in enhanced geothermal systems where it is used to stimulate fractures. Understanding of crack coalescence under the influence of water pressure is therefore very important. This chapter describes a set of experiments designed to probe the effect of water pressure on crack coalescence and the next chapter reports results and observations of those tests.

5.2 Specimen Geometry

The tests were meant as a proof-of-concept forming the basis for future studies, so only one flaw pair geometry was tested. The geometry chosen was a-60-60. It was selected because it consistently led to direct coalescence in unconfined, uniaxial tests.

5.3 Testing Procedure

5.3.1 Introduction

A method to pressurize the water in the flaws of granite specimens was developed and is illustrated in Figure 5.1. Plates were attached to the front and back of specimens (Figure 5.1 (a)). These plates were used to contain a small volume of water inside the flaws. The water was connected to a cylinder and piston (Figure 5.1 (b)), which could be used to adjust the water pressure inside the flaws. The water pressure was measured by a transducer (Figure 5.1 (c)) and recorded by a data acquisition system (Figure 5.1 (d)). The user monitored the water pressure while it was recorded and could make adjustments accordingly. Changes in the water pressure were made using a motor (Figure 5.1 (e)) attached to the piston. After a

specified water pressure was reached, uniaxial compression tests were performed until specimen failure while the pressure was maintained.

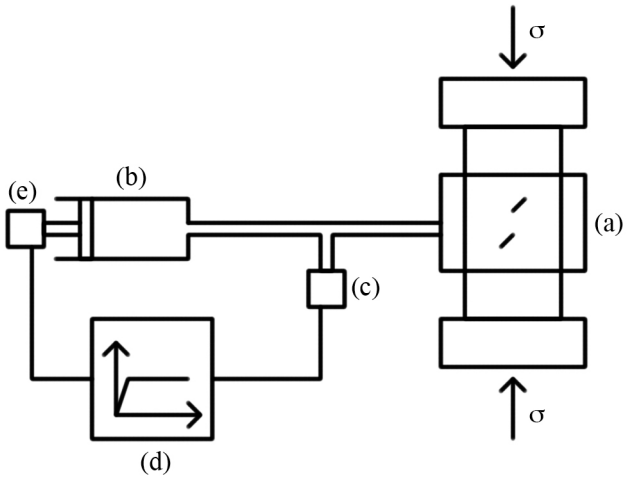

Figure 5.1. Components of system to pressurize flaws during compression test: (a) pressure plates (b) cylinder and piston (c) pressure transducer (d) data acquisition and motor control (e) piston motor.

5.3.2. Pressure Plates

To pressurize the flaws, a method to contain a small volume of water needed to be developed. Two competing boundary conditions were the deciding criteria for the design:

1. **Geometry.** Pressure should be applied to the inside of the flaws only.
2. **Uniformity.** Pressure should be uniform in all directions within the flaws.

To apply pressure exclusively inside the flaws, bladders have to be used. This method has two problems. To withstand the pressures being used, the bladders have to be made from a very stiff material. To transmit a uniform pressure to the faces of the flaws, however, the material needs to be very flexible. Even if a compromise between these two opposite demands could be made, manufacturing the bladders would be complicated and time consuming.

To apply pressure uniformly inside the flaws, water needs to be injected directly into the flaws. This can be done in a practical manner with plates holding a small volume of water in the flaws (see part (a) of Figure 5.2). While the water pressure is not applied exclusively to the inner faces of the flaws (see part (b) of Figure 5.2), the pressure is applied uniformly and the equipment can be built relatively easily. Figure 5.2 shows the basic design of the pressure plates.

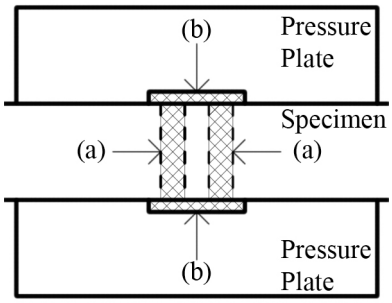

Figure 5.2. Two pressure plates hold a small volume of water (hatched area 'a') to be held inside the flaws but also have a small volume of water (hatched area 'b') between the specimen face and the pressure plate near the flaws.

As can be seen in Figure 5.2, two plates are needed. The back plate is made with steel and water is injected through it (see Figure 5.3 (a)). Water goes into a small recessed volume (Figure 5.3 (b)) sealed to the specimen with an O-ring. From this recessed volume, water is also able to enter the flaws (Figure 5.3 (c)). The front plate is made with acrylic – i.e. it is a transparent plate to allow one to observe the front face during compression tests. Once again, an O-ring was used to seal the front plate to the specimen, so there is a small volume of water between the specimen and the front plate (Figure 5.3 (d)), which is occupied by water. The recessed volume between the back plate and specimen (Figure 5.3 (b)) is necessary to guarantee water injection into both flaws. If the back plate were to be flush against the specimen, water might not be able to get into both flaws.

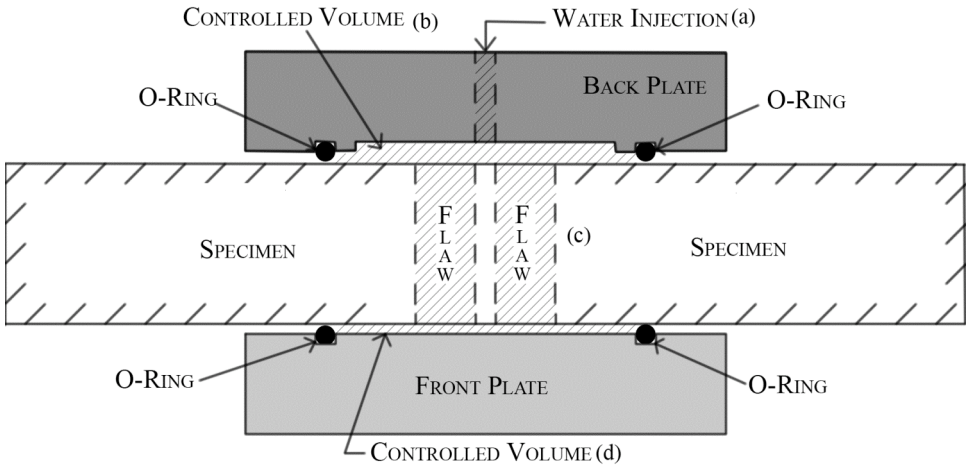

Figure 5.3. Water (hatched area) is (a) injected through the back plate into a (b) small recessed area between the back plate and the specimen. This area allows water to enter the flaws (c). Because the front plate is sealed to the specimen with an O-ring, a small volume (d) of water is between the front plate and specimen.

One final piece is needed for the pressure plate assembly (see Figure 5.4): a window frame. This steel frame is placed in front of the acrylic plate to reduce deflection, otherwise the O-ring might not make a good seal with the specimen at high water pressures. For the detailed designs of each component, see Appendix K.

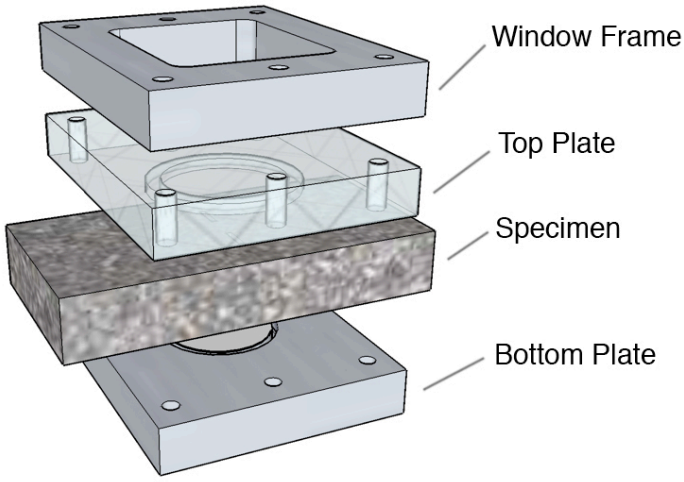

Figure 5.4. Pressure plate assembly.

Each tested specimen was sandwiched between the back and front plates, which were then bolted together with quarter-inch bolts. These bolts were used to hold the plates in the correct place as well as to produce a counter the force against the water pressure. This sandwiching did result in a confining force being applied to the front and back faces of the specimens. To ensure consistency amongst tests, the same torque was applied to each bolt prior to testing (this torque was calculated to match the force applied on each bolt by the pressurized volume).

5.3.3 Pressure Volume Controller

As discussed in Sections 5.3.1 and 5.3.2, a water control volume was used to pressurize the flaws. The pressure inside this volume was monitored and adjusted by a pressure volume controller (PVC). The PVC has several parts, which can be seen schematically in Figure 5.5. Figure 5.6 shows a photograph of the system before it is attached to the pressure plates.

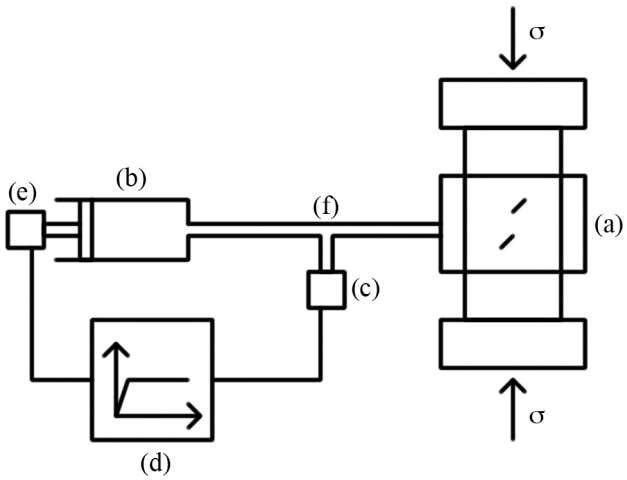

Figure 5.5. Pressure volume controller (PVC) consists of the following components: (a) pressure plates (b) cylinder and piston (c) pressure transducer (d) data acquisition and motor control (e) piston motor (f) copper pipe connected pressure plates and piston.

The entire controlled volume consisted of the volume inside the pressure plates (Figure 5.5 (a)), the copper pipe (Figure 5.5 (f)), and the cylinder and piston (Figure 5.5 (b)). The copper

pipe is used to connect the pressure plates and the cylinder and piston. A pressure transducer (c) monitors the pressure inside the entire control volume (see Appendix L for transducer calibration). A data acquisition (DAQ) unit is used to collect the voltage from the pressure transducer. This DAQ unit converts the voltage to pressure, which is displayed on a monitor (see Figure 5.6) for an operator. One can change the pressure inside the control volume by adjusting the piston. This is accomplished with the motor (Figure 5.5 (e)). The user can adjust the piston position with the motor controller (see Figure 5.6). This controller determines how much voltage is supplied to the motor, which in turn determines the force applied to the piston. A pressure release valve is also part of the system, ensuring the pressure in the control volume does not exceed 800 psi.

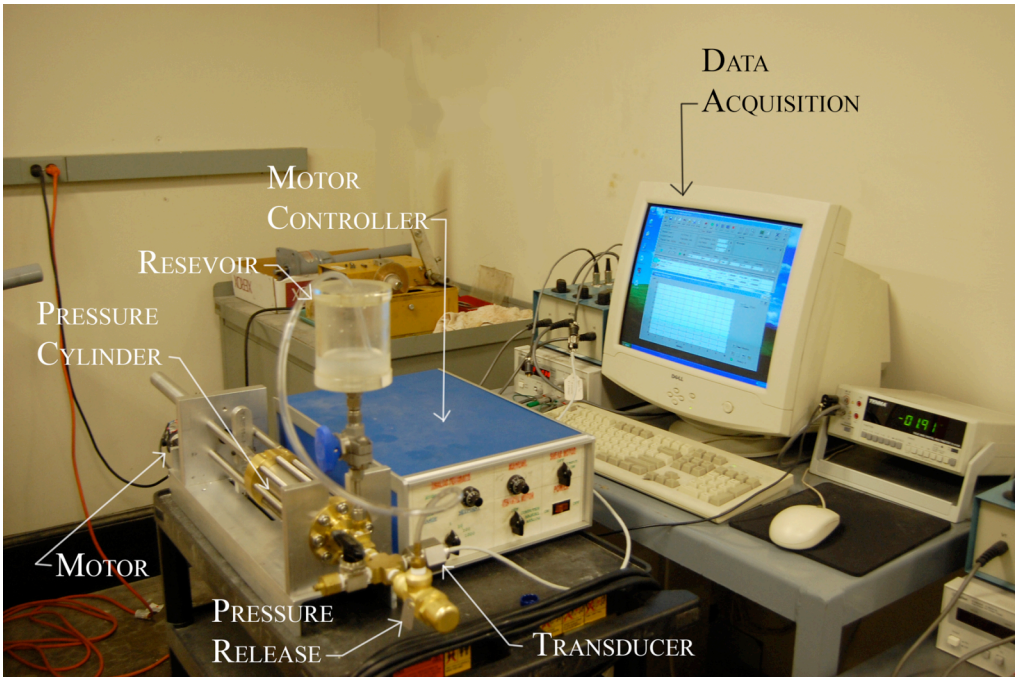

Figure 5.6. Pressure volume controller components without pressure plates. See text for explanation of each part.

The PVC system is a human-in-the-loop feedback system. This means that an operator has to be watching the system and adjusting the motor controller voltage supplied to the motor. It also means that the system is slightly less accurate and slower than an automated system. These drawbacks were deemed acceptable as the system needed to be robust near the end of each pressure test when cracks developed, compromising the control volume.

The final issue regarding the PVC is about the control volume itself. It has been assumed that the control volume consisted of water only. This assumption has to be guaranteed for two reasons:

1. If air is present inside the flaws, then pressure will not be applied uniformly over the entire face of the flaw.
2. Air is a compressible fluid, unlike water. This introduces a non-linearity into the control system, making it more difficult to control.
3.

Normally, a bleed valve would be put into the front plate to bleed any air from the system as water is injected into the pressure plates. This was impractical for two reasons: it would introduce stress concentrations in the acrylic and it would block a portion of the window from view. Therefore, the pressure plates were assembled around the specimen under water, as can be seen in Figure 5.7.

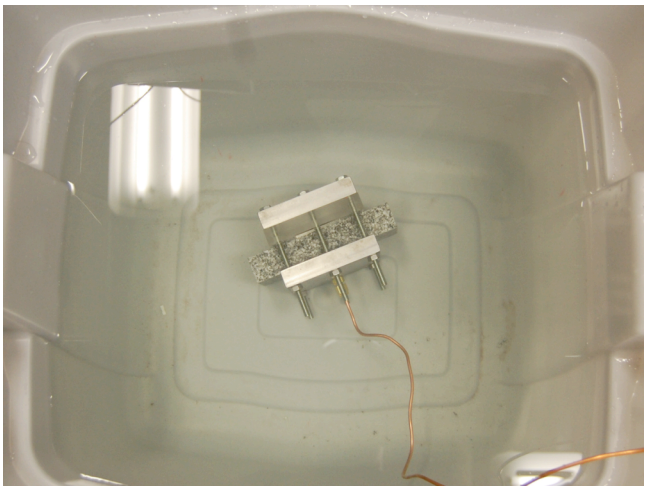

Figure 5.7. Pressure plates were assembled around the specimen underwater to ensure no air was present inside the control volume. The copper pipe is connected to the PVC.

After assembling the plates around the specimen, bolts were first tightened by hand to seal the control volume. Then the assembly was removed from underwater and the bolts were tightened with a torque wrench.

5.3.5 Pressurizing the Flaws

After the pressure plates were assembled and tightened around the specimen, the control volume was pressurized. Pressure was increased to 100, 200, or 400 psi, depending on the test. Because the PVC was manually controlled, a period of stabilization was needed to ensure the pressure level could be maintained. After the pressure was held within 10 psi of the target pressure for a short period (generally around one minute), the compression test is started.

5.3.6 Loading Profiles

Section 3.4.3 discussed the loading profile used in uniaxial compression tests. This profile was also used in the water pressure tests. It was also decided, however, to use a second, faster profile to limit the duration of tests. This was desirable because water started to leak from the control volume as cracks appeared in specimens. Maintaining pressure became difficult and eventually impossible. So the overall test time was shortened to minimize the duration of the test at a lowered pressure. Figure 5.8 shows the pressure drop for the two tests with flaw pressure set at 100 psi.

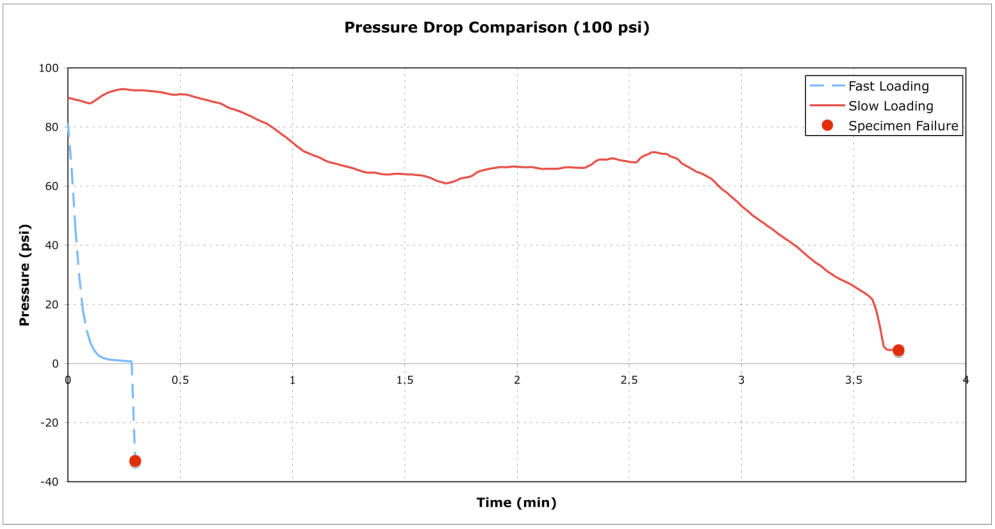

Figure 5.8. Comparison of pressure drop times for fast and slow loading profiles for specimens with flaw pressure set to 100 psi. The pressure record from the start of pressure drop to specimen failure is shown.

Similarly, Figure 5.9 shows the pressure drop time for the two tests with the flaw pressure set at 200 psi.

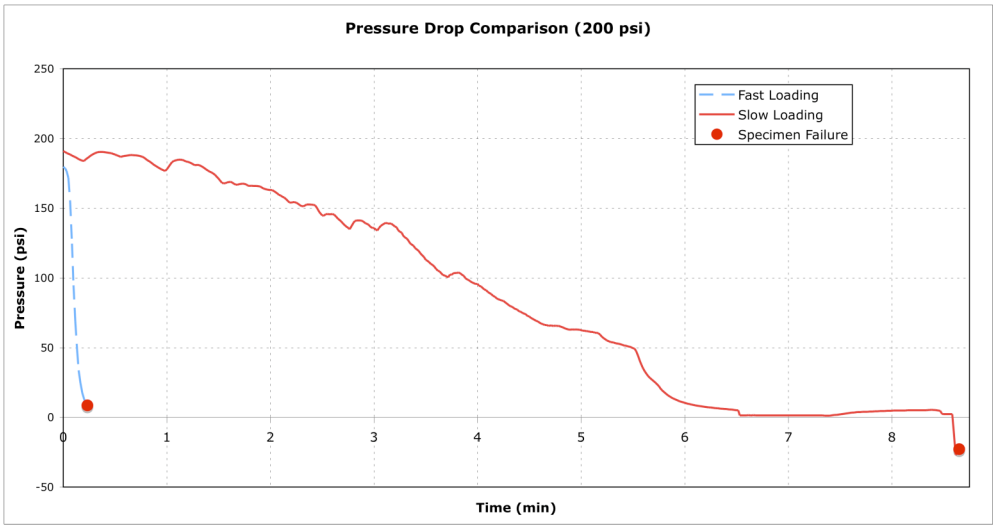

Figure 5.9. Comparison of pressure drop times for fast and slow loading profiles for specimens with flaw pressure set to 200 psi. The pressure record from the start of pressure drop to specimen failure is shown.

The original loading profile will be referred to as the "slow profile" while the other profile will be referred to as the "fast profile." The fast profile resulted in a much shorter duration of reduced pressure. The fast profile also resulted in specimen failure occurring before negative pressures (pressures below the starting pressure; caused by a loss of water from the system after crack formation) were recorded, unlike the slow profile. Table 5.2 showing the slow profile, is recreated below as Table 5.1.

Table 5.1. The four stages of the slow profile. Recreation of Table 3.2.

	Loading Rate	**Range**
Stage 1	0.0017 in/sec	0 – 1000 lbs.
Stage 2	0.0003 in/sec	1000 – 2500 lbs.
Stage 3	38.3333 lb/sec	2500 lbs – failure
Stage 4	5.0 in/min	Failure – starting position

The fast profile, in comparison, loaded at 0.0008 in/sec for the entire duration of the test. Figure 5.10 compares the two loading profiles for the two tests run with a flaw pressure of 100 psi.

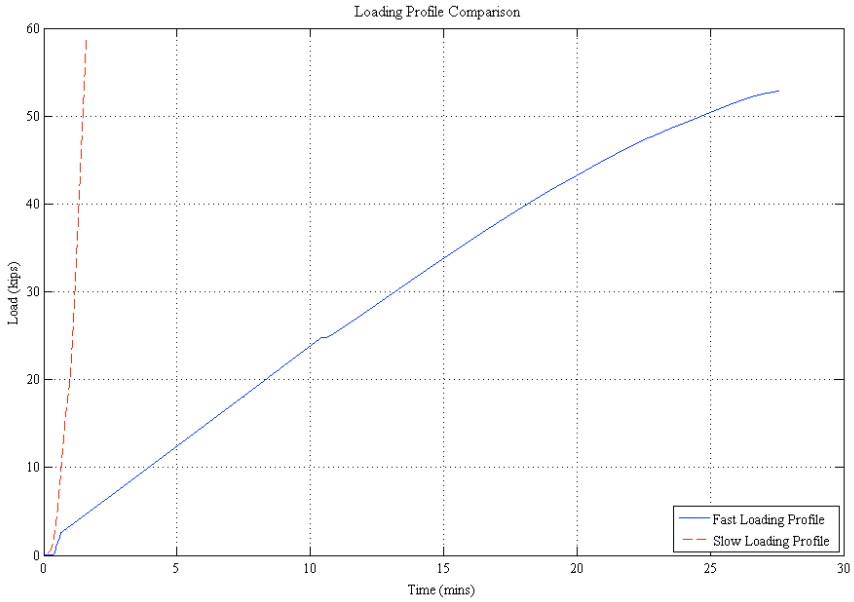

Figure 5.10. Comparison of the fast and slow loading profiles for the tests with the flaw pressure set at 100 psi. While the duration of the tests was very different, the maximum stresses were close.

Figure 5.10 shows that the duration of the two tests was different: 1 minute 36 seconds versus 27 minutes 45 seconds. The maximum stress (failure), however, was similar for the two tests: 120.6 MPa and 121.1 MPa. See Section 6.4 for more details regarding the effect of loading rate.

The slow profile was used in tests with 100, 200, and 400 psi. The fast profile was used in tests with 0, 100, and 200 psi. The effect of the loading profiles will be discussed further in Section 6.4.

Chapter 6. Results on Pressurized Flaws Tests

6.1 Introduction

Detailed summaries of the experiments described in Sections 6.2.1, 6.2.2, 6.2.3, and 6.2.4 are presented in Appendix N. In tests with water pressure, five events were identified for each test: white patch initiation, water pressure drop, crack initiation, coalescence, and failure. Water pressure drop was defined as the point when the water pressure dropped 10 psi below the average held pressure (e.g. – in a 200 psi test, the pressure drop was defined as the point when the water pressure dropped to 190 psi). The other four events are the same as those discussed in Chapters 4 and 5. White patch types were not distinguished in the pressure tests, but zones of white patching were identified. The distinction was not made because pressure tests added another level of visual complexity with the presence of air bubbles near failure, flakes of granite being pressed against acrylic, and shadows caused by the window frame on the front plate.

6.2 Experimental Results

6.2.1 Non-pressurized Flaws

One specimen was tested without water inside the flaws. Pressure plates were put on dry and tightened to the same torque as the other tests. This was done to observe the effect of confinement separately from flaw pressure. It was tested with the fast profile. Unfortunately, the loading machine software needed to be started during the test. This resulted in the beginning portion of the stress-strain data being lost and a pause during the testing. The test was resumed, and the three major events (crack initiation, coalescence, and failure) were all captured on high-speed video.

The coalescence pattern observed for non-pressurized flaws is shown in Figure 6.1. Direct coalescence by a type 1 shear crack occurred.

Figure 6.1. Coalescence pattern observed for the specimen tested with pressure plates but no water pressure inside the flaws. Coalescence is category four (direct shear coalescence).

White patch initiation was not observed and there was no pressure drop (as there was no water in the flaws). The three remaining events occurred in the order shown in Table 6.1. The detailed analysis for this test is in Appendix N.

Table 6.1. Event sequence for the specimen tested with no water pressure.

Event Number	Event
1	Crack Initiation
2	Coalescence (Category 4)
3	Failure

6.2.2 Flaws Pressurized at 100 psi

Two specimens were tested with the water pressure at 100 psi. One was tested with the slow loading profile while the other was tested with the fast. The coalescence patterns and event sequence observed in each test are summarized in Table 6.2. The detailed analyses for these tests are in Appendix N.

Table 6.2. Summary of specimens tested with 100 psi flaw pressure percentages in parentheses indicate the stress ratio (stress to maximum stress) each event occurred at.

Loading profile	Slow	Fast
Coalescence Pattern	 Category 4	 Category 5
Maximum Stress	121.10 MPa	120.58 MPa
Event 1	White Patch Initiation (81.4%)	Pressure Drop (66.2%)
Event 2	Crack Initiation (83.9%)	White Patch Initiation (68.6%)
Event 3	Pressure Drop (92.7%)	Crack initiation (97.8%)
Event 4	Coalescence (99.99%)	Coalescence (99.7%)
Event 5	Failure	Failure

Examining Table 6.2, one can see that both specimens coalesced directly, but with different crack types. White patches developed before cracks in both cases, but the pressure dropped at different points (third event in the specimen tested with the slow profile and first event in the specimen tested with the fast profile). The maximum stresses for the two tests were close to one another.

6.2.3 Flaws Pressurized at 200 psi

Two specimens were tested with the water pressure at 200 psi. One was tested with the slow loading profile while the other was tested with the fast. The coalescence patterns and event

sequence observed in each test is summarized in Table 6.3. The detailed analyses for these tests are in Appendix N.

Table 6.3. Summary of specimens tested with 200 psi flaw pressure.

Loading profile	Slow	Fast
Coalescence Pattern	 Category 4	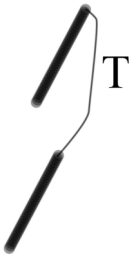 Category 8
Maximum Stress	122.32 MPa	117.01 MPa
Event 1	White Patch Initiation (76.6%)	White Patch Initiation (54.8%)
Event 2	Crack Initiation (84.7%)	Pressure Drop (77.8%)
Event 3	Pressure Drop (97.0%)	Crack initiation (99.0%)
Event 4	Coalescence (99.97%)	Coalescence (99.3%)
Event 5	Failure	Failure

Table 6.3 shows a difference between the two loading profiles. Once again, the slow loading profile resulted in direct coalescence with a shear crack. For the fast loading profile, coalescence was again direct with a single tensile crack. This time, however, the crack connected the two right flaw tips instead of the inner flaw tips. Crack initiation came before pressure drop in the slow profile and vice versa for the fast loading profile. Otherwise the events occurred in the identical order for both profiles. Once again, the maximum stresses for both specimens were close to one another.

6.2.4 Flaws Pressurized at 400 psi

Only one specimen was tested with 400 psi flaw pressure. It was tested using the slow loading profile. Figure 6.2 shows the coalescence pattern observed. The detailed analysss for this test is in Appendix N.

Figure 6.2. Coalescence pattern observed for the specimen tested with 400 psi flaw pressure. Coalescence is direct (category six).

As seen in Figure 6.2, coalescence is direct. A single tensile crack connects the two inner flaw tips in a category six coalescence pattern. Table 6.4 shows the sequence of events for the experiment.

Table 6.4. Event sequence for the specimen tested with 400 psi flaw pressure.

Event Number	Event
1	White Patch Initiation (54.0%)
2	Pressure Drop (72.1%)
3	Crack Initiation (92.6%)
4	Coalescence Category 6 (100%)
5	Failure

6.3 Effect of Pressure Plates

In order to investigate the effect of flaw pressure on coalescence, the effect of the confining stress due to the pressure plates by themselves must first be understood. Table 6.5 shows a

comparison between tests with pressure plates (confined) (no water pressure, however) and without pressure plates (unconfined).

Table 6.5. Comparison of tests with (confined) and without (unconfined) pressure plates. Note that the two types of tests were also run with different loading profiles.

	Unconfined	**Confined**
Loading Profile	Slow	Fast
Coalescence Pattern	 Category 6	 Category 4
Maximum Stress	115.95 MPa average	147.23 MPa
Crack Initiation Stress (Stress Ratio)	105.80 MPa average (91%)	146.03 MPa (99%)

As can be seen in Table 6.5, there is a substantial difference between confined and unconfined tests. The change in coalescence pattern could be due to either the pressure plates or the loading rate (see Section 6.4). The large difference in maximum stress and crack initiation stress (both absolute and ratio) are caused by the confinement since they are not likely to be caused by the loading rate, as also discussed in Section 6.4.

6.4 Effect of Loading Rate

For flaw pressures of 100 and 200 psi, two experiments were run: one with a slow loading rate and one with a fast loading rate. Table 6.6 summarizes the observed coalescence pattern for each of these four tests.

Table 6.6. Effect of loading rate on coalescence pattern for flaw pressures of 100 and 200 psi.

Flaw Pressure	Slow Loading	Fast Loading
100 psi	 Category 4	 Category 5
200 psi	 Category 4	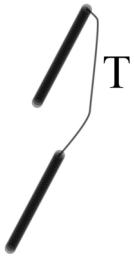 Category 8

As can be clearly seen in Table 6.6, an increase in loading rate leads to a transition from direct coalescence by shear crack to direct coalescence by a tensile crack.

Maximum stress, however, did not appear to be significantly influenced by loading rate. Figure 6.3 shows a comparison of maximum stresses between the two loading rates. As can be seen, the maximum stresses were approximately equal. Coalescence was almost simultaneous with maximum stress in all four tests.

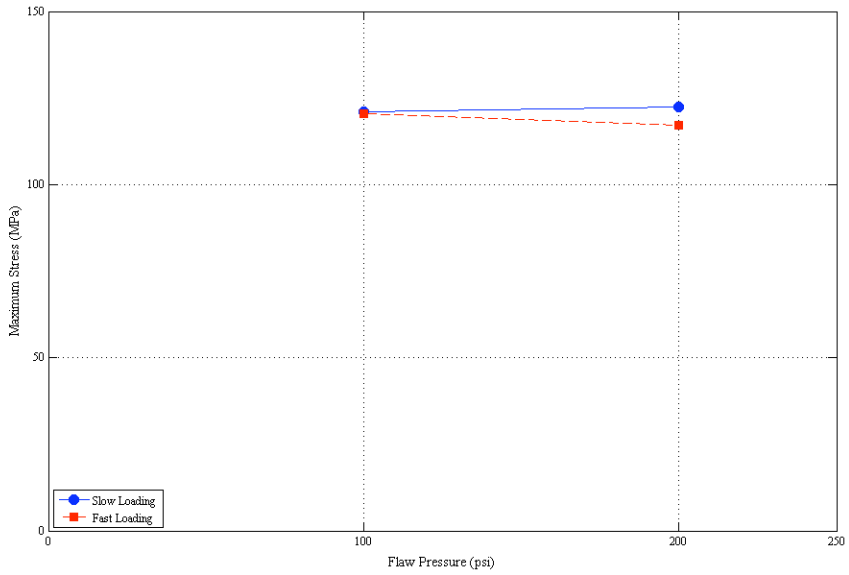

Figure 6.3. Comparison of maximum stresses for the fast and slow loading rates.

However, events other than maximum stress and coalescence did show changes with loading profile. Figure 6.4 shows the stress ratio for the three other events.

Figure 6.4 shows how the sequence of events changes between the loading profiles. For the slow profile, the order of events was always white patch formation followed by crack initiation followed by a pressure drop. For the fast profile, the first event was either a pressure drop or white patch initiation and the second event was the other. The final event was crack initiation. Events occurred at higher stress ratios for the slower loading profile.

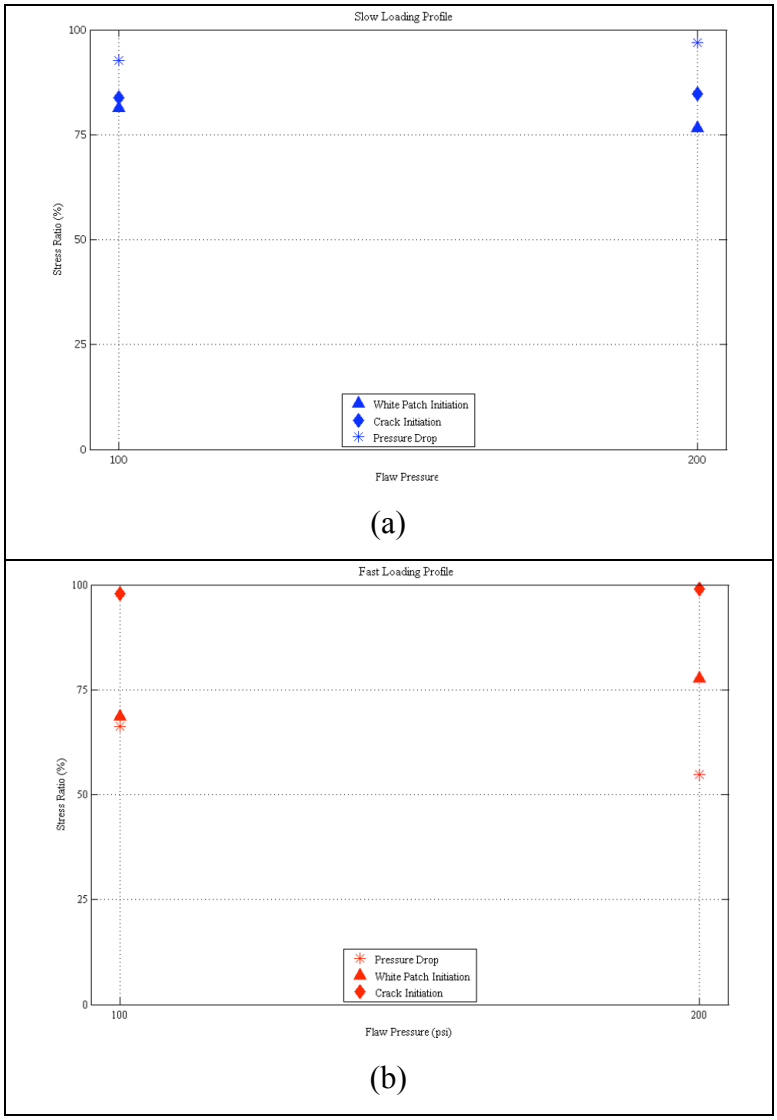

Figure 6.4. Stress ratios for crack initiation, pressure drop, and white patch initiation for (a) the slow loading profile and (b) the fast loading profile for specimens with water pressure of either 100 or 200 psi.

Perhaps the most noteworthy detail of Figure 6.4 is in regards to the pressure drop. For the slow loading profile it was always located after crack initiation and was the final event before specimen coalescence and failure. In the fast loading profile, however, the pressure drop occurred before (in terms of stress ratio, not time-wise) crack initiation in both cases. A pressure drop after crack initiation was expected because the PVC system did not have a fast response time. Visually, a small amount of water was seen flowing down the face of all

specimens before a pressure drop was observed. In the case of the fast loading profile, however, the pressure drop occurred before crack initiation. In the case of the specimen with flaw pressure of 100 psi, the first event was this pressure drop. A few explanations for this are possible:

- The O-ring couldn't maintain a proper seal with the granite with the faster loading profile.
- Small cracks had already appeared but were not visible during analysis.
- Water was leaking through microcracks.

A pressure drop from water leaking through microcracks is unlikely due to the fact that the pressure drop occurred before the first white patches were identified in one of the two specimens. This is relevant because Wong (2008) discovered that the white patches in marble were actually process zones composed of microcracks. The possibility of unidentified cracks being the cause of the pressure drop cannot be discounted. It is, however, unlikely as the first cracks identified were generally very small and occurred at a stress ratio much higher than the pressure drop noted. The most likely of the stated explanations, therefore, is that the O-ring was unable to maintain a proper seal with the granite as it deformed. This could be caused either by the granite deforming at a faster rate or deforming differently when loaded at a faster rate.

6.5 Effect of Pressurizing Flaws

As just discussed, loading rate affected white patch initiation, crack initiation, and pressure drop. It did not, however, have a strong effect on maximum stress or coalescence stress. By only examining Figure 6.3, one could conclude that maximum stress was also not strongly affected by pressurizing the flaws. Figure 6.5, however, shows the maximum stress data from all the pressurized flaw tests and shows a clear trend. Maximum stress is initially constant but then decreases with increasing water pressure. More tests are needed to understand the true nature of this trend particularly the plateau between 100 and 200 psi. This observation is the same for coalescence stress, as shown in Figure 6.6.

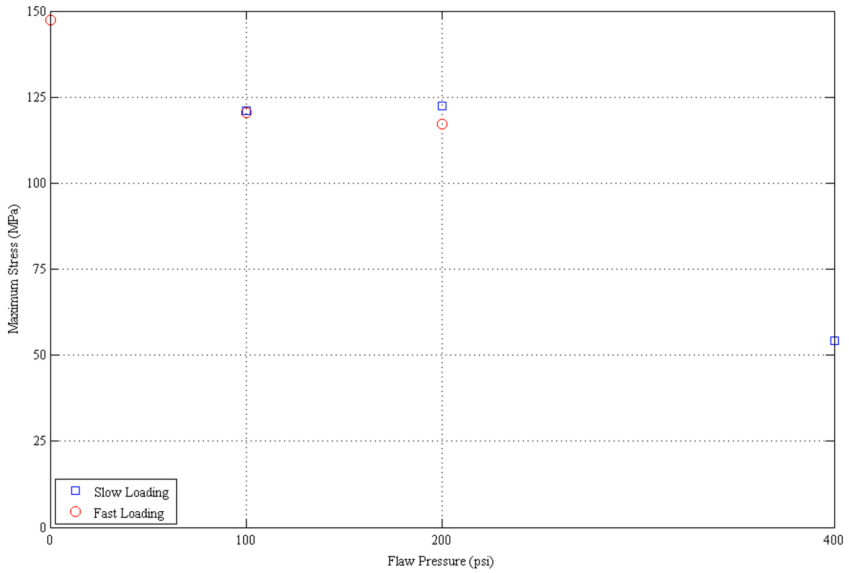

Figure 6.5. Maximum stress versus flaw pressure. Data from both slow loading and fast loading profiles are included.

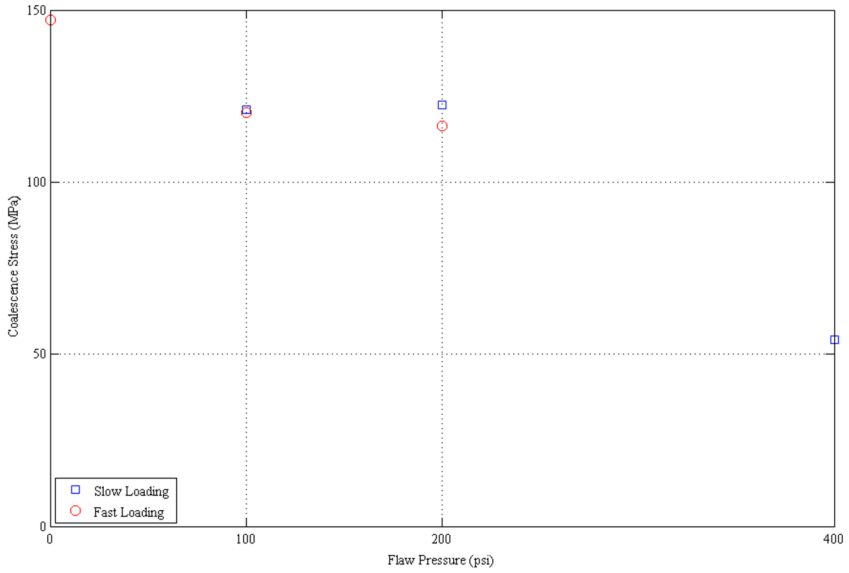

Figure 6.6. Coalescence stress versus water pressure.

Coalescence patterns, which were shown to vary with load profile in Table 6.6, also change with water pressure. Table 6.7 shows the coalescence patterns for each of the three specimens tested with pressurized flaws and the slow loading profile.

Table 6.7. Coalescence pattern observed for the slow loading profile.

100 psi	200 psi	400 psi
		
Category 4	Category 4	Category 6

Table 6.7 suggests an important trend. At first, water pressure does not affect coalescence pattern: the pattern for water pressures of 100 psi and 200 psi are the same. When water pressure is increased to 400 psi, however, coalescence is tensile. It must be emphasized that water pressure was the only parameter changed for these three tests. This same trend can be observed in Table 6.8 for specimens tested with the fast loading profile. For no water pressure, the flaws coalesced directly with a shear crack. The addition of water pressure causes direct tensile coalescence between the two inner flaw tips. Increasing water pressure to 200 psi causes coalescence between the two right flaw tips.

Table 6.8. Coalescence patterns observed for the fast loading profile

0 psi	100 psi	200 psi
		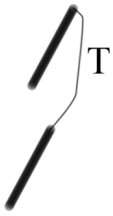
Category 4	Category 5	Category 8

6.6 Summary

A small series of tests were performed with pressurized flaws. Four flaw pressures were tested: 0, 100, 200, and 400 psi. To apply these pressures, the equipment described in

Chapter 5 was used. Five different events were observed and recorded during tests: white patch initiation, pressure drop, crack initiation, coalescence, and maximum stress (failure). Coalescence patterns were also observed in all the tests. Table 6.9 summarizes the observed coalescence patterns and shows that the coalescence pattern is affected both by the loading rate and water pressure (as well as possibly by the pressure plates).

Table 6.9. Summary of coalescence patterns for different flaw pressures and loading profiles. Note that the pattern shown for the slow profile with 0 psi flaw pressure is from the unconfined tests summarized in Chapter 4.

	0 psi	**100 psi**	**200 psi**	**400 psi**
Slow	 (unconfined)			
Fast				- -

The two coalescence patterns observed in the 0 psi column of Table 6.9 show that loading rate or pressure plates affect coalescence pattern, or that both factors do. This is uncertain. What is certain, however, is that coalescence pattern is affected by flaw pressure. In the slow loading rate, coalescence pattern changes with the introduction of water pressure, is the same for water pressures of 100 psi and 200 psi, but changes when the water pressure is increased to 400 psi. In the case of the fast loading rate, the coalescence pattern changes for each water pressure level. Table 6.10 shows what factors are influenced by loading rate and flaw pressure.

Table 6.10. Summary of observations and the parameters (loading rate, flaw pressure) that affect them (event sequence, coalescence pattern, maximum stress, and coalescence stress).

	Loading Rate	Flaw Pressure	Confinement
Event Sequence and Stress Ratio	**X**		
Coalescence Pattern	**X**	**X**	**X**
Maximum Stress and Coalescence Stress		**X**	

These tests have provided an interesting glimpse into the effects of water pressure on coalescence. Mostly, however, they provide a starting point for future research. Based on these initial experiments, the following areas should be explored:

- **Effect of pressure plates:** Tests with pressure plates and zero water pressure should be run with different loading rates. Currently, it is not known if pressure plates affect coalescence pattern, if the observed changes are a product of the loading rate only, or if they are random.
- **Effect of loading rate on maximum stress:** The conclusion that maximum stress is unaffected by loading rate should be confirmed.
- **Effect of water pressure on maximum stress:** It is clear a relationship exists between water pressure and maximum stress. More tests at different water pressures should be performed to understand this relationship better, however.
- **Effect of water pressure on coalescence pattern:** It is clear water pressure has an effect on coalescence pattern. What is the critical pressure for changes in coalescence pattern? For the slow loading rate, water pressures between 200 psi and 400 psi need to be tested to observe the transition in coalescence patterns.

Chapter 7. Modeling of Crack Initiation and Propagation

7.1 Introduction

The computer code, FROCK (**F**ractures in **Rock**) is basically well suited to model fracture initiation, propagation and coalescence. However, the failure initiation criterion is relatively simple. Some work was done in the context of this research to pave the way for improvements of FROCK.

FROCK was first developed by Chan in 1986, using LEFM (linear elastic fracture mechanics) in a hybridized indirect boundary element code. Later, with the results obtained from numerous and more sophisticated tests performed in gypsum, the model was enhanced by Bobet (1997), yielding satisfactory results when compared with the experimental work. Bobet's model introduced a new criterion for the initiation and propagation of cracks, in which both shear and tensile resistance were considered to determine the direction and critical stress at which crack initiation and propagation should occur.

7.2 Comparison between FROCK results and actual tests

The tests and numerical models developed were based on different flaw geometries, usually with 2 existing flaws. Different geometries ere obtained by varying the angles a and b and the ligament length b, as described in Figure 7.1 below.

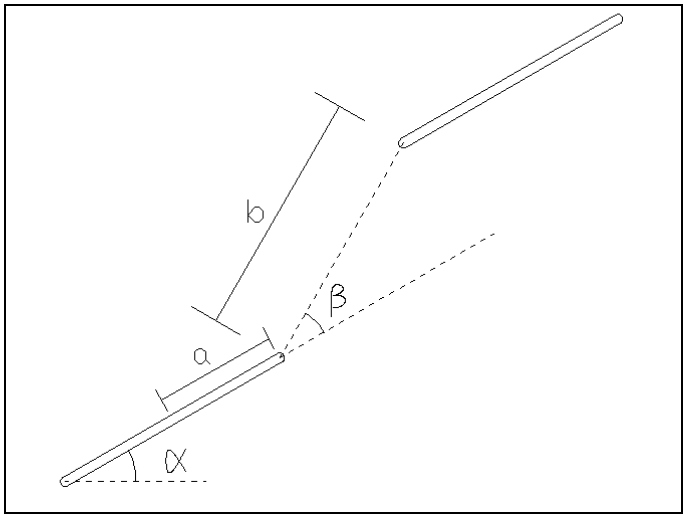

Figure 7.1. Variables used in the definition of the flaw geometry. So, a geometry 2a-30-45 has a ligament length b=2a, a= 30^{o} and b= 45 ^{o}.

For some flaw geometries, the results obtained with the existing FROCK code correspond well to those obtained in the tests (see e.g. Figure 7.2). Also, the coalescence stress obtained numerically is roughly the same as the experimental one, as shown in Figure 7.2.

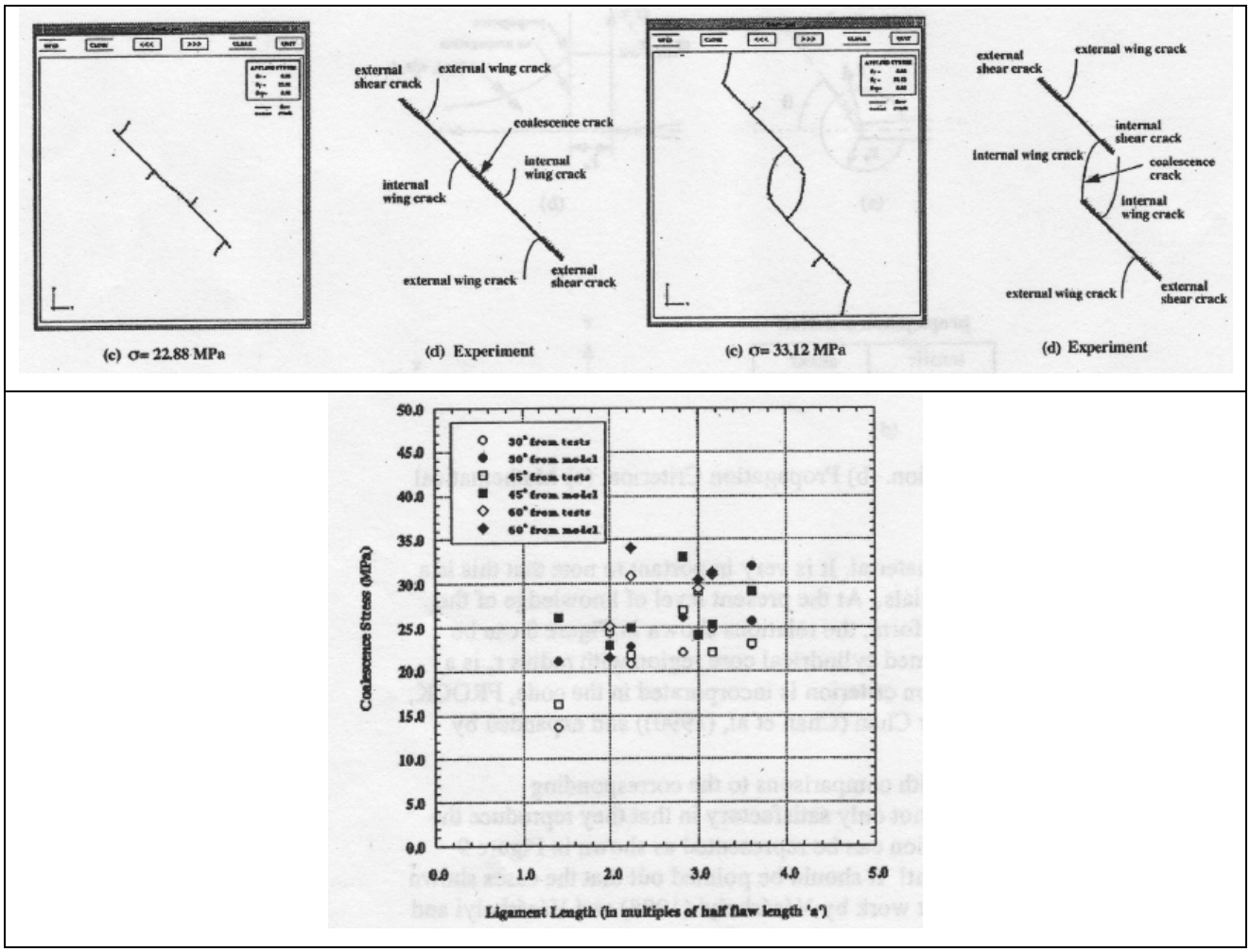

Figure 7.2. Similarities between experimental and numerical (FROCK) results, showing crack patterns for the geometries 2a-45-0 (top left) and 2a-45-45 (top right) and coalescence stresses for several geometries (bottom) based on experimental and FROCK results, white and dark dots, respectively.

However, in some tests performed by Bobet (1997) and by Wong (2008), initiation and propagation were not well simulated by FROCK. Wong, in particular, found that in some gypsum and marble geometries, the crack pattern obtained with FROCK did not correspond to that observed experimentally, as shown in Figure 7.3.

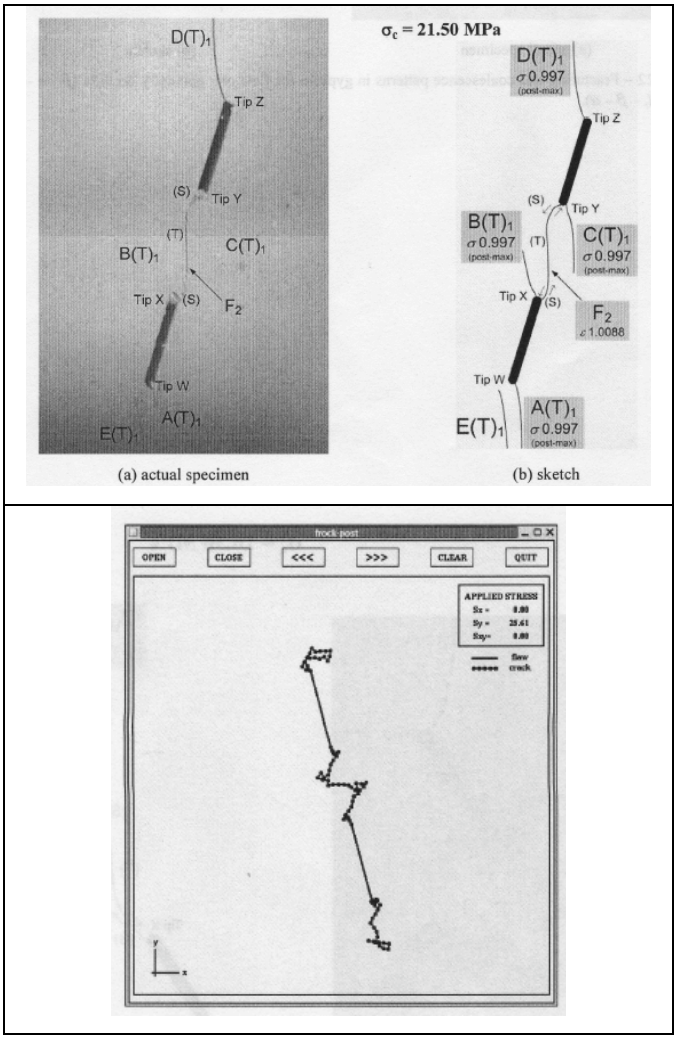

Figure 7.3. Differences between experimental (top) and FROCK (bottom) results for the geometry 2a-60-0 in gypsum (in Wong, 2008)

7.3. Modelling Work to Eventually Improve FROCK

Since the results obtained in some geometries were not always comparable to the actual results, we concluded that the FROCK code should be modified, in order to better capture the real cracking behavior observed in the tests. In order to have a good theoretical basis of the problem and to later support the modifications that will be performed on the existing FROCK code, a Finite Element study was performed using the ABAQUS code.

The Finite Element analysis consisted first of the comparison between the stress and strain fields for several geometries, in order to understand what kind of mechanism was responsible

for crack initiation and propagation. Second, the Finite Element analysis was used to understand why, how and where some cracks develop in shear and others in tension, using the stress and strain approaches.

7.4 Analysis performed in ABAQUS

7.4.1 Relation between the stress and strain fields

The following flaw geometries (please refer to Figure 7.1) were used to study the relation between the stress and strain fields:

- 2a-30-45
- 2a-30-30
- 2a-30-15
- 2a-30-0 (coplanar geometry)

Flaws and wing cracks were considered in the four geometries, since most of the tests showed that the coalescence process takes place after the wing cracks have developed. Furthermore, the partially uncoupled character of the stress and strain fields becomes more evident in models with the wing cracks in place than in models with the induced flaws only.

In Figure 7.4, the four geometries analyzed are shown. In this chapter, only the first and last geometries will be discussed.

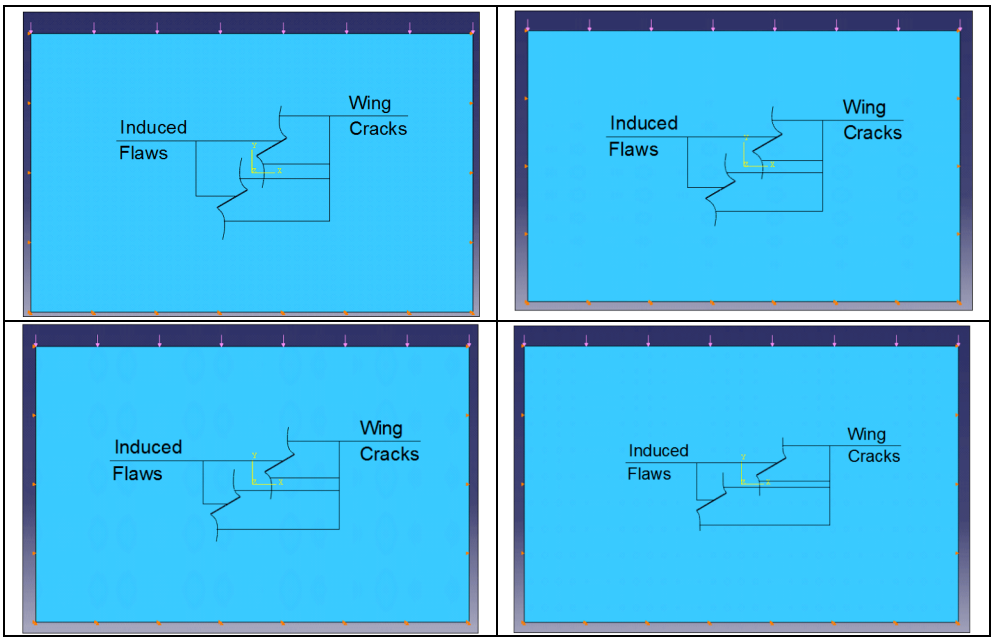

Figure 7.4. Geometries analyzed in ABAQUS: 2a-30-45 (top left), 2a-30-30 (top right), 2a-30-15 (bottom left) and 2a-30-0 (bottom right) modeled with wing cracks

The material was considered to be linearly elastic. This means that the material parameters introduced in the ABAQUS input were the modulus of elasticity E and the Poisson's ratio ν. The values of these properties were based on the tests performed on gypsum by Wong (2008) and Bobet's (1997):

$E = 6000$ MPa

$\nu = 0.28$

By analyzing the contours of the principal stresses and strains for the geometry **2a-30-45 with wing cracks**, one can notice significant similarities between the maximum principal stresses and strains (σ_I and ε_I) and between the minimum principal stresses and strains (σ_{II} and ε_{II}), as can be seen in Figures 7.5 and 7.6. However, one can also notice that there is an area between the flaw tip and the wing crack tip where the area showing contraction strains is smaller than the area showing compressive stresses.

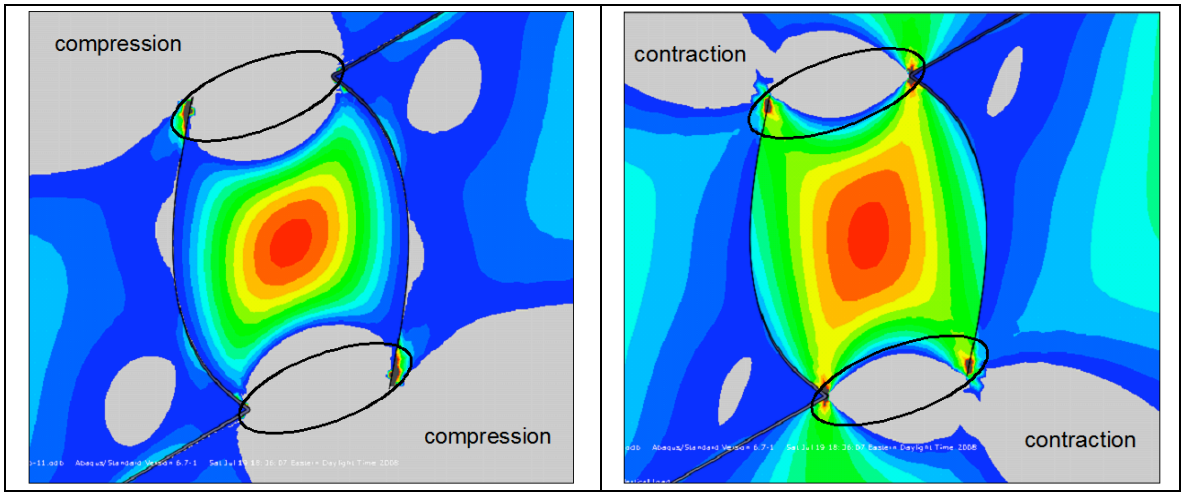

Figure 7.5. σ_I (left) and ε_I (right) contours for the geometry 2a-30-45 with wing cracks. Light grey means compression/contraction; the color scale represents several degrees of tension/elongation

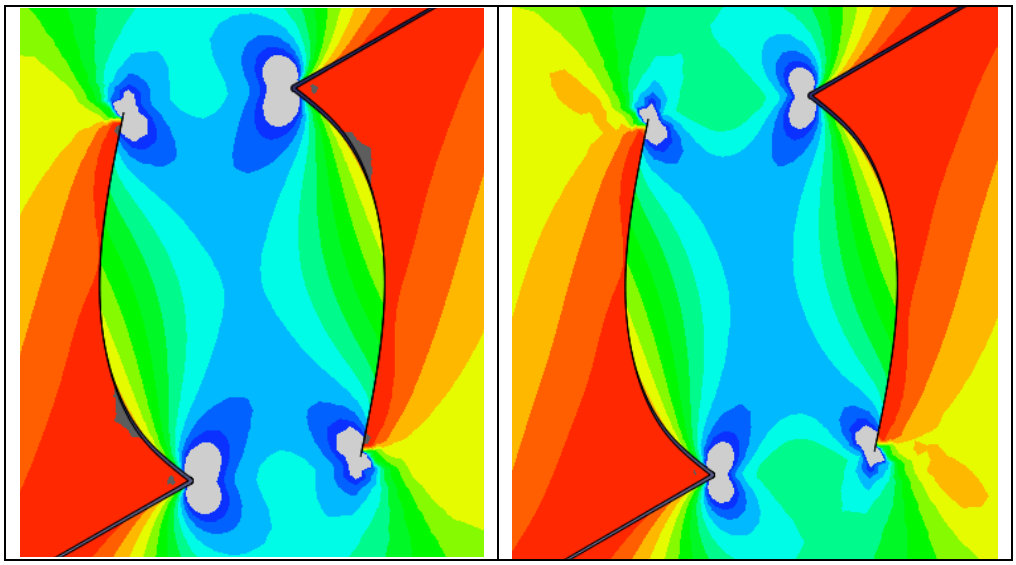

Figure 7.6 – σ_{II} (left) and ε_{II} (right) contours for the geometry 2a-30-45 with wing cracks. The color scale represents several degrees of compression/contraction

In the other geometries analyzed, the area where compressive stresses can be found is increasingly greater than the area where contraction strains occur, as b decreases.

In the coplanar geometry – **2a-30-0 with wing cracks** – the differences between maximum principal stresses and strains (σ_I and ε_I, respectively) are more significant than in any other of the investigated geometries. By analyzing Figure 7.7, it is clear that there are mostly compressive stresses in the bridge between flaw tips. In terms of strains, however, significant elongation strains can be found.

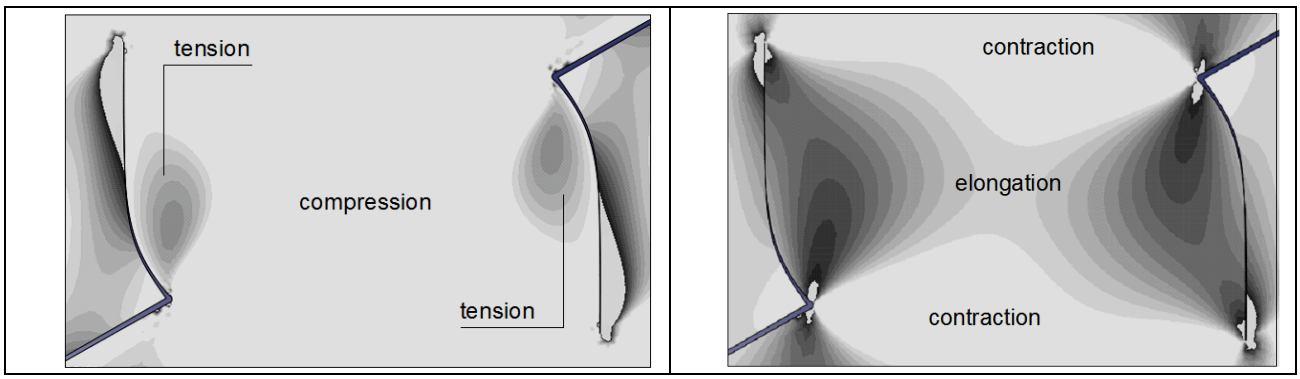

Figure 7.7. Differences between the $\boldsymbol{\sigma_I}$ (left) and $\boldsymbol{\varepsilon_I}$ (right) contours for the geometry 2a-30-0 with wing cracks

As in the other geometries studied, the difference between the minimum principal stresses and strains contours is small, as is shown in Figure 7.8.

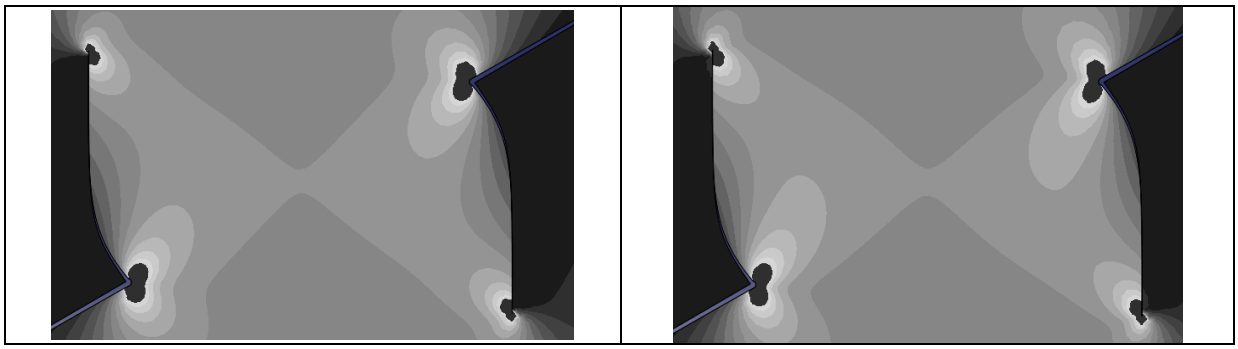

Figure 7.8. Similarities between the σ_{II} (left) and ε_{II} (right) contours for the geometry 2a-30-0 with wing cracks. The grey scale represents several degrees of compression/contraction

It is possible to show that the normal stresses and strains are not simply proportional and, as a result, the contours of a given stress will not have a direct correspondence with the strain in the same direction. So, for ε_{11}, for instance, one will have:

$$\varepsilon_{11} = \sigma_{11}/E - \nu\sigma_{22}/E \quad (7.1)$$

Therefore, ε_{11} will not only depend on σ_{11}, but it will also be a function of the perpendicular stress σ_{22}.

As a simple example, the stress and strain fields will be compared in Figure 7.9 for a 1-D compression test.

	Stress Field	Strain Field
Stresses/ Strains in a given element	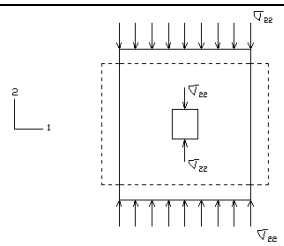	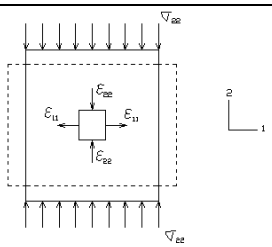
Type of stresses/ strains	Compression only	Elongation and contraction
Mohr Circle	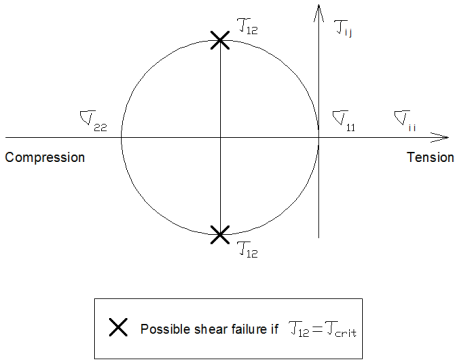	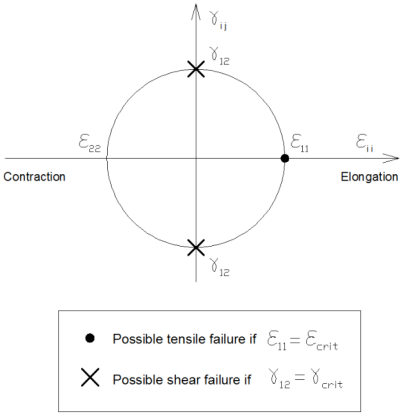
Possible types of failure	Shear only 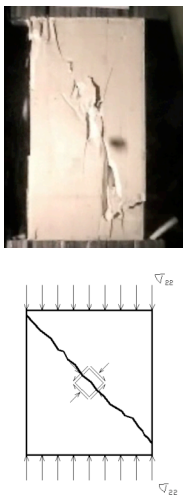	Shear and Tensile 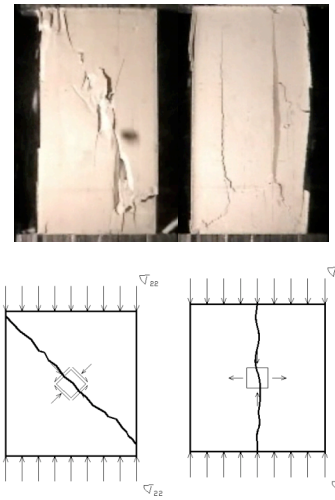

Figure 7.9 . 1-D compression test, showing results for the stress (left) and strain (right) field approaches in a 1-D compression test

If both tensile and shear failures can occur, in a similar way to what is shown at the bottom line of Figure 7.9, it is possible to understand that the stress field approach will not be able to predict tensile failure. By analyzing the Mohr circle for the stresses shown in Figure 7.9, one

can see that one of the principal stresses is always zero (σ_{11}) and the circle is always on the compression side. Consequently, only shear failure is possible in a 1-D compression test using this approach. The failure will happen when $\tau_{12} = \tau_{crit}$ as shown in the Mohr circle for the stress field.

For the strain field approach, both elongation and contraction may occur. As can be seen in the Mohr circle for strains shown in Figure 7.9, two types of failure may occur: shear failure, if $\gamma_{12} = \gamma_{crit}$, or tensile failure, if $\varepsilon_{11} = \varepsilon_{crit}$. This tensile failure was observed in the great majority of the 1-D compression tests performed on specimens consisting of Ultracal and Plaster.

In this simple example, a failure criterion based on strains seems to yield better results than one based on stresses, since it predicts the two types of failures observed in actual tests.

In contrast to what happens with normal stresses and strains, according to the constitutive relations, the shear strains (γ_{12}) and stresses (τ_{12}) are directly coupled, as shown below:

$$\gamma_{12} = \tau_{12}/G \qquad (7.2)$$

This explains why the contours of shear stresses and strains are exactly the same for a given flaw geometry and load. This result is very useful, because it shows that a shear failure can be predicted by either a stress or a strain approach, as presented at the bottom of Figure 9. This is true, because once a τ_{crit} is defined, a γ_{crit} is automatically selected and vice-versa.

Summary of stress/strain field investigation

- Normal stresses and strains are not simply proportional; therefore, their contours obtained with ABAQUS are not expected to be the same, which was confirmed in this study.
- Shear stresses and strains are proportional; therefore, their contours obtained with ABAQUS are expected to look alike, as was achieved in this study.
- A failure criterion based on stresses may not be adequate in some cases, as was shown for the 1-D compression test. In this case, tensile failure could not be predicted with the stress field approach.

7.4.2 – Crack initiation and propagation

This part of the study was done for the **2a-30-30** geometry. Both stress and strain fields were studied in this section. The cracks were modeled in the same sequence as they occurred in most of the tests: wing cracks developing first, followed by shear cracks initiating at the tip of the flaws, in the direction of the bridge between flaws. The following models were studied:

- **2a-30-30** – to study the development of wing cracks
- **2a-30-30 with wing cracks** – to study the development of shear cracks from the inner tips of the flaws in the direction of the bridge between flaws
- **2a-30-30 with shear and wing cracks** – to study the coalescence cracks that might develop between the inner tips of the flaws

These models are shown in Figure 7.10 below:

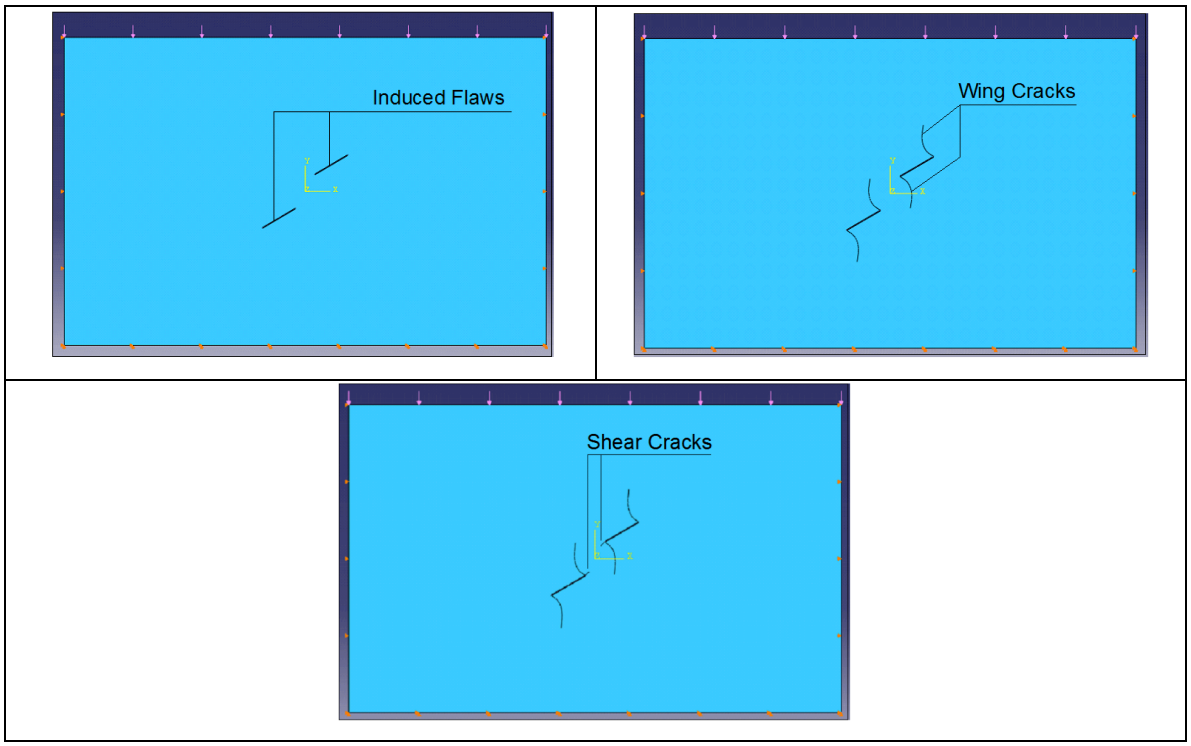

Figure 7. 10. Models used in ABAQUS for the investigation of the initiation and propagation of several types of cracks: 2a-30-30 (top left), 2a-30-30 with wing cracks (top right) and 2a-30-30 with wing and shear cracks (bottom)

The most important advantage of using the staged methodology referred to above is that not only can the initiation of the several cracks be studied, but their propagation is also considered.

- **Wing crack initiation and propagation**

In the tests performed on actual specimens, the initiation of wing cracks occurs at the same place and in roughly the same direction as predicted in the Finite Element model. The crack propagation path obtained in the experiments is also coherent with the results obtained in this part of the study, as can be seen in Figure 7.11 below.

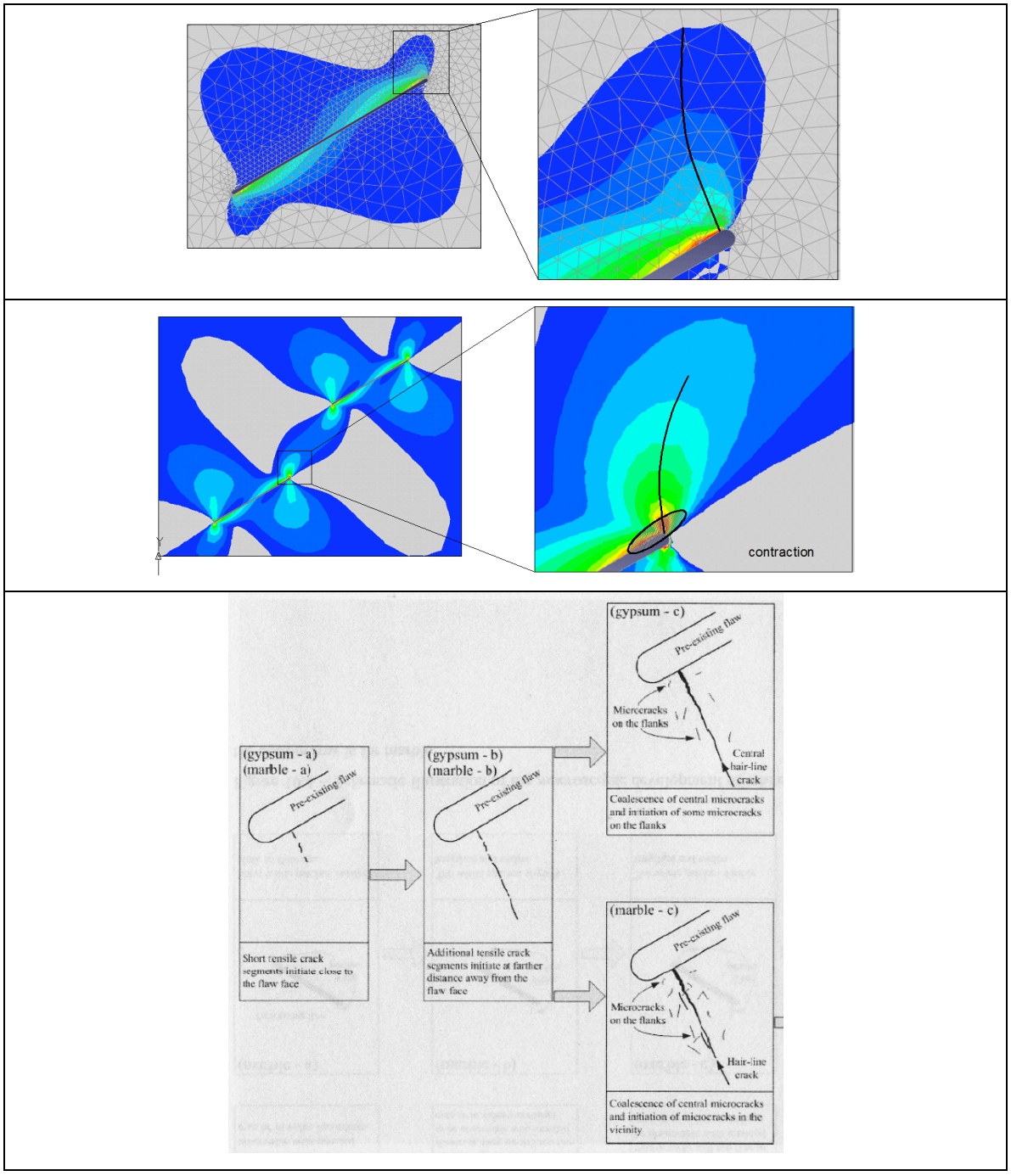

Figure 7.11 –Wing crack initiation and propagation based on stress field analysis (maximum principal stresses – top), strain field analysis (maximum principal strains – center) and in actual tests performed by Wong, 2008 (bottom). The bottom image refers to the inner tip of the upper flaw. Light grey means compression/contraction; the color scale represents several degrees of tension/elongation

- **Shear/Tensile cracks initiation and propagation at the flaw tips after wing cracks have developed**

For stepped geometries, shear cracks develop from the tip of the flaws, usually after the formation of wing cracks, as shown in Figure 7.12. This corresponds to the results obtained with the stress and strain field approaches, which are summarized in Figure 7.13.

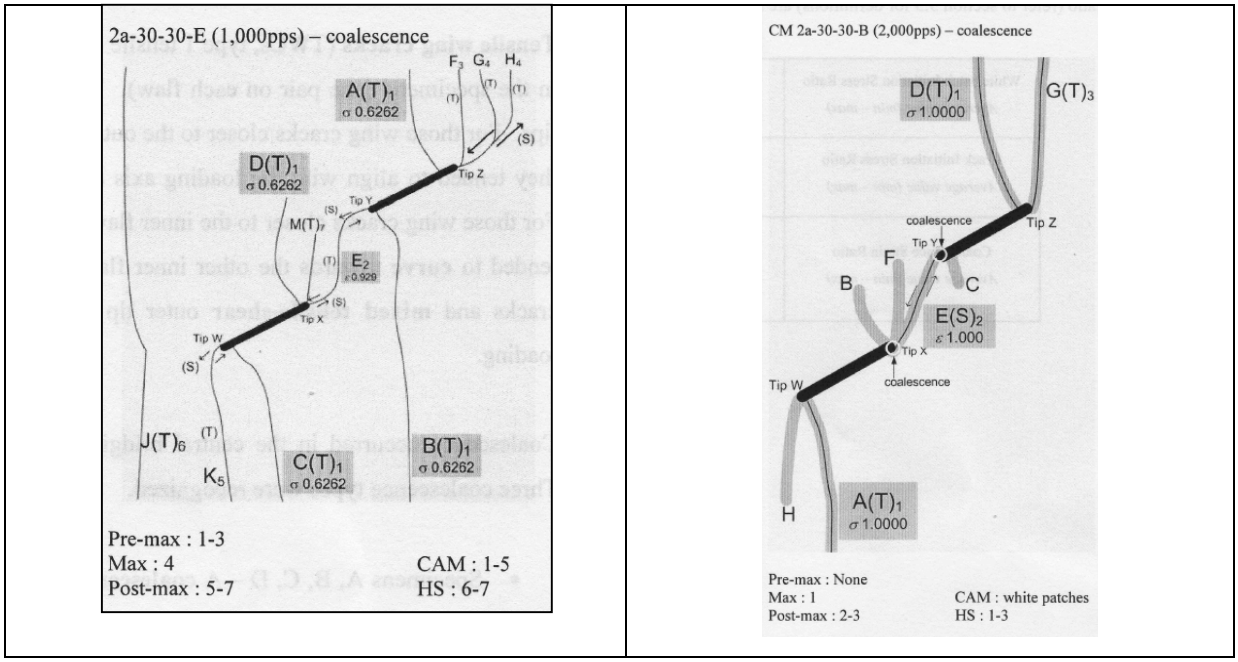

Figure 7.12. Development of shear cracks for the geometry 2a-30-30 in gypsum (left) and marble (right) – S means shear crack and T tensile crack. The letters A, B, C… indicate the order by which the different cracks develop (in Wong, 2008)

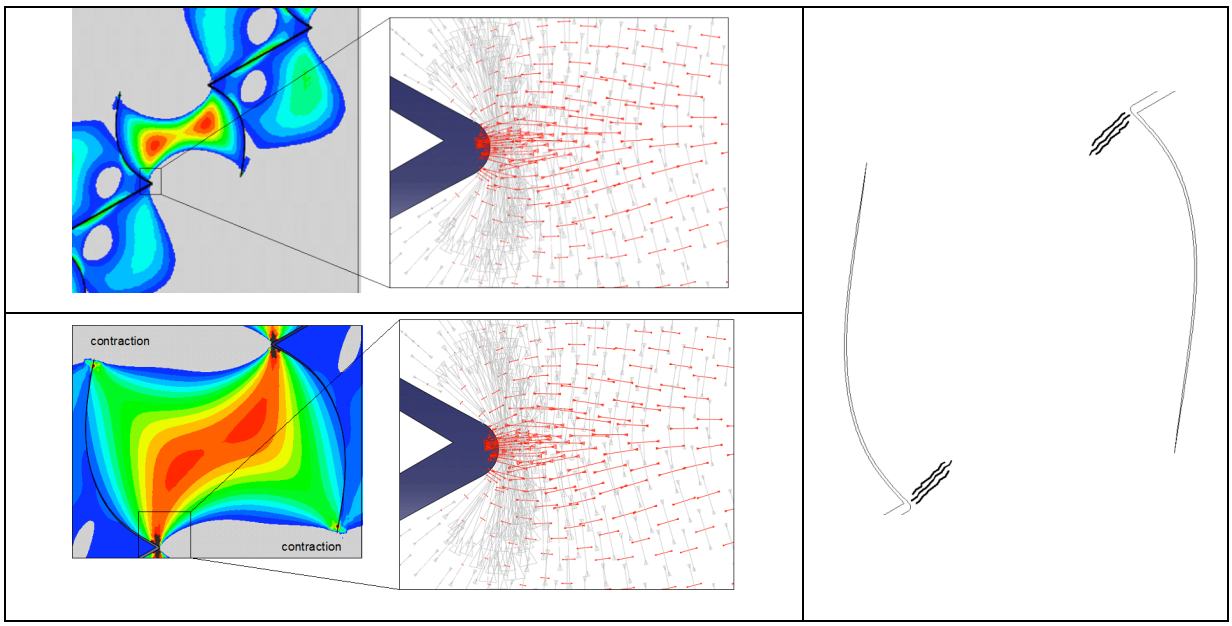

Figure 7.13. Maximum principal stress (top left) and strain (bottom left) vectors showing compression around the inner tip; Shear cracks that might develop from the flaw tips after wing crack propagation (right). Light grey means compression/contraction; the color scale represents several degrees of tension/elongation

- **Cracks involved in the coalescence**

Stress analysis

After the formation of the wing and shear cracks, the stress field near the shear crack tip is only compressive (σ_I and $\sigma_{II} < 0$). Consequently, from the stress field analysis, the propagation of tensile cracks from the tip of the shear crack is ruled out. However, due to the high concentration of compressive principal stresses (see top of Figure 7.14) with approximately horizontal and vertical directions, a shear failure is possible in a direction that is 45º with the horizontal. Basically, this would be an extension of the shear crack already developed.

In the middle of the bridge between inner flaw tips, there are significant tensile stresses. Therefore, tensile failure may occur due to the formation of cracks perpendicularly to the direction of the maximum principal stresses, i.e. almost vertical, if σ_{11} reaches σ_{crit}, as shown in Figure 7.14 (bottom right). Those tensile cracks are schematically shown in figure 7.14 below (bottom left). In the tests, especially in marble, similar cracks were observed, i.e. so called en echelon cracks.

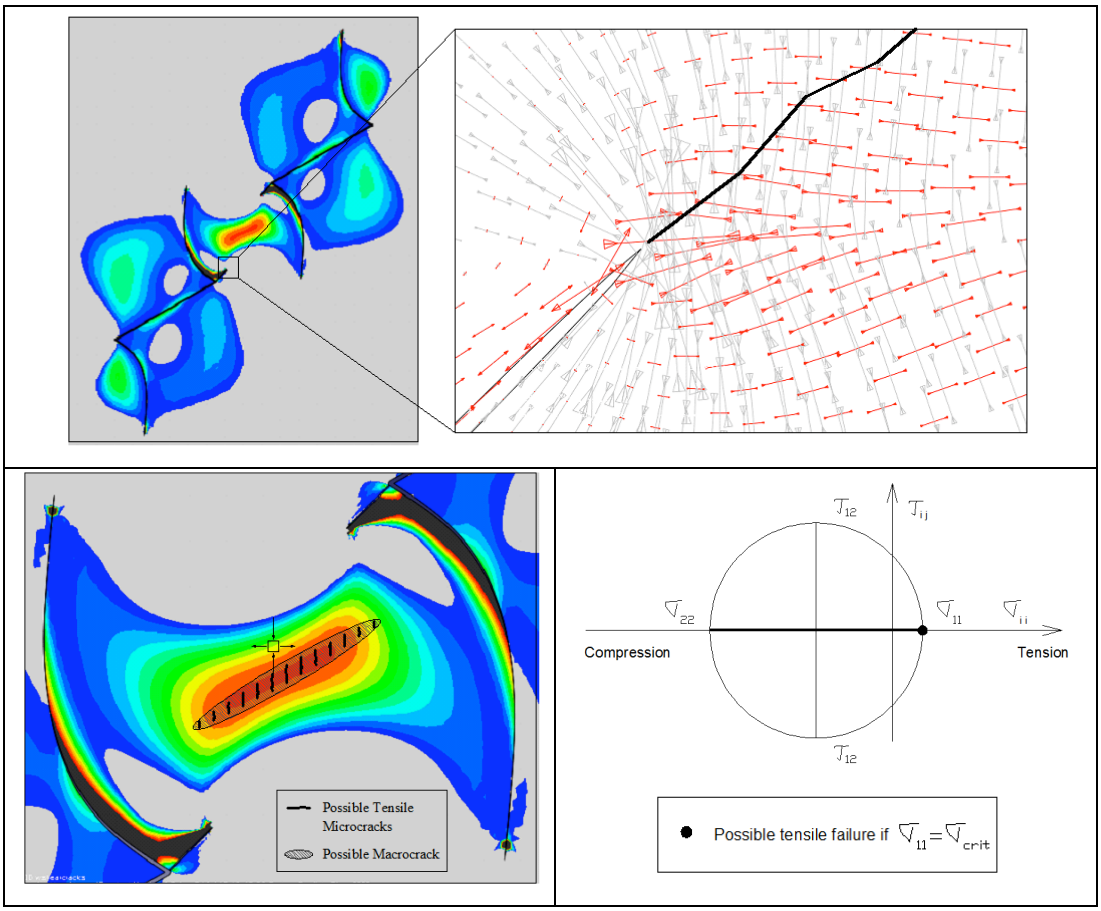

Figure 7.14. Principal stress contours and vectors showing compression stresses around the tip of the shear crack and possible propagation of the existing shear crack (top). Tensile cracks – en echelon cracks – that might develop in the bridge between inner flaw tips in a direction following the contours of maximum principal stresses (bottom left); Mohr circle for the element highlighted (bottom right). Light grey means compression; the color scale represents several degrees of tension.

Since the principal directions are roughly horizontal and vertical in the bridge between inner tips, one can argue that a shear failure caused by 45º cracks might also take place in that region, if τ_{12} reaches a critical shear stress τ_{crit}.

Obviously, the shear or tensile crack initiation will depend on the material resistance to both failures. For example, if the material resistance to shear stresses is much greater than its

resistance to tensile stresses, then a tensile failure will happen. Conversely, if the material resistance to tension is significantly greater than to shear, then a shear failure will occur.

Strain analysis

In contrast to what was discussed about the stress field, there are important elongations ($\boldsymbol{\varepsilon_I} > 0$) in the strain field around the tip of the propagated shear crack as Figure 7.15 illustrates. This means that tensile cracks may occur and propagate from the existing shear crack tip. If the propagated shear crack is long enough, coalescence might occur through a single tensile crack, as illustrated in Figure 7.15 (bottom right). Otherwise, the mechanism involved might be the formation of a coalescence macrocrack from several vertical tensile microcracks, as shown in Figure 7.15 (bottom left)

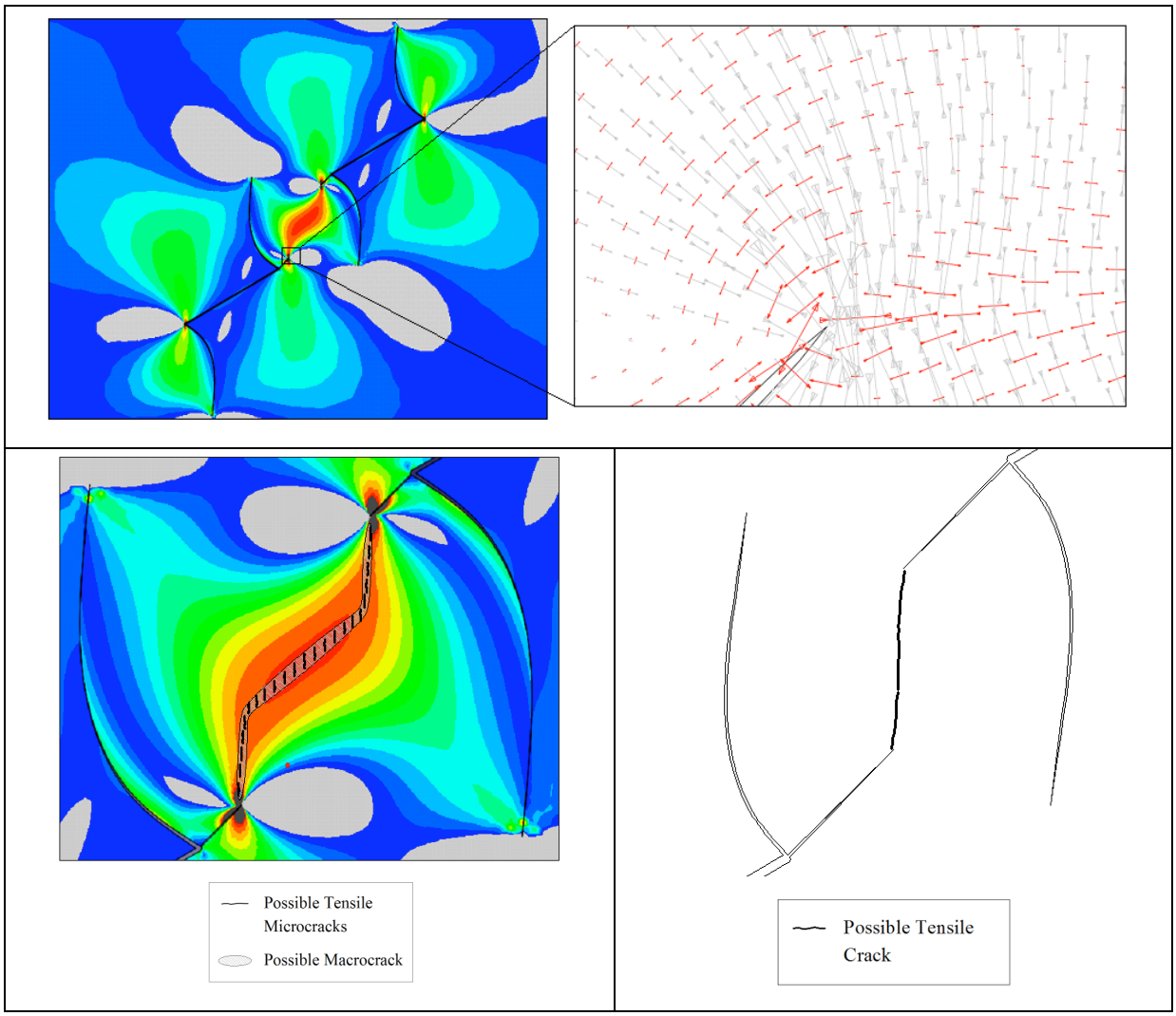

Figure 7.15. Contours of maximum principal strains (top left) and principal strain vectors around the tip of the propagated shear crack (top right). Possible coalescence through a tensile macrocrack (bottom left) and through a single tensile crack (bottom right) Light grey means contraction; the color scale represents several degrees of elongation

Shear crack propagation might also occur at the shear crack tip. The shear or tensile crack initiation will depend on the material resistance to both failures, as explained before. A shear crack will occur when γ_{12} reaches a critical shear stress γ_{crit} (as illustrated in the Mohr circle of the Figure 7.16 below), and when $\varepsilon_{11} < \varepsilon_{crit}$. This corresponds to what was shown in Figure 7.14 for the stress analysis.

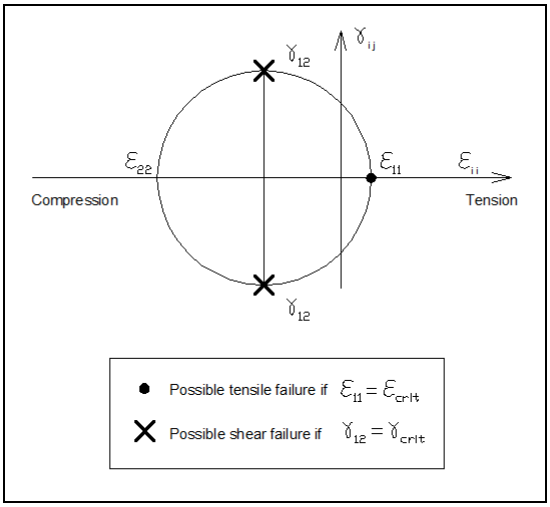

Figure 7.16 . Mohr circle for an element located near the propagated shear crack, showing possible shear and tensile failure

What was described in the stress field approach for the region in-between inner tips is also applicable for the strain field. Depending on the material capacity to absorb elongations or shear deformations, tensile or shear failure may occur.

7.5 Comparison between finite element results and actual tests

For the geometry analyzed throughout this section (**2a-30-30**), the coalescence in **gypsum** took place through a tensile crack, developed from the inner tips of the induced flaws or from shear cracks that propagated simultaneously, as depicted in Figure 7.12 (left). In this figure, the letters are used to indicate the order by which the cracks developed i.e. A develops first, followed by B and so on. The test results correspond to what was obtained for both the stress and strain field approaches, since coalescence through a tensile crack was possible to occur in both approaches, after or before the development of shear cracks from the inner flaw tips.

The only difference between the strain and the stress approaches is the place of initiation of the tensile coalescence crack. In the stress field approach, the tensile coalescence crack had theoretically to start in the middle point of the bridge between inner flaw tips. Using a strain field analysis, the tensile coalescence crack could initiate at the flaw tip, at the shear crack tips or also in the middle of the bridge between flaw tips. However, the experimental results are not clear regarding the place of initiation of the tensile coalescence crack. As a matter of

fact, what happened in many of the actual tests was that even with the high-speed camera, it was not possible to distinguish whether the coalescence crack initiated in the middle of the bridge, at the tip of an induced flaw or at the tip of a previously developed shear crack. Therefore, in these cases, the analysis performed by Wong considered that all coalescence cracks developed simultaneously. This means that unless a new technology is used and one is able to figure out where and when do the coalescence cracks initiate, both stress and strain approaches might be correct.

For **marble**, both approaches are able to predict the actual shear failure, in which coalescence is achieved through a single shear crack that makes an angle of roughly 45^{o} with the horizontal, as can be seen in Figure 7.12 (right). Therefore, both approaches yield acceptable results for marble. However, the issue of the coalescence crack initiation point also occurs here. In both approaches, the shear crack that causes coalescence to occur can start in the bridge between flaw tips, at the flaw tips or at the propagated shear crack tips. The experimental results are not conclusive regarding the initiation point of the coalescence, stating that the coalescence crack happens instantaneously, from the existing flaw tips to the middle of the bridge between inner flaw tips.

7.6 Summary and Conclusions from Models

- Both the **stress and strain field** approaches simulate reasonably well the **wing crack initiation** and **propagation**;
- Both the **stress and strain field** approaches simulate reasonably well the **shear crack initiation and propagation**, after the development of wing cracks;
- The **stress field** approach indicates that, after the wing cracks are formed, it is only possible to develop shear cracks from the inside flaw tips and never tensile cracks.
- In the **stress field** approach, tensile coalescence cracks can only initiate at the mid point of the bridge between flaws.
- The **stress field** approach simulates shear coalescence acceptably.
- With the **strain field** approach, one is able to simulate **wing and shear crack initiation and propagation**, and **tensile or shear coalescence** reasonably well;

- When both shear and tensile cracks may qualitatively occur, the resistance of the material to those failures will define which one takes place (first).

The modelling studies thus showed:

The consequence of these models results on further development of the code FROCK is that the crack propagation criterion needs to consider the strain field in addition to the stress field. Also, a more sophisticated construction of material properties is advisable.

Chapter 8. Conclusions and Future Recommendations for Fracture Research

8.1 Introduction

Fracture initiation and propagation, and particularly, coalescence in rock are complicated processes. They are very important in the creation of Enhanced Geothermal Systems. Understanding the fundamentals of these processes is an important step to eventual use and application in the field. For this reason, research sponsored by the U.S. Department of Energy in the context of Enhanced Geothermal Systems Technology Development was proposed in the following tasks:

1. Testing different rock types and fracture geometries under ambient temperature.
2. Similar to 1 but at elevated temperatures.
3. Extension of the crack initiation, propagation and coalescence criterion and incorporation in a numerical mode.
4. Initial steps toward modeling of larger/smaller fractures.

Specifically, work was done on Tasks 1 and 3 with initial work on Tasks 2 and 4. In addition, since it was thoughts to be particularly relevant, much work also done on flaws pressurized by water since this is the standard situation in the field where fractures are water filled and where hydraulic fracturing/pressurizing of fractures is used to create additional fracturing. Also, in addition to what was originally set out to be done, was an investigation of the suitability of observing acoustic emissions as part of the experimentation.

The main part of this research, the fracture experiments, concentrated on prismatic specimens of granite with two pre-cut flaws tested in unconfined, uniaxial compression. Other rock types (gypsum, marble) had been tested previously and the corresponding results were compared with those of the granite tests. Load and displacement data are recorded during testing. The front face of each specimen is also recorded by a camcorder and high-speed video camera. The camcorder records the entire test while the high-speed camera records a very short time interval (approximately one second). All three sets of data (load-

displacement, camcorder video, and high-speed video) are then synchronized and analyzed to determine crack sequence and nature. Observations regarding white patches were also made using the camcorder and high-speed video sources.

In addition to these unconfined, uniaxial compression tests, a small series of tests was run to investigate the effect of water pressure in the flaws on coalescence. Water pressure was held at 0 psi, 100 psi, 200 psi, or 400 psi with a pressure volume control system and pressure plates. These plates resulted in some confinement.

The modeling work consisted of a review of the application of the existing fracture modeling code FROCK and, specifically, a comparison of the numerical results with those of the experiments. While generally satisfactory, the fracture initiation-, propagation- and coalescence- criterion needs to be improved. First steps in this direction were taken, and they show when a stress field or a strain field approach is best suited.

8.2 Unconfined, Uniaxial Compression Tests

8.2.1 Tests on Granite

White patches appeared in granite specimens during compression tests. These white patches could be divided into two broad categories: diffuse and linear. Linear white patches were then further subdivided into boundary-following (grain boundaries) and through-going (through grains) linear features. Boundary-following linear white patches were by far the most common type of white patch. White patches could appear before, after, or even during cracking processes. Most cracks, however, did appear in zones exhibiting prior white patching. Tensile cracks were generally preceded by linear white patches while large zones of diffuse white patching generally preceded a shear crack.

Tensile wing cracks often did not originate at the tips of flaws, but rather in zones of white patching away from flaw tips. Tensile cracks generally initiated and propagated along grain boundaries. Some shear cracks were hidden by surface spalling, but those that were observed

usually initiated and propagated along grain boundaries. On rare occasions, single grains were sheared.

Unconfined tests were divided into two series, those with ligament length equal to flaw length (L = 2a) and those with ligament length equal to half flaw length. (L = a). In addition to changing ligament length, the boundary conditions were changed between the two series. Brush platens identical to those used by Bobet (1997) and Wong (2008) were used for specimens with L = 2a, and solid platens similar to those used by Martinez (1999) were used for specimens with L = a. Each of these series had coplanar (α=0°) and stepped (α=60°) flaws inclined at β = 0°, 30°, 45°, 60°, and 75°. Figure shows a summary of coalescence patterns observed in these tests. It is a compilation of figures from Section 0.

The coalescence pattern (Figure 8.1) was most strongly affected by bridging angle α. By stepping from 0° to 60°, granite specimens with the same flaw inclination were much more likely to coalesce directly. For coplanar flaw pairs, increasing flaw inclination (β) led to an increase in shear behavior (transitioning from no shear cracks to short length shear cracks to longer shear cracks). For stepped flaw pairs, increasing β actually decreased shear behavior. Comparisons with regard to the effect of ligament length on coalescence behavior are not possible as the two series with different ligament lengths also had different boundary conditions.

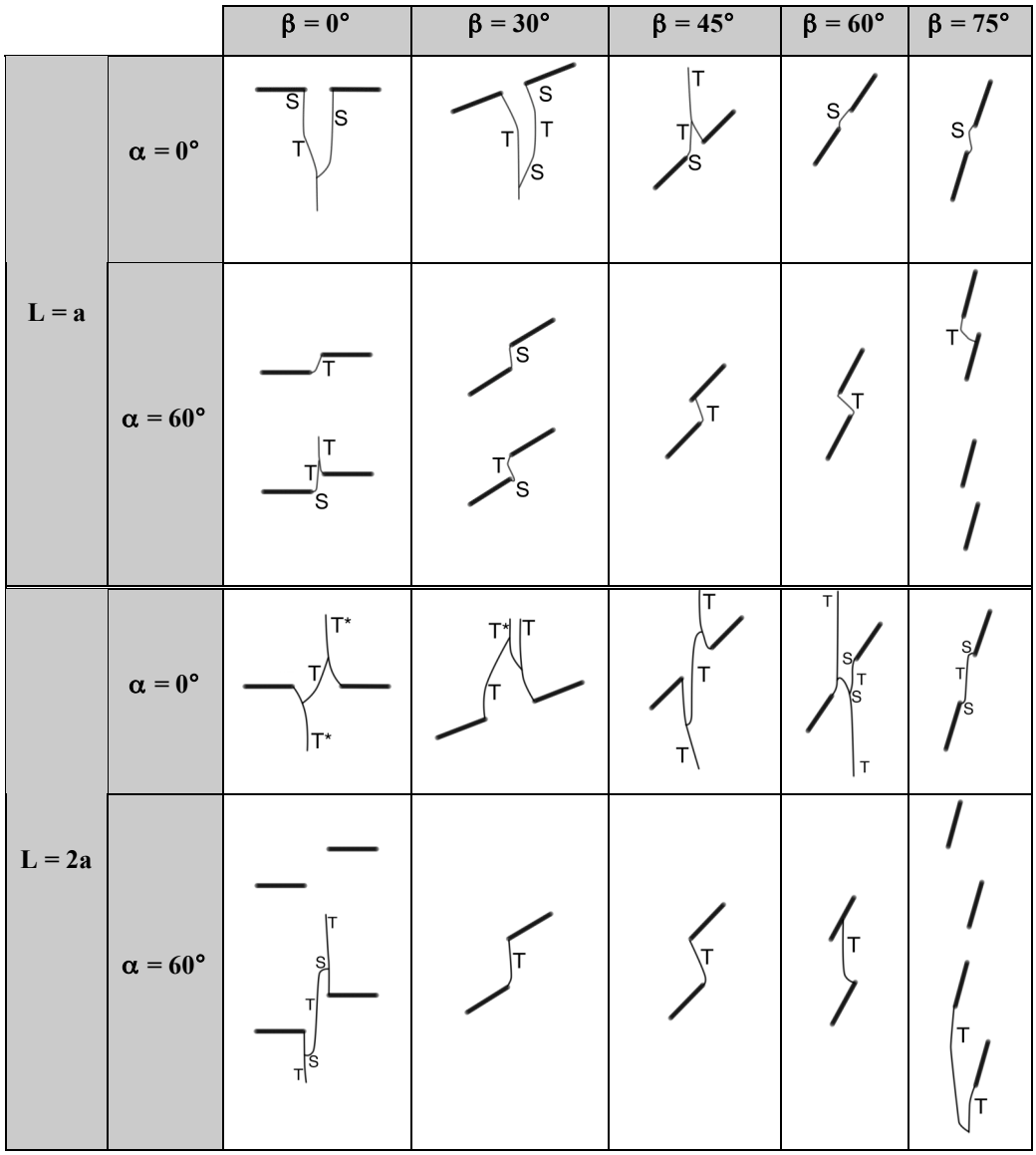

Figure 8.1. Summary of coalescence patterns seen in unconfined, uniaxial compression tests in granite.

Maximum stress was recorded for every specimen tested. Figure 8.2 reproduces the average maximum stress data presented in Figure 4.16 and Figure 4.17. For both L = 2a and L = a, increasing α from coplanar to stepped reduced the maximum stress. For L = 2a, it is interesting to note the coplanar and maximum stress curves are parallel as β increases from 0° to 30°. The two curves then follow different trends until they end at similar levels at β =

75°. For L = a, both curves start at a similar level and then deviate. The two curves, however, have similar shapes.

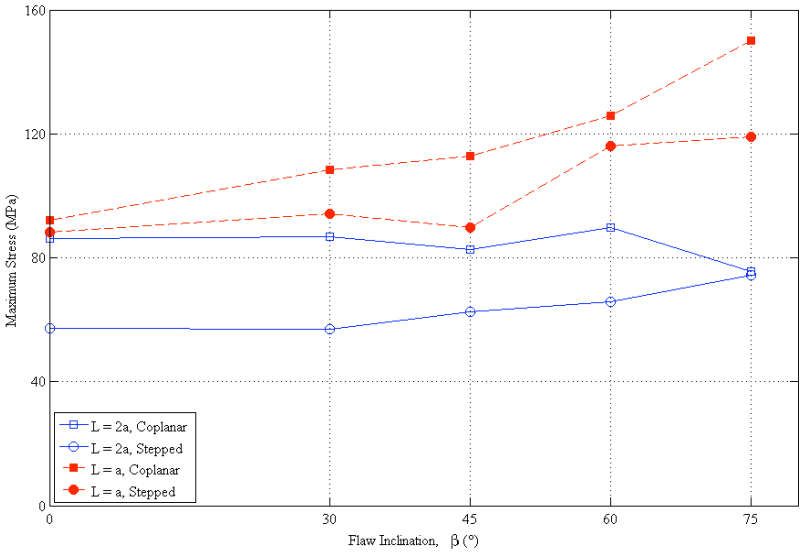

Figure 8.2. Average maximum stresses for unconfined, uniaxial compression tests in granite.

The average crack initiation stress ratio for all tested specimens is shown in Figure 8.3 again, both curves (coplanar and stepped) for L = a follow a similar pattern. The two curves for L = 2a follow different patterns, with the coplanar curve being consistently close to 100%. Once again, for both L = a and L = 2a, the coplanar curve is always higher than the stepped curve.

It should be noted that some tests were also conducted under elevated temperatures (specimens heated to 110°C). Since the behavior did not differ from the one at ambient temperatures, this is not separately reported.

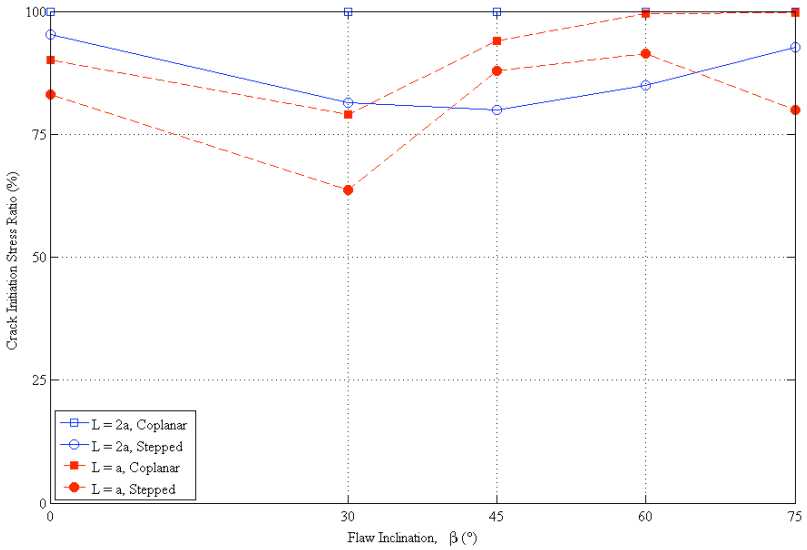

Figure 8.3– Average crack initiation stress ratios for unconfined, uniaxial granite tests.

8.2.2 Comparison with Previous Results

Unlike the observations made in this study, Martinez (1999) observed direct coalescence of all coplanar flaws in granite and tensile wing cracks originating from flaw tips. He did, however, observe sudden failure, cracks predominantly following grain boundaries, white patches, and the occasional appearance of horizontal tensile cracks.

Wong (1999) observed white patches in marble. The white patches in marble, however, were only linear patches. The linear white patches observed in this study followed more tortuous paths than those observed in marble by Wong (2008) at the macroscopic level.

Coplanar geometries with L = 2a were tested in this study to match geometries tested by Wong (2008) in both molded gypsum and Carrara marble. Wong (2008) had already observed an increase in tensile cracking and tensile coalescence patterns when changing from gypsum to marble. He postulated that this was caused by an increase in grain size. Figure 4.26 reproduced here as Figure 8.4 shows that this trend continues with granite. It also shows an increase in the number of geometries that coalesced indirectly as the material increased in grain size from gypsum to marble to granite.

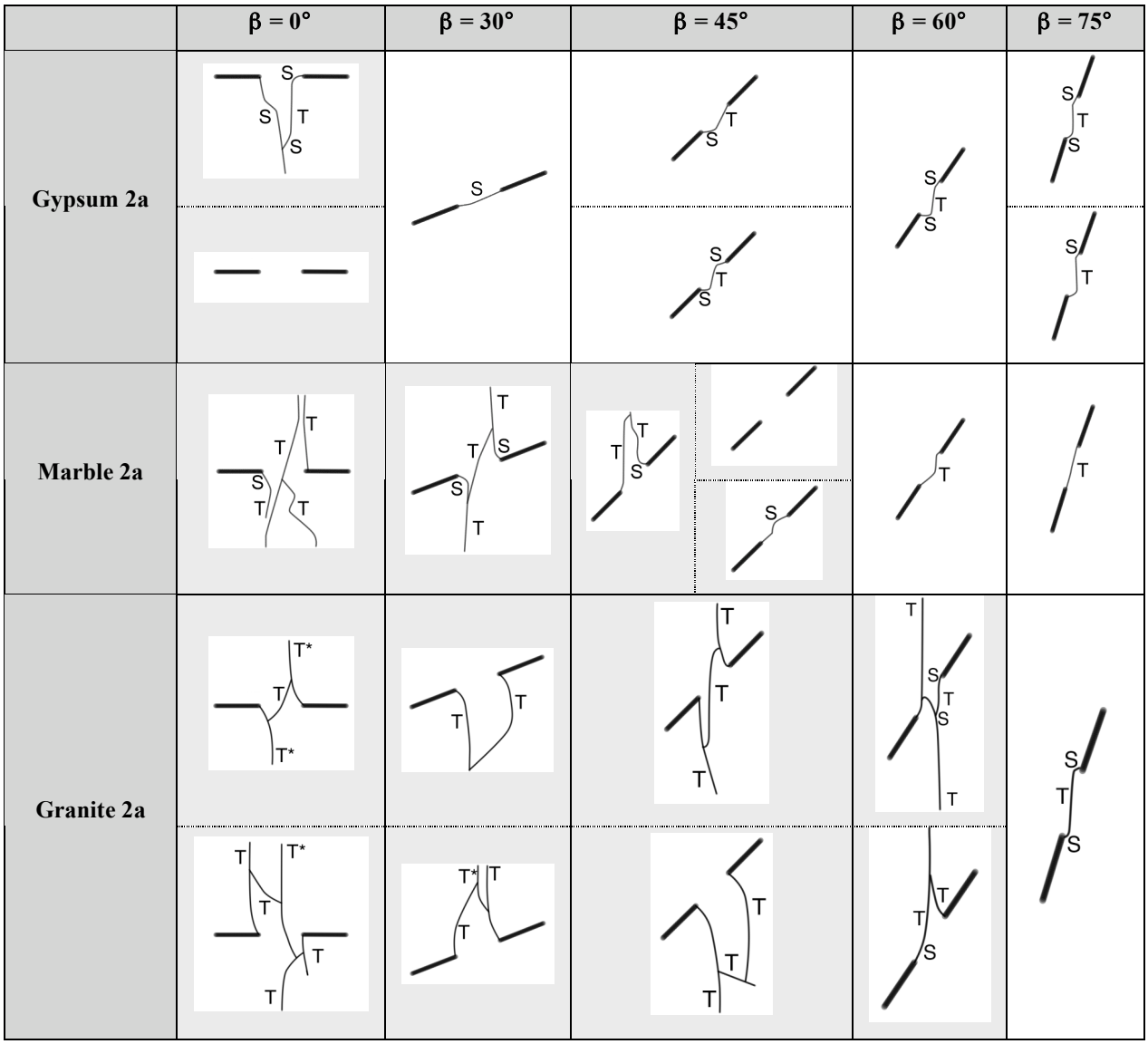

Figure 8.4. Summary of coalescence patterns for coplanar specimens with L = 2a for three different materials. Results for gypsum and marble are summarized from Wong (2008). Geometries with at least one indirect coalescence pattern are highlighted with grey.

Wong (2008) noted that the white patch initiation stress ratio in marble was similar to the crack initiation stress ratio in gypsum. A comparison of the white patch initiation stress ratios of granite and marble and the crack initiation stress ratio of gypsum was made. White

patching in granite occurred at a level close to that of marble and crack initiation in gypsum but did not vary similarly with β.

8.3 Compression Tests with Pressurized Flaws

Natural rocks often have fluid-filled flaws. Importantly, pressurizing fractures with water is often used to initiate new fractures, particularly in petroleum and geothermal applications. A small number of tests were run with the pre-cut flaws being pressurized by water to investigate the influence of water pressure on coalescence. The tests were meant as a proof-of-concept for future studies, so only one geometry was tested.

Two loading profiles and four flaw pressures were tested, as reproduced here as Table 8.1. The most important observations were in regards to water pressure. Water pressure was found to decrease maximum stress and coalescence stress. It was also observed to affect coalescence behavior. Coalescence pattern was also affected by loading rate and/or confinement (from pressure plates). Loading rate was observed to have an affect on the sequence of observed events.

Table 8.1. Summary of coalescence patterns for different flaw pressures and loading profiles. Note that the pattern shown for the slow profile with 0 psi flaw pressure is from the unconfined tests summarized in Chapter 3 (reproduction of Table 6.9).

	0 psi	100 psi	200 psi	400 psi
Slow	 (unconfined)			
fast				- -

8.4 Recommendations for Future Research

Recommendations for future research are made in four different areas:

1. Macroscopic coalescence research
2. Microscopic investigation
3. Effects of water pressure
4. Modelling

8.4.1 Macroscopic Coalescence Research

The current study extends the work done earlier on marble and gypsum to a new material: Barre Granite. To make further comparisons between gypsum, marble, and granite, however, more geometries must be tested. Specifically:

- **Bridging angle α:** intermediate values between 0° and 60° (as well as values above 60°) should be tested to better understand the effect of α on the different processes. Matching values of α tested by Wong (2008) is desirable to make comparisons amongst stepped geometries in different materials.
- **Boundary conditions:** All future tests in granite should be performed with one type of boundary condition (brush platens or solid platens). While brush platens allow one to compare with Wong's (2008) results, they may be impractical for use with a material as strong as granite.
- **Image processing:** As noted by Martinez (1999) identifying white patches in granite is difficult due to the heterogeneity of color in granite. The techniques used in this study are sufficient but time consuming. An automated method to pick out white patches would be very beneficial.

8.4.2 Microscopic Investigation

The SEM investigation by Wong (2008) provided a thorough understanding of the white patches and cracking processes observed in marble. Similar benefits may be reaped by performing a similar investigation in granite. Specifically:

- **Precursors of Tensile Cracking:** An examination of white patches at different stress levels before the visible formation of a tensile crack may lead to understanding of the tensile cracking process.
- **Precursors of Shear Cracking:** Similar to above, but with white patches preceding shear cracks.
- **White Patch Types:** Three different types of white patches were identified at the macroscopic level in this study. It would be beneficial to determine if they are different at the microscopic scale.
- **Image Processing:** The microscopic investigation may benefit from the ability to quantify microcrack density and orientation. This ability may also allow one to differentiate between the different types of microcracks (intra-granular, inter-granular, etc.).

8.4.3 Effects of Water Pressure

The summary of Chapter 6 provided recommendations for future studies regarding the effect of water pressure in flaws on coalescence. Those suggestions are repeated here:

- **Effect of Pressure Plates:** Tests with pressure plates and zero water pressure should be run with different laoding reates. Currently, it is not known if pressure plates affect the coalescence pattern, if the observed changes are a product of the loading rate only, or if they are random.
- **Effect of Loading Rate on Maximum Stress:** The conclusion that maximum stress is unaffected by loading rate should be confirmed.
- **Effect of Water Pressure on Maximum Stress:** It is clear that a relationship exists between water pressure and maximum stress. More tests at different water pressures should be performed to understand this relationship better, however.

- **Effect of Water Pressure on Coalescence Pattern:** It is clear that water pressure has an effect on coalescence pattern. The pressure at which the coalescence pattern changes is not known. For the slow loading rate, water pressures between 200 psi and 400 psi need to be tested to observe the transition in coalescence pattern.

8.4.4 Modelling

It was shown in Chapter 7 that consideration of the strain field in addition to the stress field might lead to improved modeling of the cracking process. In addition, it is necessary to expand the crack initiation-, propagation- and coalescence- criterion to make it normal stress dependent. Right now the development of cracks only depends on the existence of tensile or shear strength where the latter is independent of normal stresses. This is sufficient for open cracks/fractures but not closed ones. Also, while the model has been compared against experiments in gypsum and marble, this has not yet been done for granite.

APPENDIX A. References

Anderson, Minster, and Cole. 1974. The Effect Of Oriented Cracks On Seismic Velocities, *J. Geophys. Res.*, 79, pp 4011-4015.

Anderson. (2005) Fracture mechanics: Fundamentals and Applications, 3rd Ed., CRC Press, Boca Raton, Florida.

Anon. 1981. "In-Situ Sensitivity Calibration of Acoustic Emission Systems," *Technical Review*, No. 2, Appendix C, Bruel and Kjaer, Denmark.

Argon, A.S.; Safoglu. 1975. Cavity Formation From Inclusions In Ductile Fracture, *Metallurgical Transactions*, Vol. 6A, pp 825-837.

Ashby; Hallam. 1986. The Failure Of Brittle Solids Containing Small Cracks Under Compressive Stress States. *Acta Metall.*, 34, pp 497-510.

Ashby; Sammis. 1990. The Damage Mechanics if Brittle Solids in Compression, *Pure Appl. Geophys.*, 133, pp 489-521.

Backers; Stanchits; Dresen, 2005. "Tensile Fracture Propagation and Acoustic Emission Activity in Sandstone: The Effect of Loading Rate," *International Journal of Rock Mechanics and Mining Sciences*, Vol. 42, pp 1094-1101.

Barenblatt. 1962. The Mathematical Theory of Equilibrium Cracks in Brittle Fracture. In Advances in Applied Mechanics, Vol. 7, Academic Press, NY, pp. 55-109.

Bieniawski, Z. 1967. Mechanisms of Brittle Fracture of Rock, Part II – Experimental Studies, *Int. J. Rock. Mech. Min. Sci.*, Vol. 4, pp 407-423.

Bobet, A.; Einstein, H.H. 1998. Fracture Coalescence in Rock-Type Materials Under Uniaxial and Biaxial Compression. *Int. J Rock Mech Min Sci*, 35:7, pp. 863-888.

Bobet, A. 1997. Fracture Coalescence in Rock Materials: Experimental Observations and Numerical Predictions, Sc. D. Thesis, Massachusetts Institute of Technology.

Bombolakis, E. 1963. Photoelastic Stress Analysis Of Crack Propagation Within A Compressive Stress Field, Ph.D. Thesis, Massachusetts Institute of Technology, 38p.

Brace, W.; Bombolakis, E. 1963. A Note on Brittle Crack Growth in Compression, *J. Geophys. Res.*, 68 (12), pp 3709-3713.

Cai, Z. 2000. "Effects of Multiple Parallel Fractures on Apparent Attenuation of Stress Wave in Rock Masses," *International Journal of Rock Mechanics & Mining Sciences*, 37, pp 661-682.

Chaker; Barquins. 1996. Sliding effect on branch crack, *Phys. Chem. Earth*, 21 (4) pp 319-323.

Chan, H.C.M. 1986. Automatic Two-dimensional Multi-Fracture Propagation Modelling of Brittle Solids with Particular Application to Rock, Ph.D. Thesis, Massachusetts Institute of Technology.

Chan, H.C.M. 1991. "Equivalent Crack Formation by Propagating Cracks Under Tension", *Engineering Fracture Mechanics*, Vol. 39, No. 2, pp. 433-441.

Chan, H.C.M.; Li, V.; Einstein, H.H. 1990. "A Hybridized Displacement Discontinuity and Indirect Boundary Element Method to Model Fracture Propagation". *Int'l. Journal of Fracture*, Vol. 45, pp. 263-282.

Chayes, 1952. The Finer-Grained Calcalkaline Granites of New England, *J. Geol.*, 60, pp 207-254.

Chen, G.; Kemeny, J; Harpalani, S. 1995. Fracture propagation and coalescence in marble plates with pre-cut notches under compression, in Myer, Cook, Goodman, and Tsang (Eds.), *Symposium on Fractured and Jointed Rock Mass*, Lake Tahoe, CA, pp 435-439.

Chen; Nishiyama; Kusuda; Kita; Sato. 1999. Correlation between microcrack distribution patterns and granitic rock splitting planes, *International Journal of Rock Mechanics and Mining Sciences*, Vol. 36, pp 535-541.

Costin. 1985. Damage mechanics in the post-failure region. *Mech. Mat.*, 4, pp 149-160.

Crampin. 1984. An introduction to wave propagation in anisotropic media, *Geophys. J. R. Aston. Soc.*, 76, pp 17-28.

Dai; Labuz, J. 1997. Damage and failure analysis of brittle materials by acoustic emission," *Journal of Materials in Civil Engineering*, pp 200-205.

Dale. 1923. The commercial granite of New England, *Bull. US Geol. Surv.*, No. 738.

David, C.; Barton, C.C. 1966. Two Space-time interaction tests for epidemicity, *British Journal of Preventative and Social Medicine*, 20, pp 44-48.

Dugdale. 1960. Yielding in steel sheets containing slits. *Journal of the Mechanics and Physics of Solids*, 8, pp 100-104.

Egle; Tatro. 1967. Analysis of Acoustic-Emission Strain Waves," *The Journal of the Acoustical Society of America*, Vol. 41, No. 2, pp 321-327.

Einstein, H.H.; Hirschfeld, R.C. 1973. Model studies on mechanics of jointed rocks, ASCE Journal of the Geotechnical Division, Vol. 99, SM3.

Einstein, H.H.; Nelson, R. A.; Bruhn, R.W.; Hirschfeld, R.C. 1969. Model studies of jointed rock behavior, *Proc. 11th Symposium on Rock Mechanics*, pp. 83-103.

Erdogan, F.; Sih, G.C. 1963. On the crack extension in plates under plane loading and transverse shear. *Journal of Basic Engineering*, 85, pp 305-321.

Fenwick; Paulay. 1968. Mechanisms of Shear Resistance of Concrete Beams, *journal of the Structural Division, ASCE*, 94 (ST10), pp. 2235-2350.

Fishman, Yu. A. 2008. Features of Shear Failure of Brittle Materials and Concrete Structures on Rock Foundations, *International Journal of Rock Mechanics & Mining Sciences*, 45, pp 976-992

Forster, Scheil. 1936. Akustische Untersuchung der Bildung von martensitnadeln Z Metallk, 29.

Friedman; Handin; Alani. 1972. Fracture energy of rocks. *Int. J. Rock. Mech. Min. Sci.*, 9, pp 757-766.

Germanovich, R.J.; Dyskin, A.V. 2000. Fracture mechanisms and instability of openings in compression. *Int. J. Rock. Mech. Min. Sci.*, 37, pp 263-284.

Gidley et al. (Ed). 1989. Recent advances in hydraulic fracturing, SPE Monograph, SPE, Richardson, Texas.

Glaser; Nelson. 1992. "High-Fidelity Waveform Detection of Acoustic Emissions from Rock Fracture," *Materials Evaluation*, March 1992, pp. 254-359.

Goldsmith; Sackman; Ewert. 1976. Static and dynamic fracture strength of Barre Granite, *Int. J. Rock Mech. Min. Sci. and Geomech. Abstr.*, Vol. 13, pp 303-309.

Gramberg. 1965. Axial cleavage fracturing, a significant process in mining and geology, *Engineering Geology*, 1(1), pp 31-72.

Griffith, A.A. 1920. The phenomenon of rupture and flwo in solids. *Philosophical Transactions*, Series A, 22a, pp 163-198.

Griffith, A.A. 1927. Tech. Rpt. *Aeronaut. Res. Comm.*, 2, pp 668.

Hallam; Ashby. 1990. Compressive brittle fracture and the construction of multi-axial failure maps. In Barber and Meredith (eds) Deformation Processes in Minerals, Ceramics and Rocks. London: Unwin Hyman, pp 84-108.
Hardy, Jr. 2003. Acoustic Emission/Microseismic Activity: Vol. 1, A.A. Balkema Publishers, Exton.
Hillerborg; Modeer; Petersson. 1976. Analysis of crack formation and crack growth in concrete by means of frature mechanics and finite elements. *Cement and Concrete Research*, 6, pp 773-782.
Hillerborg. 1991. Application of the fictitious crack model to different materials. *International Journal of Fracture*, 51, pp 95-102.
Hoek, E.; Bieniawski, Z. 1965. Brittle fracture propagation in rock under compression, *Int. J. of Fracture Mechanics*, Vol. 1, pp 137-155.
Hoenig. 1979. Elastic moduli of a non-randomly cracked body, *Int. J. Solids Struct.*, 15, pp 137-154.
Horii, H.; Nemat-Nasser, S. 1985. Compression-induced microcrack growth in brittle solids: Axial splitting and shear failure, *J Geophys. Res.*, 90 (B40), pp 3105-3125.
Horii, H.; Nemat-Nasser, S. 1986. Brittle failure in compression, splitting, faulting and brittle-ductile transition, *Philo. Trans. Roy. Soc. London*, 319, pp 337-347.
Hsu; Simmons; Hardy. 1979. "An Approach to Acoustic Emission Signal Analysis-Theory and Experiment," *Material Evaluation*, Vol. 35, No. 10, pp. 100-106.
Huang; Chen; Zhao; Wang. 1990. An experimental study of the strain field development prior to failure of a marble plate under compression, *Tectonophysics*, 175, pp 283-290.
Hudson, J.A. 1981. Wave speeds and attenuation of elastic waves in material containing cracks, *Geophys. J. R. Astron. Soc.*, 65, pp 133-150.
Hussain, M. A., S. L. Pu, and J. Underwood. 1974. Strain energy release rate for a crack under combined mode I and mode II. *Fract. Anal. ASTM STP*, 560, pp 2-28.
Inglis. 1913. Stresses in a plate due to the presence of cracks and sharp corners, *Inst. Naval Architecture, London*, 55, pp 219-230.
Ingraffea and Heuze. (1980) Finite element models for rock fracture mechanics, *Int. J. Num. Anal. Meths. In Geomechs.*, 4, pp 25.
Ingraffea, A.R.; Heuze. F.E. 1980. Finite Element Models for Rock Fracture Mechanics. International *Journal for Numerical and Analytical Methods in Geomechanics*, Vol. 4, 25-43, 1980
Iqbal; Mohanty. 2006. Experimental calibration of stress intensity factors of the ISRM suggested cracked chevron-notched Brazilian disc specimen used for determination of mode-I fracture toughness, *Int. J Rock Mech. Min. Sci.*, 43, pp 1270-1276.
Irwin. 1956. Onset of fast crack propagation in high strength steel and aluminum alloys. *Sagamore Research Conference Proceedings*, 2, pp 289-305.
Irwin. 1957. Analysis of stresses and strains near the end of a crack traversing a plate. *Journal of Applied Mechanics*, 24, pp 361-364.
Isnard; Leymarie. 1964. Observations sur le fil du granite dans les carriers du Sidobre (Tarn), *Sci. Terre*, 9, pp 423-437.
Kachanov. 1985. A simple technique of stress analysis in elastic solids with many cracks, *Int. J. Fracture*, 28, R11-R-19.

Kaiser. 1953. "Erkenntnisse und Folgerungen aus der Messung von Gerauschen bei Zubeanspruchung von metallischen Werkstofen [Results and conclustions from measurements of sound in metallic materials under tensile stress], Archiv Eisenhuttenwess, 24, p43.

Kani; Huggins; Wittkipp. 1979. Kani on Shear in Reinforced Concrete, University of Toronto Press, Toronto, Canada, 225 pp.

Kemeny, J.; Cook, N. 1987. Crack models for the failure of rocks in compression. In *Proc. 2nd Int. Conf. on Constitutive Laws for Engineering Materials*, Tucson, Arizona.

Kemeny, J.; Cook, N. 1991. Micromechanics of deformation in rocks, in Shah (Ed) Toughening Mechanisms in Quasi-Brittle Materials, Kluwer Academic, Norwell, USA, pp 155-188.

Kessler et al. 1940. Physical, Mineralogical, and durability studies on the building and monumental granites of the United States, *Journal of Research of the National Bureau of Standards*, Vol. 25, No. 2, Paper RPI1320.

Ko, T.Y. .2005. Crack coalescence in rock-like material under cyclic loading, Civ. Eng. Thesis, Massachusetts Institute of Technology, 184 p.

Ko, T.Y.; Einstein, H.H.; Kemeny, J. 2006. Crack coalescence in brittle material under cyclic loading. Golden Rocks 2006, Proc. of the 41st U.S. Symposium on Rock Mechanics (USRMS): "50 Years of Rock Mechanics – Landmarks and Future Challenges.", Golden, Colorado, June 17-21. ARMA/USRMS 06-930.

Krech; Hendersen; Hjelmstad. 1974. A standard rock suite for rapid excavation research. *U.S.Bureau of Mines*, Report Investigations 7865.

Kurz; Grosse; Reinhardt. 2005. Strategies for Reliable Automatic Onset Time Picking of Acoustic Emissions and of Ultrasound Signals in Concrete, *Ultrasonics*, Vol. 43, pp 538-546, 2005.

Labuz; Cattaneo; Chen. 2001. Acoustic Emission at Failure in Quasi-brittle Materials, *Construction and Building Materials*, 15, 2001, pp225-233.

Lajtai, E.Z. 1971. A theoretical and experimental evaluation of the Griffith theory of brittle fracture, *Tectonophysics*, 11, pp 129-156.

Lei; Nishizawa; Kusunose; Satoh. 1992. Fractal Structure of the Hypocenter Distributions and Focal Mechanism Solutions of Acoustic Emission in Two Granites of Different Grain Sizes, *Journal of the Physics of Earth*, Vol. 40, pp 617-634.

Li, S; Chen, Z.; Wang. 2005. Experimental research on pre-cracked marble under compression, *International Journal of Solids and Structures*, 42, pp 2505-2516.

Liebowitz, H. *Fracture: An advanced Treatise*. Academic Press, New York, 1968

Lo; Coyner; Toksoz. 1986. Experimental determination of elastic anisotropy of Berea sandstone, Chicopee shale, and Chelmsford granite, *Geophysics*, Vol. 51, No. 1, pp 164-171.

Lockner; Byerlee, J. 1977. Acoustic Emission and Fault Formation in Rocks," *Proc. 2nd Conf. on Acoustic Emission/Micro Seismic Activity in Geological Structures and Materials*, Ed. HR Hardy and FW Leighton, Trans-Tech Publications, Clausthal-Zellerfeld, pp 99-107.

Lockner; Byerlee, J. 1980. Development of Fracture Planes During Creep in Granite, *Proc. 1st Conf. on Acoustic Emission/Micro Seismic Activity in Geological Structures and Materials*, Ed. HR Hardy and FW Leighton, Trans-Tech Publications, Clausthal-Zellerfeld, pp 11-25.

Lockner; Byerlee, J. 1978. Velocity Anomalies: An Alternative Explanation Based on Data from Laboratory Experiments," *Pure and Applied Geophysics*, Vol. 116, pp 765-772.
Lockner, 1993. The role of acoustic emission in the study of rock fracture. International Journal of Rock mechanics, Mining Science and Geomechanic Abstracts, 30, pp 883-889.
Lockner; Byerlee; Kuksenko; Ponomarev; Sidorin, 1992. Observations of Quasistatic Fault Growth from Acoustic Emissions. Fault Mechanics and Transport Properties of Rocks. Eds. B Evans and T Wong, Academy, London, pp. 3-31.
MacGregor. 1964. Discussion of "The Riddle of Shear Failure and its Solution" by G.N.J. Kai, *ACI Journal, Proceedings*, 61(12), pp. 1598-1604.
Maji, A.K.; Wang, J. 1992. Fracture mechanics of a tension-shear macrocrack in rocks. *Experimental Mechanics* 32(2), pp 190-196.
Mansfield, C.; Cartwright, J. 2001. Fault Growth by linkage: Observations and Implications from Analogue Models. *Journal of Structural Geology*, 23, pp. 745-763.
Martinez, A. 1999. Fracture Coalescence in Natural Rocks, M.Sc. Thesis, Massachusetts Institute of Technology, 341 p.
Meglis; Chow; Young. 1995. Progressive Microcrack Development in Tests on Lac du Bonnet Granite – I. Acoustic Emission Source Location and Velocity Measurements, *International Journal of Rock Mechanics, Mining Science and Geomechanics Abstracts*, Vol. 32, No. 8, 1995, pp 741-750.
Michaels; Michaels; Sachse, 1981.Applications of Deconvolution to Acoustic Emission Signal Analysis, *Materials Evaluation*, Vol. 29, pp. 1032-1036.
Miller, J. 2008. Crack Coalescence in Granite, M.Sc. Thesis, Massachusetts Institute of Technology, 474 p.
Miller, J.; Einstein, H. H. 2008. Crack Coalescence Tests on Granite. 42nd U.S. Rock Mechanics Symposium, Proc. 2nd U.S.-Canada Rock Mechanics Symposium, San Francisco.
Moss; Gupta. 1982. A constitutive model describing dilatancy and cracking in brittle rocks. *Journal of Geophysical Research*, 87 (B40), pp 2985-2998.
Motoyama; Hirschfeld. 1971. The effect of joint configurations on the strength and deformability of model rock masses, Final Report, Federal Railroad Administration, Department of Transportation, Washington, D.C. 20591, 183 p.
Mughieda; Alzo'ubi. 2004. Fracture mechanics of offset rock joints – a laboratory investigation, *Geotechnical and Geological Engineering*, 22, pp 545-562.
Nasseri; Mohanty. 2008. Fracture toughness anisotropy in granitic rocks, *International Journal of Rock Mechanics and Mining Sciences*, 45, pp. 167-193.
Nelson; Glaser, 1992. Acoustic Emissions Produced by Discrete Fracture in Rock: Part1, *International Journal of Rock Mechanics, Mining Science and Geomechanic Abstracts*, Vol. 29, No. 3, 1992, pp. 237-251.
Nelson. 1968. Modeling a Jointed Rock Mass, MSc Thesis, Massachusetts Institute of Technology, 218p.
Nemat-Nasser, S.; Horii, H. 1982. Compression-induced nonplanar crack extension with application to splitting, exfoliation, and rockburst, *J. Geophys. Res.*, 87 (8), pp 6805-6821.
Nesatova; Lajtai, E.Z. 1973. Fracture from compressive stress concentrations around elastic flaws, *Int J. Rock Mech. Min. Sci. & Geomech. Abstr.*, 10, pp 265-284.
Nishiyama; Kusuda. 1994. Identification of pore spaces and microcracks using fluorescent resins, *Int. J. Rock Mech. Min. Sci. Abstr.*, 31(4), pp 369-375.

Nur, A.; Simmons, G. 1969. Stress-induced velocity anisotropy in rocks: an experimental study, *J. Geophys. Res.*, 74, pp 6667-6674.
Obert. 1941. Use of subaudible noise for the prediction of rock bursts. RI 3555, *US Bureau of Mines.*
Osborne. 1935. Rift, grain, hardway in some pre-Cambrian granites, Quebec, *Econ. Geol.*, 30, pp 540-551.
Peng; Johnson. 1972. Crack growth and faulting in cylindrical specimens of Chelmsford granite, *Int. J. Rock Mech. Min. Sci.*, 9, pp 37-86.
Petit, J.-P.; Barquins, M. 1988. Can natural faults propagate under Mode II conditions? *Tectonics*, 7 (6), pp 1246-1265.
Physical Acoustics Corporation, 2007. <http://www.pacndt.com>, Last Accessed 28 August 2007.
Press; Flannery; Tenkolsky; Vetterling. 1987. Numerical Recipes. Cambridge University Press, Cambridge, pp. 502-507.
Proctor, Jr. 1982. An improved piezoelectric acoustic emission transducer, *The Journal of the Acoustical Society of America*, Vol. 71, No. 5, 1982, pp 1163-1168.
Proctor, Jr. 1980. Improved Piezoelectric Transducer for Acoustical Emission Reception, *The Journal of the Acoustical Society of American Supplements*, Vol. 1, pp S68.
Reyes, O; Einstein, H.H. 1991. Failure mechanism of fractured rock – a fracture coalescence model. In W. Wittke (ed) *Proceedings of the 7th International Congress of Rock Mechanics,* Aachen, Germany, 1, pp.333-340. Rotterdam: Balkema.
Reyes, O. 1987. Numerical Modeling of Fracture Propagation in tension softening materials, S.M. Thesis, Massachusetts Institute of Technology.
Reyes, O. 1991. Experimental Study and Analytical Modeling of Compressive Fracture in Brittle Materials, Ph.D. Thesis, Massachusetts Institute of Technology.
Reyes, O.; Einstein, H. H. 1991. Failure mechanism of fractured rock – a fracture coalescence model. In W. Wittke (ed) Proc. of the 7th International Congress of Rock Mechanics 1991, Aachen, Germany, 1, pp.333-340. Rotterdam: Balkema.
Sagong, M.; Bobet, A. 2002. Coalescence of multiple flaws in a rock-model material in uniaxial compression, *Int. J. Rock Mech. Min. Sci.*, 39, pp 229-241.
Sagong, M. 2001. The study of the fracture of multiple flaw specimens, Ph.D. Thesis, Purdue University, Indiana.
Salamon; Wiebols. 1974. Digital Location of Seismic Events by an Underground Network of Seismometers using the Arrival Times of Compressional Waves, *Rock Mechanics*, Vol. 6, 1974, pp 141-166.
Sano; Kudo; Mizuta. 1992. Experimental Determination of Elastic Constants of Oshima Granite, Barre Granite, and Chelmsford Granite, *Journal of Geophysical Research*, Vol. 97, No. B3, pp. 3367 – 3379.
Satoh; Idehara; Nishizawa; Kusunose, 1986. Hypocenters Distribution and Focal Mechanisms of AE Events Under Triaxial Compression – Focal Mechanisms of AE events in Yugawara Andesite, *Zisin*, Vol. 39, 1986, pp 351-360.
Scott, 1991. Basic Acoustic Emission, Gordon and Break Science Publishers, New York.
Scruby, 1985. Quantitative Acoustic Emission Techniques, Research Techniques in Nondestructive Testing, Vol. 8, ed. By RS Sharpe, Academic Press, London (1985).
Segall, P.; Pollard, D.D. 1983. Nucleation and growth of strike slip faults in granite. *J. Geophys. Res.*, 88, pp 555-568.

Shah; Labuz, 1995. Damage Mechanisms in Stressed Rock from Acoustic Emission, *Journal of Geophysical Research*, Vol. 100, No. B8, 1995, pp15, 527-15,539.
Shen, B., O. Stephansson, H.H. Einstein and B. Ghahreman. 1995. Coalescence of fractures under shear stress experiments. *J. Geophs Res*, 100 (6), pp. 5975-5990.
Sherwood; Bentz; Collins. 2007. Effect of Aggregate Size on Beam-Shear Strength of Thick Slabs. *ACI Materials Journal*, 104 (2), pp. 180 – 191.
Sih, G. 1973. Some basic problems in fracture mechanics and new concepts. *Engineering Fracture Mechanics*, 5, pp 365-377.
Sih, G. 1974. Strain-energy-density factory applied to mixed mode crack problems. *International Journal of Fracture*, 10(3), pp 305-321.
Simmons; Todd; Baldridge. 1975. Toward a quantitative relationship between elastic properties and cracks in low porosity rocks, *Am. J. Sci.*, 275, pp 318-345.
Stephens; Pollock. 1971. Waveforms and Frequency Spectra of Acoustic Emissions, *The Journal of the Acoustical Society of America*, Vol. 50, No. 3, 1971, pp 904-910.
Taylor. 1970. Investigation of Forces Carried across Cracks in Reinforced Concrete Beams by Interlock of Aggregates, TRA 42.447, Cement and Concrete Association, London, 22p.
Tester; Drake; Driscoll; Golay; Peters. 2005. Sustainable Energy: Choosing Among Options, The MIT Press, Cambridge, Massachusetts, 846 pp.
Vallen System website, 2007. <http://www.vallen.de/>, Last accessed 28 August 2007.
Wang; Shrive. 1995. Brittle fracture in compression: mechanics, models and criteria, *Engineering Fracture Mechanics*, 52 (6), pp 1107-1126.
Wong, L.N.Y. 2008. Crack coalescence in molded gypsum and Carrara Marble, Ph.D. Thesis, Massachusetts Institute of Technology, 876 p.
Wong, L.N.Y.; Einstein, H. H. 2006. Fracturing behavior of prismatic specimens containing single flaws. Proc. Golden Rocks 2006, The 41st U.S. Symposium on Rock Mechanics (USRMS): "50 Years of Rock mechanics – Landmarks and Future Challenges.", Golden, Colorado, June 17-21, 2006, ARMA/USRMS 06-899.
Wong, L.N.Y.; Einstein, H. H. 2008. Crack Coalescence in Molded Gypsum and Carrara Marble: Part 1. Macroscopic Observations and Interpretation. *Rock Mech. and Rock Eng.*
Wong, L.N.Y.; Einstein, H. H. 2008. Crack Coalescence in Molded Gypsum and Carrara Marble: Part 2. Microscopic Observations and Interpretation. *Rock Mech. and Rock Eng.*
Wong, L.N.Y.; Einstein, H. H. 2008. Using high speed video images in the study of cracking process in rock. Accepted for publication in *Geotechnical Testing Journal*.
Wong, R.H.C.; Chau, K.T. 1998. Crack coalescence in rock-like material containing two cracks. *Int. J. Rock Mech. Min. Sci*., 35 (2), pp 147-164.
Wood. 2006. Tools and Machinery of the Granite Industry, *The Chronicle of the Early American Industries Association*, June.
Xia; Nasseri; Mohanty; Lu; Chen; Luo. 2008. Effects of microstructures on dynamic compression of Barre granite, *International Journal of Rock Mechanics and Mining Sciences*, 45, pp 879-887.
Yew, 1997. Mechanics of Hydraulic Fracturing, Gulf Publishing Company, Houston, Texas, 1997.

Zang; Wagner; Dresen. 1996. Acoustic Emission, Microstructure, and Damage Model of Dry and Wet Sandstone Stressed to Failure, *Journal of Geophysical Research*, Vol. 101, No. B8, pp 17,507 – 17,521.

Zang; Wagner; Stanchits; Dresen; Andresen; Haidekker. 1998. Source Analysis of Acoustic Emissions in Aue Granite Cores Under Symmetric and Asymmetric Compressive Loads," *Geophysics Journal International*, Vol. 135, pp 1113-1130.

Zietlow; Labuz, 1998. Measurement of the intrinsic process zone in rock using acoustic emission," *International Journal of Rock Mechanics, Mining Science and Geomechanic Abstracts*, Vol. 35, No. 3, pp 291-299.

APPENDIX B– Acoustic Emission Review

B.1 Introduction

When a structure deforms, it releases energy in the form of elastic waves. These elastic waves cause small movements on the structure's surface, which can in turn be detected. This is the foundation of the field of acoustic emission. Obert first observed the phenomenon in rocks in 1941 while studying rock bursts in underground mines (Obert, 1941). However, acoustic emissions had been observed in metals much earlier. Jabir ibn Hayyan first wrote about the sounds metal made while being forged in the 8th century. Forster and Scheil discussed clicks made by rapidly cooling high-nickel steel (Forster and Scheil, 1936). Since then, the method has been adapted to several fields, such as safety monitoring of structures, weld cracking, the testing of thin-walled structures, corrosion detection, and even as an indicator of martensitic transformations (Scott, 1991).

Acoustic emission observation is an indirect method. It does not measure a material property, but the behavior of the particular structure being observed. The method can alert the user to an impending failure of the structure. In this way, it is similar to sonic methods. Unlike sonic transmission methods, however, acoustic emission techniques are passive. This difference can be seen in Figure B.1.

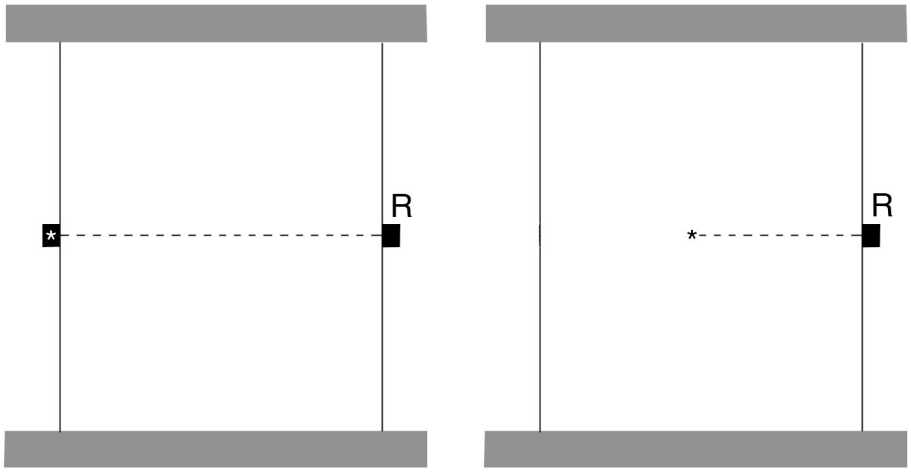

(a) **(b)**

Figure B.1 – Illustration of (a) sonic transmission where the source (*) is a transmitter mounted to the specimen versus (b) acoustic emission where the source is inside the specimen. In this case, the source is natural instead of artificial.

In fact, Obert and Duvall were using the sonic technique as shown in Figure B.1(a) while studying rock bursts for the US Bureau of Mines when they noticed even after removing the transmitter, the receiver would still record signals (Obert and Duvall, 1942). They had inadvertently switched to an experimental set-up resembling Figure B.1 (b). In Obert's original paper, he noted that the rate (e.g. signals per second) of these signals increased with loading of the columns being observed.

In 1950, Kaiser laid the foundations for the modern field of acoustic emission with his PhD thesis at theTechnische Hochschule Munchen and his first publication (Kaiser, 1953). He discovered the Kaiser effect, which is observed in most materials. The effect is a phenomenon, in which there will be no new acoustic emissions until a material has passed the maximum load is has previously experienced. Some materials follow this pattern strictly, others merely have decreased emissions during reloading, and still other materials follow the effect until some percentage of their maximum load, as reported by Lockner (1993) and Dai and Labuz (1997). Figure B.2 illustrates the Kaiser effect.

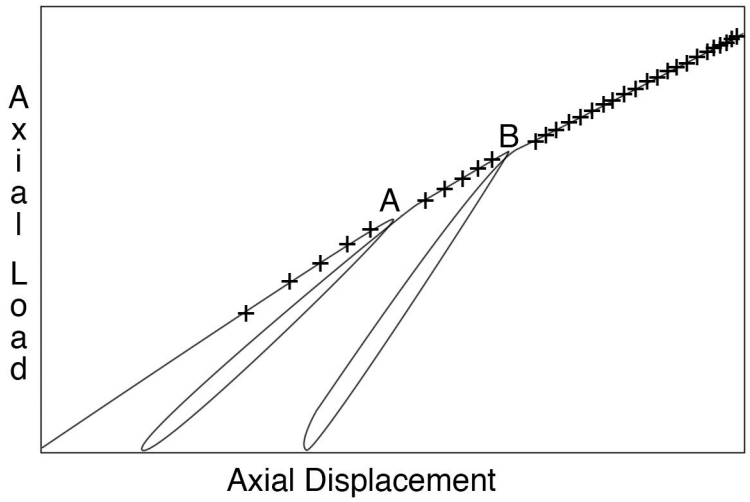

Figure B.2 – Illustration of the Kaiser effect for a material undergoing multiple load-unload cycles. Crosses indicate acoustic emission events. As the specimen is loaded up to point A, there are a few sparse events. As the specimen is unloaded and then loaded back to the same axial load as point A, there are no new events. As the load increases past point A to point B, events resume. Again, no events take place as the specimen is unloaded and reloaded to an equivalent stress level. Events resume as the specimen is loaded further. Note the increasing number of events with increasing load as reported by Obert.

More recent studies involving acoustic emission techniques have studied stability and failure, source location, and source characterization. These will be discussed in greater depth, later.

B.2 Mechanisms of Acoustic Emission

Acoustic emission comes from the sudden release of strain energy within a material. This sudden release of strain energy is often related to crack formation and propagation. When a crack forms (the case of a propagating crack is analogous), the stress on the face of the crack goes to zero. As shown in Figure A.3, the stress in the material on a plane with the crack goes from an initial stress of $\sigma = \sigma_0$ to $\sigma = \sigma_0\left(\frac{A}{A_0 - A}\right)$, where A_0 is the cross-sectional area

before the crack formed, and A is the area after crack formation. The stress is redistributed by elastic waves traveling at the speed of sound within the material (Scruby, 1985).

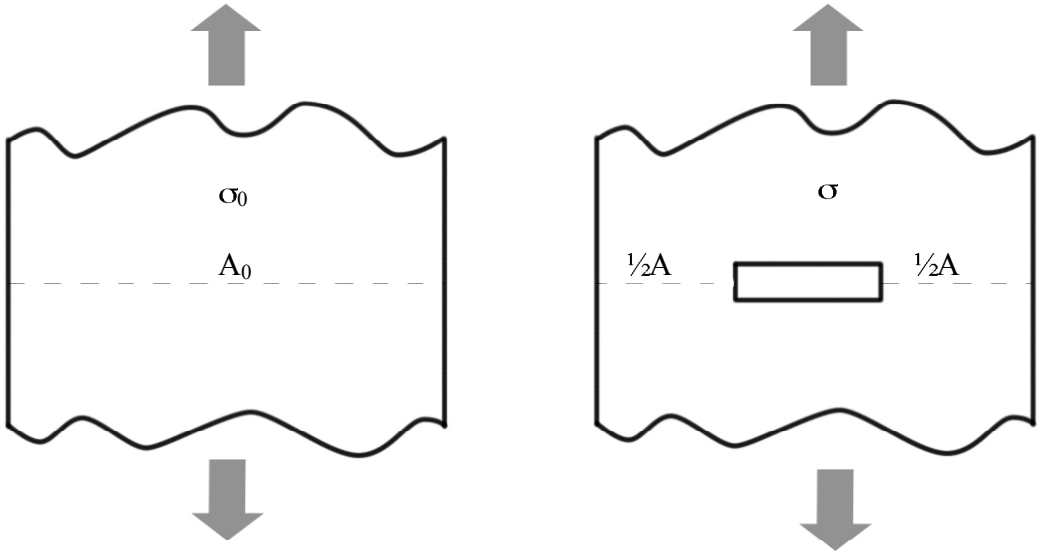

Figure B.3 – Illustration of the effect of crack formation on stresses within a specimen. The left figure shows a specimen with a horizontal cross section with area A_0 and a uniform stress field of σ_0. With the formation of a crack in the right figure, the stress state is changed. Because there are zero stresses on the faces of the crack, the effective cross sectional area is decreased to A (equal to A_0 minus the area of the crack face).

While crack formation and propagation is the main source of acoustic emission in metallic materials, there are many other sources in rock, not all of which are well understood. These sources occur on many different scales and can be broken into three levels: micro (below grain level), macro (at grain level), and mega (far above grain level). Possible sources of elastic waves within rock and rock-like materials include (from Hardy, 2003):

- Micro-level: dislocations
- Macro-level: twinning, grain boundary movement, or initiation and propagation of cracks (through and/or between mineral grains)
- Mega-level: failure of large areas or the movement of whole structural units

These elastic waves propagate in cylindrical or spherical waves (depending on boundary conditions as well as the source itself), although they can be assumed to be planar in the far field or over small distances along the wave front in the near field. The waves themselves will primarily take one of two possible forms. The first, known as P-waves (also known as primary, pressure, longitudinal, dilational, or irrotational waves), are compression waves in the direction of propagation. The second type, known as S-waves (also known as secondary, shear, transverse, or distortional waves), are associated with particle movement perpendicular to the direction of wave propagation. These two wave types are illustrated in Figure B.4.

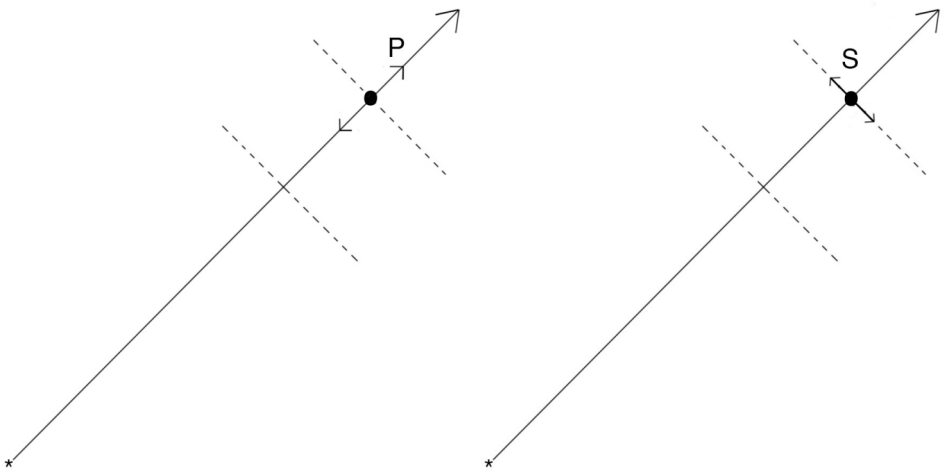

Figure B.4 – Two main wave types. Dashed lines are wave fronts and solid lines indicate the direction the wave is traveling or particle motion. Note that particle motion is in the same direction as wave propagation in P-waves (left) while it is perpendicular to wave propagation in S-waves (right).

P-waves travel faster than S-waves and the difference can be expressed using only the Poisson's ratio. This can be done because both P-wave velocity (C_1) and S-wave velocity (C_2) can be expressed in terms of material density and the elastic constants. The ratio of C_1 to C_2 can then be found to be

$$\frac{C_1}{C_2} = \sqrt{\frac{2(1-\upsilon)}{(1-2\upsilon)}}$$, where υ is the Poisson ratio.

So for a Poisson's ratio of 0.3 (typical for many rock types), C_1 is $1.87 \bullet C_2$, or almost twice the S-wave velocity. Typical values of C_1 and C_2 in rock are a few thousand meters per

second. These values are also variable in rock depending on many factors, including stress, temperature, composition, mechanical history, and mechanical state (Hardy, 2003).

Stress waves traveling through a rock mass often travel at different speeds in different directions. This effect is known as velocity anisotropy. This velocity anisotropy can be an inherent property or develop with changing conditions. Rocks with material anisotropy (bedding or rift planes, for example) display velocity anisotropy at all stress states. The presence or formation of pores or micro-cracks will also contribute to this velocity anisotropy as they behave inelastically (Lo, Coyner, and Toksoz, 1986). By behaving inelastically, a stress wave travels across or around these features differently, changing the speed of the wave. Macro cracks attenuate elastic waves (Cai and Zhao, 2000). In most situations involving rock, these features mentioned are not random, but have an orientation or multiple orientations. It is this orientation of features that causes an overall velocity anisotropy. Impending failure will also contribute to velocity anisotropy (Lockner and Byerlee, 1977).

To study acoustic emissions, the waves created by the source mechanisms must be recorded. Transducers measuring displacement are either mounted on free surfaces of the specimen (most common technique in laboratory studies) or are embedded in the specimen itself (common in field studies). Waves created by a source mechanism inside the specimen propagate away from their origin and eventually to the transducers (see Figure A.1(b)).

The recordings of the stress waves made by the transducers represent a signal emitted from the source mechanism. Seismogram recordings from earthquakes provide a good example of how these signals look. The frequency content of these acoustic emission signals can be quite wide. Field studies in rock have involved frequencies lower than 1 Hz while laboratory studies have had frequencies in excess of 500 kHz. The discrepancy in frequency is due to source lifetime. Sources with a short lifetime (like almost all sources in laboratory experiments) have wider frequency content while sources with longer lifetimes will have a narrow frequency content centered at low frequencies. It is important to note that the signal generated by the source mechanism is not the signal which will reach the surface of the rock mass. The rock mass will attenuate the signal, but not uniformly. Attenuation is a process by which energy is removed from a signal. In the case of elastic waves, this translates to smaller

amplitudes of particle motion. Higher frequency signals are attenuated more strongly than lower frequency signals (Hardy, 2003). So the high frequency content of the waves will become increasingly weaker the farther a transducer is from a source mechanism. In effect, the rock behaves as a low-pass filter.

B.3 Acoustic Emission Experiments in Rock

Obert (1941) was the first to observe acoustic emissions in rock in 1941 inside a coalmine. While the technique has been studied extensively for metallic materials (e.g. Kaiser's thesis (1953)), it has also continued to be used within rock mechanics.

As will be seen later, being able to locate the sources of acoustic events within a rock mass can be extremely useful. To locate events, one can use one of three methods: the travel-time-difference method (Hardy, 2003), the Gaussian method (Lockner and Byerlee, 1980 and Lockner et. al., 1992), or the downhill simplex method (Press et. al., 1987). The travel-time-difference method requires at least five transducers to locate a source in three dimensions while the other two methods require only four.

The travel-time-difference method is based on methods developed in seismology. The method compares arrival times at the different transducers to locate a source. By solving a system of equations, the method calculates a location for the source, and the least-squares method should be used to minimize errors when more transducers are used (Salamon and Wiebols, 1974). The method relies on a very good wave speed estimate and also assumes an isotropic velocity field within the rock mass (Hardy, 2003). Because of the number of transducers required, this method is not commonly used in modern acoustic emission studies. The method can be modified to account for velocity anisotropy.

The assumption of an isotropic velocity field can be a good assumption for some rock masses in the early stages of a compression test. Some rocks, however, have bedding or rift planes, making the assumption false from the start. More importantly, however, deformation of a test specimen will lead to velocity anisotropy as microcracks open in the direction parallel to loading (Lockner et. al., 1992). By placing four transducers on a specimen and then using one as a source and the other three as receivers, P-wave velocity at three different

inclinations with respect to the direction of maximum velocity (parallel to loading) could be measured at different times during a compression test (Lockner et. al., 1992). This method assumes a radial symmetry about the loading axis and an overall ellipsoidal velocity field. While these assumptions do not match reality perfectly, they are much better than the assumption of an isotropic velocity field.

Whereas the travel-time-difference method derives several locations for a source and then aims to minimize the difference amongst the solutions, both the Gaussian and downhill simplex methods look to minimize the difference (residual) between arrival times observed at all transducers and those predicted by a model. Both methods take an initial estimate for source location and then search all the nearby points within the rock mass for a smaller residual. The difference between the two methods is in the search algorithm used. As source location is an integral part of most acoustic emission studies, it is worthwhile to explain the search algorithms used.

The Gaussian method (Lockner et. al., 1992) first uses an estimate of an event source **m** = $[T_e, X_e, Y_e, Z_e]$ and the following parameters for the travel path from the source to the i^{th} transducer:

$(x,y,z)_i$ – spatial coordinates of i^{th} transducer

d_i – distance from event to transducer

ϕ_i – declination of travel path relative to direction of maximum loading (axial direction)

v_i – average P-wave velocity along travel path to transducer

t_i – observed arrival time of P-wave at transducer

t_i^m - model estimated arrival time = $T_e + d_i/v_i$

R_i – travel time residual = $t_i - t_i^m$

To calculate v_i, the velocity anisotropy factor (ζ) is introduced, where $\zeta = v^{transverse}/v^{axial}$. The transverse direction is perpendicular to the axial direction, which is the direction of loading. ζ will normally begin with a unitary value and decrease as a test progresses. The velocity along the travel path (which is assumed to be a straight line), v_i, is then equal to

$$\frac{\zeta \cdot v^{axial}}{\sqrt{\sin^2(\phi_i) + \zeta^2 \cdot \cos^2(\phi)}}.$$

A model adjustment factor $\partial\mathbf{m}$ is then calculated by solving $\mathbf{A}\partial\mathbf{m} = \mathbf{b}$, where $\mathbf{A} = \mathbf{P}^T\mathbf{P}$ and $\mathbf{b} = \mathbf{P}^T\mathbf{R}$. $P_{ij} = \partial R_i/\partial m_j$, or, more explicitly,

$$\frac{\partial R_i}{\partial m_1} = 1 \qquad \frac{\partial R_i}{\partial m_2} \cong \frac{(X_e - x_i)\cdot v_i}{d_i \cdot (\zeta \cdot v^{axial})^2}$$

$$\frac{\partial R_i}{\partial m_3} \cong \frac{(Y_e - y_i)\cdot v_i}{d_i \cdot (\zeta \cdot v^{axial})^2} \qquad \frac{\partial R_i}{\partial m_4} \cong \frac{(Z_e - z_i)\cdot v_i}{d_i \cdot (\zeta \cdot v^{axial})^2}$$

The $(k+1)^{th}$ estimate of the event source is then $\mathbf{m}^{k+1} = \mathbf{m}^k + \partial\mathbf{m}^k$. The number of iterations performed needs to have a set maximum or a criterion for deciding a source has been located. Some experimenters have used a smaller value for the model adjustment factor (10% of the original) and have set the stop point for iterations for when a local minimum for **m** has been found (Zang, et. al., 1996).

The downhill simplex method (Press et. al., 1987) uses a more geometric approach for finding the source location. First, a model of arrival times needs to be developed. This model should predict when each transducer used would detect a P-wave arrival from each point within the specimen. The magnitude of the residual between model and observation would then be calculated for each point for every transducer. The sum of all these residuals for each point could then be plotted, as seen in Figure B.5.

Figure B.5 - sum of the residuals for a six transducer array for a rectangular specimen with a source located at (3,1). While this is for a two dimensional case, it could easily be extended to three dimensions. This surface was calculated using a velocity anisotropy factor of 0.5.

Figure B.5 shows a surface of residual times with only one local minimum. This will be the case when three or more transducers are used. The downhill simplex method then searches this surface (function) for a local minimum. Three initial points must be first chosen. These three points cannot lie along a line, and should be separated by some characteristic length of the problem or by some unit length. The function is evaluated at all three of the points of the triangle constructed. This is triangle BGW in Figure B.6, with vertex B having the lowest function value, G the next lowest, and W the highest. The method then starts looking for a better point for W. To accomplish this, W can be reflected to point R. If the function is lower at point R than W, then point E is evaluated. If E is a better point than R, it is selected. If not, then point R is selected. If R is no better than W, points C_1 and C_2 are evaluated. If either or both are better than W, then the best option (the one with the lower function value) is chosen. If neither are better than point W, then the whole triangle is contracted to triangle BMS.

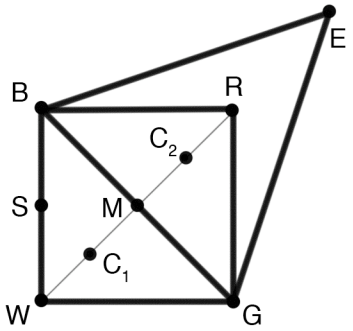

Figure B.6 – Possible options during a downhill simplex search.

After any selection, the whole process begins again. Eventually, the triangle will contract about a single point: the local minimum. Again, a criterion must be selected for when the search should stop, be it a number of iterations or a minimum triangle size.

One important note should be made about both search algorithms. Both algorithms search for local minima. This will correspond to an event source location when an adequate number of transducers register an event. In the three dimensional case, this corresponds to four transducers and three in the two dimensional case. If fewer transducers register the event, at least two local minima will be present, as can be seen in Figure B.7.

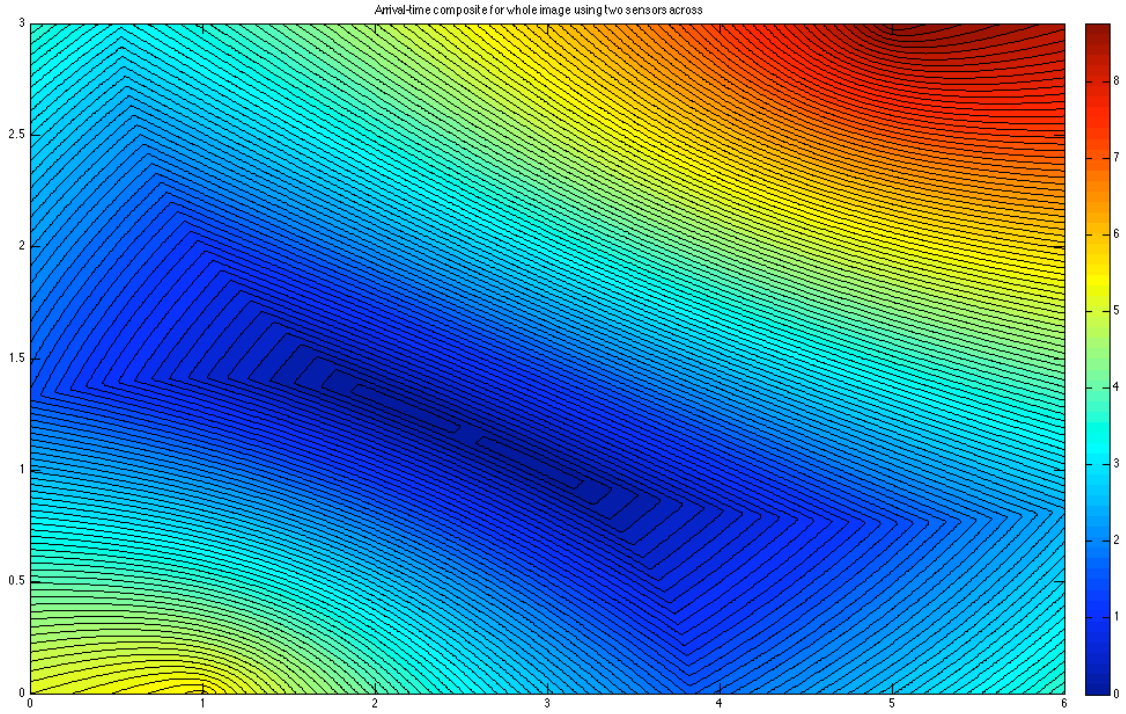

Figure B.7 – Sum of the residuals for a two transducer array for an event located at (3,1). Note that two locations are possible interpretations: (3,1) and ~(2,1.5).

Figure B.7 shows both minima for travel time residuals for a two transducer array. Neither search algorithm would report the presence of two minima, but would merely report one of them. For this reason, events for source location should first be filtered to include only those with an adequate number of transducers registering the event.

A third complication arises when locating sources. Each method mentioned relies upon accurate arrival time measurements. Obviously, this necessitates picking the time at which a wave arrives at a transducer. This is done in one of two ways: manually or automatically. Manual methods involve a researcher examining each sensor record and deciding when a wave has arrived at that sensor. This method becomes impractical with most modern acoustic emission experiments, as the number of registered events can number in the tens of thousands for each specimen tested.

Automatic methods can be subdivided into two further categories: those based on thresholding and those based on statistics. Threshold methods declare a wave to arrive once the magnitude of a signal is greater than a specified value (called the threshold). This threshold must be set carefully. Some methods set the threshold a specified amount above ambient noise recorded for the first segment of testing. Other threshold methods also calculate the energy content of a signal after a potential trigger. This is valuable because noise contains less energy than an actual wave. A series of if statements are then used to see if a trigger is from a spike in noise or from an actual arrival. Using these if statements allows one to set a lower threshold, thus reducing the chance of false negatives. Other automated arrival time pickers use statistical methods (primarily based on the Kinkely Criterion or the Akaike information criteria) that try to determine if a signal's basic characteristic is changing (i.e. if a wave is arriving). These methods are similar to regression analysis used for stock market forecasting.

Complication arises when one considers the effect of errors in selecting arrival times. Both manual and automatic methods generally record an arrival time later than appropriate in the case of low amplitude events (Lockner and Byerlee, 1978). Arrival time is considered to be the first particle motion associated with a wave front. For low amplitude events, this first motion may be indistinguishable (or nearly so) from noise. If later parts of the wave's signal are then of higher amplitude (a reflection of the wave, the S-wave arrival for waves traveling nearly parallel to the surface being monitored, or transducer resonance), however, these parts of the wave may be selected as an arrival. This pick would then be later than the actual arrival time. This bias toward later arrival times for low amplitude events introduces an error into source location for both automatic and manual methods. To counteract this problem, some automated pickers also associate every location calculation with a confidence value. This value measures how certain the picker is that the arrival time picked is accurate. A threshold can then be set for confidence values and those with too much uncertainty will not be used for source location.

By accounting for velocity anisotropy (either anisotropy that is inherent in the rock or that develops as a test progresses), one can locate the sources of acoustic emissions with algorithms based on seismic methods. By examining the sources of these locations, as will be

discussed in the coming paragraphs, other phenomena can be observed, giving greater insight into the failure process.

Dai and Labuz (1997) observed that acoustic event rate increases with increasing load. They expanded upon this well-known observation (first reported by Obert, 1941) to include the general effects of porosity and/or pre-existing cracks. Dai and Labuz monitored how many acoustic emission events (referred to as events from now on) occurred as the test progressed. For materials with pre-existing cracks or those that were more porous, events occurred relatively uniformly over the whole test. For materials without pre-existing cracks and that were less porous, most events occurred at or after 95-98% of the peak stress. That is, most events occurred near peak stress for these materials. Dai and Labuz also located the sources they were recording. They found that at loads before 95% of peak stress, events occurred at relatively random locations, which indicated a homogeneous deformation of the rock mass. After 95% of the peak stress, however, events clustered along what was to become the failure plane, as can be seen in Figure B.8.

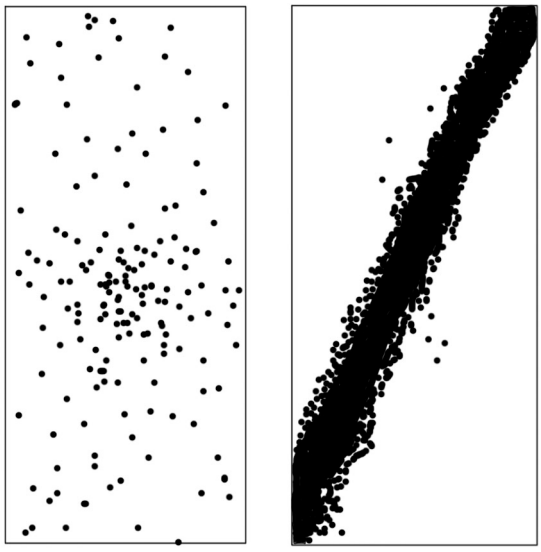

Figure B.8 – An idealized clustering of acoustic events. The left image shows a typical spacing of acoustic emission events during the initial stage of compression, during homogeneous deformation of the specimen. The image

on the right shows a typical distribution of events during fault propagating at or beyond 95-98% of the peak stress.

The observation of event clustering made by Dai and Labuz agreed with other experiments that had previously been conducted. Lockner and Byerlee (1977) found that acoustic events would cluster about an eventual failure plane in sandstone but not in granite specimens. They later found, however, that a failure plane would form in granite during tertiary creep (Lockner and Byerlee, 1980). This clustering of events into a failure plane is indeed noted in later experiments in both granite and sandstone.

Shah and Labuz (1995) looked to explore the clustering of events in granite more thoroughly. They used statistical techniques originally developed in biostatistics by David and Barton (1966) to study whether events were clustered in space, time, or both. The diffuse pattern of acoustic emission events during the initial stage of loading as reported in other experiments was observed. It was found, however, that events were slightly clustered even during this initial stage. Near the peak stress, events started to occur only in a localized region. Within this region, events were evenly clustered. Events were also clustered in the time domain, meaning that if there was an event, it was then more likely for another event to occur. Finally, space-time clustering was studied and showed that the distance and time between two events was correlated. This implied that if an event occurred, it became more likely for another event to occur close to it in both space and time. A critical radius was found wherein the next event was likely to occur, and this radius corresponded to the size of the region of damage that was initially observed.

Zietlow and Labuz (1998) also investigated the location of acoustic emission events near failure. Instead of the compression tests used in the experiments mentioned above, Zietlow and Labuz used a three-point bending test (without a notch cut). They found that the region of localized microcracking (also known as the intrinsic process zone) could be characterized by the location of acoustic emission events near the peak stress level. They also found that this zone's size varied between rock types. The process zone would form along the surface of the specimen that experienced the maximum moment and extend perpendicularly into the specimen. Near the peak stress, events would cluster in a well-defined zone, as shown in

Figure B.9. It was found that the width (W) of this zone was related to the logarithm of grain size. W was defined as the distance perpendicular to crack growth in which these cluster events were contained. In Figure B.9, W is measured in a horizontal direction. Scatter in their data was larger for larger grain sizes. The length (l) of the process zone (depth of the process zone into the specimen), however, was not found to be related to any material property. The authors speculated it might be related to loading configuration.

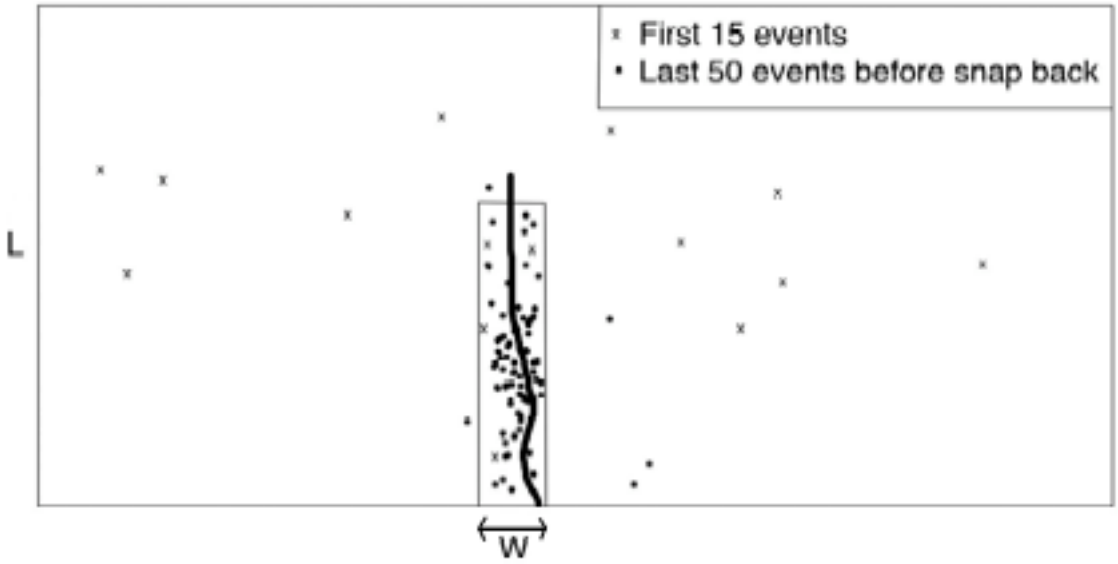

Figure B.9 – Idealized image depicting the process zone investigated by Zietlow and Labuz. The first events are disperse, while the final events cluster about the eventual crack that forms (shown as a heavy, dark line).

Labuz et al. (2001) continued this vein of research by varying loading configurations as well as material type. Again, events were found to be relatively diffuse throughout the specimen at first. As loads approached peak stress level, events occurred in a more localized zone. This process zone was affected by grain size (larger grain size corresponding to wider zone) and porosity (higher porosity corresponding to longer zone). This result disagreed with Zietlow and Labuz in that it found process zone length was dependent upon a material property as well as loading condition.

Lockner, et al. (1992) conducted a novel experiment in which the failure process itself was slowed to occur over minutes or hours instead of a fraction of a second. They were able to

slow fault growth by using acoustic emission rate as the feedback variable during their triaxial tests. For granite they found no clustering of events as reported in unconfined experiments. Sandstone specimens, however, showed a strong localization of events with loading. At peak load, granite formed a zone of intense acoustic emission activity (similar to that reported by Lockner and Byerlee, 1980) which then spread to a half disc shape that formed at the position and orientation of the eventual fracture. In sandstone, events localized more strongly into a planar feature. The fault in both granite and sandstone grew with a process zone of acoustic event activity propagating across the specimen. The process zone in granite was smaller than in sandstone (both parallel and perpendicular to the direction of propagation). Granite had a process zone 10-50 mm parallel to the direction of propagation of the process zone (width) and 1-5 mm normal to the direction of propagation (thickness). In sandstone, the process zone was 60-90 mm wide and 10mm thick.

Still more information can be gathered with acoustic emission techniques. Rate and location of events allow investigators to visualize damage as it occurs within a rock mass. Neither technique, however, gives insight as to the source mechanisms. By analyzing the waveforms that are received at the transducer, some investigators hope to gather more insight into the internal processes of rock.

Egle and Tatro (1967) were able to distinguish between P- and S-waves in a metallic specimen under tension. They accomplished this by characterizing their specimen's response to different modes of excitation as well as a frequency analysis of received signals. They were using resonant transducers, which are tuned to be more responsive to certain frequencies. This fact made the transducers "ring," which corresponds to the transducer being driven at its resonant frequency, so Egle and Tatro could not count the number of events accurately. Resonant transducers will be discussed more in depth later. They found that the dominant frequency of emissions varied with load and the point of highest dominant frequency corresponded to yield stress.

Stephens and Pollock (1971) tested the influence of the specimen upon the observed waveform. By finding the frequency response of the specimen itself, they tested the influence of the specimen on the received waveforms. Stephens and Pollock also theorized about the

type of failure occurring (single grain fractures versus coalescing fractures). Lastly, they derived and experimentally confirmed that the frequency spectrum as well as energy carried by the wave was inversely proportional to the duration of the source event.

At this point, an important distinction needs to be made regarding the transducers used in acoustic emission research. Commercially available transducers designed for acoustic emission techniques are a type of transducer known as resonant transducers. These transducers have a resonant frequency to allow them to detect events within a narrow band of certain frequencies very well. Figure B.10 shows an idealized frequency response of one of these resonant transducers as well as their basic design.

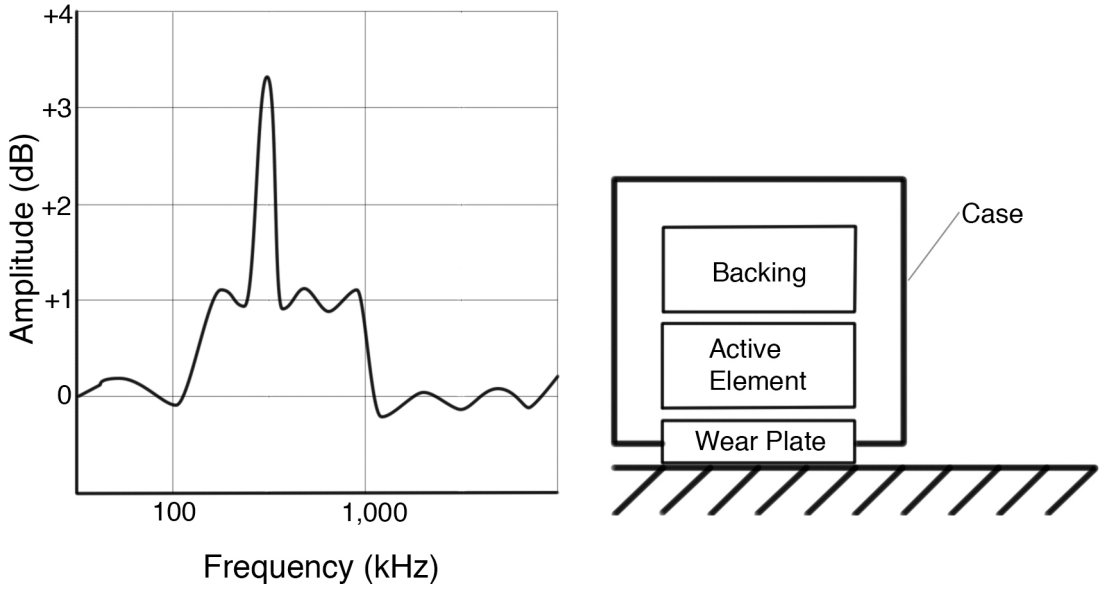

(a) (b)

Figure B.10 – a) Idealized frequency response of a broadband transducer. For signal frequencies roughly between 100 kHz to 1 MHz, the transducer amplifies the signal. However, signal content around 300 kHz is amplified to a much greater degree than any of the other frequencies. The sensor is said to have a resonant peak around 300 kHz. b) The typical design of one of these transducers is shown in part. Because of the multiple structural elements, the transducer will generally have several resonant peaks.

Other transducers, which are specifically designed for waveform analysis, are known as broadband transducers. These transducers have a relatively flat frequency response over a

very large range. The range of frequencies these transducers are typically designed for is 100kHZ to 1 MHz (frequencies below 100kHz are not common in the laboratory setting). An example of a frequency response for a broadband sensor as well as basic sensor design can be seen in Figure B.11.

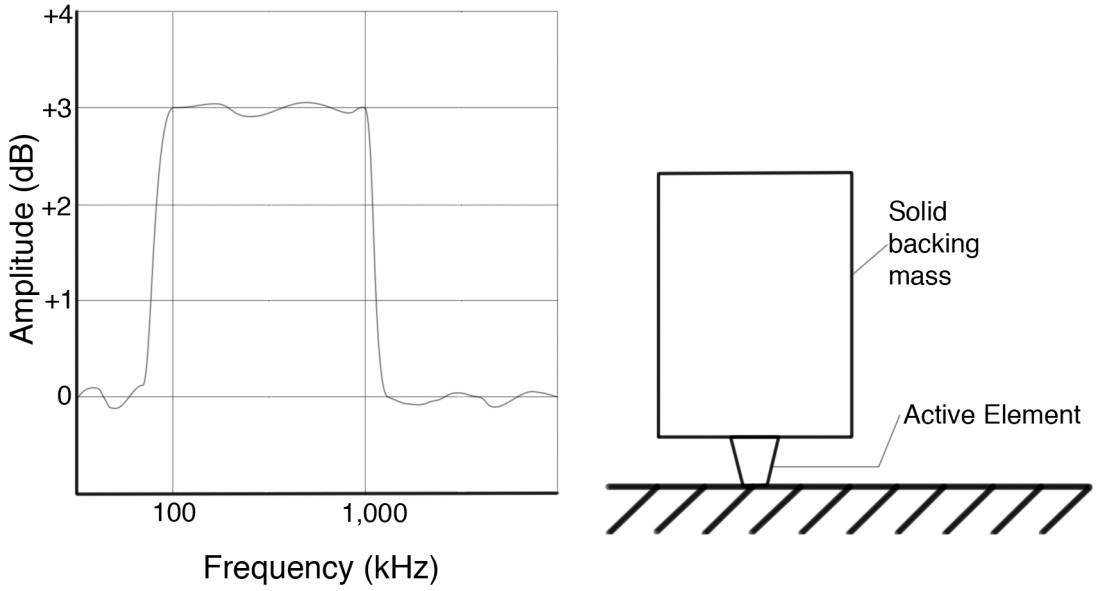

(a) **(b)**

Figure B.11 – a) Idealized frequency response of a broadband sensor (a). Like the resonant sensor, signal content in the 100 kHz to 1 MHz window is amplified. Unlike the resonant transducer, however, the signal is amplified roughly equally within that window. Because of this fact, the waveform is kept relatively intact while boosted above noise levels. b) Basic design of the transducer. Note the conical transducer and large backing mass.

Obviously, when performing rigorous analyses on a waveform, it is important to have a flat frequency response so the actual wave at the surface of the specimen is the wave that is recorded. Proctor developed the first broadband transducer (see Proctor, 1980 and 1982). The transducer is conical and has a very small contact area with the specimen surface being monitored. The larger the contact area, the larger the interference created within the sensor itself from waves hitting the transducer at an angle. The transducer also has a large backing mass to dampen out resonances within the range of frequencies being examined. For event rate and location calculations, either sensor type can work. Work described here up to this

point was all accomplished using resonant transducers. The experiments mentioned in the following paragraphs all used broadband transducers

The work of Egle and Tatro as well as Stephens and Pollock was a step toward gaining more information from acoustic emission events. More recent work has focused on the ability to "read" the waveforms from acoustic emissions. Nelson and Glaser recorded transducer outputs continuously during four-point bending tests on large rock beams (Nelson and Glaser, 1992 and Glaser and Nelson, 1992). They then later analyzed these waveforms and discovered five main categories of wave-types in their experiments. Three were associated with a mechanism extending a crack along its plane (each waveform recorded assumed to be from a small, step-like extension). There were three categories depending on the orientation of the crack extension with respect to the transducer receiving the wave. See Figure B.12 for these waveforms.

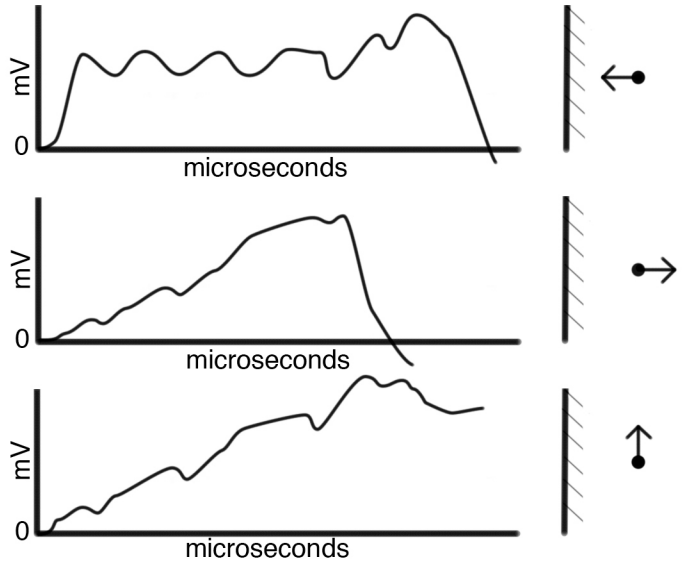

Figure B.12 – Waveforms recorded associated with a simple step force mechanism extending a crack in plane. The top waveform is for a crack extending toward the surface being monitored while the middle waveform is for a crack extending away from the surface being monitored. The bottom waveform is for a crack extending in a direction nearly parallel to the surface being monitored.

Another waveform was complex and its mechanism was not understood. The last waveform category was thought to be caused by interaction between the specimen and testing equipment. These two waveforms are shown in Figure B.13.

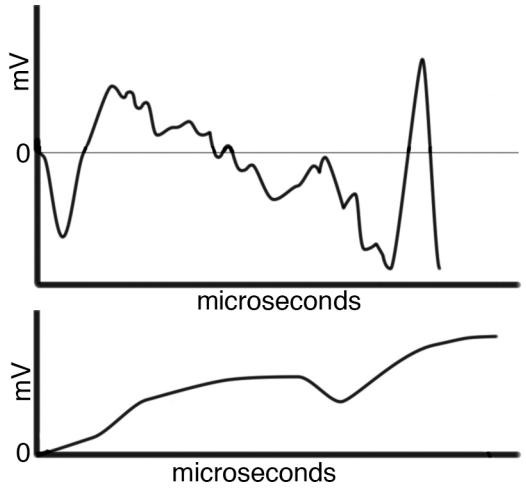

Figure B.13 – Complex waveform associated with an unknown source mechanism (top) as well as rolling waveform believed to be associated with loading equipment (bottom). Note how the bottom waveform does not have high frequency components like the other waveforms.

Instead of looking at the entire waveform, as Nelson and Glaser did, other researchers look only at the first motion of an arriving P-wave (Satoh et. al., 1986, Lei et. al., 1992, Meglis et. al., 1995, Zang et. al., 1998, and Backers et. al. 2005). It should be noted that these studies can be performed with resonant transducers. In these studies, the first motion of the P-wave received at each transducer in an array is recorded and later analyzed instead of the entire waveform. If all the transducers receive a dilatational first motion, the event is interpreted to be a pore closure (type-C event). The pore face moving away from the transducers causes these dilational first motions. If both dilatational and compressive first motions are recorded matching a quadrupole source mechanism, the event is interpreted as a shear crack (type-S). By two planes sliding past one another, we get two zones of dilational first motions and two zones of compressive first motions. If only compressive first motions are observed, the crack is said to be initiating/propagating in a tensile mode (type-T event). Again, this can be explained by the fact that an extending crack's face will be moving toward all the

transducers, causing compressive first motions (Lei et. al., 1992). These source mechanisms and their associated first motions can be seen in Figure B.14.

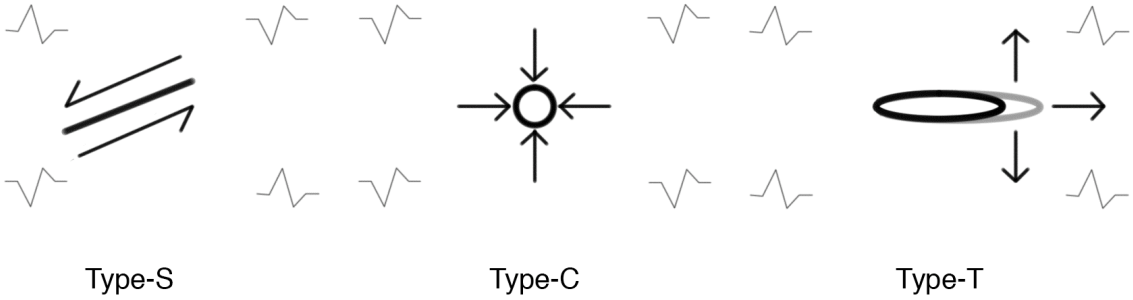

Figure B.14 – The three source mechanisms outlined in Lei et. al. (1992) and associated first motions.

To make a clear decision regarding source mechanism, every transducer must register an event. Often, however, not all transducers would record an event (only 10% of located events registered on all 20 transducers used). Lei et. al. (1992) used the ratio of dilatational first motions to total number of clear first motions recorded. Comparison between this ratio of dilatational first motions to total clear first motions was compared to hand solutions of source mechanisms. They then estimated that events with dilatational first motions more than 70% of first motions were type-C events, events with dilatational first motions between 30% and 70% of first motions were type-S events, and those with dilatational first motions less than 30% of first motions were type-T events (Lei et. al., 1992). One quick check for this method is to compare the cracking volume change to the dominant source mechanism. Type-T events cause a larger volume change than type-S events. Because of this, portions of the test with predominantly type-T events should see larger volume changes due to cracking than those with predominantly type-S events. Note this only works for portions of the test with either a low number of type-C events compared to the total number of events.

Zang et. al. (1998) also used first motion (polarity) of events to find source mechanisms. Analogous to the statistical approach used by Lei et. al. (1992), they defined a value to

differentiate between the three source mechanisms. Their value was polarity (pol) and was defined as

$$pol \equiv \sum_{i=1}^{k} sign(A_i),$$

where k is the number of transducers used for a particular source mechanism determination, and A_i is the amplitude of the event recorded at the i^{th} transducer. This value can range from -1 (all transducers recording a compressive first motion) to 1 (all transducers recording a dilatational first motion). Zang et. al. (1998) recommended the following intervals: events with polarity greater than 0.25 are defined as type-C, those with polarity between -.25 and .25 are defined as type-S, and those with polarity less than -.25 are defined as type-T. These intervals are similar to those proposed by Lei et. al. (1992), but with a small zone of values being defined as type-S events. These polarities were calibrated with pencil lead breaks, steel ball drops, and tensile wing crack formation.

It is important to describe these calibrations mentioned, as they are relevant to several tests involving waveform analysis. Calibration is performed to compare the output of the whole acoustic emission system to a known input (known as end-to-end calibration). In these situations, a simulated source is created at a known location, and then compared to the output of the whole system (i.e. sample, sensor, pre-amplifier, and signal conditioner). The known source can vary. The most commonly used source is the pencil lead break test. In this test, a length of pencil lead is let out from a mechanical pencil and pressed against the sample's surface. When the lead finally breaks, the surface is relieved of a point force. The exact amount of force (on the order of a few Newtons) depends on the type of lead, length of lead, and angle the pencil is pressed down at. Hsu (Hsu et al., 1977) and Nielsen (Anon., 1981) are credited with coming up with the procedure. A Pentel pencil with 2H, 0.5 mm diameter lead projecting out 3 mm is usually used. A Teflon guide may also be used to guarantee a consistent angle (see Anon., 1981 for specifications). The steel-ball drop causes a sudden increase in stress on the surface, modeling a point force application. The tensile wing crack provides tensile mode extension (not as common as the other two tests) by initiating an actual tensile crack. It is known to be purely a tensile crack, so one can observe first motions for pure tensile initiation and propagation. For a detailed calibration, the magnitude of the sources must be known and controlled (length and angle of pencil lead or height and weight

of steel ball). For this reason, wing crack formation is used for more qualitative calibrations, as the mode of cracking is known, whereas the source strength is not.

While Nelson and Glaser were able to get information from the waveforms and other studies have garnered some clues as to source mechanisms with first motions, other researchers (such as Shah and Labuz, 1995) went deeper into waveform analysis. By deconvoluting the waveforms with the system response of both the transducers and the recording system, one can find the system response of the specimen (Michaels, et al, 1981). This requires providing a known input to the system, such as the pencil lead break test or the capillary break test. Knowing the system response gives information about an event source's mechanism. Examples of such sources include the implosion/explosion of a void or the extension of a crack (with the ability to differentiate between shear and tensile extension). Information about the orientation of the event can also be computed. The results of the analysis, however, are very sensitive to the duration of the signal being analyzed. Too short of a duration and it is impossible to distinguish between possible source mechanisms, while too long of a duration can include too much noise and give a false source mechanism. Experimenters set a window after an arrival time has been detected. This window is based on sample size and material but generally set so only the P-wave is analyzed. These windows can either be a fixed duration or vary depending on source location.

Shah and Labuz were performing calculations requiring very detailed calibrations. Before every test, a known input would need to be applied to the system (transducers attached to specimen as well as recording system). Complicated calculations could then be performed to gather insight into source mechanisms of events. Dai and Labuz (1997), on the other hand, performed relatively simple calculations and were still able to benefit from using full-waveform recording. In their experiment, they found a key failure indication. The root-mean-square (RMS) value of an acoustic emission event is the time-averaged magnitude of the voltage recorded at a transducer, or $RMS = \sqrt{\left(\frac{1}{T}\int_0^T [g(t)]^2 dt\right)}$, where T is the length of time the value is calculated for and g(t) is the voltage as a function of time recorded by a transducer. The RMS is related to the magnitude of the emission, and if it is averaged among several sensors for a series of events, the relative energies of the events can be compared.

Computing the actual amount of energy released requires calibration like that used by Shah and Labuz. The RMS value-based approach allows one to represent in real-time the energy being released within a specimen with no calibration beforehand. By keeping track of the cumulative RMS (the sum of RMS values recorded so far) one can track the stress-induced damage. Dai and Labuz plotted the cumulative RMS versus the number of recorded events and the applied load and found a linear relationship between cumulative RMS and event number. They also noticed a sudden increase in slope at 95-98% of the peak stress as can be seen in Figure A.15. This increase in slope indicated that the specimen was close to failure. This method is a superior failure-predictor when compared to event rate tracking based on the sharp change in slope. It is also superior in that it is capable of predicting failure in more porous materials or those with pre-existing cracks. The cumulative RMS, event number, and load are all values that can be calculated in real-time. This means that impending failure of a specimen can be predicted so long as those three values are available.

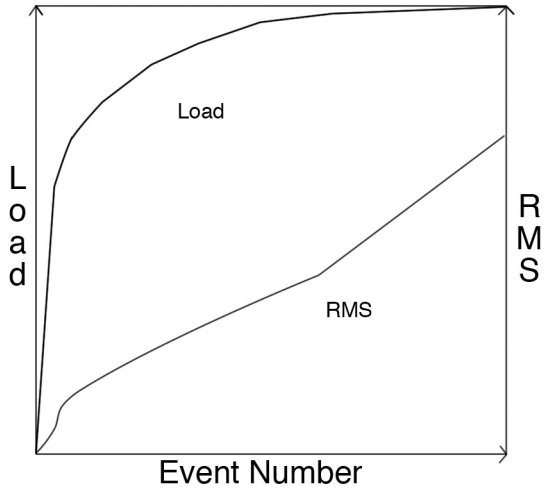

Figure B.15 – Idealization of load vs. event number and cumulative RMS vs. event number as reported by Dai and Labuz. Note the sudden change in slope of the RMS curve as the load reaches 95-98% of its peak level.

This discovery provides a method of predicting failure in real-time with observations of the recorded voltages from transducers versus the event number. Care must be taken, however, in calculating the value of the RMS values to avoid including energy from reflected waves or

any resonant effects (Dai and Labuz only used the first 2.5 μs of each received wave in their calculations).

B.4 Acoustic Emission Systems

A laboratory setup for detecting acoustic emissions has several components. First there are the sensors, which must attach directly to the specimen. Researchers must choose between resonant or broadband transducers. For waveform analysis of any kind, broadband transducers should be selected. This choice currently necessitates the design and manufacturing of the transducers as well. Because they are detecting such small signals, each transducer must have its own preamplifier. From there, the signal is passed into an amplifier and then must be converted from analog to digital. This means the signal must be sampled at a rapid rate (typical systems sample at rates between 5 and 20 MHz) and then stored. This requires a data acquisition system and memory.

There are several companies offering commercial acoustic emission systems such as Vallen and the Physical Acoustics Corporation (see References for website addresses). These systems, however, utilize resonant sensors. Location algorithms are proprietary and their accuracy is unknown, so the level of error in source location is uncertain.

The option many researchers take is to build a customized system. Data acquisition systems are standard and can easily be purchased. The only requirement on this part of the acoustic emission system is that it is a fast sampling systems (to avoid aliasing, the system must sample at above 2 MHz for most broadband transducers while 20 MHz is preferable) with many channels (typically eight to twelve channels will be required). Transducers are either built (broadband transducers) or purchased (resonant transducers). Many experimenters choose broadband transducers either for waveform analysis or for more accurate arrival time picking. It is important to note that many companies advertise broadband transducers for sale, but inspection of their frequency responses will show they are not truly broadband. These systems are then attached to a desktop computer for transferring data to. Any analysis is done with software written by the lab performing the analysis for the most part. Developing programs to select arrival times is difficult.

B.5 Acoustic Emission Techniques in Coalescence Research

The coalescence research being performed by the MIT Rock Mechanics Group involves recording crack propagation in brittle geo-materials. Tests are recorded with both low-speed and high-speed video cameras. Stress-strain data are also recorded. The coalescence of the two prefabricated flaws is the event of highest interest and it is this event that is captured on high-speed video. The high-speed video is recorded at between 5,000 and 10,000 frames per second. By linking the two recordings and stress-strain data from each test, it is possible to reconstruct the test. By examining high-speed video, cracks can be classified as tensile or shear (and sometimes the direction of shearing can be determined).

Obviously, this approach is limited. The front surface of each specimen is the only part observed directly. Hairline cracks on the front face may be through-going or they may just be on the surface; acoustic emission source location could help differentiate. The way in which cracks propagate within the specimen can also be investigated. The time between a process zone developing and a visible crack propagating can be found, as could the size of the process zone. This process zone could be compared to the white patches observed in marble and granite.

Cumulative RMS values could prove an interesting measurement to compare to visual recordings and stress-strain history. Dai and Labuz observed a bifurcation in cumulative RMS versus event number for a specimen loaded to failure (refer to Figure B.11). That specimen, however, did not have prefabricated cracks present, as do the current specimens. How would the formation of tensile wing cracks, coalescence, and the failure of a specimen affect the cumulative RMS versus event number? By integrating the visual, stress-strain, and acoustic waveform records, these questions could be investigated. RMS calculations are beneficial in that they do not require long time intervals for computing (important as we have such small specimens) and are simple computation-wise (beneficial for any software that must be written) but still offer a method of computing the relative amount of energy being released by the sample.

Using broadband sensors would enable one to calculate RMS values, but an in-depth examination of the waveforms and system response may not be as useful. While the prospect of gaining so much information about events is tempting, there are two problems. The first problem is simply a matter of time. Calibration before every test, development of analysis programs, and performing the actual analysis would take a significant amount of time. The second problem is more subtle. With the development of tensile wing cracks and secondary cracks, waves originating from coalescing cracks will be significantly attenuated and the system response may change greatly. If this were to occur, the original system calibration would be rendered null and void. Further investigation of this possibility is needed to determine whether rigorous full waveform analysis is even feasible (more to the point: source location may become difficult to impossible after the formation of too many wing and secondary cracks). Finally, even if these rigorous techniques were still possible, the window for analysis before reflections and S-waves begin to arrive will be very short within our specimens. Initial calculations estimate the window for events originating from coalescing cracks being at most 12 microseconds.

Investigation using first-motions to determine source-mechanism appears a tempting option. Two possible problems exist with this approach for the current research. First of all, identifying the first motion for sources near failure may be difficult. Small amplitude sources making picking arrival times as well as first motion difficult. Only strong sources could be used to find source mechanisms, introducing a bias in the source mechanisms analyzed. To combat this problem, resonant transducers could be used to amplify the received signals. This possible solution, however, comes with a price in the number of events that could then be analyzed. Because resonant transducers "ring," events occurring immediately after another event will not be distinguishable from transducer ringing. A period of time after every registered event will be a blind spot for the system. For this approach to be implemented, these two problems would need to be balanced.

The last problem that must be addressed is the synchronization of the acoustic emission observations with the other observational records of each test. The acoustic emission signals' acquisition could be combined with the stress-strain data acquisition system, thereby allowing the two data streams to be integrated. This would make analysis significantly easier.

B.6 Conclusions

Acoustic emission techniques have been extensively developed since the first observation of the phenomenon. They offer a nondestructive and passive method to investigate processes occurring in visually inaccessible parts of rock masses. By examining other researchers' solutions to the complications arising from applying acoustic emission techniques to rocks, many problems can be circumvented.

Transducer choice needs to be made after the acoustic emission investigation has been decided upon. Broadband transducers are recommended for any study involving full waveform analysis. Cumulative RMS would benefit from the use of broadband transducers as well by producing a larger window for calculating the value. Resonant transducers could be used for cumulative RMS calculation, but instead of secondary arrivals being the determining duration, the resonance of the sensor would govern the window of useful waveform for calculations. Resonant transducers might be better for a first-motion investigation. Of course, resonant transducers will "ring," causing a blind spot for the system. If possible, broadband transducers should be preferred for this reason. Broadband transducers would have to be manufactured in-house. There is a great deal of helpful information available in this regard (see Proctor 1980 and 1982 especially).

A data acquisition system would also need to be purchased, which could be used by a computer already present or a student laptop. The largest investments in time would come from two main areas: troubleshooting and analysis techniques. Troubleshooting would be performed while setting the whole system up and trying to integrate all the subsystems needed. Programming an arrival time picker would be necessary given the amount of data that will be produced with each test. While this will pose a difficult problem, there is a wealth of literature (for a good review, see Kurz, Gross, and Reinhardt, 2005) within the fields of acoustic emission, seismology, and financial forecasting.

The application of acoustic emission techniques (such as source location, event rate, and cumulative RMS value) would help enhance the current research. All three dimensions of specimens will become observable instead of just the front face. Cumulative RMS values

may give some insight into the coalescence process. Some other methods may be too complicated or time-consuming to implement as they require large amounts of time for calibration and/or analysis or they may be physically impossible with changing system response.

B.1 References

Anon. "In-Situ Sensitivity Calibration of Acoustic Emission Systems," *Technical Review*, No. 2, Appendix C, Bruel and Kjaer, Denmark, 1981.

Backers, Stanchits, and Dresen, "Tensile Fracture Propagation and Acoustic Emission Activity in Sandstone: The Effect of Loading Rate," *International Journal of Rock Mechanics and Mining Sciences*, Vol. 42, 2005, pp 1094-1101.

Cai, Zhao, "Effects of multiple parallel fractures on apparent attenuation of stress wave in rock masses," *International Journal of Rock Mechanics & Mining Sciences*, 37, pp 661-682, 2000.

Dai and Labuz, "Damage and failure analysis of brittle materials by acoustic emission," Journal of Materials in Civil Engineering, Nov 1997, pp 200-205.

David and Barton, "Two Space-time interaction tests for epidemicity," *British Journal of Preventative and Social Medicine*, 20, 1966, pp 44-48.

Egle and Tatro, "analysis of Acoustic-Emission Strain Waves," *The Journal of the Acoustical Society of America*, Vol. 41, No. 2, 1967, pp 321-327.

Forster and Scheil. Akustische Untersuchung der Bildung von martensitnadeln Z Metallk, 29, 1936.

Glaser and Nelson, "High-Fidelity Waveform Detection of Acoustic Emissions from Rock Fracture," *Materials Evaluation*, March 1992, pp. 254-359.

Hardy, Jr., Acoustic Emission/Microseismic Activity: Vol. 1, A.A. Balkema Publishers, Exton (2003).

Hsu, Simmons, and Hardy, "An Approach to Acoustic Emission Signal Analysis-Theory and Experiment," *Material Evaluation*, Vol. 35, No. 10, (1979), pp. 100-106.

Kaiser "Erkenntnisse und Folgerungen aus der Messung von Gerauschen bei Zubeanspruchung von metallischen Werkstofen [Results and conclustions from measurements of sound in metallic materials under tensile stress], Archiv Eisenhuttenwess, 24, (1953) p43.

Kurz, Grosse, and Reinhardt, "Strategies for Reliable Automatic Onset Time Picking of Acoustic Emissions and of Ultrasound Signals in Concrete," *Ultrasonics*, Vol. 43, pp 538-546, 2005.

Labuz, Cattaneo, and Chen, "Acoustic Emission at Failure in Quasi-brittle Materials," *Construction and Building Materials*, 15, 2001, pp225-233.

Lei, Nishizawa, Kusunose, and Satoh, "Fractal Structure of the Hypocenter Distributions and Focal Mechanism Solutions of Acoustic Emission in Two Granites of Different Grain Sizes", *Journal of the Physics of Earth*, Vol. 40, 1992, pp 617-634.

Lo, Coyner, and Toksoz, "Experimental determination of elastic anisotropy of Berea sandstone, Chicopee shale, and Chelmsford granite," *Geophysics*, Vol. 51, No. 1, pp 164-171, 1986.

Lockner and Byerlee, "Acoustic Emission and Fault Formation in Rocks," *Proc. 2nd Conf. on Acoustic Emission/Micro Seismic Activity in Geological Structures and Materials*, Ed. HR Hardy and FW Leighton, Trans-Tech Publications, Clausthal-Zellerfeld, 1977, pp 99-107.

Lockner and Byerlee, "Velocity Anomalies: An Alternative Explanation Based on Data from Laboratory Experiments," *Pure and Applied Geophysics*, Vol. 116, 1978, pp 765-772.

Lockner and Byerlee, "Development of Fracture Planes During Creep in Granite," *Proc. 1st Conf. on Acoustic Emission/Micro Seismic Activity in Geological Structures and Materials*, Ed. HR Hardy and FW Leighton, Trans-Tech Publications, Clausthal-Zellerfeld, 1980, pp 11-25.

Lockner, Byerlee, Kuksenko, Ponomarev, and Sidorin, "Observations of Quasistatic Fault Growth from Acoustic Emissions" in Fault Mechanics and Transport Properties of Rocks. Eds. B Evans and T Wong, Academy, London, 1992, pp. 3-31.

Lockner, "The role of acoustic emission in the study of rock fracture" International Journal of Rock mechanics, Mining Science and Geomechanic Abstracts, 30, (1993), pp 883-889.

Meglis, Chow, and Young, "Progressive Microcrack Development in Tests on Lac du Bonnet Granite – I. Acoustic Emission Source Location and Velocity Measurements", *International Journal of Rock Mechanics, Mining Science and Geomechanics Abstracts*, Vol. 32, No. 8, 1995, pp 741-750.

Michaels, Michaels, and Sachse, "Applications of Deconvolution to Acoustic Emission Signal Analysis," *Materials Evaluation*, Vol. 29, 1981, pp. 1032-1036.

Nelson and Glaser, "Acoustic Emissions Produced by Discrete Fracture in Rock: Part1," *International Journal of Rock Mechanics, Mining Science and Geomechanic Abstracts*, Vol. 29, No. 3, 1992, pp. 237-251.

Nelson and Glaser, "Acoustic Emissions Produced by Discrete Fracture in Rock: Part 2," *International Journal of Rock Mechanics, Mining Science and Geomechanic Abstracts*, Vol. 29, No. 3, 1992, pp. 253-265.

Obert, "Use of subaudible noise for the prediction of rock bursts" RI 3555 US Bureau of Mines (1941).

Obert and Duvall, "Use of subaudible noises for the prediction of rock bursts, part II" RI 3654 USBM (1942).

Physical Acoustics Corporation, <http://www.pacndt.com>, Last Accessed 28 August 2007.

Press, Flannery, Tenkolsky, and Vetterling, Numerical Recipes. Cambridge University Press, Cambridge, 1987, pp. 502-507.

Proctor, Jr., "Improved Piezoelectric Transducer for Acoustical Emission Reception," *The Journal of the Acoustical Society of American Supplements*, Vol. 1, 1980, pp S68.

Proctor, Jr. "An improved piezoelectric acoustic emission transducer," *The Journal of the Acoustical Society of America*, Vol. 71, No. 5, 1982, pp 1163-1168.

Salamon and Wiebols, "Digital Location of Seismic Events by an Underground Network of Seismometers using the Arrival Times of Compressional Waves," *Rock Mechanics*, Vol. 6, 1974, pp 141-166.

Satoh, Idehara, Nishizawa, and Kusunose, "Hypocenters Distribution and Focal Mechanisms of AE Events Under Triaxial Compression – Focal Mechanisms of AE events in Yugawara Andesite", *Zisin*, Vol. 39, 1986, pp 351-360.

Scott, Basic Acoustic Emission, Gordon and Break Science Publishers, New York (1991).

Scruby, "Quantitative Acoustic Emission Techniques" in Research Techniques in Nondestructive Testing, Vol. 8, ed. By RS Sharpe, Academic Press, London (1985).

Shah and Labuz, "Damage Mechanisms in Stressed Rock from Acoustic Emission," *Journal of Geophysical Research*, Vol. 100, No. B8, 1995, pp15, 527-15,539.

Stephens and Pollock, "Waveforms and Frequency Spectra of Acoustic Emissions," *The Journal of the Acoustical Society of America*, Vol. 50, No. 3, 1971, pp 904-910.

Vallen System website, <http://www.vallen.de/>, Last accessed 28 August 2007.

Zang, Wagner, and Dresen, "Acoustic Emission, Microstructure, and Damage Model of Dry and Wet Sandstone Stressed to Failure," *Journal of Geophysical Research*, Vol. 101, No. B8, 1996, pp 17,507 – 17,521.

Zang, Wagner, Stanchits, Dresen, Andresen, and Haidekker, "Source Analysis of Acoustic Emissions in Aue Granite Cores Under Symmetric and Asymmetric Compressive Loads," *Geophysics Journal International*, Vol. 135, 1998, pp 1113-1130.

Zietlow and Labuz, "Measurement of the intrinsic process zone in rock using acoustic emission," *International Journal of Rock Mechanics, Mining Science and Geomechanic Abstracts*, Vol. 35, No. 3, 1998, pp 291-299.

APPENDIX C– Unconfined Compressive Strength and Modulus of Elasticity of Granite

A specimen of granite with no pre-cut flaws was loaded until failure. The end pieces and loading profile were both identical to those used for granite specimens with ligament length "a" (see Section 0 for a description of flaw geometry). The stress-strain curve of the test is shown in Figure C.1.

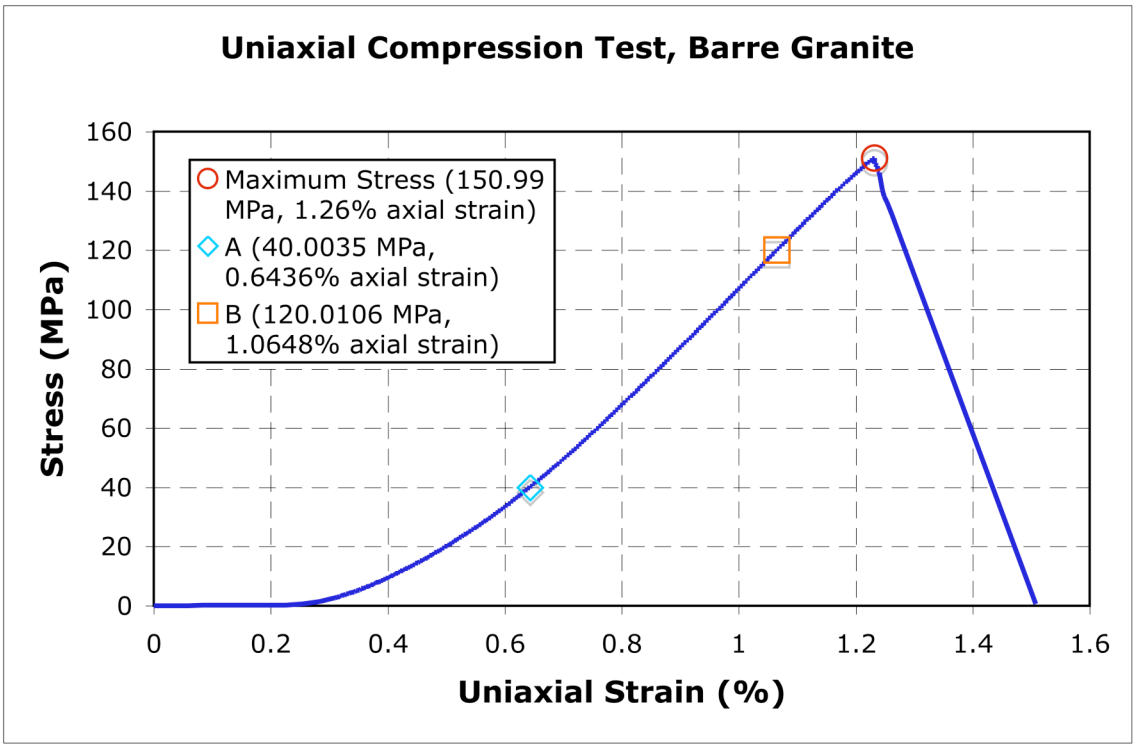

Figure C.1 – Stress-strain curve for an unconfined uniaxial test performed on a Barre Granite specimen with now waterjetted flaws. Points A and B are the limits of the interval used for the calculation of the Young's modulus.

As can be seen in Figure C.1, the compressive strength of the specimen was 150.99 MPa. This value is slightly higher than the 140 MPa found by Martinez (1999) but lower than the lower bound of 170 MPa found by Kessler et al. (1940). A linear portion of the curve (the

portion between points A and B in Figure C.1) was used to calculate the Young's modulus of the specimen. Figure C.2 shows this linear portion as well as the line fit to the data.

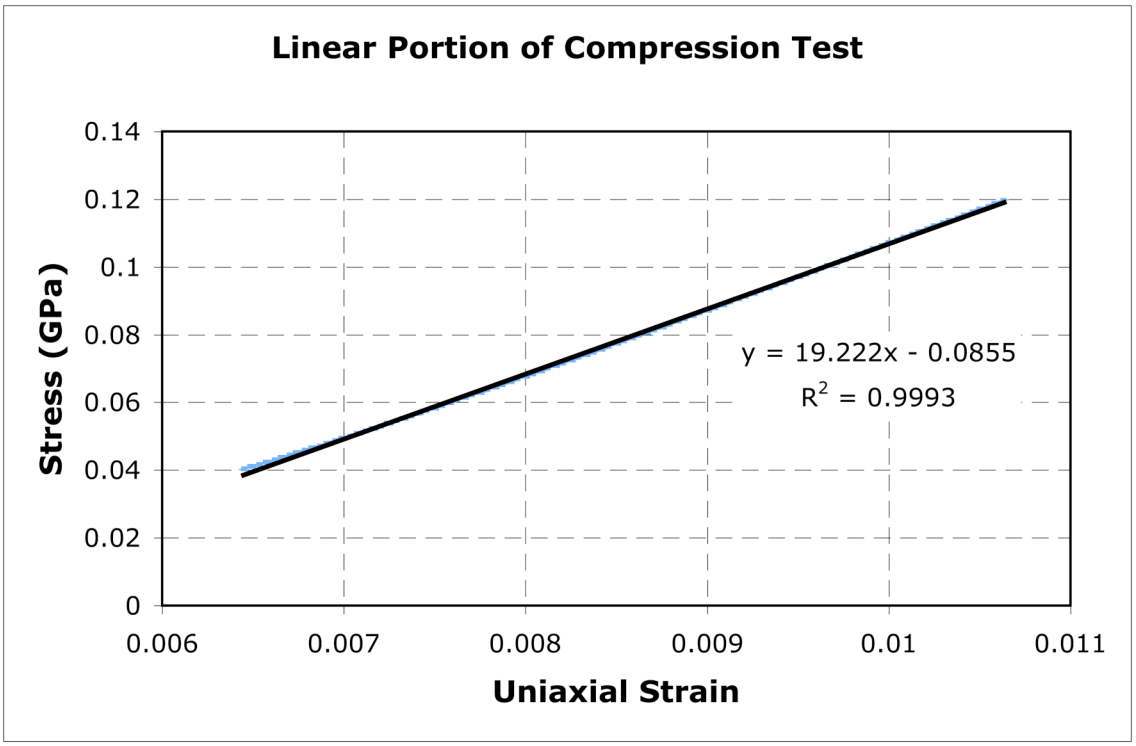

Figure C.2 – Linear portion of the unconfined uniaxial test of Barre Granite. Note the different units for both axes than those used in Figure A.1.

The Young's modulus was calculated to be 19.22 GPa, a value within the bounds of 11.9 Gpa and 23.1 Gpa found by Kesser et al. (1940) and close to the value of 17.5 Gpa found by Martinez (1999).

APPENDIX D– Platen Design

Figures D.1 and D.2 provide schematics for platens with vertical teeth (brush platens). The solid platens used were made from the base piece drawing in Figure D.2. Drawings were made in AutoCAD by Raymond Janeiro.

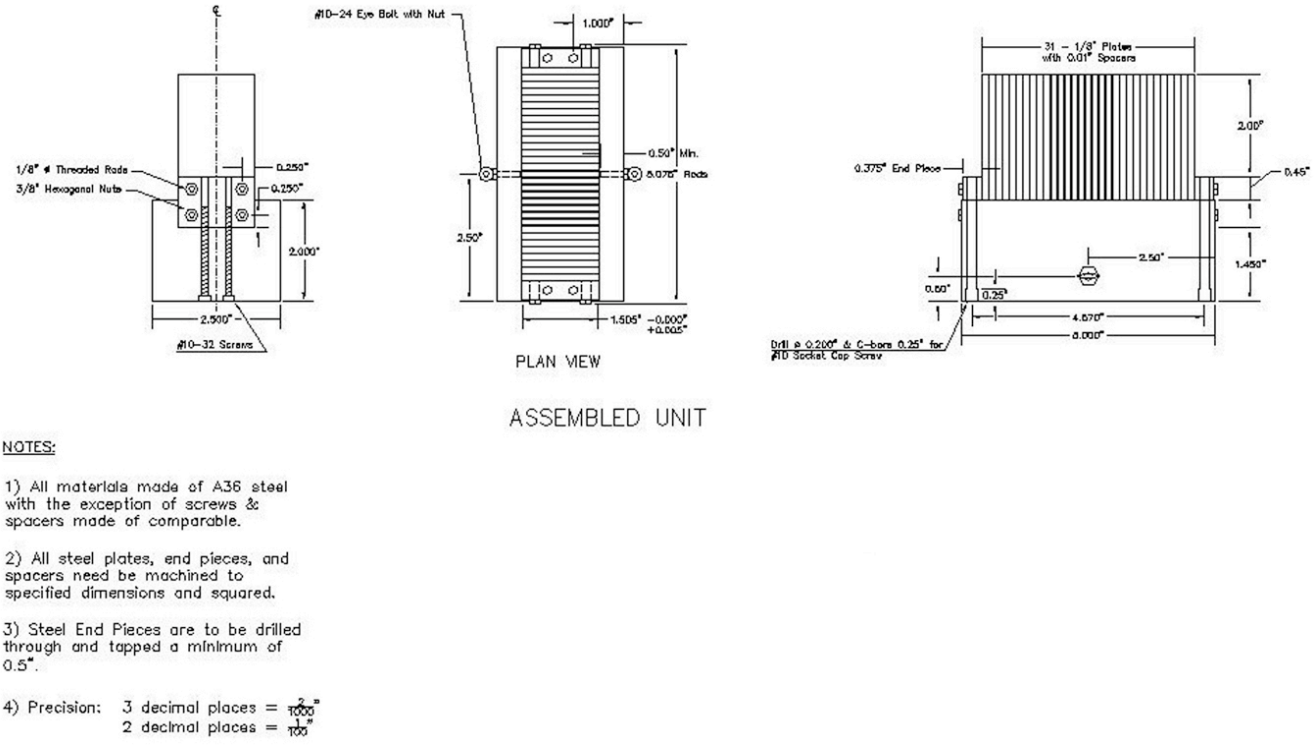

NOTES:

1) All materials made of A36 steel with the exception of screws & spacers made of comparable.

2) All steel plates, end pieces, and spacers need be machined to specified dimensions and squared.

3) Steel End Pieces are to be drilled through and tapped a minimum of 0.5".

4) Precision: 3 decimal places = $\frac{2}{1000}$"
2 decimal places = $\frac{1}{100}$"

Figure D.1 – Plan and elevation views of assembled platen with vertical teeth.

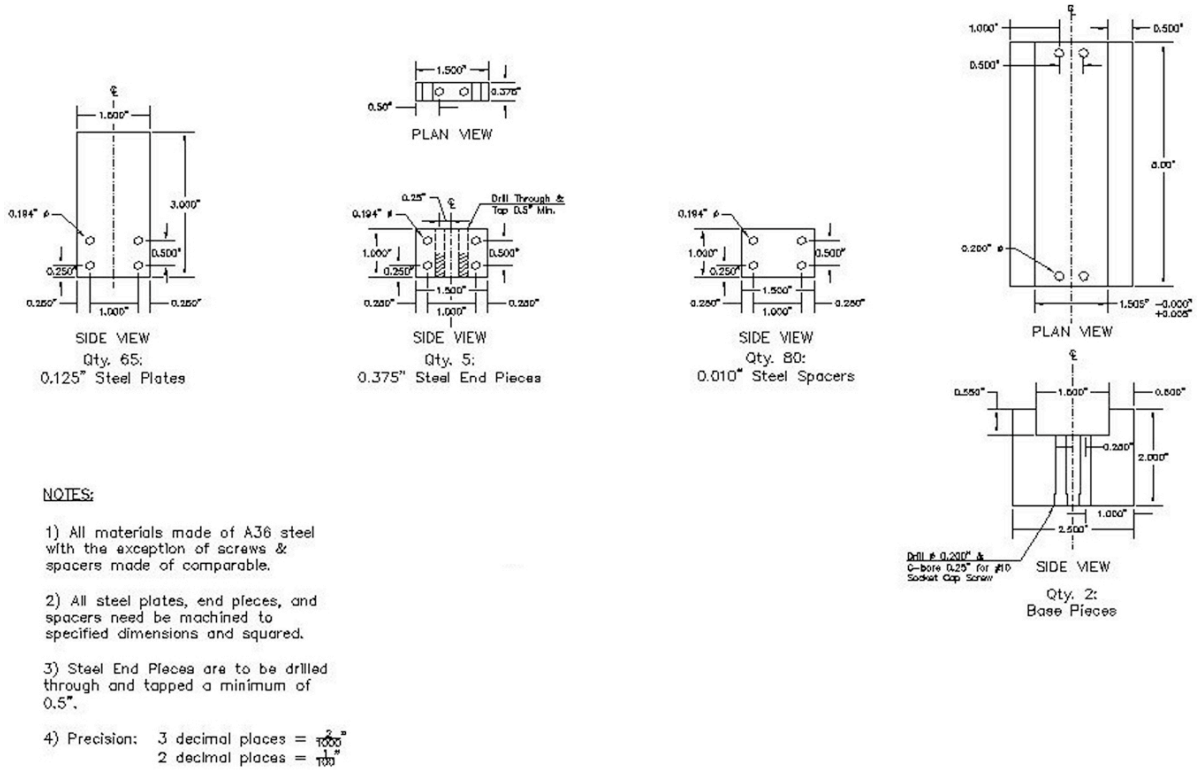

Figure D.2 – Plan and elevation views of individual parts making up platen with vertical teeth. The "base piece" design corresponds also to the "solid platens".

APPENDIX E. Confining Stress from Solid Platens

As mentioned in Section 3.4.2, solid platens may introduce a confining stress at the top and bottom of the specimen being tested. This is actually the reason for using brush platens as mentioned in Section 3.4.2. It was, however, not possible to use brush platens in the tests with ligament length "a" (see Section 3.2 for a description of specimen geometries). This Appendix explains and calculates the confinement introduced by the solid platens.

Confinement is the result of a difference in elastic properties between the granite specimen and steel end piece. More specifically, the confinement comes from a difference in Poisson's ratios between the two materials.

To find the confinement stress, it is helpful to think of an axial compression test in three stages: initial, deformed with slipping ("no confinement"), deformed without slipping. All three steps are shown in Figure E.1. In the undeformed condition, the specimen is in contact with the platens, but no compression is applied. In the deformed with slipping condition, compression is applied. Friction is neglected, however, so both parts (specimen and platens) expand due to the Poisson effect. As the granite has a higher Poisson's ratio, it will expand laterally more than the steel will. In the third and final step, the frictional resistance is superimposed on the second step. Assuming the friction between steel and granite is high enough, this force will limit the granite's expansion to that of the steel.

To calculate the confinement stress, one must know the Poisson's ratio (ν) and the Young's modulus (E) of both materials. Platens were constructed with A36 steel, which has a Poisson's ratio of 0.26 and a Young's modulus of 200 GPa (MatWeb, 2008). Granite, as explained in Section 0, is not an isotropic material, so two values of the Young's modulus will be used: 11.9 GPa and 23.1 GPa (Kessler et al., 1940). These two values are the minimum and maximum values, respectively, reported by Kessler et al. (1940). The Poisson's ratio is taken to be 0.23 (Krech et al., 1974) as an average value.

Only one value is used as Poisson's ratio generally does not vary greatly in different directions.

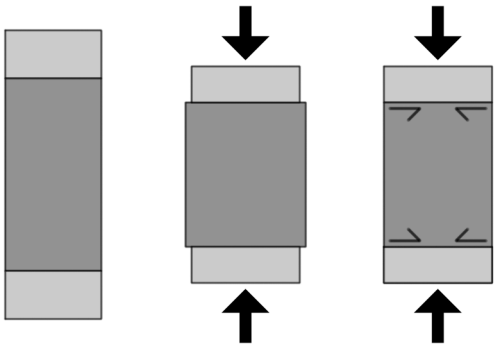

Figure E.1 – Three steps used to visualize confinement stress. 1) Initial state. 2) Deformed with slipping. 3) Deformed without slipping.

Granite specimens can be oriented in two ways: with the stiff direction parallel or perpendicular to the axis of compression. As described in Section 0, it is assumed that specimens in this study are tested with the rift plane perpendicular to the axis compression. As such, the stiff direction is oriented perpendicular to the axis of compression, as shown in Figure E.2.

To find the confinement stress, the transverse strains of both the end pieces and the granite must be calculated. Calculations will be performed for one end, because both ends are symmetric to one another.

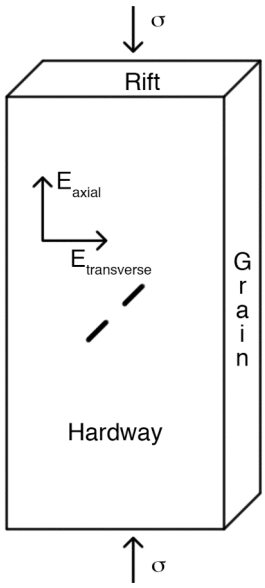

Figure E.2 – Illustration of assumed orientation of granite during testing. $E_{transverse}$ is the maximum Young's modulus and E_{axial} is the minimum Young's modulus (Kessler et al., 1940).

The transverse strain of the end piece can be calculated using the definitions of Young's modulus and Poissons ratio. Young's modulus in the axial direction (the direction parallel to the applied load) is defined $E_{axial} = \frac{\sigma_{axial}}{\varepsilon_{axial}}$, where σ_{axial} and ε_{axial} are stress and strain, respectively, in the axial direction. Poisson's ratio is defined $\nu = -\frac{\varepsilon_{transverse}}{\varepsilon_{axial}}$ for an axially applied load. Then, the transverse strain in the steel end piece can be calculated:

$$\varepsilon_{transverse}^{steel} = -\nu^{steel} \cdot \varepsilon_{axial}^{steel} = -\frac{\nu^{steel} \cdot \sigma_{axial}}{E^{steel}},$$

where negative strain is taken as expansion. Similarly, the transverse strain in granite can be calculated:

$$\varepsilon_{transverse}^{granite} = -\nu^{granite} \cdot \varepsilon_{axial}^{granite} = -\frac{\nu^{granite} \cdot \sigma_{axial}}{E_{axial}^{granite}},$$

where the axial direction for granite is the minimum Young's modulus value. The transverse strain can then be calculated with the physical properties given earlier as well as the applied axial stress.

To find the confining stress, the difference in transverse expansion for the two materials must be calculated:

$$\Delta\varepsilon_{transverse} = \varepsilon_{transverse}^{granite} - \varepsilon_{transverse}^{steel} = \left(\frac{\nu^{steel}}{E^{steel}} - \frac{\nu^{granite}}{E_{axial}^{granite}} \right) \cdot \sigma_{axial} .$$

The confining stress, then, is the stress required to reverse this difference in strain in the granite, or:

$$\sigma_{confine} = -\Delta\varepsilon \cdot E_{transverse}^{granite} = -\left(\frac{\nu^{steel}}{E^{steel}} - \frac{\nu^{granite}}{E_{axial}^{granite}} \right) \cdot E_{transverse}^{granite} \cdot \sigma_{axial} .$$

For the transverse direction for granite, the maximum value of the Young's modulus has to be used. So the confinement stress is linearly dependent on the applied axial stress. Using the values given earlier, the expression reduces to $\sigma_{confine} = 0.42 \cdot \sigma_{axial}$. This means that the confinement stress is nearly half the applied stress at both ends. This assumes no slipping between the granite and end piece, so is the maximum limit for confinement stress.

E.1 References

Kessler et al. (1940) Physical, mineralogical, and durability studies on the building and monumental granites of the United States, *Journal of Research of the National Bureau of Standsards*, Vol. 25, No. 2, Paper RPI1320.

MatWeb: Material Property Data, *ASTM A36 Steel Bar*, <http://www.matweb.com/search/DataSheet.aspx?MatGUID=d1844977c5c8440cb9a3a967f8909c3a>. Last accessed August, 2008.

APPENDIX F. MATLAB for White Patch Visualization

F.1 Introduction

The simplest technique to find white patches is to compare two frames from the high-speed footage. This method has its limitations, however. One needs to switch between the frames many times over in able to find the white patches in different areas, and small details are difficult to find. Another method uses the image processing toolbox of Matlab. By subtracting two images from one another, the noise of the granite grains is eliminated. Any two pixels which do not change color are shown as black. A change in pixel color will show up as a shade of gray.

Using Matlab to find white patches is thus very useful. After one operation, the difference between images can be used to trace white patches that might be hard to find or not noticed with the standard frames. If a more thorough investigation of the white patches takes place, the Matlab technique may also prove useful. Images imported into Matlab are intensity images (grayscale) with each pixel having a value between 0 (black) and 255 (white). This is valuable because the degree to which an area of an image lightened can be determined. This, in turn, may be related to the extent of micro damage taking place.

However, this method is not without its problems. Because the process does not have any knowledge of its application, differences are computed for identical pixels between two images. This can be problematic in a number of situations; all caused by relative movement of units within a specimen: the high-speed camera being bumped, the light sources being repositioned, Poisson expansion of the specimen, the opening of tensile cracks, the closing of prefabricated flaws, or rotation of structural units can also cause this changing in pixel color. By using Matlab to compare images early in the testing (before tensile crack formation), many of these problems can be eliminated. While limitations of the method still remain, the problems are readily seen: three frame comparisons for specimen Gr 2a-45-0 C (20071002) are shown below in Figures F.1, F.2, and F.3. Each demonstrates a different problem and what information, if any, that can be

gained from the subtraction. In each figure, the image has been inverted so that white indicates no color change and gray/black indicates lightening between the two images.

Figure F.1 – Loading from 2,067 pounds per square inch to 5,000 pounds per square inch. In this case the camera was moved slightly, so the entire image was moved. Grain edges are highlighted (a typical edge is traced). This results in a general appearance of features being oriented diagonally upward to the left. The arrow indicates the direction of motion of the camera. No meaningful information can be obtained from this image.

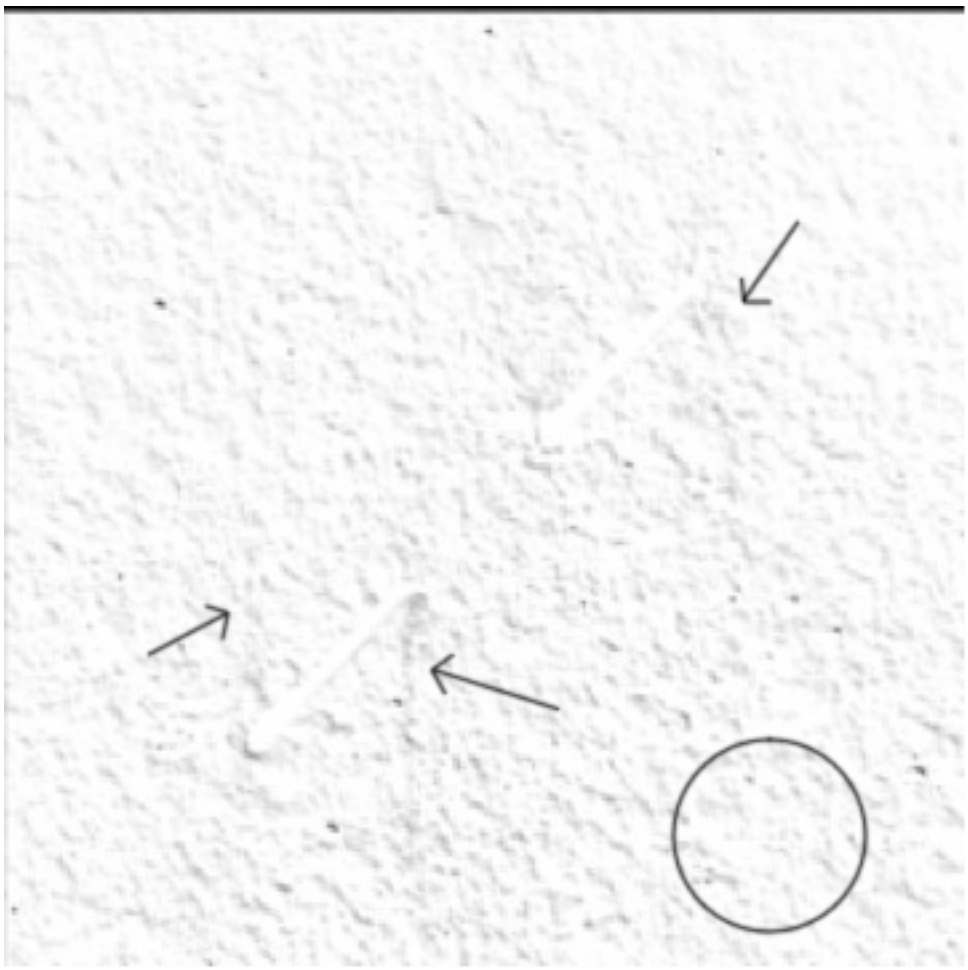

Figure F.2 – Loading from 5,000 pounds per square inch to 10,000 pounds per square inch. Here a large amount of horizontal spreading has occurred (5,000 psi have been applied between images). As a result, many grains have moved slightly. This results in most areas looking “rough”. One such area is circled. One can see linear features extending from the flaw tips, however. These features are indicated with arrows. This could be from the horizontal spreading of the specimen or from actual white patch development. The features show areas of interest that should be examined in the images, narrowing the search.

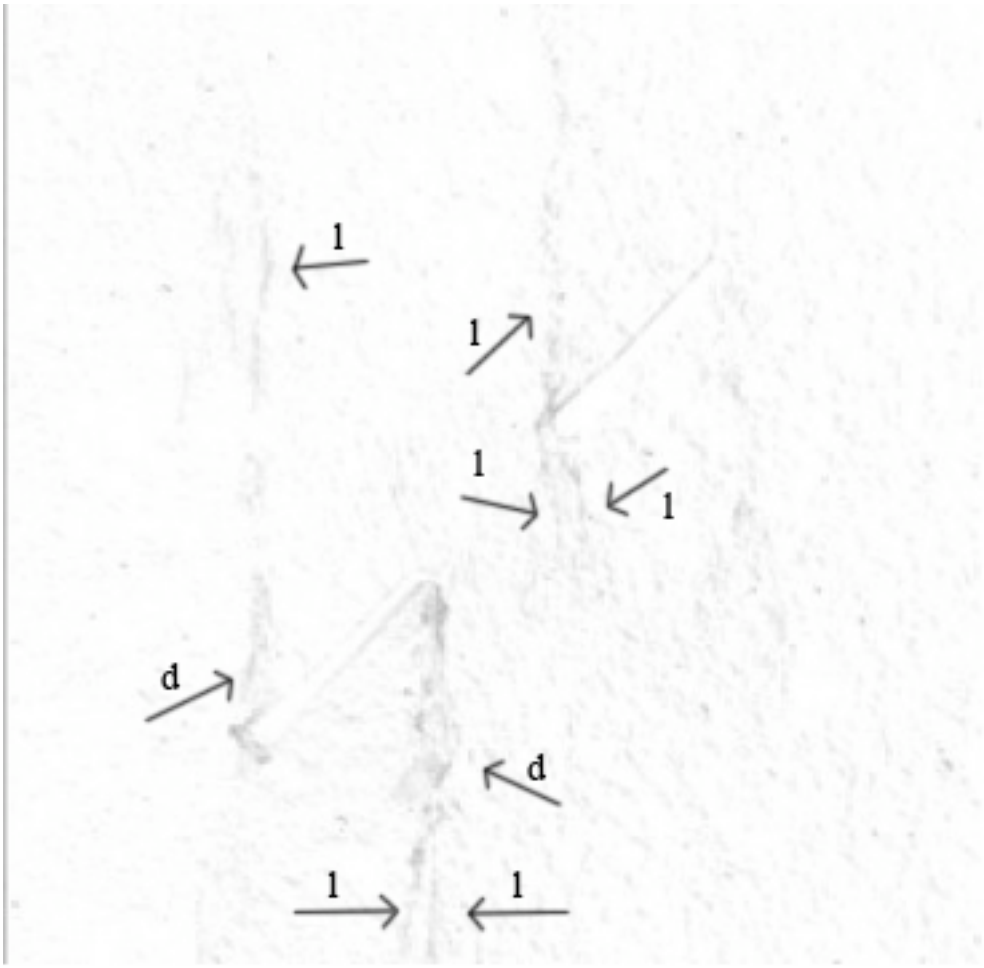

Figure F.3 – 10,667 pounds per square inch to 11,000 pounds per square inch. Here again one sees the effect of horizontal spreading, but can see a significant development of linear white patches. Diffuse features (d) and linear features (l) can be seen. As in Figure F.2, the use of a difference image allows one to see areas of interest.

F.2 Matlab Commands

Making these figures is easy within Matlab. To compare two JPEG images, first put them both in Matlab's working directory. For this example we will assume the two images are "1.jpg" and "2.jpg." First, load the two images as variable in the Matlab workspace:

```
>>first = imread('1.jpg');
>>second = imread('2.jpg');
```

Next, subtract the first image from the second and store this resulting image as a variable:

```
>>delta = second – first;
```

Finally, to produce the image:

```
>>imshow('delta');
```

APPENDIX G. Coplanar Flaws Separated by '2a'

The following detailed analyses are for specimens with coplanar flaws ($\alpha = 0°$) and L = 2a (see Section 3.2 for an explanation of flaw geometry) tested as described in Chapter 3. Brush platens (see Section 3.4.2 for a description of platens) were used in all cases. For an overall summary of the results of these experiments, see Section 4.3.2

Gr 2a-0-0 A (20070918)

Summary

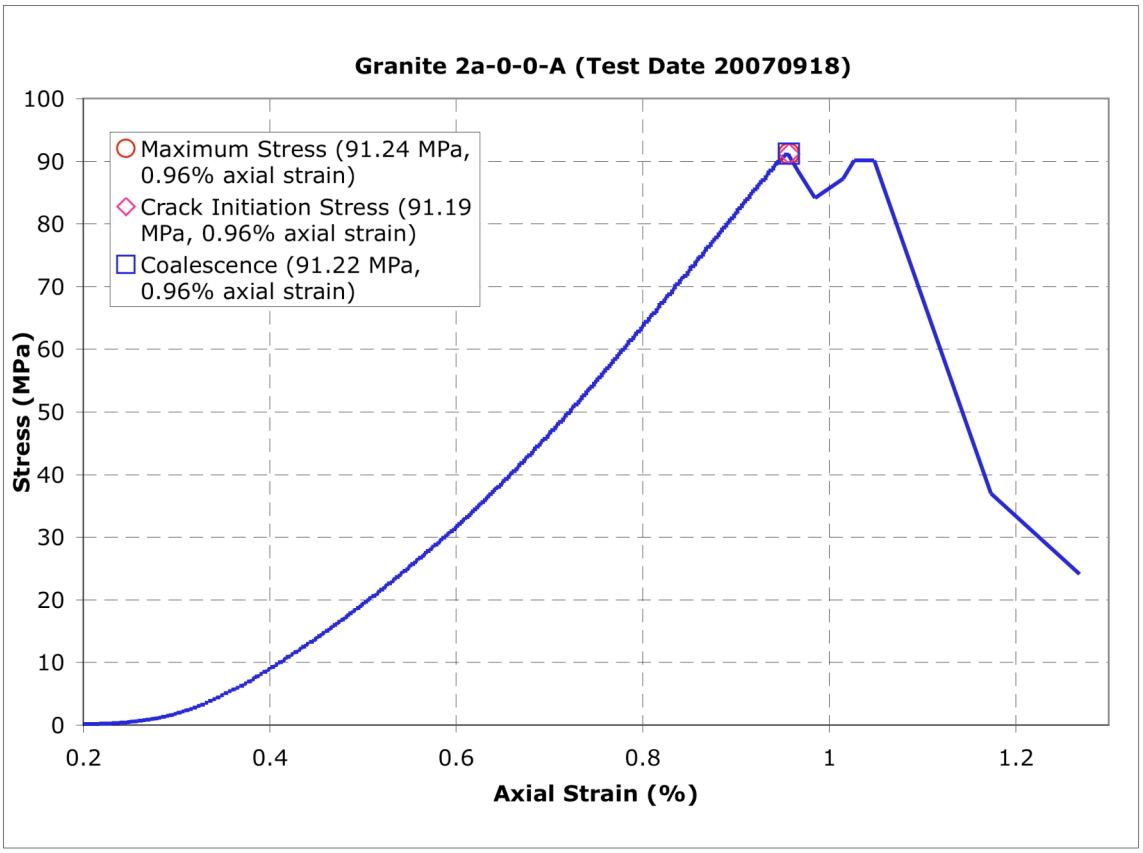

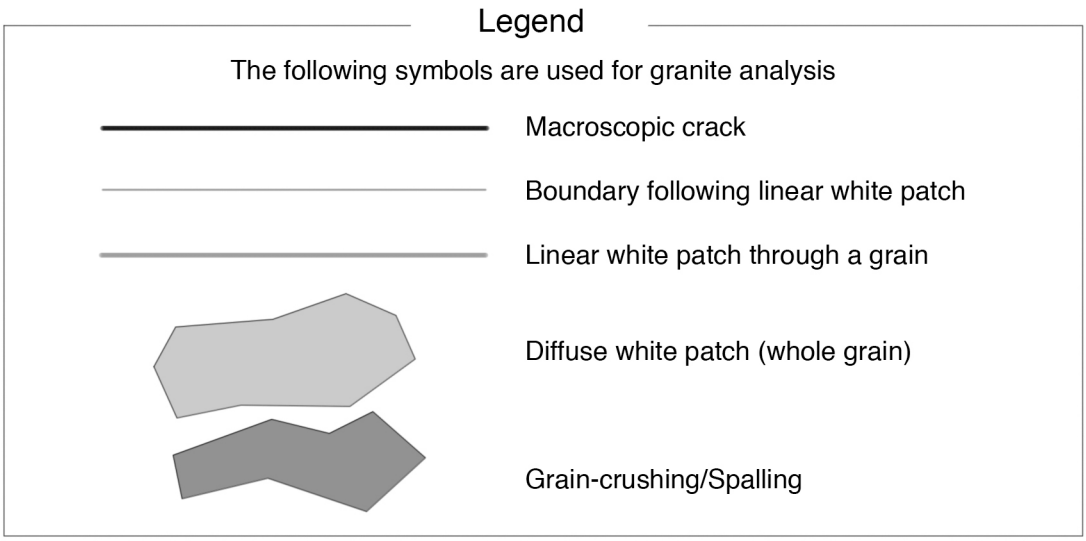

Category 2 coalescence
Images taken from high-speed camera

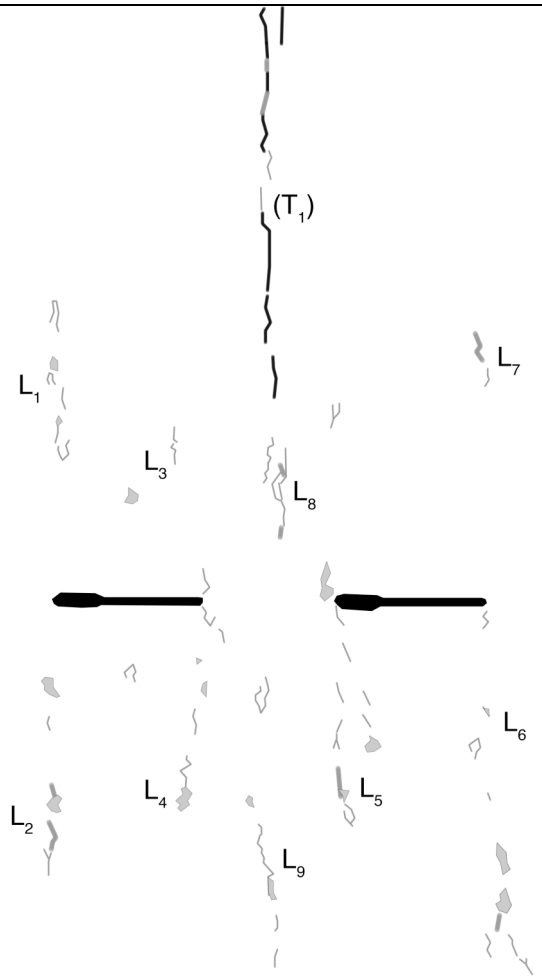

Time: 0.284s before failure

Linear white patches open in nine regions (L_1 through L_9). L_1 through L_7 are near flaw tips, while L_8 and L_9 are above and below the bridge area, respectively. Boundary following and through-going linear features are present as are lightened grains. Boundary-following tensile cracks open above the bridge area. These cracks are labeled as (T_1).

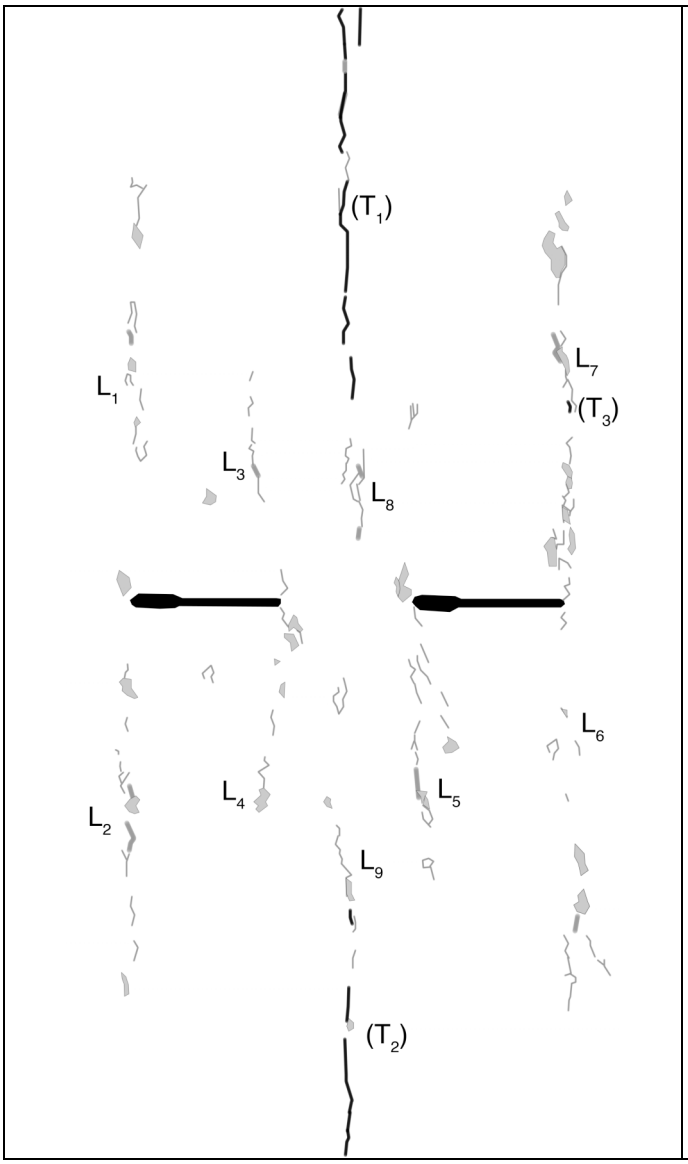

Time: 0.2741s before failure

Tensile cracks within the (T_1) group extend and grow together. Some tensile cracks form below the bridge area in the L_9 region and are labeled as (T_2). White patching continues in linear white patches L_1 through L_7 with all types of white patches (boundary-following linear features, those going through grains, as well as diffusely lightening grains). A small tensile crack opens in the L_7 region as well. It is called (T_3).

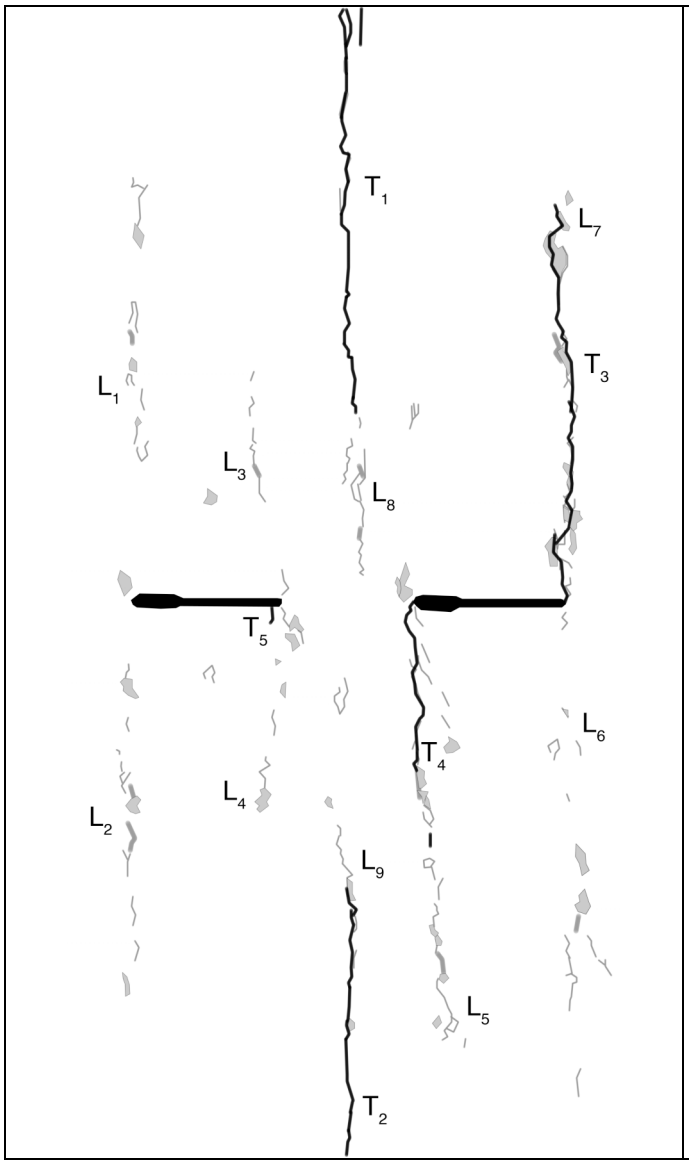

Time: 0.2735s before failure

Tensile cracks T_1 and T_2 form when (T_1) and (T_2) have their smaller cracks grow and link together to form large tensile features. Linear white patches continue to grow along grain boundaries below T_1 in the L_8 region. Tensile wing cracks T_3, T_4, and T_5 all form with T_3 growing from (T_3). L_5 extends downward with all three types of white patching.

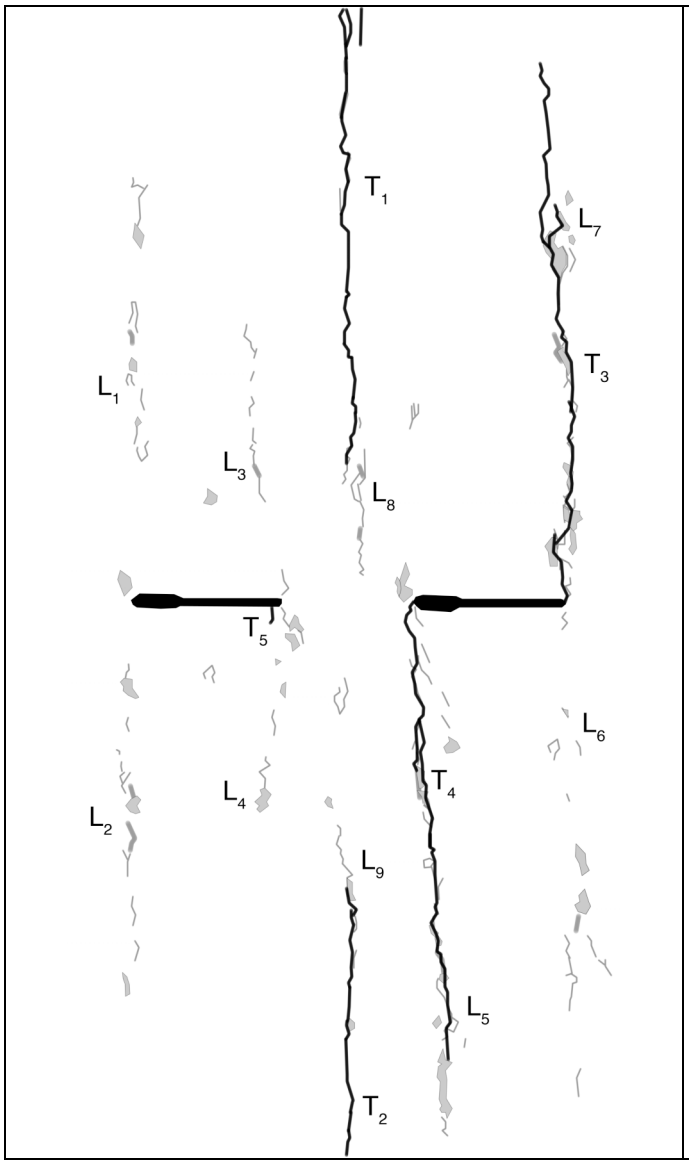

Time: 0.272s before failure

Tensile cracks T_1, T_3, and T_4 all lengthen. Linear white patches L_3 and L_5 also extend. L_3 extends along grain boundaries while L_5 extends with a long, thin area of lightened grains.

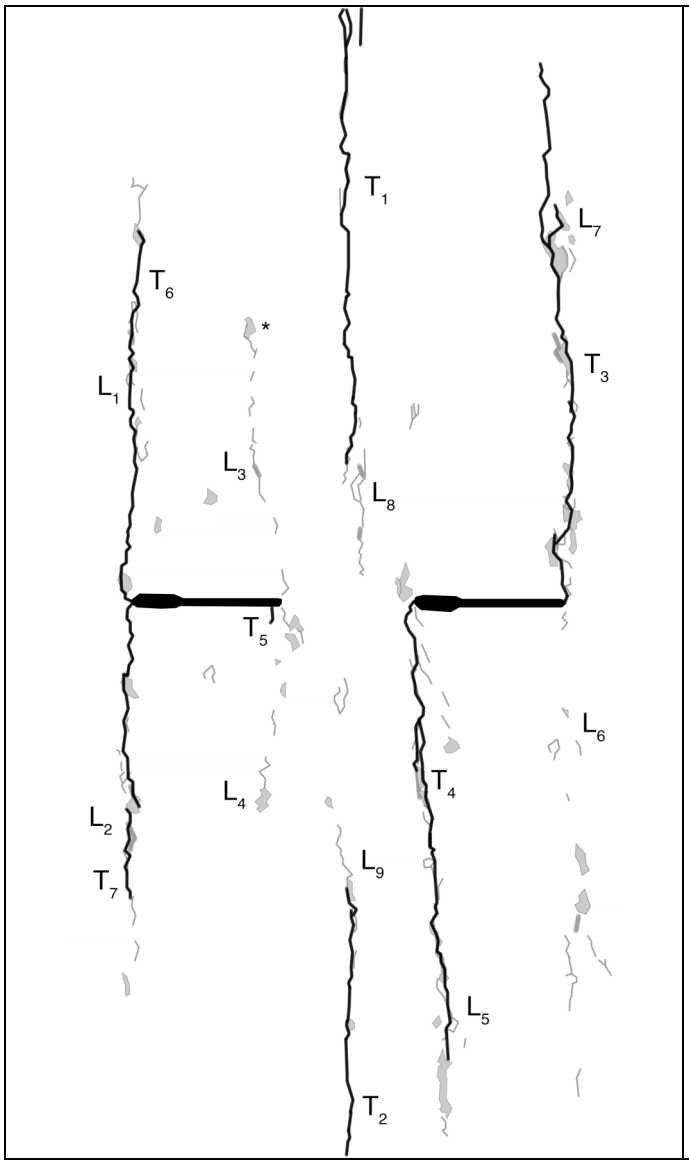

Time: 0.271s before failure

Tensile wing cracks T_6 and T_7 open above and below the outside tip of the left flaw. L_3 has a lightened grain form at its tip and is indicated by the *.

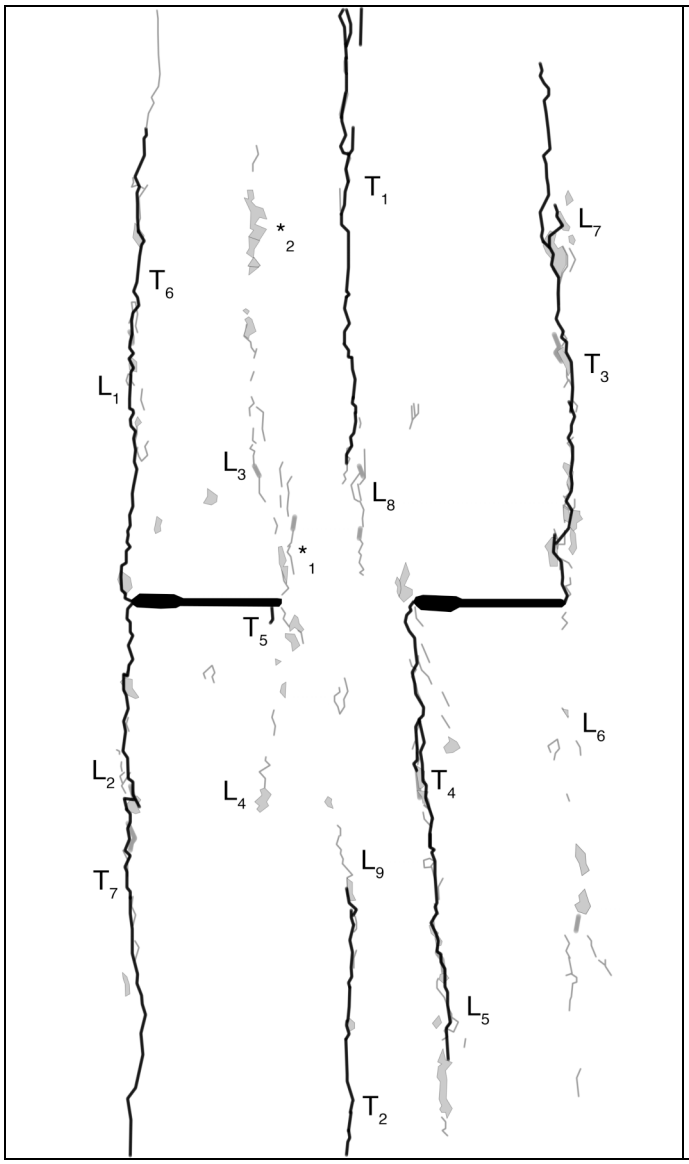

Time: 0.270s before failure

Tensile wing cracks T_6 and T_7 lengthen (along with their corresponding linear white patches L_1 and L_2, respectively). L_3 lengthens with mostly lightening grains in the area marked $*_1$ and widens in the area marked $*_2$.

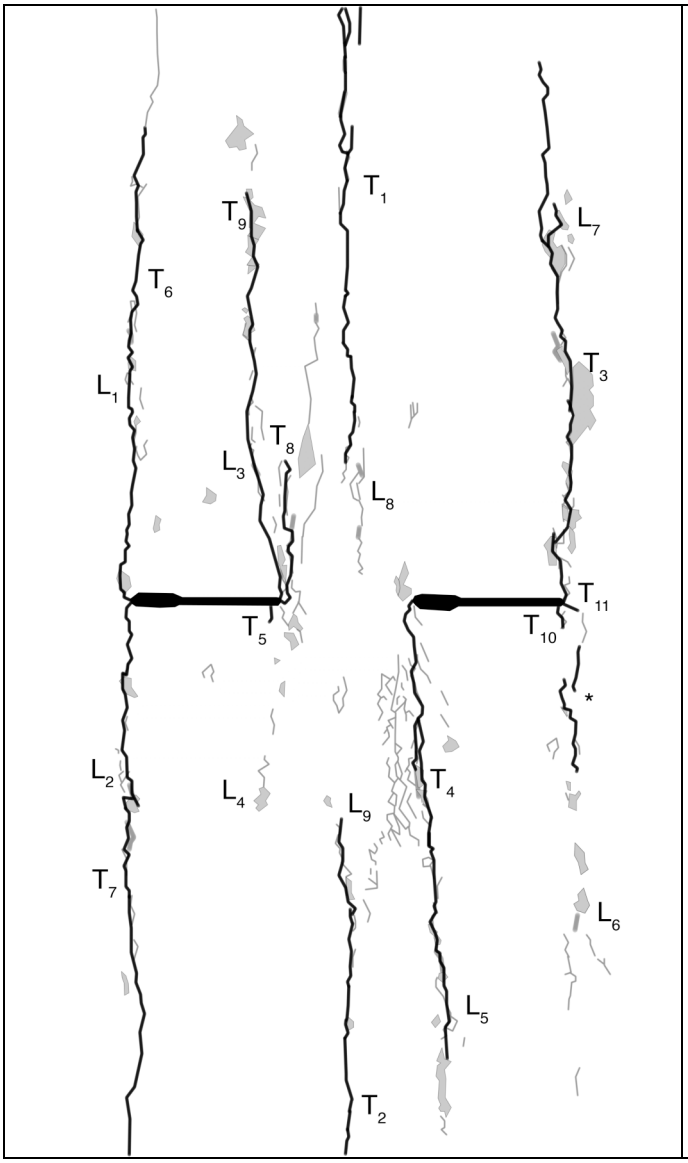

Time: 0.142s before failure

Tensile wing cracks T_8 and T_9 both extend up from the left inner flaw tip. Both cracks also have linear white patches extending beyond their tips. Boundary following linear white patches develop along T_4 and extending toward T_2. Tensile wing cracks T_{10} and T_{11} open below the outer tip of the right flaw. Tensile cracks open below T_{10} and T_{11} near the *. White patches develop within L_6 near these new tensile cracks. The white patches are both boundary following linear features as well as lightened grains.

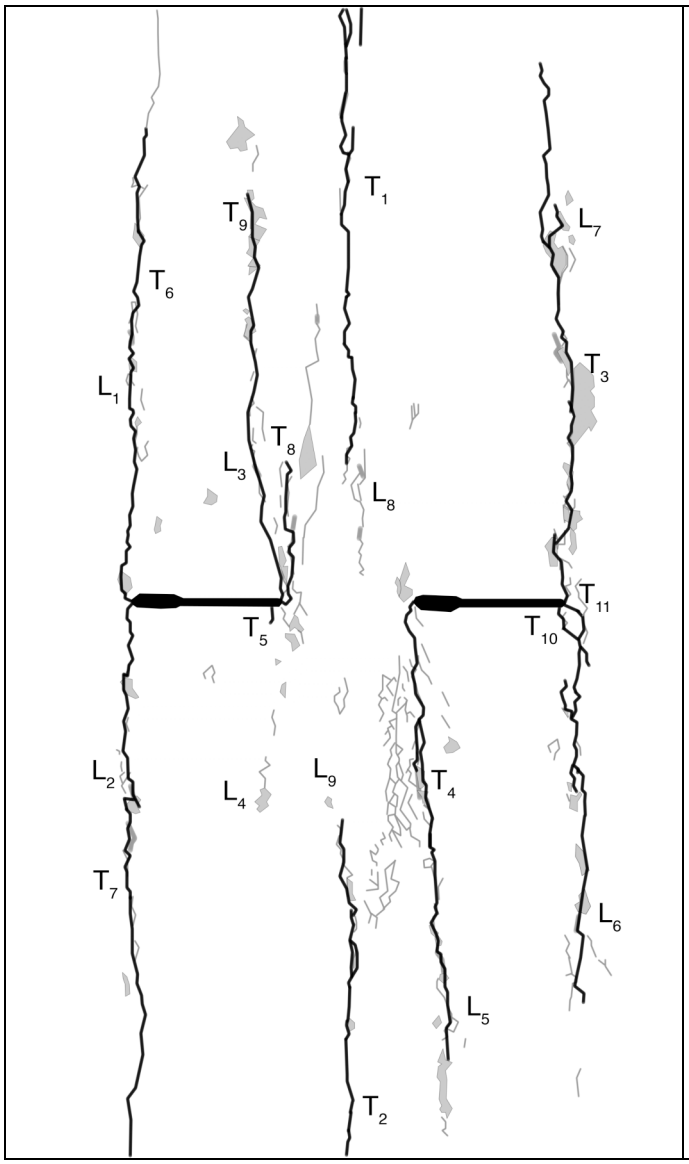

Time: 0.140s before failure

T_{10} and T_{11} grow together and link with the tensile cracks that had opened below them. The new T_{10}/T_{11} tensile crack grows downward. The zone of boundary-following linear white patches between T_2 and T_4 intensifies.

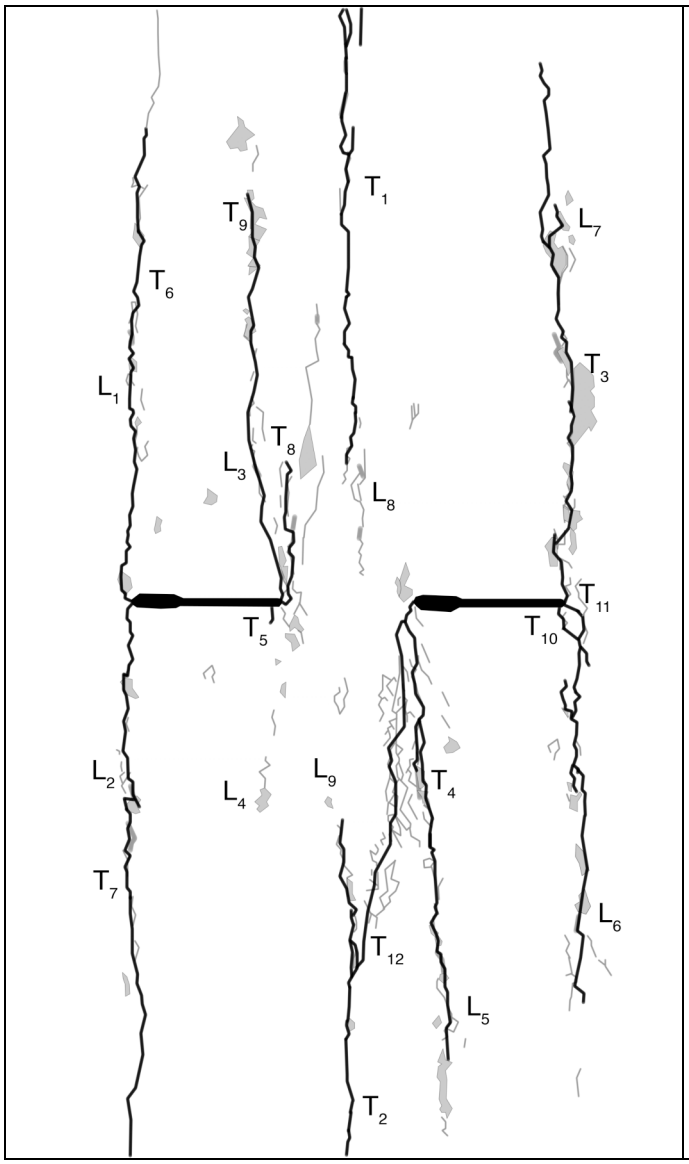

Time: 0.139s before failure

Tensile crack T_{12} grows from T_2 to T_4 through the zone of granite which had the network of linear white patches in it.

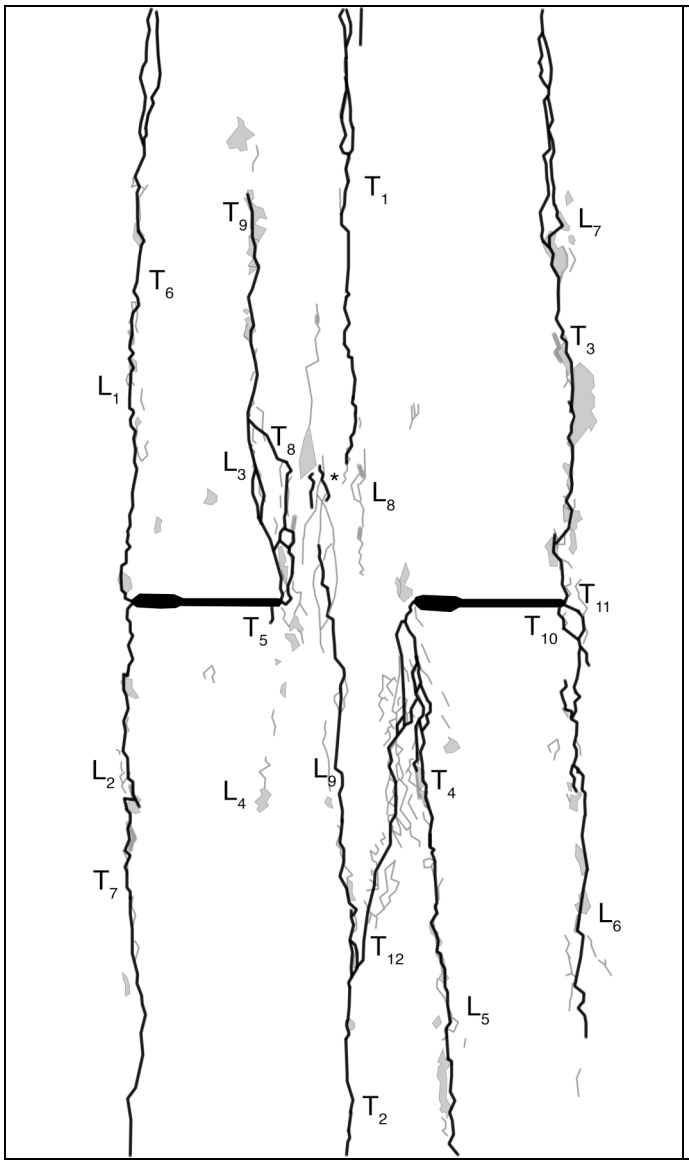

Time: 0.134s before failure

Tensile crack T_2 grows upward through the bridge area past the left inner flaw tip and "bends" toward T_8. Linear white patches develop between the two tensile cracks as do two smaller tensile cracks (labeled as *). T_4 extends downward through L_5. T_8 grows and links with T_9 at multiple points.

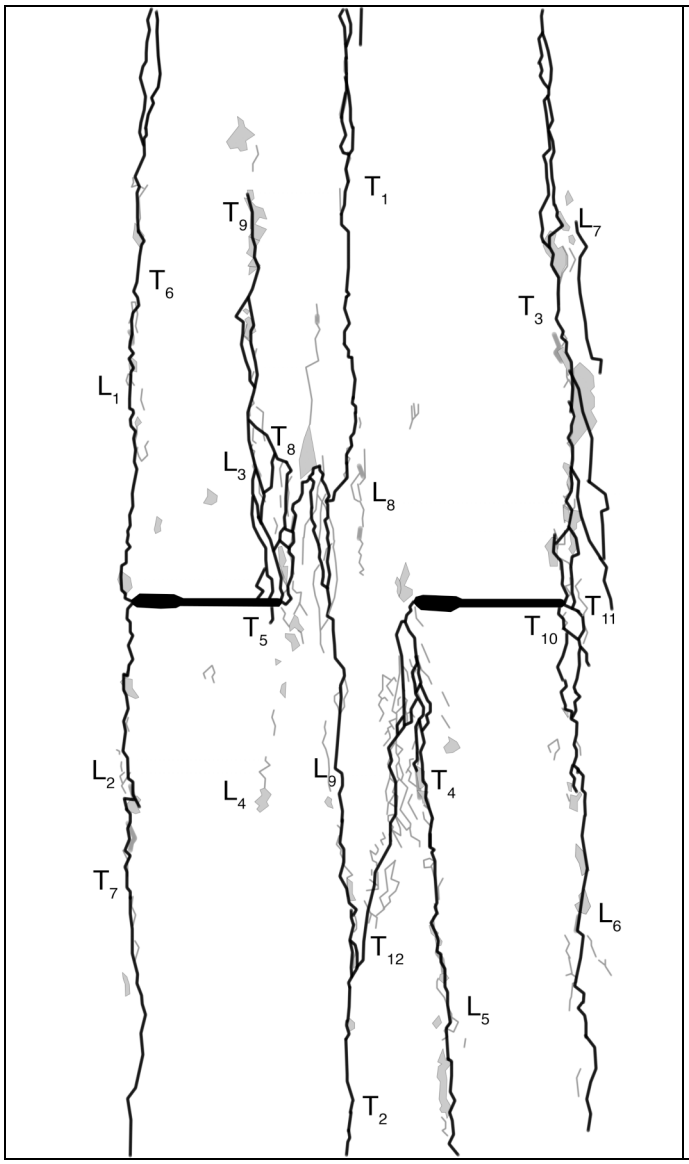

Time: 0.0261s before failure

Tensile cracks T_1, T_2, and T_8 link together. Several tensile cracks branch off of both T_5 and T_9. The T_{10}/T_{11} tensile cracks extend.

The sample has coalesced indirectly (category 2).

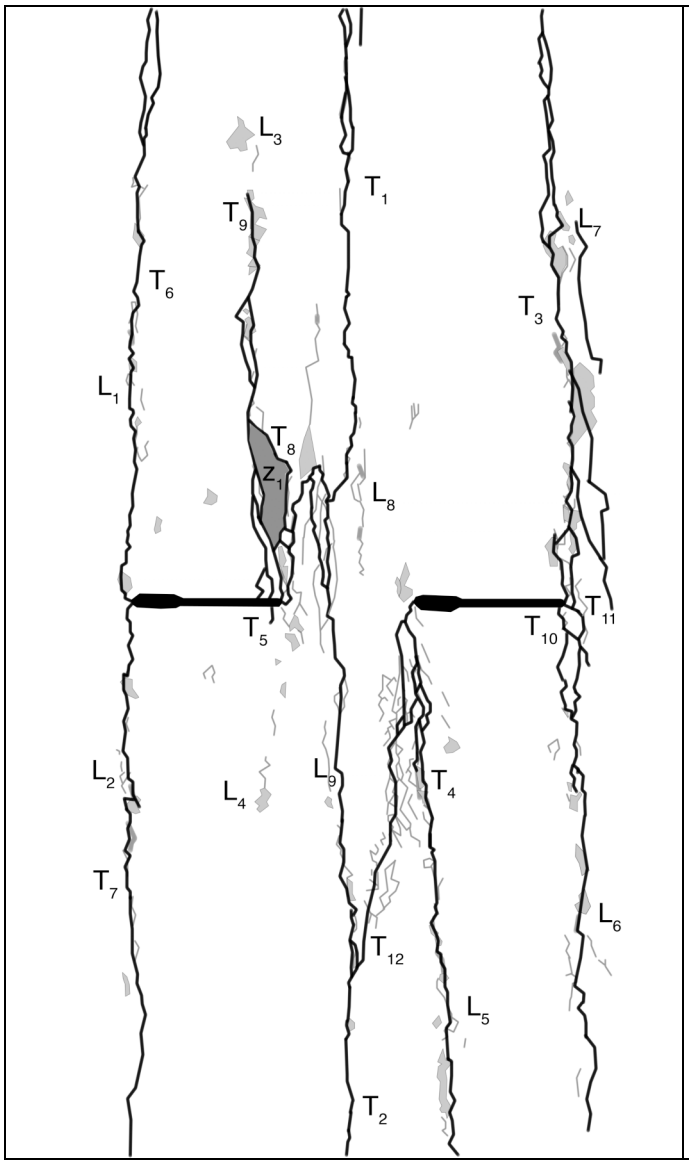

Time:16min49.404s
σ: 91.2399 MPa

Failure of the sample occurs when material within the network of tensile cracks between T_8 and T_9 bursts. The region of bursting is labeled z_1 for zone 1.

Gr 2a-0-0 B (20070918)

Summary

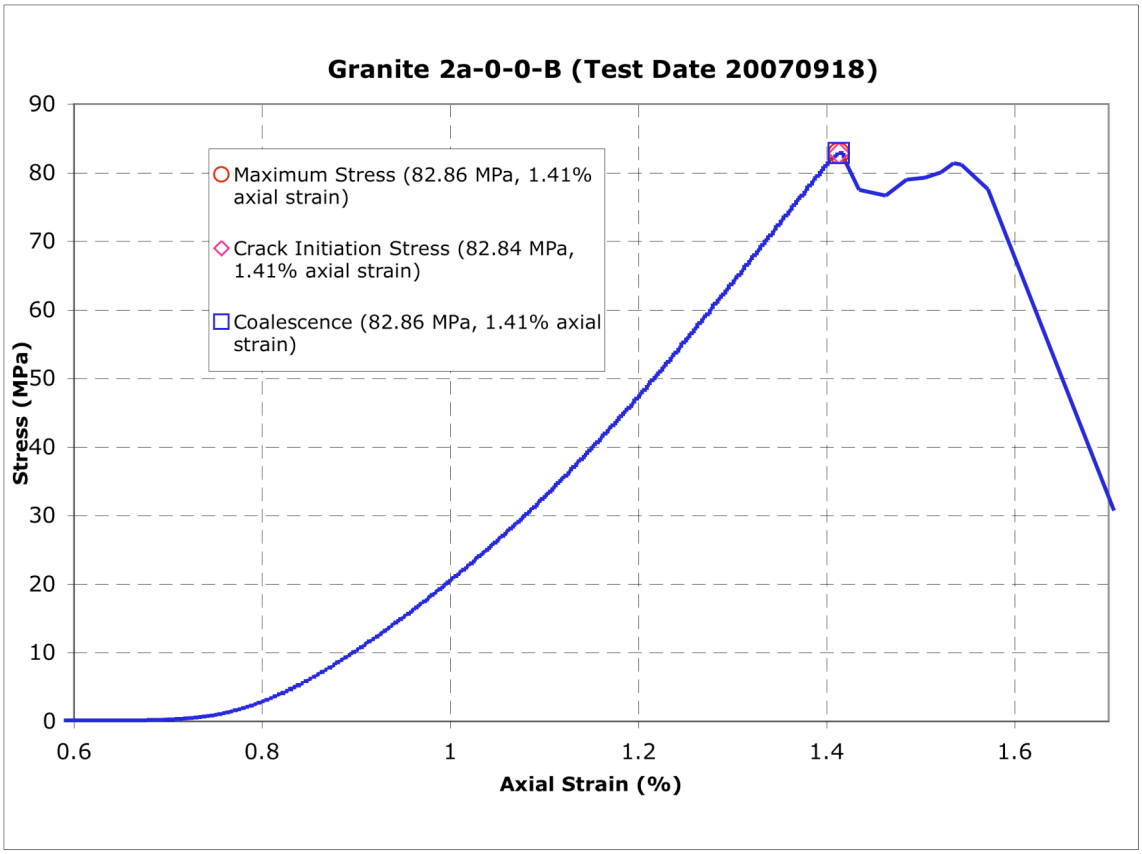

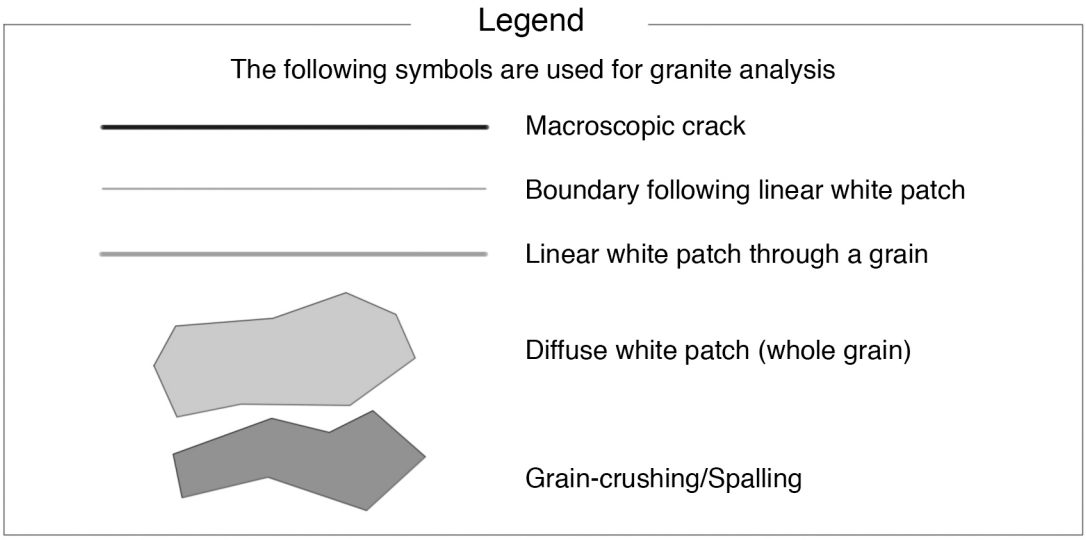

Category 2 coalescence
Images taken from high-speed camera

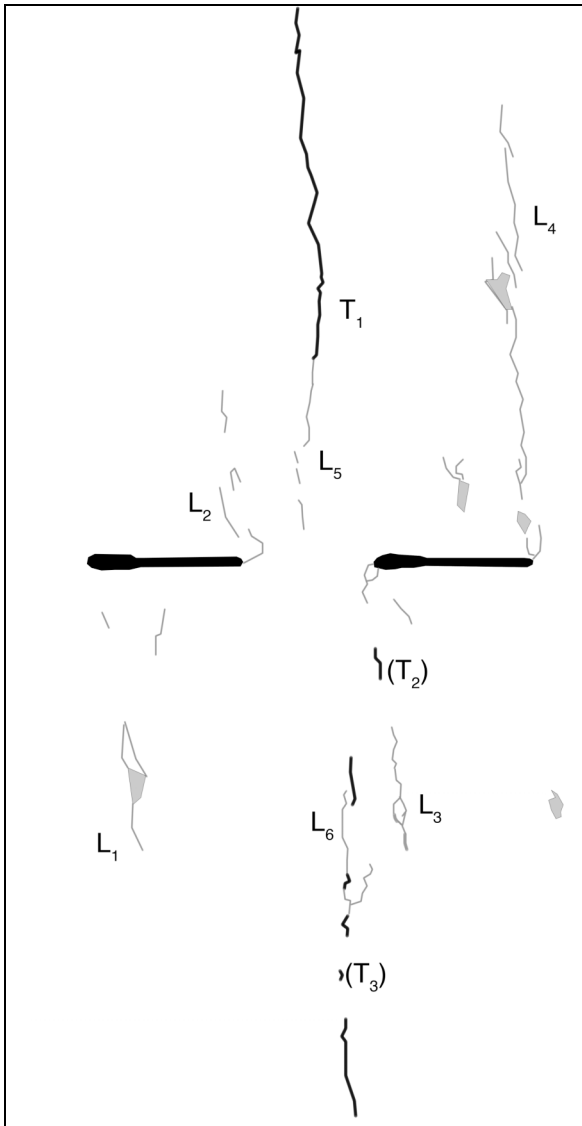

Time: 0.259s before failure

Linear white patches form on all four flaw tips (labeled as L_1 through L_4). They are in the positions of the expected tensile wing cracks. There is a small tensile crack which opens along grain boundaries in the L_3 region and it is labeled as (T_2). There is also a long, continuous tensile crack T_1 extending down the middle of the sample toward the bridge area. There are boundary following linear white patches extending further than T_1 (labeled as L_5). A series of tensile cracks are also below the bridge area in the (T_3) group. Boundary following linear white patches in the L_6 area link several of these tensile cracks.

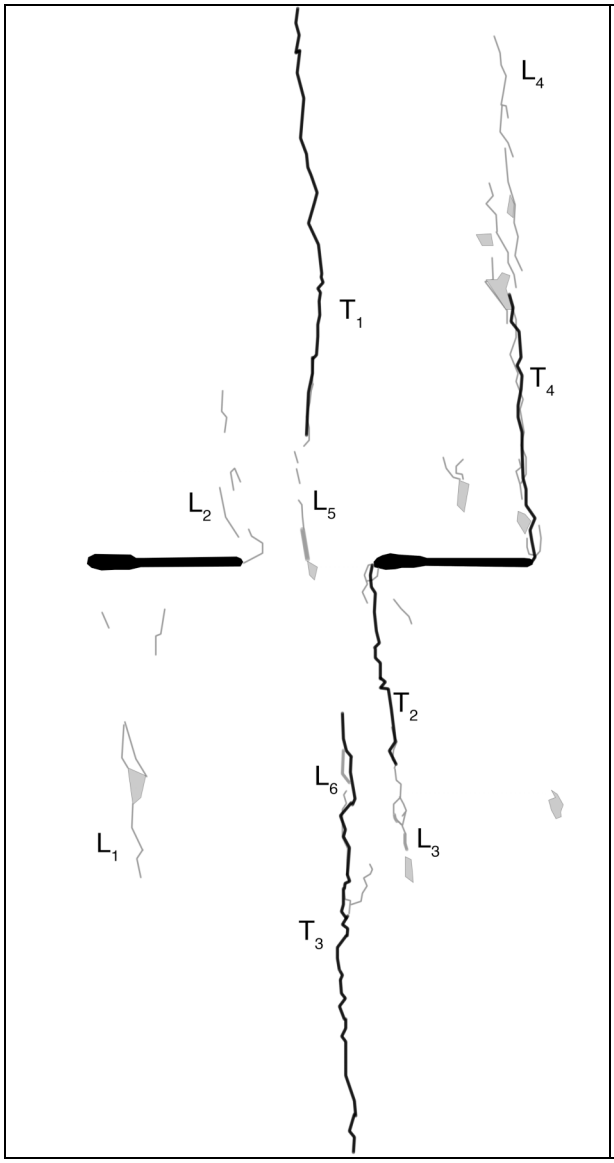

Time: 0.246s before failure

(T_2) extends up to the inner tip of the right flaw and downward away from the tip to form tensile wing crack T_2. Another tensile wing crack – T_4 – forms, extending up from the outer tip of the right flaw. L_1, L_3, and L_4 all extend. T_1 extends further toward the bridge area while the tensile cracks below the bridge area grow and link to form tensile crack T_3. White patch development here sees grain lightening and linear features going through grains.

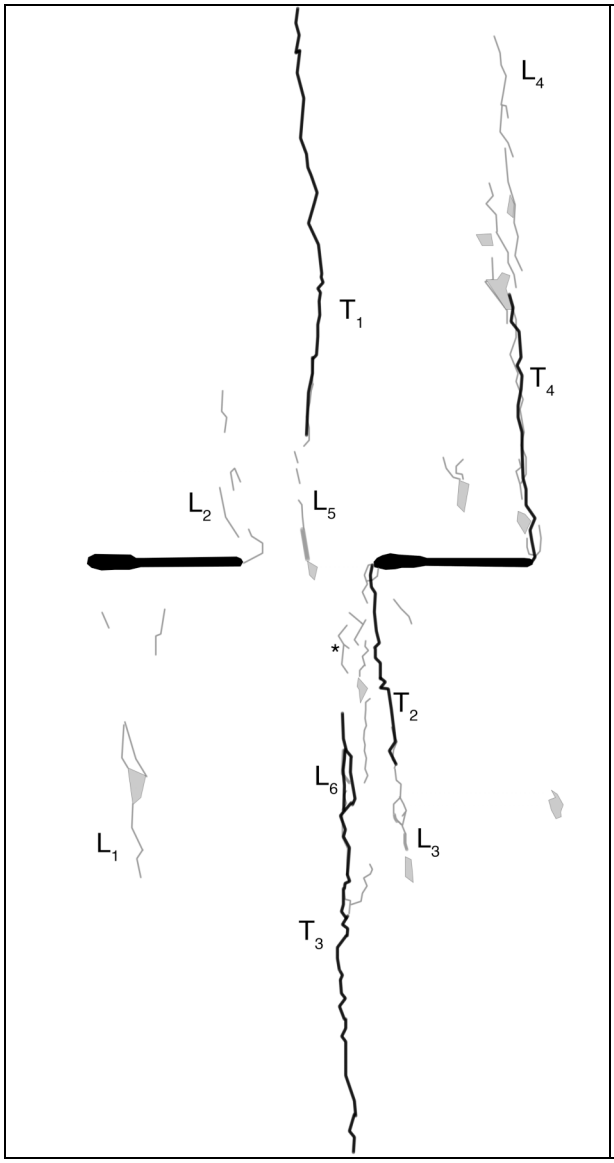

Time: 0.244s before failure

T_3 forms another branch which connects back to itself along linear white patches. L_6 extends upward toward L_3 in the region indicated by a *.

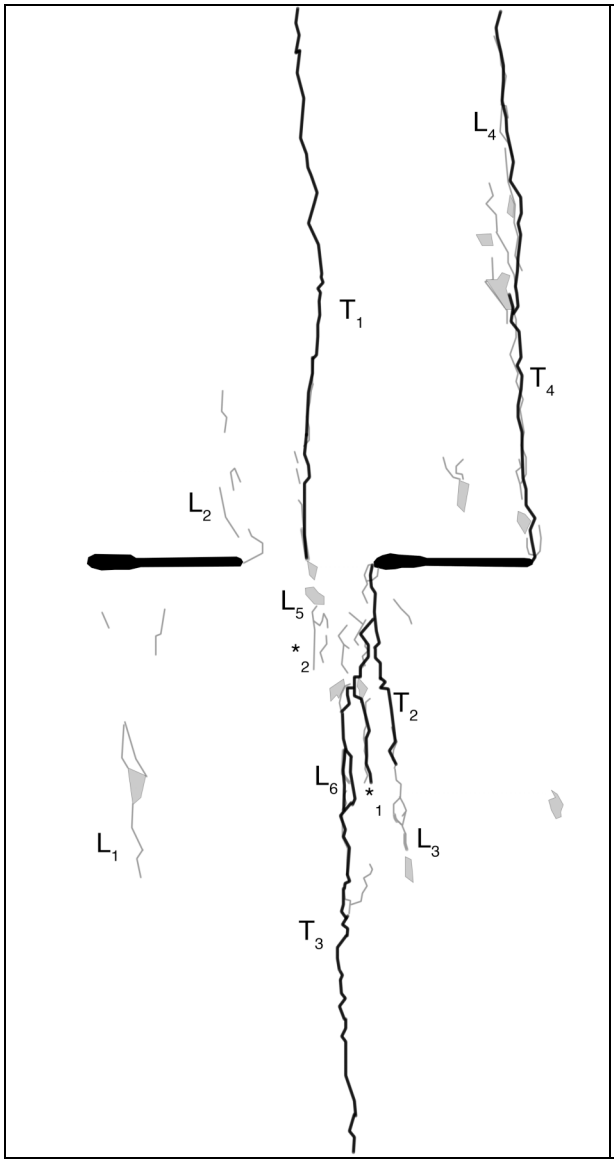

Time: 0.243s before failure

T_3 grows and connects with tensile wing crack T_2. During this connection, another tensile crack approximately halfway between T_2 and the previous location of T_3 extends downward parallel to T_2 and to roughly the same distance from the flaw tip. This tensile crack is indicated by $*_1$. T_1 grows down into the bridge area. L_5 grows toward the L_3-L_5 connection (labeled $*_2$). Tensile wing crack T_4 also grows upward.

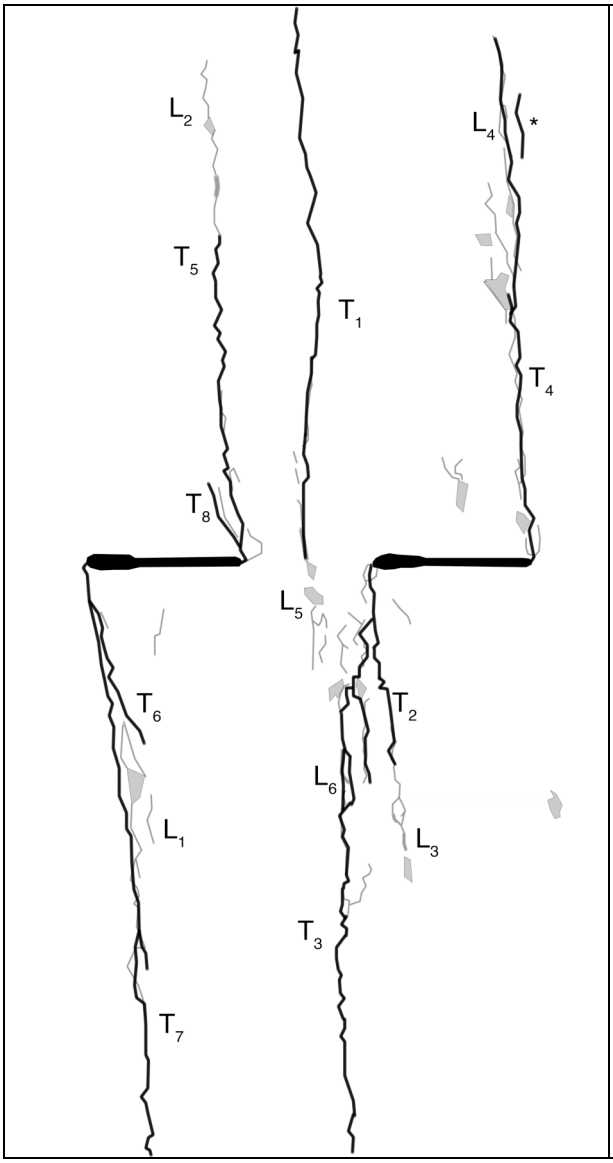

Time: 0.242s before failure

Four tensile cracks appear. T_5 appears above the left flaw's inner tip with T_8 branching off of it and T_6 and T_7 appearing below the left flaw's outer tip. Both L_1 and L_2 extend as well. Next to the *, a small tensile crack opens parallel to T_4.

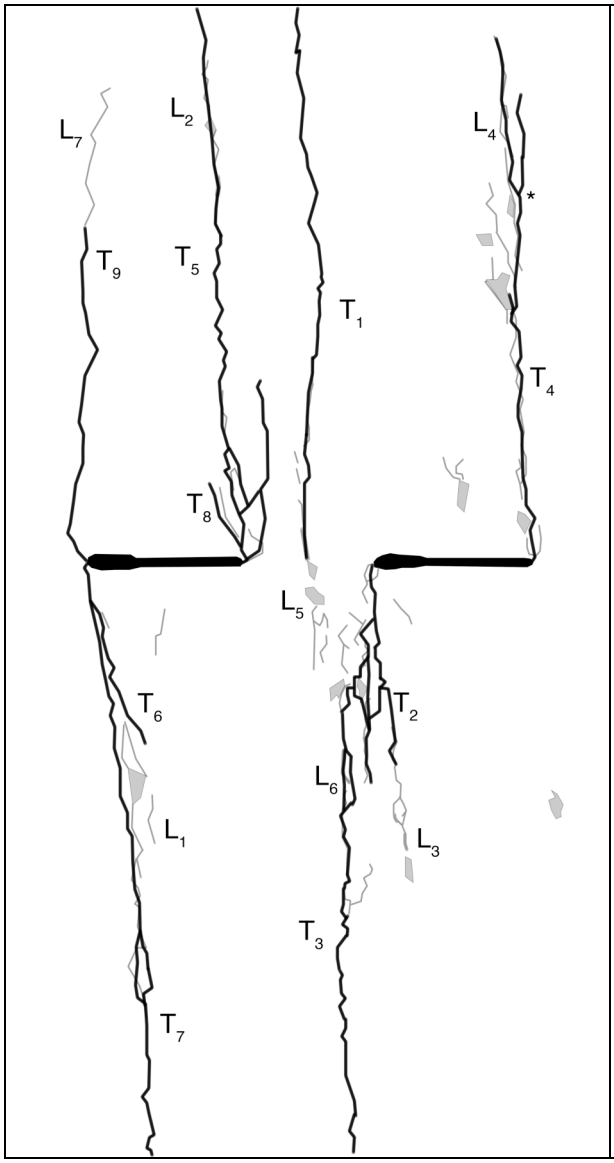

Time: 0.139s before failure

Tensile wing crack T_9 opens upward from the left flaw's outer tip with L_7 extending further upward. T_5 branches and connects with itself near the left flaw's inner tip. T_5 extends up and out of the camera's field of view. T_4 connects with the tensile crack that formed near the wing crack previously at the point indicated by the *. T_2 and T_3 become more connected with tensile cracks. A branch of T_7 grows to reattach to the crack.

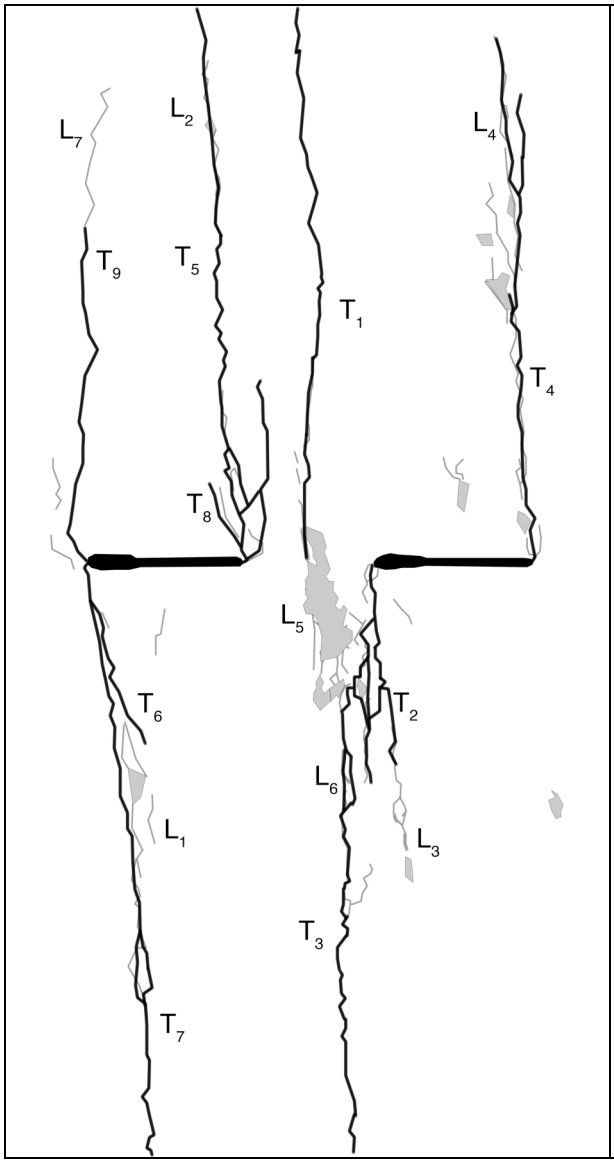

Time: 0.005s before failure

Some linear white patches (boundary following) form near the left crack's outer tip. A large zone of lightening grains forms between the junction of L_5 and connection between L_3 and L_6.

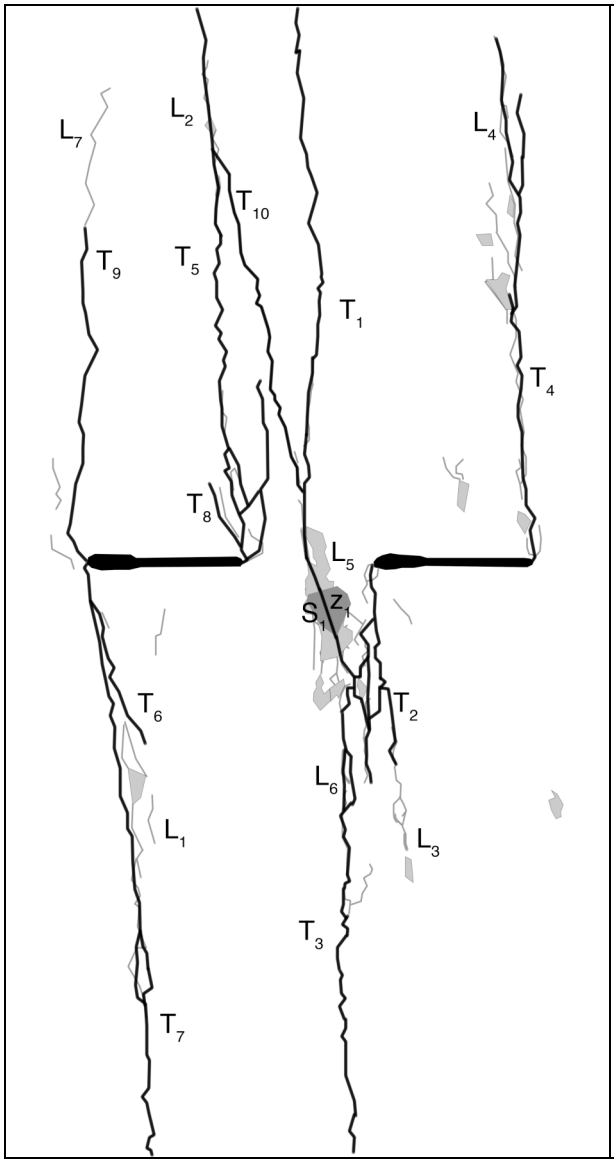

Time: 0.003s before failure

T_1 extends down through L_5 to the network of tensile cracks connecting T_2 and T_3. A small group of grains (labeled z_1 for zone 1) spall as the crack propagates and after the grains have been removed from the surface, the crack appears to have propagated in a shear mode (marked S_1) through this area. Spalling is taken as evidence of shearing, but sense of shear is not determinable. Tensile crack T_{10} also grows up from T_1 connecting with T_5. Indirect (Category 2) coalescence has occurred.

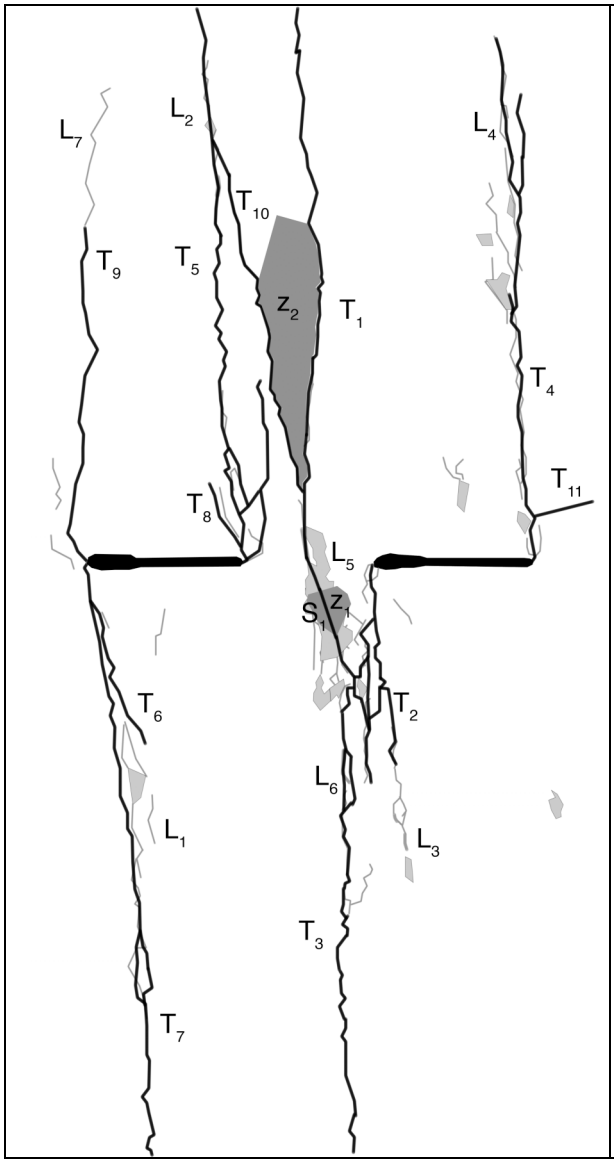

Time: 15min54.498s
σ: 82.8559 MPa

Sample failure occurs when a large zone of material between cracks T_1 and T_{10} (labeled z_2) bursts. Tensile crack T_{11} extends perpendicular to tensile wing crack T_3.

Gr 2a-0-0 C (20070918)

Summary

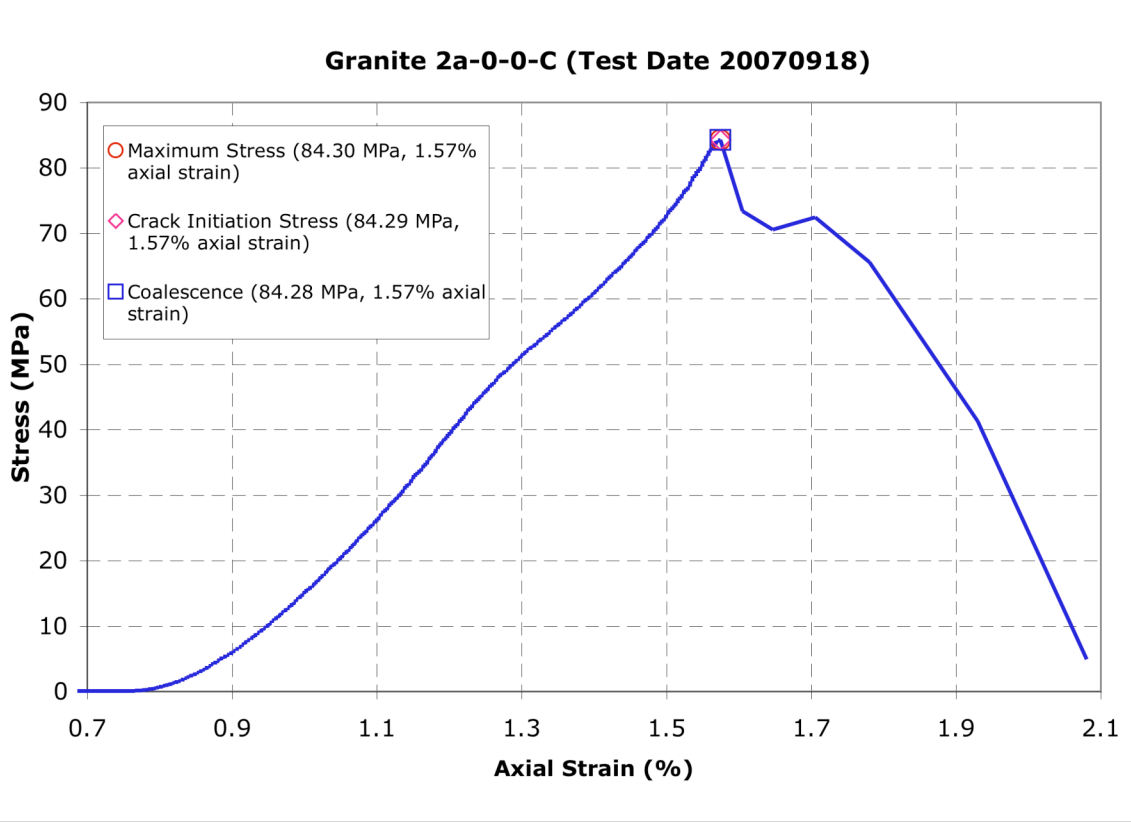

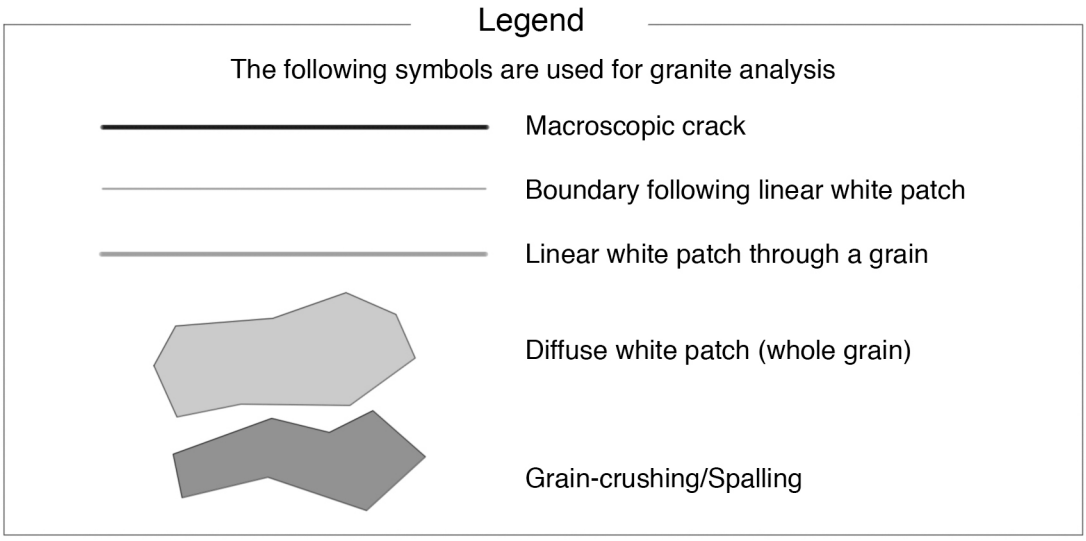

Category 2 coalescence
Images taken from high-speed camera

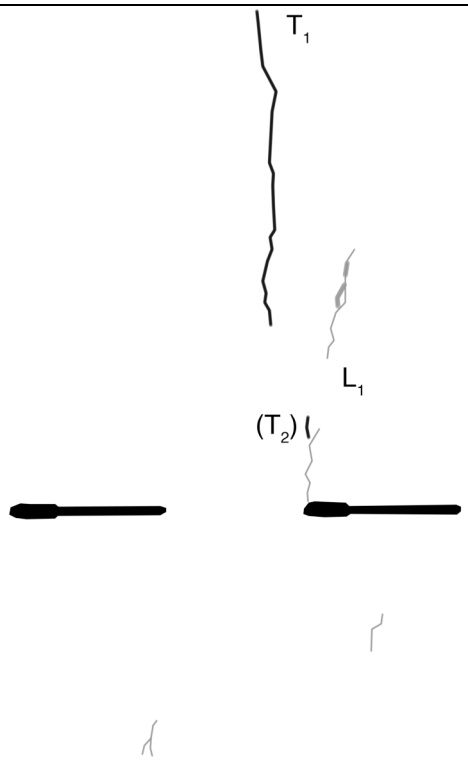	**Time:** 0.149s before failure Tensile crack T_1 comes down toward the bridge area. A boundary following white patch extends up from the inner tip of the right flaw (labeled L_1) and a small tension crack forms along grain boundaries in this same area. This tensile crack is labeled (T_2). Boundary following as well as some features going through grains form farther from the tip. Some small linear white patches form beneath both flaws.

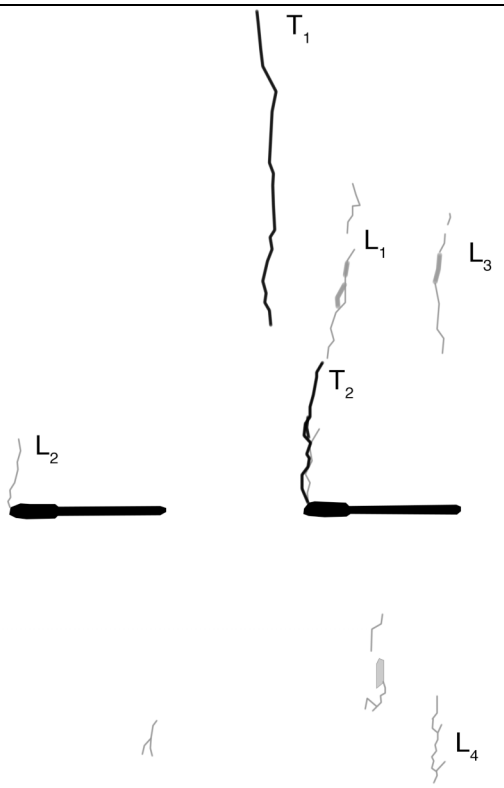	**Time:** 0.145s before failure (T_2) extends and connects with the flaw tip becoming tensile wing crack T_2. L_1 extends. More linear white patches form (both boundary following and through-going). L_2 is connected to the outer tip of the left flaw while L_3 and L_4 are above and below the outer tip of the right flaw, but not connected to the flaw.

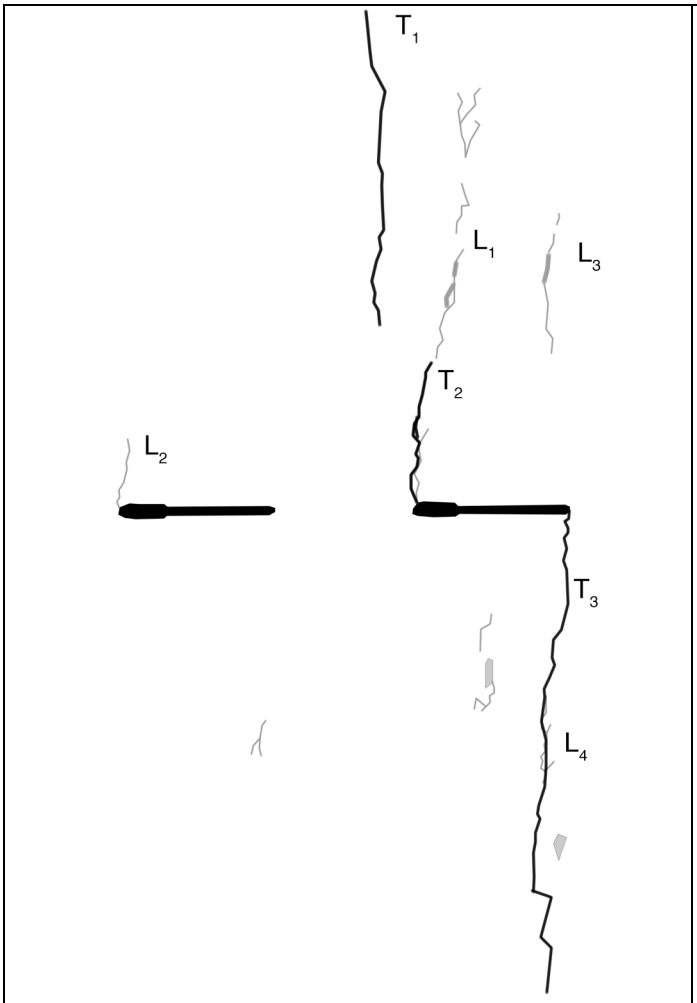	**Time:** 0.144s before failure Linear white patch L_1 grows upward with a branching boundary following white patch while L_4 extends downward with a lightened grain. Tensile wing crack T_3 extends downward from the outer tip of the right flaw and through L_4.

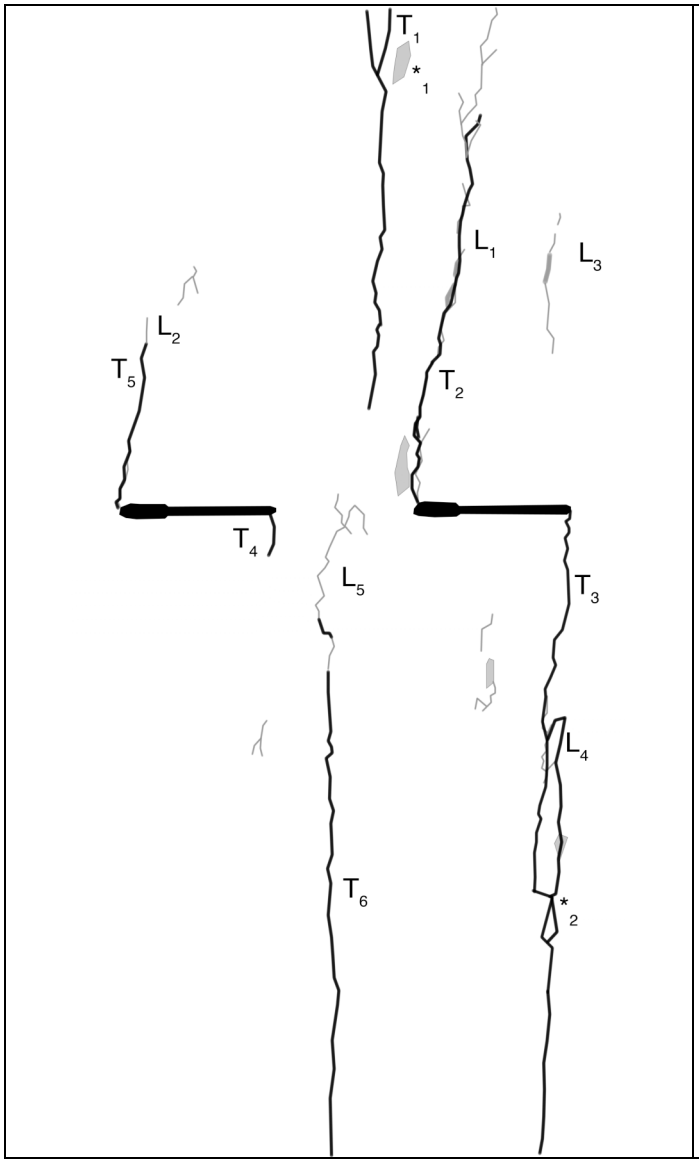

Time: 0.1437s before failure

Tensile cracks T_1, T_2, and T_3 all extend. T_1 branches near the top of the camera's field of view and a group of grains lighten near this branching. This area is indicated by $*_1$. T_3 branches at $*_2$ and extends up to connect with itself. Tensile wing cracks T_4 and T_5 form on the left flaw. T_5 follows L_2. Tensile crack T_6 extends up toward the bridge area with a boundary following white patch (labeled L_5) extending into the bridge area.

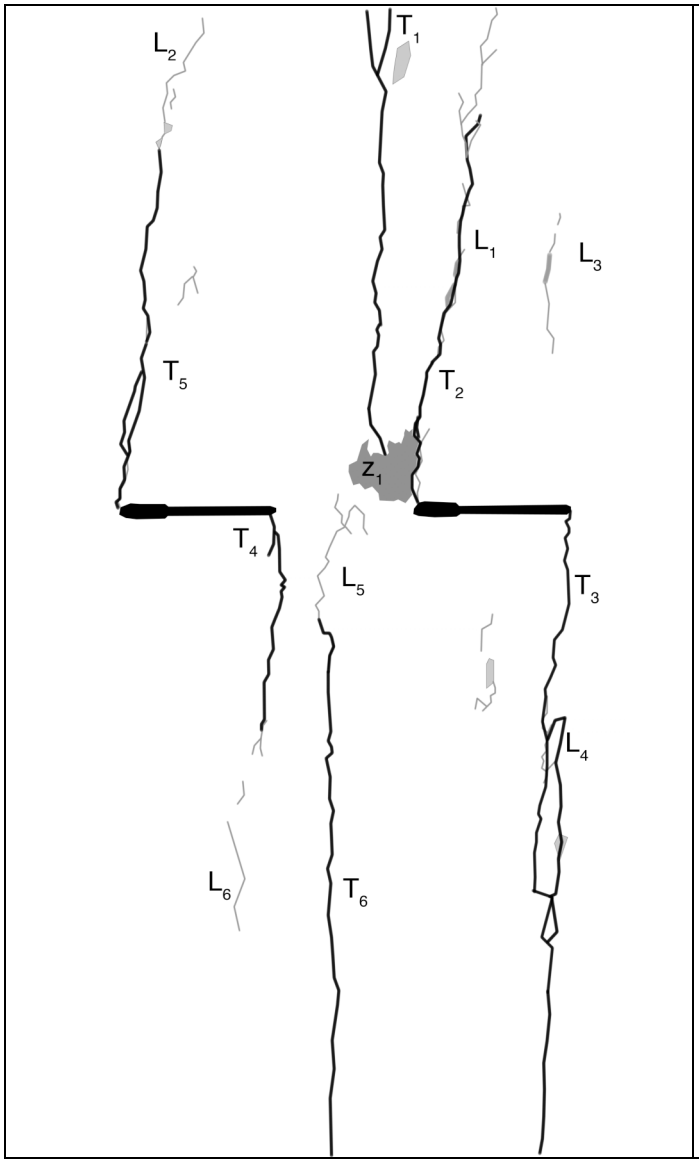

Time: 0.1435s before failure

Tensile wing crack T_5 extends upward, as does L_2. T_4 branches downward. L_6 also extends downward. T_6 extends upward slightly. T_1 curves toward the inner tip of the right flaw and a large patch of spalling forms (labeled z_1) at the tip of T_1 and is bounded on the right by T_2.

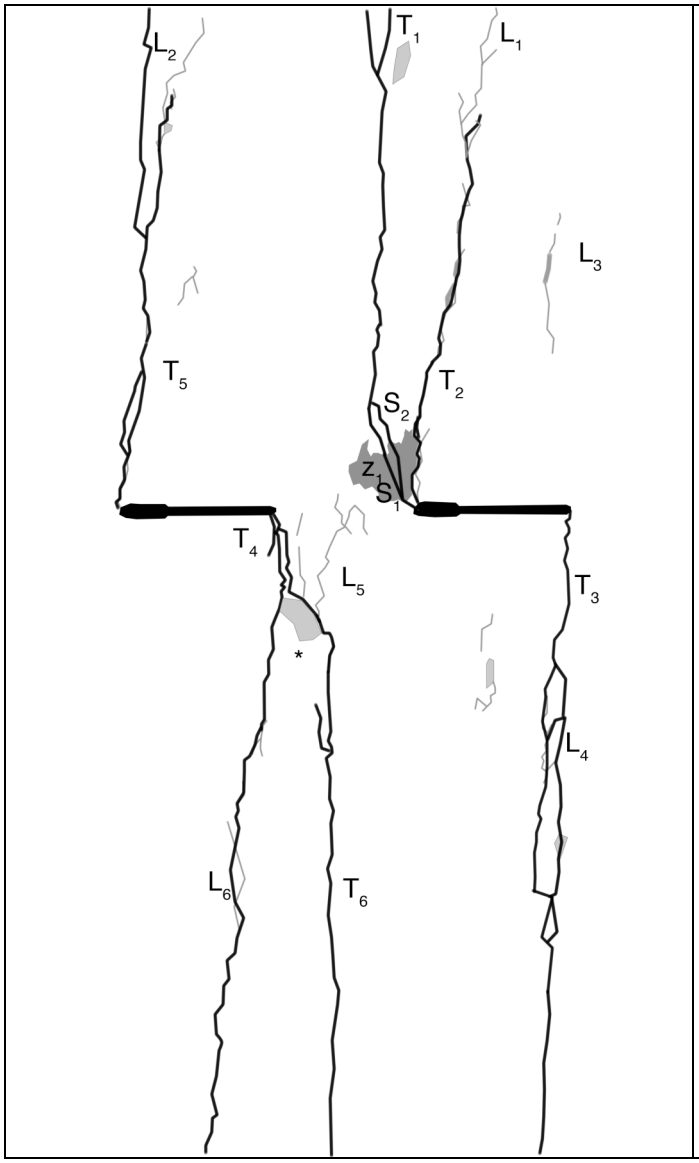

Time: 0.142s before failure

T_4 and T_5 both propagate further. Tensile crack T_1 connects with the inner tip of the right flaw with two shear cracks (S_1 and S_2) cutting across area 1 (direction of shearing not discernable, but spalling is taken as evidence of shearing). T_6 connects with the inner tip of the left flaw as well as with T_4. As it extends, a patch of grains lighten in the region indicated by the *.

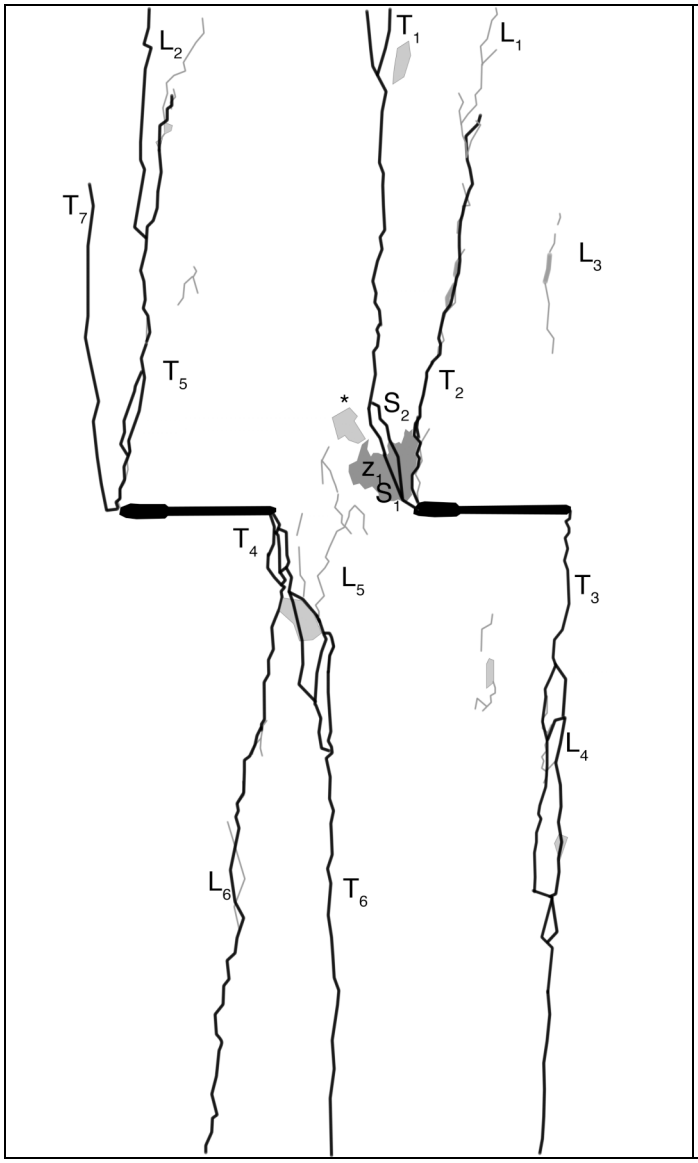

Time: 0.039s before failure

A second tensile wing crack extends off of the outer tip of the left flaw (labeled as T_7). L_5 extends upward and some grains between it and T_1 lighten (below the *). A network of tensile cracks form connecting T_4 and T_6 more intensely.

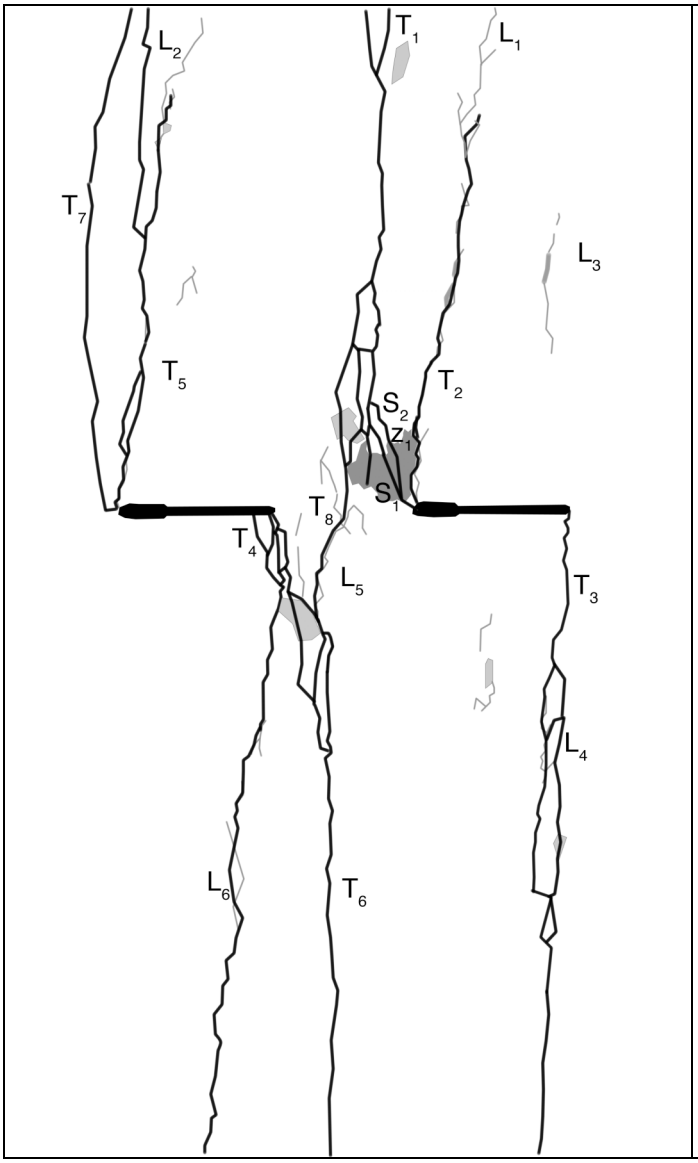

Time: 0.017s before failure

Tensile crack T_7 extends upward. The sample coalesces in an indirect fashion (category 2) when tensile crack T_8 along the linear white patches that had developed between T_1 and T_6. T_8 connects with T_1 and S_1 with a network of small tensile cracks.

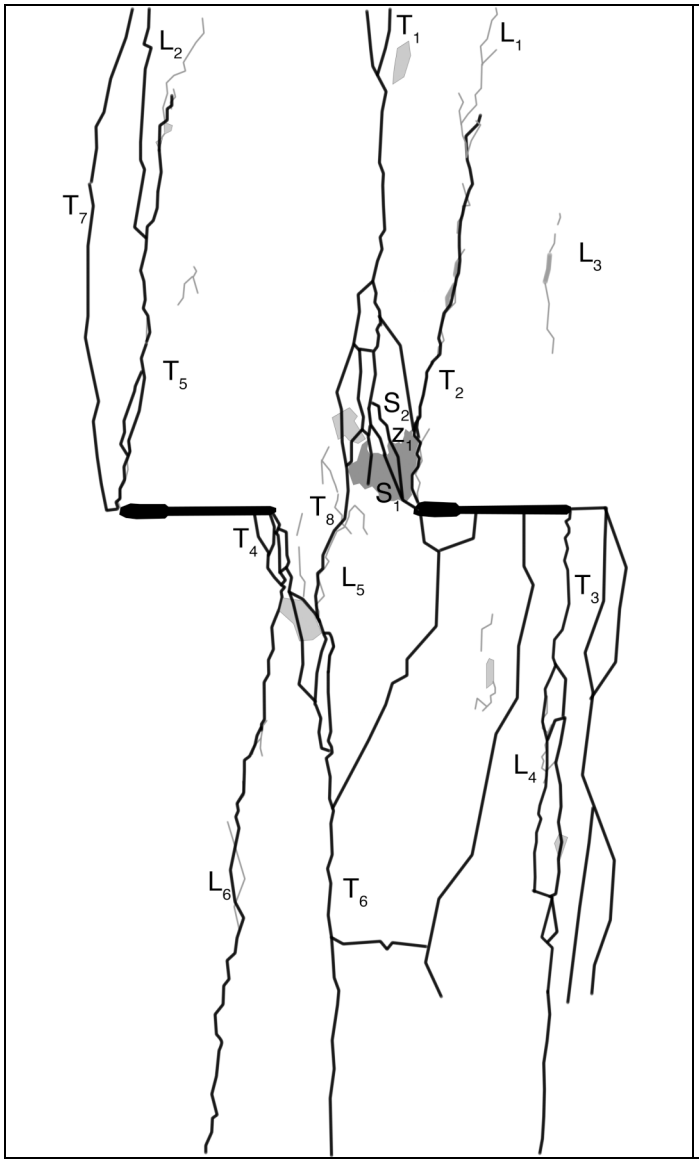

Time: 15min50.532s
σ: 84.3043 MPa

Failure occurs with a large number of tensile cracks form along the right flaw.

Gr 2a-30-0 A (20070925)

Summary

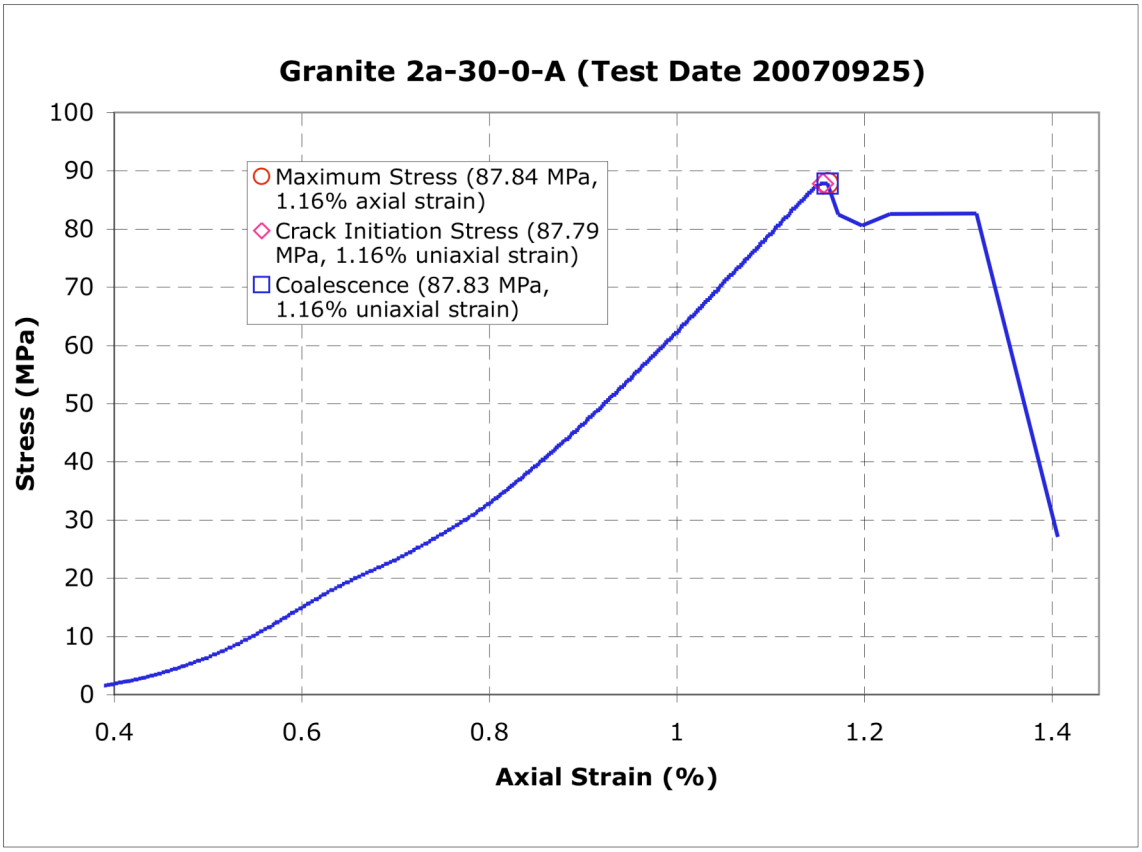

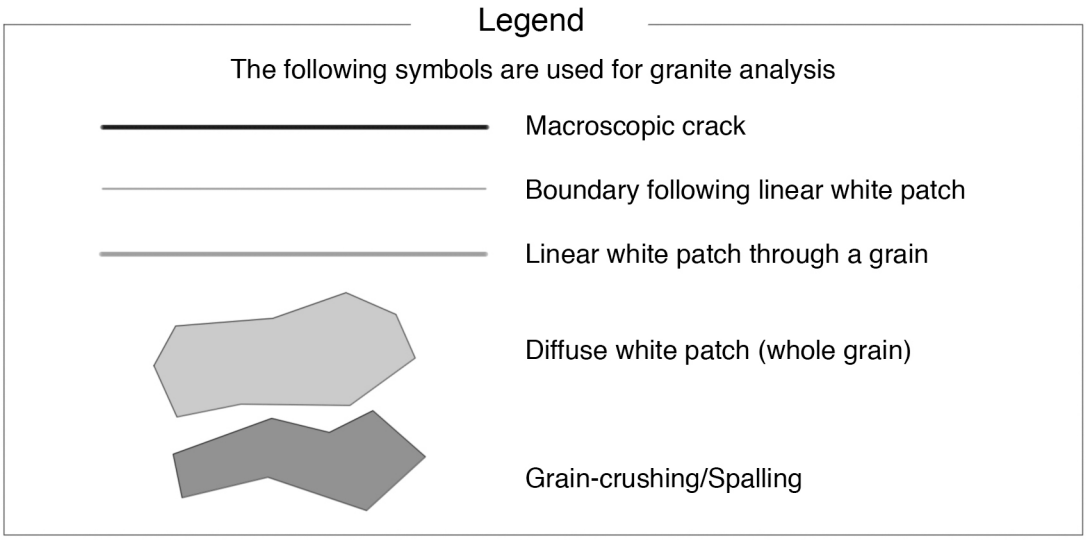

Category 2 coalescence
Images taken from high-speed camera

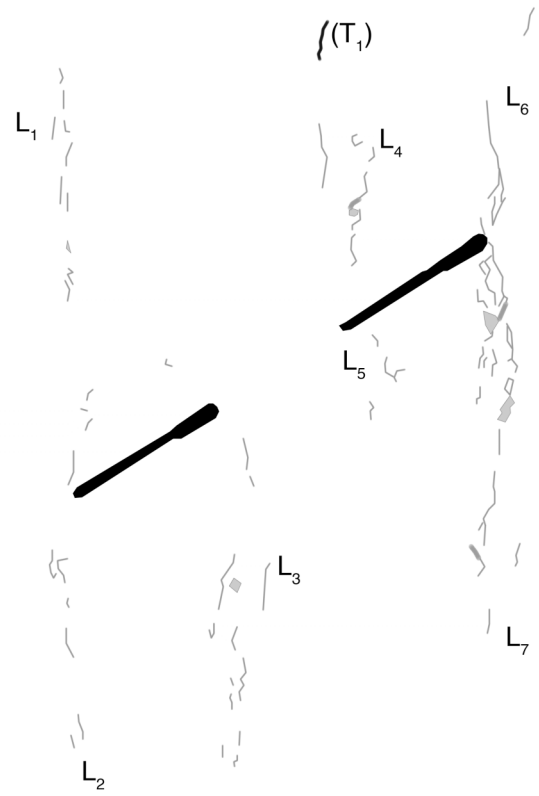	**Time:** 0.284s before failure Linear white patches L_1 through L_3 on the left flaw and linear white patches L_4 through L_7 open on the right flaw. Most white patches are boundary following, although some go through grains as well. Several grains lighten. A tensile crack labeled (T_1) opens above the inner tip of the right flaw. It follows along grain boundaries.

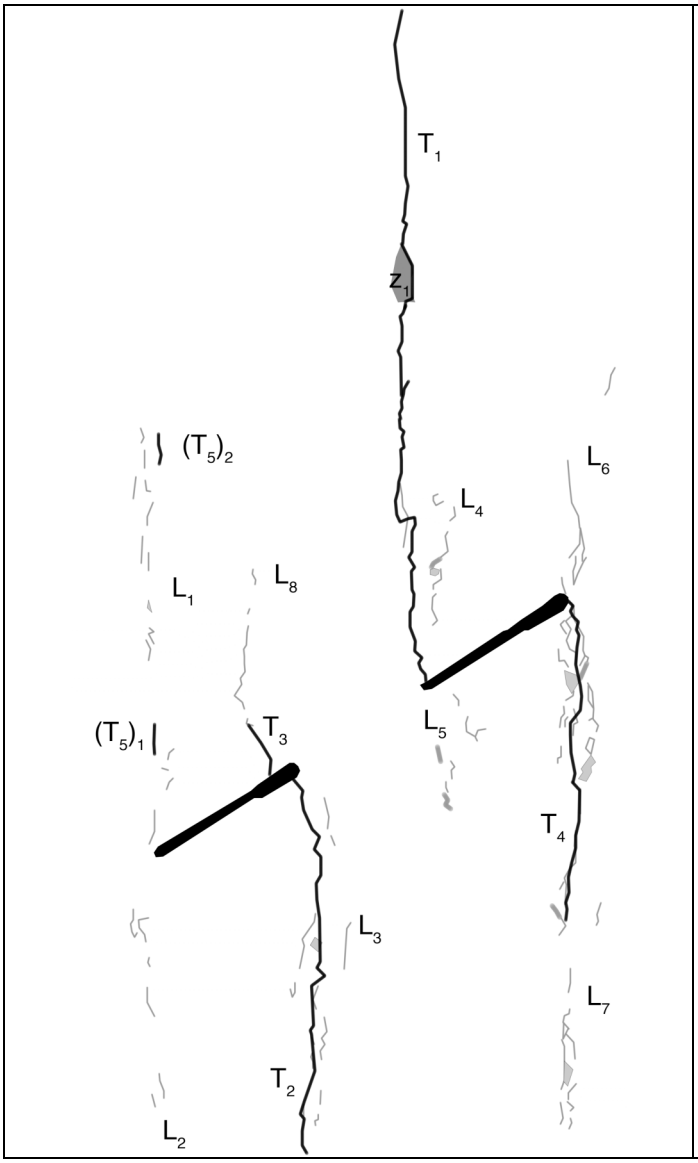

Time: 0.117s before failure

Linear white patch L_7 extends downward.

Two short tensile cracks open along grain boundaries above the outer tip of the left flaw. The lower tensile crack is labeled $(T_5)_1$ and the upper tensile crack is labeled $(T_5)_2$. Tensile wing cracks T_1 through T_4 open. T_2 and T_3 open above and below the inner tip of the left flaw. T_1 opens above the left inner flaw and T_4 opens below the outer tip of the right flaw. A zone of spalling (labeled z_1) grows along T_1.

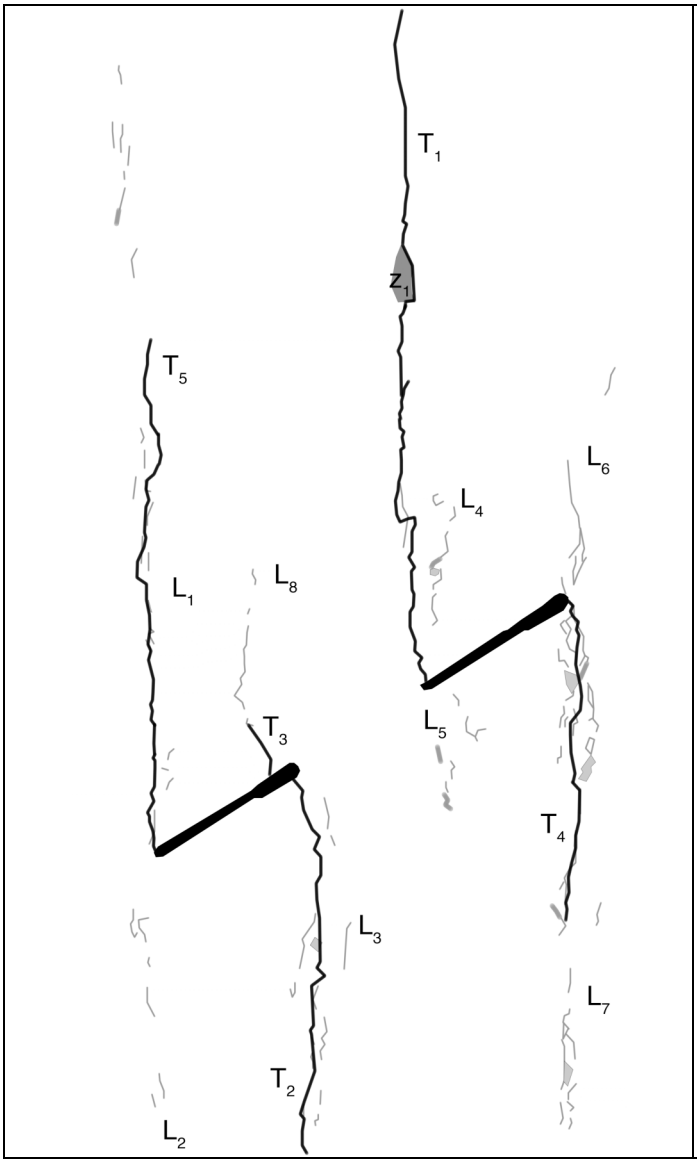

Time: 0.116s before failure

Linear white patch L_1 extends upward. $(T_5)_1$ and $(T_5)_2$ lengthen and connect with each other and then to the outer tip of the left crack forming tensile wing crack T_5.

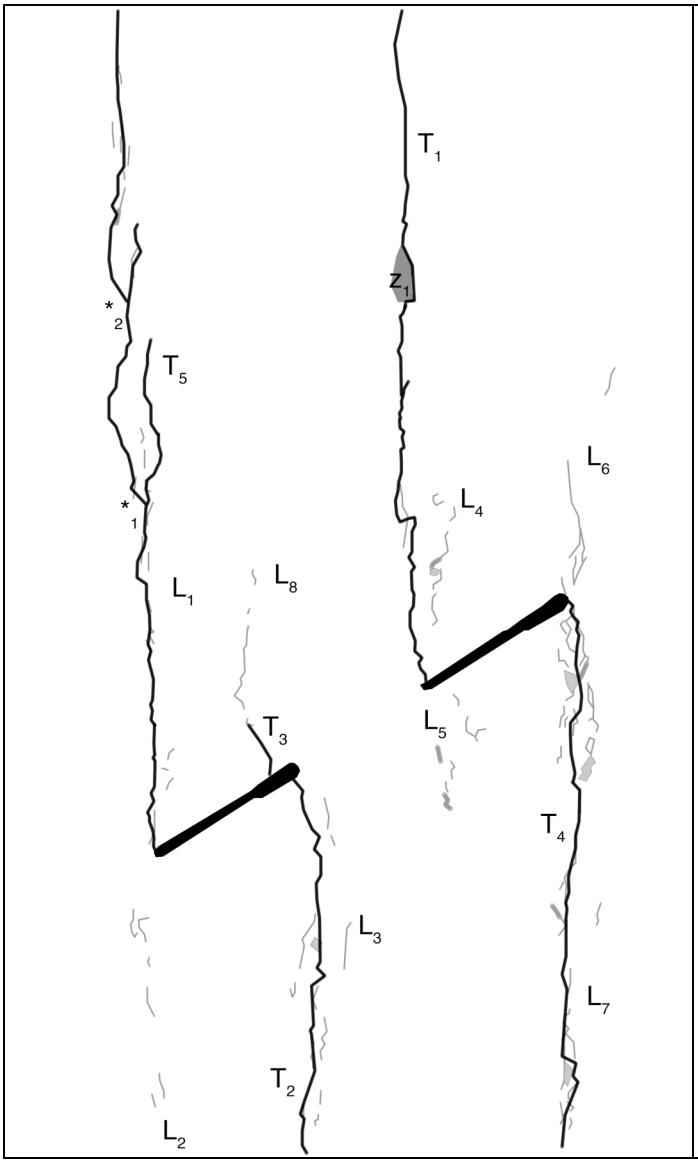

Time: 0.115s before failure

Outside tensile wing cracks T_4 and T_5 extend. T_4 extends in a linear fashion, but T_5 branches at two points while extending upward. These branch points (indicated by $*_1$ and $*_2$) experience some shearing as the specimen continues to deform. It is important to note these cracks opened as tensile cracks before they experienced any shearing.

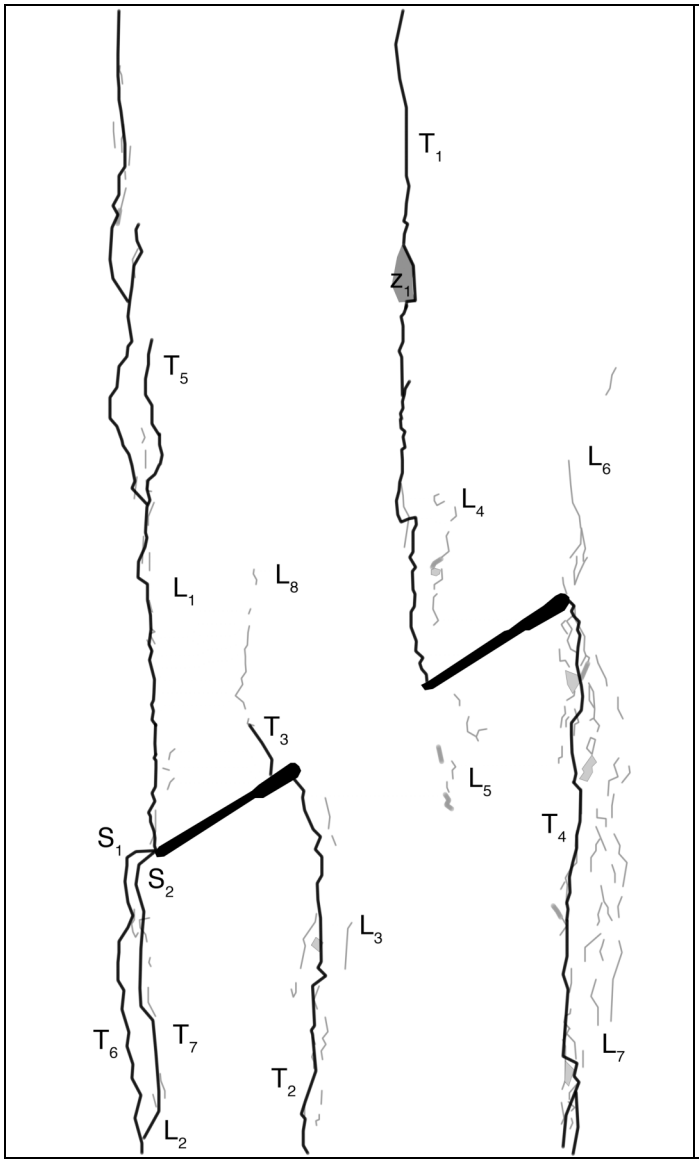

Time: 16min36.75s
σ: 87.8379 MPa

Sample failure occurs when tensile cracks T_6 and T_7 open and connect to the outer tip of the left flaw with shear portions S_1 and S_2. Linear white patch L_7 broadens.

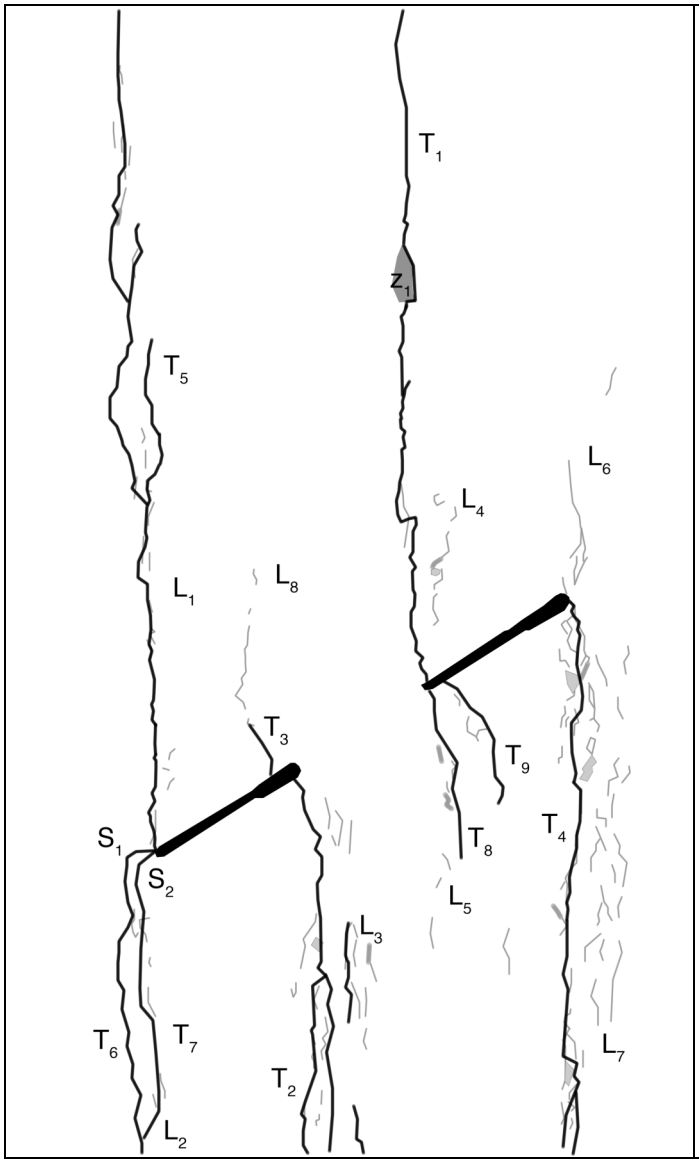

Time: 0.003s after failure

More tensile cracks open, including T_8 and T_9 which connect to the inner tip of the right flaw.

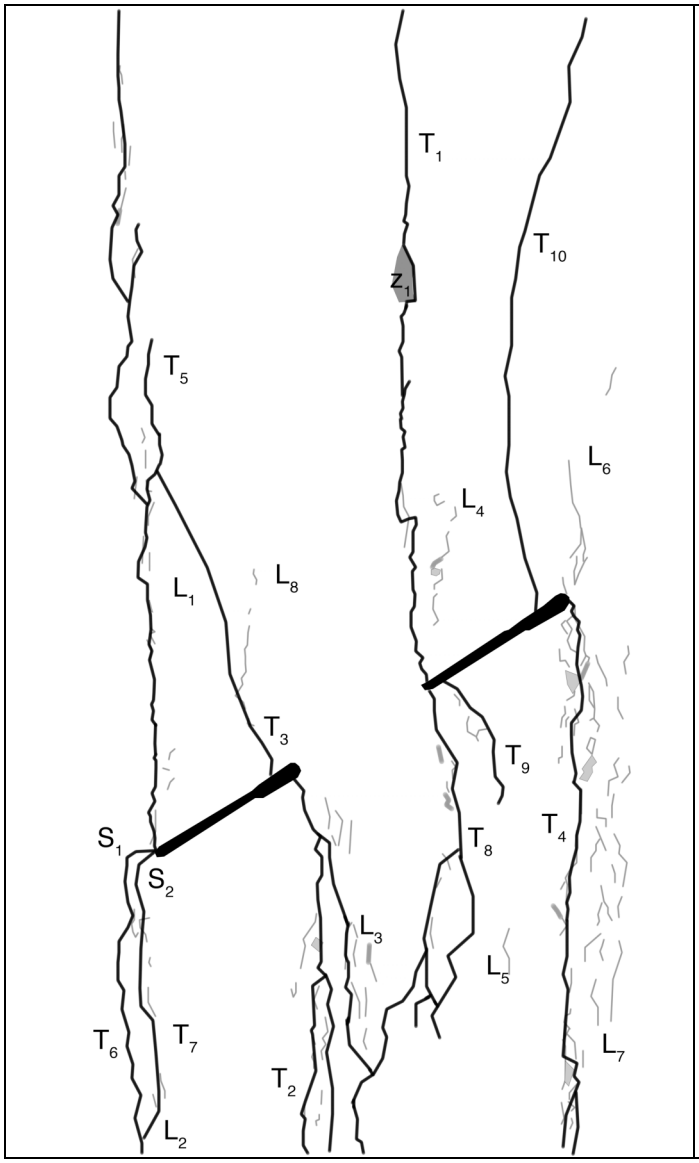

Time: 0.046s after failure

Indirect (category 2) coalescence occurs when T_8 extends and connects to T_2.

Gr 2a-30-0 C (20070925)

Summary

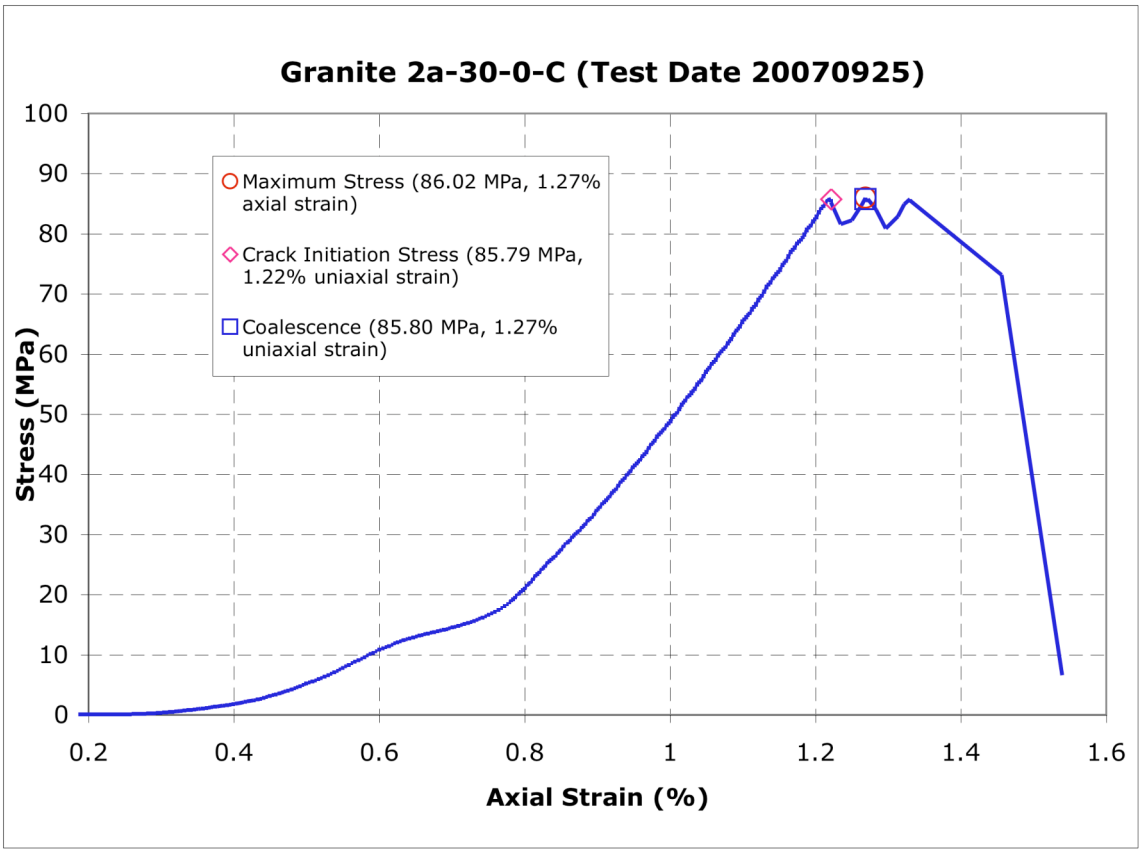

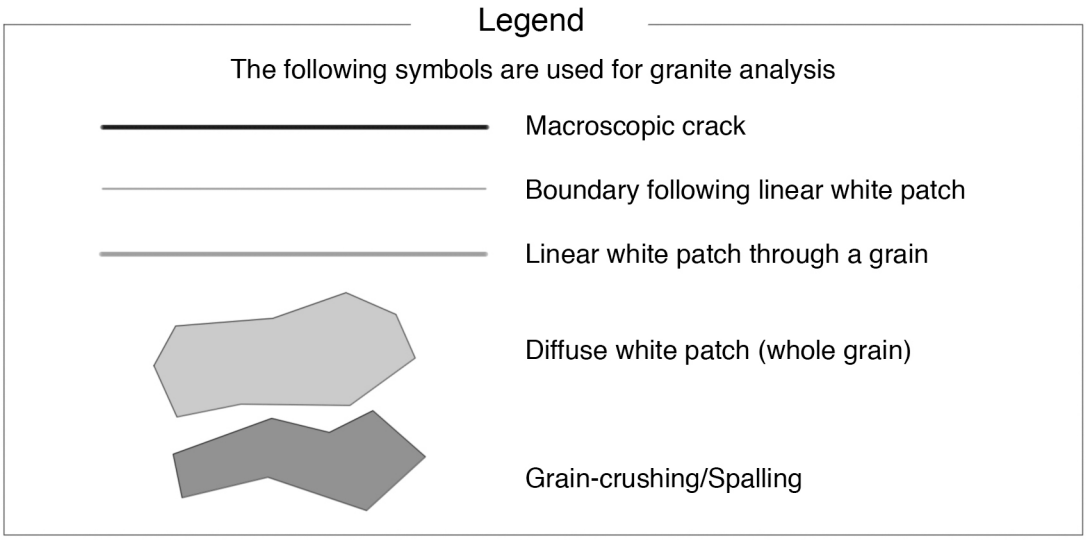

Category 2 coalescence

Images taken from high-speed camera

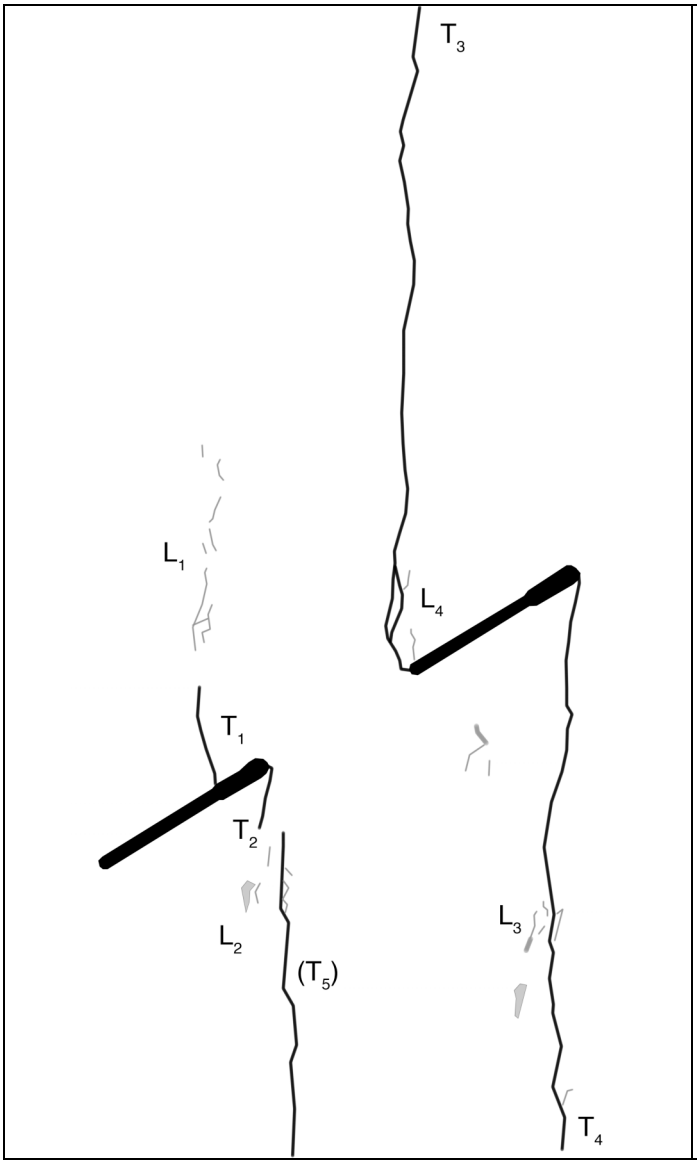

Time: 0.585s before failure

Linear white patches L_1 through L_4 grow as do corresponding tensile wing cracks T_1 through T_4. A long tensile crack opens below T_2. As it will later form a tensile crack distinct from T_2, it is labeled (T_5). Tensile wing crack T_3 branches and comes back together near the inner tip of the right flaw. All but one of the linear white patches are boundary following. A few grains lighten.

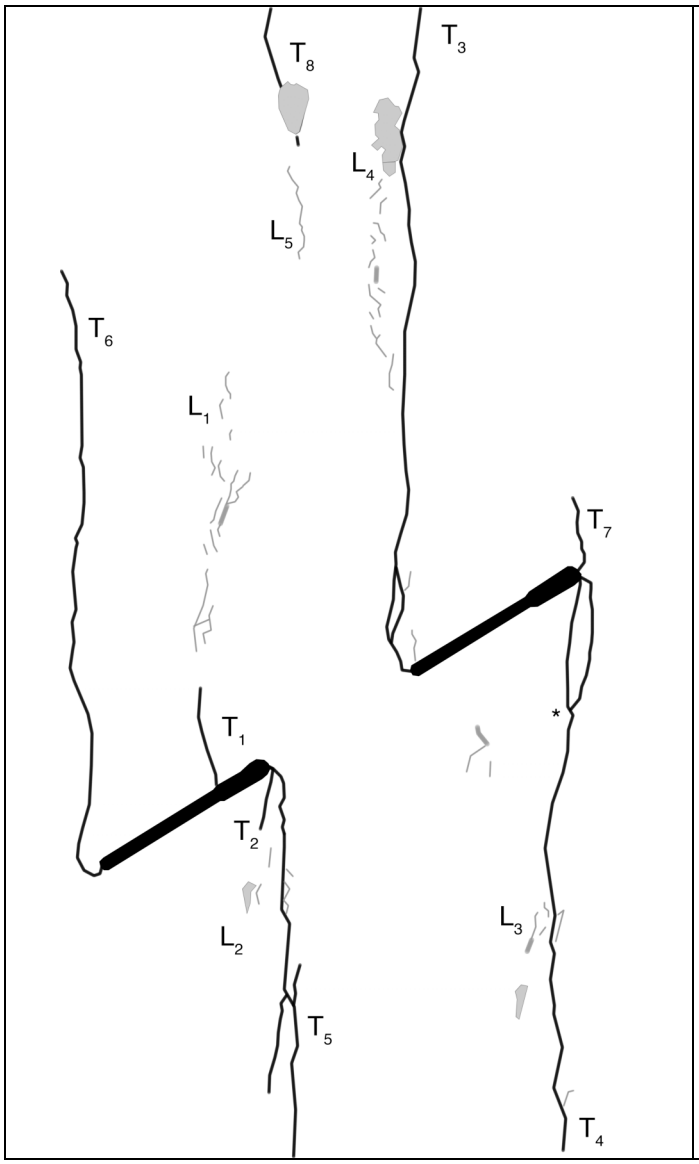

Time: 0.227s before failure

Tensile wing crack T_6 opens above the outer tip of the left flaw. (T_5) extends up and connects to the inner tip of the left flaw, becoming tensile wing crack T_5. Tensile wing crack T_7 appears above the outer tip of the right flaw. T_4 branches at the point indicated by a * and this branch also connects to the right flaw's outer tip. L_4 extends to the side of T_3 with a large patch of lightened grains. Tensile crack T_8 opens downward toward the bridge area. Near its lower tip there is a large white patch. Beyond T_8 there is a linear white patch labeled L_5. L_1 also extends.

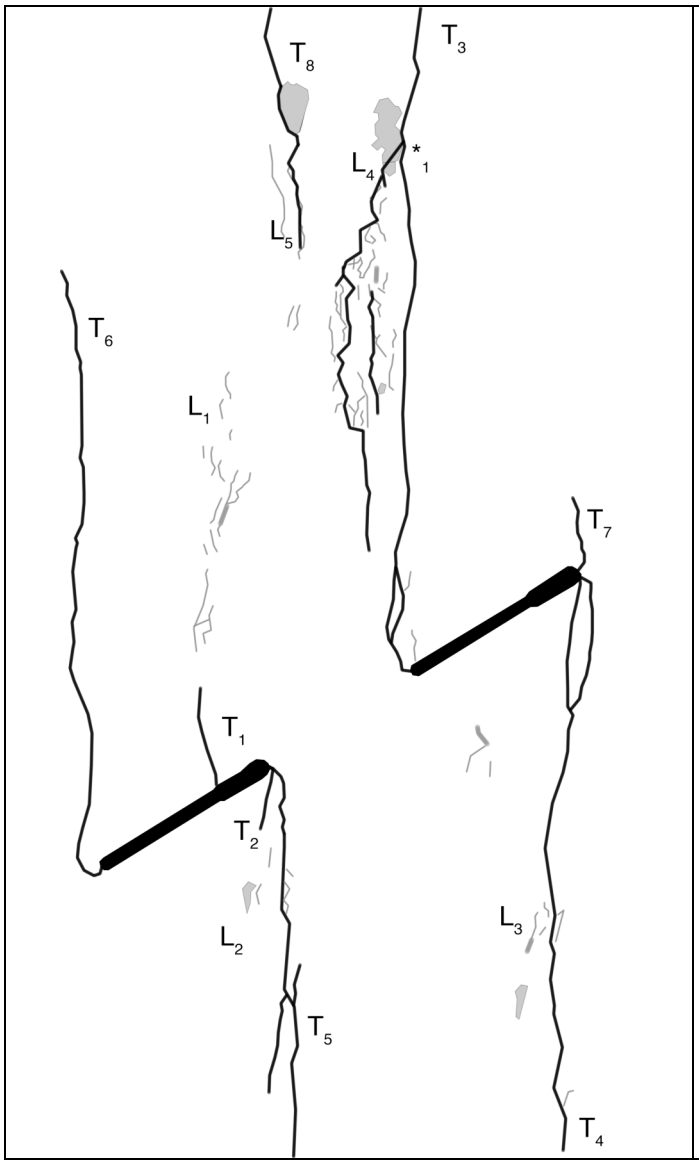

Time: 0.136s before failure

T_8 extends around and past the lightened grains. T_3 branches downward from the point labeled $*_1$ and down through the L_4 region (which also intensifies). This branch experiences some shearing directly after opening along some of the small straight portions.

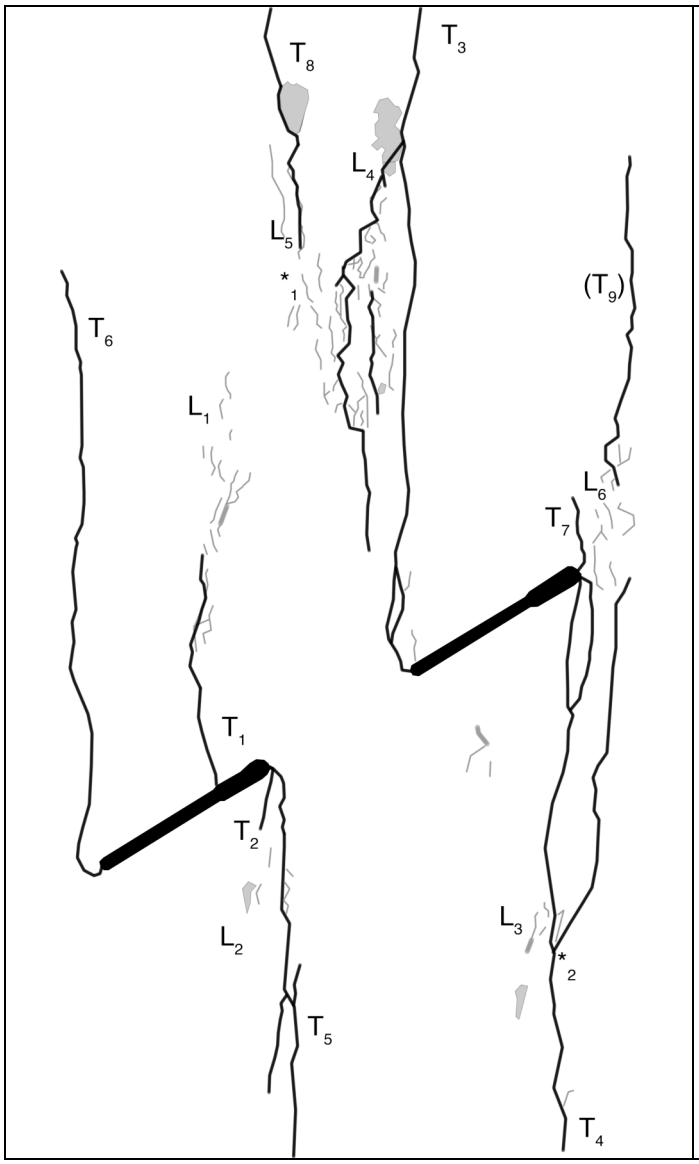

Time: 0.003s before failure

T_1 extends upward. L_4 and L_5 link together below T_8 in the region indicated by $*_1$. T_4 branches at point $*_2$ and grows upward until it's even with the outer tip of the right flaw. There are some linear white patches and then another tensile crack opens beyond that point. This tensile crack is labeled (T_9).

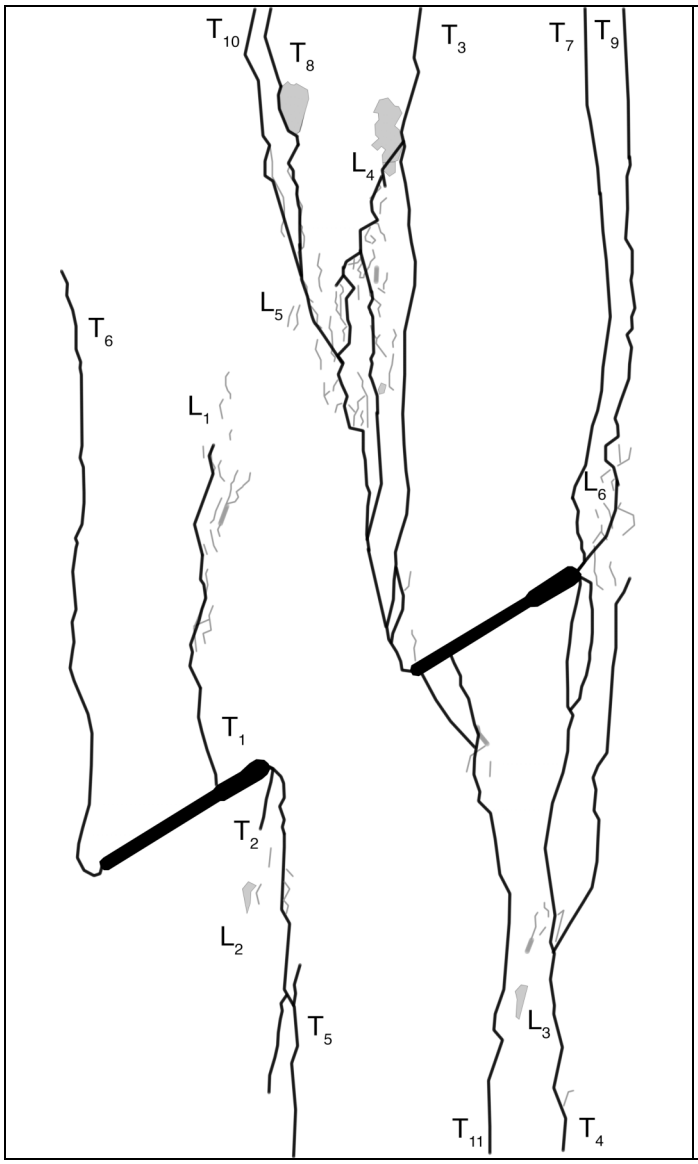

Time: 15min50.532s
σ: 86.0239 MPa

Tensile cracks T_9, T_{10}, and T_{11} open. T_1 also extends. Sample failure occurs with these new cracks opening.

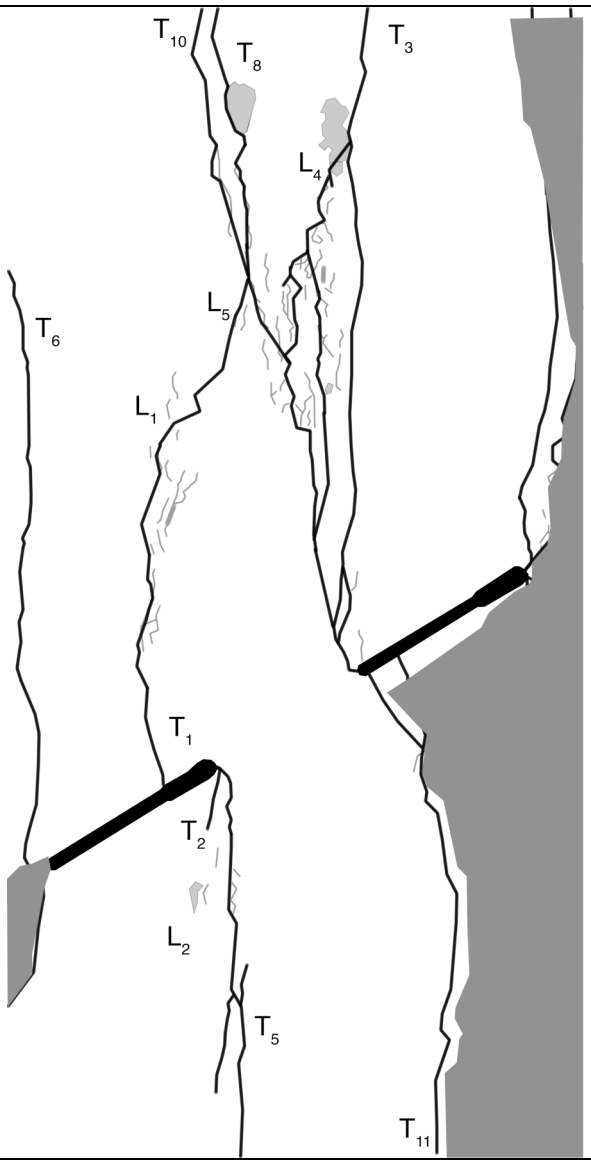

Time: 0.040s after failure

T_1 extends toward T_8 and joins at the same point T_{10} connects with T_8 also. Gray areas marked are zones of the sample that have fallen away during sample collapse. Indirect (category 2) coalescence.

Gr 2a-45-0 A (20071002)

Summary

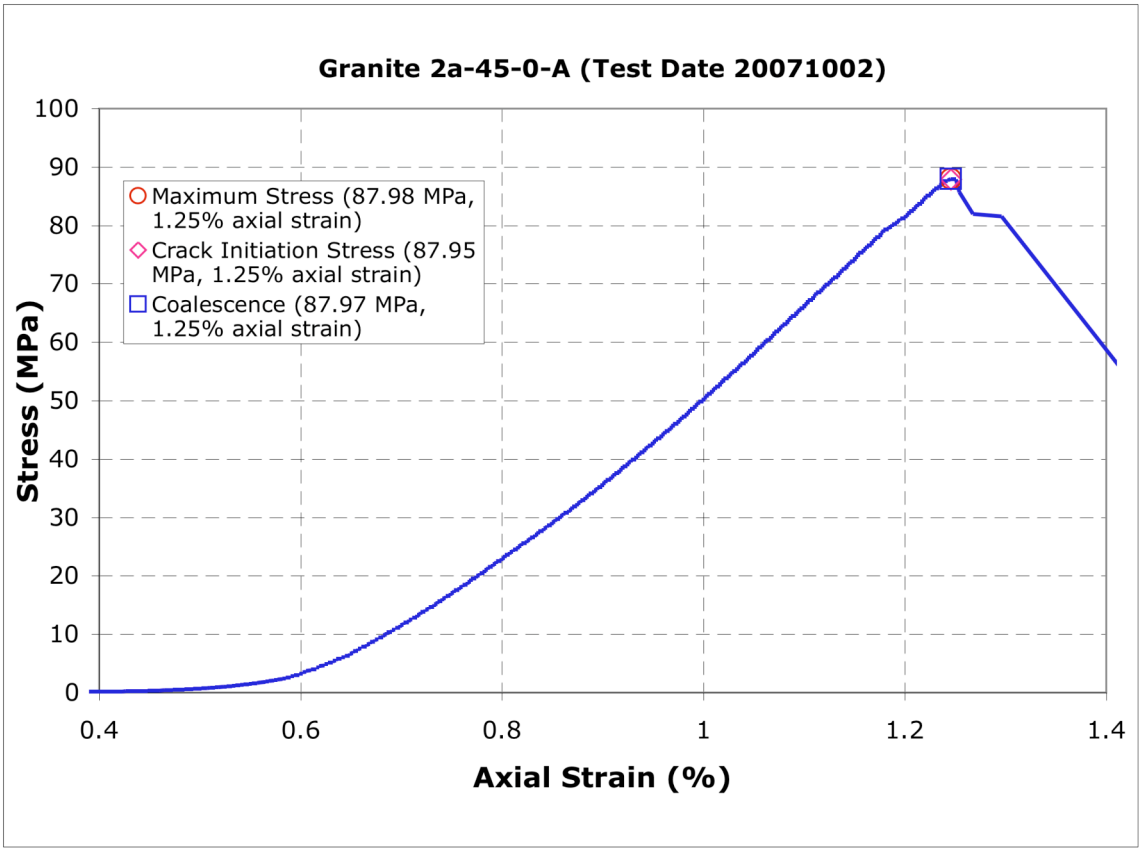

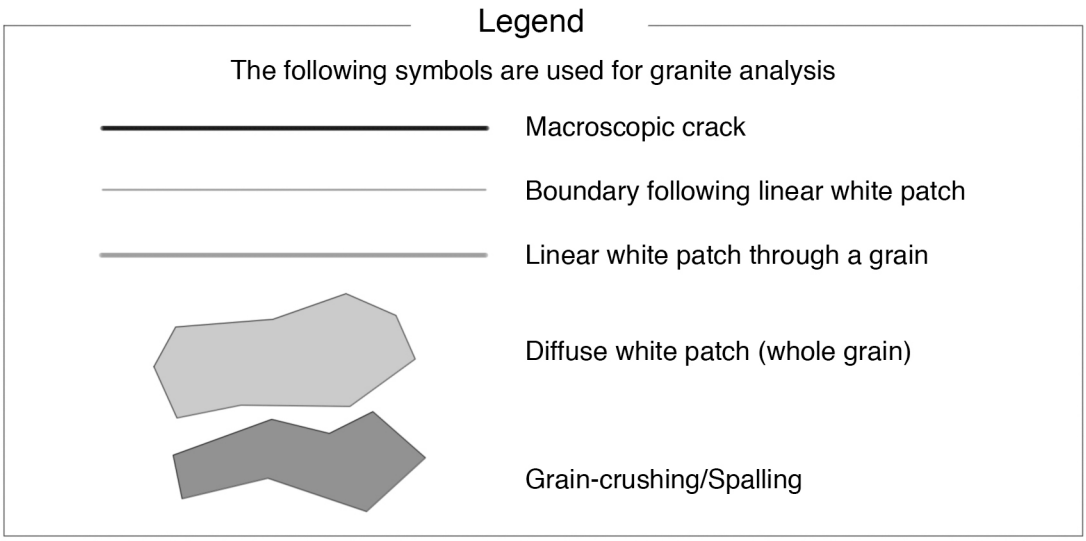

Category 2 coalescence
Images taken from high-speed camera

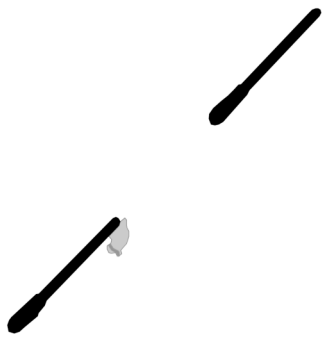	**Time:** 0.4558s before failure Grains lighten at the inner tip of the left flaw 0.4754s before failure and then a linear white patch passes through a grain.
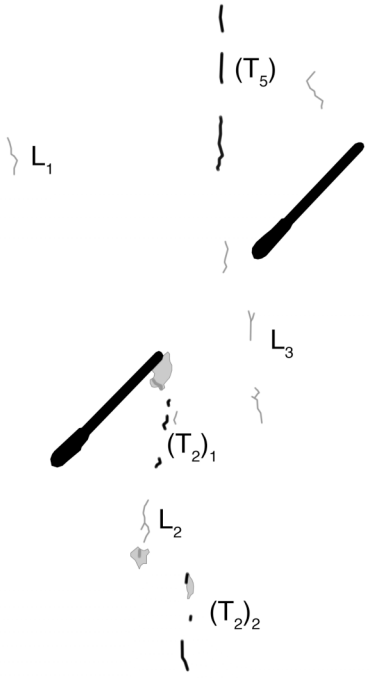	**Time:** 0.3296s before failure LWPs L_1, L_2, and L_3 form. Some diffuse lightening also begins. Tensile crack groups $(T_2)_1$ and $(T_2)_2$ open within the L_2 region. Tensile crack group (T_5) opens above the bridge area. Tensile cracks are on the order of one to ten grain lengths.

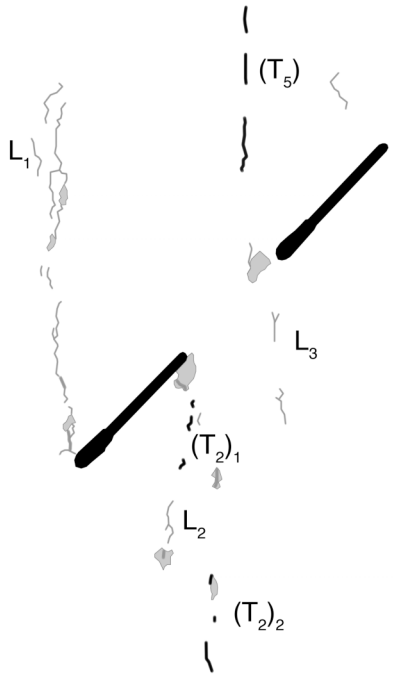	**Time:** 0.2076s before failure L_1 grows both upwards and downwards. Some grains also lighten near the right flaw's inner tip.
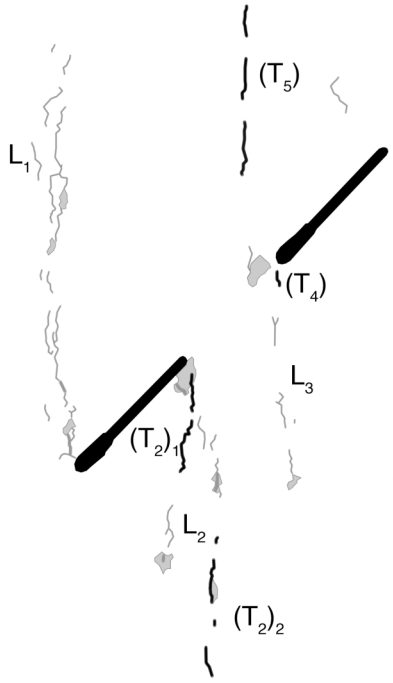	**Time:** 0.1376s before failure Tensile cracks along L_2 grow in length and link together. More LWPs form along L_3 as does a small tensile crack – labeled (T_4). L_1 also grows with linear white patches becoming more dense.

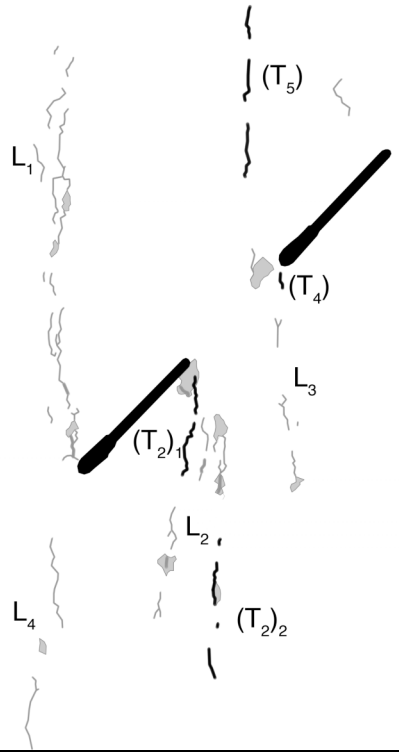	**Time:** 0.1192s before failure Linear white patch L_4 forms. More LWPs form along L_2.
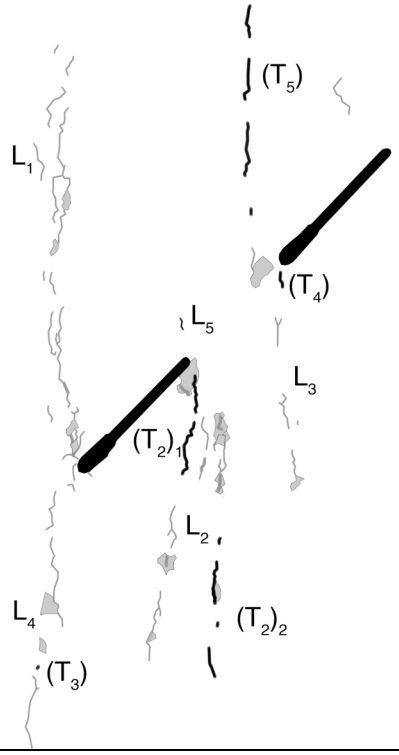	**Time:** 0.112s before failure Increasing linear white patch formation in L_1, L_2, and L_4. The first tensile crack opens along L_4. It is labeled (T_3). L_5 is the first linear white patch to form above the left inner flaw tip.

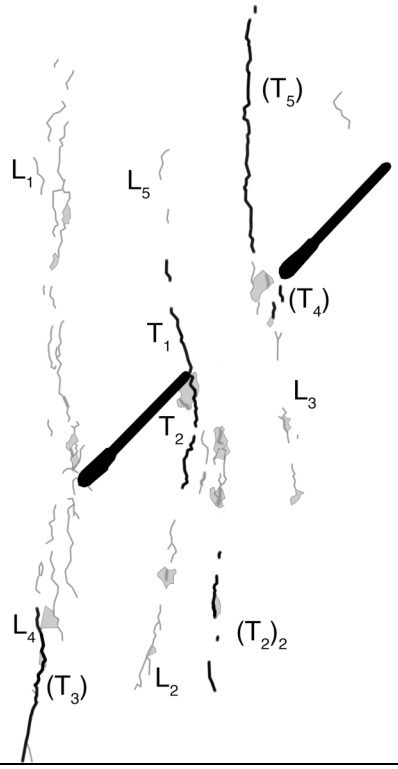	**Time:** 0.1098s before failure T_1 and T_2 form, becoming the first attached tensile wing cracks. Linking and growing of other tensile cracks occurs in (T_3) and (T_5). Another tensile crack opens in (T_4).
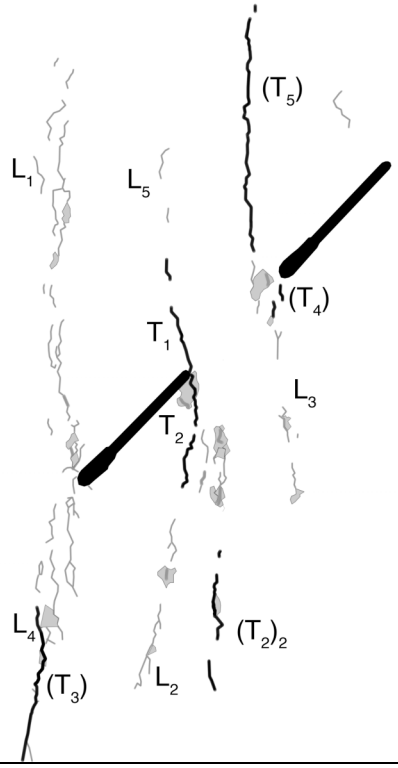	**Time:** 0.1092s before failure Tensile cracks in $(T_2)_2$ grow and link together. Linear white patches in the upper regions of L_4 grow.

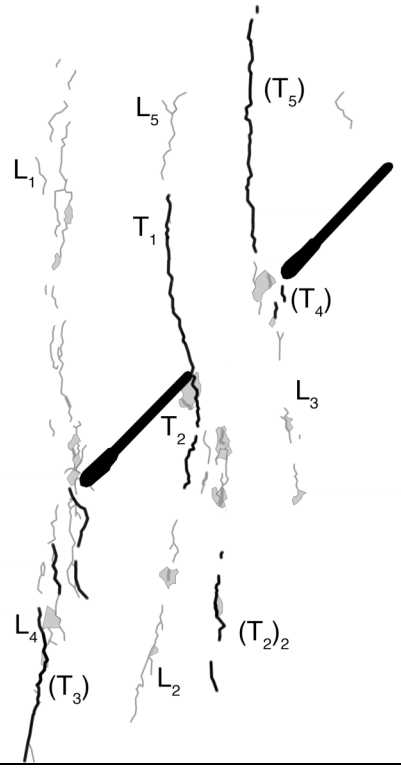	**Time:** 0.1088s before failure (T_3) grows upward through L_4 closer to the outer left flaw tip. T_1 extends upward as do linear white patches within L_5.
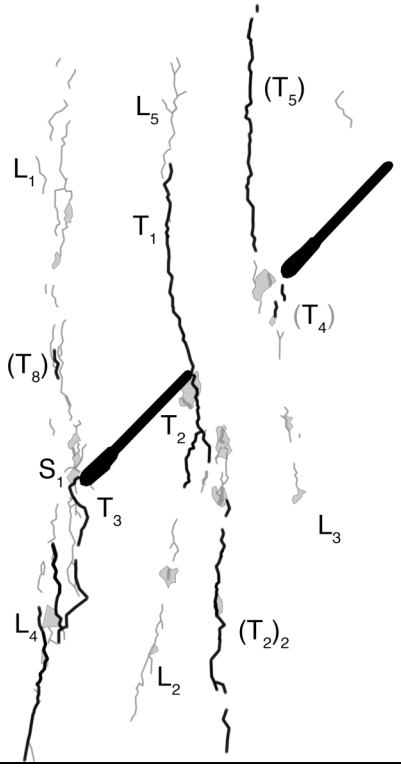	**Time:** 0.1086s before failure The first tensile crack opens above the left outer flaw tip. This crack is labeled (T_8). A mixed tensile-shear crack forms at the left outer flaw tip as well. The shear portion goes across a single grain and is labeled S_1 before the crack becomes tensile (the tensile portion is labeled T_3). Cracks within $(T_2)_2$ grow and link together and T_2 extends downward and branches.

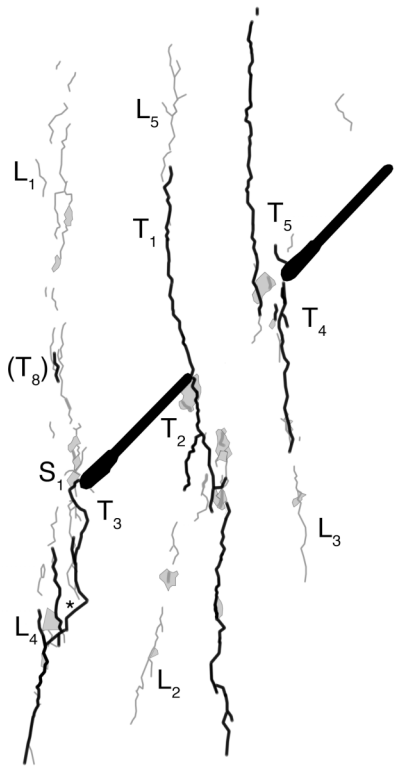	**Time:** 0.1084s before failure T_3 grows and connects with other tensile cracks. Some sliding occurs along T_3 (along the section labeled *) where a tensile crack initially formed. Further growing and linking of tensile cracks below T_2 occurs. Linear white patches in L_5 grow upward. T_4 initiates from the lower part of the right inner flaw tip and connects tensile cracks previously labeled (T_4). T_5 initiates from the upper part of the same flaw tip. The tensile crack previously labeled (T_5) grows downward past the flaw tip.
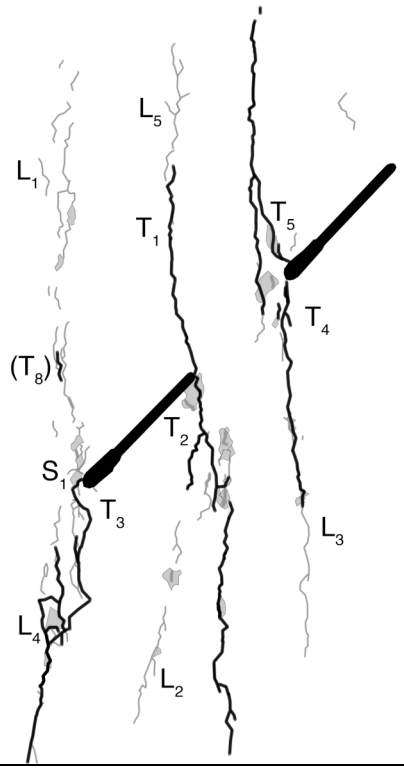	**Time:** 0.1078s before failure Tensile cracks along T_3 interconnect more. T_5 connects to the previously existing tensile crack that had been labeled (T_5).

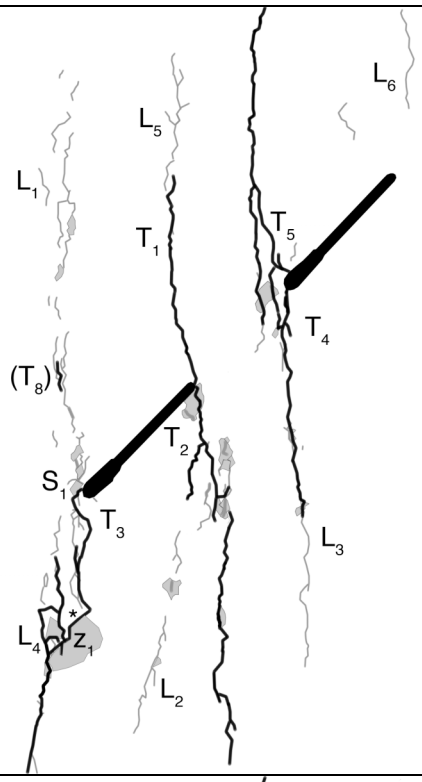	**Time:** 0.0562s before failure Some grains are crushed in zone z_1 below the point labeled with a * where more sliding occurs along existing tensile cracks. Tensile cracks T_4 and T_5 connect with a tensile crack. A linear white patch labeled L_6 extends down toward the right outer flaw tip.
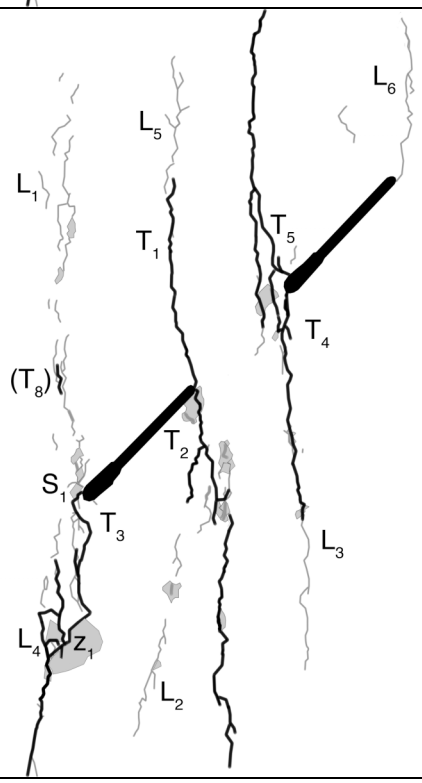	**Time:** 0.0548s before failure L_6 connects to the right outer flaw tip.

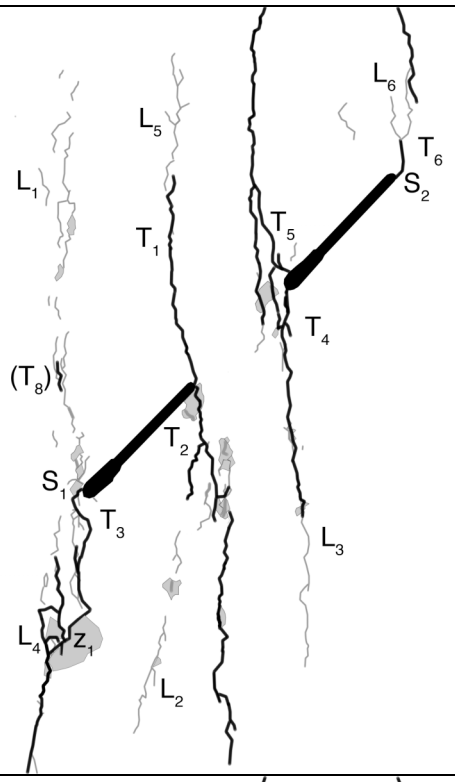	**Time:** 0.546s before failure A tensile crack opens downward along L_6 while a mixed tensile-shear crack simultaneously opens at the right outer flaw tip. Again, the shear crack is across a single grain.
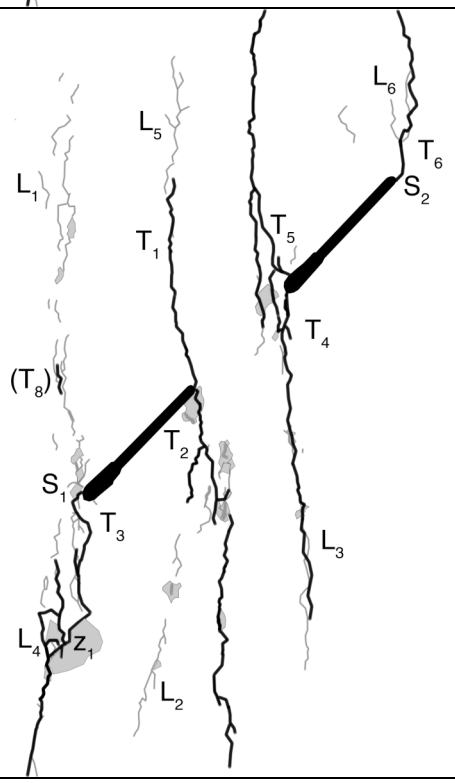	**Time:** 0.544s before failure T_6 connects to the tensile crack that had opened downward above it.

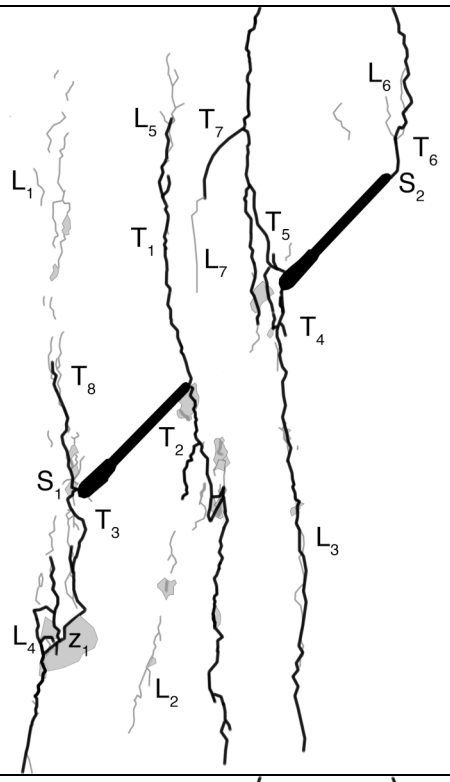	**Time:** 0.0158s before failure T_2 connects to the tensile cracks below it and T_1 grows upward. Tensile crack T_7 grows off of T_5 downward into the bridge area led by linear white patch L_7. Tensile crack T_8 is formed when the tensile crack previously labeled (T_8) connects to the left outer flaw tip.
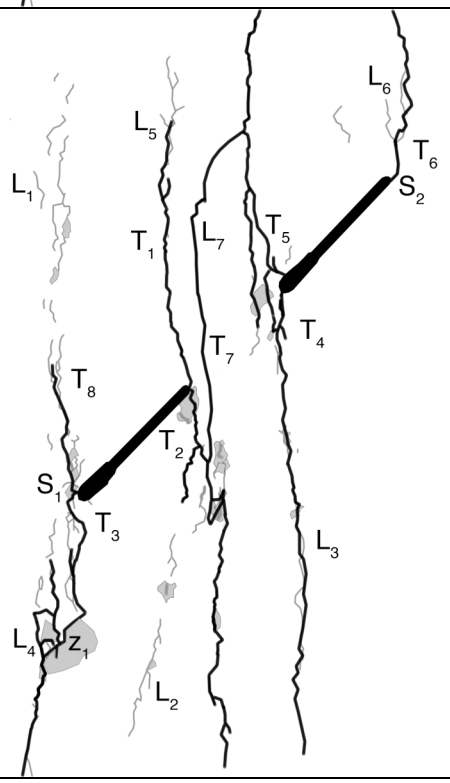	**Time:** 0.0156s before failure Indirect coalescence (category 2) occurs when tensile crack T_7 grows down to connect T_5 and T_2.

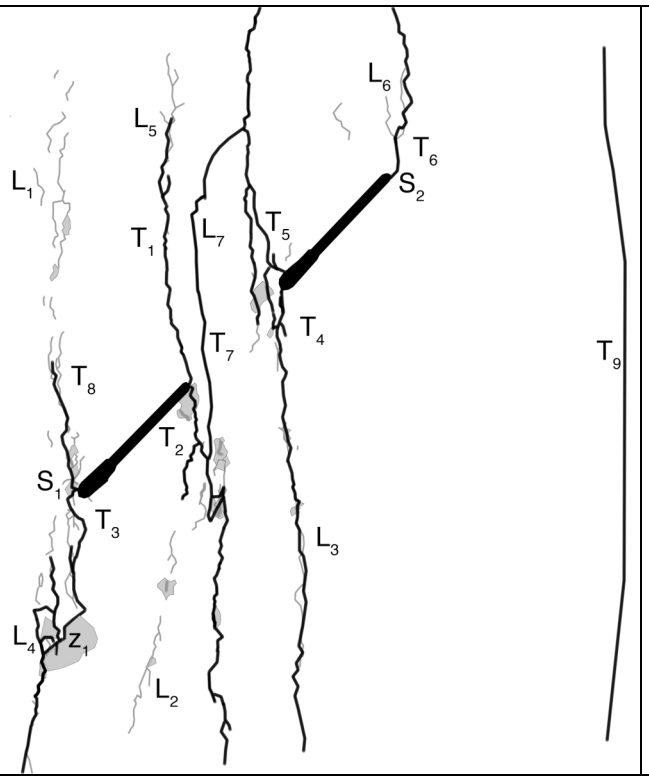

Time:16m36.016s
σ: 87.9791 MPa

Failure of sample. The right side of the sample falls away with the opening of tensile crack T_9.

Gr 2a-45-0 C (20071002)

Summary

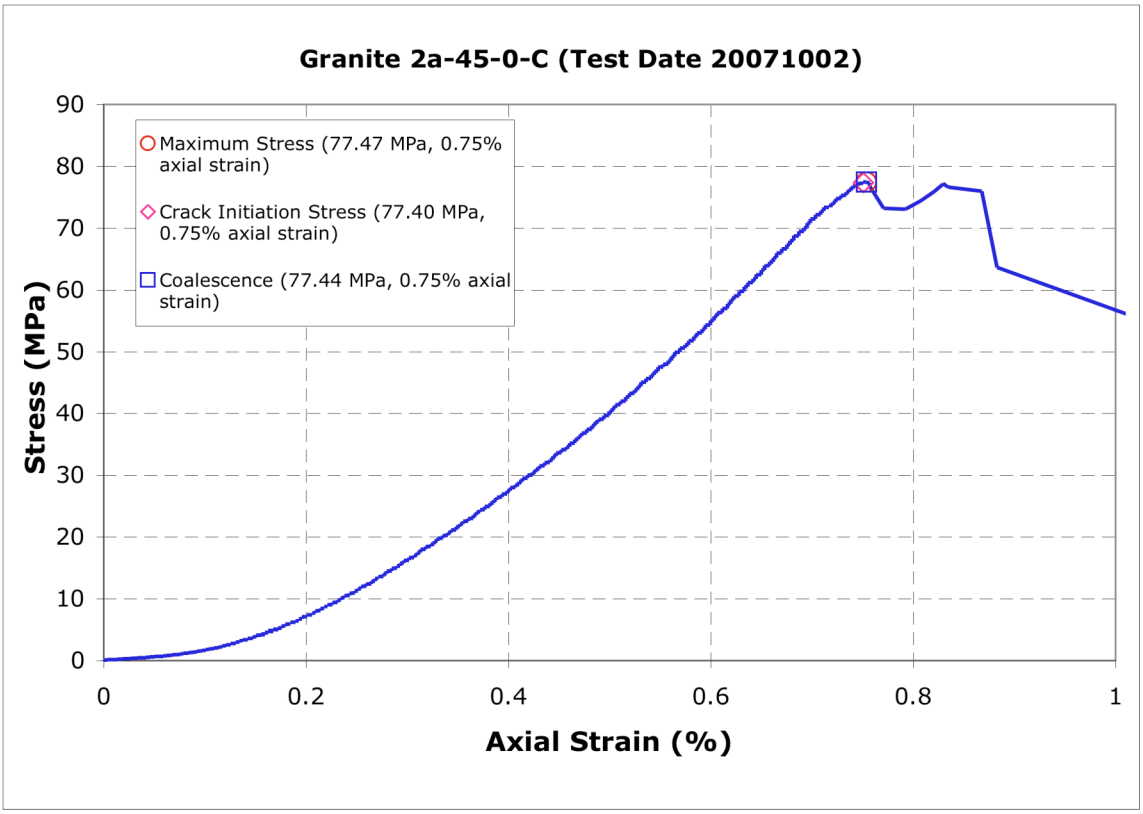

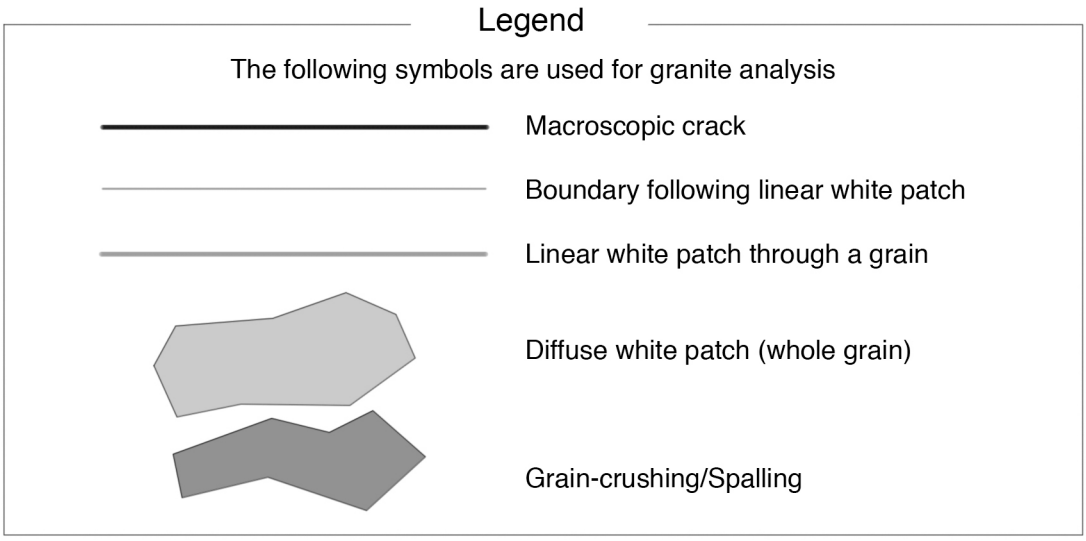

Category 2 Coalescence

Images taken from high-speed footage unless otherwise noted

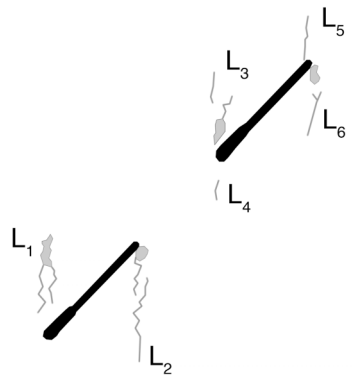	**Time:** ~12m25s **σ:** ~68.3 MPa Still-frame captured during loading. Linear white patches L_1 through L_6 have started developing on flaw tips. There are also some lightened grains near some of the flaw tips.
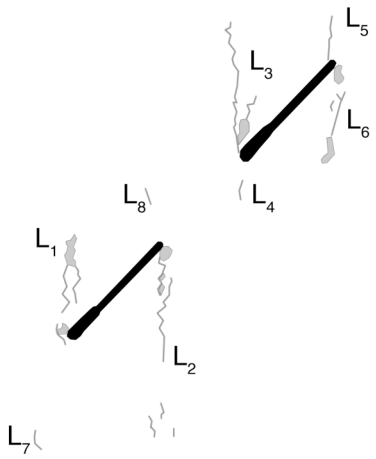	**Time:** ~13m17s **σ:** ~72.9 MPa Still-frame captured during loading. LWPs continue growing and L_7 and L_8 form (also on flaw tips).

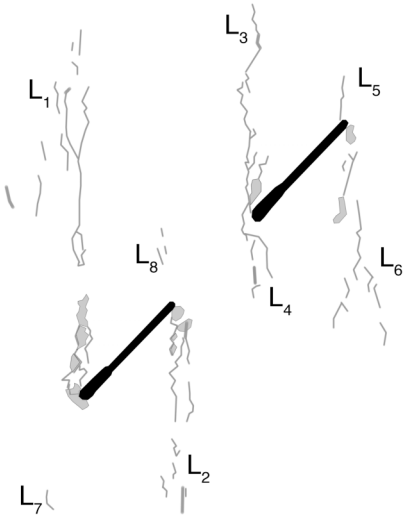	**Time:** 0.7976s before failure First frame of high-speed recording. Linear white patches have continued to grow, except for L_7. Note that boundary-following linear white patches are more prevalent than those going through grains and that more grains have lightened near the left flaw tips.
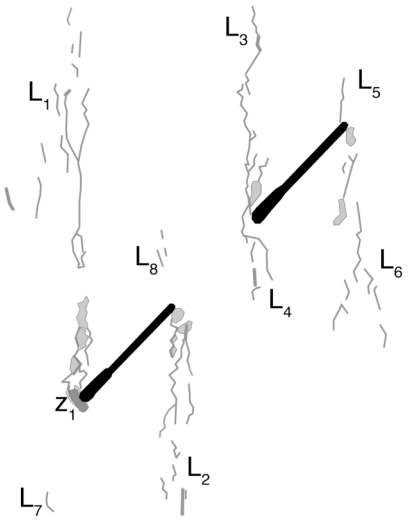	**Time**: 0.7208s before failure Grain at left outer flaw tip (zone z_1) spalls off of surface. Linear white patches in L_2 grow.

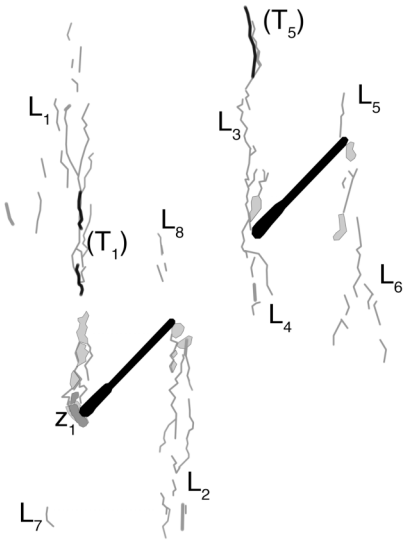	**Time:** 0.5898s before failure First tensile cracks appear. (T_1) opens aboe the left flaw's outer tip while (T_5) opens above the right flaw's inner tip. These tensile cracks open mostly along linear white patches, although not entirely.
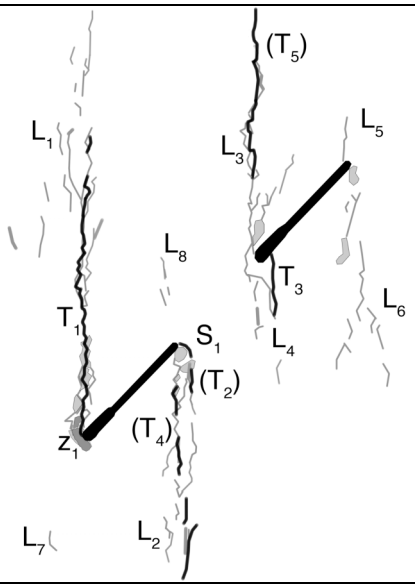	**Time:** 0.5374s before failure Tensile wing crack T_1 forms when tensile cracks previously labeled (T_1) grow downward along the boundaries of diffuse white patches and connect with the outer left flaw tip. On the left inner flaw tip, a mixed tensile-shear crack (S_1/T_2) opens with the shear portion of the crack being along the boundary of two grains. Tensile wing crack T_3 opens on the right inner flaw tip and (T_5) grows downward.

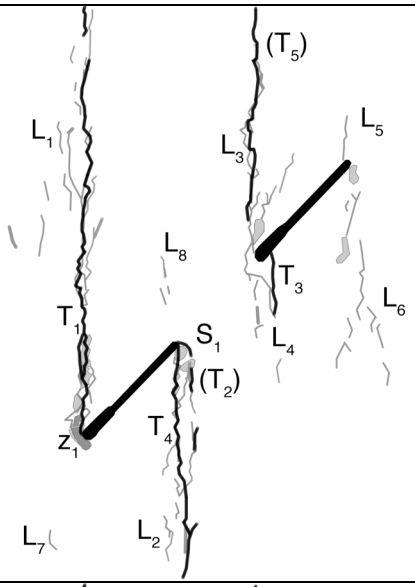	**Time:** 0.5362s before failure Tensile cracks below the left inner flaw tip connect to the flaw tip, creating tensile wing crack T_4 – a second wing crack at the tip. Tensile wing crack T_1 grows upward and (T_5) grows downward.
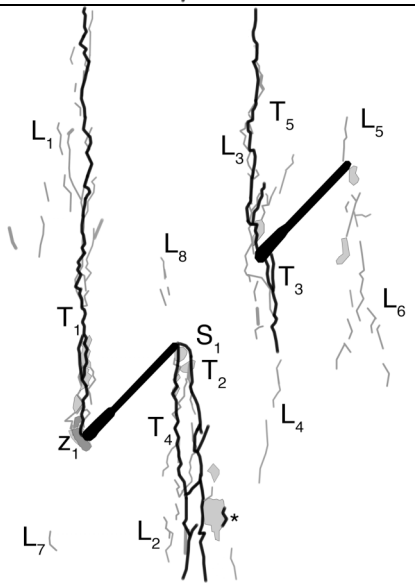	**Time:** 0.4822s before failure Tensile wing cracks T_2 and T_4 join with increased LWP formation in L_2 as well as some lightened grains. Along one edge of this area of lightened grains (indicated by a *) a tensile crack also opens. Tensile wing crack T_5 is formed when the tensile crack previously labeled (T_5) connects to the left flaw's inner tip. Tensile wing crack T_3 extends downward and has a second branch meet the flaw tip as well. Tensile wing crack T_1 extends upward.

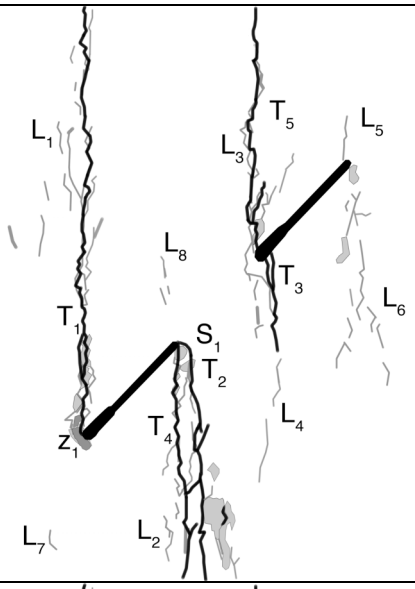	**Time:** 0.4820s before failure More grains lighten in the lower portion of L_2.
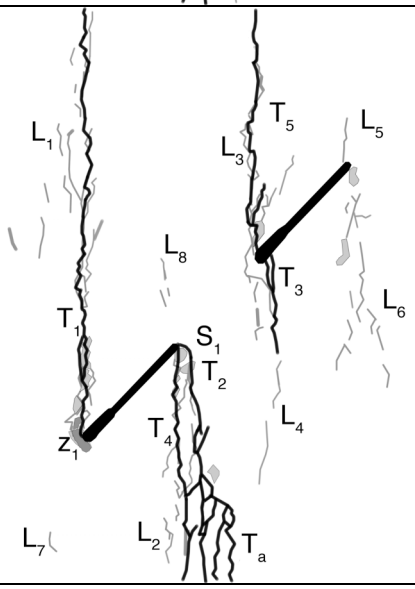	**Time:** 0.4816s before failure Several tensile cracks form where the grains had lightened at the bottom of L_2. This network of tensile cracks is labeled T_a. Any grains that were not already lightened became brighter. Several grains within T_a were also crushed.

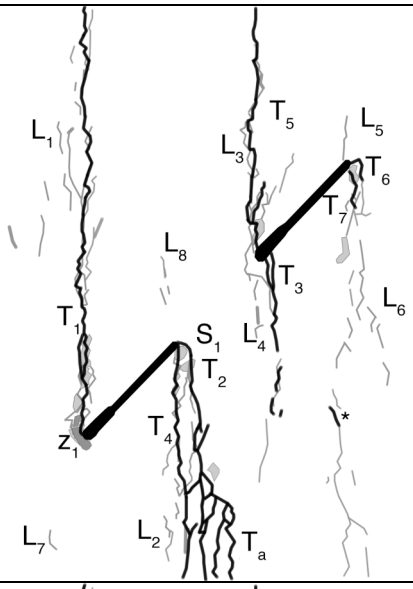	**Time:** 0.4658s before failure L_6 extends downward with a small tensile crack (labeled with a *) also forming in that same region. More tensile cracks form below T_3 along previous linear white patches. Two tensile wing cracks, T_6 and T_7 form at the right outer flaw tip.
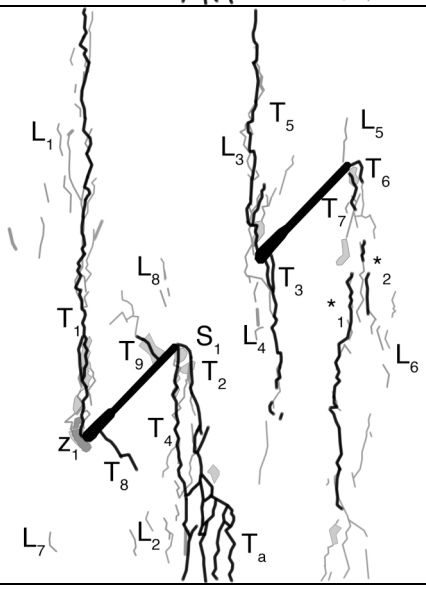	**Time:** 0.2614s before failure T_3 extends downward by linking to previous tensile cracks. Tensile cracks open below T_7 and are labeled $*_1$ while tensile cracks forming underneath T_6 are labeled $*_2$. More white patches form within the lower parts of L_6. Tensile cracks T_8 and T_9 form farther in from both tips of the left flaw. T_9 goes through a grain that becomes lighter with the crack's formation.

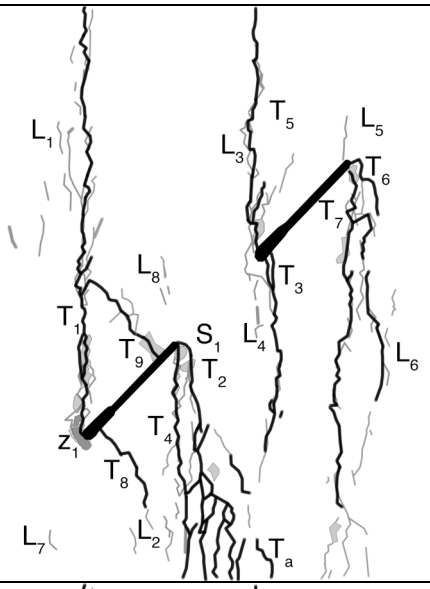	**Time:** 0.2510s before failure Tensile wing crack T_3 continues growing down toward T_a. Region T_a had more tensile crack growth as well as linear white patch growth. Tensile crack T_9 connects with T_1. T_8 grows toward T_4.
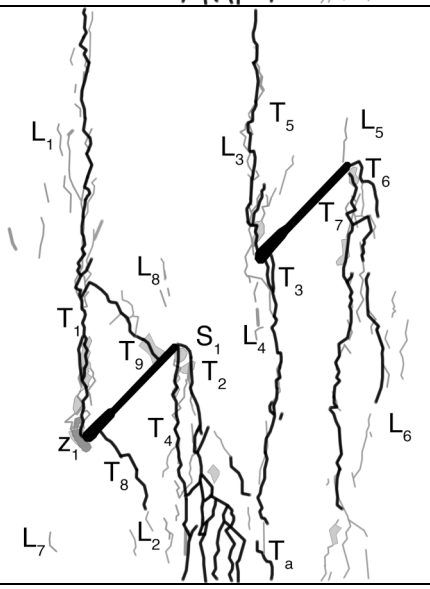	**Time:** 0.2162s before failure Tensile wing crack T_3 continues extending downward toward T_a.

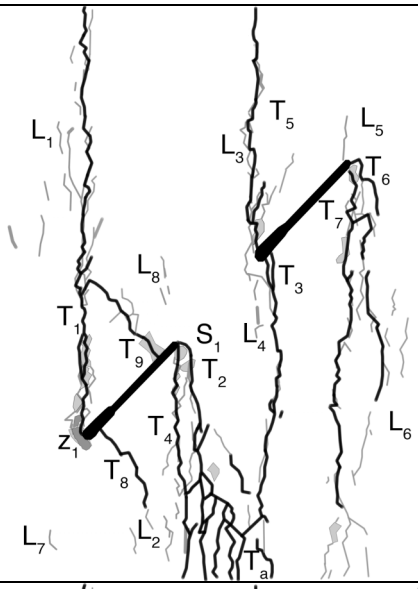	**Time:** 0.2092s before failure Indirect (category 2) coalescence. Tensile wing crack T_3 connects with tensile cracks in T_a (which are connected to tensile wing cracks T_2 and T_4.
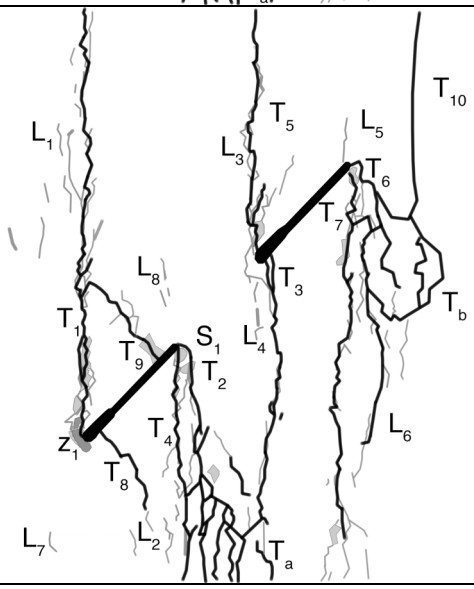	**Time:** 0.2062s before failure Tensile crack T_{10} opens downward and links up with tensile wing cracks T_6 and T_7 with a region of tensile cracking (labeled as T_b).

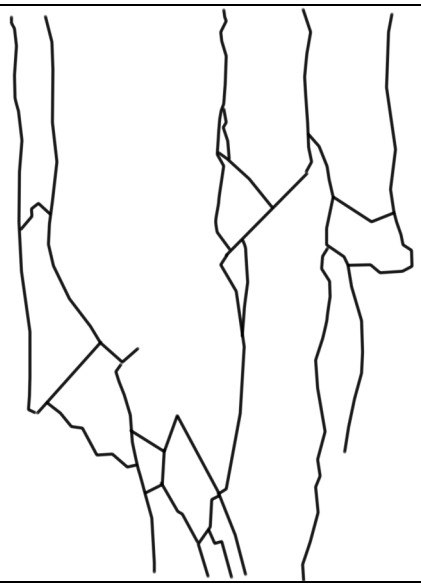	**Time:** 14m10.716s **σ:** 77.4694 MPa Sample failure occurs with sudden widening and sliding along tensile wing cracks. Several other tensile cracks form. Sliding along some of these new cracks cause the left flaw to be split and then rotated so it is no longer continuous.

Gr 2a-60-0 A (20071002)

Summary

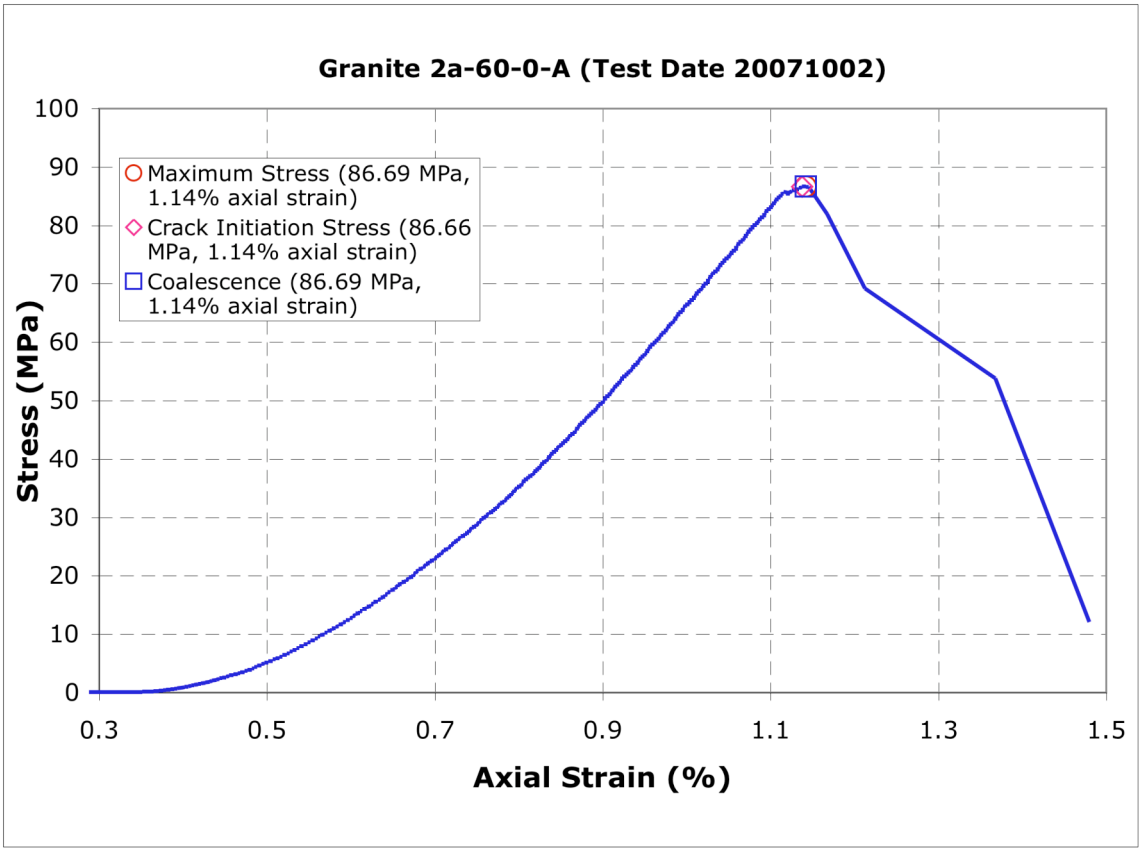

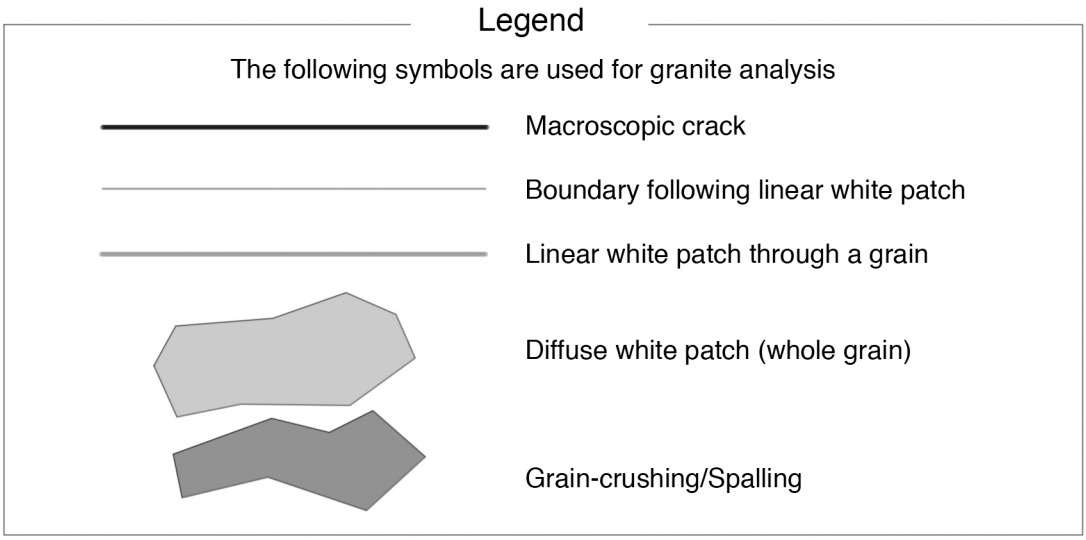

Category two coalescence
Images taken from high-speed camera

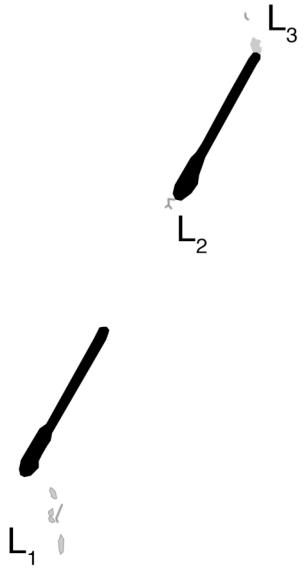	**Time:** ~15m41s **σ:** ~85 MPa Image capured before high-speed recording started. Three zones of white patches form. L_1 and L_3 are made up of both linear white patches as well as grains which have lightened. L_2 is composed of a single linear white patch.
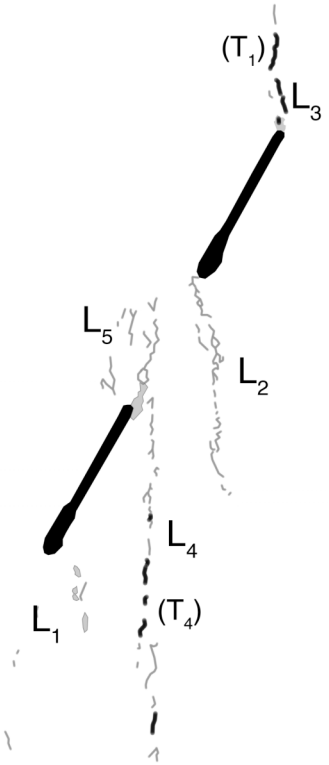	**Time:** 0.3748s before failure First frame of high-speed recording. L_4 and L_5 develop and the other linear white patches continue to grow. Small tensile cracks within the L_3 and L_4 regions form. The cracks inside the L_3 region are labeled as (T_1) and those inside the L_4 region are labeled (T_4). Of note is that L_4 seems to pass the flaw tip and connect with L_5 instead.

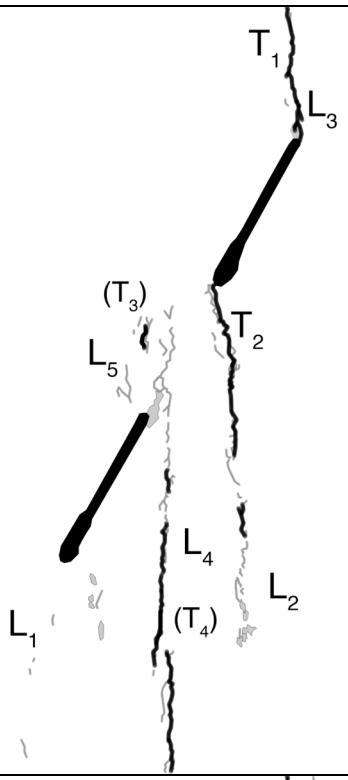	**Time:** 0.0834s before failure (T_1) and (T_4) grow within L_3 and L_4. (T_1) connects with the right flaw to make a tensile wing crack, so it is labeled T_1. Tensile wing crack T_2 forms and grows downward. (T_3) opens in the L_5 region.
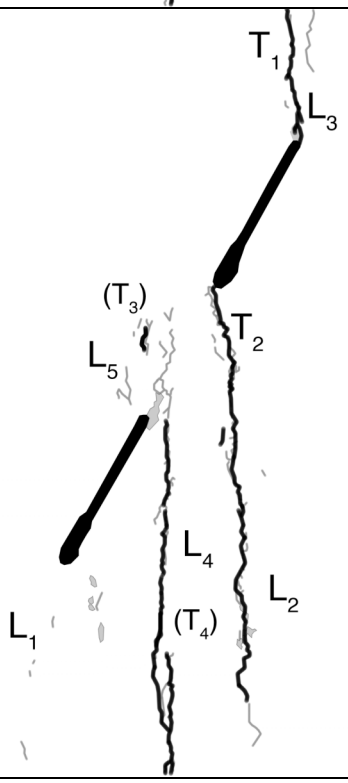	**Time:** 0.0730s before failure Tensile cracks within (T_4) continue to grow and link with one another. T_2 continues growing downward.

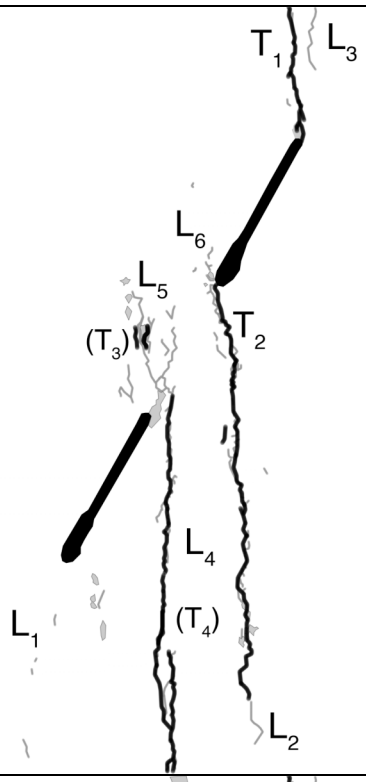	**Time:** 0.0694s before failure Further linking of (T_4) takes place. It grows up past the inner tip of the left flaw. (T_5) forms within L_5 along with more linear white patches.
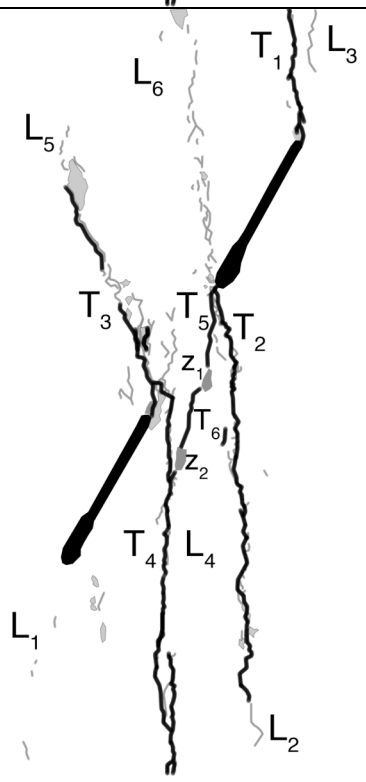	**Time:** 0.0692s before failure Increased linear white patch formation and growth occurs in both L_5 and L_6. Tensile wing crack T_3 forms and grows upward from the inner tip of the left flaw. (T_4) connects with T_3 and is now labeled as T_4. Notice that it bypassed the flaw tip. A second crack forms on the inner right flaw tip – labeled T_5 – and grows toward T_4. There are two zones of spalling (z_1 and z_2) in the bridge area, separated by tensile crack T_6. It is likely that coalescence has occurred at this point.

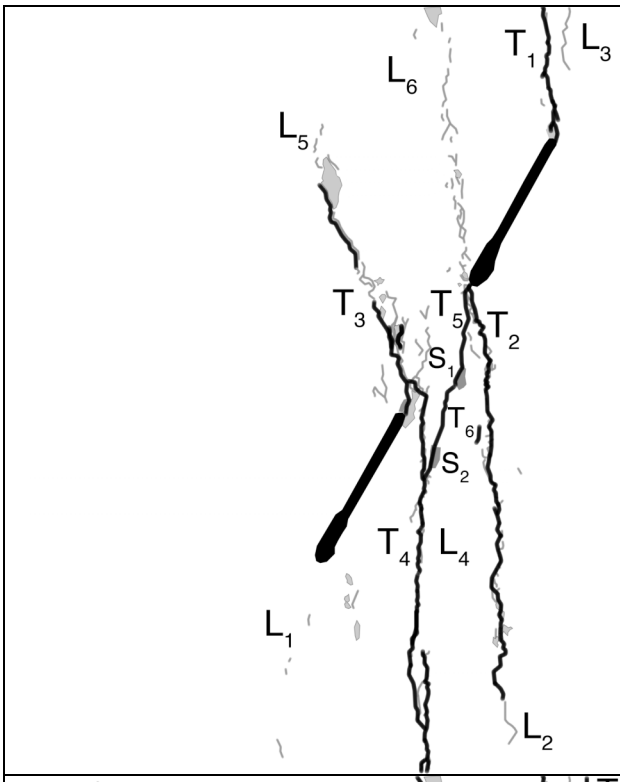	**Time:** 0.0690s before failure Shear cracks S_1 and S_2 are exposed after spalled material falls away from z_1 and z_2. Coalescence has definitely occurred by this point. It is indirect (category 2) coalescence.
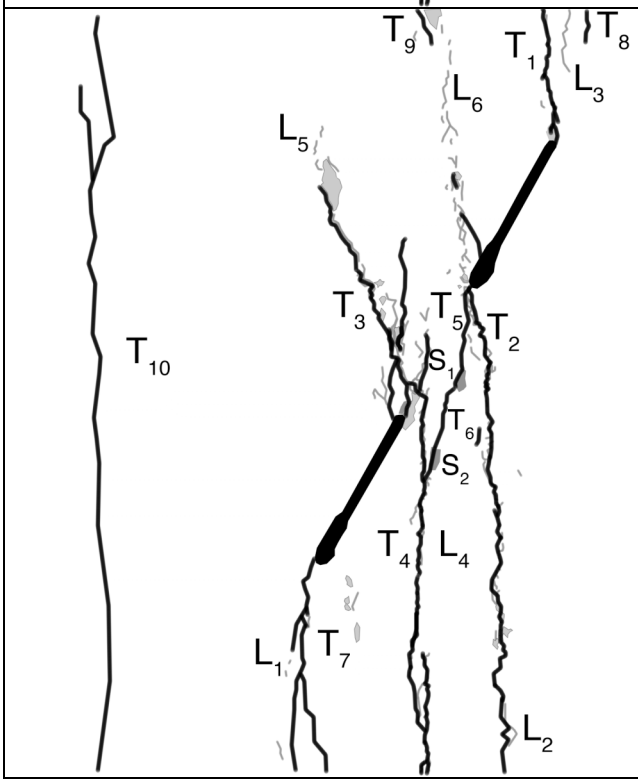	**Time:** 16m00.156s **σ:** 86.6946 MPa Tensile cracks T_7, T_8, and T_9 form before tensile crack T_{10} opens upward from the bottom of the sample and causes failure.

Gr 2a-60-0 B (20071002)

Summary

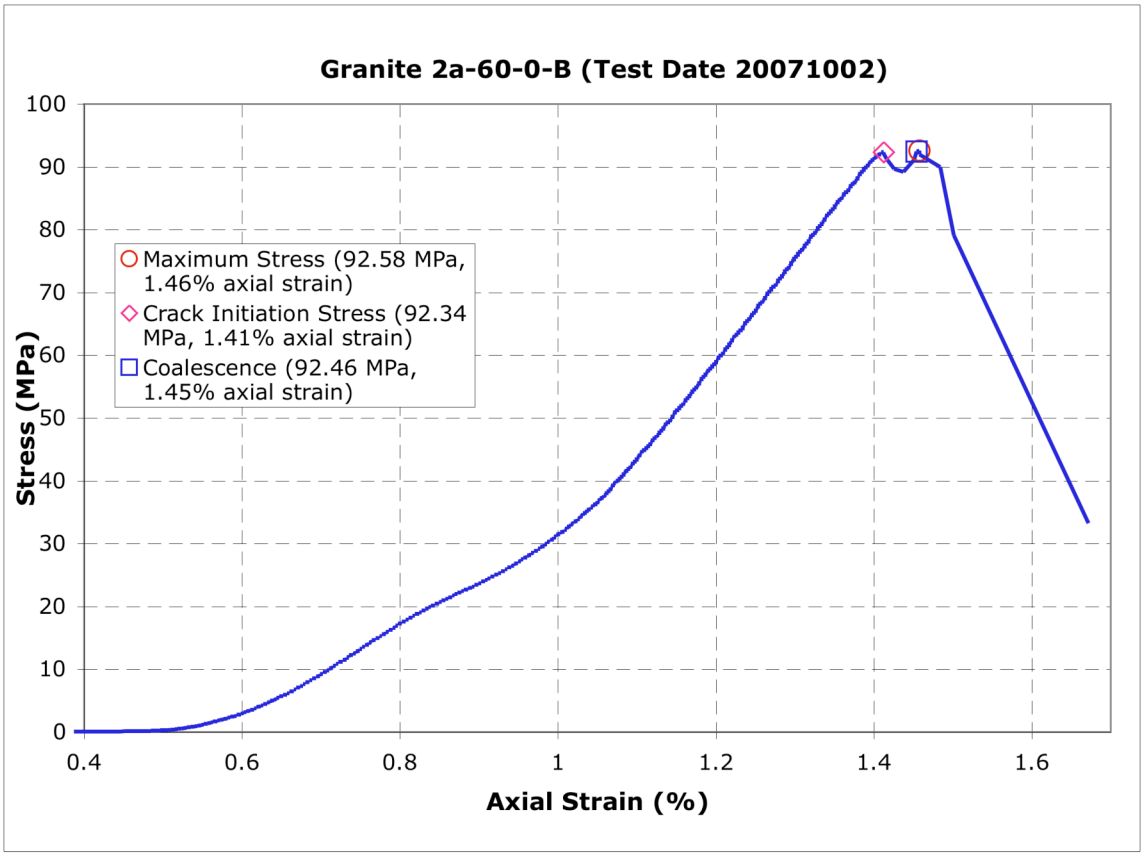

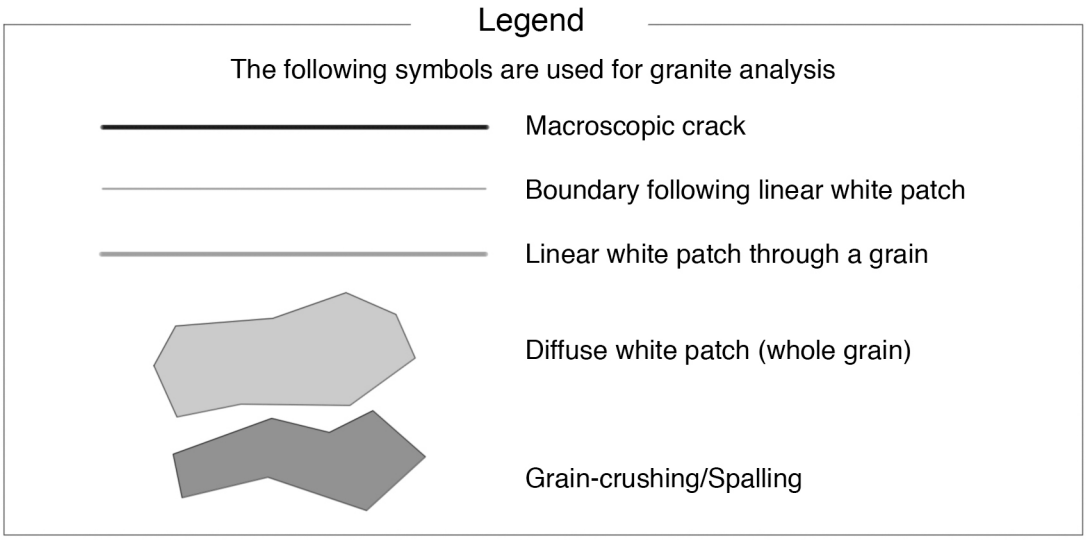

Category two coalescence
Images taken from high-speed camera

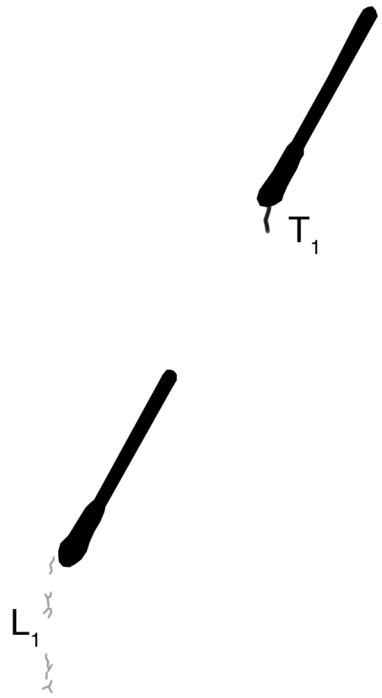	**Time:** ~17m03s **σ:** ~90.3 MPa The first tensile crack T_1 opens on the inner tip of the right flaw. The first set of linear white patches (all grain boundary-following), L_1, forms on the outer tip of the left flaw.
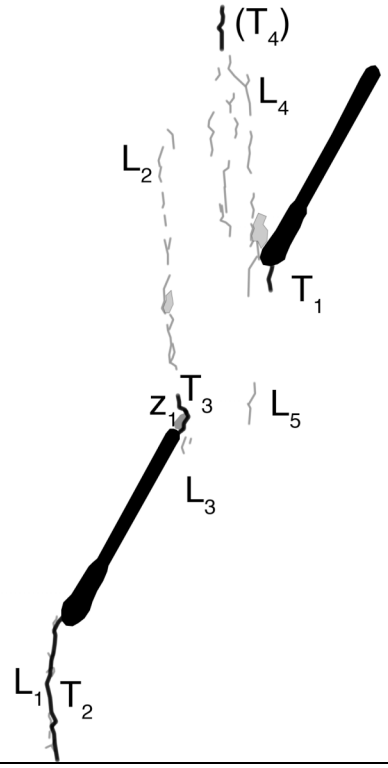	**Time:** 0.6438s before failure Tensile wing cracks T_2 and T_3 form on the left flaw. Regions of linear white patches form on the inner flaw tips (L_2 through L_5). There is some grain lightening near the two inner flaw tips. A single grain starts to spall off the surface near the left inner flaw tip (labeled z_1). A tensile crack also opens in the L_4 region. This crack is labeled (T_4).

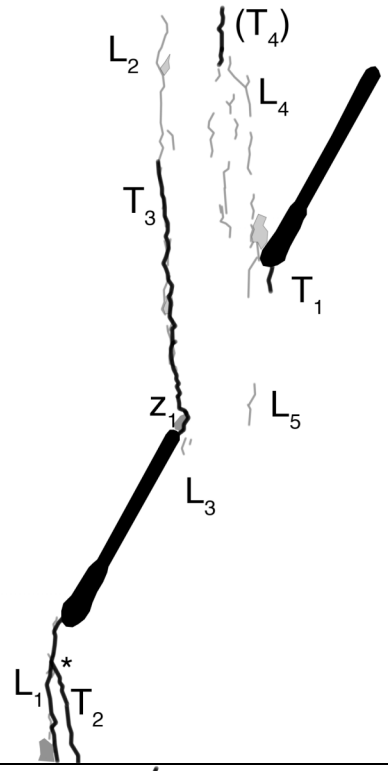	**Time:** 0.4283s before failure Another tensile crack branches off of T_2 at a point indicated by a * and some grains burst off the surface (labeled z_2). More linear white patches form in the L_4 region. Both T_3 and L_2 grow upward.
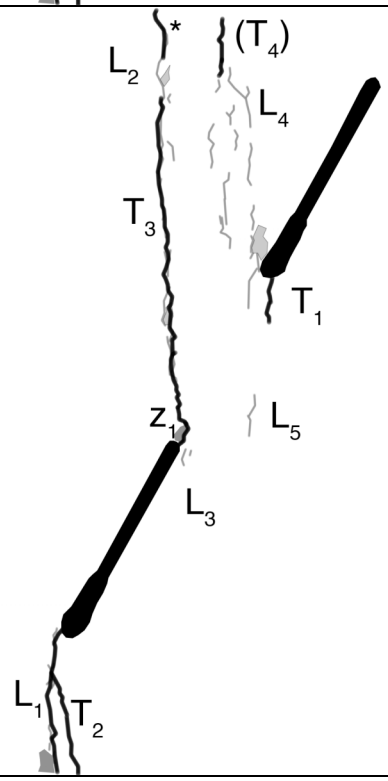	**Time:** 0.3314s before failure A tensile crack forms above T_3 and is indicated by a *.

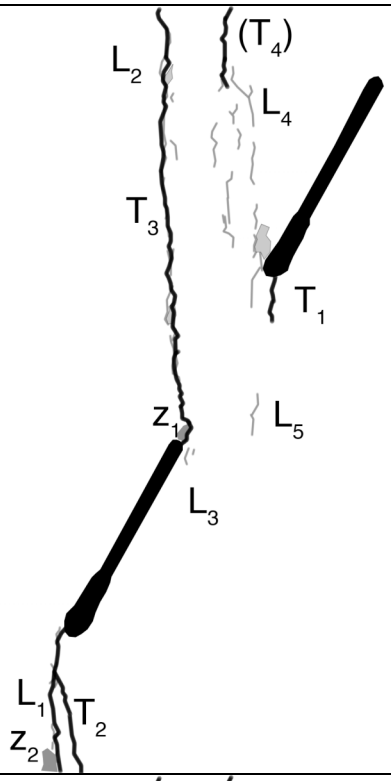	**Time:** 0.3294s before failure Tensile crack T_3 grows and links with the tensile crack that was above it. (T_4) grows downward slightly.
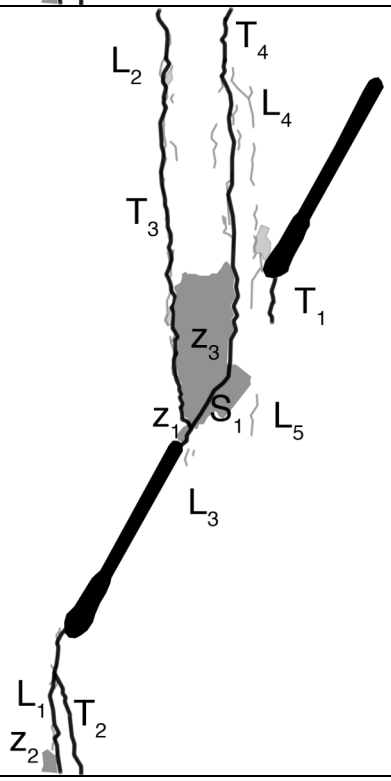	**Time:** 0.2950s before failure A large zone in the bridge area spalls and falls off the surface of the sample (labeled z_3). A shear crack, S_1, connects with the inner flaw tip of the left flaw and cuts across the region (as seen in later frames). As the crack turns upward, it transforms into a tensile crack, T_4, which links with the previously existing tensile crack in the L_4 region.

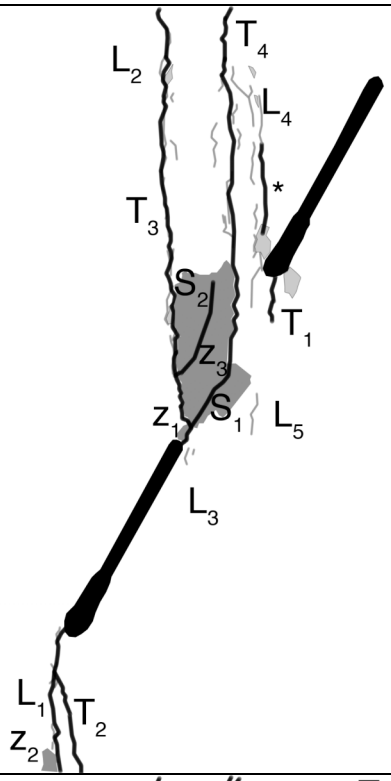	**Time:** 0.0476s before failure Increased white patch activity near the inner right flaw tip (both linear features as well as grain lightening). Another tensile crack forms in this region along grain boundaries and is labeled with a *. S_2 is a second shear crack that forms within zone 3. It stops propagating near the edge of the region of spalling. Of interest is the fact that linear white patches in L_4 start "curving" toward T_4.
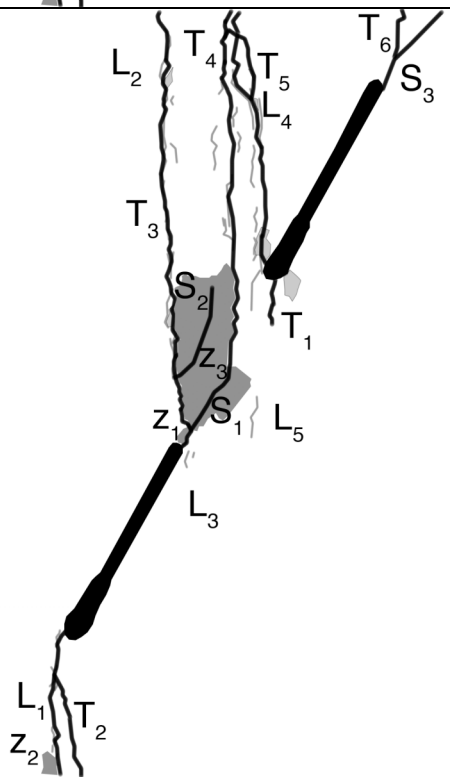	**Time:** 0.0438s before failure The second tensile crack (labeled T_5 in this frame, indicated by a * in the last frame) in the L_4 region connects to the inner flaw tip by extending downward. This crack also extends up to meet T_4 leading to category two (indirect) coalescence. Several small cracks near the coalescing region form, making T_5 have a branched nature at this point. Simultaneously, a mixed shear-tensile wing crack forms. S_3 is connected to the outer tip of the right flaw. Tensile crack T_6 branches off of S_3 upward.

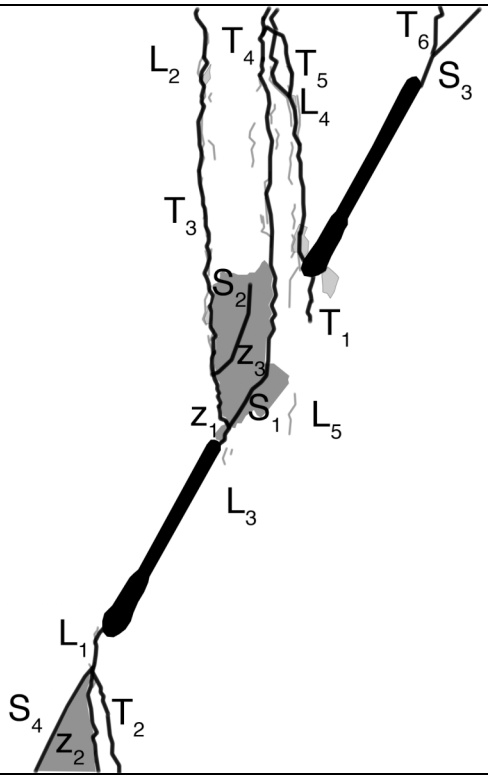

Time: 17m27.498s
σ: 92.5750 MPa

Failure occurs when shear crack S_4 forms with the crushing and spalling of material within an expanded region 2. Both flaws become wider as do previously formed cracks.

Gr 2a-75-0 A (20071002)

Summary

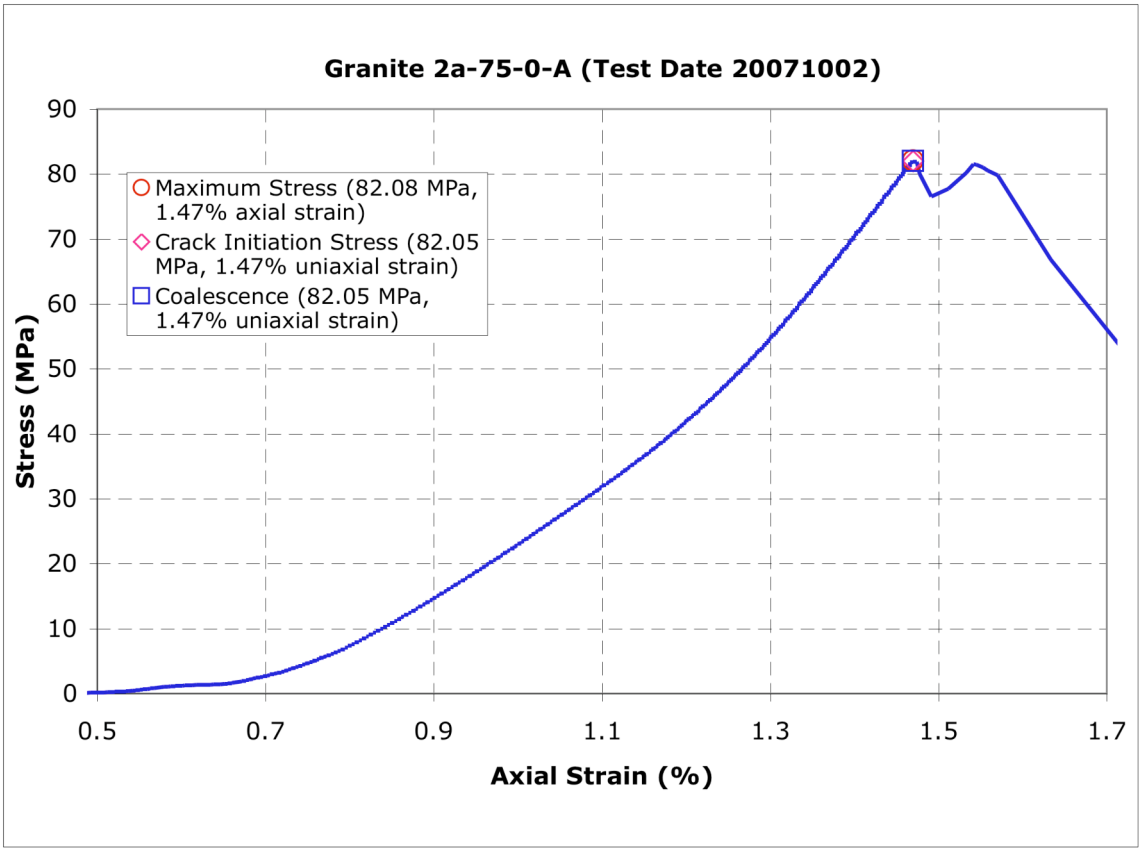

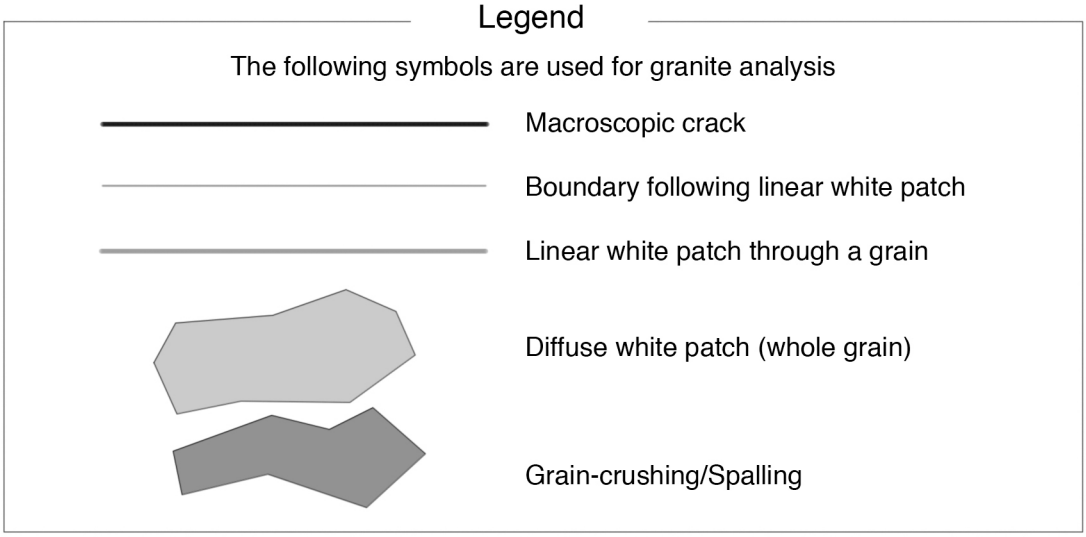

Category 5 Coalescence

Images captured from high-speed video unless otherwise noted

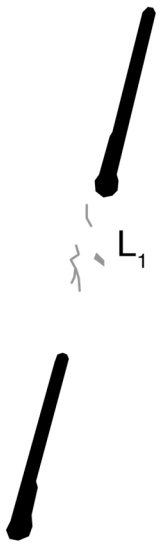	**Time:** ~12m22s **σ:** ~65.8 MPa Still image captured before high-speed recording with high-speed camera. Linear white patch L_1 appears between the two flaws. L_1 is predominantly boundary-following linear white patches with a small patch of lightened grains.
	**Time:** ~13m14s **σ:** ~70.3 MPa Still image captured before high-speed recording with high-speed camera. L_1 grows slightly and L_2 appears below the outer left flaw tip. Note that L_2 is connected to the left outer flaw tip while L_1 is connected to neither of the inner flaw tips. Both L_1 and L_2 do not have any through-going linear white patches.

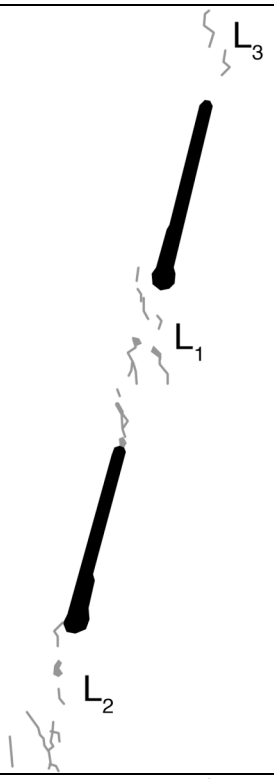	**Time:** ~15m25s **σ:** ~81.6 MPa Still image captured before high-speed recording with high-speed camera. L_3 appears above the right outer flaw tip and only has boundary-following linear white patches. Both the L_1 and L_2 regions have more linear white patches grow. Of note is that L_1 now connects to the left inner flaw tip and has a through-going linear white patch near the left inner flaw tip.
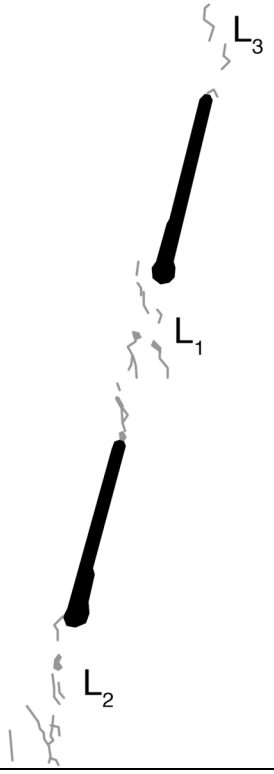	**Time:** 0.5124s before failure First frame of high-speed video. L_3 connects to the right outer flaw tip. It still only has boundary-following linear white patches. L_2 also has more boundary-following white patches appear.

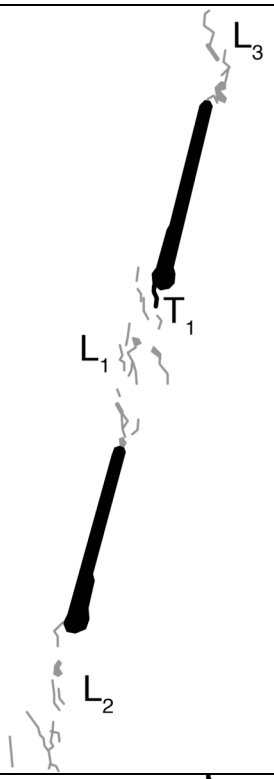	**Time:** 0.3780s before failure First tensile wing crack forms on the inner right flaw tip. It is labeled T_1. More boundary-following linear white patches form in the middle of L_1. L_3 also grows away from the right outer flaw tip. L_3 now includes all three types of white patches.
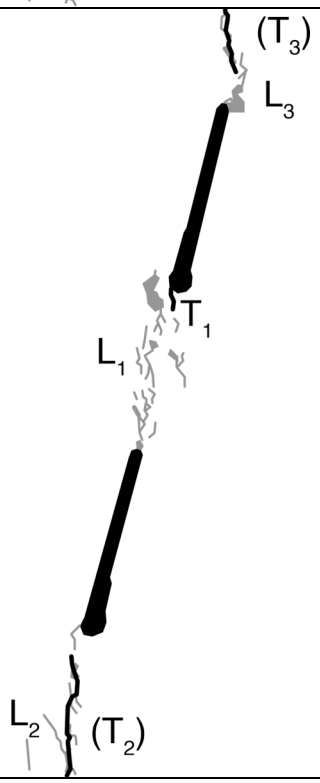	**Time:** 0.2988s before failure Tensile cracks (T_2) and (T_3) grow from outside the camera's field of view toward the outer flaw tips. L_1 has several more white patches develop. The new white patches are boundary-following linear white patches and lightened grains.

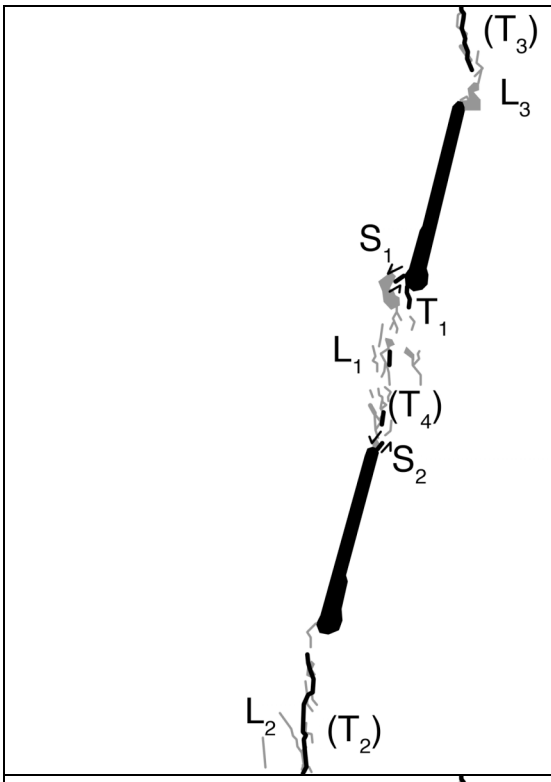	**Time:** 0.2928s before failure Shear cracks S_1 and S_2 develop on the inner flaw tips and shear in the direction indicated. Small tensile cracks labeled (T_4) open in the bridge area.
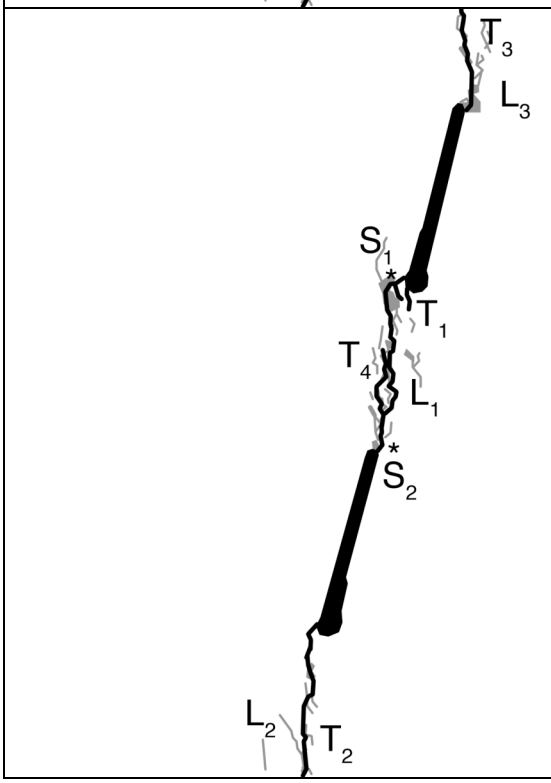	**Time:** 0.2916s before failure Tensile cracks previously labeled as (T_4) grow and connect with each other and shear cracks S_1 and S_2. This is now labeled as tensile crack T_4. T_4 connects with S_1 and S_2 at the points indicated by '*'s. The sample has now coalesced (category five). Tensile cracks (T_2) and (T_3) also connect to the outer flaw tips, becoming T_2 and T_3, respectively.

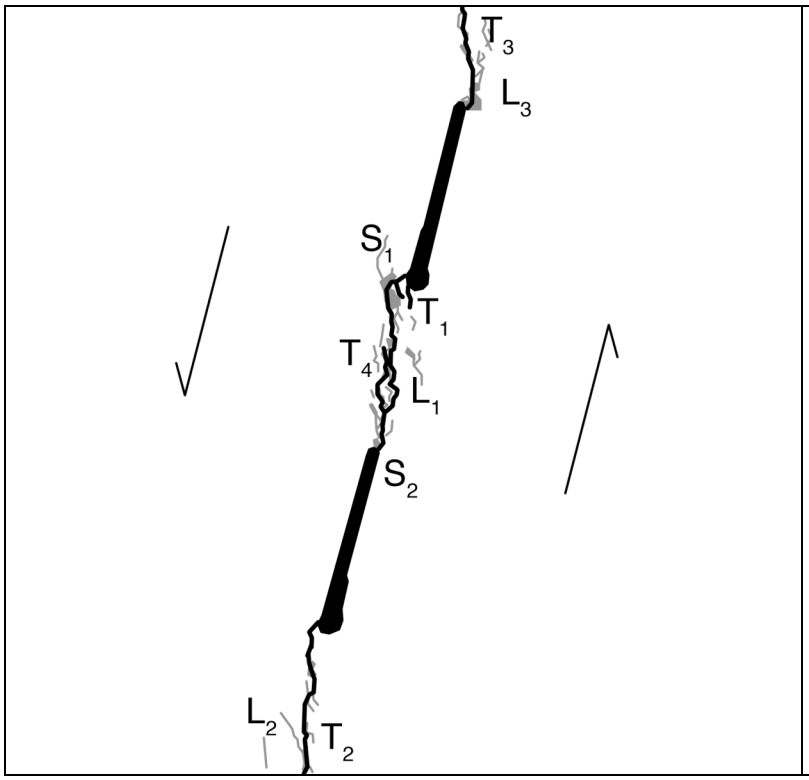

Time: 15m30.126s
σ: 82.0817 MPa

The sample fails with sliding along T_2, T_3, and T_4 in the sense indicated.

Gr 2a-75-0 B (20071002)

Summary

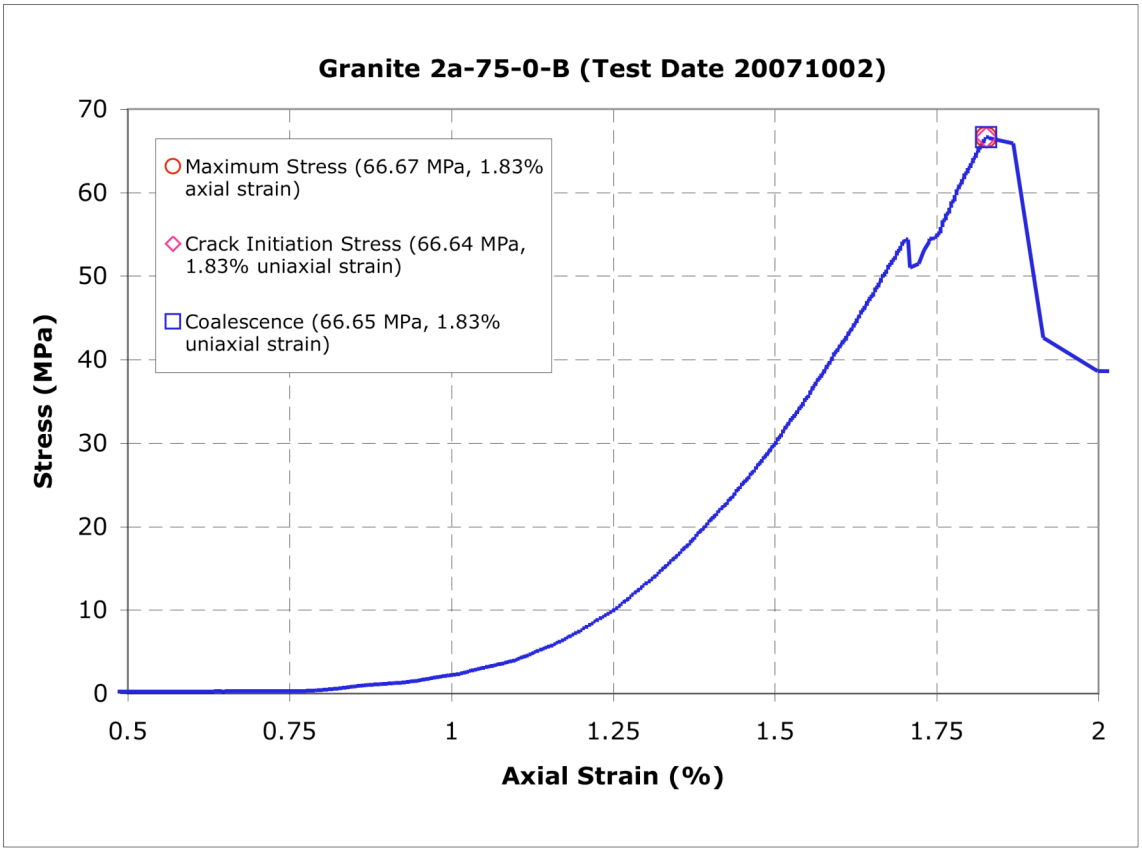

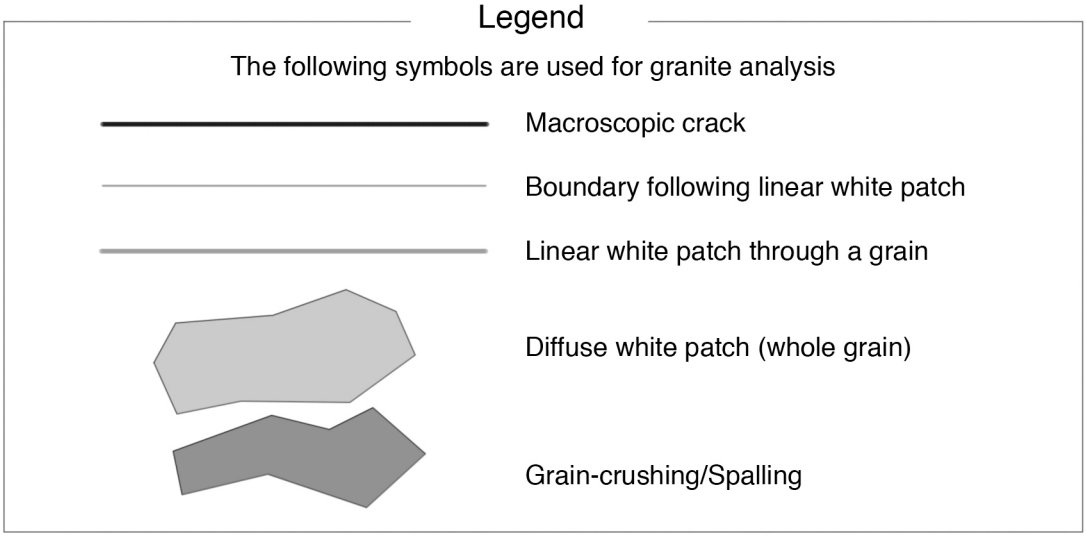

Category 5 Coalescence
Images taken from high-speed camera

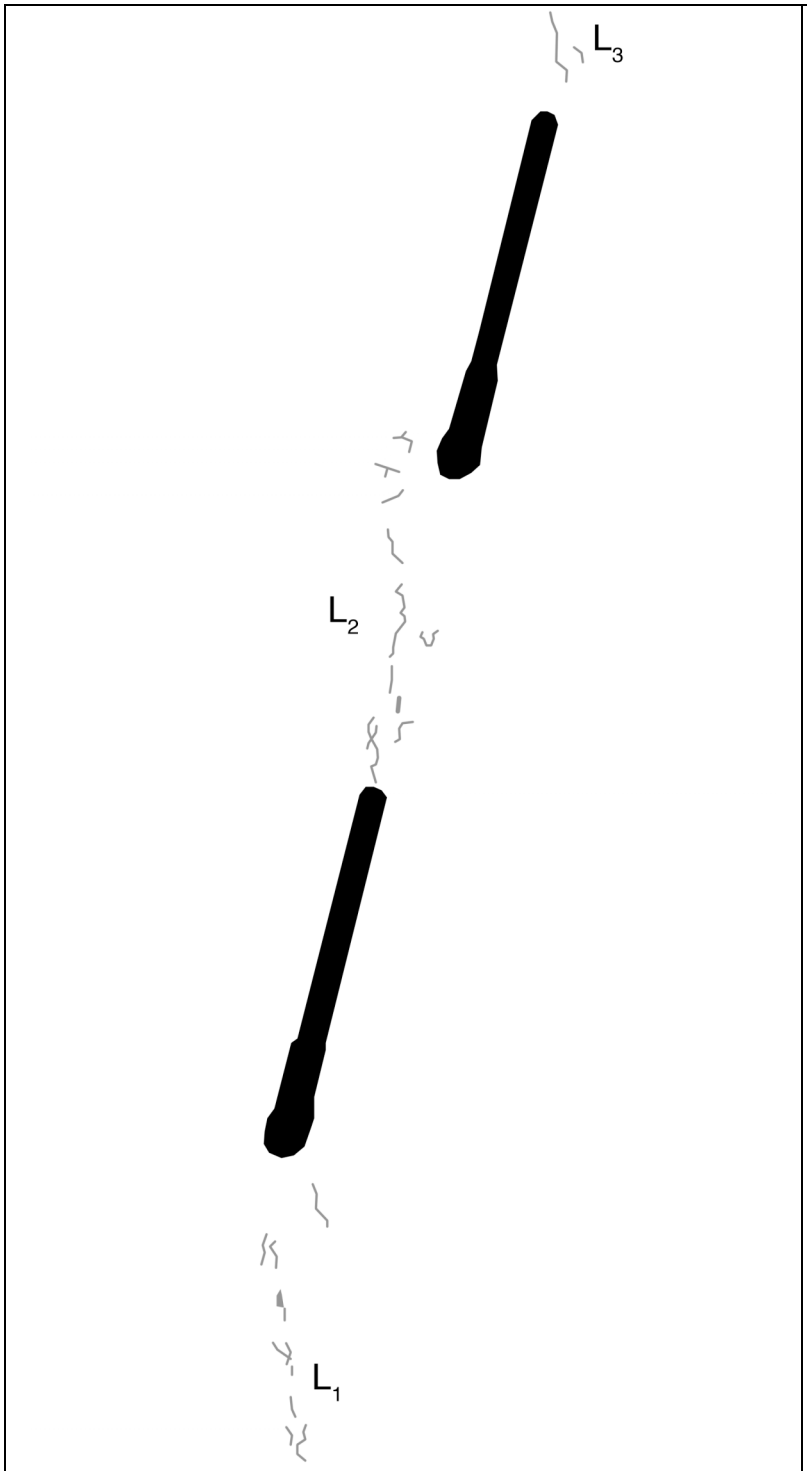	**Time:** 0.4625s before failure Linear white patches L_1, L_2, and L_3 form. L_3 is composed of boundary-following linear white patches. L_1 has boundary-following linear white patches as well as a small patch of lightened grains. L_2 also has boundary-following linear white patches but also has a through-going linear white patch.

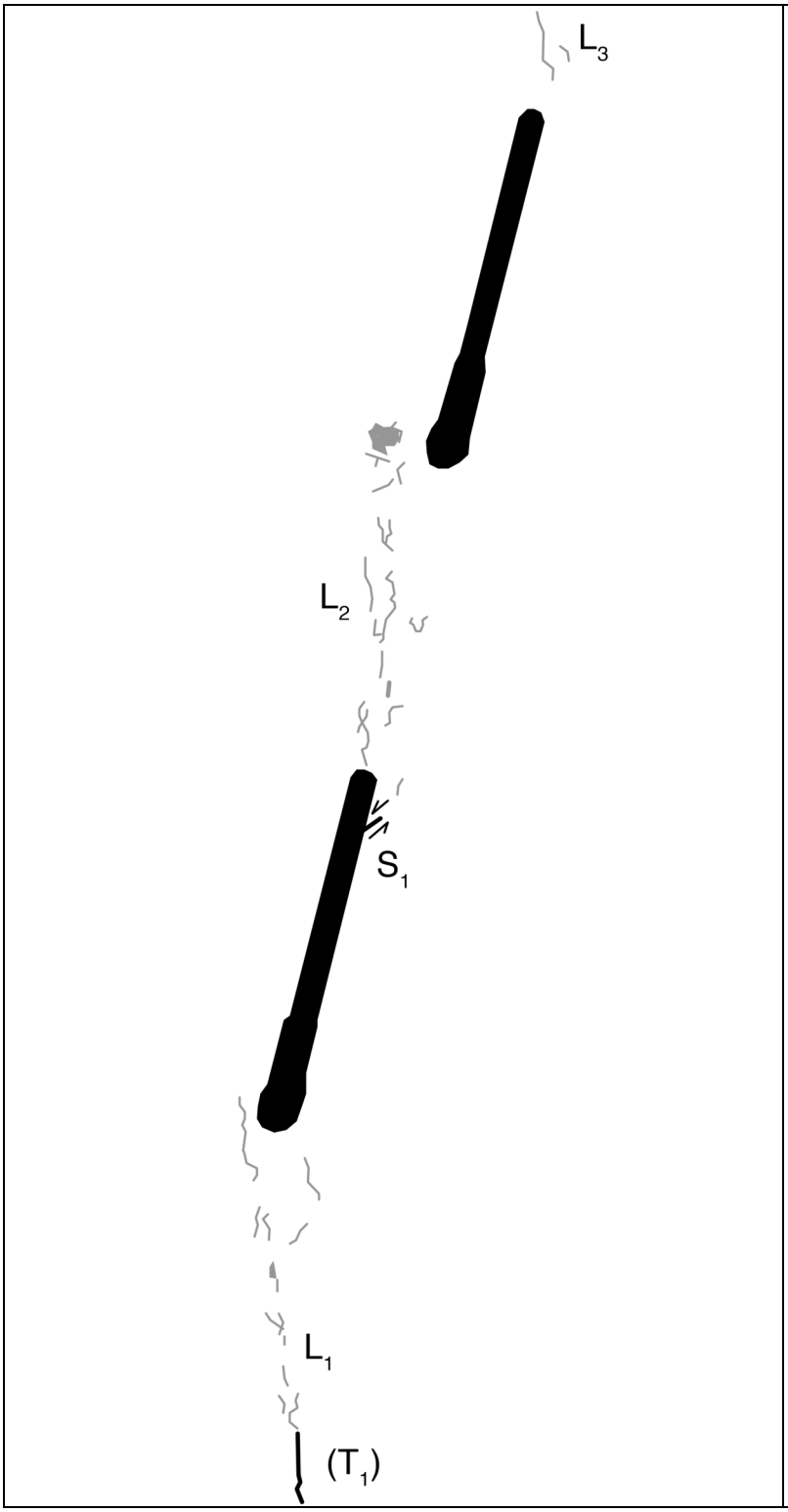

Time: 0.1816s before failure

L_1 and L_2 both develop more linear white patches (all along grain boundaries). L_2 also has a small group of grains near the right inner flaw tip lighten. Tensile crack (T_1) opens upward from below the camera's field of view toward the left outer flaw tip. Shear crack S_1 starts on the left flaw's inner flaw tip, shearing in the sense indicated.

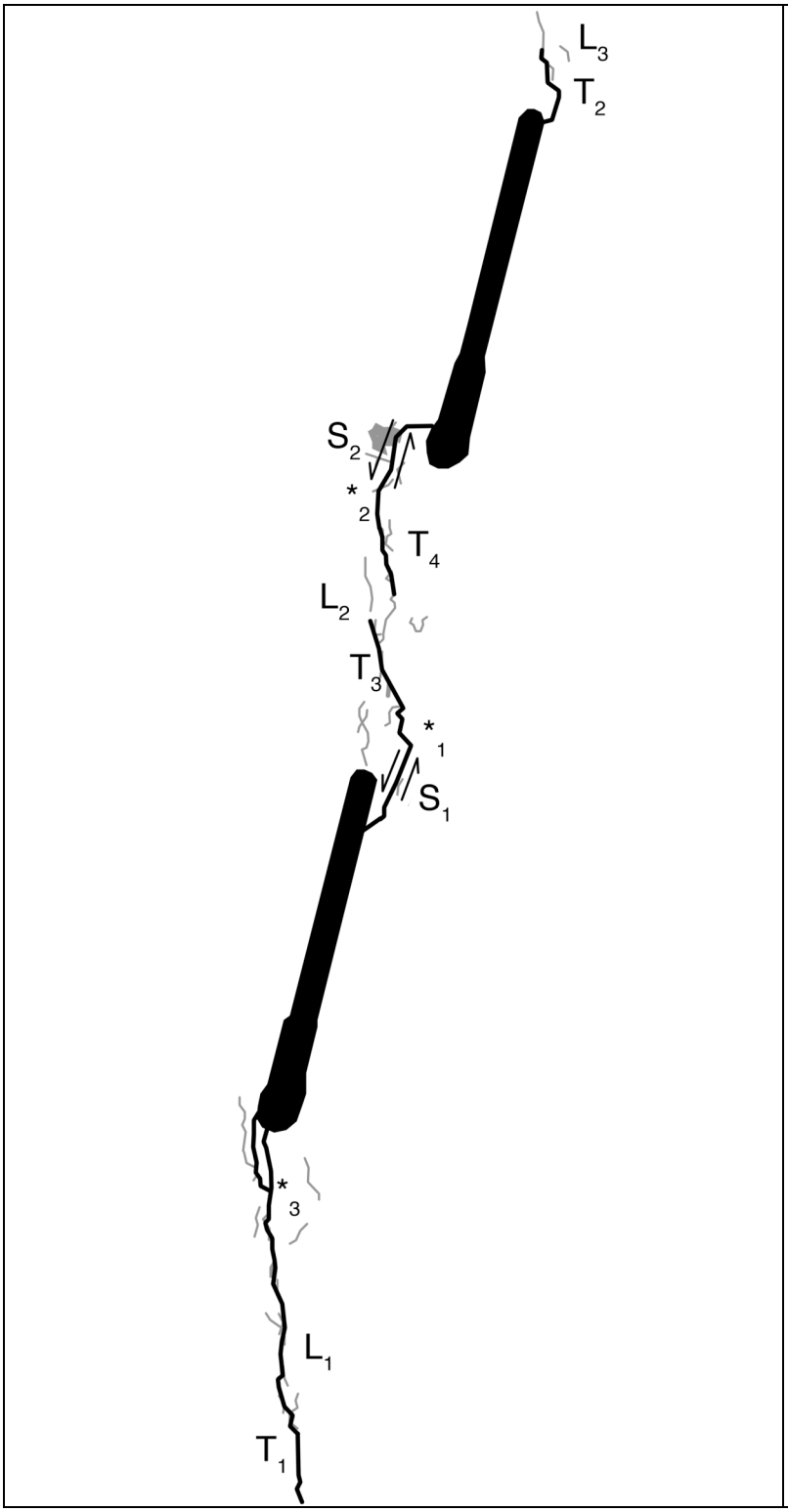

Time: 0.0454s before failure

S_1 grows upward and continues to shear in the sense indicated. At point $*_1$, the wing crack is no longer only a shear crack, but also has a tensile portion (labeled T_3). Similarly, the right flaw's inner tip also has both shear and tensile portions. The portion closest to the flaw is shear and labeled S_2 (shearing in the sense indicated). At point $*_2$ the crack changes into a tensile crack that is labeled T_4. S_2 appears before T_4.

(T_1) continues to grow upward, eventually branching at point $*_3$ and connecting with the left outer flaw at two locations. It will now be referred to as crack T_1. Tensile wing crack T_2 appears on the right outer flaw tip.

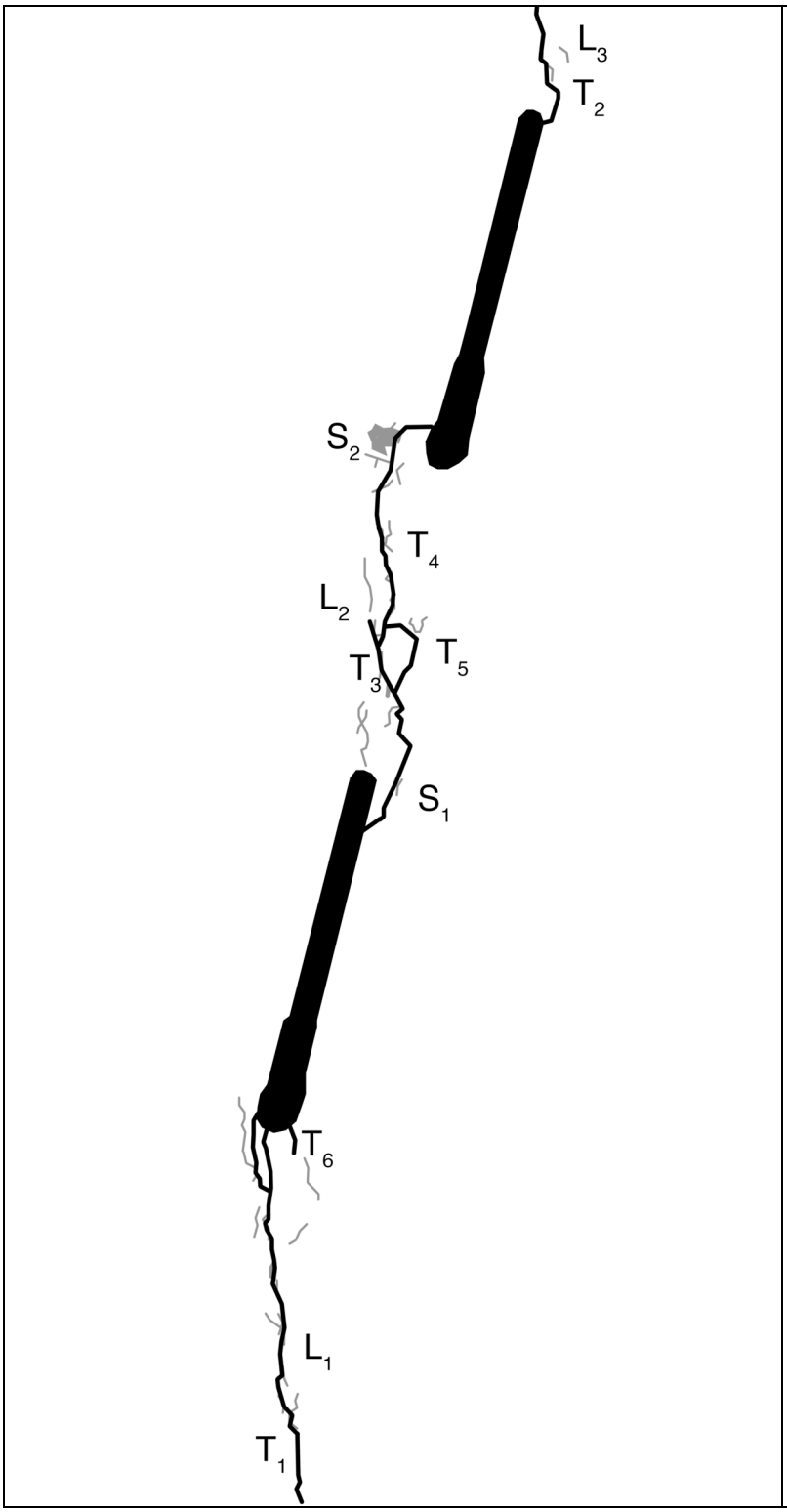

Time: 0.0328s before failure

T_3 and T_4 grow and link with one another. Tensile crack T_5 branches off both cracks and also joins the two original cracks. The sample has coalesced (category 5).

T_2 grows upward and out of the camera's field of view. Tensile crack T_6 also appears on the left flaw's outer tip.

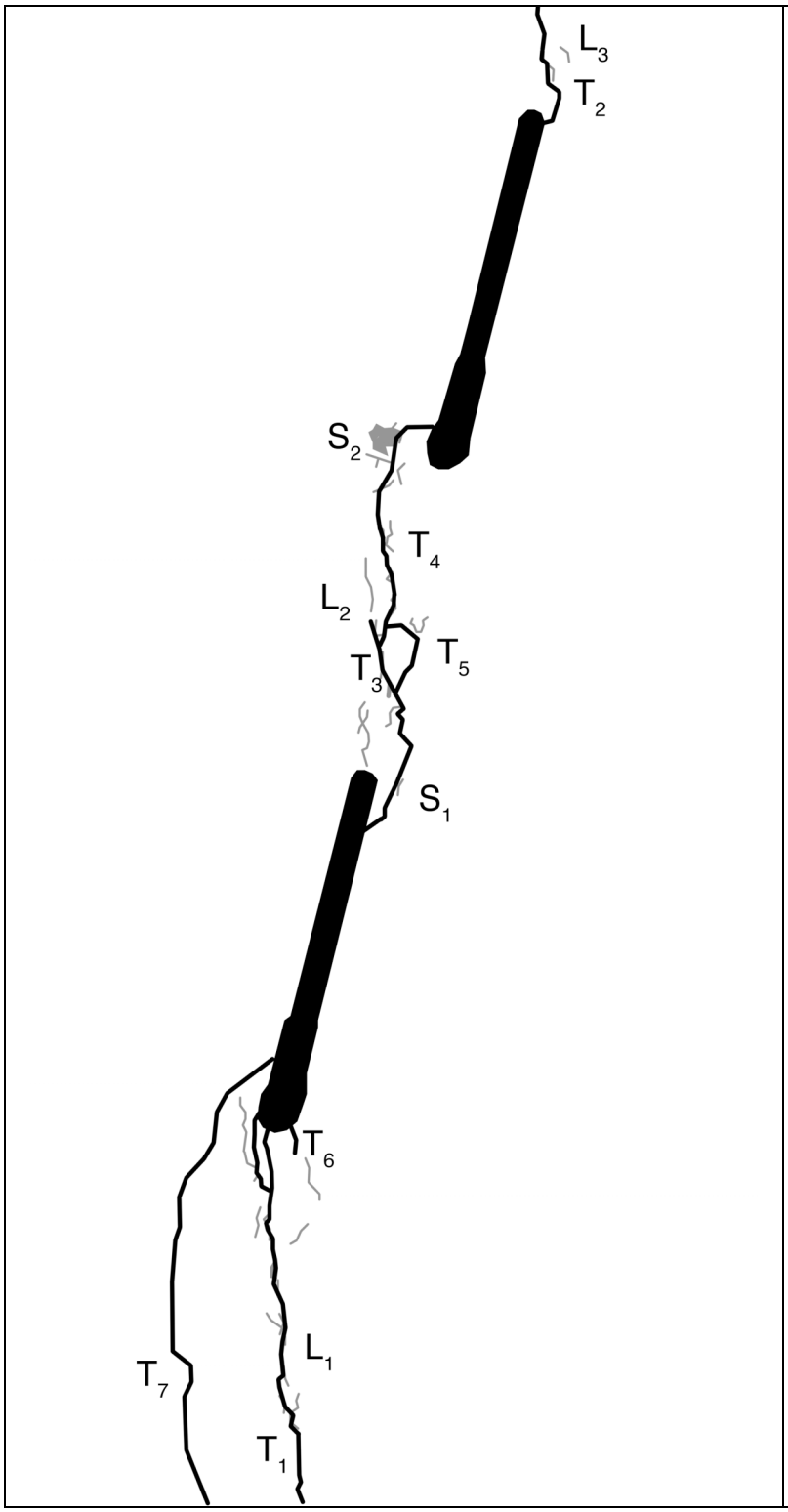

Time: 13m11.346s
σ: 66.6652 MPa

Sample failure occurs with the growth of tensile crack T_7 downward from the left flaw.

Gr 2a-75-0 C (20071002)

Summary

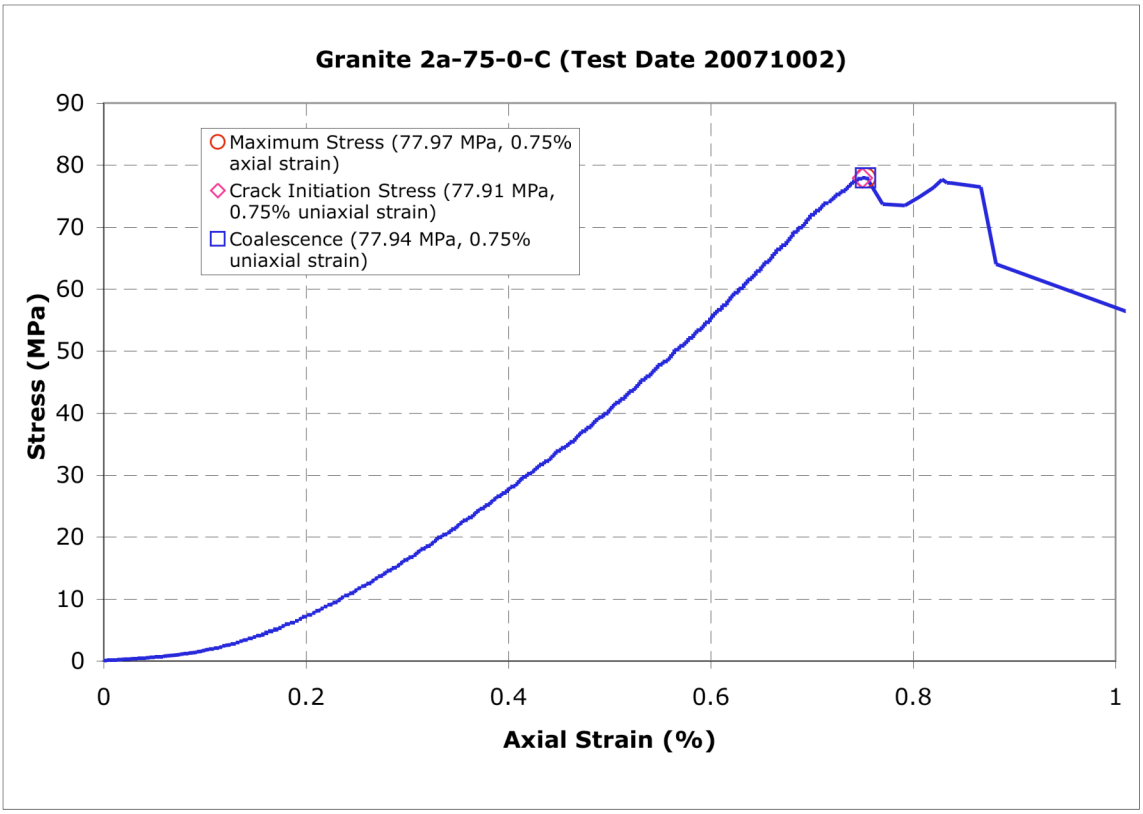

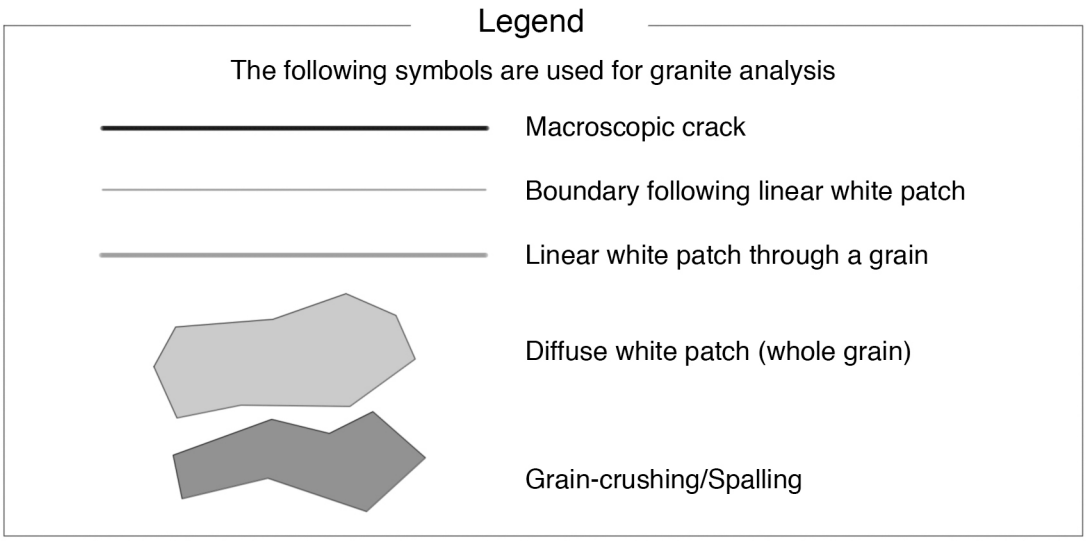

Category 5 Coalescence
Images taken from high-speed video

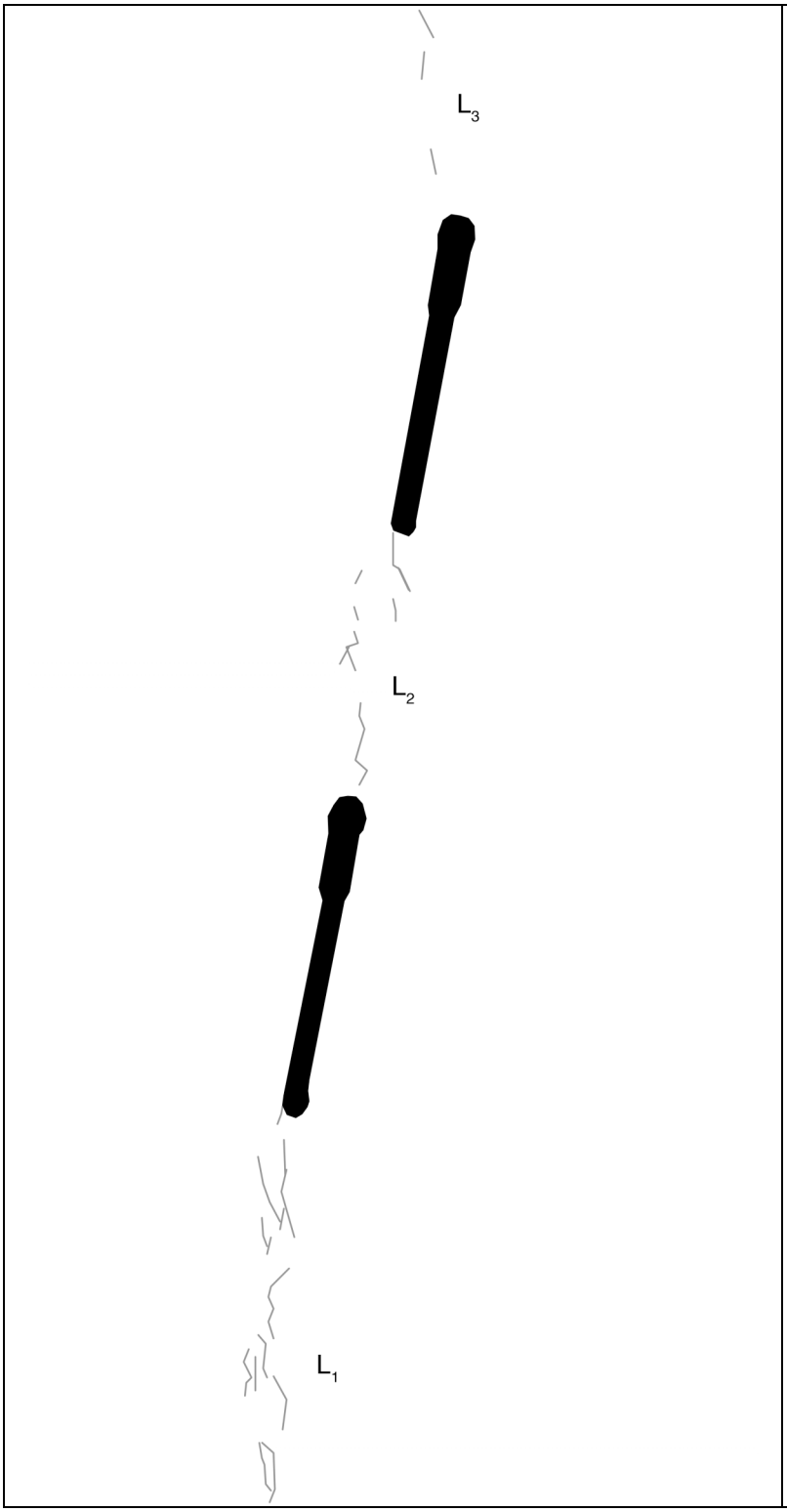

Time: 0.6656s before failure

Linear white patches L_1, L_2, and L_3 appear. All three only have boundary following features.

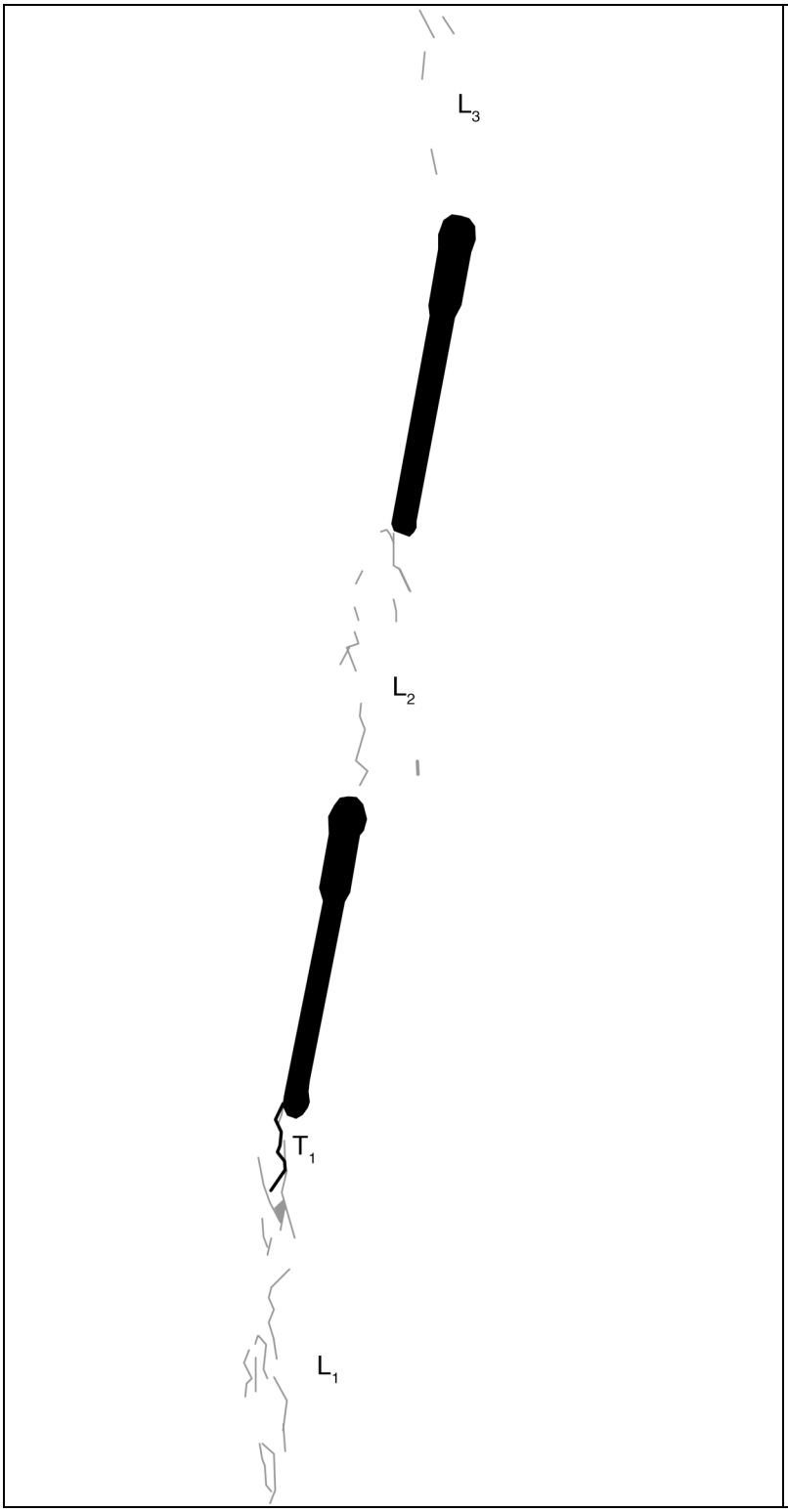

Time: 0.3847s before failure

More linear white patches appear in all three regions. A grain lightens in L_1 and a through-going linear white patch develops in L_2.

Tensile wing crack T_1 appears and extends down from the left flaw's outer tip.

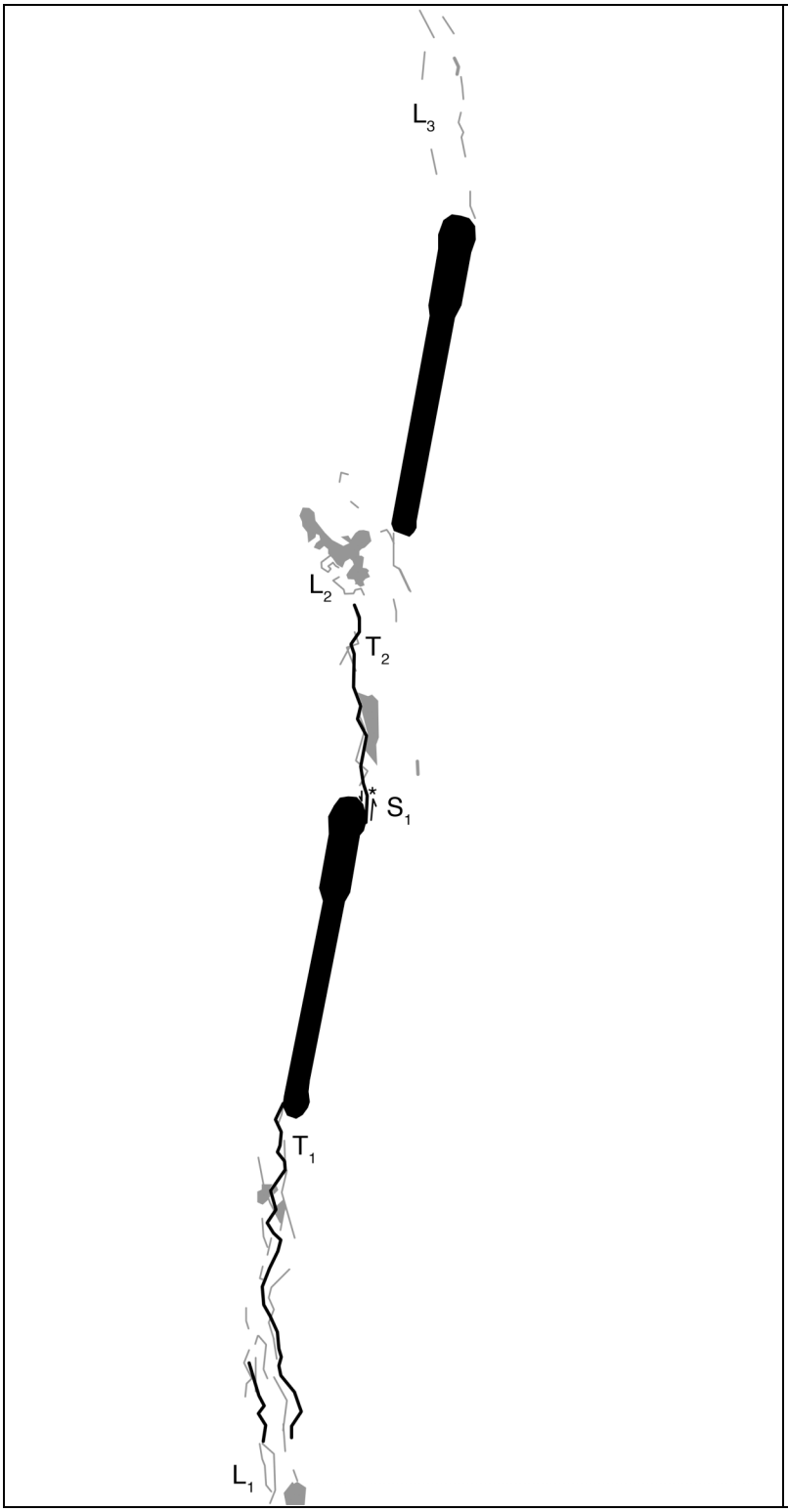

Time: 0.2214s before failure

More grains lighten in the L_1 region. T_1 extends downward. A second tensile crack opens to the left of the lower portion of T_1. Large zones of grains lighten in the L_2 region. A tensile wing crack extends up from the left flaw's inner tip. From the flaw tip to the point indicated by the '*', the crack is a shear crack (labeled S_1) shearing in the sense shown while beyond that point, the crack is a tensile crack (labeled T_2). It is unclear if the shear crack initiates before or simultaneous with the tensile crack. More linear features also appear in the L_3 region (mostly boundary-following, but including one through-going feature).

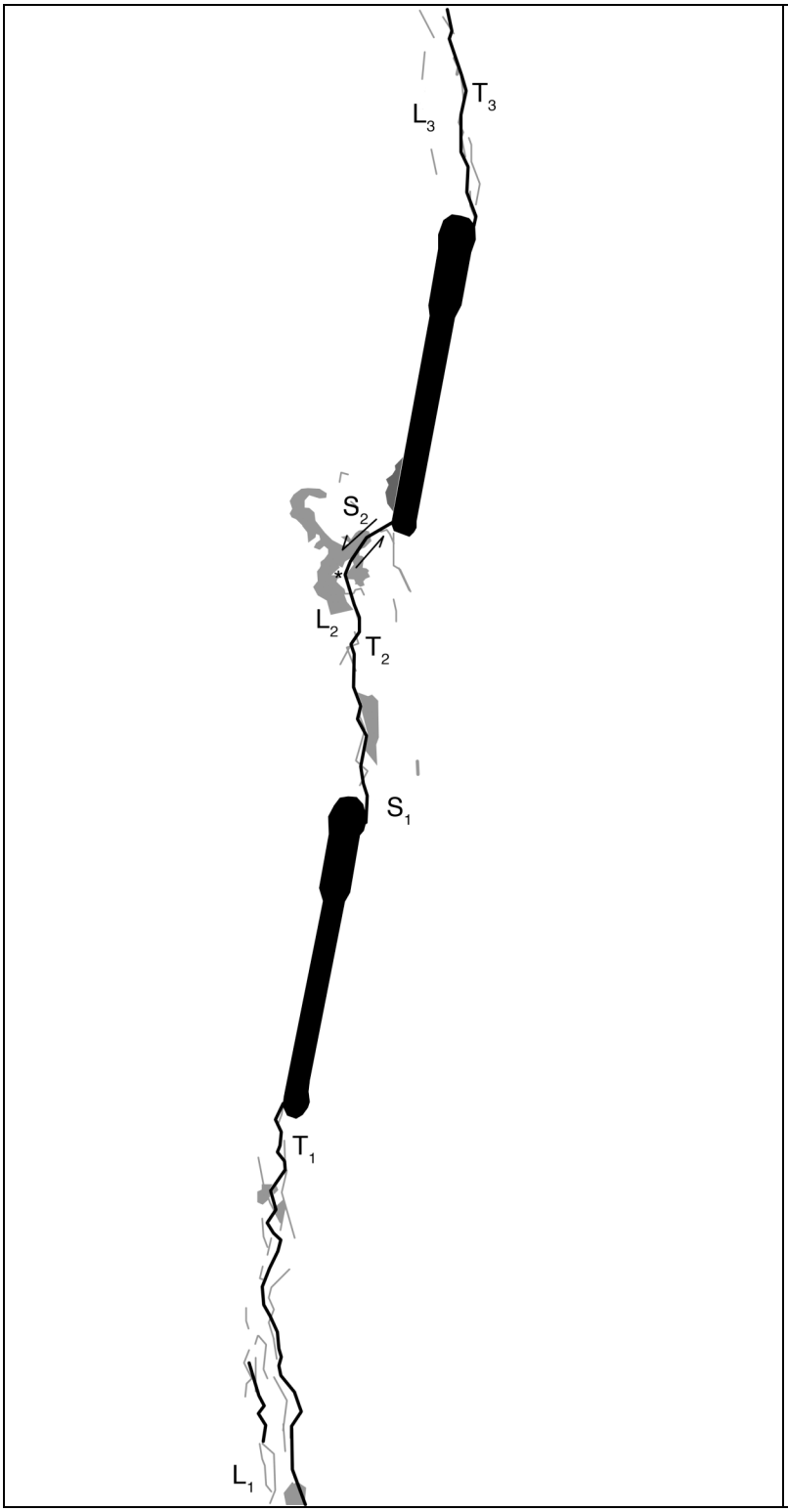

Time: 0.2165s before failure

Sample coalescence occurs as T_2 extends upward toward the right flaw's inner tip. After this extension, the crack then transitions to a shear crack again (labeled S_2) at the point indicated by the '*'. S_2 shears in the direction shown. Above the point where S_2 connects with the flaw tip, several grains spall. More grains in L_2 lighten. Tensile wing crack T_3 appears and extends upward from the right flaw's outer tip. T_1 also extends downward.

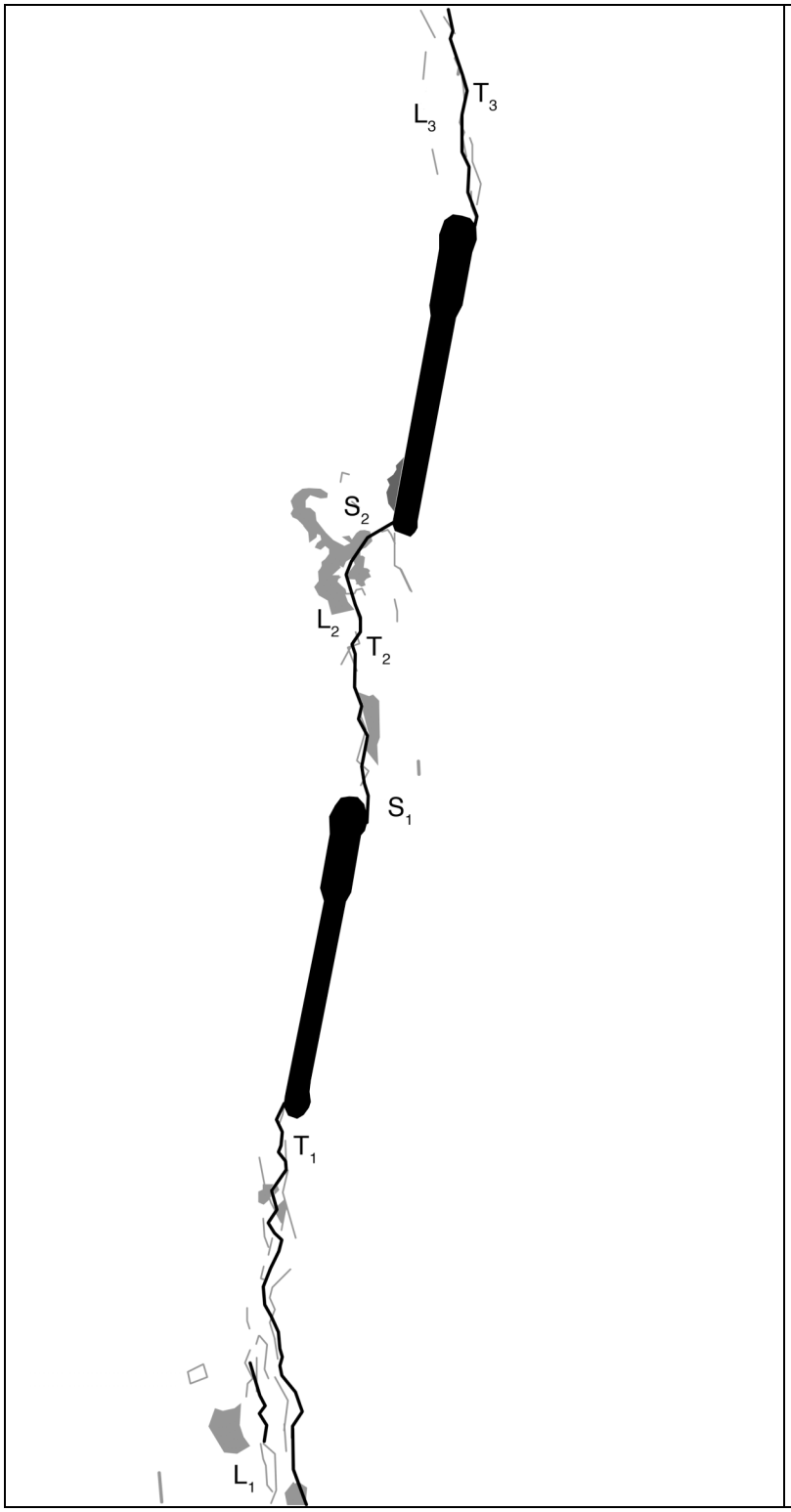

Time: 0.1399s before failure

A group of grains lighten near the bottom of L_1 and other linear features also appear in the same area. Most are boundary-following while one is through-going.

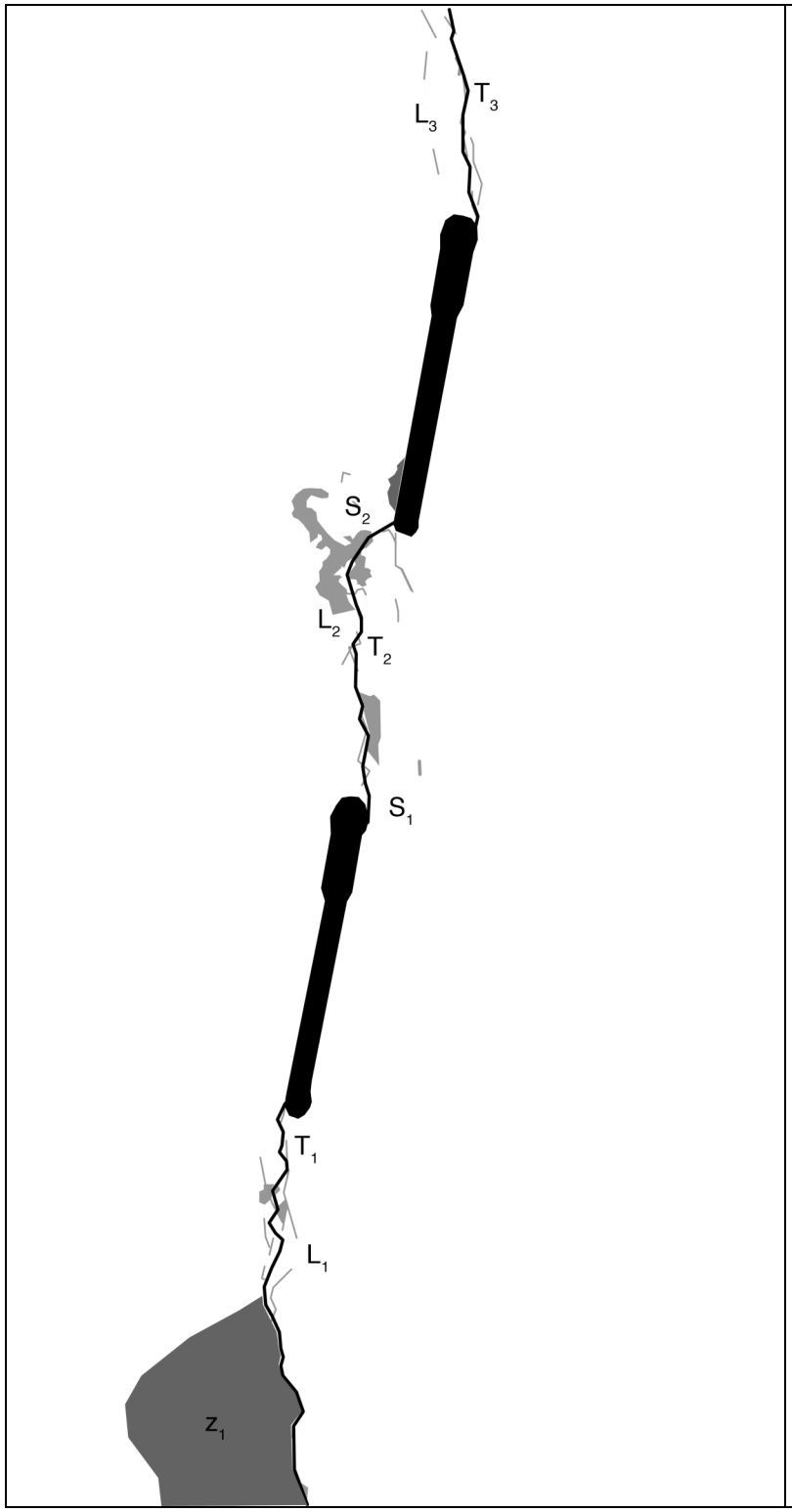

Time: 0.1398s before failure

A large zone (labeled z_1) in the lower half of L_1 bursts and all grains are crushed.

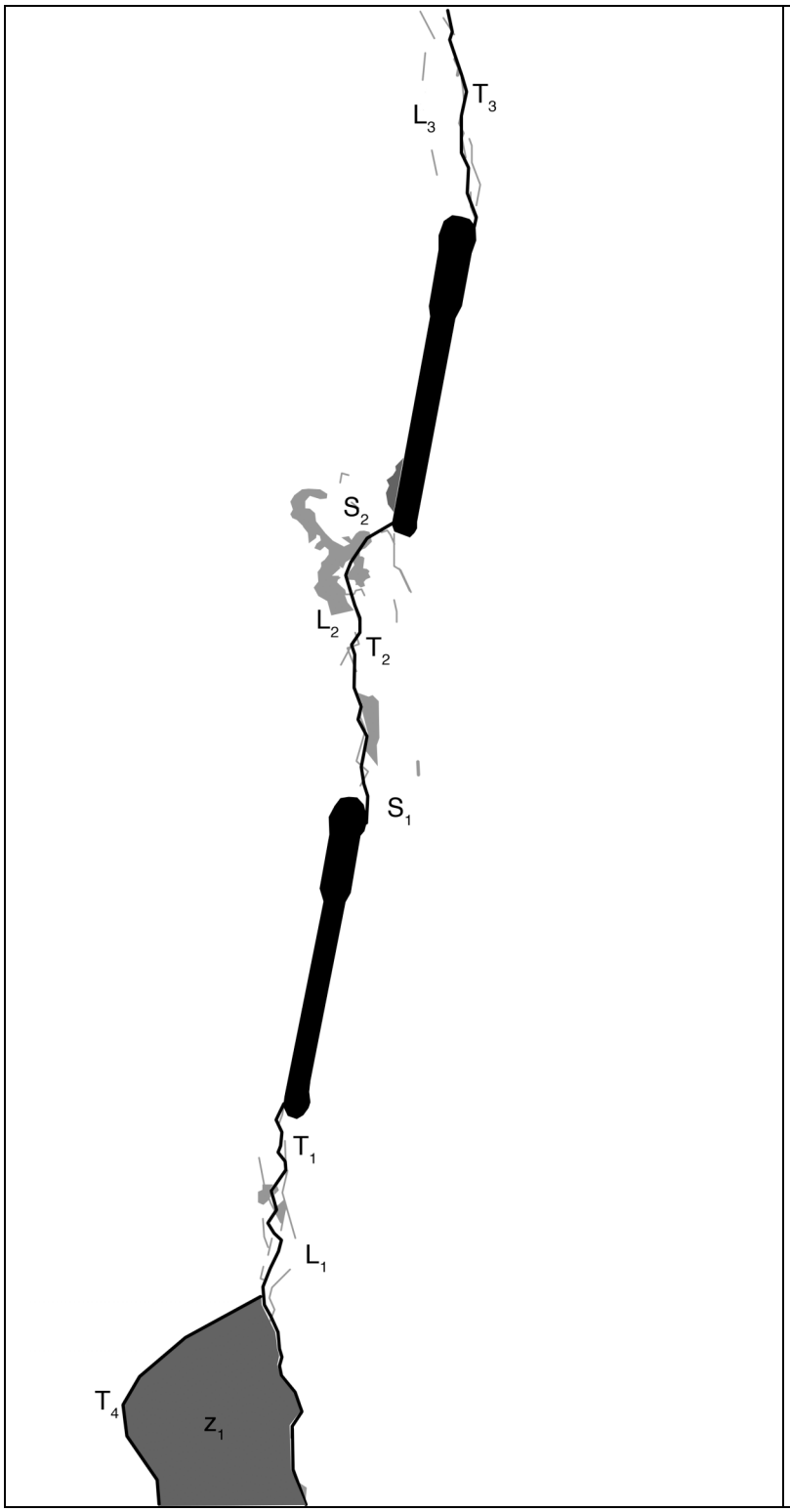

Time: 14m10.716s
σ: 77.9722 MPa

Specimen failure occurs when grains within zone z_1 are ejected as tensile crack T_4 appears along its boundary.

APPENDIX H – Stepped Flaws Separated by '2a'

The following detailed analyses are for specimens with stepped flaws ($\alpha = 60°$) and L = 2a (see Section 3.2 for an explanation of flaw geometry). Brush platens (see Section 3.2 for a description of platens) were used in all cases. For an overall summary of the results of these experiments, see Section 4.3.3.

Gr 2a-0-60 B (20071006)

Summary

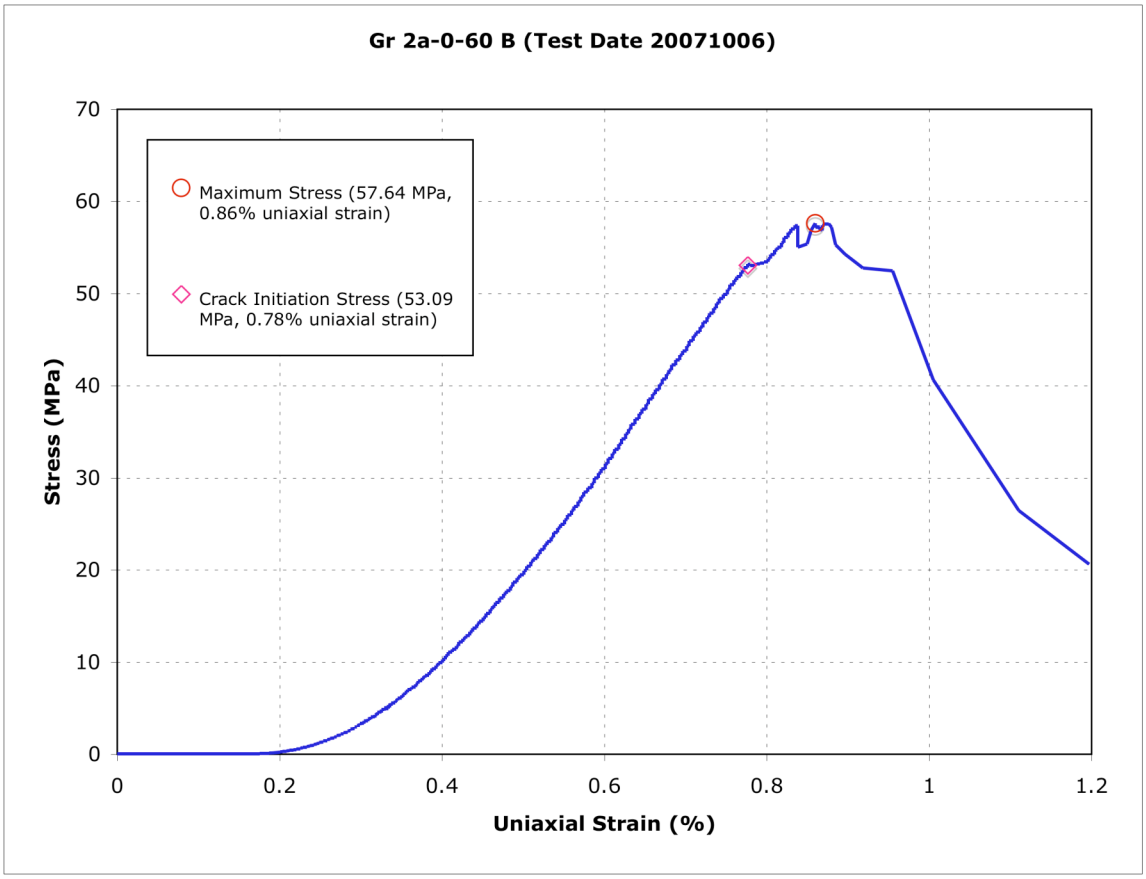

Legend

The following symbols are used for granite analysis

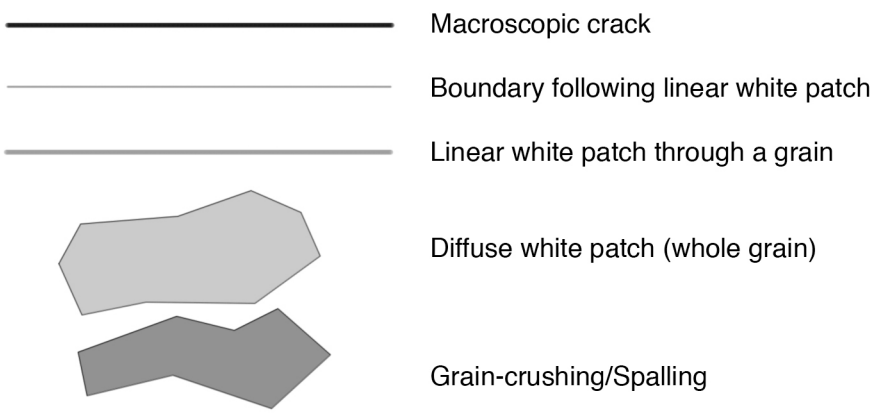

Category one coalescence

Images taken from high-speed video unless otherwise noted

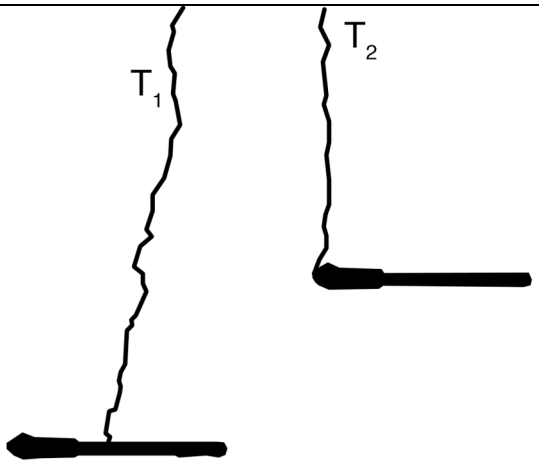	**Time:** 10m12.74s **σ:** 53.09 MPa Image taken from camcorder video. Tensile crack T_1 appears above the middle of the left flaw while tensile wing crack T_2 opens from the right flaw's inner tip. *Note: Images taken from camcorder do not show linear white patches or diffuse white patches well enough for analysis purposes.
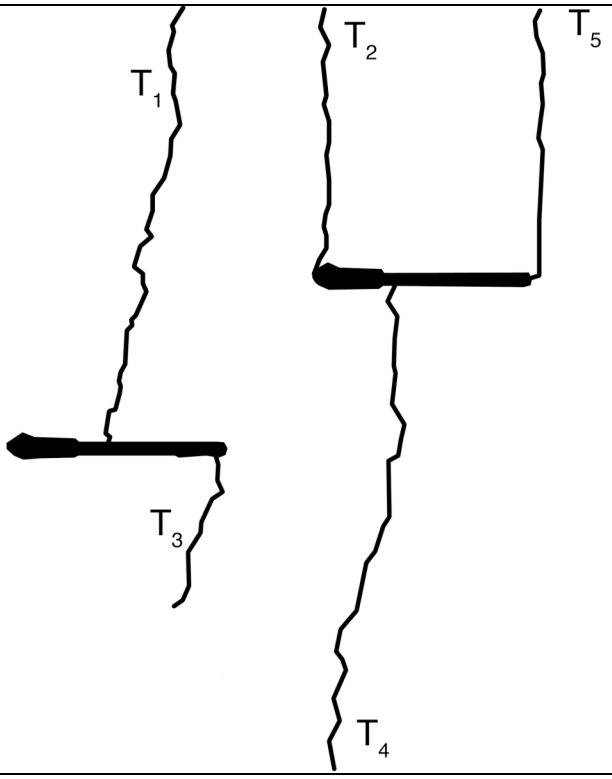	**Time:** 11m03.50s **σ:** 57.21 MPa Image taken from camcorder video Tensile cracks T_3, T_4, and T_5 open. T_3 is a tensile wing crack on the left flaw while the other two are on the right flaw.

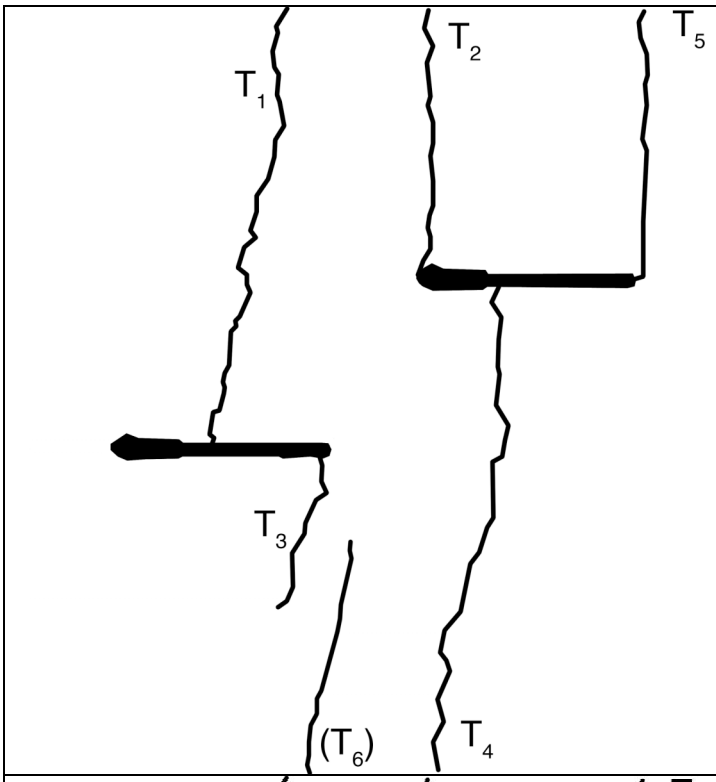	**Time:** 0.3798s before failure First image taken from high-speed video Tensile crack (T_6) appears and propagates upward toward the left flaw's inner tip.
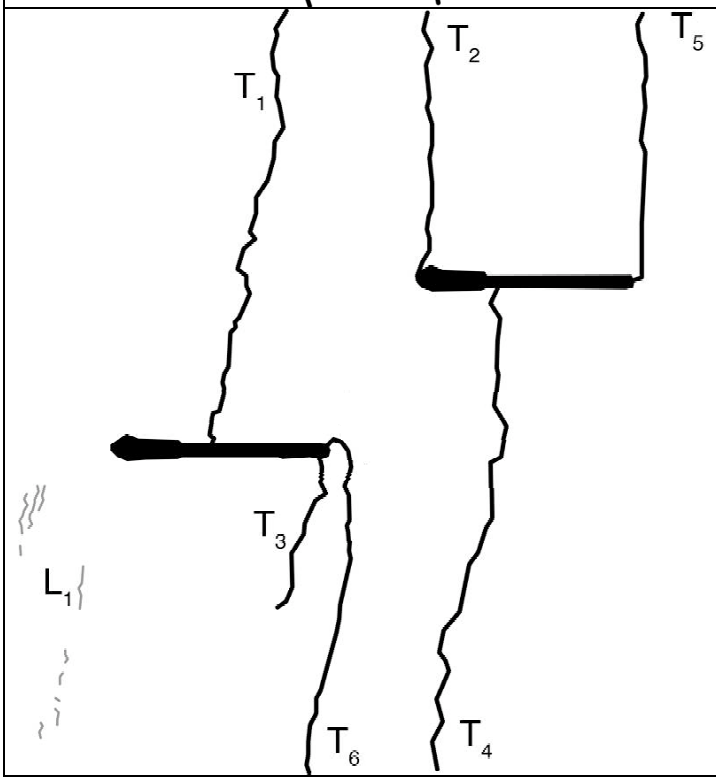	**Time:** 0.306s before failure (T_6) continues upward until it connects with the left flaw's inner tip (and becomes T_6) . Note: These may not be the first white features in the loading history, but the first seen with high-speed video.

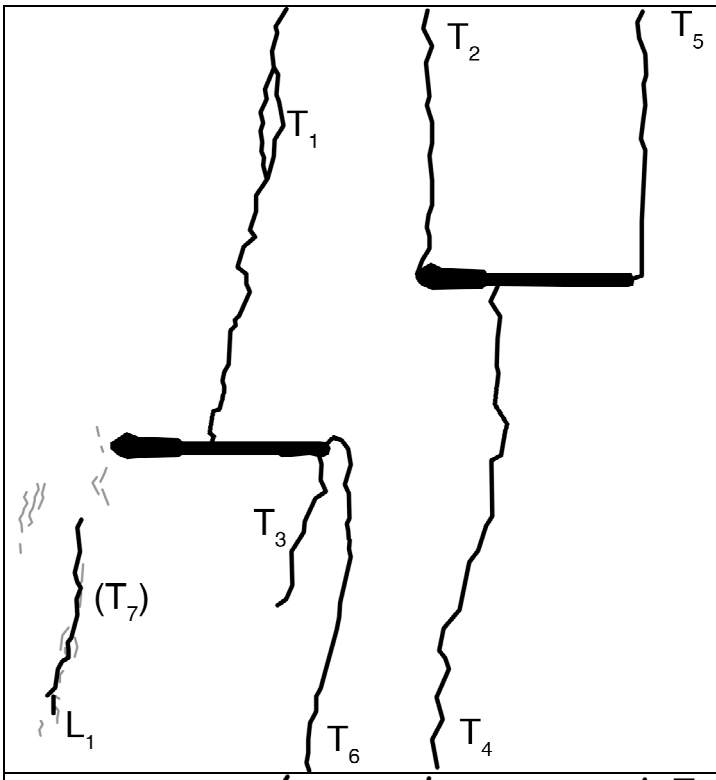	**Time:** 0.2472s before failure Tensile crack (T_7) appears within the L_1 region. More boundary-following white patches appear closer to the flaw tip. T_1 branches and connects with itself.
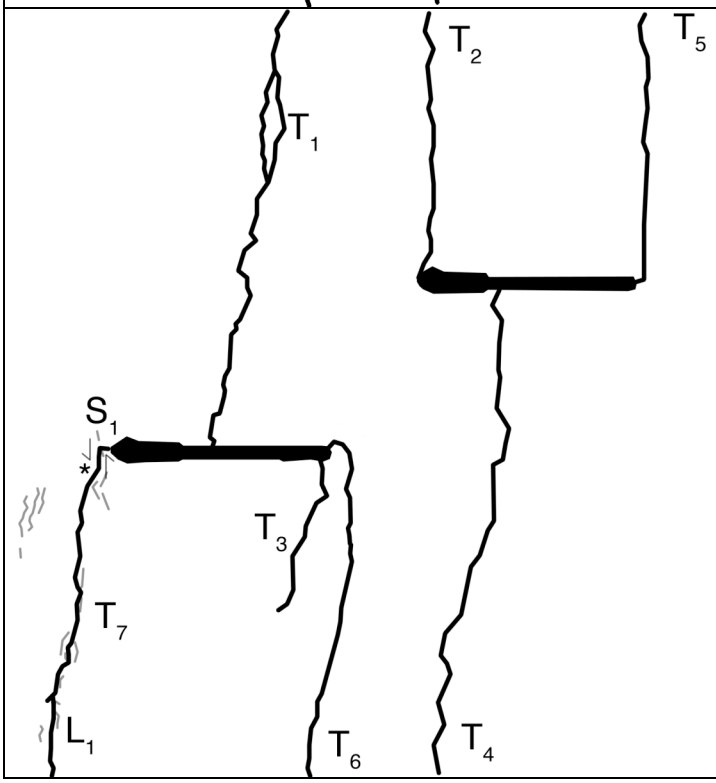	**Time:** 0.2282s before failure (T_7) grows both upward and downward. Shear crack S_2 connects with T_7 at a point labeled '*' and with the left flaw's outer tip. S_2 shears in the sense indicated.

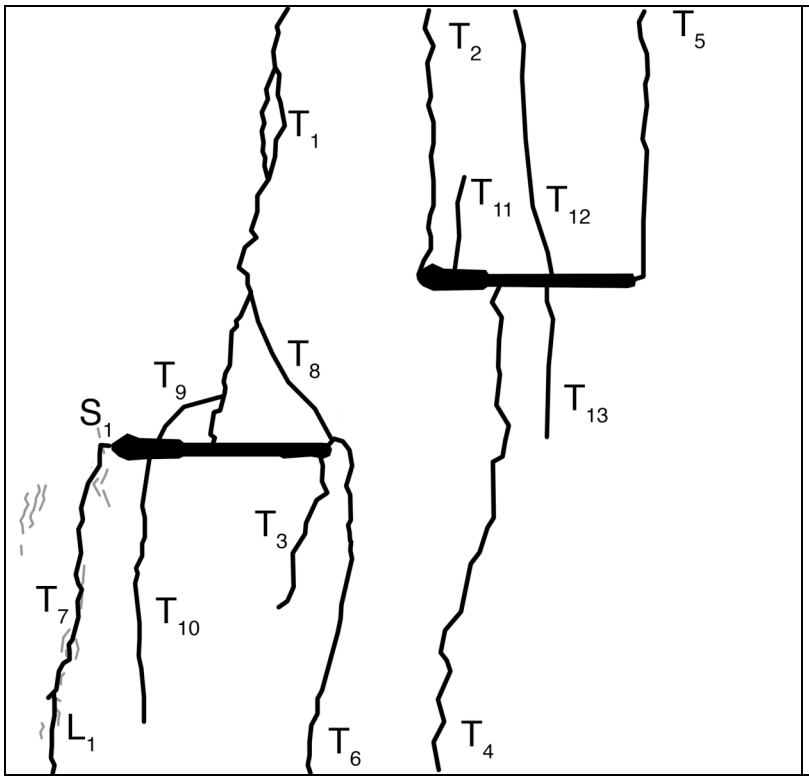

Time: 11m05.940s
σ: 57.64 MPa

Sample failure occurs with the formation of tensile cracks T_8 through T_{13}.

Gr 2a-0-60 C (20071006)

Summary

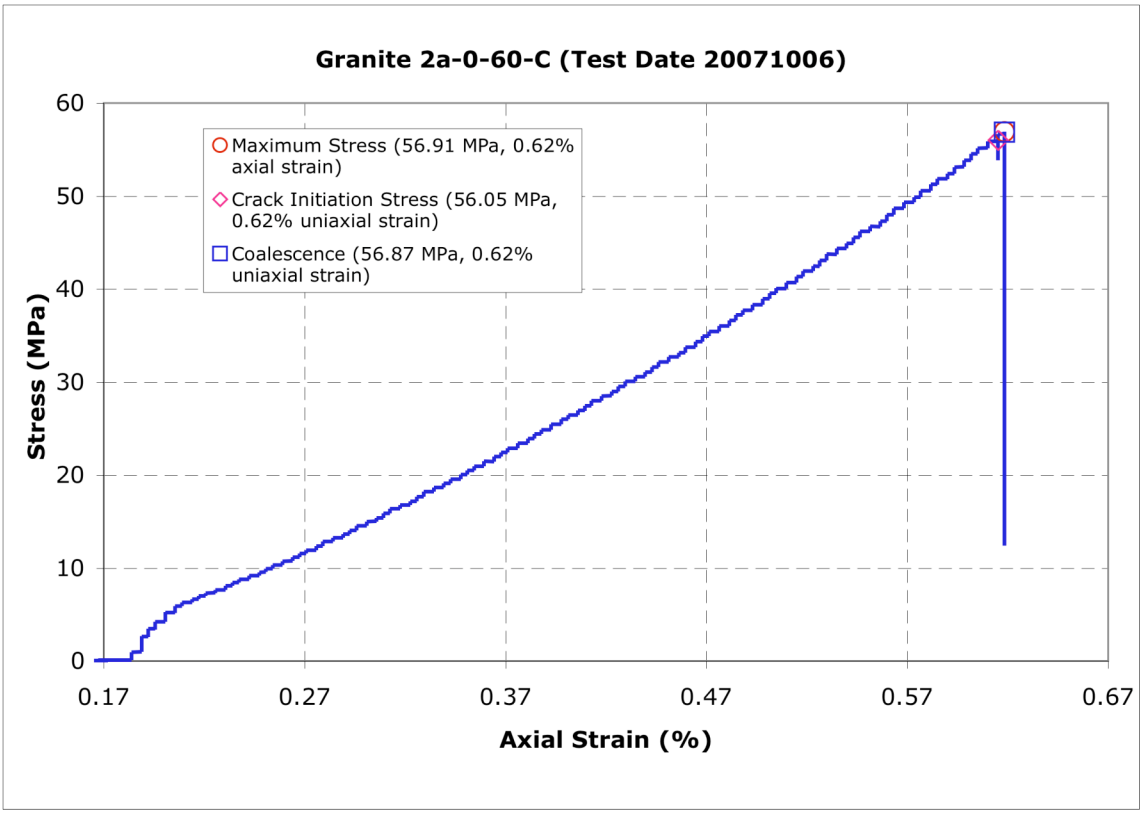

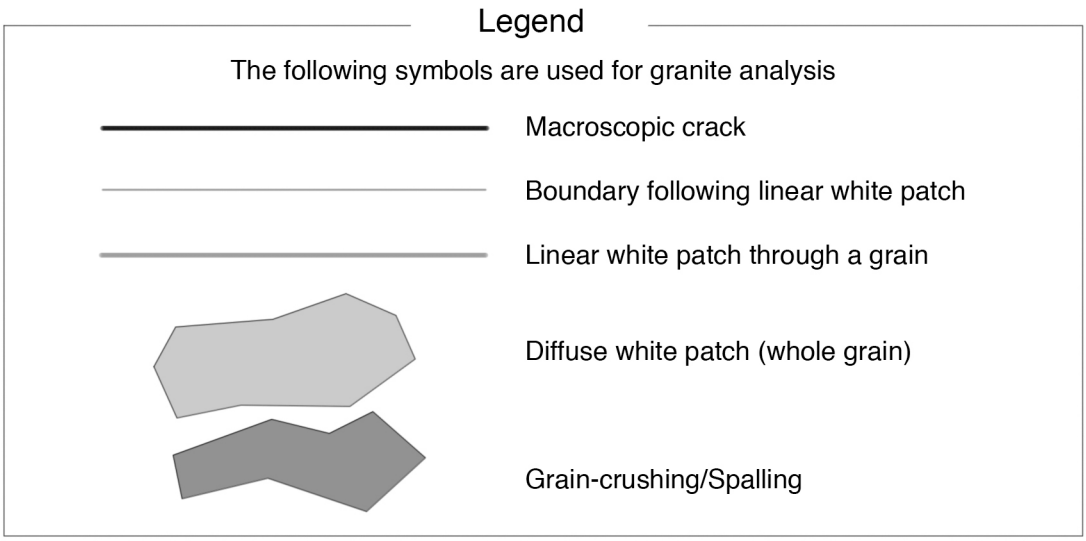

Category two coalescence

Images taken from high-speed video unless otherwise noted

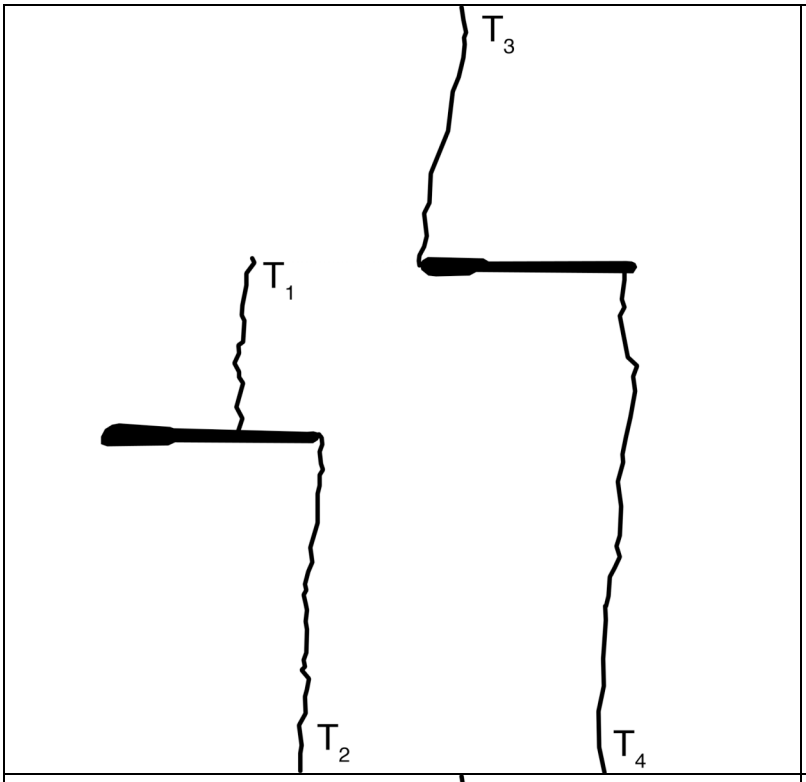	**Time:** 10m16.76s Image taken from camcorder video. Tensile cracks T_1 through T_4 appear. *Note: Images taken from camcorder do not show linear white patches or diffuse white patches well enough for analysis purposes.
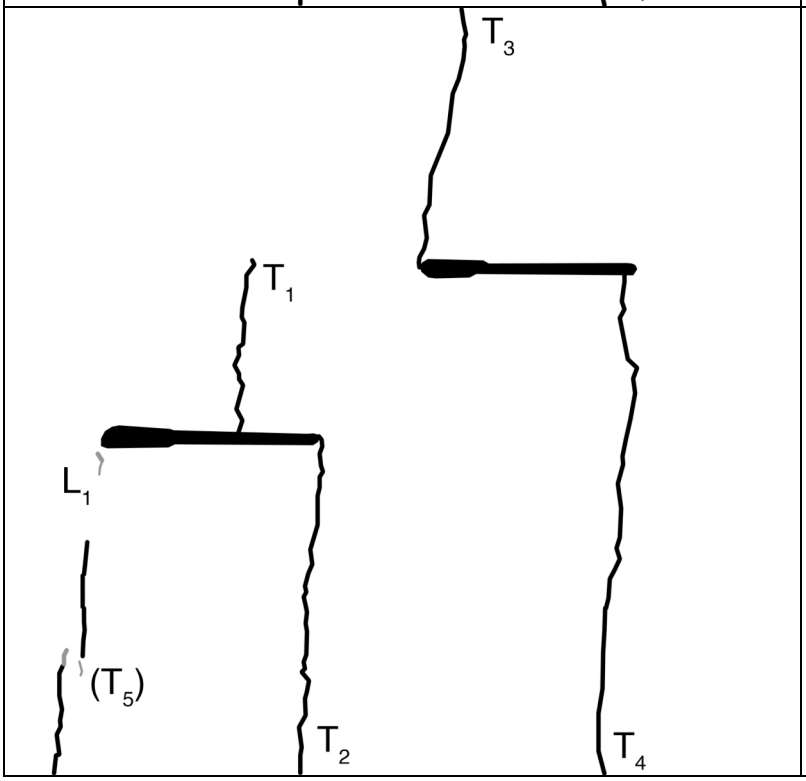	**Time:** 0.4874s before failure Image taken from high-speed video. Two tensile cracks appear below the outer tip of the left flaw. They are labeled (T_5). Linear white patches (labeled L_1) form in the same region. Both boundary-following and through-going linear features are present.

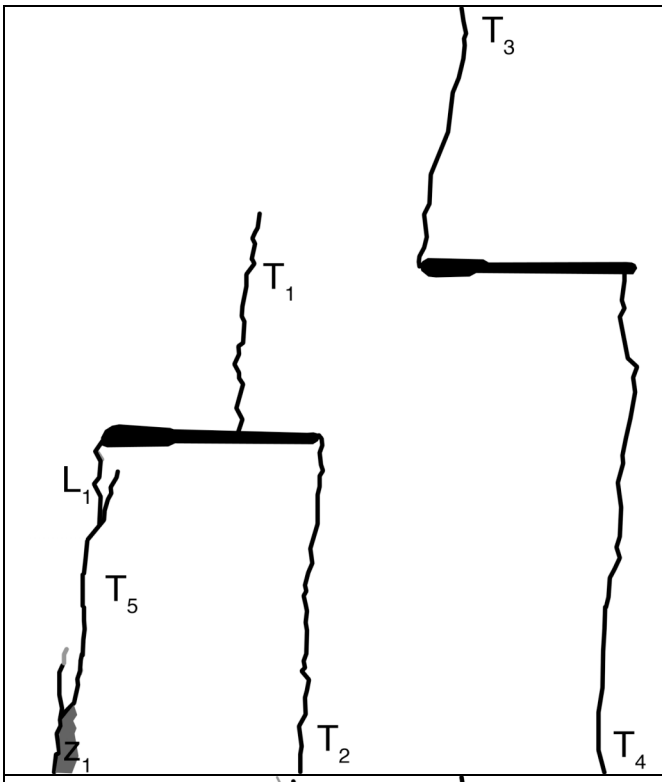	**Time:** 0.4872s before failure (T_5) grows upward and downward (branching at two points as well) and connects with the left flaw's outer tip, becoming tensile wing crack T_5. Some grains are crushed in the zone labeled z_1.
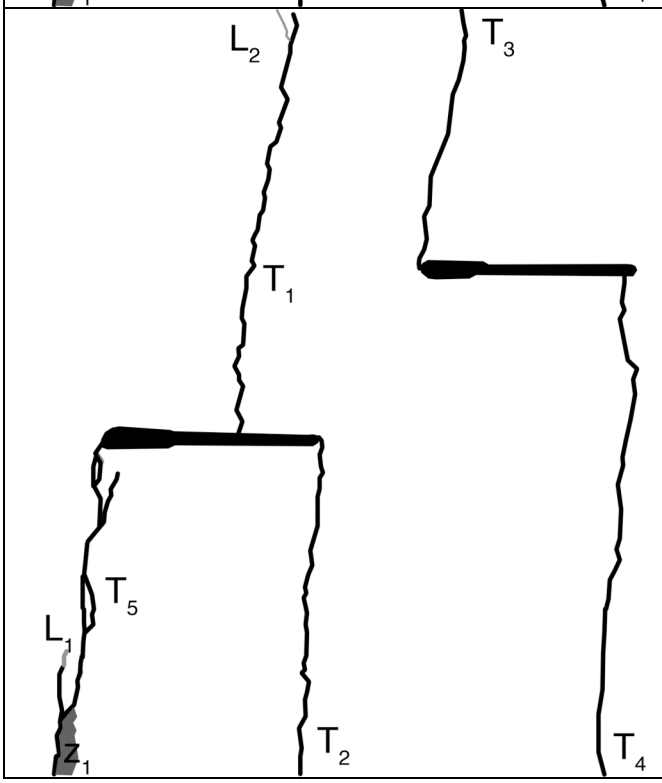	**Time:** 0.4870s before failure More branching occurs along T_5. T_1 extends upward and has a boundary-following linear white patch (labeled L_2) extend near it as well.

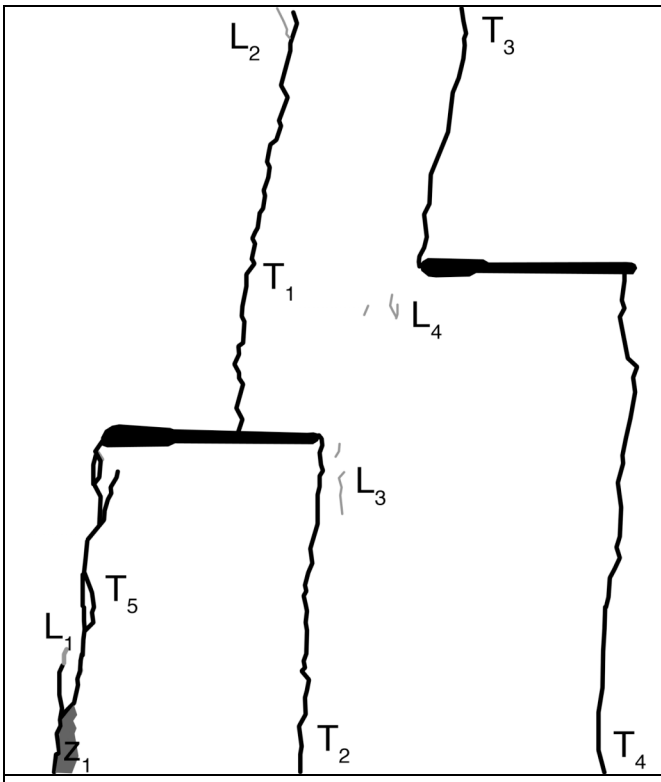	**Time:** 0.4778s before failure Two groups of linear white patches form in the bridge area. L_3 forms near the left flaw's inner tip, while L_4 forms near the right flaw's inner tip. Both are composed solely of boundary-following linear white patches.
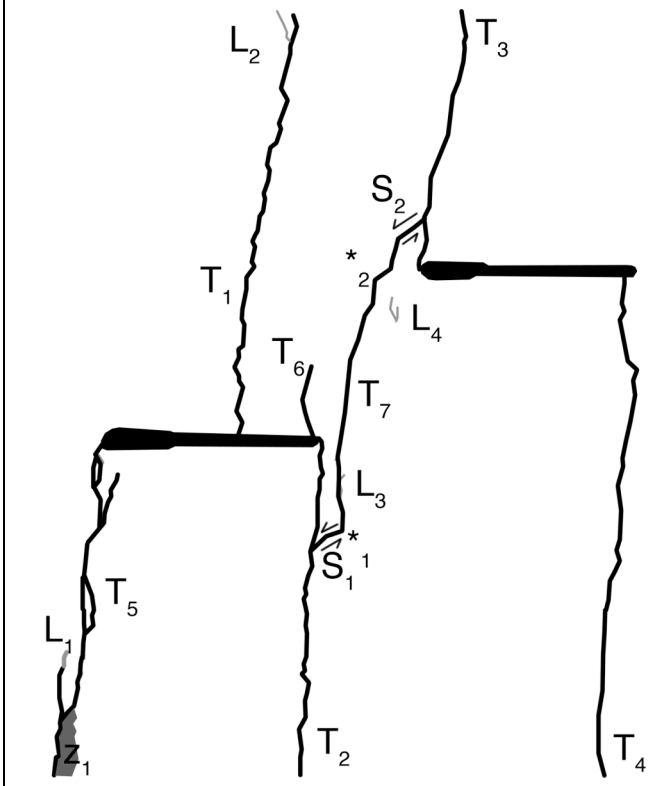	**Time:** 0.4776s before failure Indirect coalescence occurs when tensile wing cracks T_2 and T_3 are connected. The coalescing crack is composed of shear portions near the wing cracks with a central tensile portion. S_1 is the shear crack near T_2 (extending from T_2 to the point labeled $*_1$) and S_2 is the shear crack near T_3 (extending from T_3 to $*_2$). Both shear cracks shear in the direction indicated. The central portion of the coalescing crack is T_7. S_1, S_2, and T_7 appear in a single high-speed frame. Tensile wing crack T_6 appears above the left flaw's inner tip.

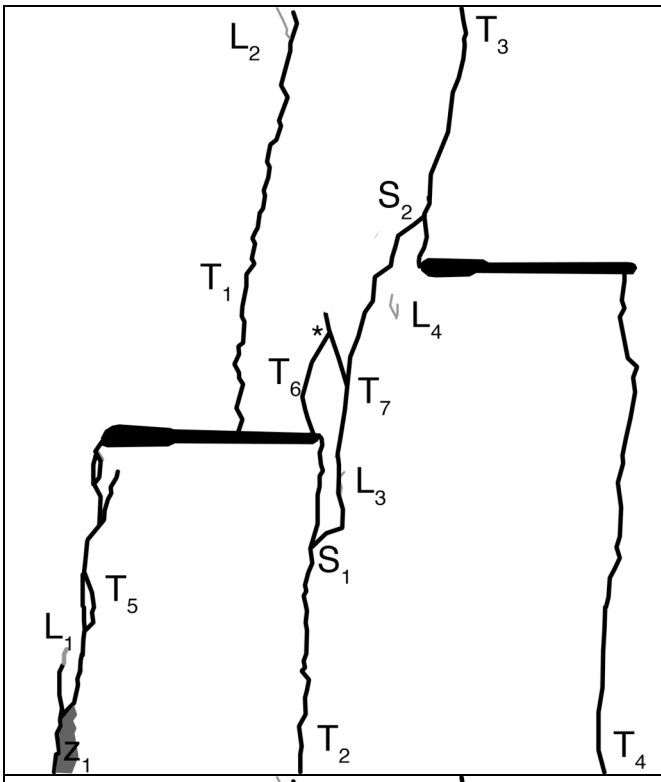	**Time:** 0.3786s before failure T_6 and T_7 connect at the point labeled with a '*'.
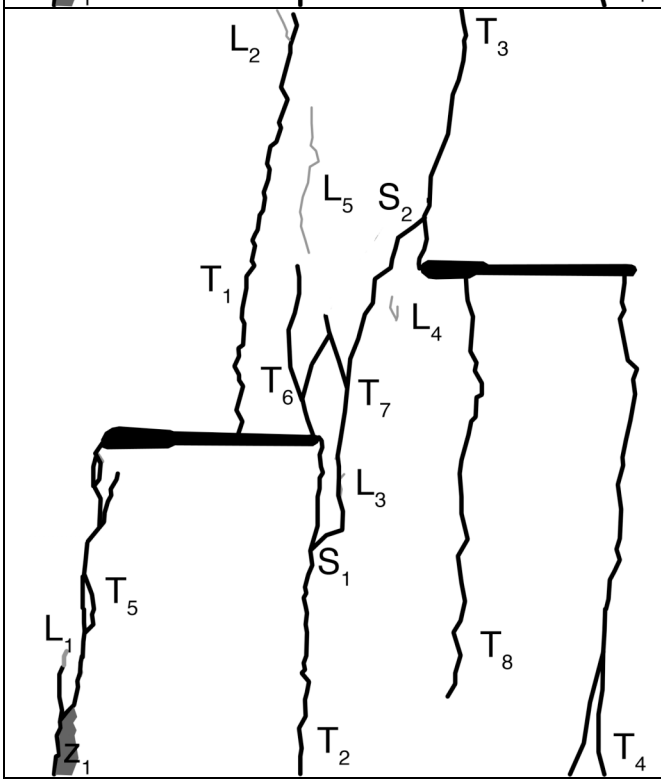	**Time:** 0.1012s before failure Linear white patch L_5 appears above T_6. It is composed of boundary-following white patches only.

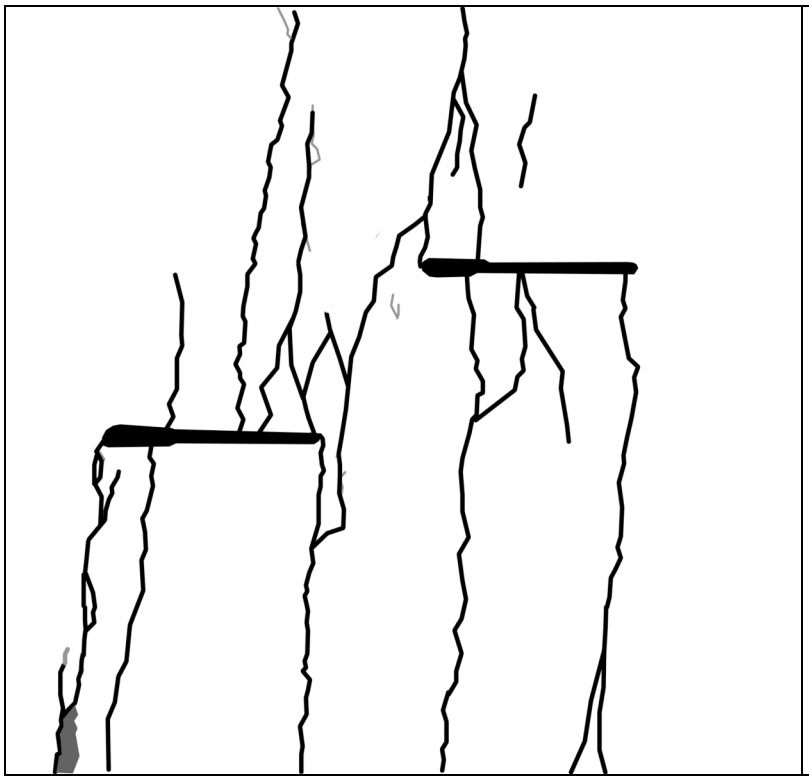

Time: 10m26.97s
σ: 56.9126 MPa

Sample failure occurs with the formation of several new tensile cracks.

Gr 2a-30-60 B (20071006)
Summary

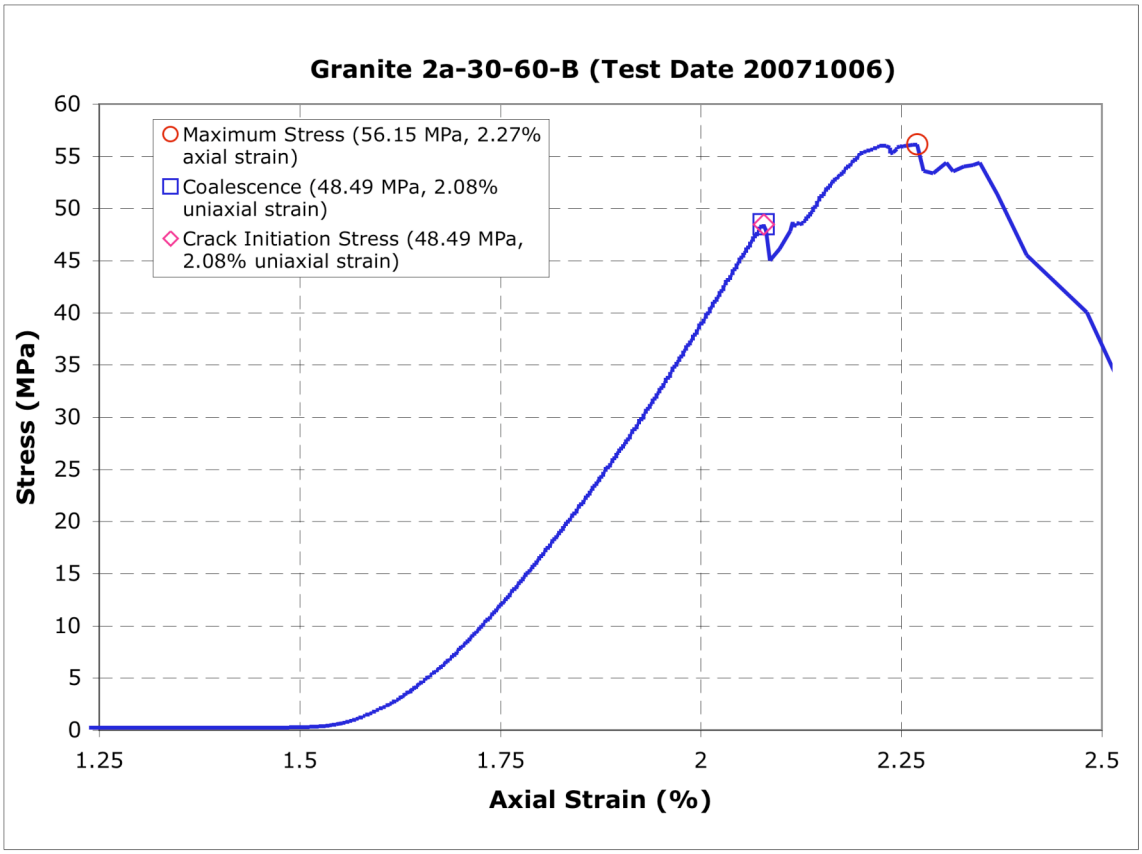

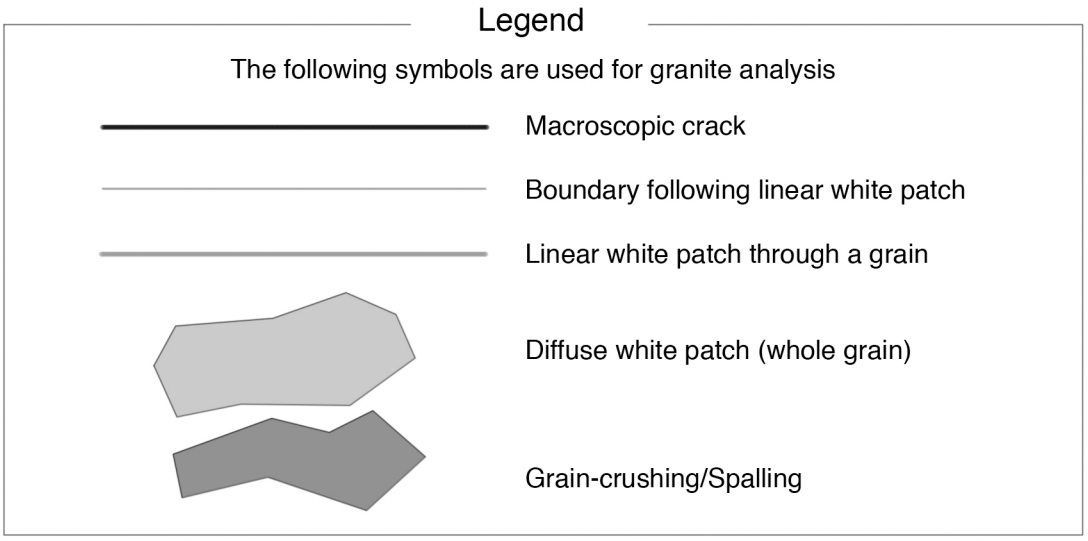

Category six coalescence
Images taken from high-speed video unless otherwise noted

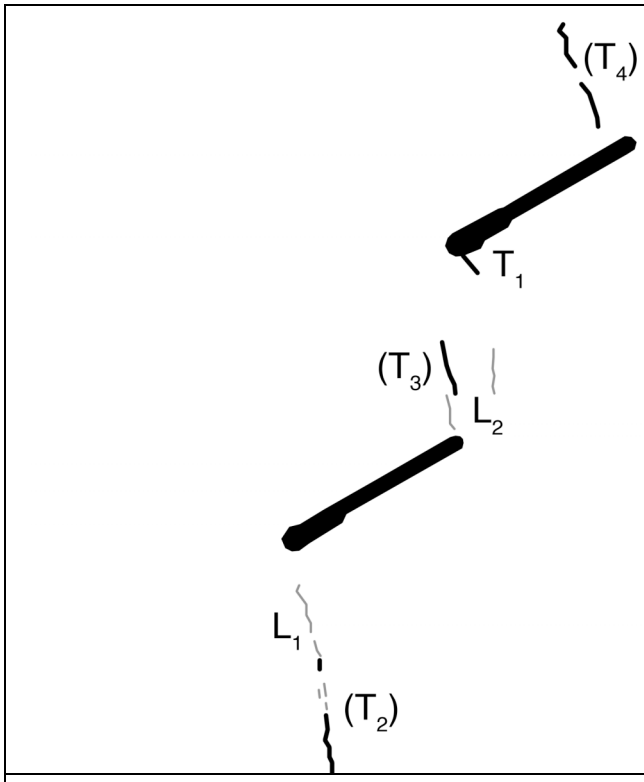	**Time:** 0.0036s before coalescence Tensile wing crack T_1 forms on the inner tip of the right flaw. Tensile cracks (T_2), (T_3), and (T_4) also appear near flaw tips. Linear white patches L_1 and L_2 also appear. They are composed only of boundary-following white patches.
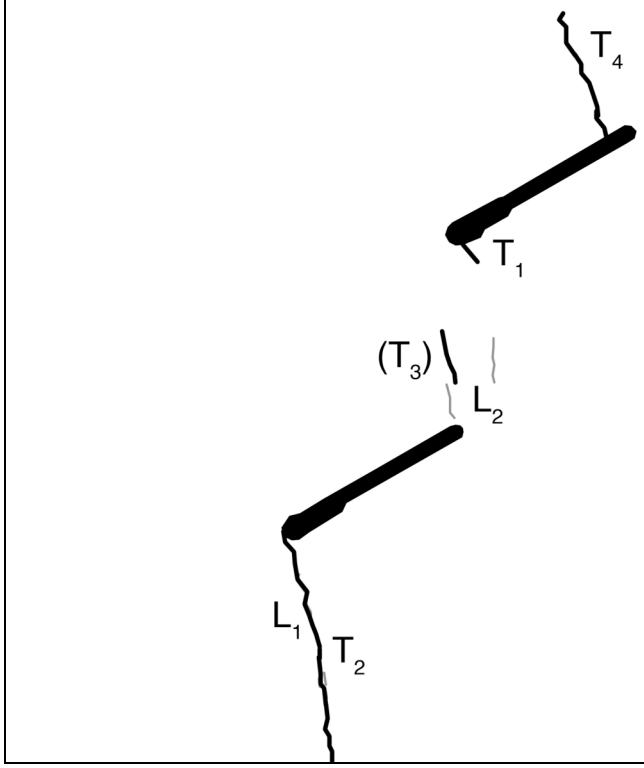	**Time:** 0.003s before coalescence (T_2) and (T_4) extend and connect with the flaw tips, becoming T_2 and T_4, respectively.

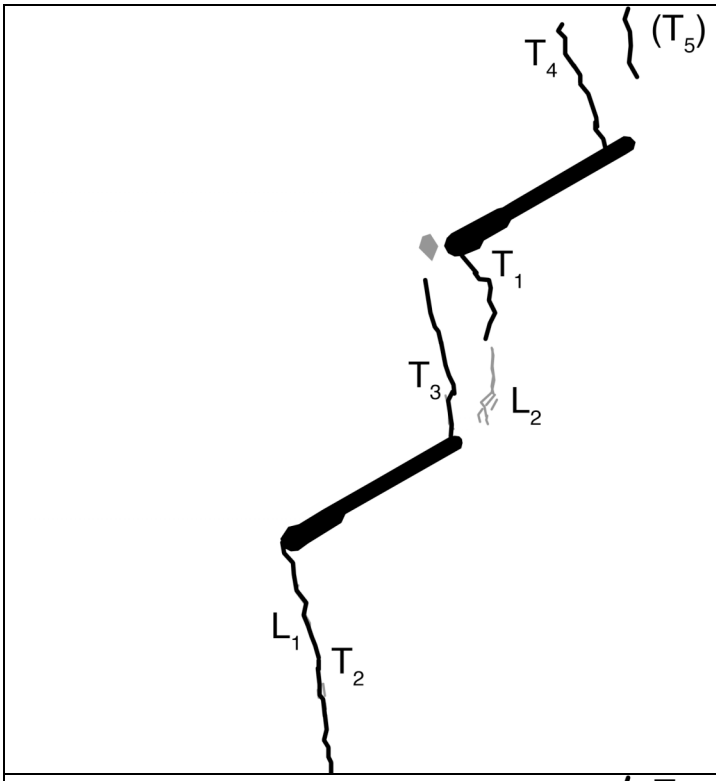	**Time:** 0.0002s before coalescence (T_3) extends both upward and downward, connecting to the inner tip of the left flaw, becoming T_3. T_1 extends downward. Several grains lighten near the inner tip of the right flaw. L_2 extends and branches downward. T_5 also appears and extends downward from above the camera's field of view.
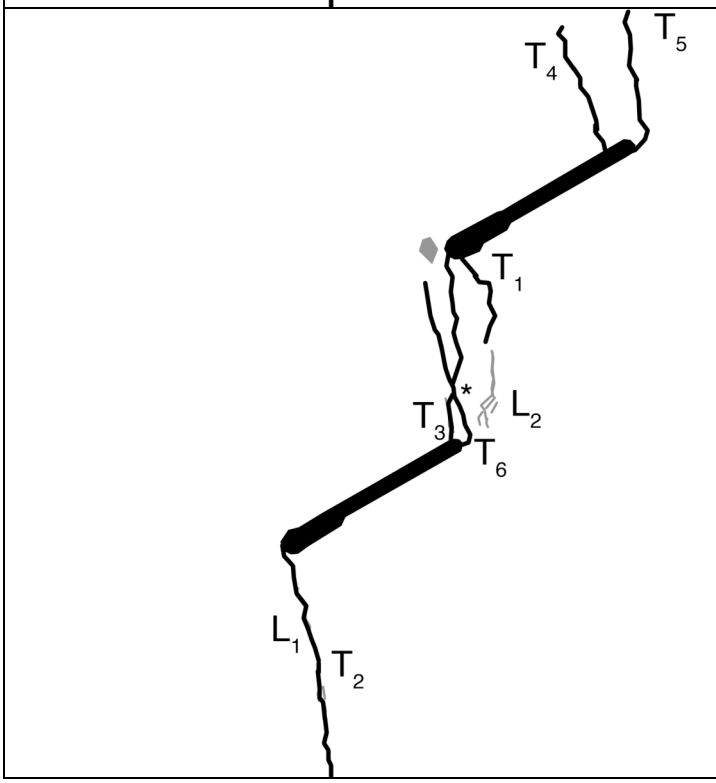	**Time:** 10m0.83s (T_5) extends downward and connects with the right flaw's outer tip, becoming tensile wing crack T_5. Tensile wing crack T_6 appears and extends upward from the left flaw's inner tip to the right flaw's inner tip. It connects with T_3 at the point indicated by the '*'. The specimen has coalesced (category six) at this point.

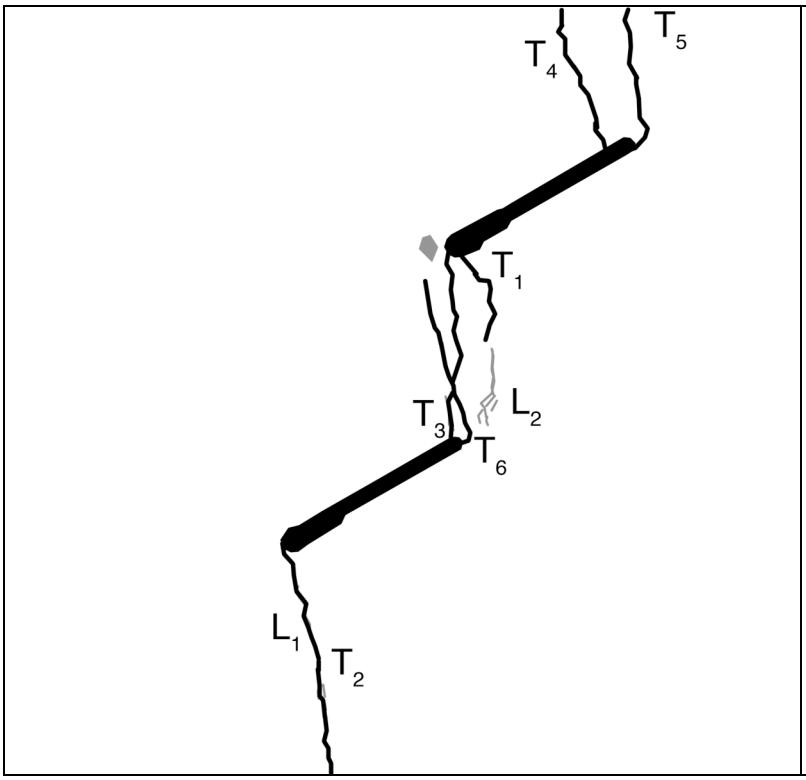	**Time:** 11m34.686s **σ:** 56.1497 MPa Specimen fails with tensile crack formation outside the camera's field of view.

Gr 2a-30-60 C (20071006)

Summary

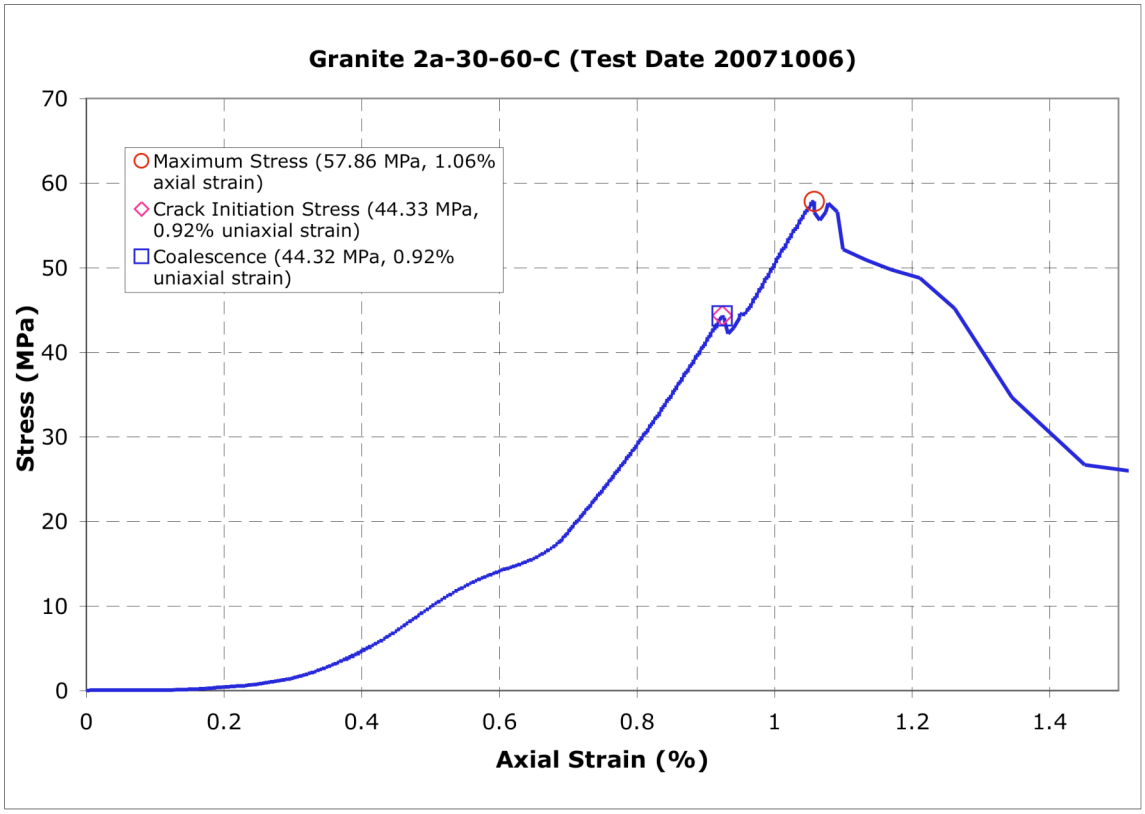

Legend

The following symbols are used for granite analysis

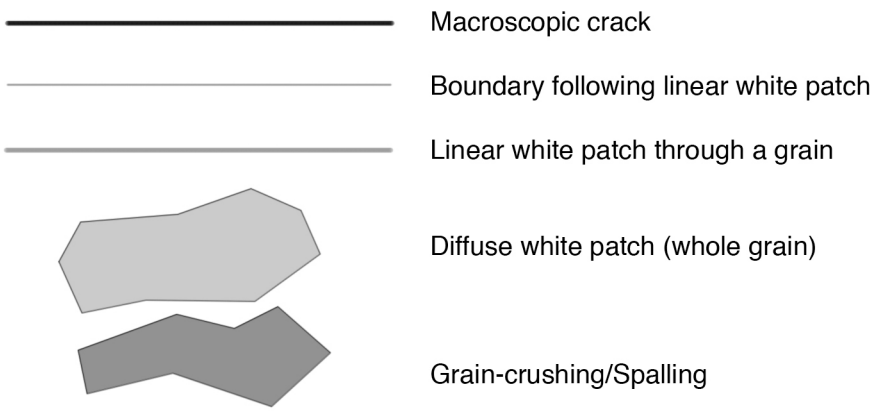

Category six coalescence

Images taken from high-speed video unless otherwise noted

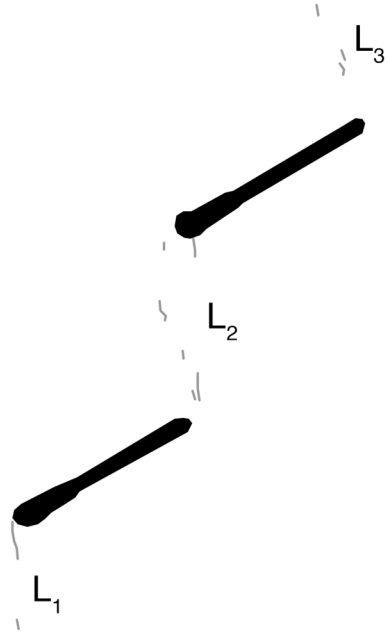	**Time:** 0.0978s before coalescence Linear white patches appear near the outer tips of both flaw as well as in the bridge area. These are labeled as L_1, L_2, and L_3. All are boundary-following linear features.
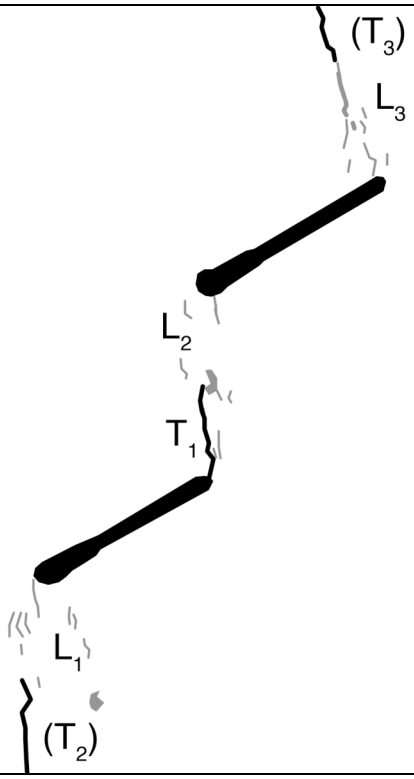	**Time:** 0.0228s before coalescence L_1, L_2, and L_3 all grow. L_1 and L_2 both have grains lighten while L_3 develops some through-going linear white patches. Tensile wing crack T_1 appears over the right flaw's inner tip. Two tensile cracks grow from outside the camera's field of view toward the outer flaw tips (labeled as (T_2) and (T_3)).

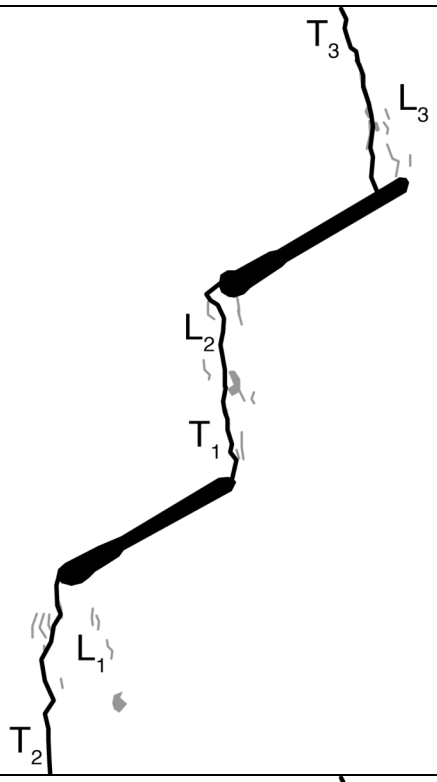	**Time:** 8m42.45s (T_2) and (T_3) both extend and connect with the outer flaw tips, becoming T_2 and T_3, respectively. T_1 extends upward and connects with the left flaw's inner tip, causing sample coalescence (category six).
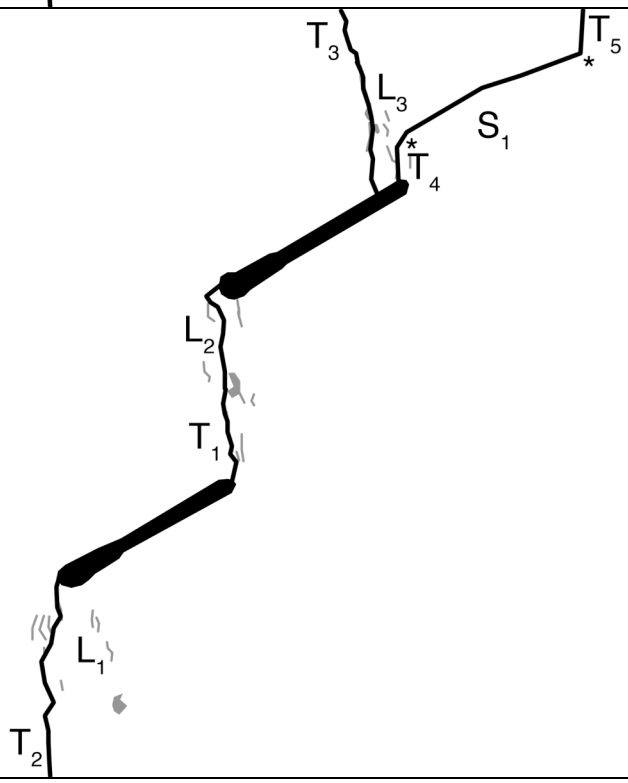	**Time:** 11m42.4555s **σ:** 57.8560 MPa Specimen failure occurs with a new wing crack that appears and extends with three distinct stages. The crack first extends from the outside tip of the right flaw as tensile crack T_4. The crack then transitions to a shear crack S_1 at the asterisk closest to the flaw. Finally, the crack becomes tensile crack T_5 at the second asterisk.

Gr 2a-45-60 A (20071006)

Summary

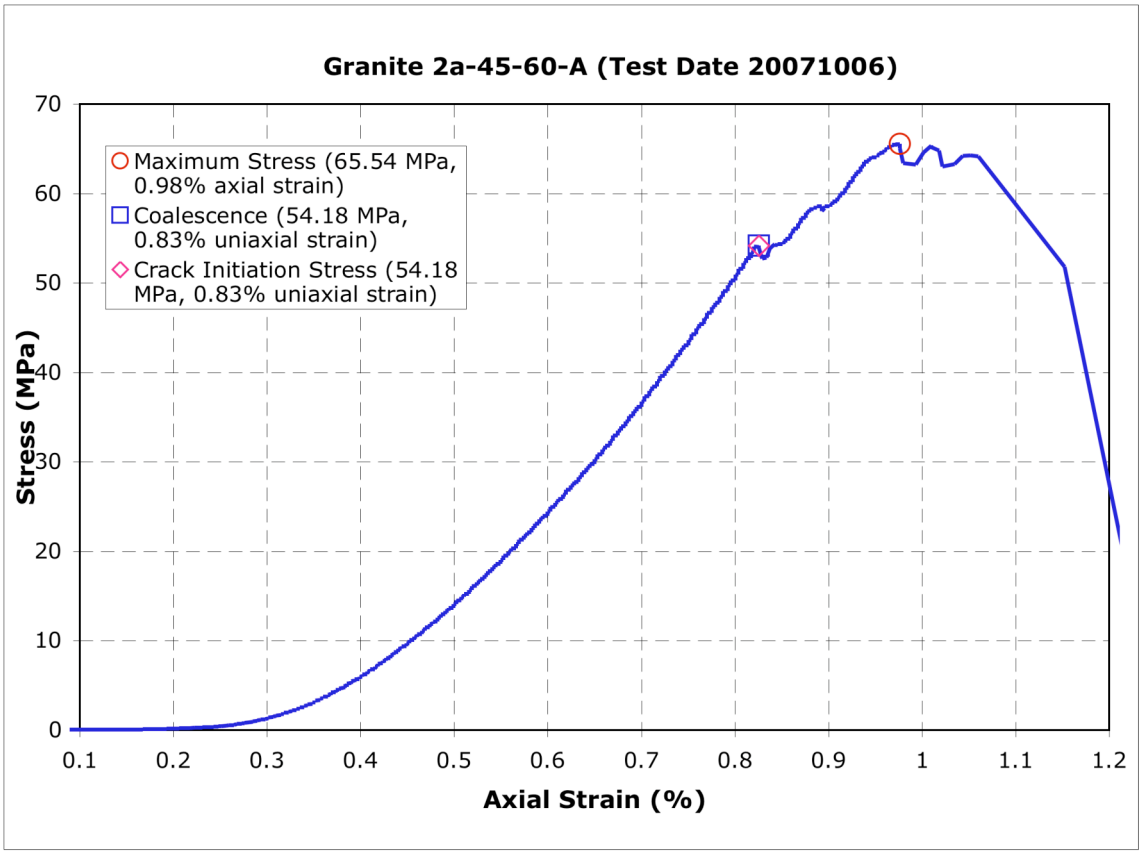

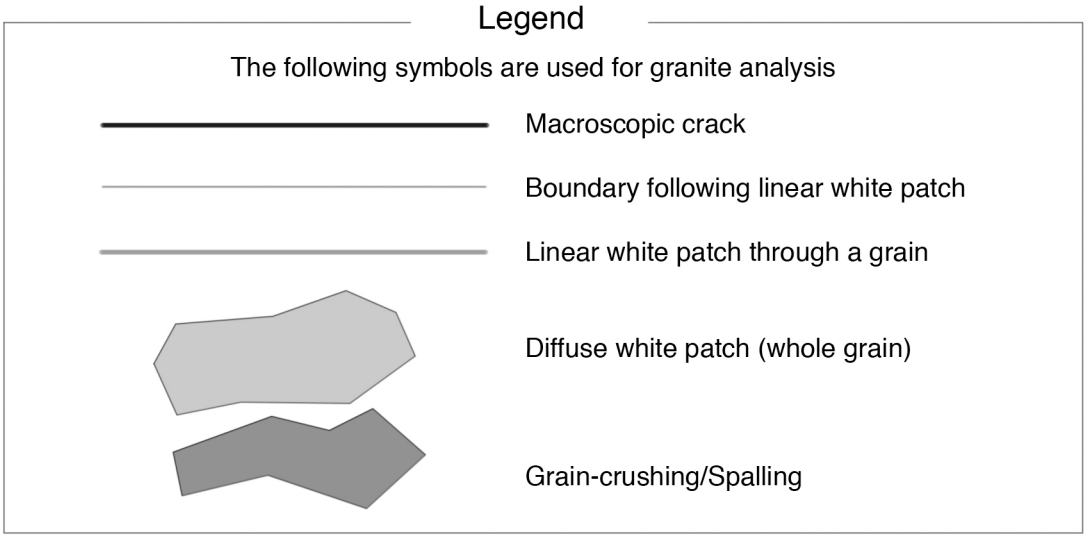

Category Six Coalescence

Images taken from high-speed video unless noted otherwise

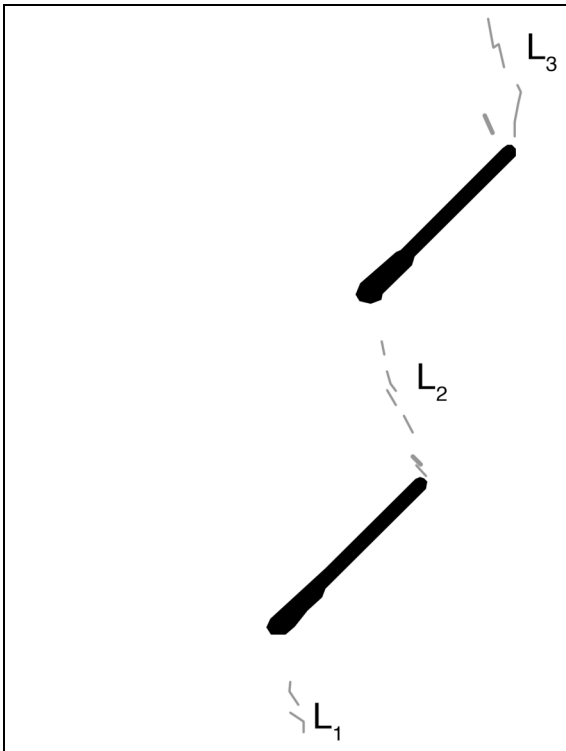	**Time:** ~9m06s **σ:** ~49.4 MPa Image taken before high-speed video. Linear white patches L_1, L_2, and L_3 appear. L_1 only has boundary following linear white patches while L_2 and L_3 each have a single through-going linear white patch. L_2 appears to extend from the left inner flaw tip toward the right inner flaw tip.
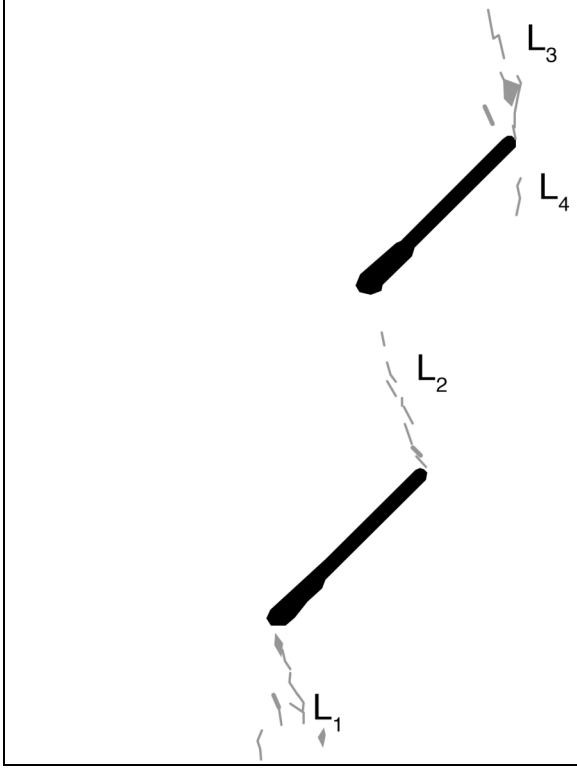	**Time:** ~9m59s **σ:** ~53.9 MPa Image taken before high-speed video. More linear features appear in $L_1 - L_3$. Small groups of grains lighten in L_2 and L_3. L_1 also has a through-going linear white patch appear. A boundary following linear white patch develops below the outer right flaw tip and is labeled L_4.

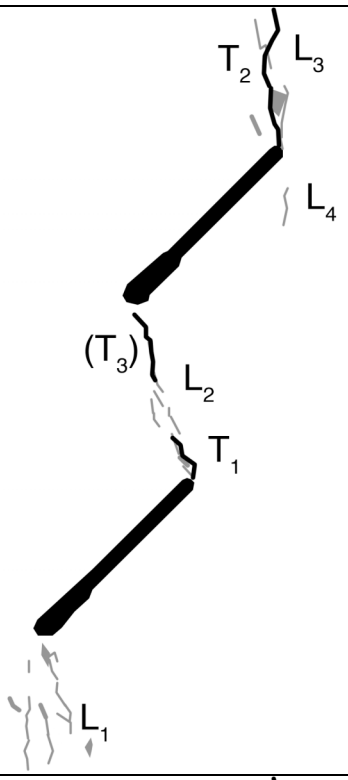	**Time:** 0.0122s before coalescence Tensile wing cracks T_1 and T_2 appear. A tensile crack (T_3) also forms. It is in the bridge area but unconnected to either flaw. L_1 and L_2 see more linear white patches form. L_1 has some through-going linear white patches while L_2 only has boundary-following features.
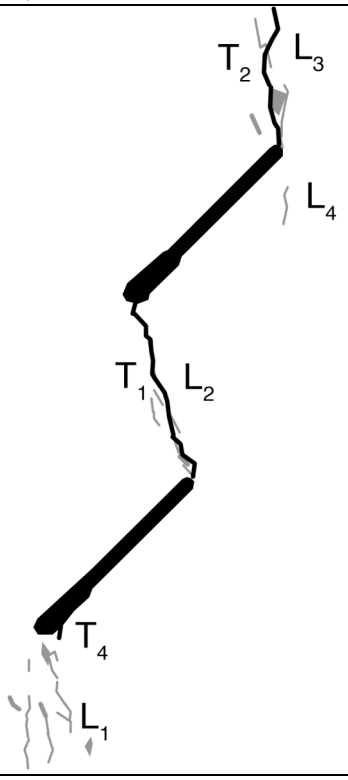	**Time:** 10m02.013s **σ:** 54.1813 MPa Sample coalesces (category six) when T_1 connects with (T_3) and the right flaw's inner tip. Tensile wing crack T_4 also forms.

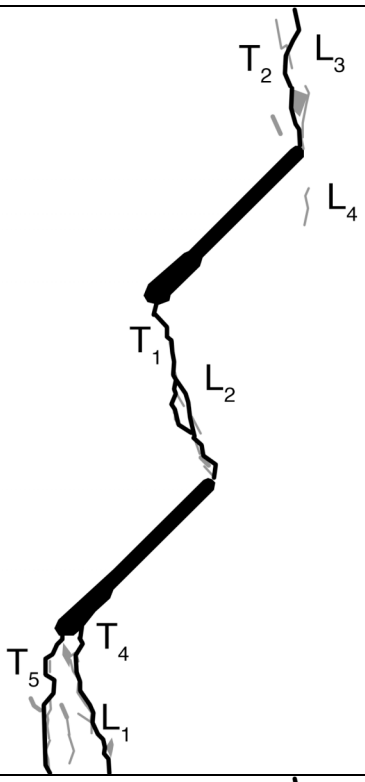	**Time:** 0.0006s after coalescence T_4 extends downward while T_1 branches and connects with itself in the center of the bridge area. A second tensile wing crack forms on the left outer flaw tip. It is labeled T_5.
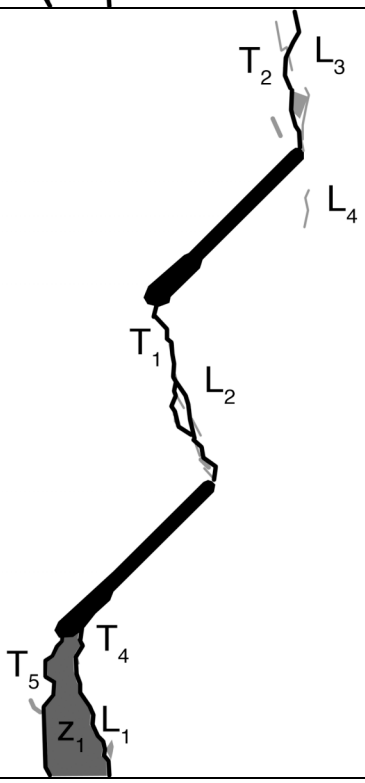	**Time:** 12m15.09s **σ:** 65.5445 MPa Image taken from camcorder. Sample failure occurs when the grains in zone 1 (labeled z_1) between T_4 and T_5 are crushed and ejected. Vertical tensile cracks simultaneously form in the specimen, although these are outside the camera's field of view.

Gr 2a-45-60 C (20012006)

Summary

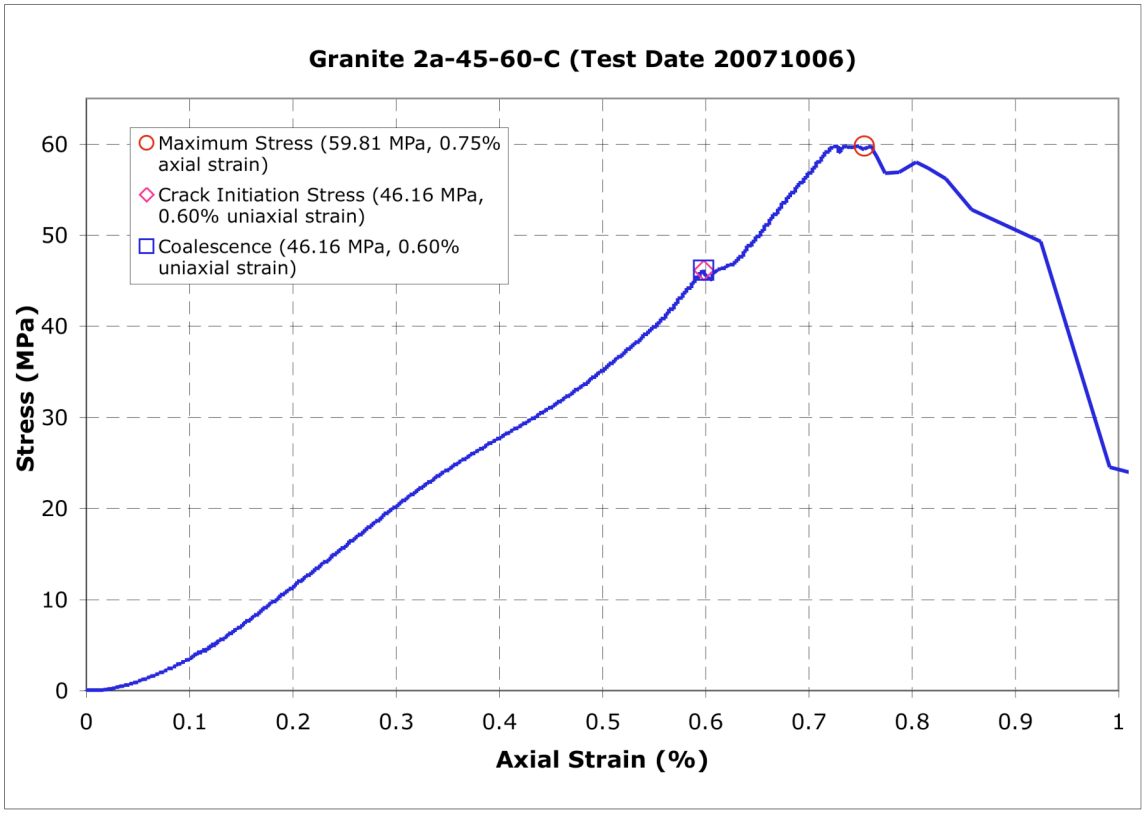

Legend

The following symbols are used for granite analysis

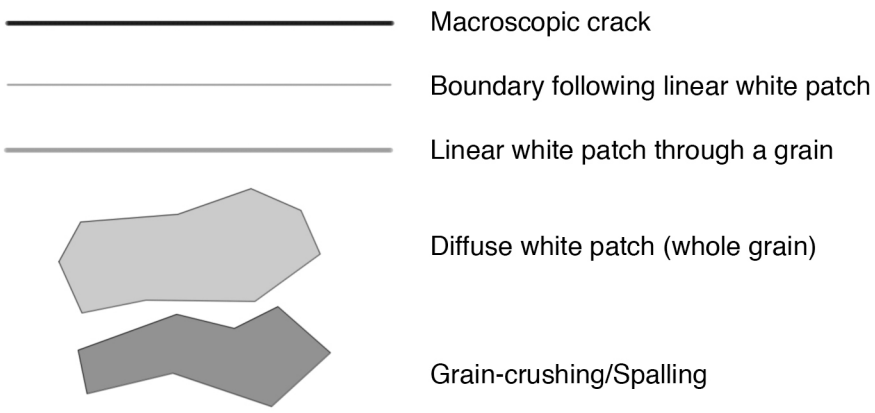

Category Six Coalescence

Images taken from high-speed video unless otherwise noted

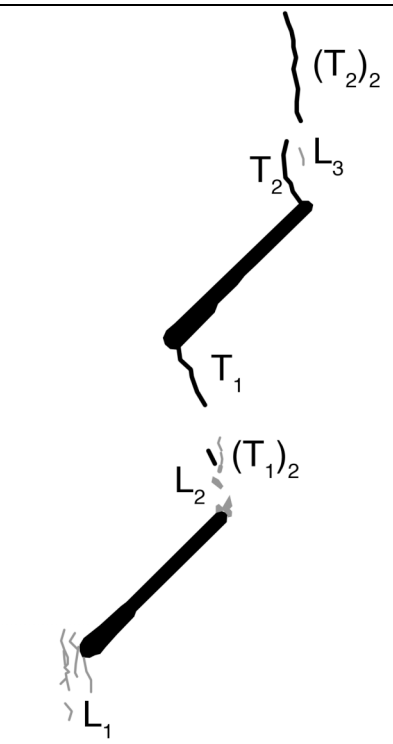	**Time:** 0.0260s before coalescence Tensile wing cracks T_1 and T_2 form on the tips of the right flaw. Tensile features $(T_1)_2$ and $(T_2)_2$ are unconnected to these wing cracks, but their formation appears related to T_1 and T_2, respectively. L_1, L_2, and L_3 all form as well. L_2 includes lightened grains. The remainder of the white patches are all boundary-following linear white patches.
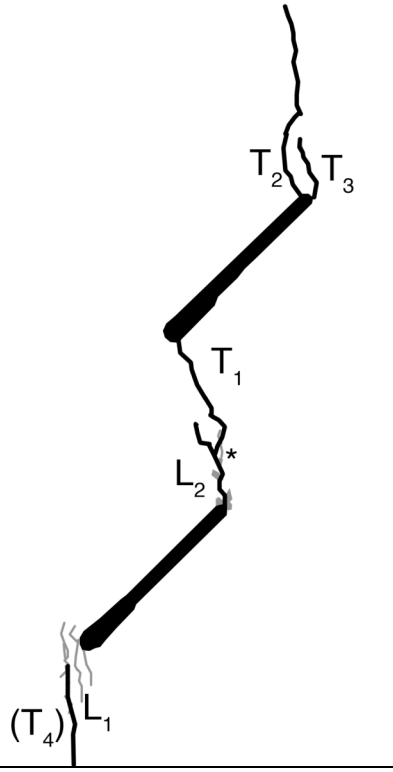	**Time:** 8m11.369s **σ:** 46.1623 MPa T_1 and $(T_1)_2$ both grow and link together (at the point labeled *) as well as connect to the left flaw's inner tip. The sample has coalesced (category six). T_2 and $(T_2)_2$ also link together. A second wing crack – labeled T_3 – appears on the right flaw's outer tip. Tensile crack (T_4) appears below the left flaw's outer tip.

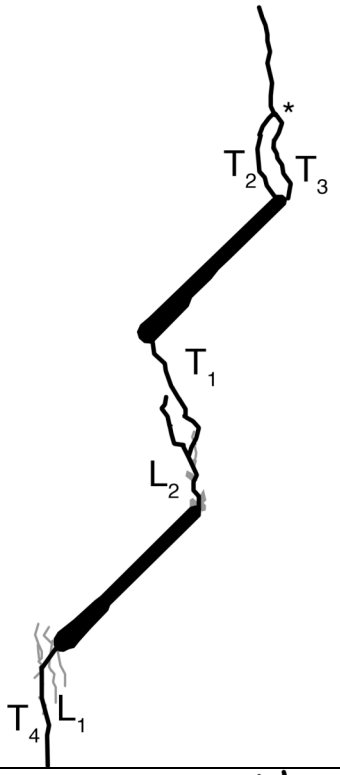	**Time:** 0.0026s before failure T_3 grows upward and connects with T_2 at the point labeled by a '*.' (T_4) grows and connects with the left flaw, becoming tensile wing crack T_4.
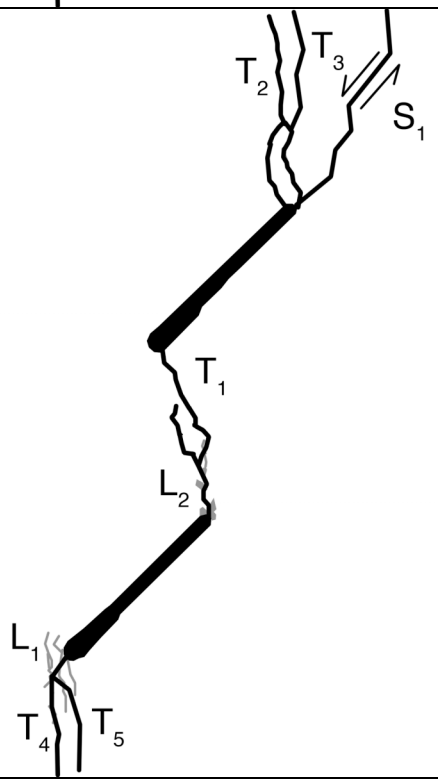	**Time:** 10m51.282s **σ:** 59.8056 MPa Image taken from camcorder video. T_3 branches away from T_2 and grows upward. Tensile crack T_5 branches off of T_4 and grows downward. Shear crack S_1 forms and connects with the right flaw's outer tip and shears in the direction indicated. Sample failure occurs with this shearing.

Gr 2a-60-60 B (20071006)

Summary

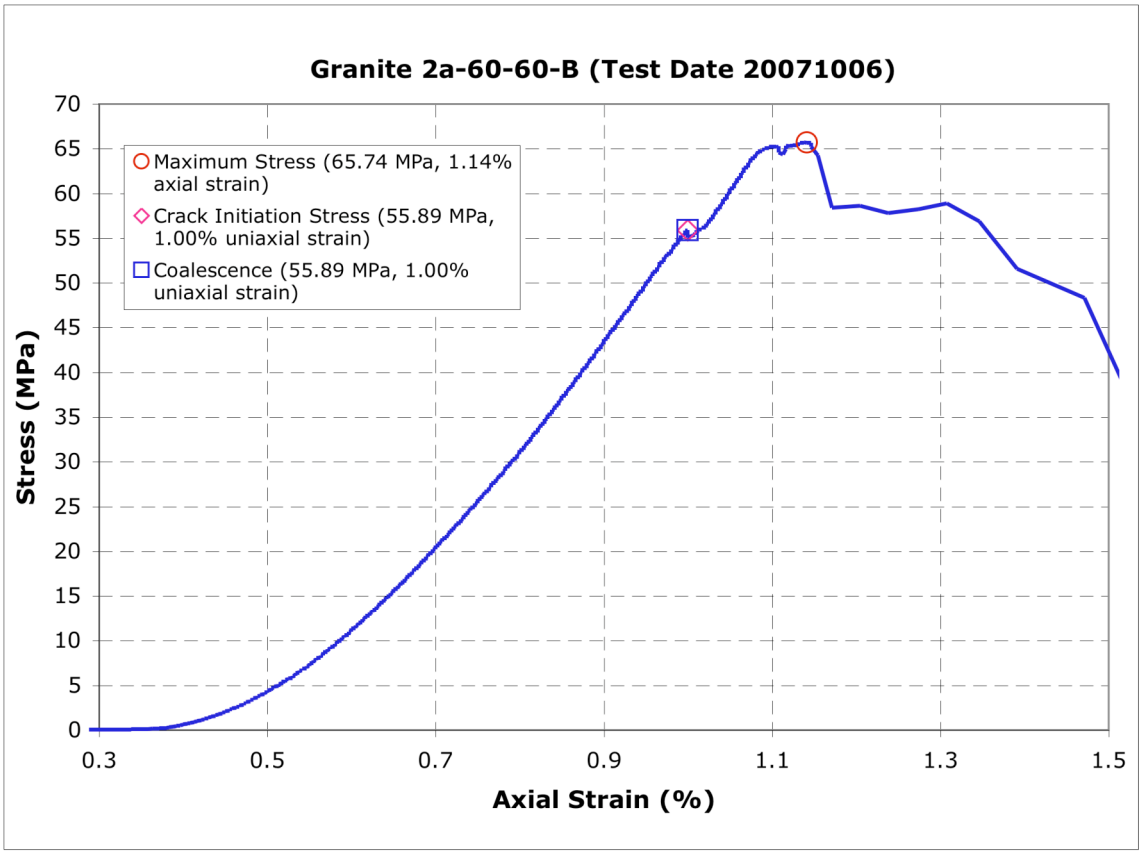

Legend

The following symbols are used for granite analysis

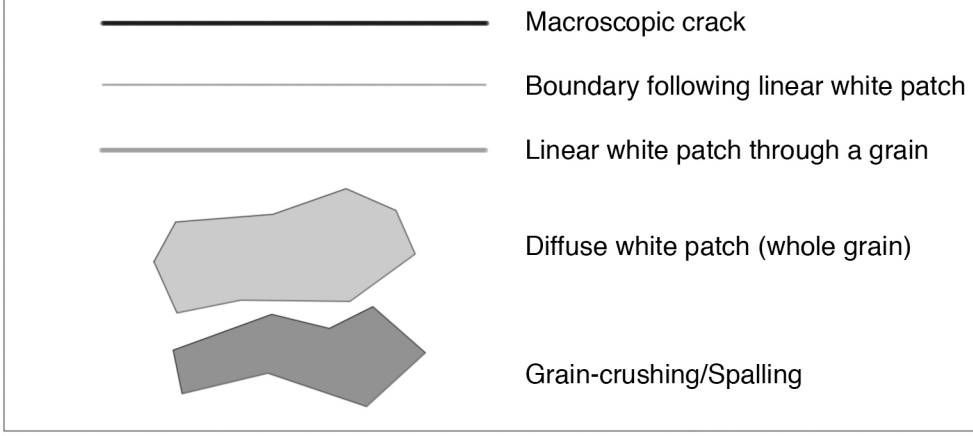

Category seven coalescence

Images taken from high-speed video unless otherwise noted

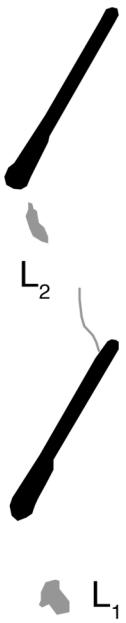	**Time:** ~10m01s **σ:** ~54.5 MPa Image taken with high-speed camera before video recorded. Lightened grains appear below the left tip of the lower crack (labeled L_1). A linear, boundary-following white patch and lightened grains appear in the bridge area (labeled L_2).
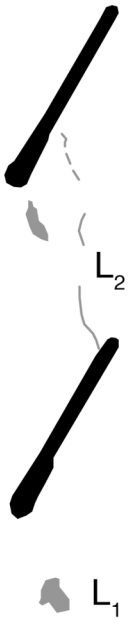	**Time:** 0.477s before coalescence L_2 extends upward with boundary-following linear white patches.

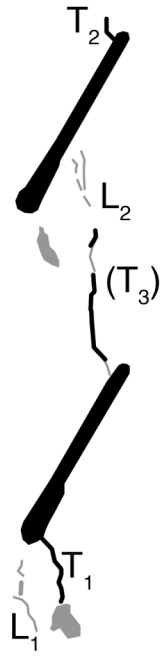	**Time:** 0.0184s before coalescence Tensile wing crack T_1 appears and grows down from the left tip of the lower flaw while L_1 expands with boundary-following and through-going linear white patches. Tensile wing crack T_2 appears and grows upward from the right tip of the upper flaw. Tensile cracks (T_3) appear in the bridge area.
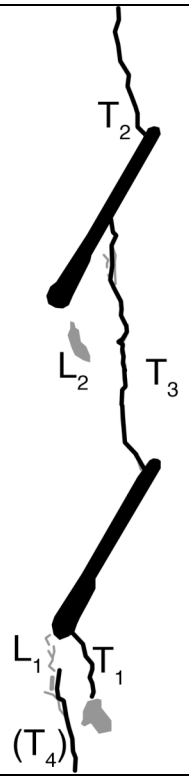	**Time:** 10m17.97s **σ:** 55.8949 MPa T_2 extends upward. (T_3) extends both upward and downward and links both flaws. Sample has coalesced with category seven coalescence. Tensile crack (T_4) extends upward toward the outer tip of the lower flaw.

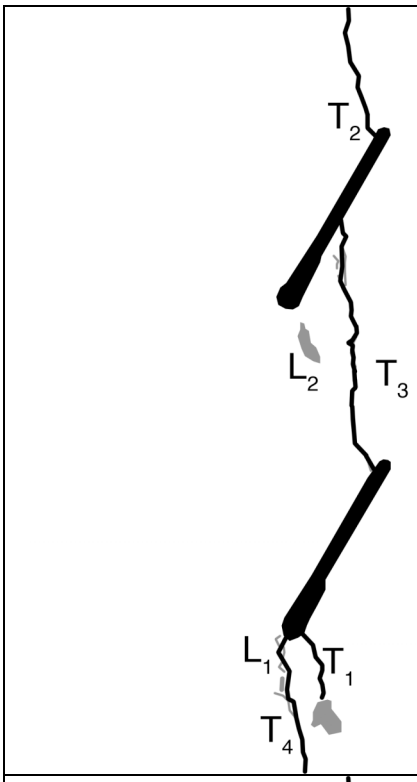	**Time:** 0.0552s after coalescence (T_4) extends upward and connects with the left tip of the lower flaw becoming crack T_4.
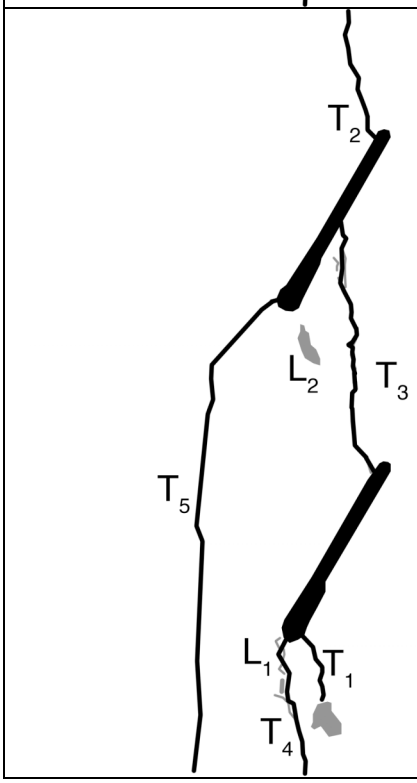	**Time:** 12m12.156s **σ:** 65.7376 MPa Sample failure occurs with tensile crack T_5 growing downward from the left tip of the upper flaw.

Gr 2a-75-60 B (20071006)

Summary

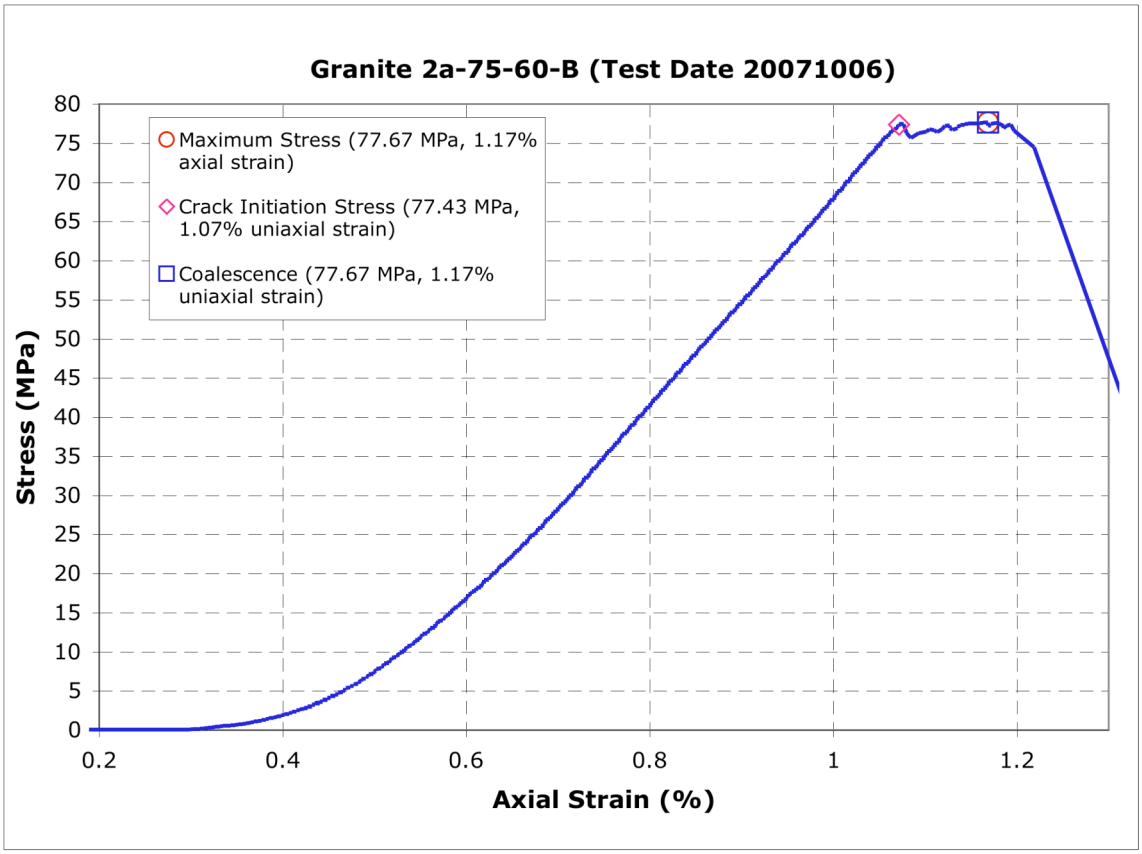

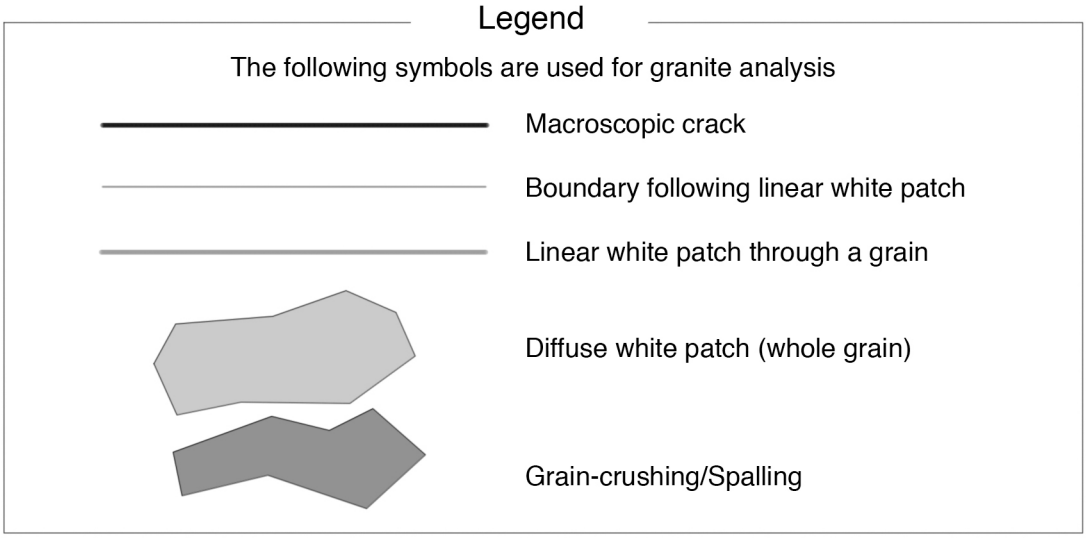

Category two coalescence
Images taken from high-speed video unless otherwise noted
Time correlation between high-speed video and camcorder less certain than normal

	**Time:** ~13m53s **σ:** ~75.47 MPa Image taken with high-speed camera before video was captured. Boundary-following linear white patches appear on the lower flaw's left tip (labeled L_1) and the upper flaw's right tip (labeled L_2).
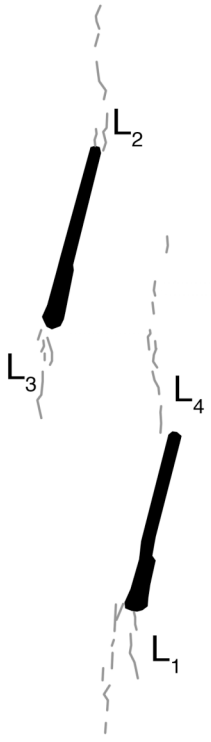	**Time:** 3.14s before failure Both L_1 and L_2 extend away from their respective flaw tips while L_3 and L_4 appear on the left flaw's lower tip and the right flaw's upper tip, respectively. All linear white patches at this points are boundary-following linear features.

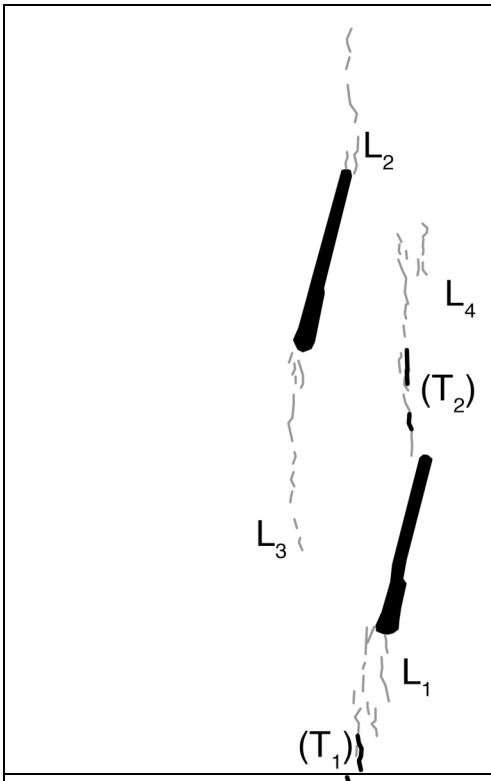	**Time:** 2.99s before failure L_1, L_3, and L_4 extend with boundary-following linear white patches. Tensile crack (T_1) appears near the lower flaw's left tip and tensile cracks (T_2) appear near the lower flaw's right tip.
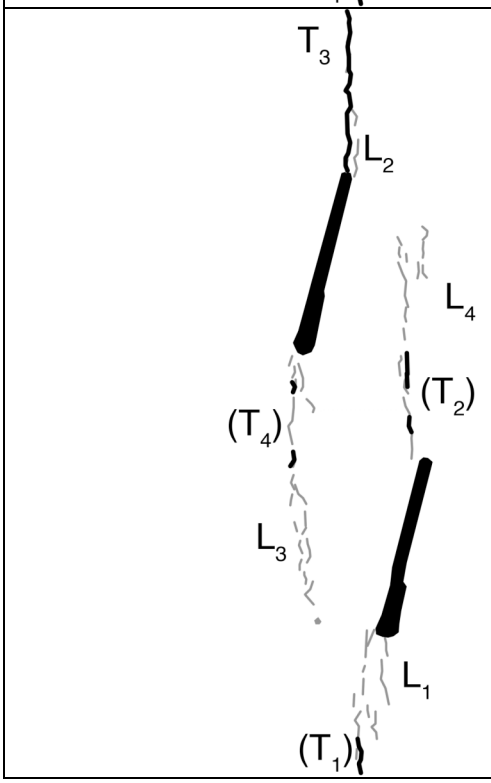	**Time:** 2.98s before failure Small tensile cracks appear within the L_3 region (which also grows slightly). These tensile cracks are labeled (T_4). Tensile wing crack T_3 appears on the right tip of the upper flaw.

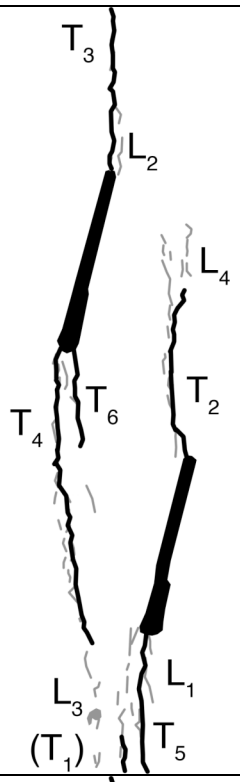	**Time:** 14m16.03s (T_2) extends upward and downward, connecting with the lower flaw (becoming crack T_2). (T_4) also extends in both directions – connecting with the upper flaw – becoming T_4. Tensile wing cracks T_5 and T_6 appear and extend down from the lower tips both flaws. Boundary-following linear white patches and lightening grains appear between L_3 and L_1.
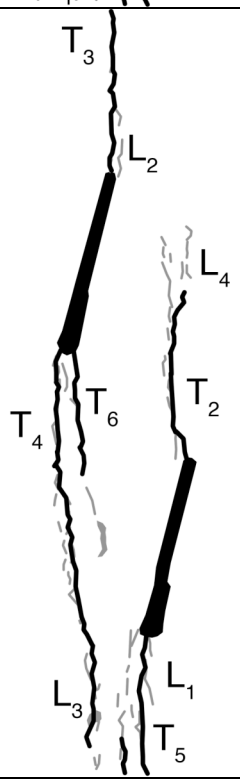	**Time:** 2.76s before failure A group of lightened grains appears between the left flaw tips while T_4 extends downward.

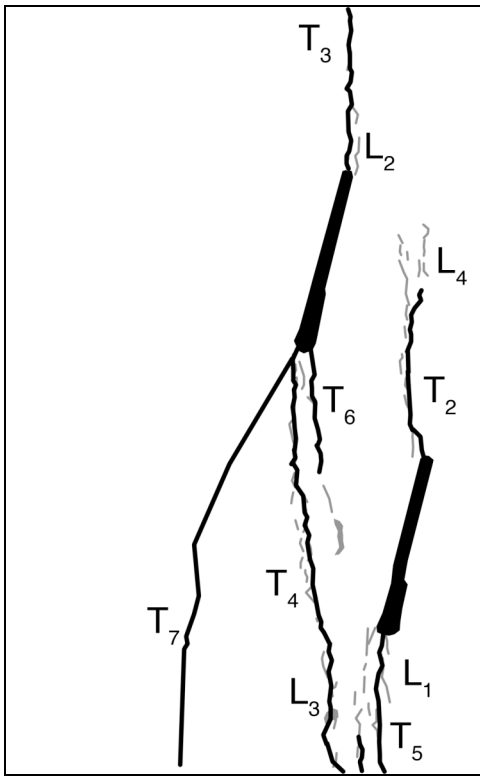

Time: 14m18.97s
σ: 77.6652 MPa

Image taken from camcorder video after high-speed video was captured. As such, the time can only be taken to be within 0.03s of time indicated.

Sample failure occurs with the appearance and downward propagation of tensile wing crack T_7. Simultaneously, Tensile crack T_4 grows downward and connects with T_5 causing category two (indirect) coalescence.

Gr 2a-75-60 C (20071006)

Summary

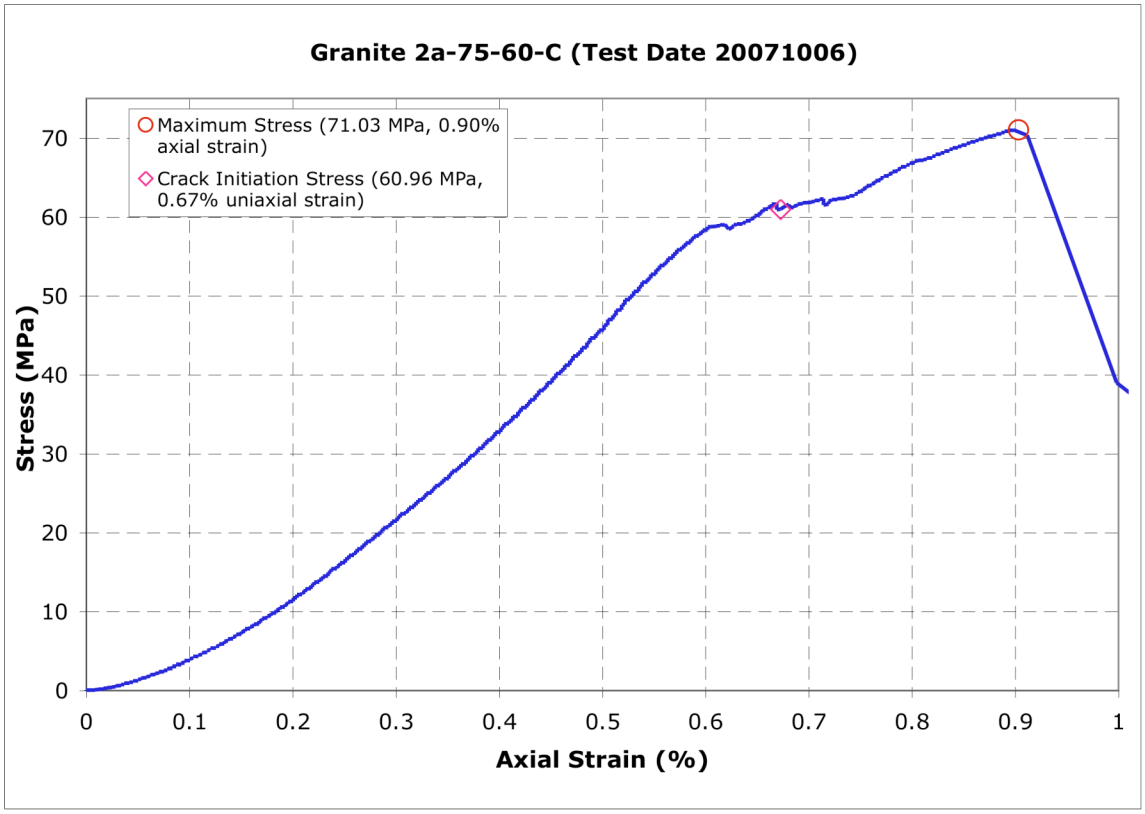

Legend

The following symbols are used for granite analysis

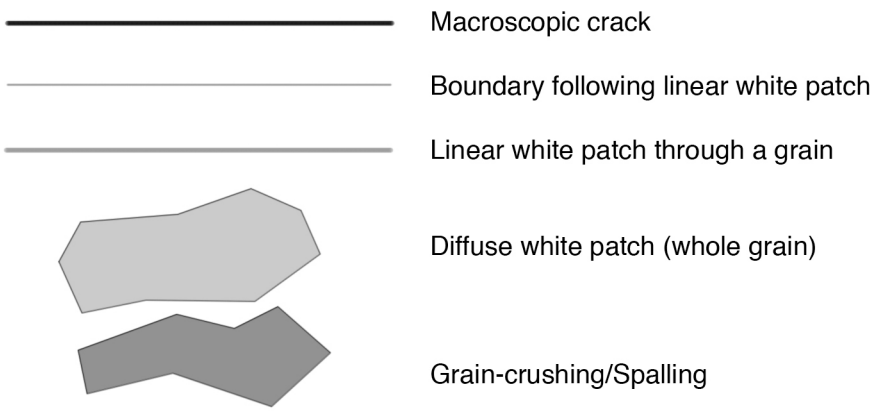

Category one coalescence

Images taken from high-speed video unless otherwise noted

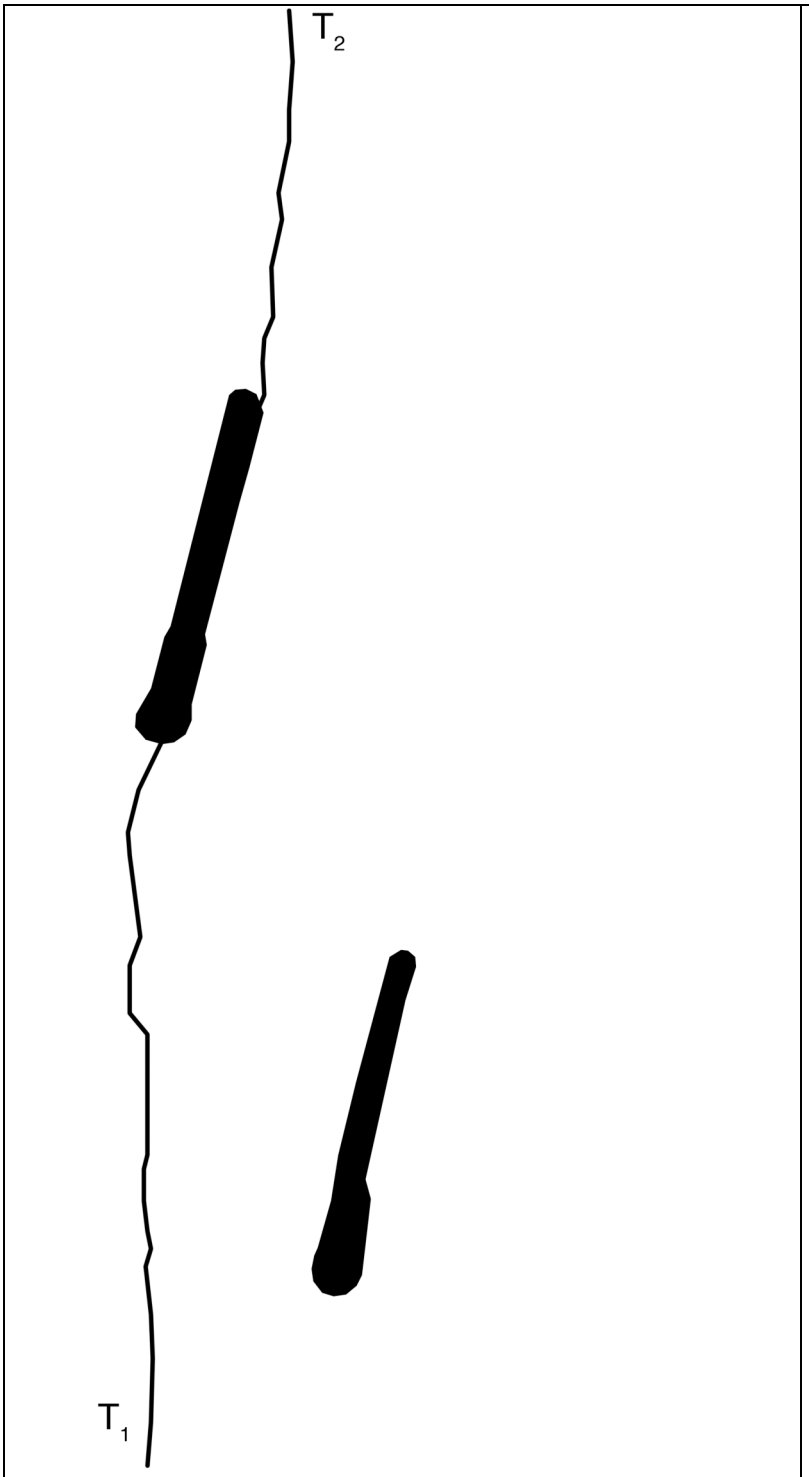

Time: 12m19.16s
σ: 60.96 MPa

Image captured from camcorder video before high-speed video.

Tensile wing cracks T_1 and T_2 appear above and below the upper crack.

*Note: Image taken from camcorder so quality not sufficient to identify white patches.

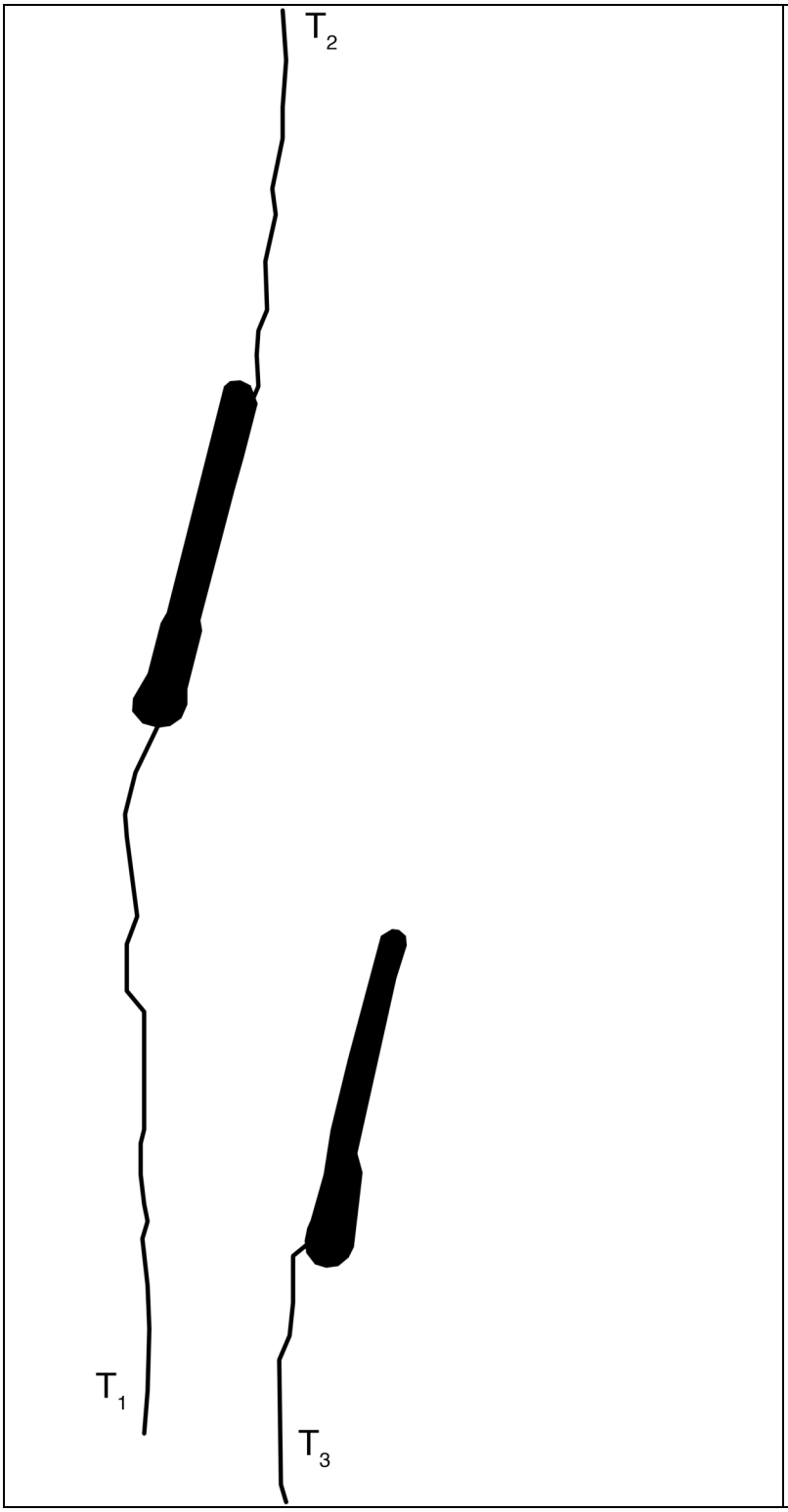

Time: 12m25.54s
σ: 62.31 MPa

Image taken from camcorder video before high-speed video

Tensile wing crack T_3 extends downward from the left tip of the lower flaw.

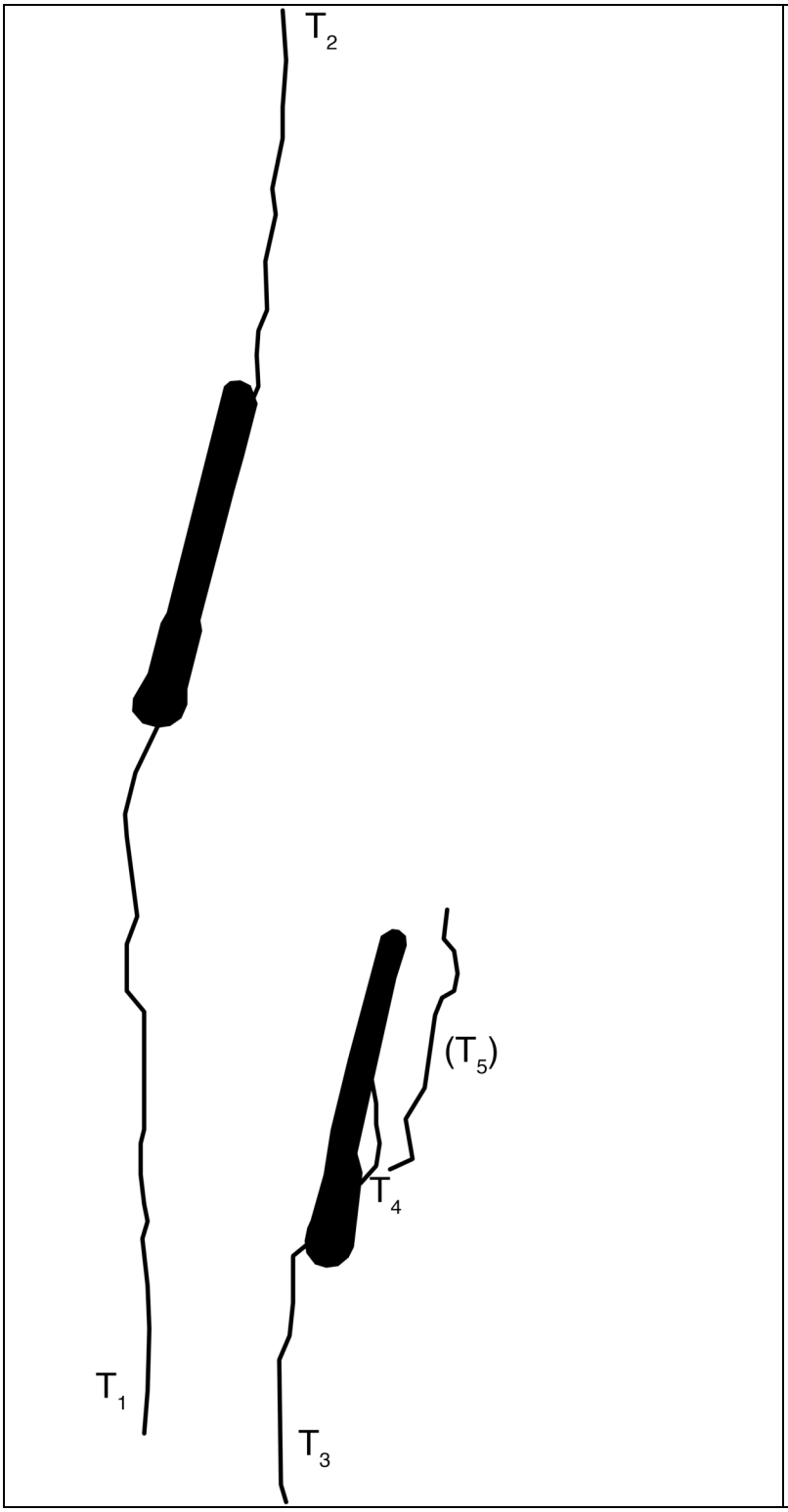

Time: 14m04.54s
σ: 70.09 MPa

Image taken from camcorder video before high-speed video.

Tensile crack T_4 appears on the lower crack. Tensile crack (T_5) also appears next to lower crack.

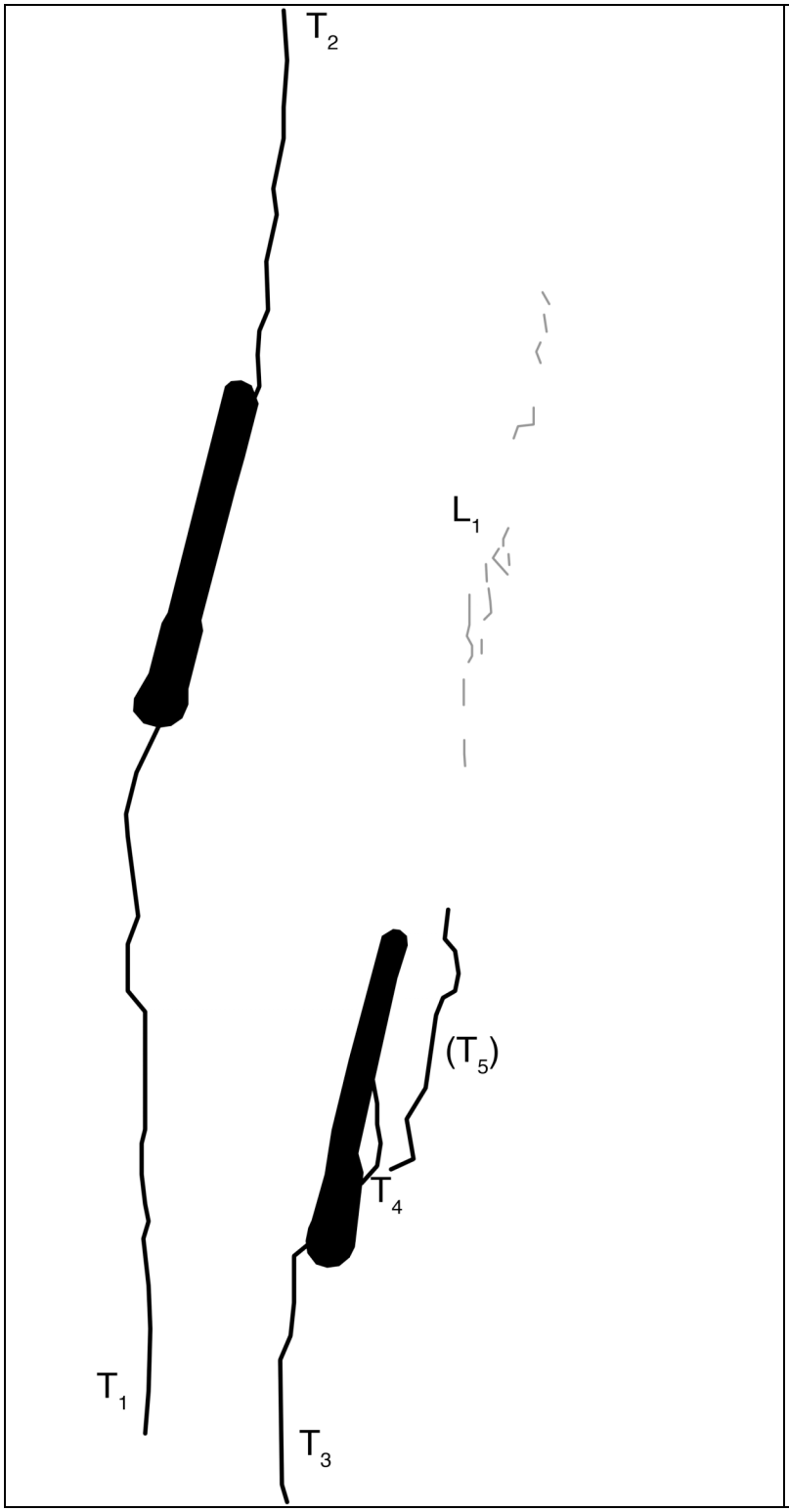

Time: 0.8773s before failure

Image taken from high-speed video.

Linear white patch L_1 extends upward from the lower flaw. All features are boundary-following.

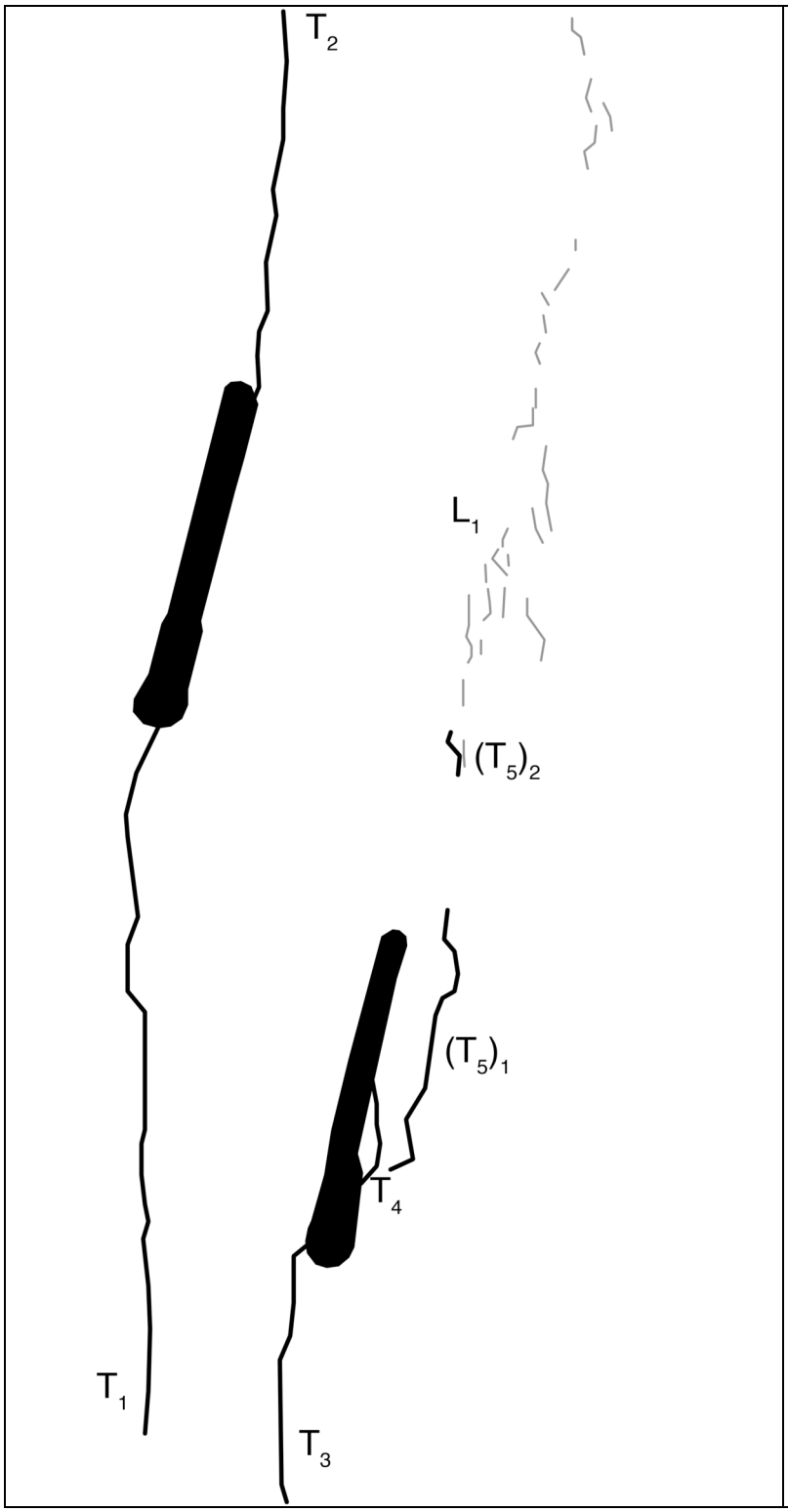

Time: 0.0495s before failure

L_1 continues extending upward with boundary-following linear white patches. A small tensile crack opens within L_1. It is labeled $(T_5)_2$.

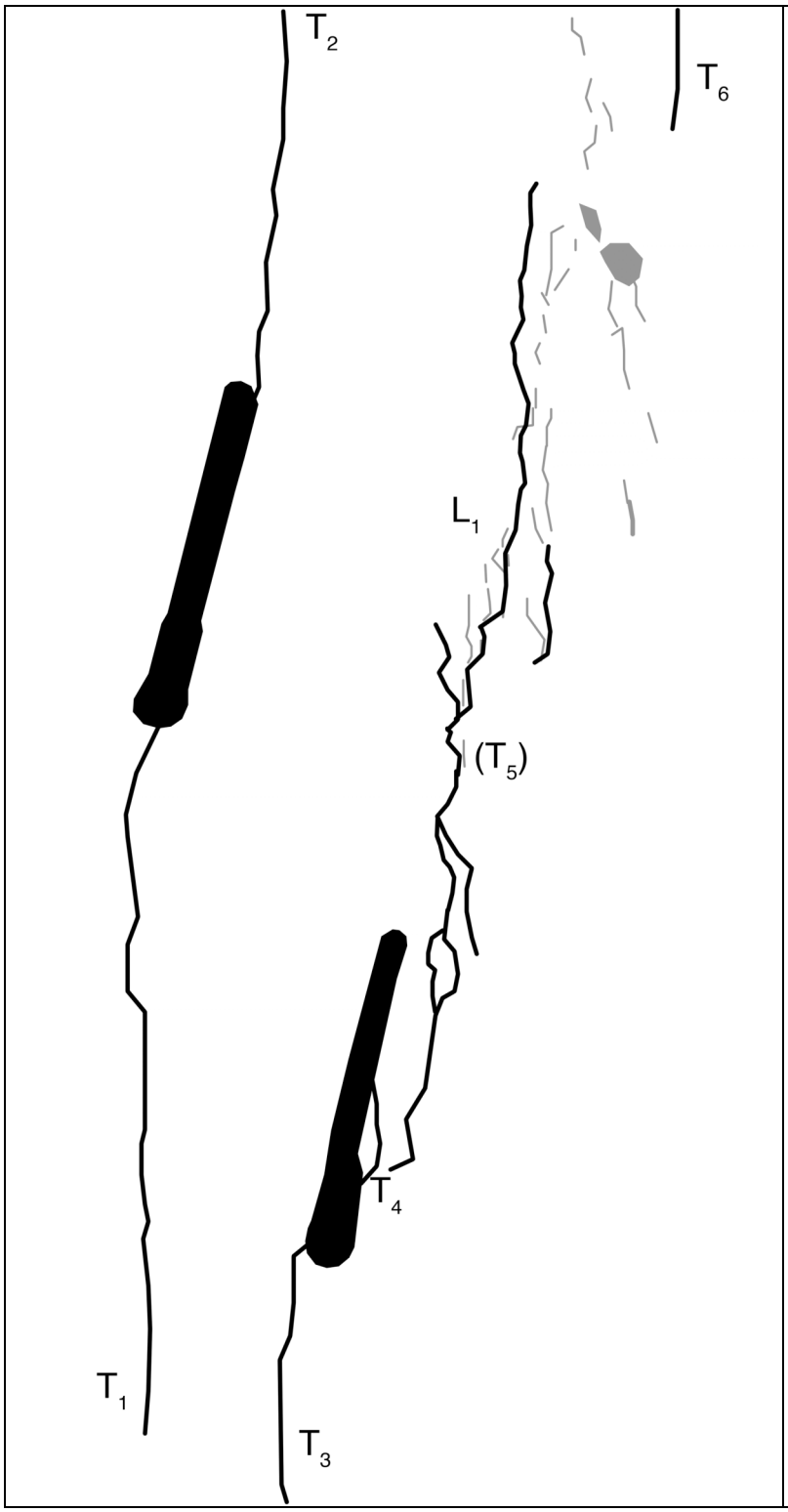

Time: 0.0235s before failure

L_1 broadens. It includes lightening grains as well as one through-going linear white patch. The two tensile cracks labeled $(T_5)_1$ and $(T_5)_2$ in the previous image grow and link together to form crack (T_5). Tensile crack T_6 appears and extends downward from above the camera's field of view.

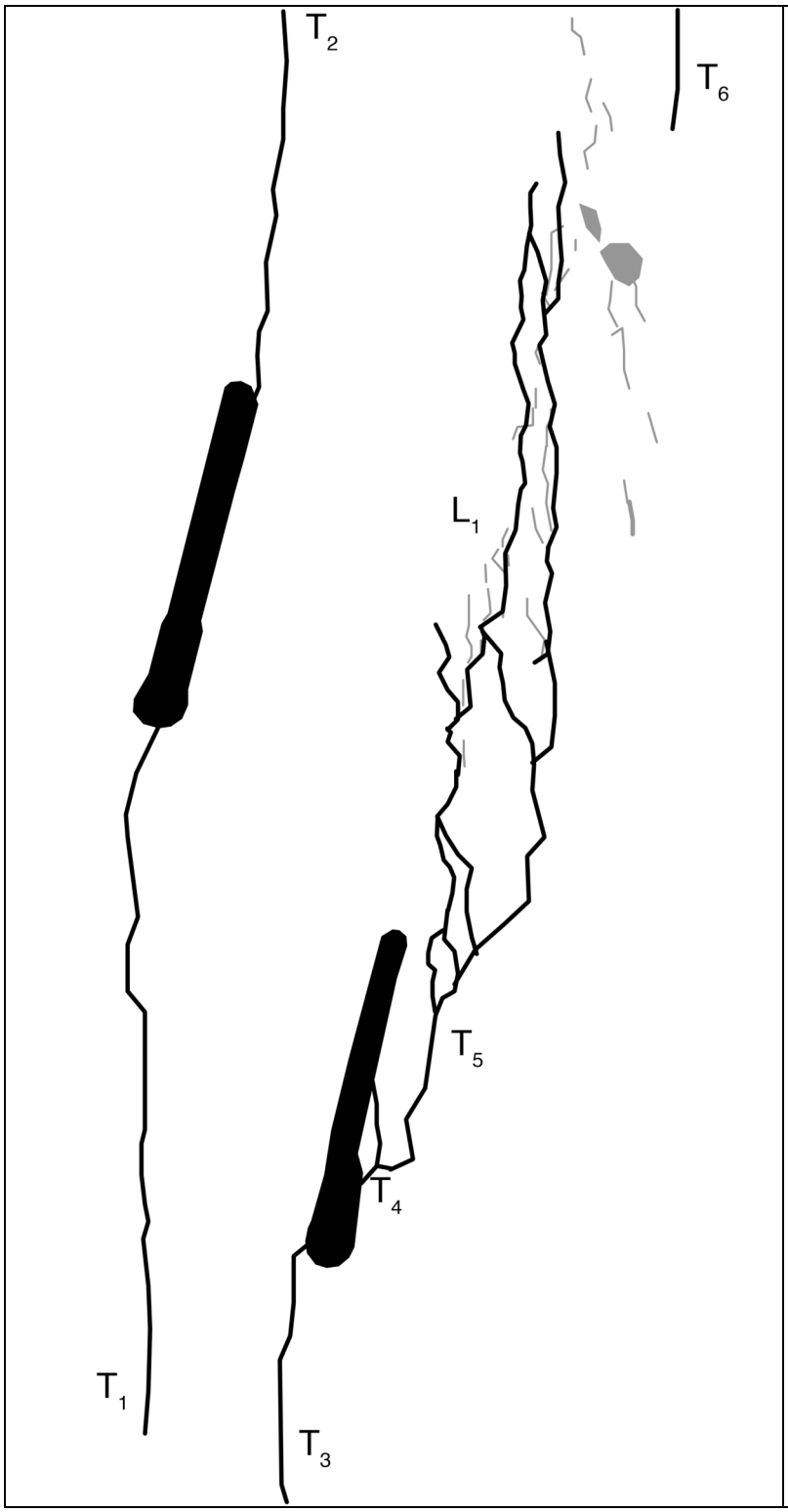

Time: 14m16.314s
σ: 71.0310 MPa

(T_5) extends downward connecting with T_4. It is now labeled T_5. The specimen fails as T_5 and T_6 continue upward. The sample does not coalesce after failure.

APPENDIX I - Coplanar Flaws Separated by 'a'

The following detailed analyses are for specimens with coplanar flaws ($\alpha = 0°$) and L = a (see Section 3.2 for an explanation of flaw geometry) tested as described in Chapter 3. Solid platens (see Section 3.4.2 for a description of platens) were used in all cases. For an overall summary of the results of these experiments, see Section 4.3.4.

Granite a-0-0 C (20080229)

Summary

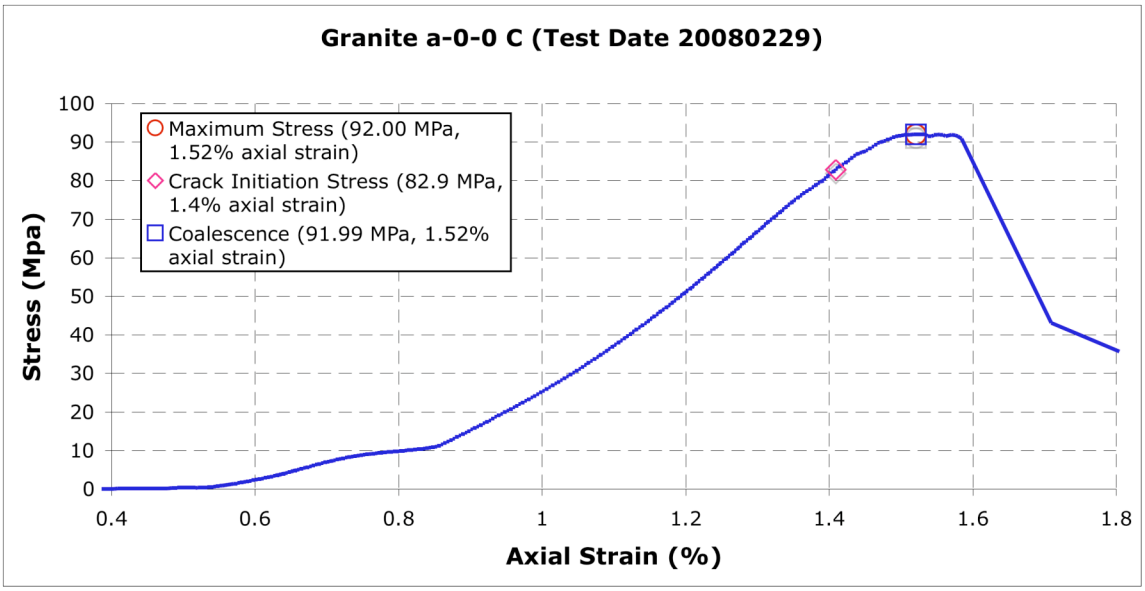

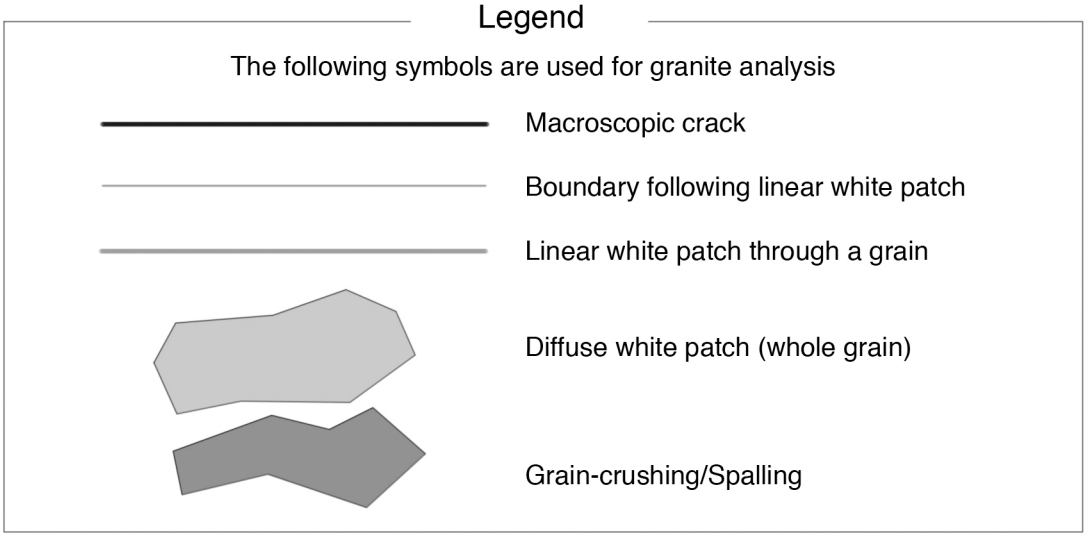

Category 2 Coalescence

Images captured from high-speed video unless otherwise noted

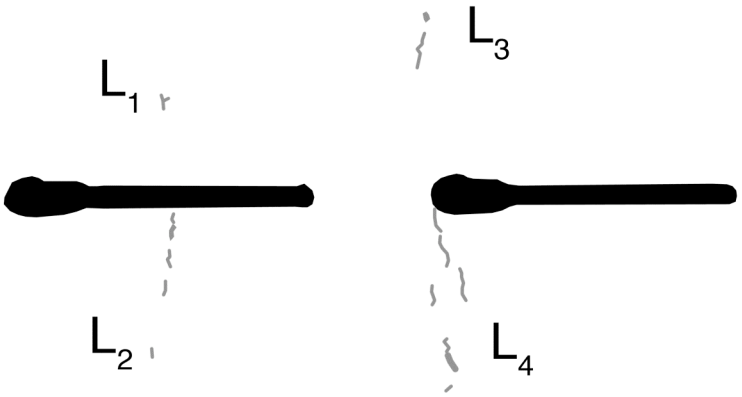	**Time:** ~18m18s **σ:** ~43.4 MPa Still image captured before high-speed recording with high-speed camera Linear white patches L_1 through L_4 appear. L_1 and L_2 are located above and below the middle of the left flaw, respectively. L_3 and L_4 are located above and below the right flaw's inner tip, respectively. L_1 is a boundary-following linear white patch while L_2 through L_4 are composed of both boundary-following and through-going linear white patches.

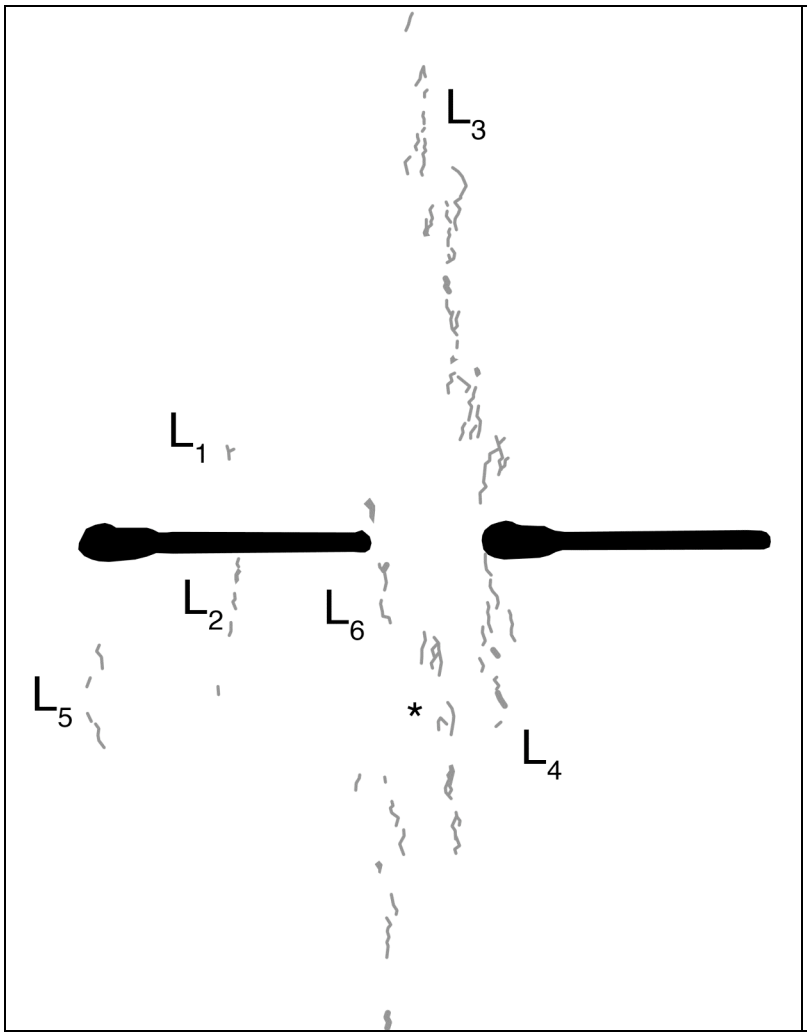

Time: ~12m43s
σ: ~65.4 MPa

Still image captured before high-speed recording with high-speed camera

L_3 grows (predominantly boundary-following, but some through-going features) and more linear features appear in L_4. Linear white patches L_5 and L_6 appear below the left and right tips of the left flaw, respectively. L_5 only has boundary-following white patches while L_6 has both types of linear features. There is a small area of linear white patches (both types), marked with an '*', between and parallel to L_4 and L_6.

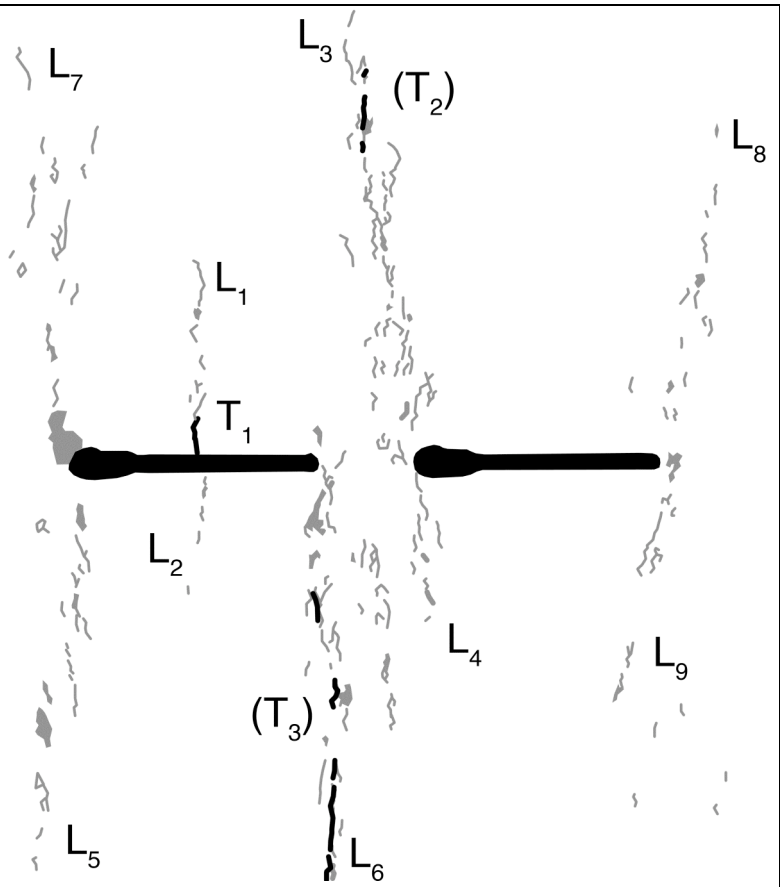

Time: ~16m12s
σ: ~82.9 MPa

Still image captured before high-speed recording with high-speed camera

L_1, L_3, L_5, and L_6 all grow with both types of linear white patches. In addition, some grains lighten in the L_5 and L_6 groups. L_7 through L_9 also form. All three new white patches have both types of linear features as well as lightened grains. Tensile wing crack T_1 forms from the middle of the top of the left flaw. Small tensile cracks also form near the inner flaw tips and are labeled (T_2) and (T_3).

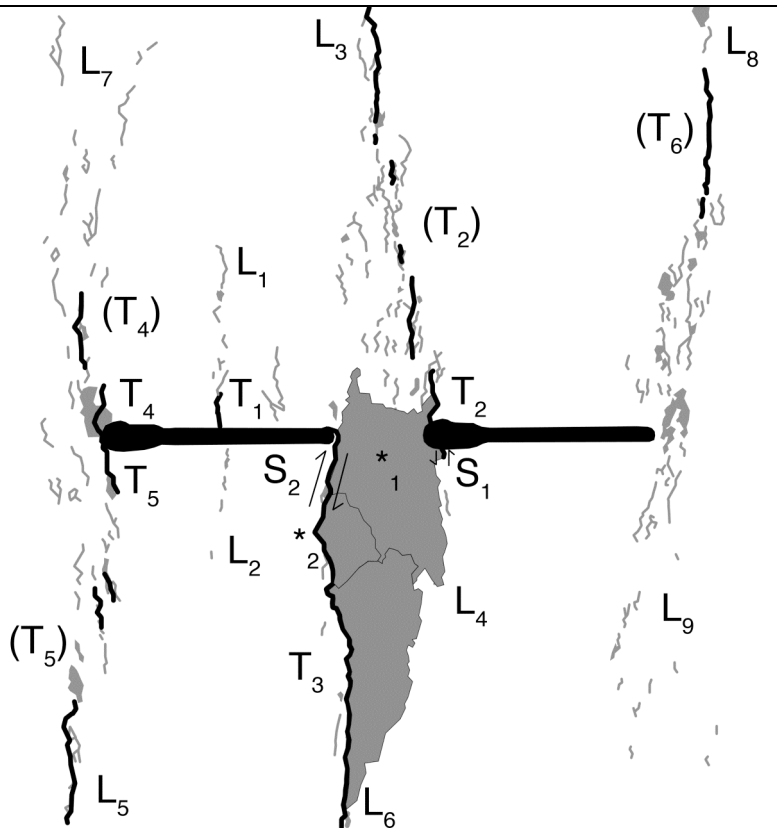

Time: ~17m57s
σ: ~91.6 MPa

Still image captured before high-speed recording with high-speed camera

A large zone of spalling appears in the bridge area, and is labeled $*_1$. The thin lines indicate different pieces of spalling material. Tensile cracks within (T_2) lengthen and connect and new cracks form. T_2 appears on the right flaw's inner tip. S_1 also forms on the right flaw's inner tip and shears in the sense indicated. T_3 grows upward and connects with S_2 at point $*_2$. S_2 shears in the sense indicated.

Tensile crack groups (T_4) through (T_6) also form, as do tensile wing cracks T_4 and T_5.

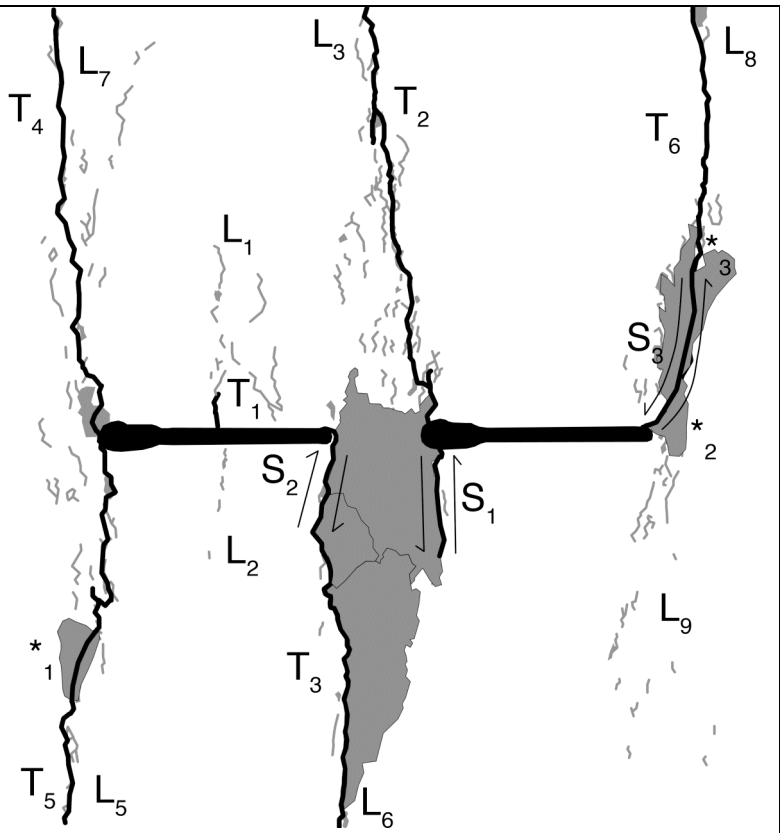

Time: 0.2477s before failure

First frame of high-speed video.

Tensile groups (T_2), (T_4), and (T_5) simultaneously connect with their tensile wing cracks becoming T_2, T_4, and T_5, respectively. A zone of spalling appears along T_5 (labeled $*_1$). (T_6) connects to the right flaw's outer tip via S_3, a new shear crack (shear sense indicated). The two cracks join at point $*_3$. S_3 also has an associated zone of spalling, $*_2$.

S_1 lengthens, continuing to shear in the same direction. S_2 also experiences more sliding along the crack – in the sense indicated.

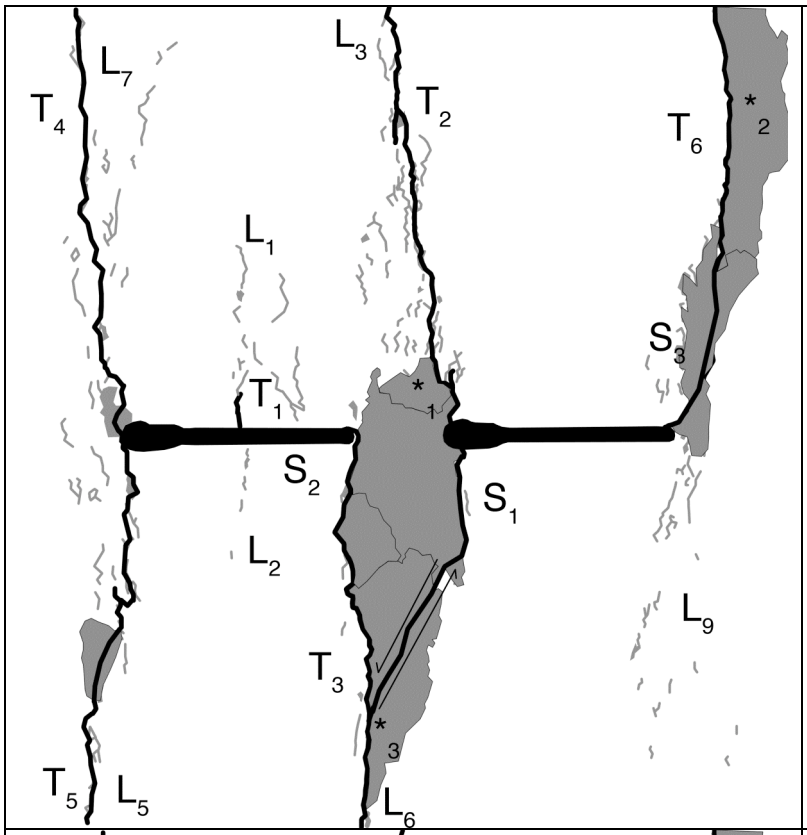

Time: 0.0014s before failure

A sudden increase in spalling occurs with both $*_1$ and $*_2$ appearing simultaneously. This is interpreted as coalescence. An extension of S_1 connecting with T_3 at point $*_3$ can be seen in later frames. Shear sense is discernable in this frame, however, and is indicated.

Coalescence is indirect (category 2)

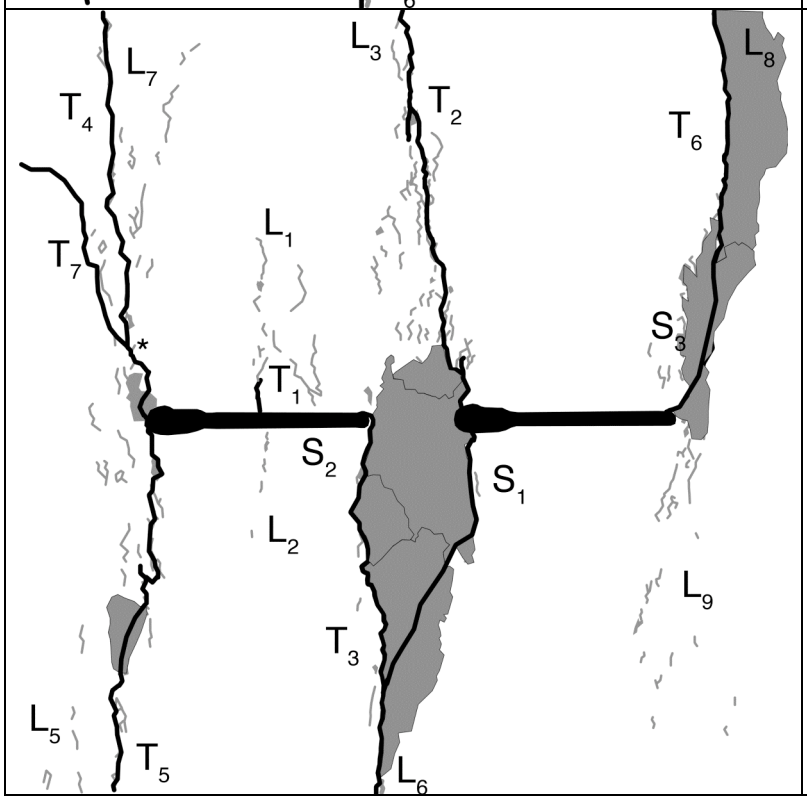

Time: 18m02.406s
σ: 92.0069 MPa

Specimen failure occurs with the development of tensile crack T_7, which branches off of T_4 at the point indicated with the '*'.

Granite a-30-0 B (20080229)

Summary

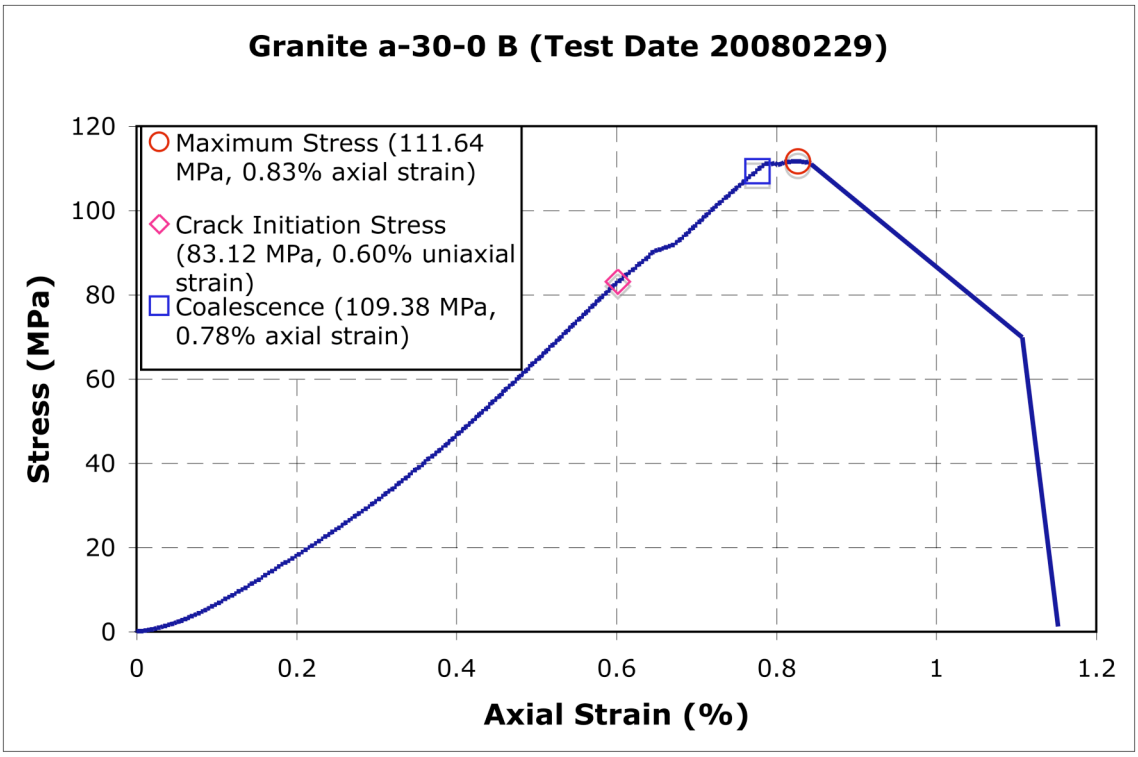

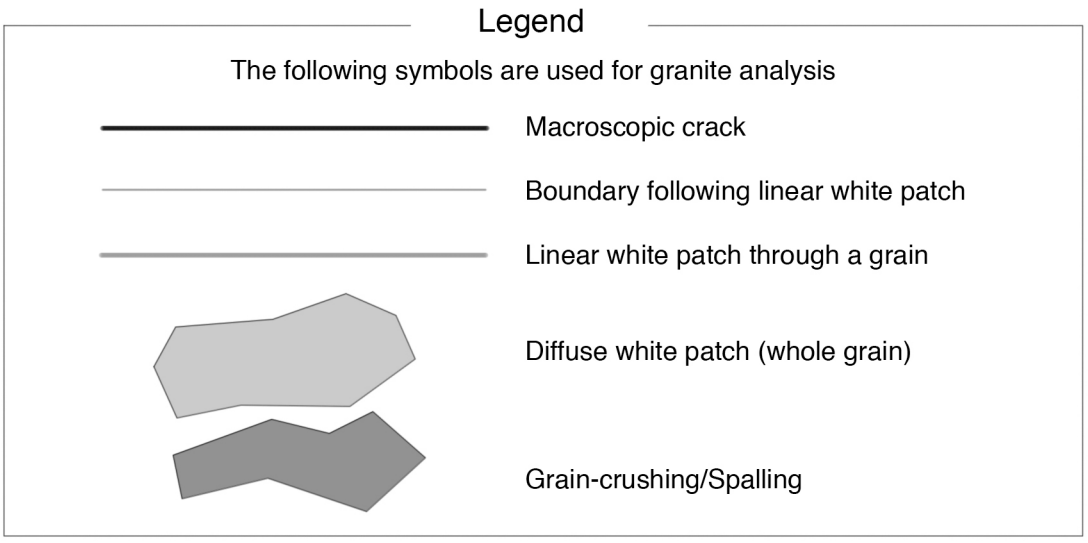

Category 2 coalescence

Images captured from high-speed video unless otherwise noted

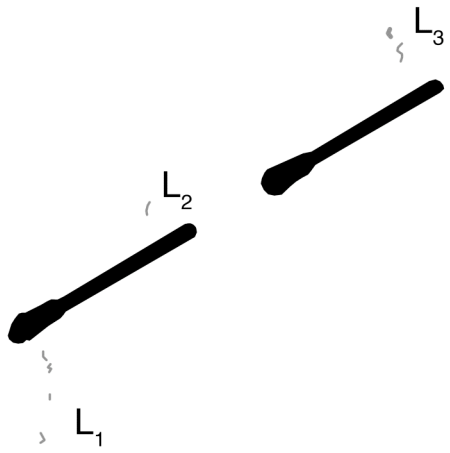	**Time:** ~7m52s **σ:** ~43.8 MPa Still image captured before high-speed recording with high-speed camera. Linear white patches L_1, L_2, and L_3 appear. L_1 and L_2 contain both boundary-following and through-going white patches, while L_2 has a single boundary-following linear white patch.
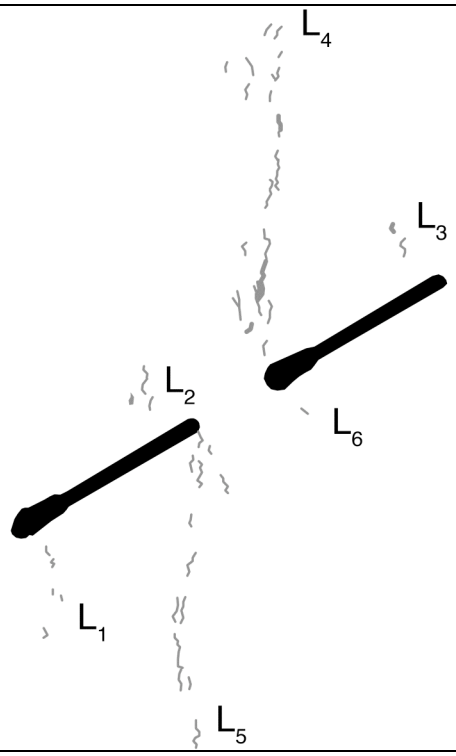	**Time:** ~12m15s **σ:** ~65.6 MPa Still image captured before high-speed recording with high-speed camera. L_2 expands with one boundary-following and one through-going linear white patch. Linear white patches L_4, L_5, and L_6 appear. L_5 and L_6 are composed solely of boundary-following linear white patches. L_4 includes all three types of white patch: boundary-following, through-going, and lightened grains.

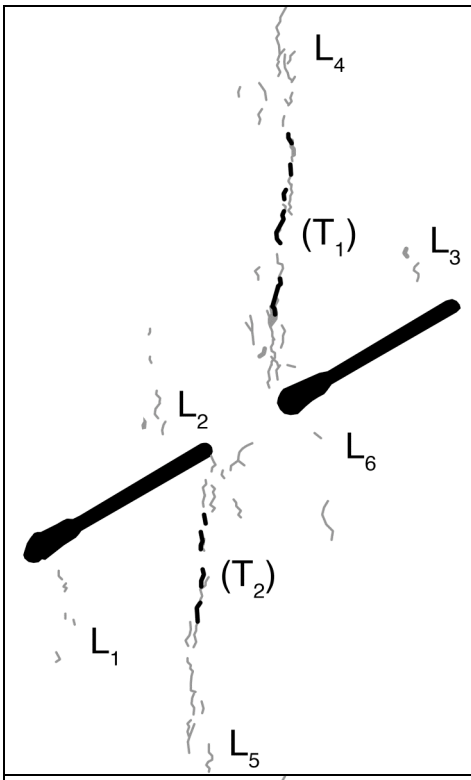	**Time:** ~15m44s **σ:** ~83.1 MPa Still image captured before high-speed recording with high-speed camera. Linear white patches L_2, L_4, L_5, and L_6 all grow and expand with boundary-following linear white patches. Note that some linear white patches in L_5 near the inner tip of the left flaw reach into the bridging zone. Tensile cracks also appear within the L_4 and L_5 regions. Those cracks within L_4 are labeled (T_1) and those within L_5 are labeled (T_2).
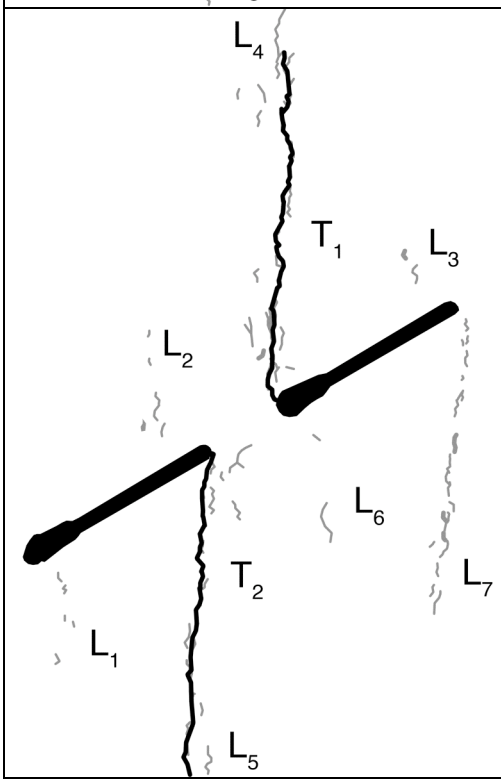	**Time:** ~16m38s **σ:** ~87.6 MPa Still image captured before high-speed recording with high-speed camera. The tensile cracks within (T_1) and (T_2) grown and connect and form tensile wing cracks T_1 and T_2, respectively. Linear white patch L_7 also appears below the right flaw's outer tip. L_7 is composed of both boundary-following and through-going linear white patches.

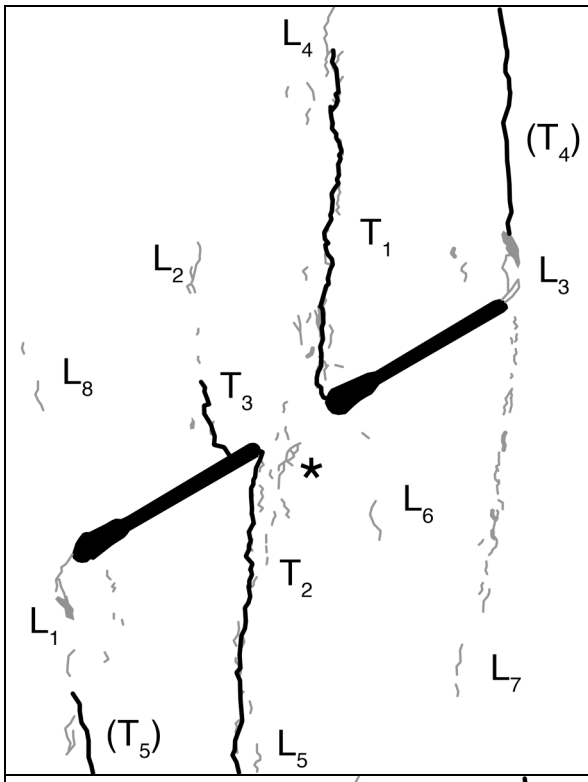	**Time:** ~17m03s **σ:** ~89.7MPa Still image captured before high-speed recording with high-speed camera. All linear white patches with the exception of L_4 and L_6 grow and expand. L_8 also appears above the left flaw's outer tip. It is composed of boundary-following white patches. Of particular note is the region of white patches in the bridging zone (marked by the '*') expanding. Tensile wing crack T_3 appears on the left flaw's inner tip. Tensile crack (T_4) appears above the right flaw's outer tip while (T_5) appears below the left flaw's outer tip.
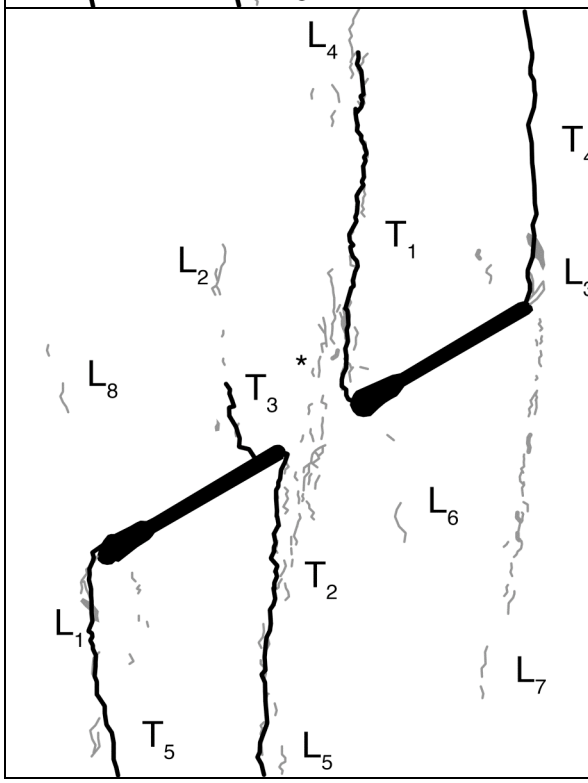	**Time:** ~18m47s **σ:** ~98.4 MPa Still image captured before high-speed recording with high-speed camera. (T_4) and (T_5) connect with their respective flaw tips and become tensile wing cracks T_4 and T_5, respectively. The linear white patches within L_5 that had expanded into the bridging continue expanding and connect with L_4. They are again labeled '*'.

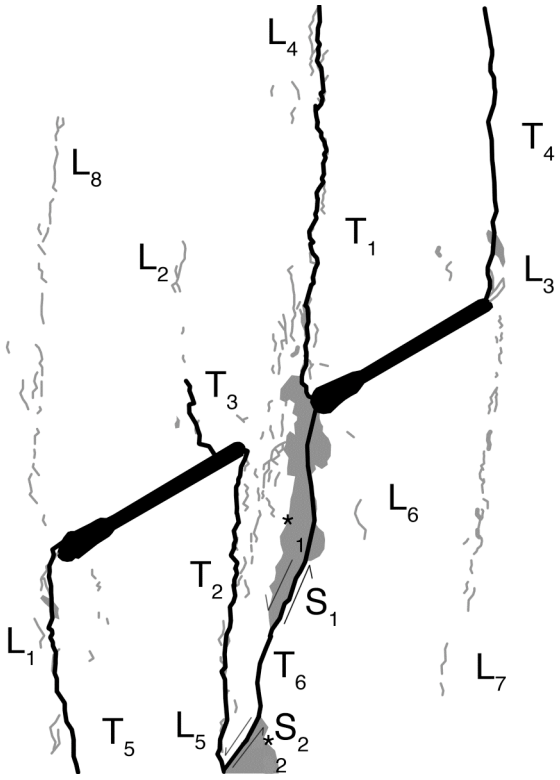

Time: ~20m58s
σ: ~109.4 MPa

Still image captured before high-speed recording with high-speed camera.

Coalescence occurs and is missed by high-speed video. Tensile wing crack T_6 appears to extend down from the inner tip of the right flaw and connect with T_2 causing indirect coalescence (category 2). This crack is accompanied by two zones of spalling: $*_1$ along the upper part and $*_2$ along the lower part. This spalling, as well as relative motion is seen as evidence for two segments of shearing along this coalescence crack. S_1 and S_2 both shear in the sense indicated and in the segments indicated by the arrows only.

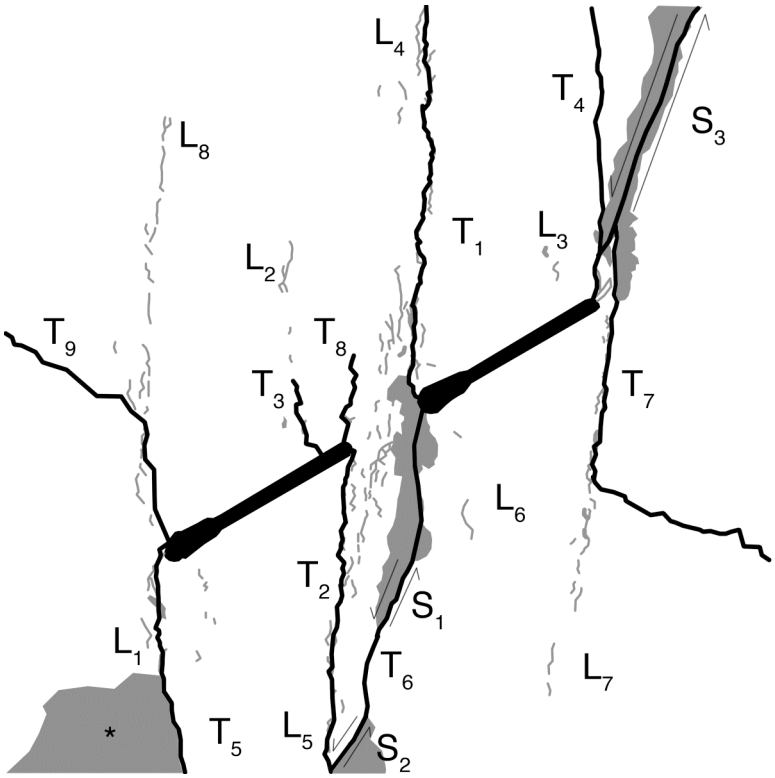

Time: 21m25.56s
σ: 111.64 MPa

Still image captured before high-speed recording with high-speed camera.

Specimen failure occurs over a short period of time (800 μs). Shear crack S_3 appears, shearing in the sense indicated. S_3 is accompanied by spalling. Tensile crack T_7 appears to branch off of S_3. It extends down along the L_7 region before abruptly turning away from the flaw's and out of the camera's field of view. Finally, tensile wing cracks T_8 and T_9 appear concurrent with specimen failure. T_8 appears above the inner tip of the left flaw. T_9 appears above the outer tip of the left flaw and extends up along the L_8 region before abruptly turning away from the flaw's and out of the camera's field of view.

Granite a-30-0 C (20080229)

Summary

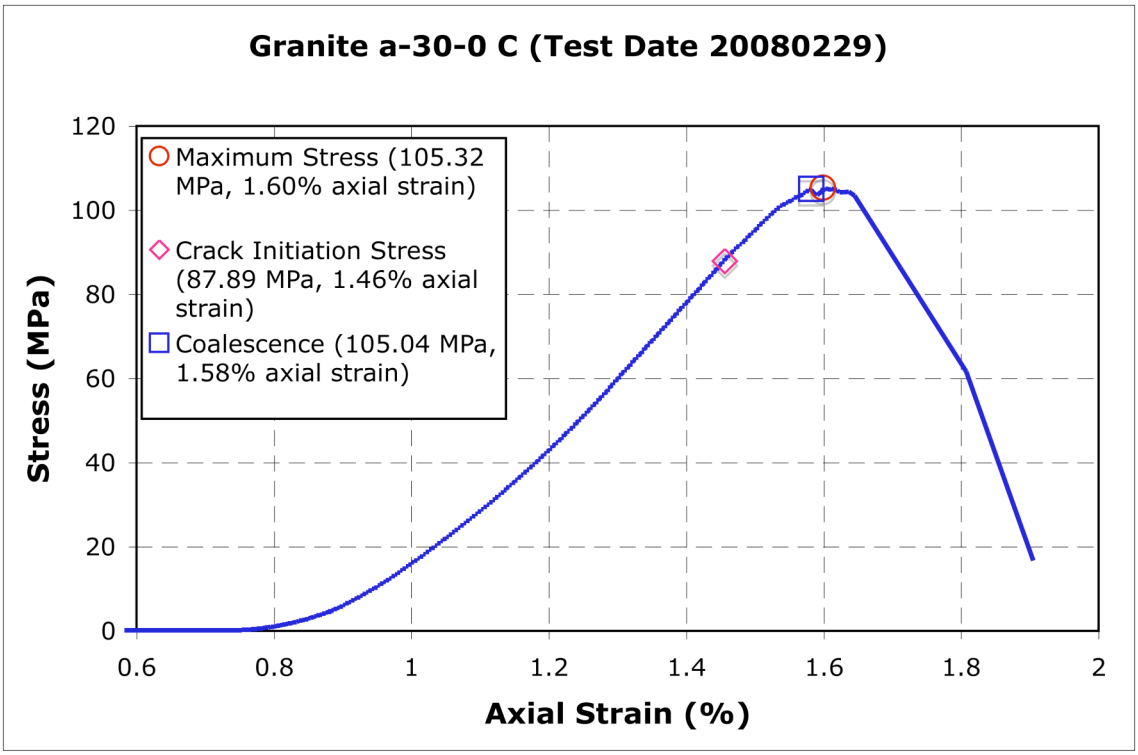

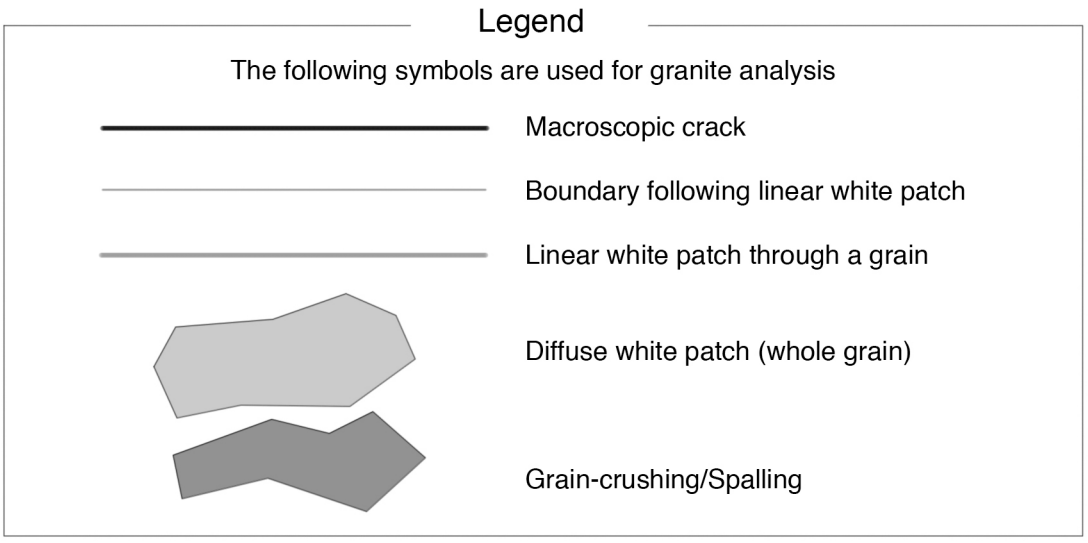

Category 2 Coalescence

Images captured from high-speed video unless otherwise noted

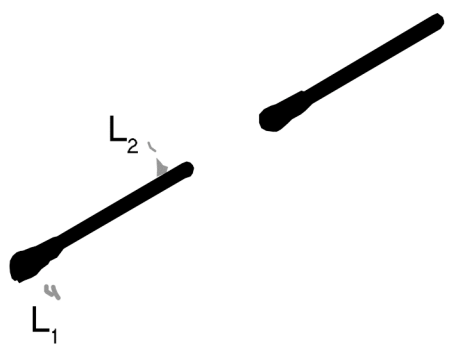	**Time:** ~6m13s **σ:** ~34.7 MPa Still image captured before high-speed recording with high-speed camera. Linear white patches L_1 and L_2 appear on the outer and inner tips, respectively of the left flaw. L_1 is composed solely of through-going linear features. L_2 has a zone of lightened grains as well as a boundary-following feature.
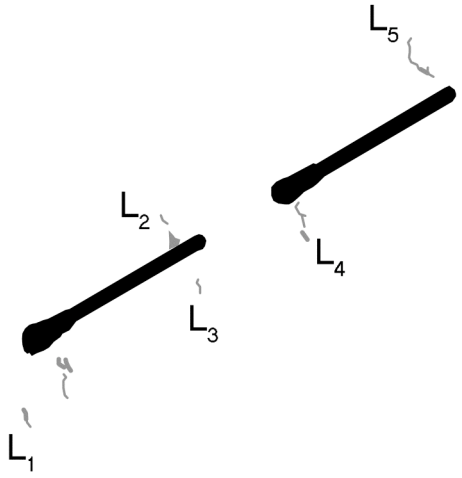	**Time:** ~10m35s **σ:** ~57.8 MPa Still image captured before high-speed recording with high-speed camera. L_1 extends downward with both boundary-following and through-going features. L_3 through L_5 also appear. L_3 has a boundary-following feature while L_4 and L_5 have both boundary-following and through-going features.
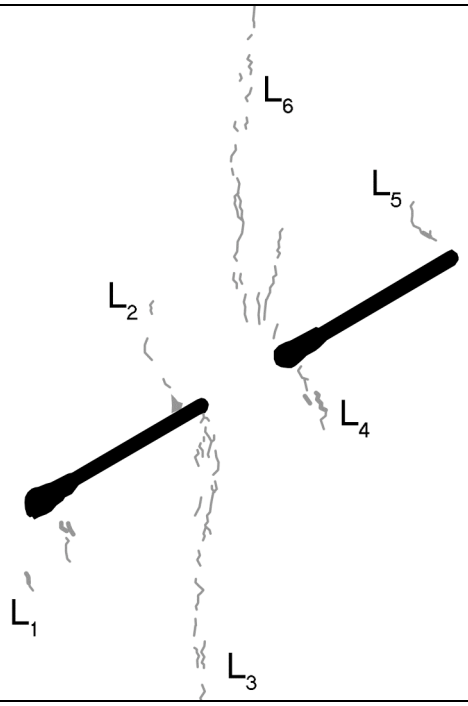	**Time:** ~14m56s **σ:** ~80.9 MPa Still image captured before high-speed recording with high-speed camera. L_2 and L_3 both extend with boundary-following features while L_6 appears. L_6 is composed solely of boundary-following features.

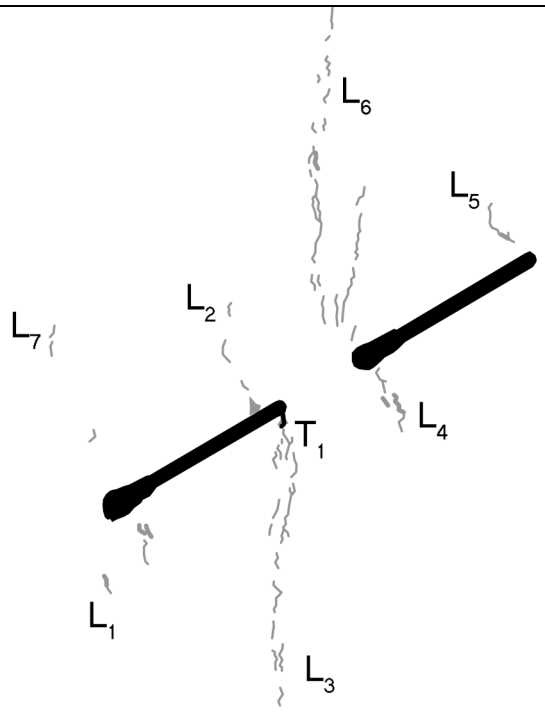	**Time:** ~16m15s **σ:** ~87.9 MPa Still image captured before high-speed recording with high-speed camera. Tensile crack T_1 appears below the inner tip of the left flaw. L_6 extends and has more features appear within it (both boundary-following and through-going). L_7 also appears above the left flaw's outer tip and is composed of boundary-following features.
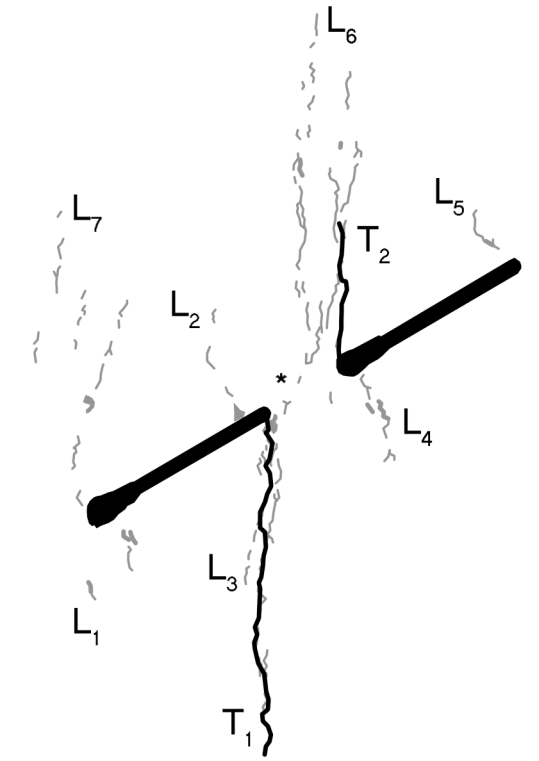	**Time:** ~17m07s **σ:** ~92.5 MPa Still image captured before high-speed recording with high-speed camera. L_4 extends slightly with a boundary-following feature. L_6 extends both up and down. Of note is the part of L_6 (labeled '*') that extends across the bridge area and connects with L_3. L_7 also extends with both boundary-following features and one small patch of lightened grains. Tensile crack T_1 extends downward while tensile crack T_2 appears.

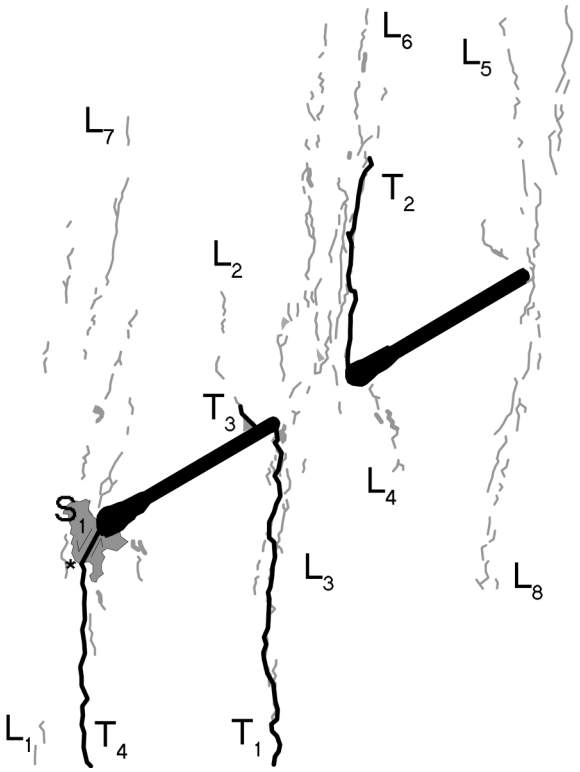

Time: ~19m18s
σ: ~104.0 MPa

Still image captured before high-speed recording with high-speed camera.

With the exception of L_3 and L_4, all linear white patches extend and have new features appear. L_8 also appears beneath the right tip's outer flaw. It is composed of boundary-following features only.

T_2 extends upward. Tensile wing crack T_3 appears above the left flaw's inner tip. Shear crack S_1 and tensile crack T_4 appear on the outer tip of the left flaw. S_1 shears in the sense indicated within a zone of spalling. The wing crack transitions to a tensile crack at the point labeled '*'. Because this was captured before high-speed recording, the sequence of these two cracks is indeterminable.

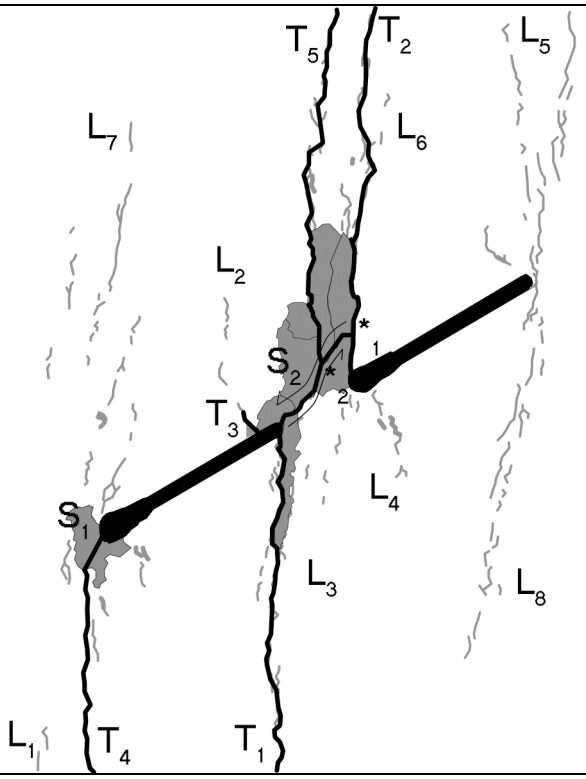

Time: 0.843s before failure

First frame of high-speed video.

A large zone of spalling occurs in the bridge zone. Shear crack S_1 (which shears in the sense indicated) causes sample coalescence as it extends from the left flaw's inner tip to a point on T_2 labeled '$*_1$'. The trace of the crack is seen in later frames. Tensile crack T_5 appears and connects with S_2 at a point labeled '$*_2$'.

Indirect (category 2) coalescence.

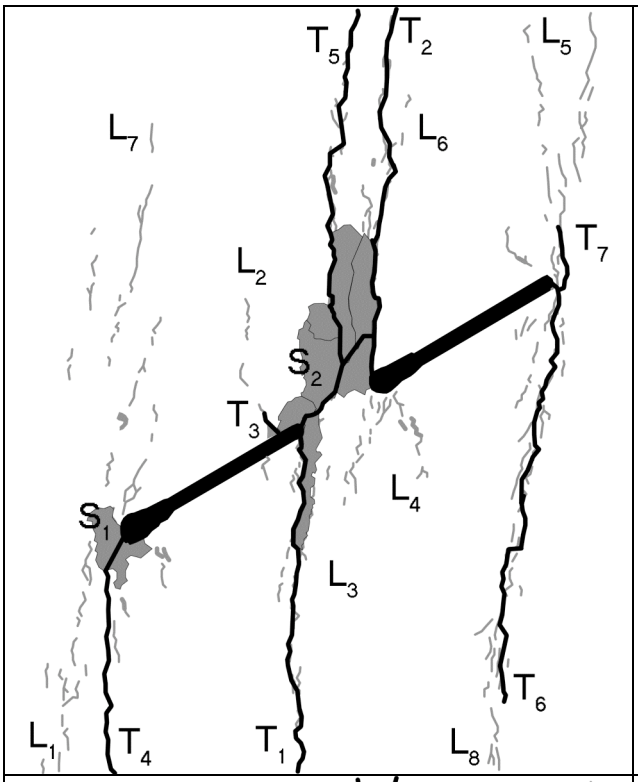	**Time:** 0.6206s before failure Tensile wing cracks T_6 and T_7 form.
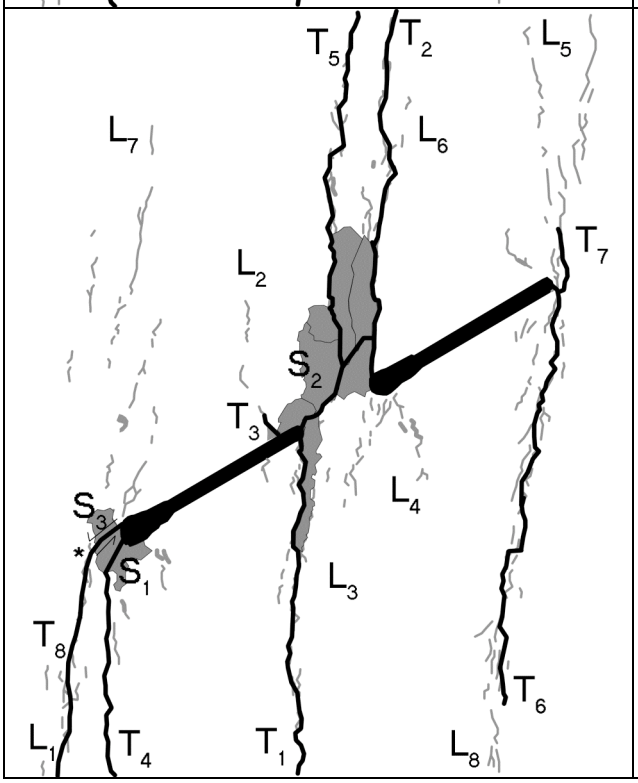	**Time:** 0.6208s before failure A second wing crack forms on the outer tip of the left flaw (labeled T_8). Shear crack S_3 starts and then transitions to tensile crack T_8. Shearing sense is as indicated

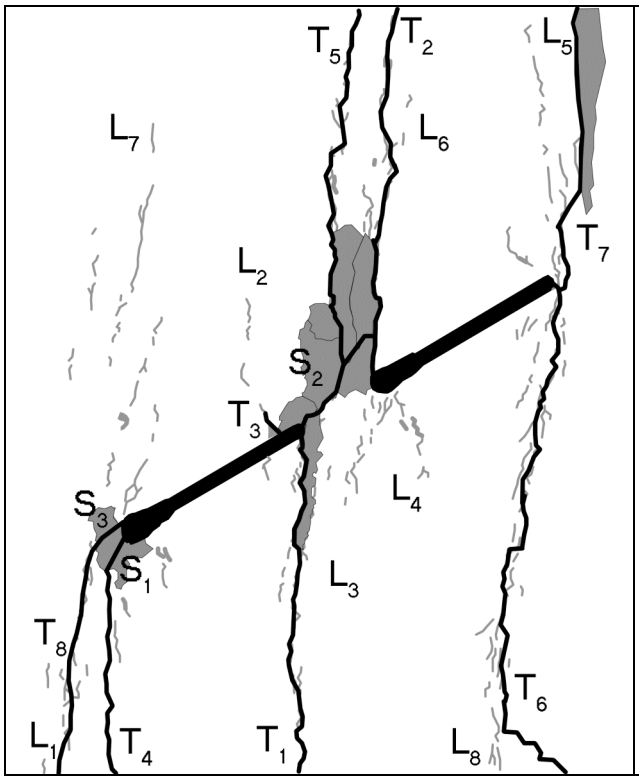

Time: 19m26.628s
σ: 105.3221 MPa

Sample failure occurs with the extension of T_6. First T_7 extends upward and a large zone of grains are crushed along its trace. Then T_6 suddenly curves in a more horizontal direction as the sample fails.

Granite a-45-0 C (20080229)

Summary

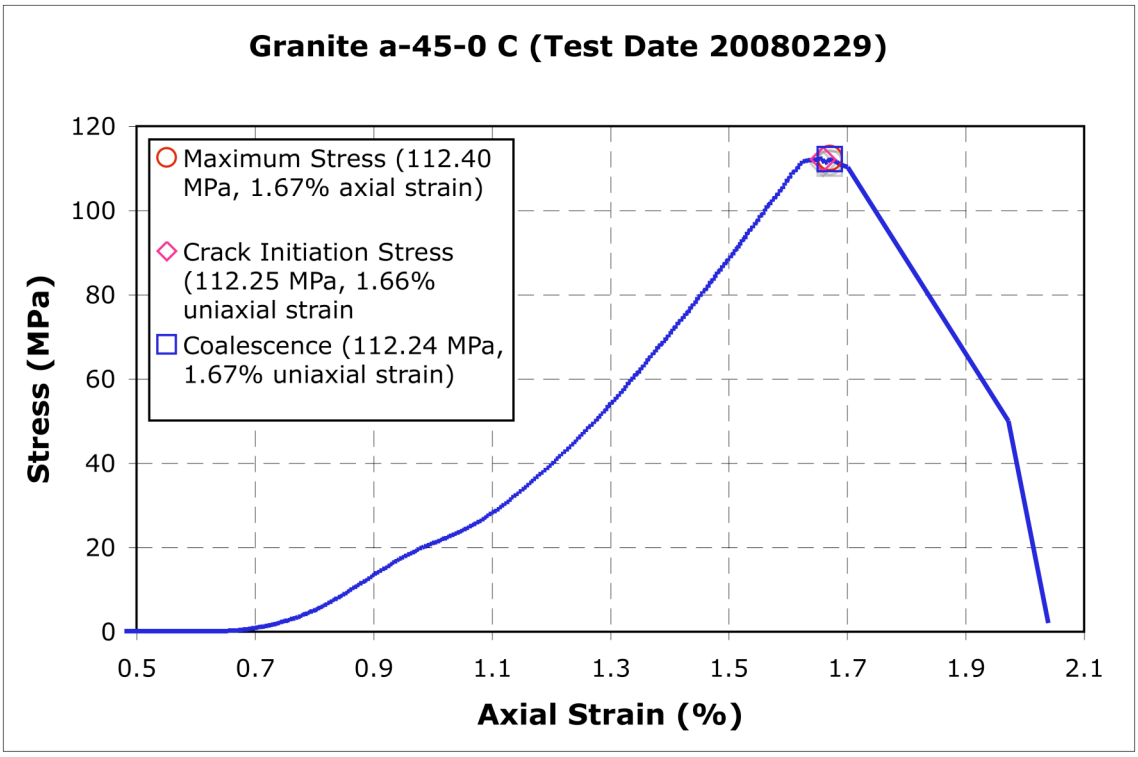

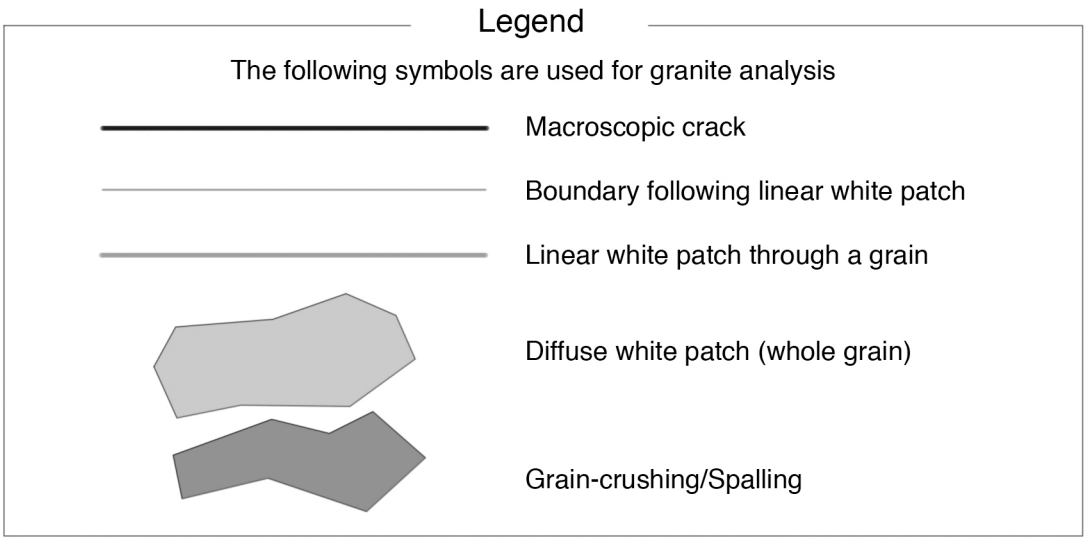

Category 2 Coalescence

Images captured from high-speed video unless otherwise noted

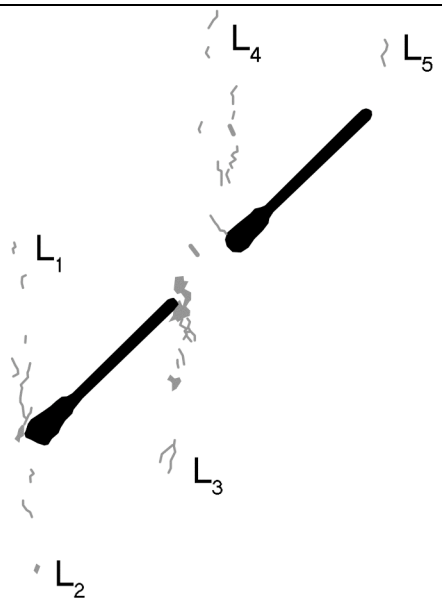	**Time:** ~17m10s **σ:** ~88.1 MPa Still image captured before high-speed recording with high-speed camera. Linear white patches L_1 through L_5 appear. All have boundary-following white patches, while L_3 and L_4 also contain through-going white patches. L_1, L_2, and L_3 also contain lightened grains.
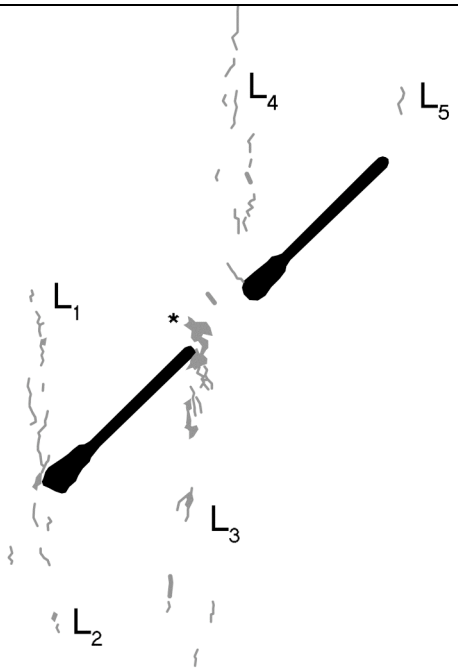	**Time:** ~19m21s **σ:** ~99.1 MPa Still image captured before high-speed recording with high-speed camera. L_1 through L_4 extend. Most extension is composed of boundary-following white patches, although some features are through-going and lightened grains. Of particular note is the increasing number of lightened grains in the bridge zone (labeled '*') as a part of L_3.

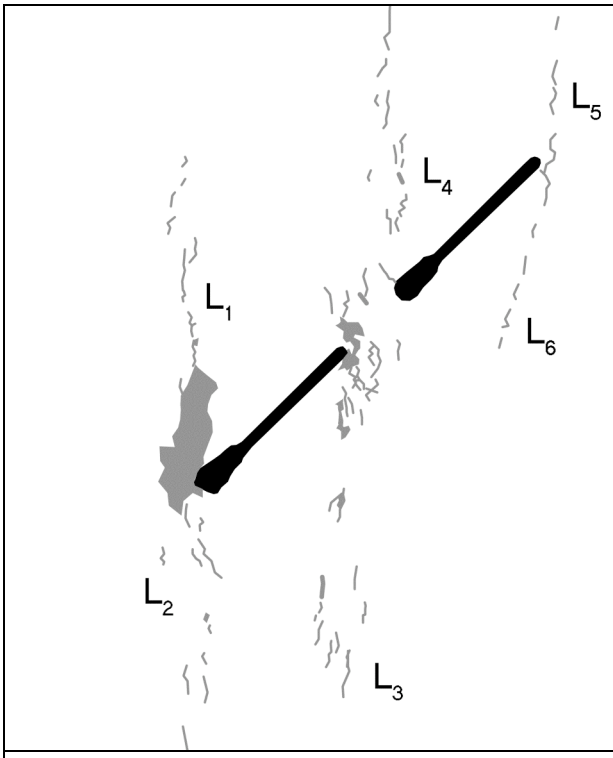	**Time:** ~21m32s **σ:** ~110.1 MPa Still image captured before high-speed recording with high-speed camera. With the exception of L_4, linear white patches continue to expand and extend. Linear white patch L_6 also appears below the right flaw's outer tip. It is composed of boundary-following linear white patches. A large zone of lightened grains appears in the L_1 region connected to the left flaw's outer tip.
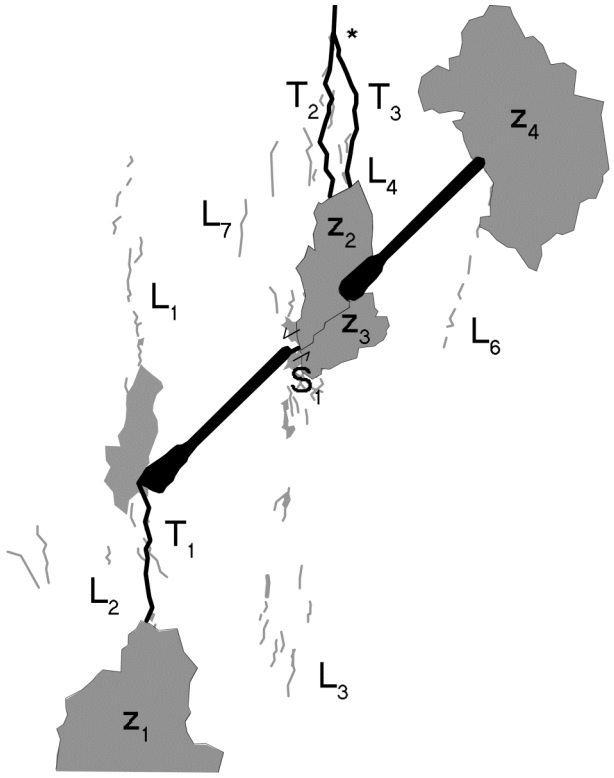	**Time:** 0.2652s before failure First frame of high-speed video analyzed. Four cracks appear along with some spalling. T_1 appears below the left flaw's outer tip and extends downward until it is hidden behind a patch of spalling (z_1). T_2 extends downward from outside the camera's field of view. T_3 branches off of T_2 at the point labeled '*'. Both tensile cracks run into the second zone of spalling (z_2), which is also attached to another patch of spalling (z_3). A small shear crack (S_1) appears at the inner tip of the left flaw and shears in the sense indicated. Finally, a large zone of spalling also appears on the outer tip of the right flaw.

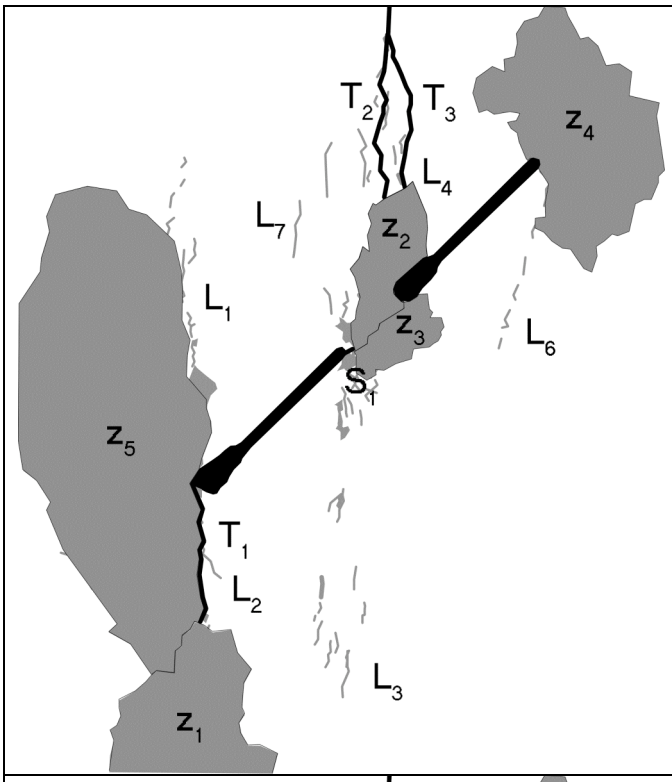	**Time:** 0.1978s before failure A very large zone of spalling appears (z_5).
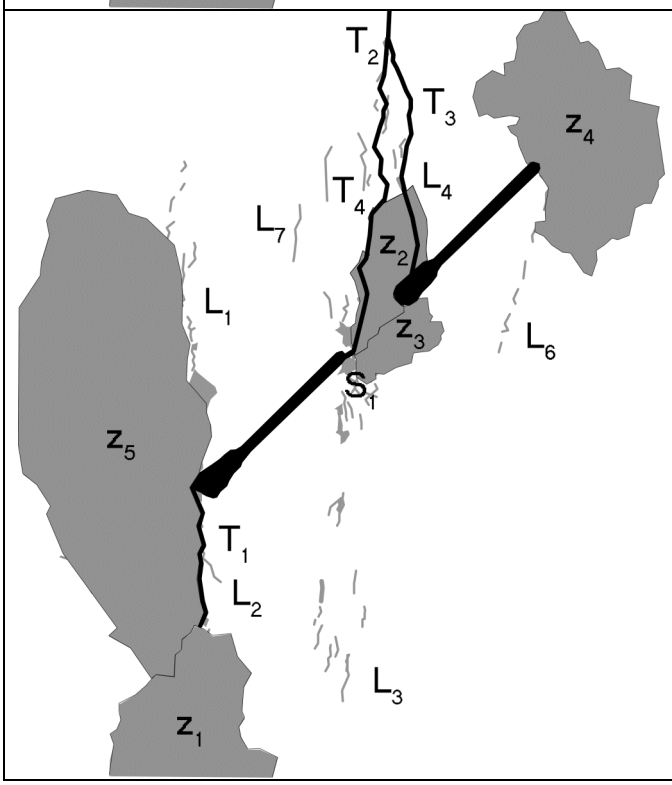	**Time:** 0.0012s before failure Sample coalescence occurs with the extension of both T_3 and T_4. T_3 connects with the right flaw's inner tip while T_4 extends to connect with S_1. Coalescence is assumed to accompany a sudden shift in the specimen (especially strong in the z_2/z_3 region). Crack traces are taken from later frames. As crack traces aren't visible in this frame, it is possible that some small portions of the cracks are of a shear nature.

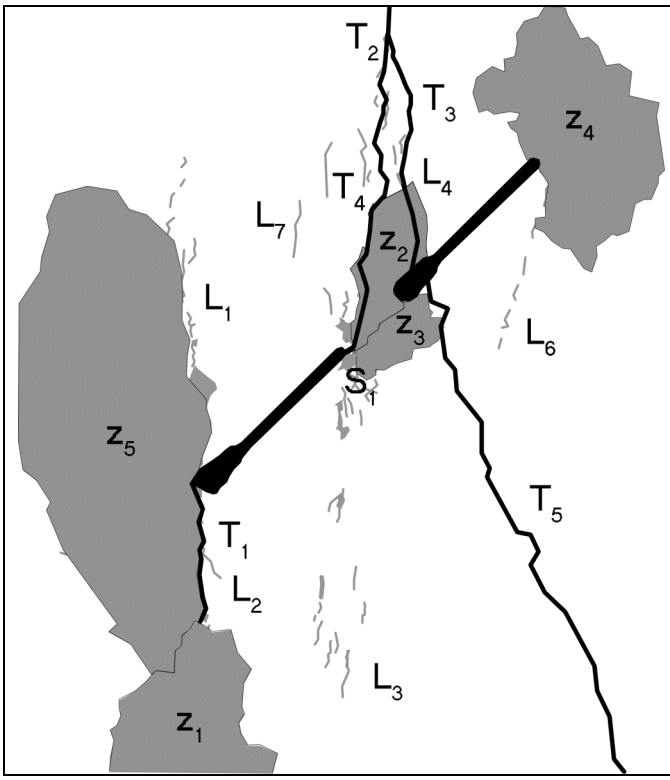

Time: 21m58.656s
σ: 112.4020 MPa

Specimen failure occurs with the formation of tensile wing crack T_5, which appears below the inner tip of the right flaw.

Granite a-45-0 D (20080420)

Summary

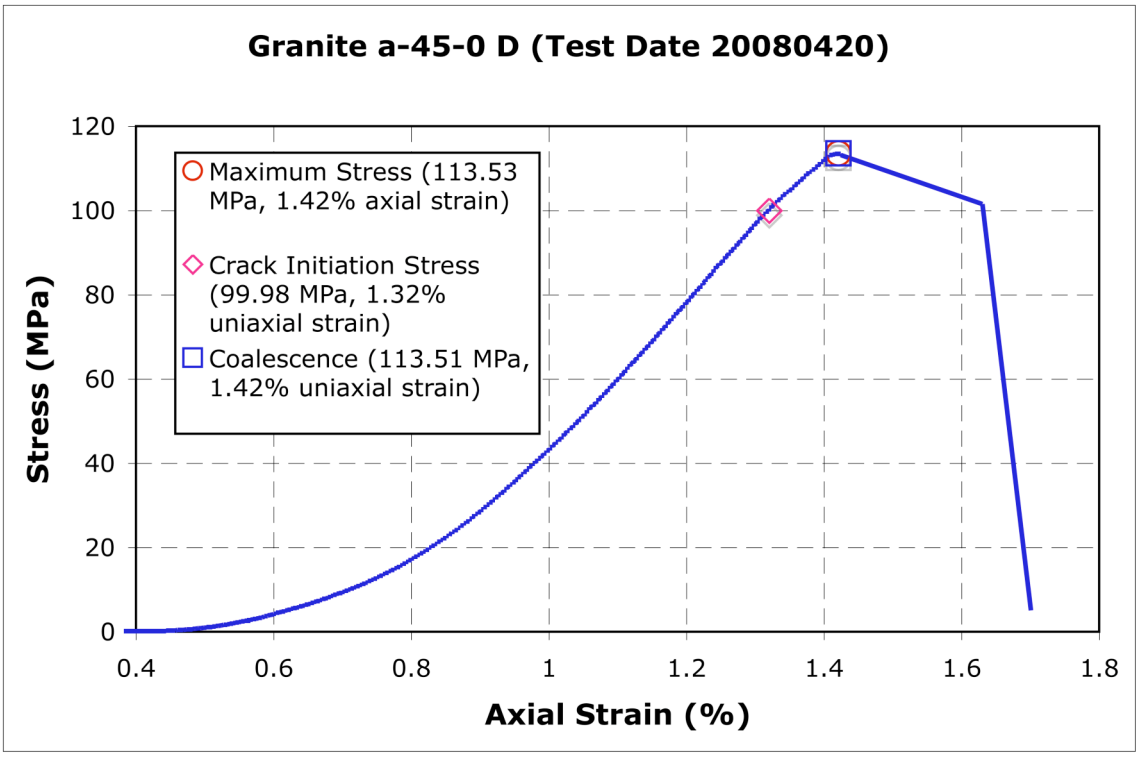

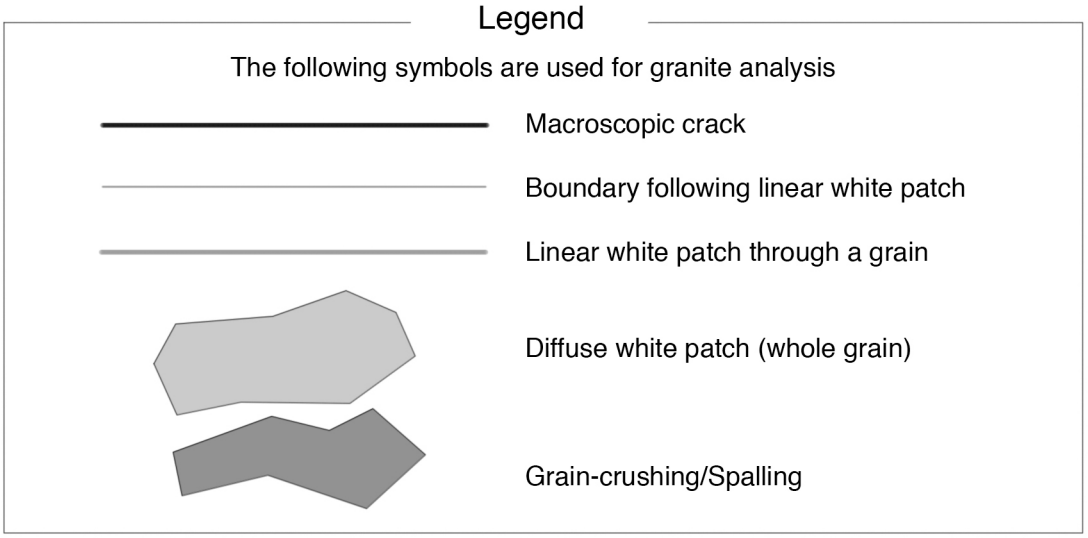

Category 2 Coalescence

Images captured from high-speed video unless otherwise noted

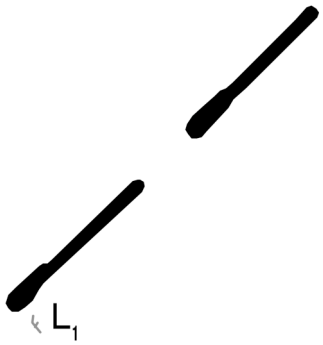	**Time:** ~8m20s **σ:** ~42.5 MPa Still image captured before high-speed recording with high-speed camera. L_1 appears below the left flaw's outer tip. It is composed of boundary-following linear features only.
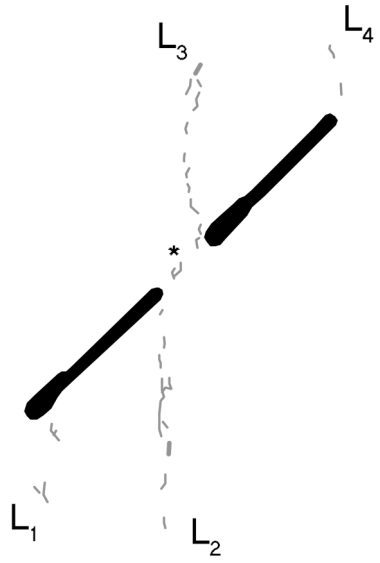	**Time:** ~85.1 MPa **σ:** ~17m04s Still image captured before high-speed recording with high-speed camera. L_1 extends slightly with more boundary-following linear white patches. L_2, L_3, and L_4 appear. L_2 and L_3 have both boundary-following and through-going linear white patches, while L_4 is composed of only boundary-following linear white patches. There are also some boundary-following linear white patches in the bridge zone (indicated by the '*').

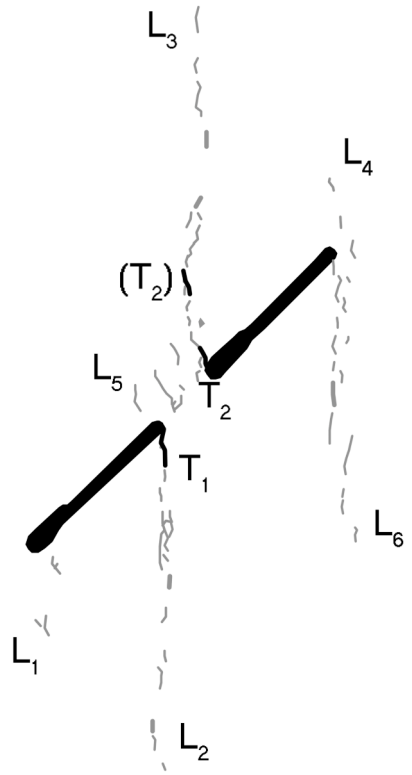	**Time:** ~20m08s **σ:** ~100.0 MPa Still image captured before high-speed recording with high-speed camera. L_2 and L_3 extend. L_5 and L_6 also appear. L_5 is composed solely of boundary-following linear white patches, while L_6 is composed of both linear feature types. More boundary-following linear white patches appear in the bridge zone. Tensile wing crack T_1 appears below the left flaw's inner tip. Tensile wing crack T_2 appears above the right flaw's inner tip. Another tensile crack appears slightly above T_2 and is labeled (T_2).
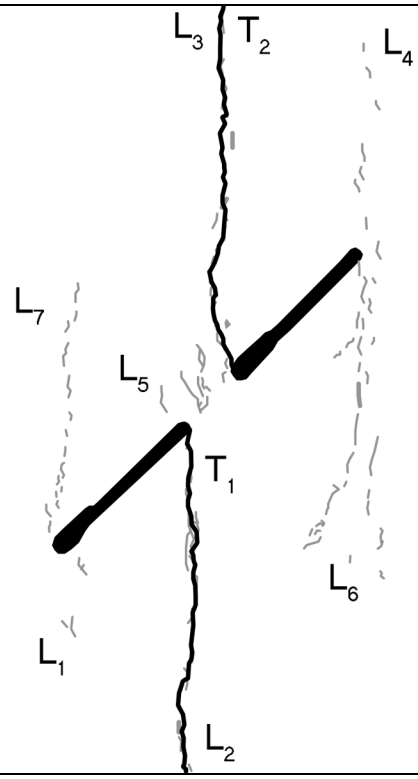	**Time:** ~21m05s **σ:** ~107.9 MPa Still image captured before high-speed recording with high-speed camera. Tensile wing cracks T_1 and T_2 extend out of the camera's field of view. T_2 extends and joins (T_2). Linear white patch L_7 forms and is composed of boundary-following linear white patches. L_4 and L_6 extend and more boundary-following linear white patches form in the bridge zone.

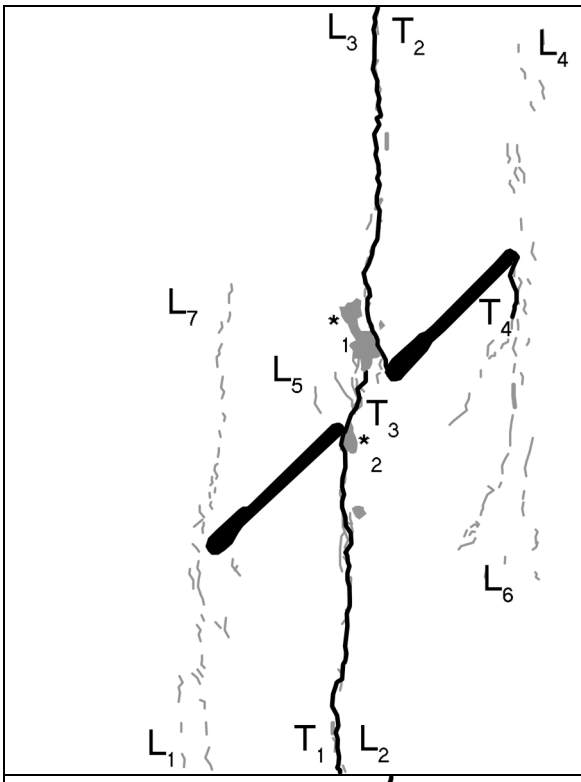	**Time**: ~22m44s **σ:** ~112.8 MPa Still image captured before high-speed recording with high-speed camera. Tensile crack T_3 appears and extends from the inner tip of the left flaw toward T_2. Joining T_3 and T_2 is a small patch of spalling labeled '$*_1$'. At the junction of T_1 and T_3 there is also a small patch of spalling (labeled '$*_2$'). While it is possible coalescence has occurred at this point, it is thought coalescence happens at a later point. Tensile wing crack T_4 appears below the outer tip of the right flaw.
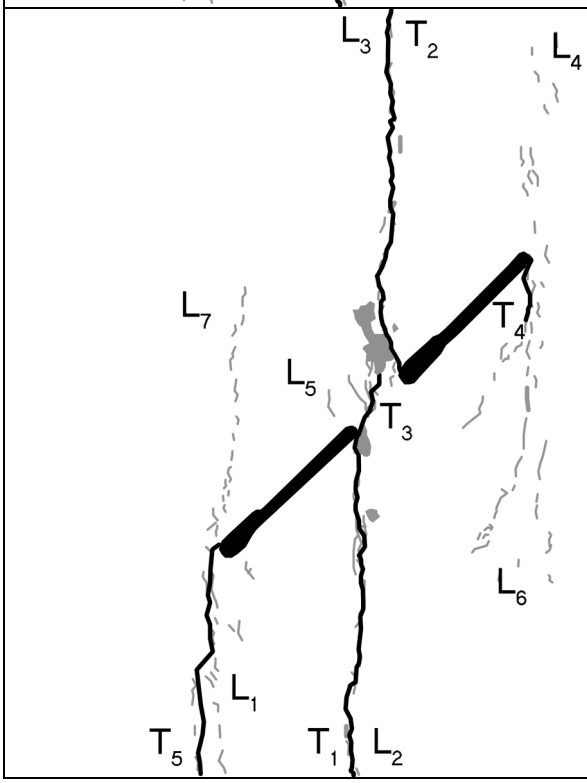	**Time:** 0.7432s before failure First frame of high-speed video. Tensile wing crack T_5 appears below the outer tip of the left flaw and extends down and out of the camera's field of view.

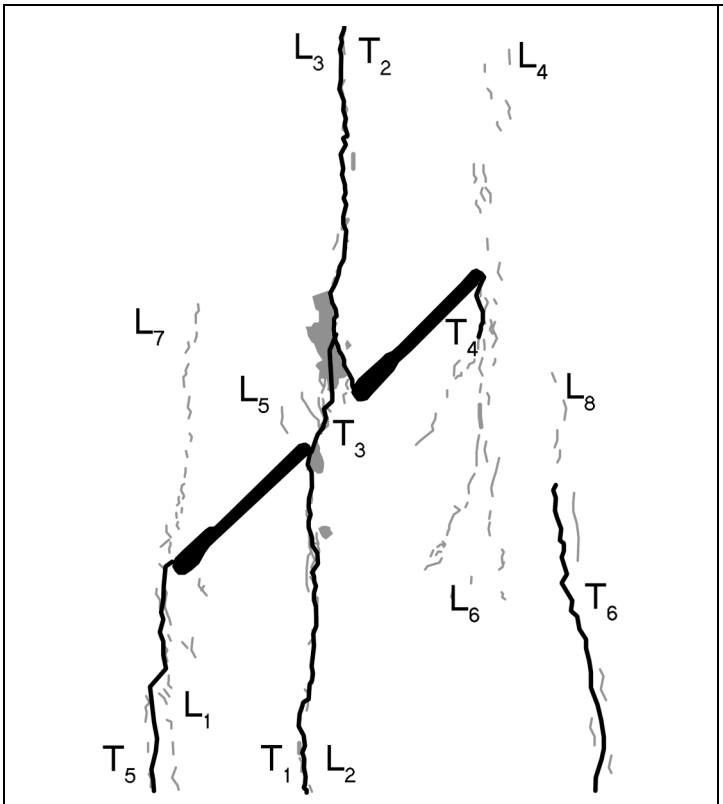

Time: 0.0004s before failure

A sudden increase in the surface spalling between T_3 and T_2 along with the widening of T_2 is taken as an indication of coalescence. The crack trace is not clearly visible and is estimated from later frames. There are no clear shear sense indicators at the time of coalescence, so the crack is assumed to be tensile in nature. Coalescence is indirect (category 2).

A tensile crack T_6 appears from outside the camera's point of view along with associated linear white patches (boundary-following). The white patches are labeled L_8. L_8 also extends beyond T_6.

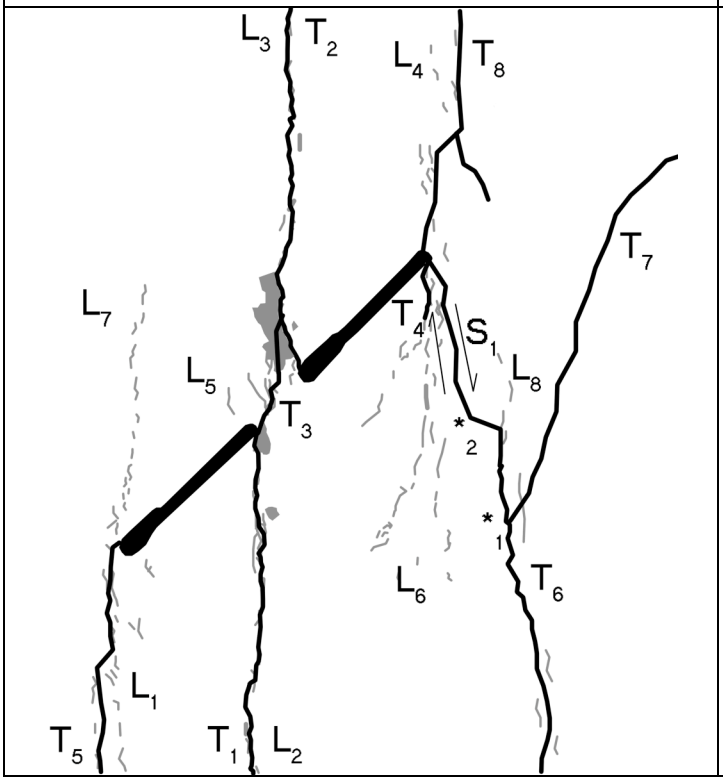

Time: 22m53.592s
σ: 113.5280 MPa

Sample failure occurs as T_6 connects with the outer tip of the right flaw with a shear crack (labeled S_1, shearing in the sense indicated). The shear nature of the crack extends from the point labeled with '$*_2$' until the flaw tip. Tensile crack T_7 branches off of T_6 at the point labeled with the '$*_1$'. Tensile wing crack T_8 appears above the right flaw's outer tip as well.

Granite a-60-0 A (20080229)

Summary

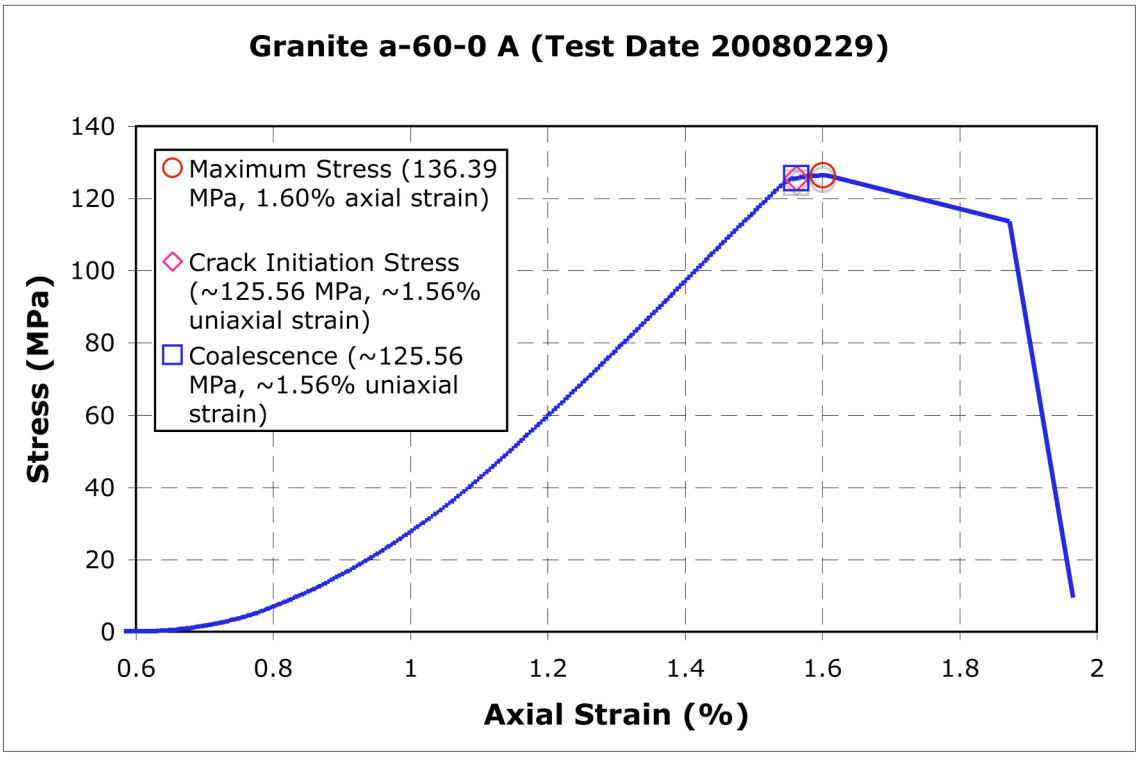

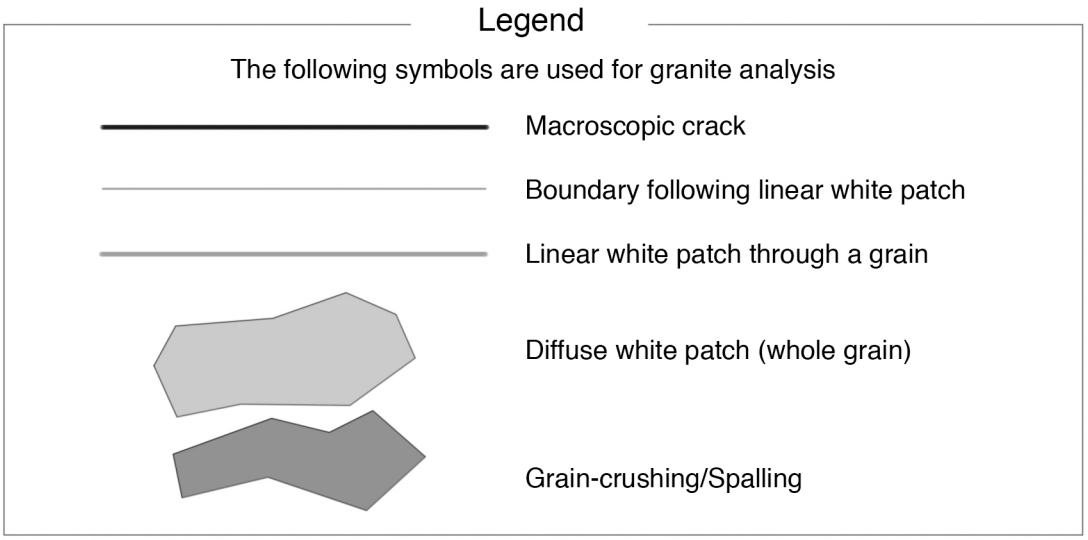

Category 3 Coalescence

Images captured from high-speed video unless otherwise noted

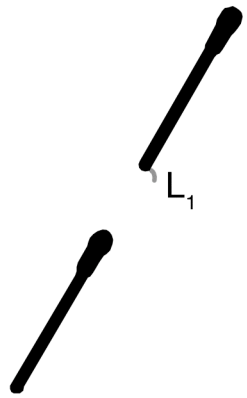	**Time:** ~6m9s **σ:** 30.9 MPa Linear white patch L_1 appears below the right flaw's inner tip. It is a through-going linear feature.
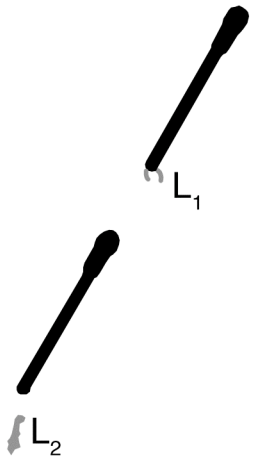	**Time:** ~12m43s **σ:** ~61.8MPa Another through-going linear white patch forms on the right flaw's inner tip. A group of lightened grains also appears near the left flaw's outer tip. They are labeled as L_2.
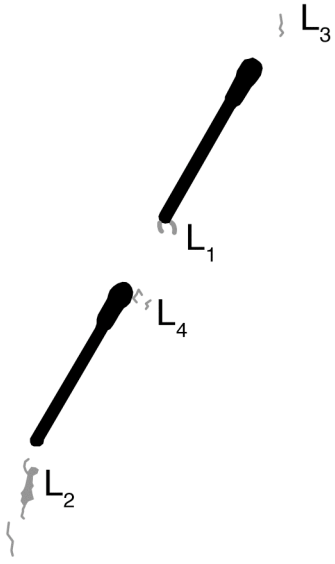	**Time:** ~17m4s **σ:** ~82.3 MPa L_2 extends both toward and away from the left flaw's outer tip. The features are all boundary-following linear features. Other boundary-following linear patches also form on the inner tip of the left flaw and the outer tip of the right flaw. They are labeled L_3 and L_4, respectively.

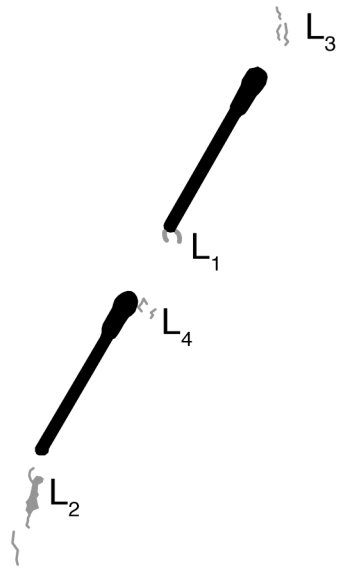	**Time:** ~19m15s **σ:** ~92.6 MPa L_3 extends with more boundary-following features.
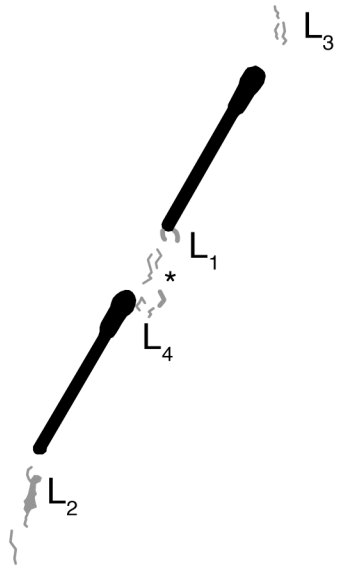	**Time:** ~21m26s **σ:** ~102.9 MPa L_4 extends up toward the right flaw's inner tip in the region marked "*". The features are mostly boundary-following, but there is one through-going feature.

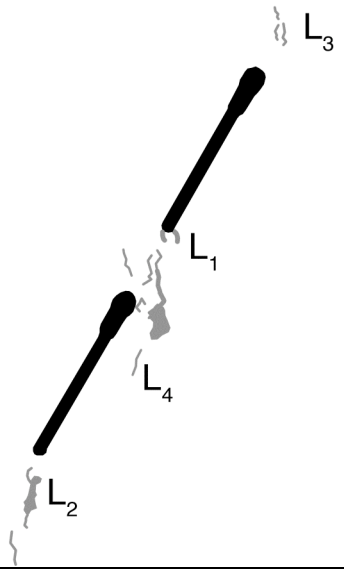	**Time:** ~24m55s **σ:** ~119.4 MPa More white patches form in the L_4 region. All three types of white patches form, with through-going white patches extending from a group of lightening grains. Other features are boundary-following.
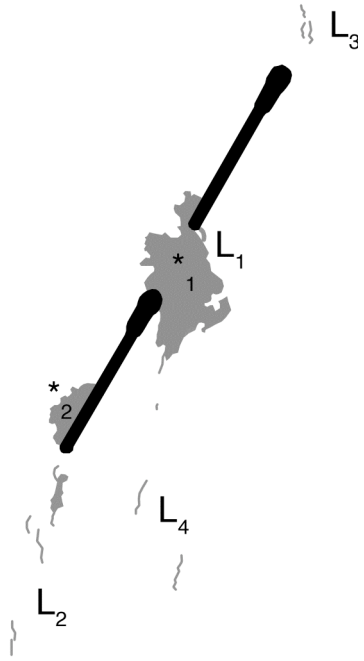	**Time:** ~25m47s **σ:** ~123.5 MPa Linear white patches L_2 and L_4 extend downward with boundary-following linear white patches. Two zones of spalling also appear. The region marked "$*_1$" is a large zone in the bridging area while the region marked "$*_2$" is on the outer tip of the left flaw.

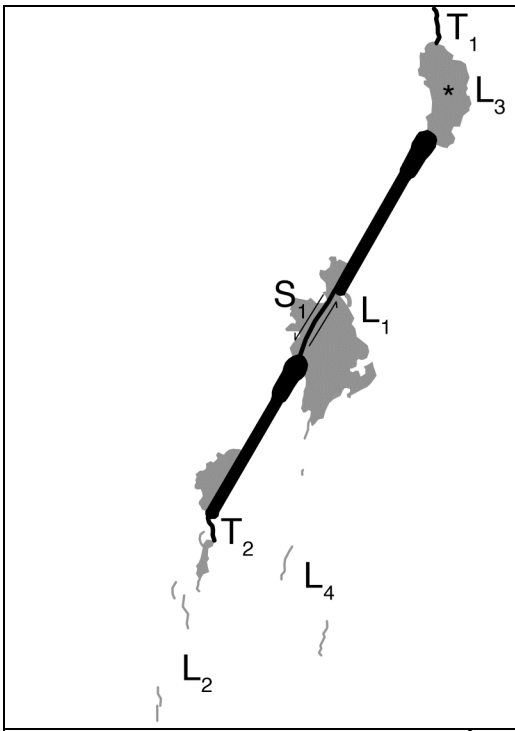	**Time:** ~26m14s **σ:** 125.6 MPa Another zone of spalling appears in the L_3 region (marked "*"). Two tensile cracks also appear. T_1 extends upward from the spalling in the L_3 region. Tensile wing crack T_2 appears on the outer tip of the left flaw. Sample coalescence occurs (category 3) with a shear crack (labeled S_1) forming directly between the two inner flaw tips. The trace of the crack is traced from later images because it is hidden behind spalling. Coalescence is evidenced by a sudden shift by both halves of the specimen in the direction indicated along the crack trace.
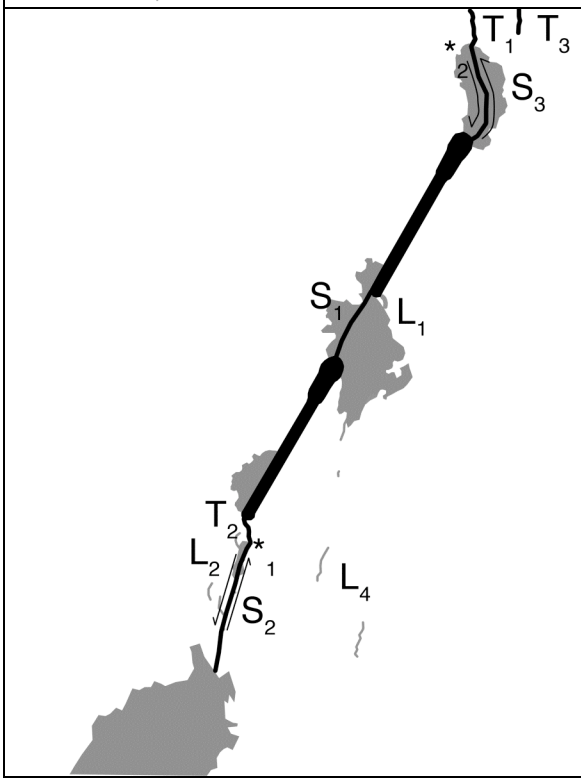	**Time:** 0.6092s before failure Two additional shear cracks form. S_2 extends from T_2 at the point marked "$*_1$" and shears in the sense indicated. Beyond S_2 a large zone of spalling forms. S_2 may extend further, but there isn't sufficient evidence. S_3 connects T_1 with the outer tip of the right flaw. S_3 is shearing in the sense indicated and connects with T_1 at the point marked "$*_2$". Tensile crack T_3 also forms near T_1.

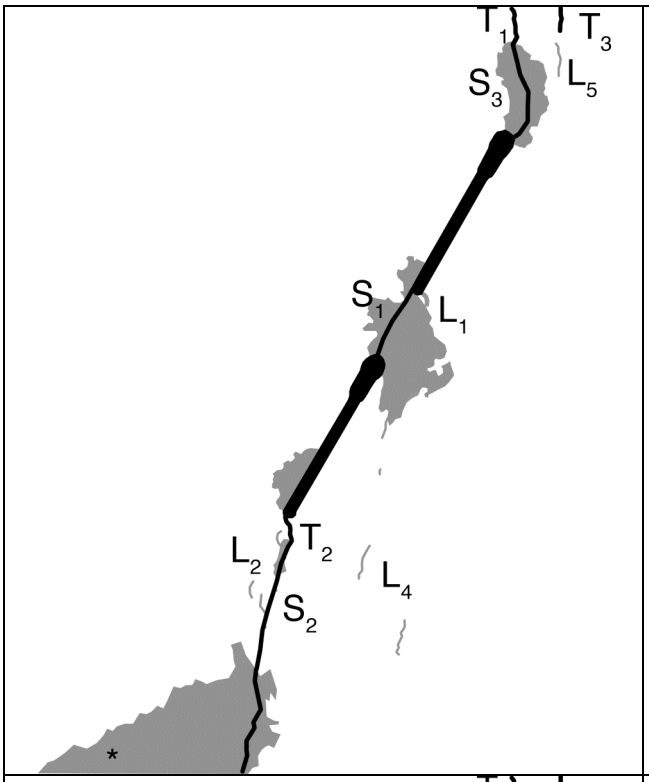	**Time:** 0.0046s before failure Linear white patch L_5 appears below T_3 as a boundary following white patch. S_2 also extends downward shearing in the same sense as the previous frame. The zone of spalling below S_2 also extends in the region marked "*".
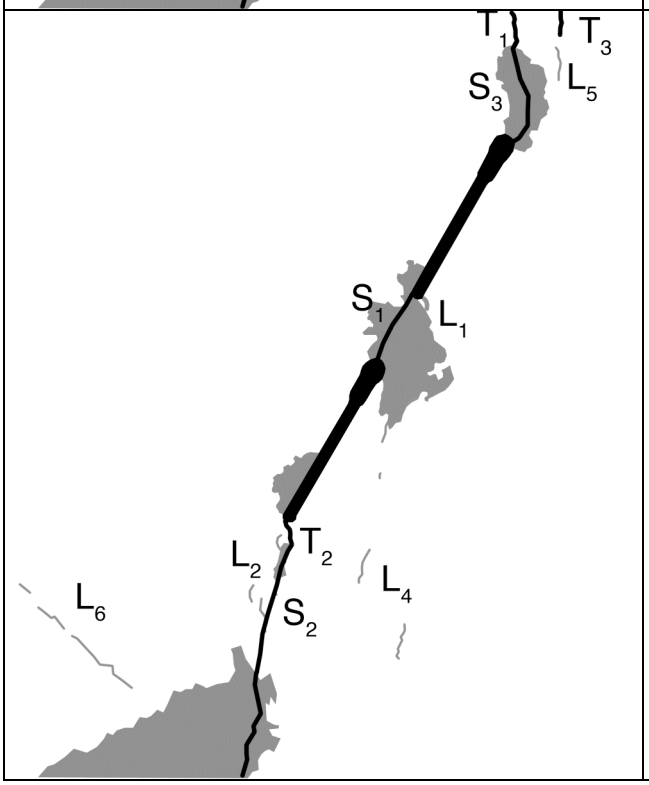	**Time:** 0.0002s before failure Linear white patch L_6 appears. It is composed of boundary-following features and has a more horizontal nature than the other linear white patches previously indicated.

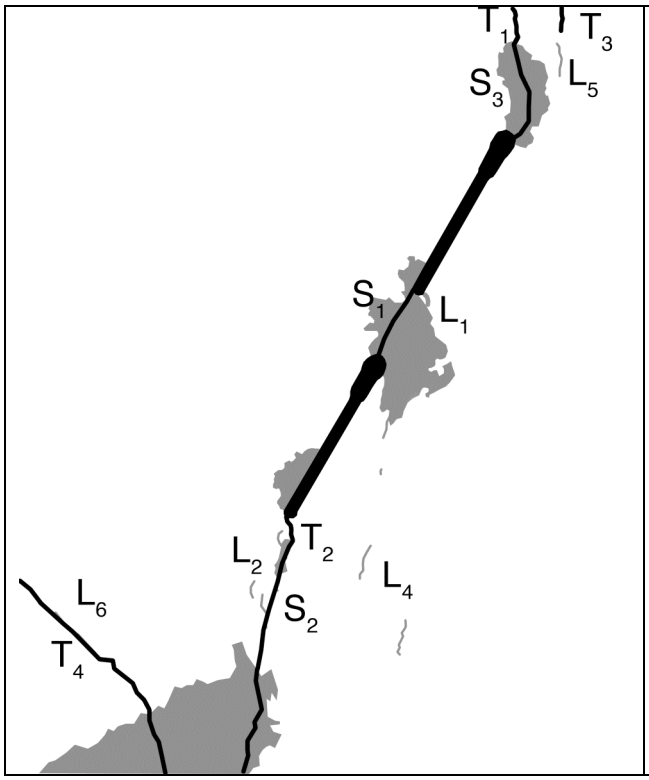

Time: 26m24.438s
σ: 126.3863 MPa

Tensile crack T_4 appears with sample failure. It follows the path of L_6 and 'turns' more vertical as it enters the zone of spalling.

Granite a-60-0 C (20080302)

Summary

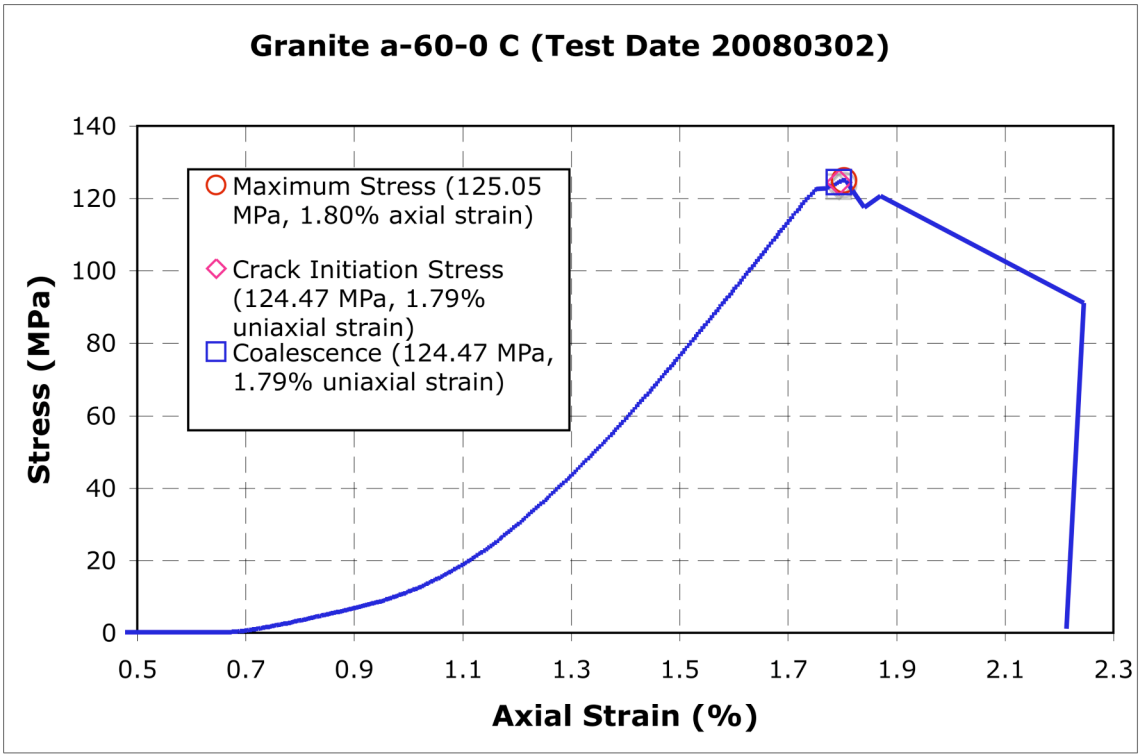

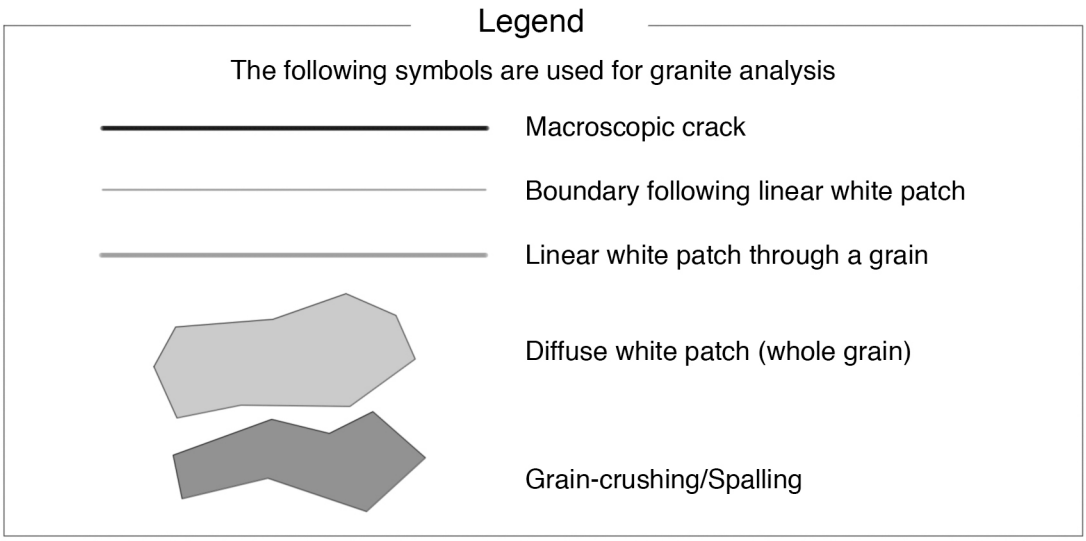

Category 4 Coalescence

Images taken from high-speed video unless otherwise noted

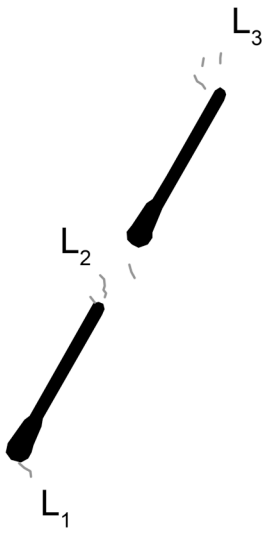	**Time:** ~10m44s **σ:** ~53.6 MPa Still image captured before high-speed recording with high-speed camera. Linear white patches L_1, L_2 and L_3 appear. All white patches are boundary-following linear features. L_2 appears to be in the bridge zone.
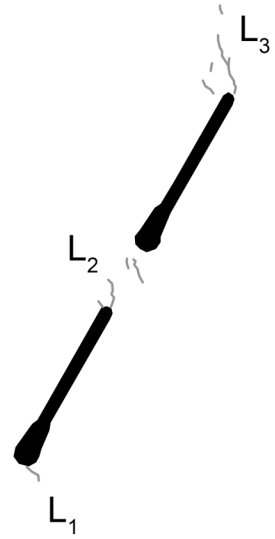	**Time:** ~17m17s **σ:** ~85.8 MPa Still image captured before high-speed recording with high-speed camera. L_2 and L_3 extend with more boundary-following linear white patches.

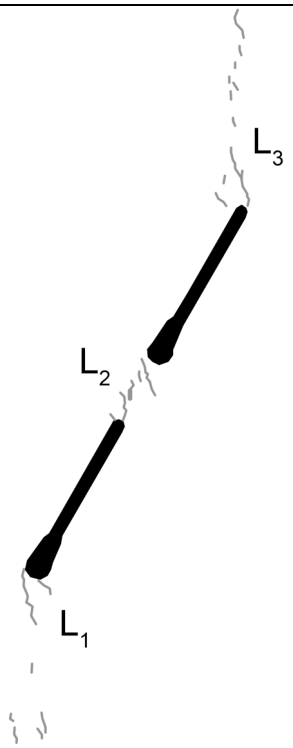	**Time:** ~21m39s **σ:** ~107.3 MPa Still image captured before high-speed recording with high-speed camera. All three linear white patches extend. A through-going linear white patch appears in L_2 and all other white patches are boundary-following.
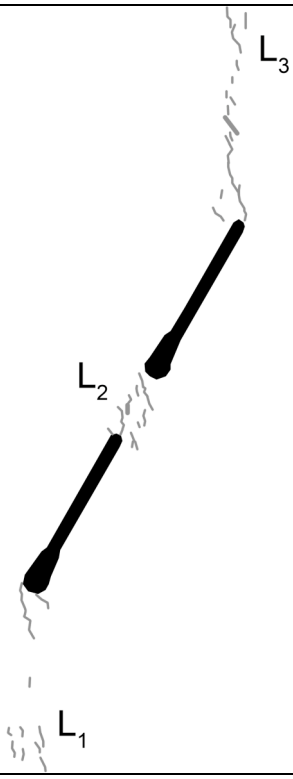	**Time:** ~24m42s **σ:** ~122.3 MPa Still image captured before high-speed recording with high-speed camera. More white patch extension and expansion

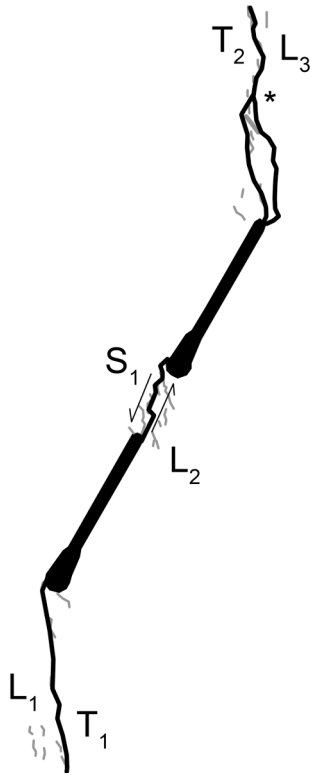	**Time:** ~25m08s **σ:** ~124.5 MPa Still image captured before high-speed recording with high-speed camera. Tensile wing cracks T_1 and T_2 appear on the outside tips of the left and right flaws, respectively. T_2 immediately branches and then reconnects at the point labeled '*'. The specimen also coalesces with the formation of a shear crack (labeled S_1). The shear crack shears in the sense indicated. Coalescence is direct (category 4). It is important to note that this is an approximate time of these events. It is doubtful they happened simultaneously as indicated, however the events were not captured in the recording and are indistinguishable on the camcorder recording.

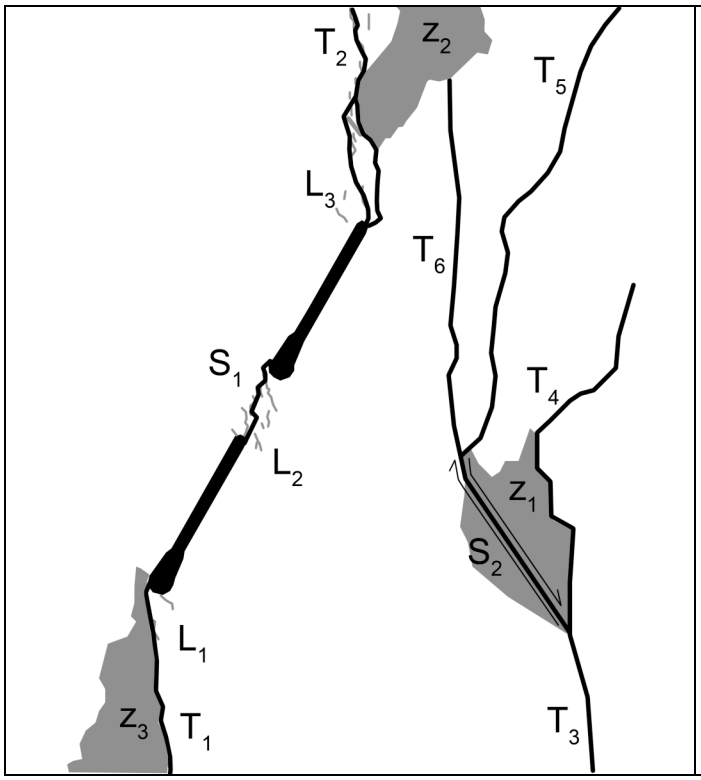

Time: 25m14.372s
σ: 125.0456 MPa

Specimen failure occurs when tensile crack T_3 appears from outside the camera's field of view. It transitions into shear crack S_2 and tensile crack T_4. Shear crack S_2 shears in the sense indicated through zone z_1 where there is surface spalling. The crack then transitions back to a tensile crack and branches into T_5 and T_6. T_6 extends until zone z_2 where a large group of grains are crushed and ejected. The zone labeled z_3 indicates another patch of surface spalling.

Granite a-75-0 C (20080418)

Summary

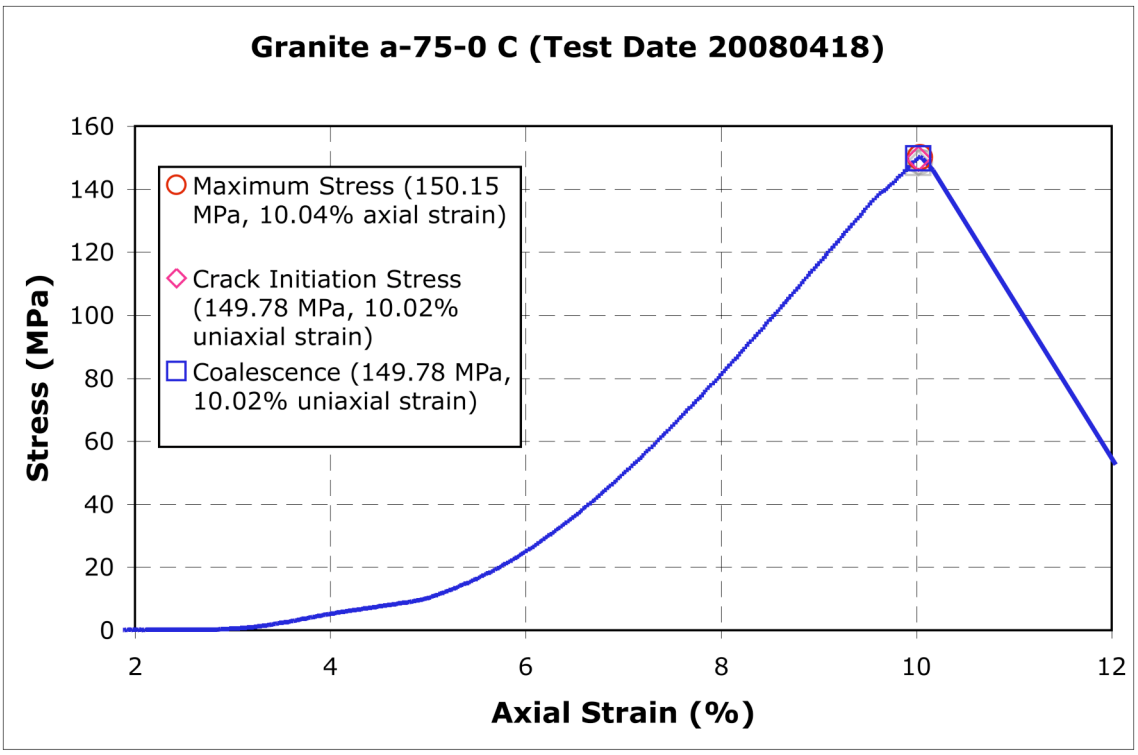

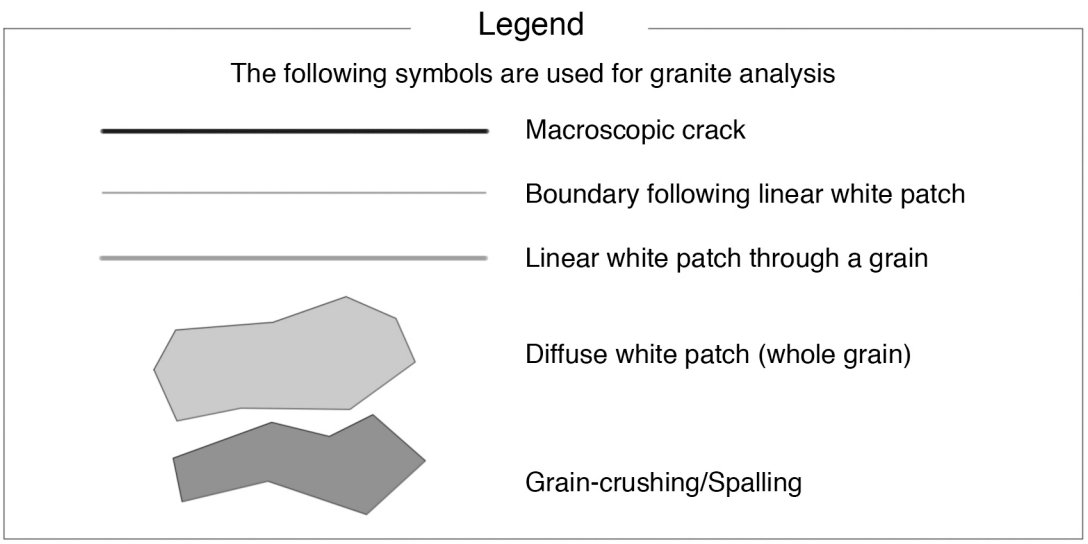

Category 4 Coalescence

Images taken from high-speed video unless otherwise noted

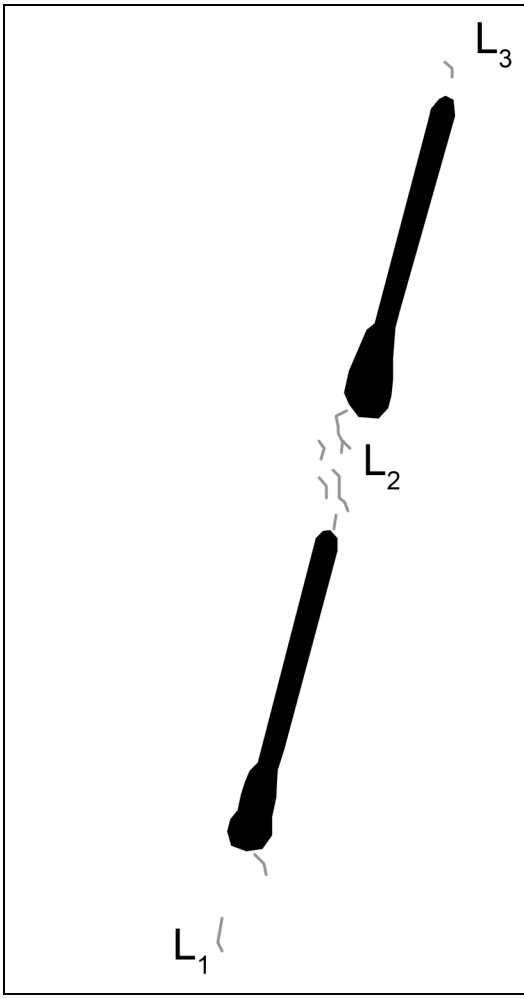	**Time:** ~12m51s **σ:** ~62.4 MPa Still image captured before high-speed recording with high-speed camera. Three linear white patches appear: L_1, L_2, and L_3. All have boundary following linear white patches.

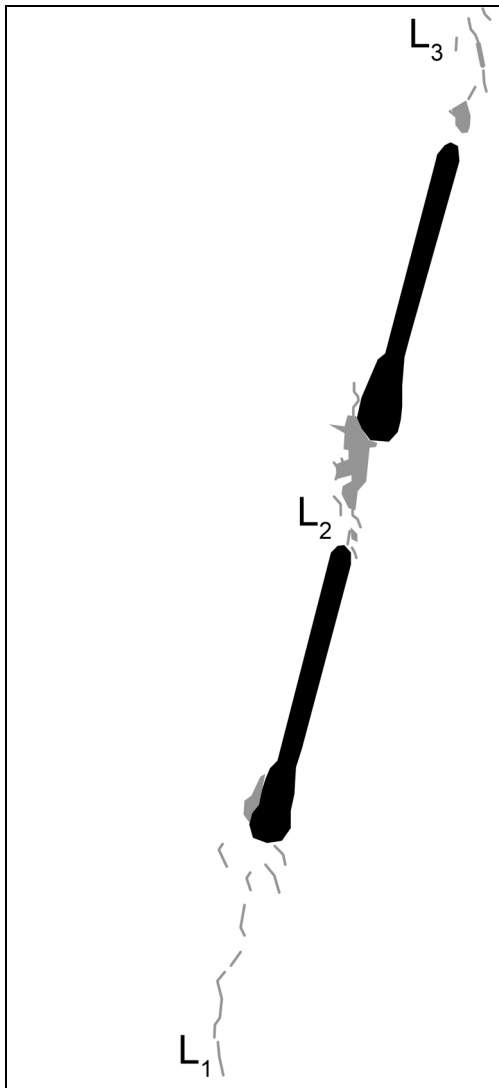

Time: ~25m56s
σ: ~124.8 MPa

Still image captured before high-speed recording with high-speed camera.

L_1 and L_2 extend. L_1 extends with boundary-following linear white patches. L_3 extends with all three types of white patch. L_2 has two groups of grains lighten.

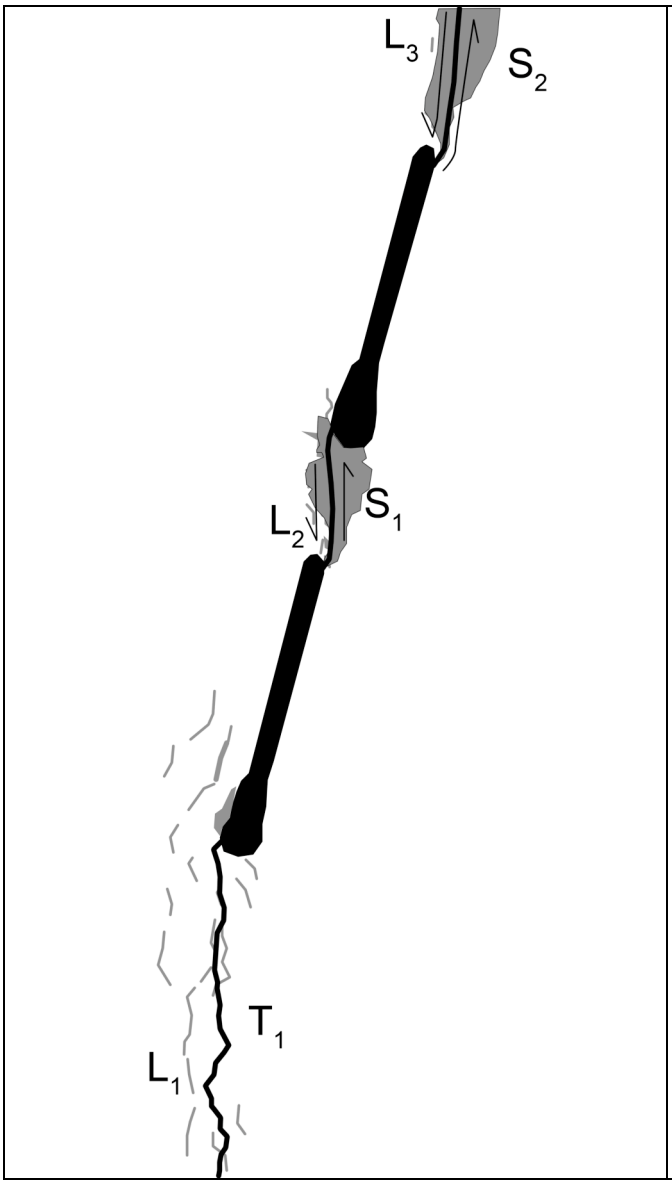

Time: ~31m09s
σ: ~149.78 MPa

Still image captured before high-speed recording with high-speed camera.

Sample coalescence occurs with crack initiation. Tensile wing crack T_1 appears below the left flaw's outer tip. Surface spalling appears in the bridge zone as well as above the right flaw's outer tip. Shear cracks S_1 and S_2 are inferred from relative motions between the two units (divided by T_1, S_1, S_2, and the flaws). Crack traces are estimated as they do not become visible at any point during the recording. Coalescence is direct (category 4).

It is important to make two notes: 1) Coalescence and crack initiation may not be (and indeed probably are not) simultaneous; the camera simply had not started recording at high speed and cracks are not distinguishable in camcorder footage. 2) Coalescence is <u>assumed</u>. This assumption is based on the evidence mentioned, but it is an assumption nonetheless.

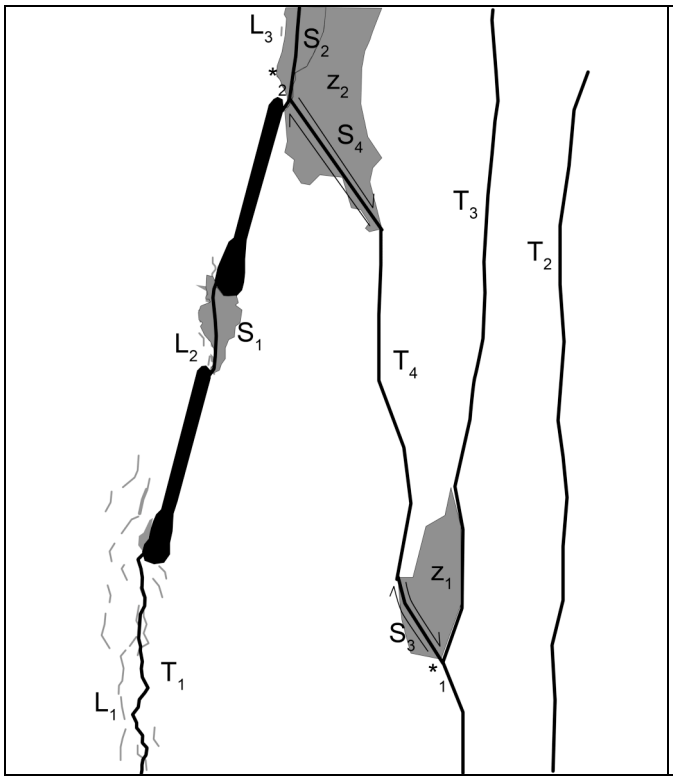

Time: 31m14.346s
σ: 150.1457 MPa

Specimen failure occurs (starting 2370) with the formation of two vertical tensile cracks (T_2 and then T_3) followed by a crack connecting T_3 and S_2 at the points labeled '$*_1$' and '$*_2$'. The crack has two shear cracks (S_3 and S_4, shearing in the sense indicated) on either side of a tensile crack (labeled T_4). Zones z_1 and z_2 indicate zones of spalling followed by bursting.

APPENDIX J – Stepped Flaws Separated by ‘a’

The following detailed analyses are for specimens with coplanar flaws ($\alpha = 60°$) and L = a (see Section 3.2 for an explanation of flaw geometry) tested as described in Chapter 3. Solid platens (see Section 3.4.2 for a description of platens) were used in all cases. For an overall summary of the results of these experiments, see Section 4.3.5.

Gr a-0-60 D

Summary

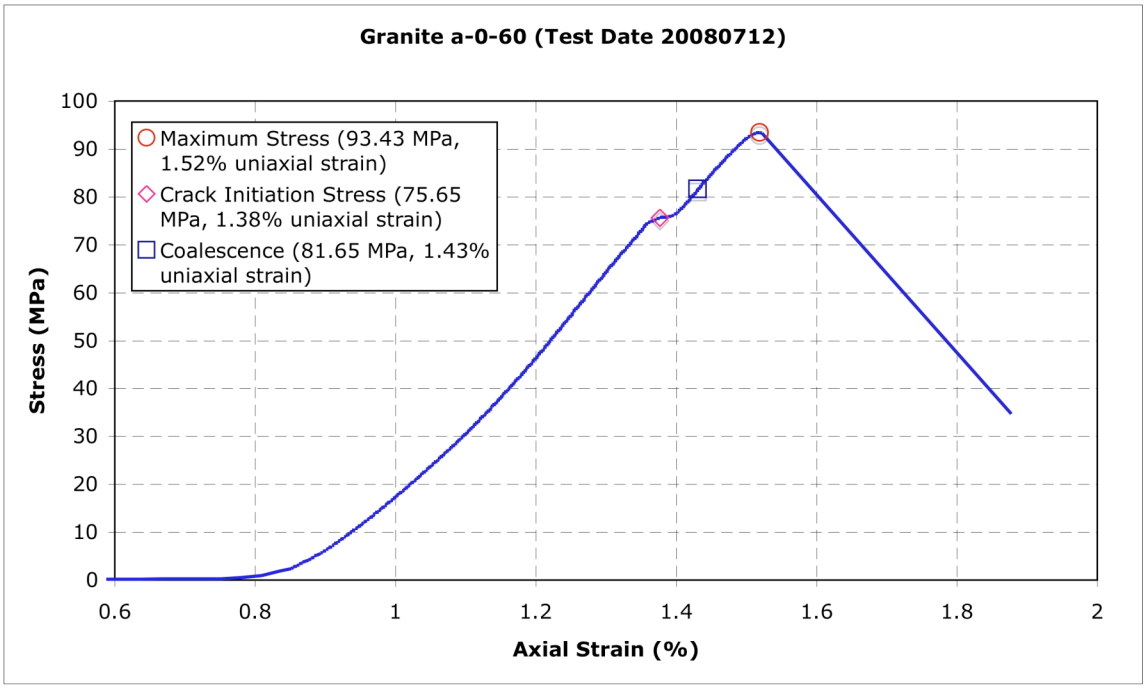

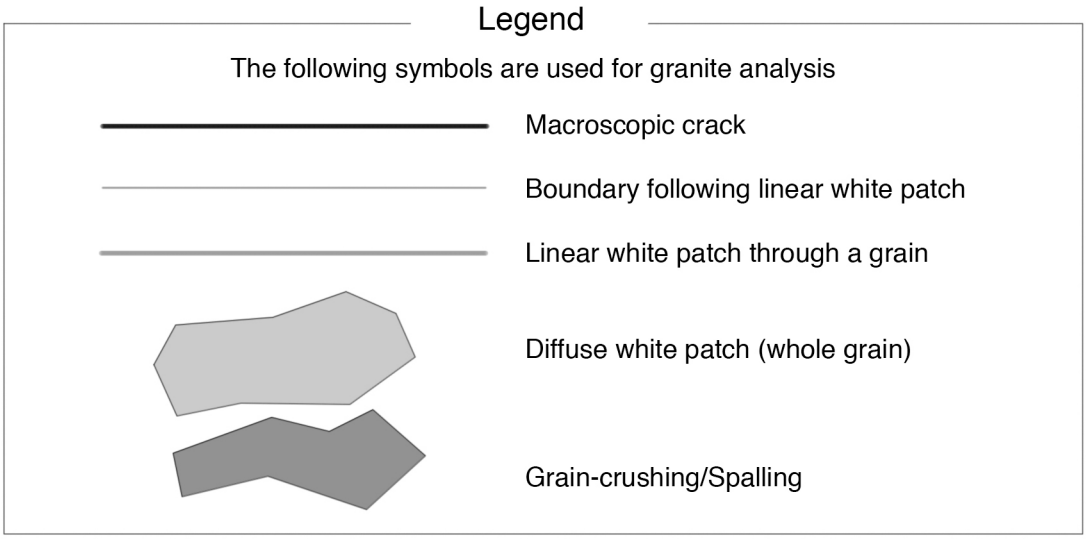

Category 6 Coalescence

Images taken from high-speed video unless otherwise noted.

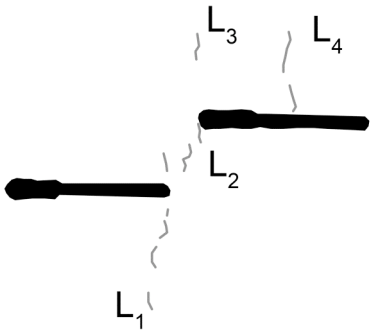	**Time:** ~9m14s **σ:** ~47.3 MPa Still image captured before high-speed recording with high-speed camera. Linear white patches L_1 through L_4 appear. All are composed of boundary-following linear white patches. Of note is the presence of L_2 in the bridging area.
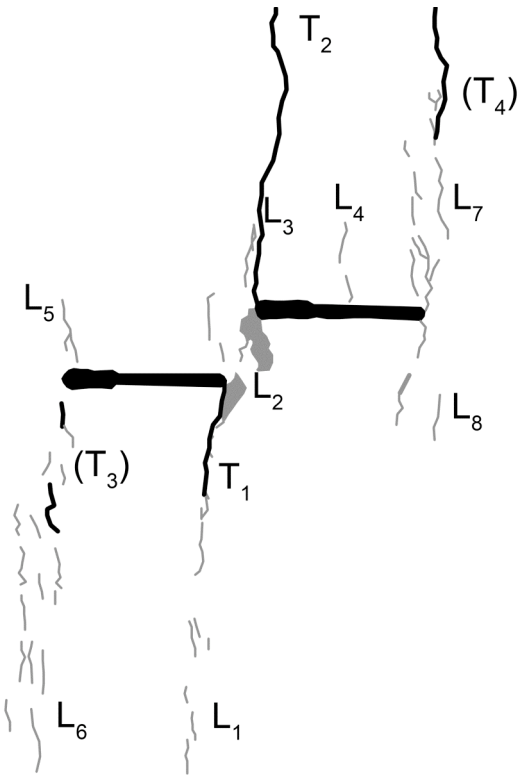	**Time:** ~15m00s **σ:** ~75.7 MPa Still image captured before high-speed recording with high-speed camera. L_1 extends downward with boundary-following linear features. L_2 extends and expands with both boundary-following linear white patches and two zones of lightening grains. L_3 extends downward with boundary-following linear features. L_5 through L_8 all appear. All but L_8 are composed solely of boundary-following linear white patches. L_8 includes a through-going feature. Tensile wing cracks T_1 and T_2 appear below and above the left and right flaws' inner tips, respectively. Tensile cracks (T_1) and (T_2) appear below and above the left and right flaws' outer tips, respectively.

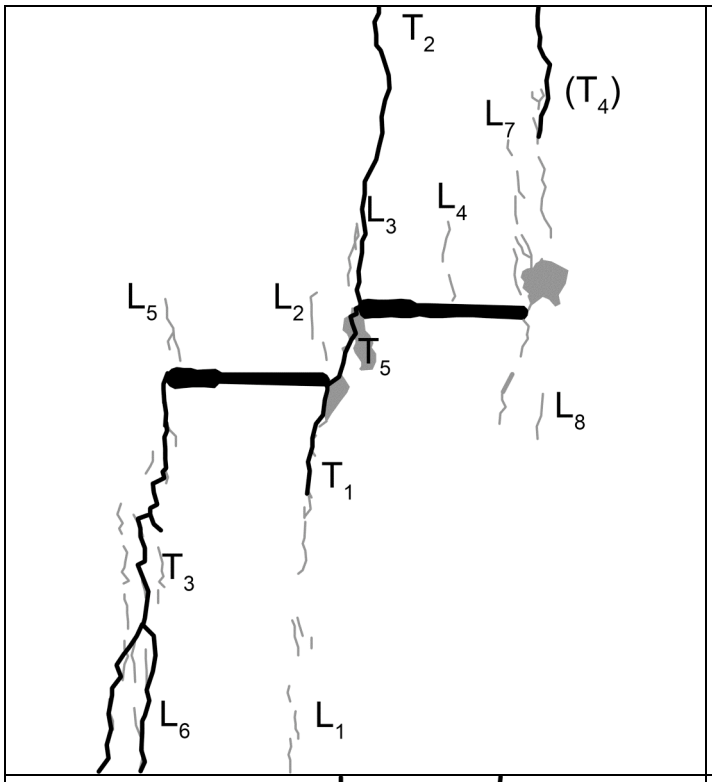

Time: ~16m13s
σ: ~81.6 MPa

Still image captured before high-speed recording with high-speed camera.

Specimen coalesces with the appearance of tensile crack T_5 directly connecting the two inner flaw tips. (T_3) extends in both directions, becoming tensile wing crack T_3. Some grains lighten in the L_7 region.

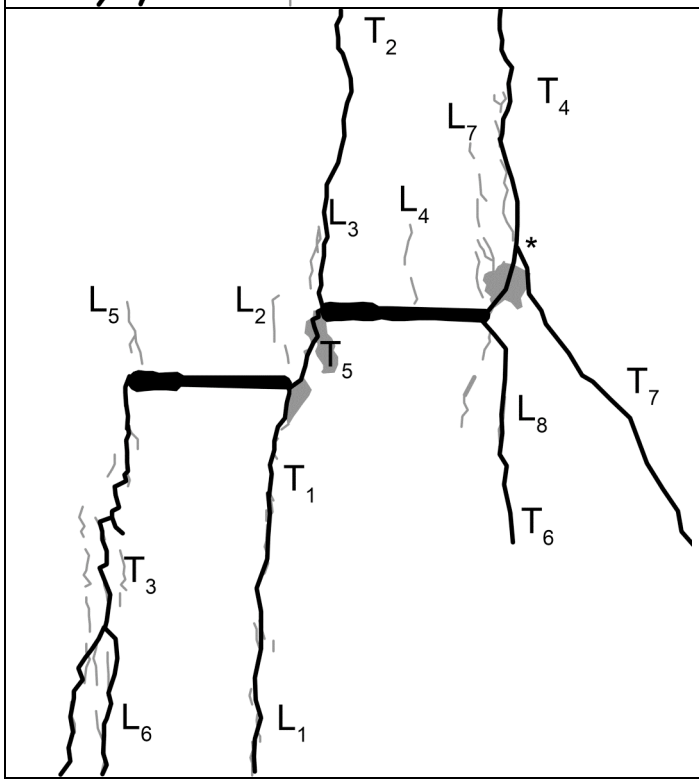

Time: 18m37.32s
σ: 93.4320 MPa

Image taken from high-speed video.

Tensile crack (T_4) extends downward and becomes tensile wing crack T_4. Specimen failure occurs when tensile cracks T_6 and T_7 appear simultaneously. T_6 is a tensile wing crack while T_7 branches off of T_4 at the point indicated by the "*".

Gr a-0-60 E

Summary

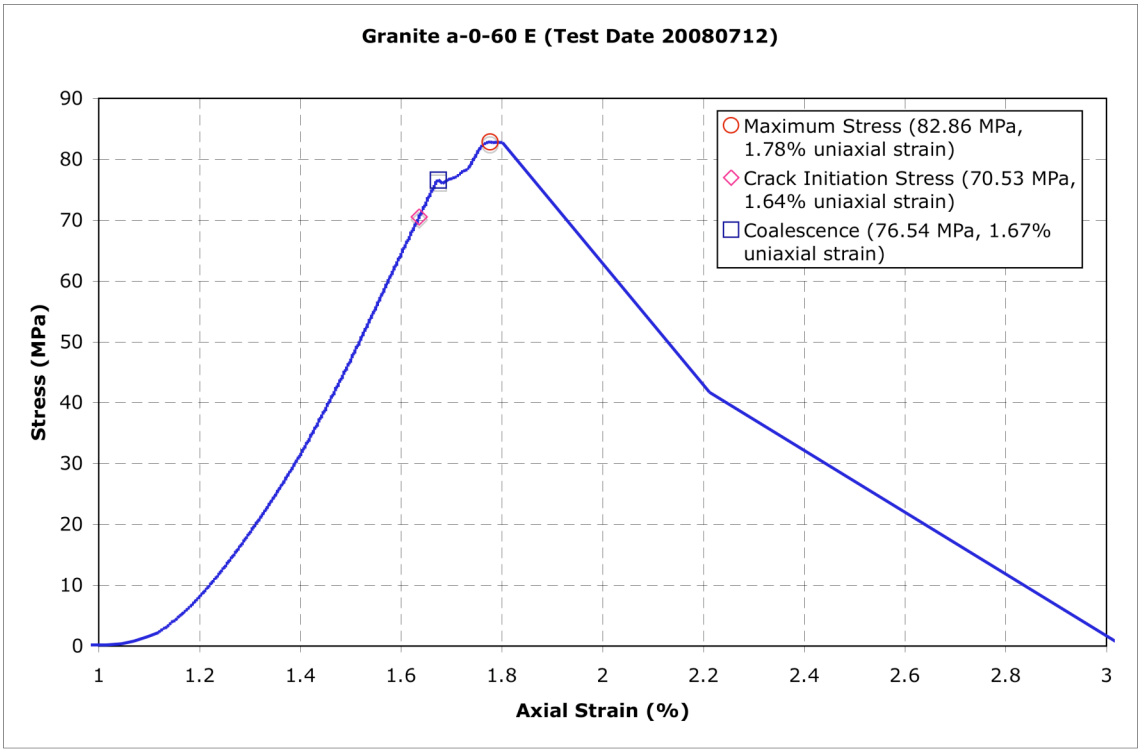

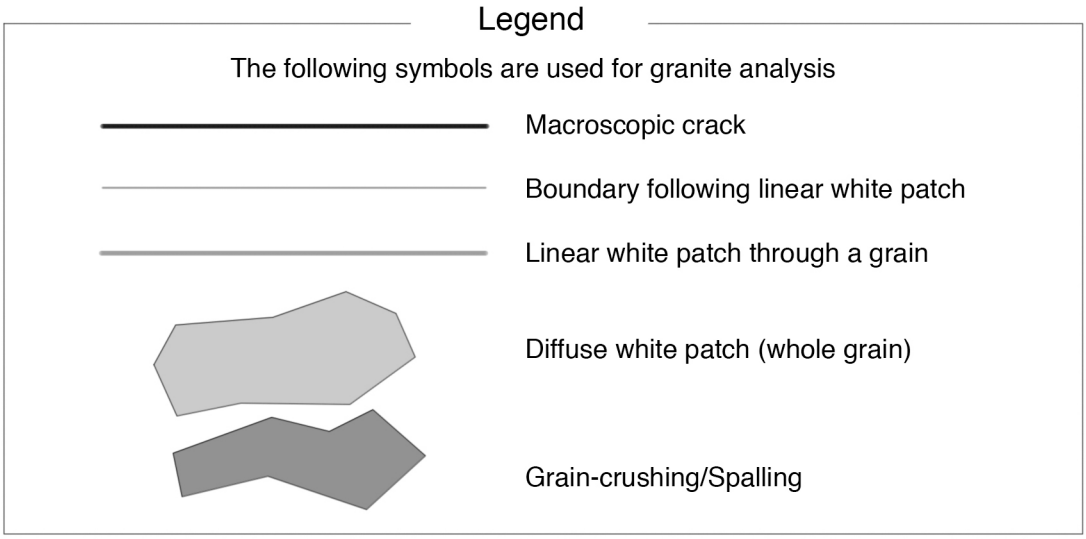

Category 2 (indirect) Coalescence
Images take from high-speed video unless otherwise noted

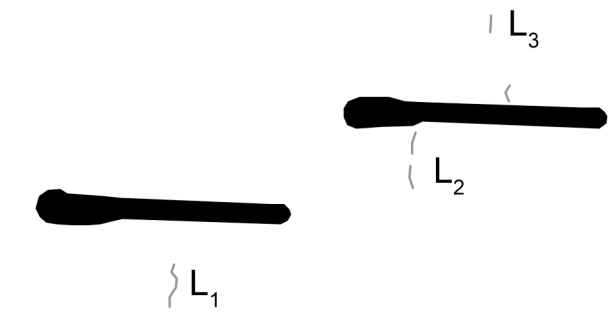	**Time:** ~6m47s **σ:** ~34.2 MPa Still image captured before high-speed recording with high-speed camera. Linear white patches L_1, L_2, and L_3 appear. All are composed solely of boundary-following white patches.
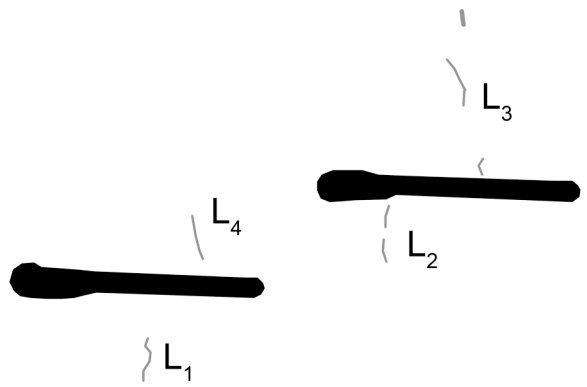	**Time:** ~8m33s **σ:** ~42.8 MPa Still image captured before high-speed recording with high-speed camera. L_3 extends with both boundary-following and through-going features. Linear white patch L_4 appears above the inner tip of the left flaw.
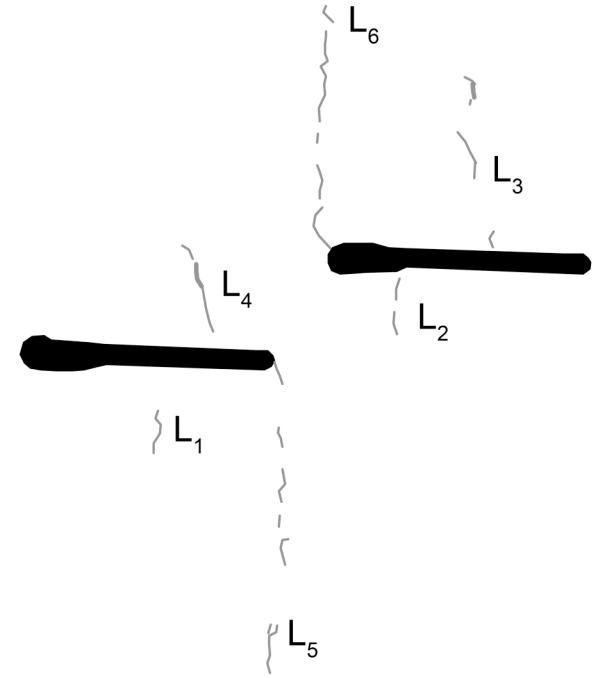	**Time:** ~10m44s **σ:** ~53.4 MPa Still image captured before high-speed recording with high-speed camera. Linear white patches L_5 and L_6 appear below and above the left and right flaws' inner tips, respectively. Both are composed solely of boundary-following linear white patches.

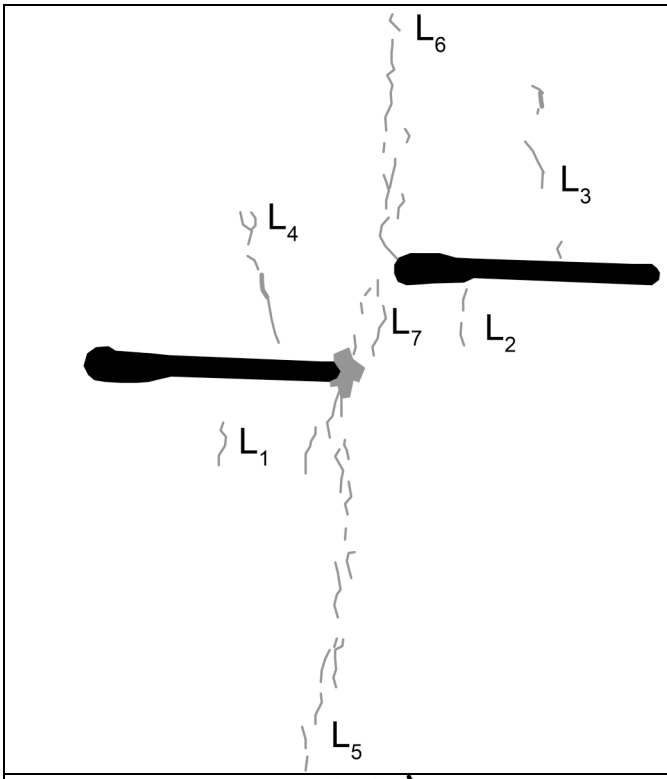	**Time:** ~13m21s **σ:** ~66.3 MPa Still image captured before high-speed recording with high-speed camera. Linear white patches L_5 and L_6 extend with boundary-following linear features. The two inner flaw tips are connected by linear white patch L_7. L_7 includes both boundary-following linear white patches and a zone of lightened grains on the inner tip of the left flaw.
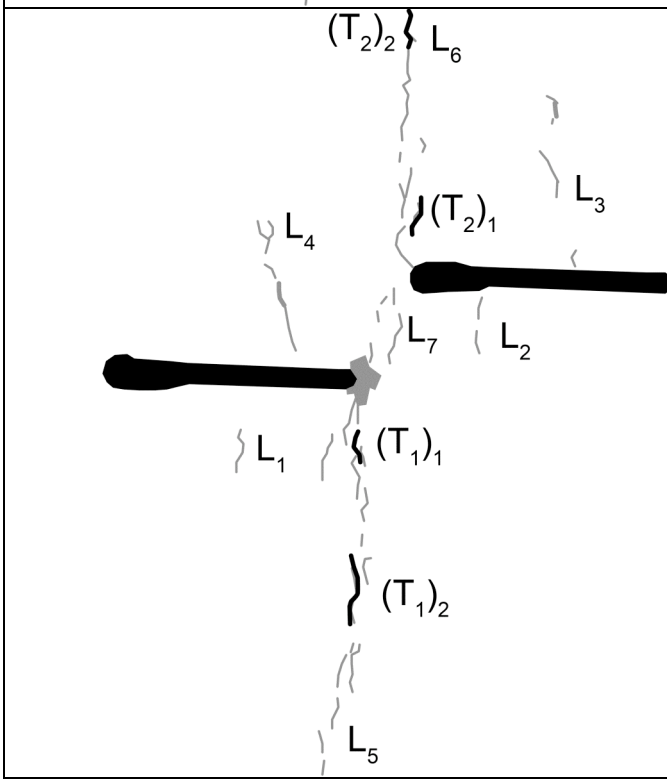	**Time:** ~14m14s **σ:** ~70.5 MPa Still image captured before high-speed recording with high-speed camera. Tensile cracks appear in the L_5 and L_6 regions. $(T_1)_1$ and $(T_1)_2$ appear in the L_5 region while $(T_2)_1$ and $(T_2)_2$ appear in the L_6 region.

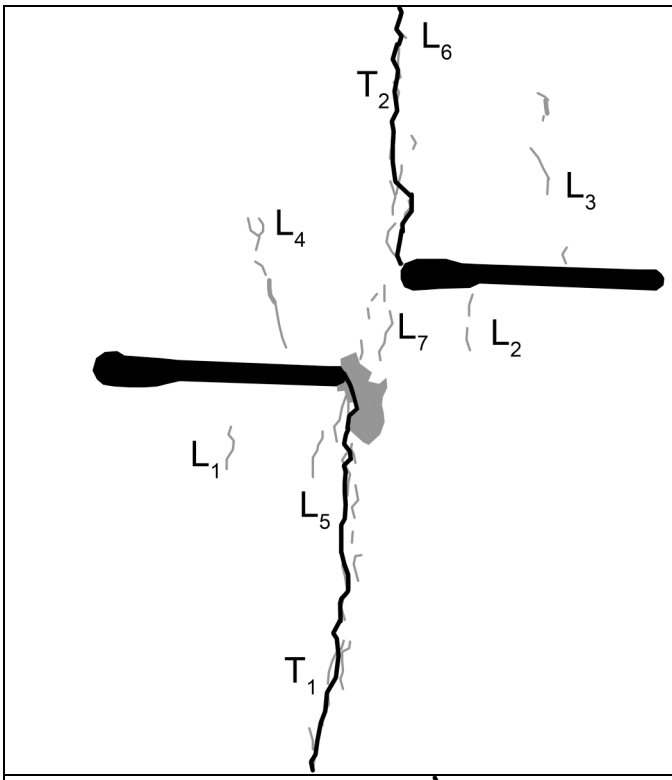	**Time:** ~15m06s **σ:** ~74.8 MPa Still image captured before high-speed recording with high-speed camera. (T_1) and (T_2) extend and link and become tensile wing cracks T_1 and T_2, respectively. The patch of lightened grains in the L_7 region expands downward.
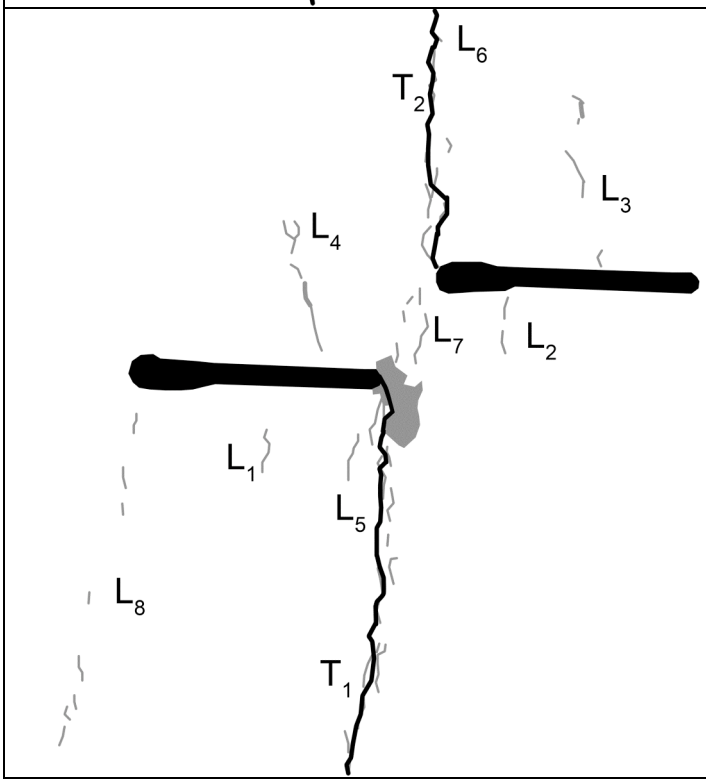	**Time:** 6.1035s before coalescence **σ:** 76.06 MPa First frame of high-speed video. Linear white patch L_8 appears below the outer tip of the left flaw. It is composed solely of boundary-following linear white patches.

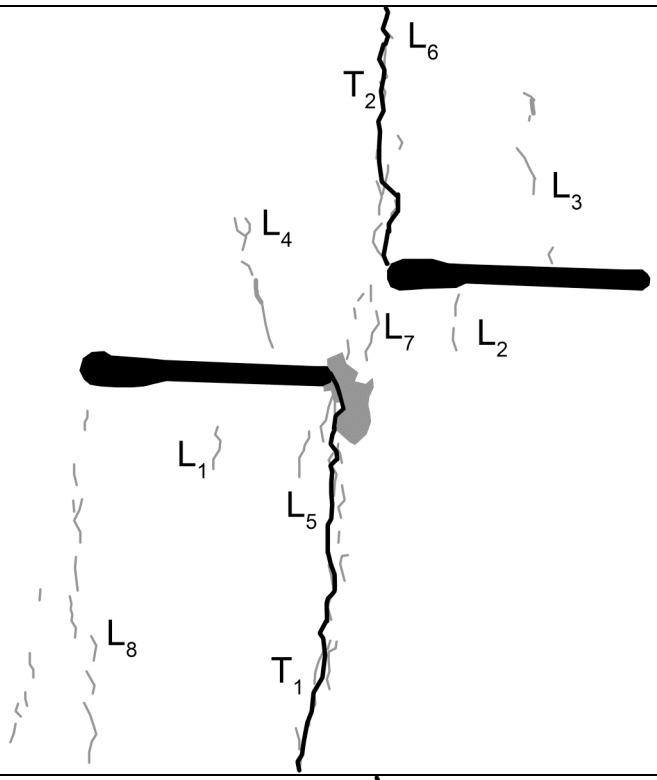	**Time:** 4.1855s before coalescence **σ:** 76.22 MPa L_8 extends and widens with more boundary-following linear white patches.
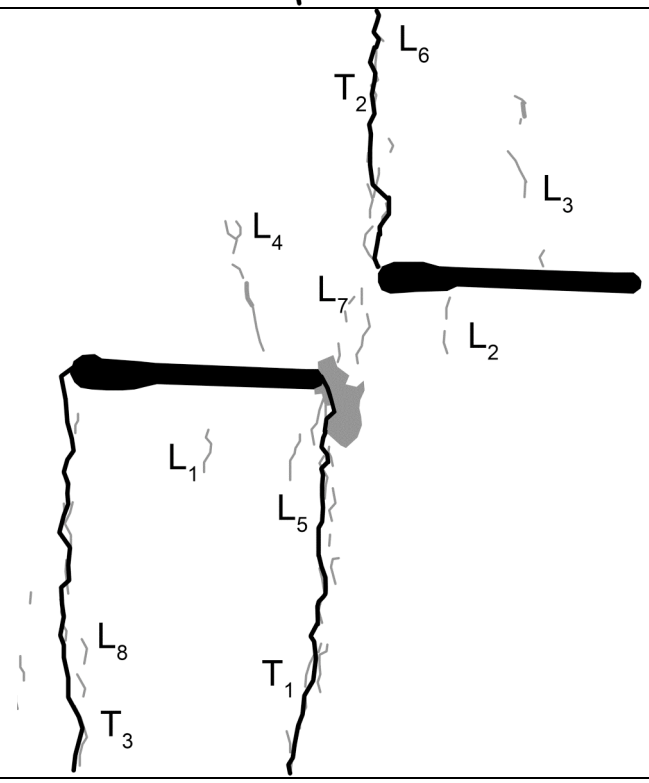	**Time:** 0.6855s before coalescence **σ:** 76.54 MPa Tensile wing crack T_3 appears below the left flaw's outer tip.

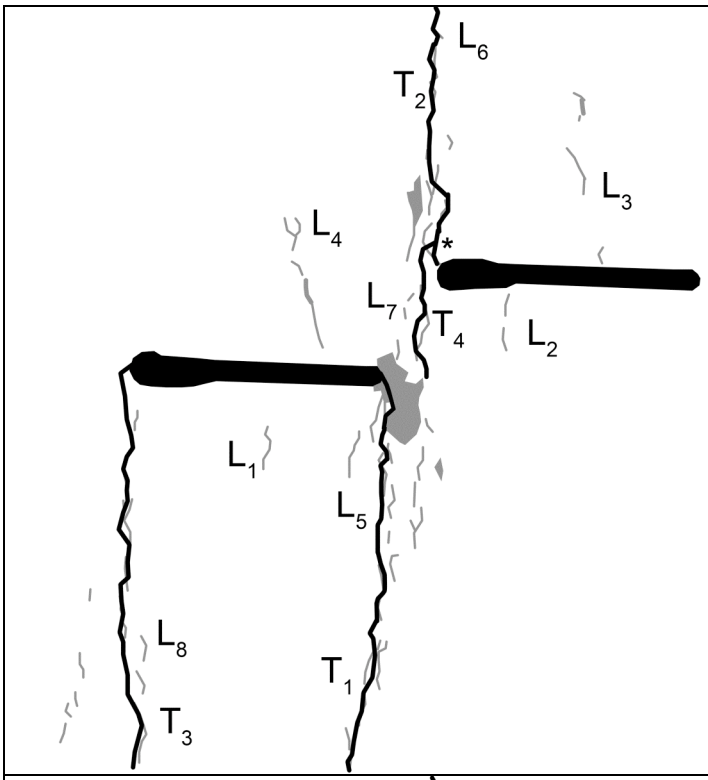	**Time:** 0.003s before coalescence **σ:** 76.62 MPa White patching continues in the bridge area with lightening grains as well as boundary-following linear white patches. Tensile crack T_4 branches off of T_2 (at the point labeled "*") and extends down into the bridging zone.
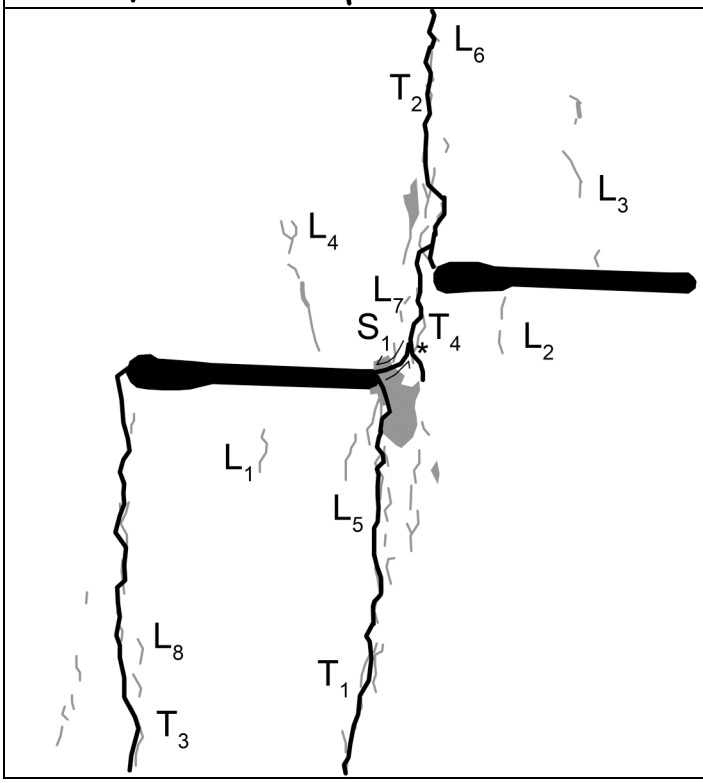	**Time:** 15m27.972s **σ:** 76.54 MPa Specimen coalescence occurs when shear crack S_1 appears (shearing in the sense indicated) linking the inner tip of the left flaw with T_4 (at the point labeled "*"). Coalescence is indirect.

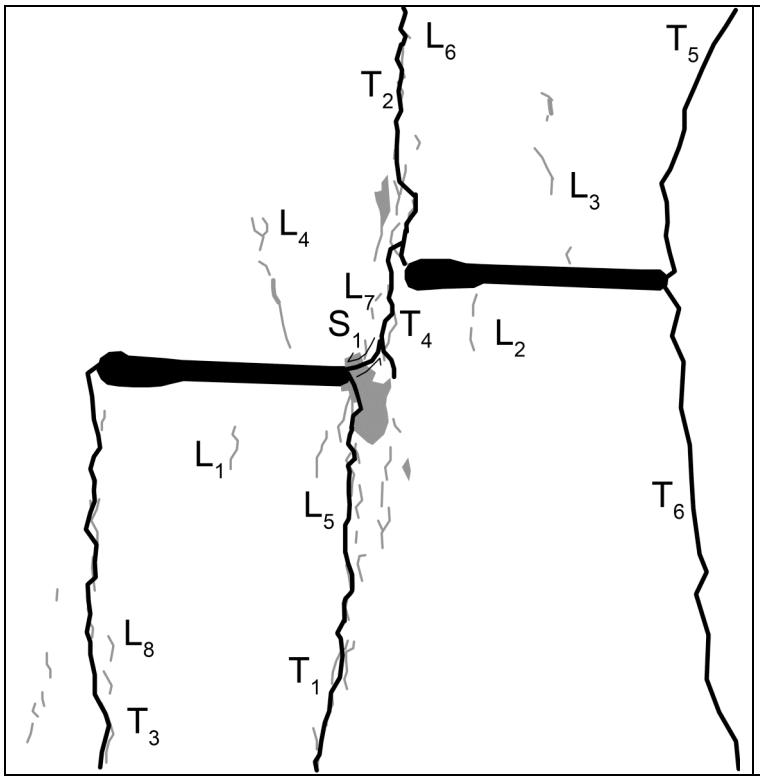

Time: 16m45.474s
σ: 82.8559 MPa

Still image captured after high-speed recording with high-speed camera.

Specimen failure occurs when tensile wing cracks T_5 and then T_6 appear.

Granite a-30-60 A (20080301)

Summary

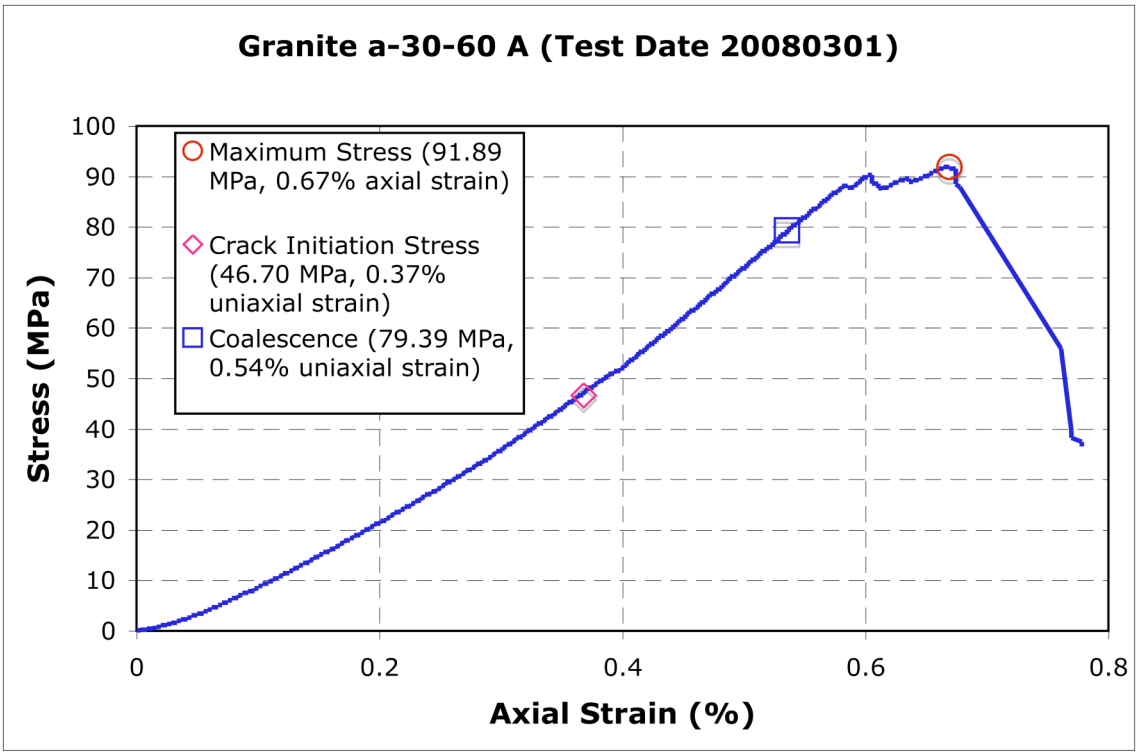

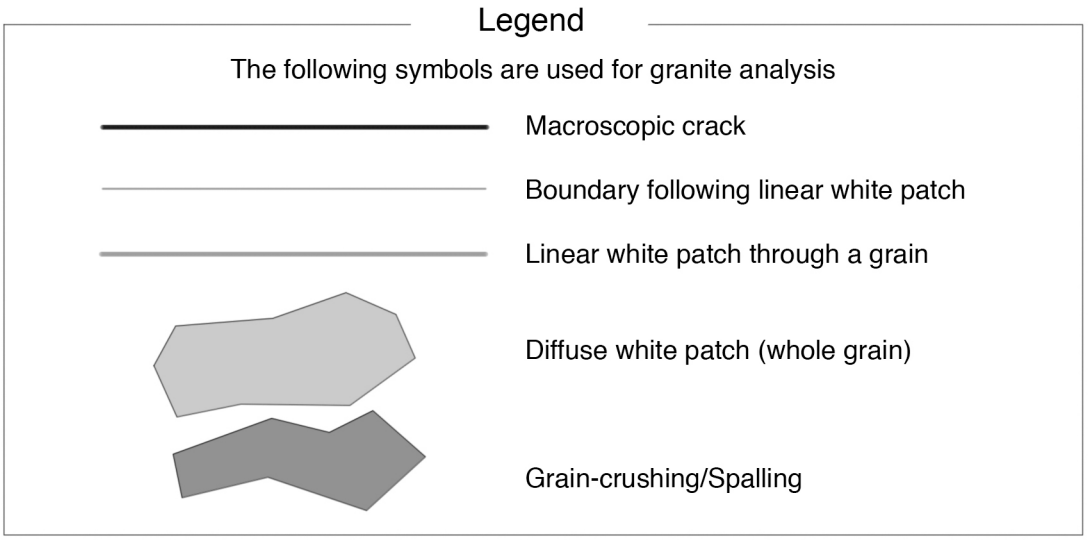

Category 3 Coalescence

Images taken from high-speed video unless otherwise noted

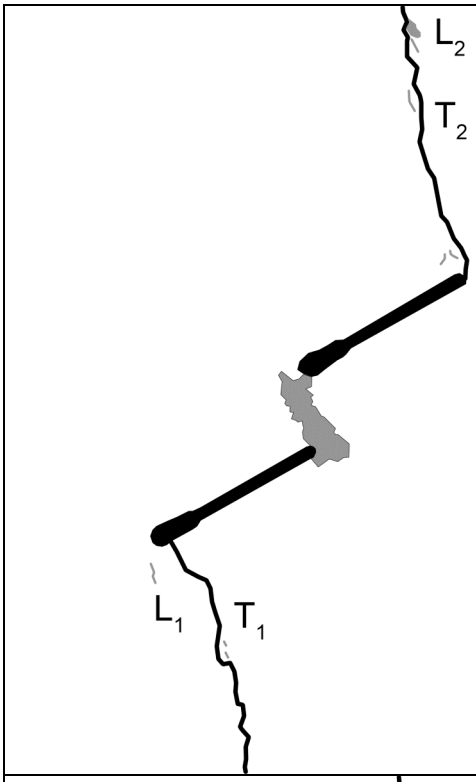	**Time:** ~11m43s **σ:** 46.7 MPa Still image captured before high-speed recording with high-speed camera. Tensile wing cracks T_1 and T_2 appear simultaneous with spalling in the bridge zone. Linear white patches L_1 and L_2 appear alongside T_1 and T_2, respectively. L_1 is composed solely of boundary following linear white patches while L_2 also includes a patch of lightening grains.
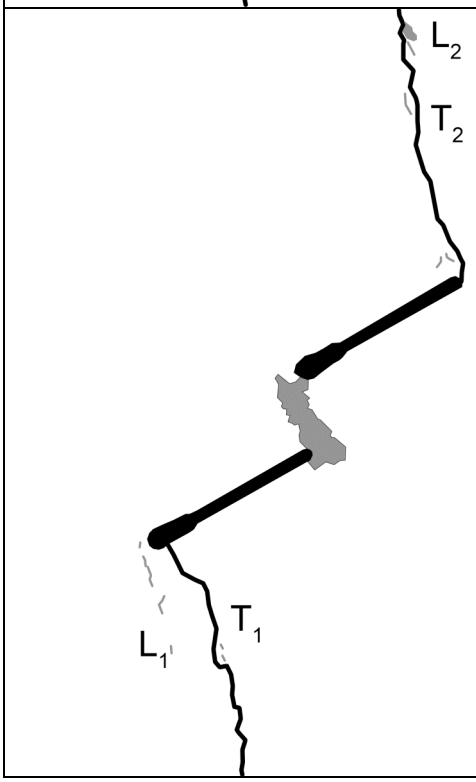	**Time:** ~14m27s **σ:** ~58.4 MPa Still image captured before high-speed recording with high-speed camera. L_1 extends with more boundary-following linear white patches.

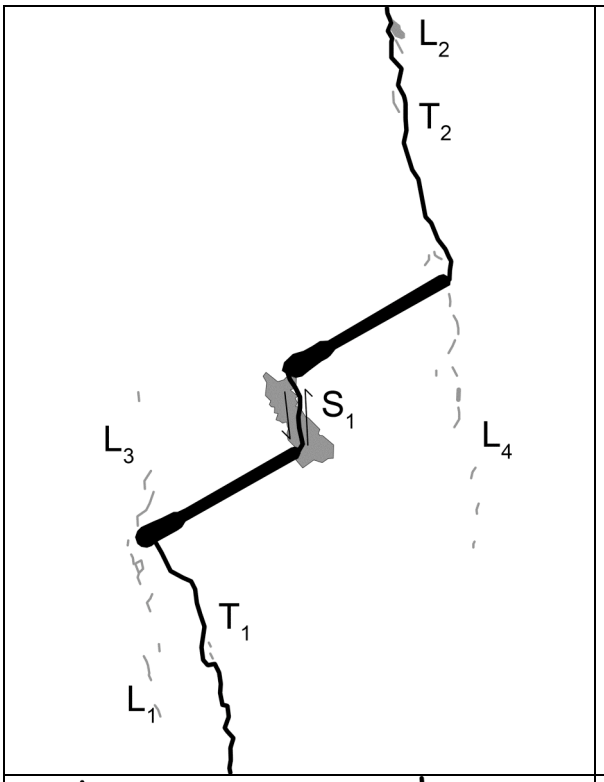	**Time:** ~19m24s **σ:** ~79.4 MPa Still image captured before high-speed recording with high-speed camera. Specimen coalescence occurs when shear crack S_1 (shearing in the sense indicated) appears connecting the two inner flaw tips. Coalescence is assumed based on relative motion between the two sides of S_1. Coalescence is direct (type 3). L_1 extends with more boundary-following linear white patches. L_3 and L_4 also appear. L_3 is composed solely of boundary-following linear white patches while L_4 also contains a through-going linear white patch.
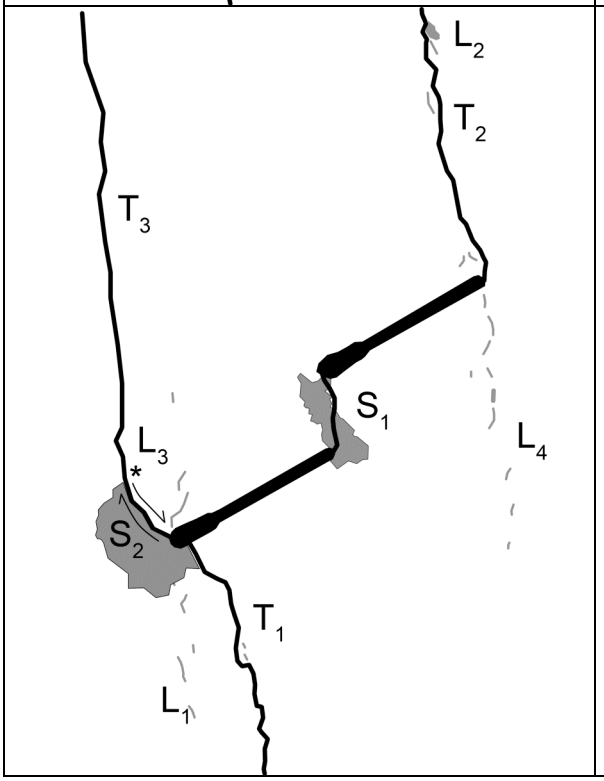	**Time:** 25m0.000s **σ:** 91.8930 MPa Specimen failure occurs when S_2 appears (shearing in the sense indicated and with surface spalling shown) followed by tensile crack T_3. S_2 transitions into T_3 at the point indicated by the '*'.

Granite a-30-60 B (20080418)

Summary

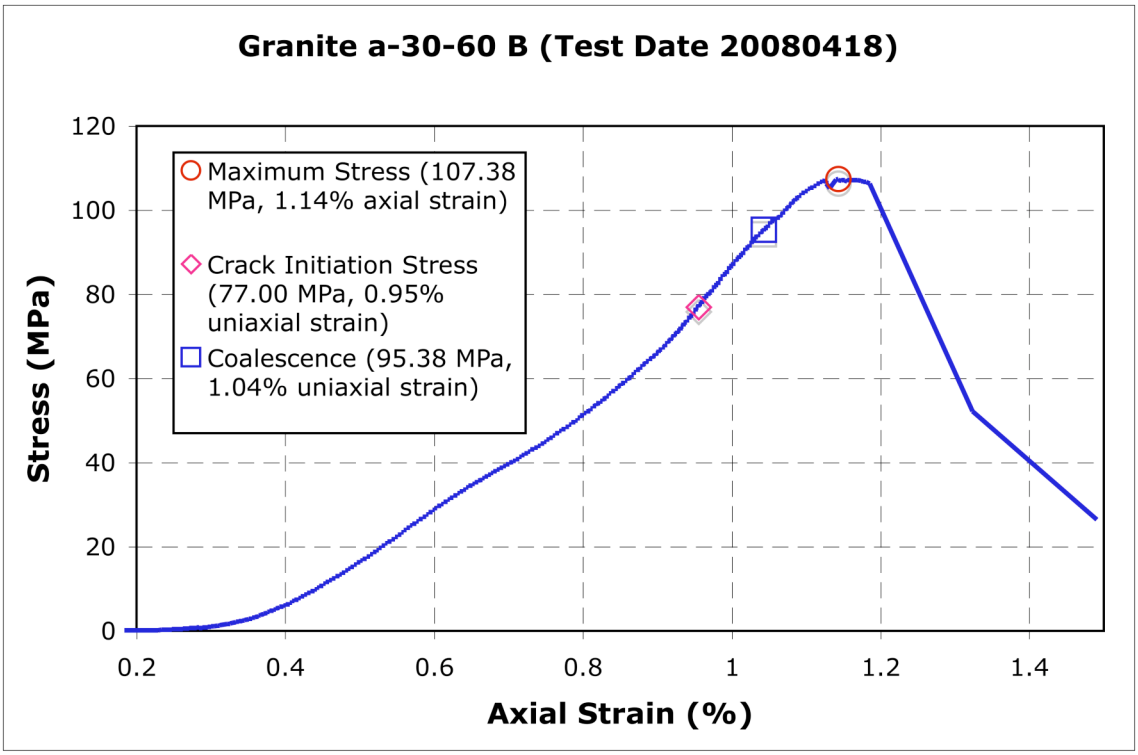

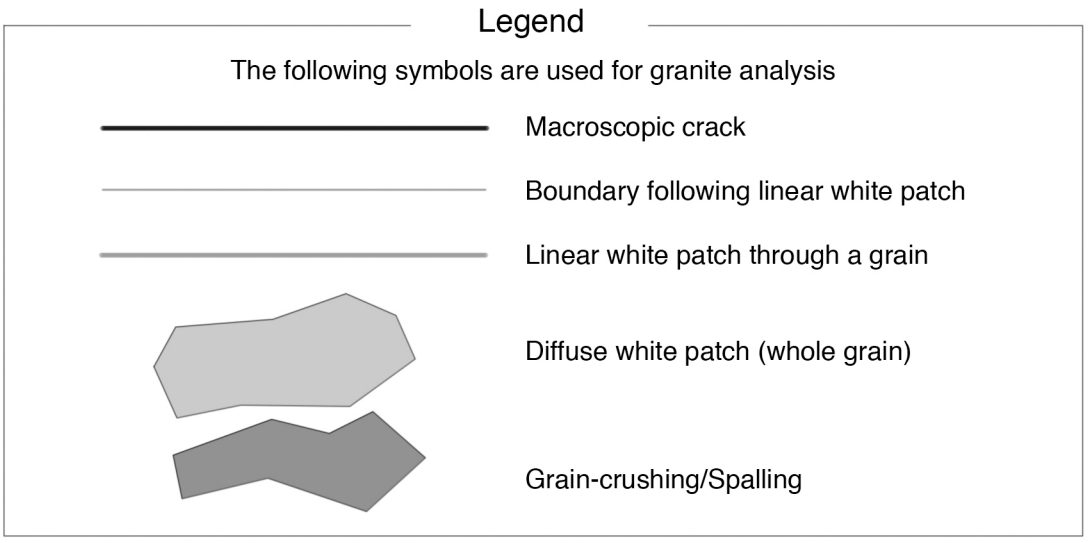

Category 3 Coalescence

Images taken from high-speed recording unless otherwise noted

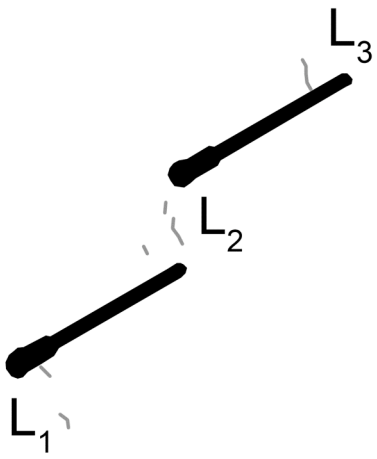	**Time:** ~5m56s **σ:** ~34.9 MPa Still image captured before high-speed recording with high-speed camera. Linear white patches L_1, L_2, and L_3 appear. All three are composed solely of boundary-following linear white patches.
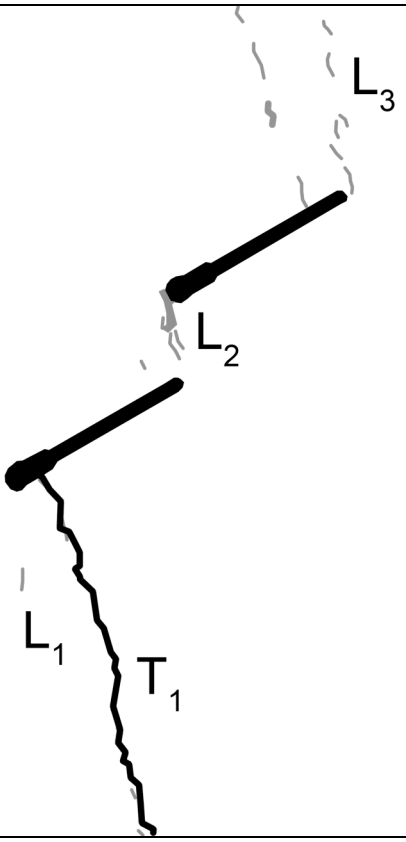	**Time:** ~13m51s **σ:** ~77.0 MPa Still image captured before high-speed recording with high-speed camera. All three linear white patches extend. L_2 now includes a zone of lightened grains and L_3 now includes a through-going linear white patch. Tensile wing crack T_1 appears below the outer tip of the left flaw.

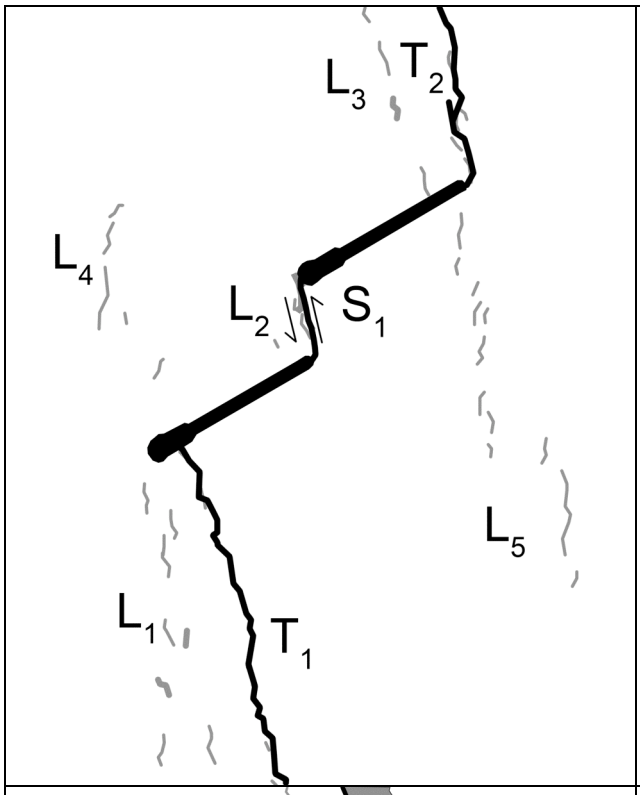

Time: ~17m18s
σ: ~95.4 MPa

Still image captured before high-speed recording with high-speed camera.

The specimen coalesces directly (category 3) when shear crack S_1 connects both inner flaw tips. Tensile wing crack T_2 also appears. It is important to note that these two events are observed to be simultaneous because the high-speed recording still had not started at this point.

Linear white patches L_1 and L_3 extend and expand (including both boundary-following and through-going linear features). L_4 and L_5 appear. Both are composed solely of boundary-following linear white patches.

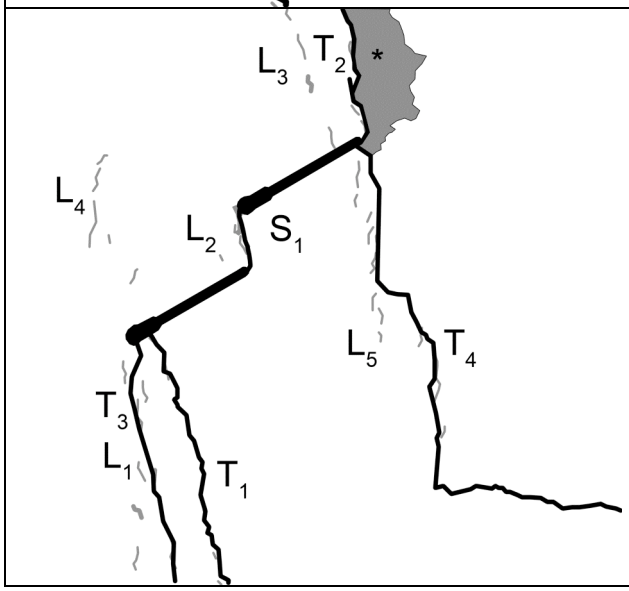

Time: 19m29.124s
σ: 107.3772 MPa

Tensile wing cracks T_3 and T_4 appear. Note how T_4 turns abruptly to the right and out of the camera's field of view. Failure occurs when a large patch of grains bursts (no good view exists after this burst to see if there is a crack trace) in the region marked with the '*'.

Granite a-30-60 C (20071213)

Summary

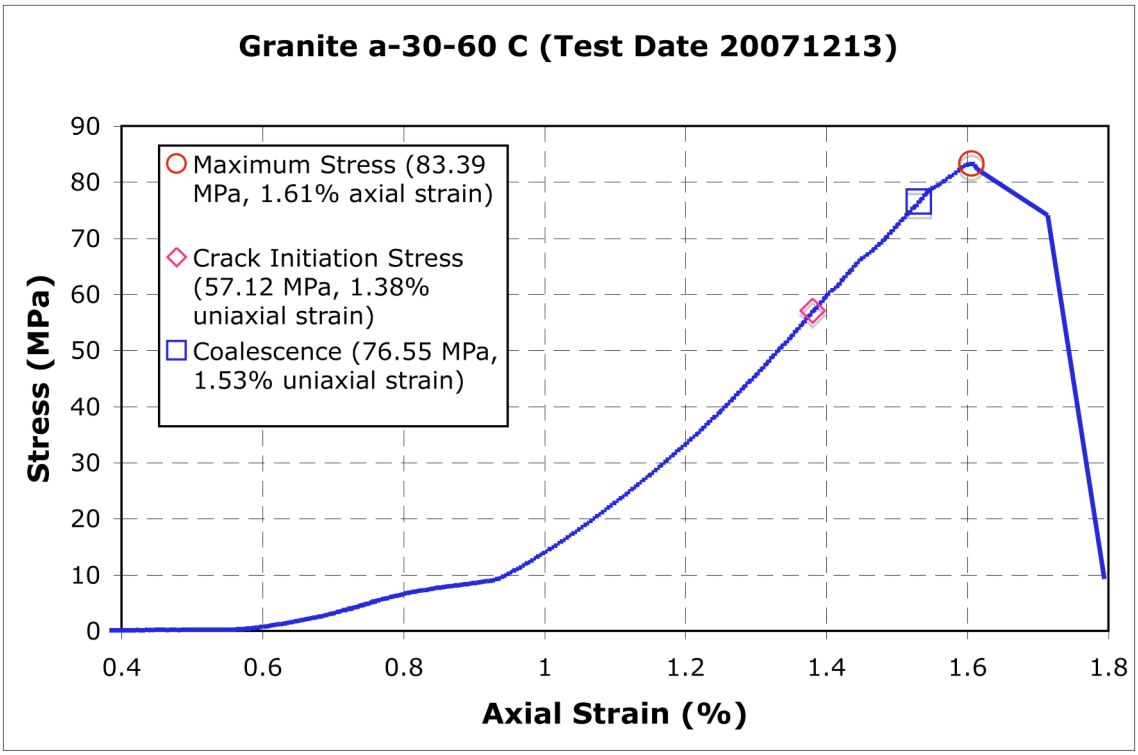

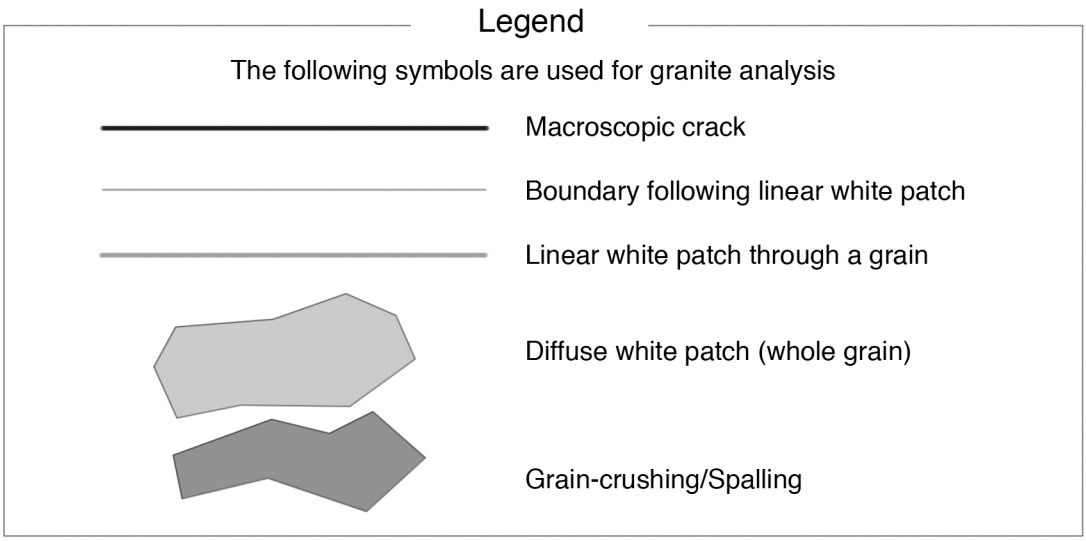

Category 5 Coalescence

Images taken from high-speed video unless otherwise noted

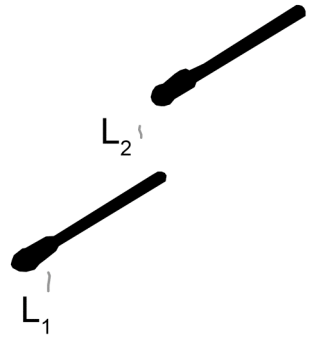	**Time:** ~4m07s **σ:** ~22.8 MPa Still image captured before high-speed recording with high-speed camera. Linear white patches L_1 and L_2 appear. Each composed of a single boundary-following linear white patch.
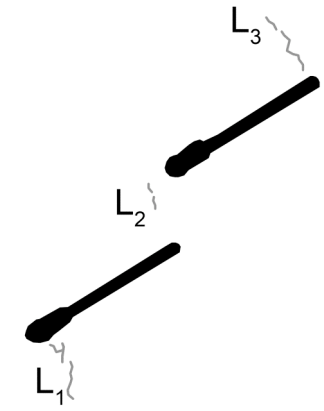	**Time:** ~6m18s **σ:** ~34.3 MPa Still image captured before high-speed recording with high-speed camera. L_1 and L_2 both extend with boundary-following linear features. L_3 also appears. It is also composed solely of boundary-following linear white patches.
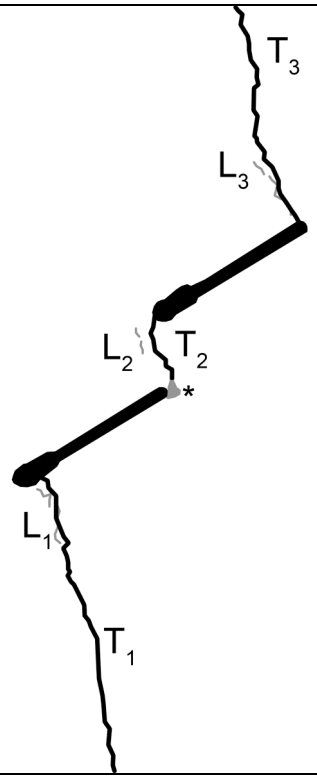	**Time:** ~10m42s **σ:** ~57.1 MPa Still image captured before high-speed recording with high-speed camera. Tensile wing cracks T_1 and T_3 appear on the outer tips of the left and right flaws, respectively. Tensile wing crack T_2 appears below the inner tip of the right flaw and extends toward the inner tip of the left flaw. A small group of grains between the wing crack and the opposite flaw tip brighten (and are indicated by the '*').

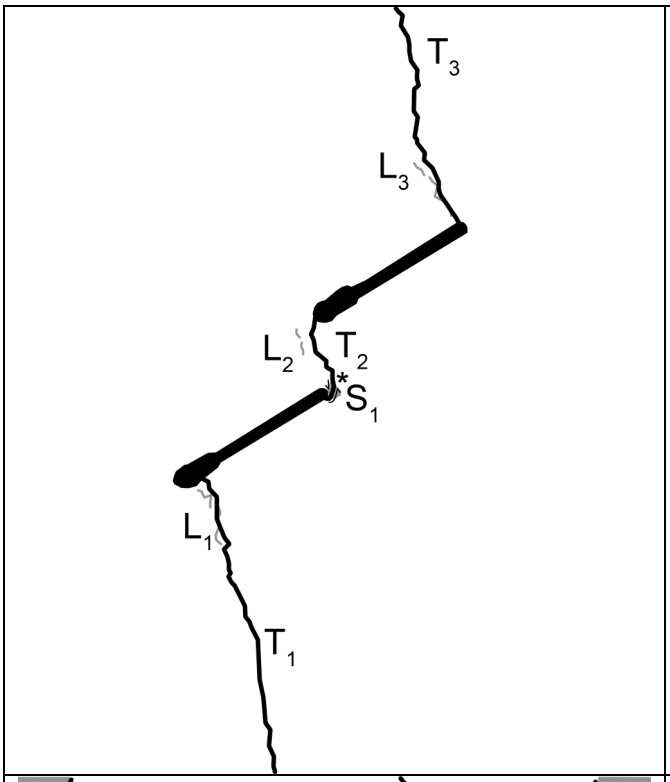	**Time:** ~14m25s **σ:** ~76.5 MPa Still image captured before high-speed recording with high-speed camera. Specimen coalescence when a shear crack connects T_2 with the left flaw's inner tip. The shear crack extends from the point indicated by the '*' to the flaw tip and shears in the sense indicated. The crack trace is taken from later pictures after the lightened grains from the previous picture are ejected. Coalescence is direct (category 5).
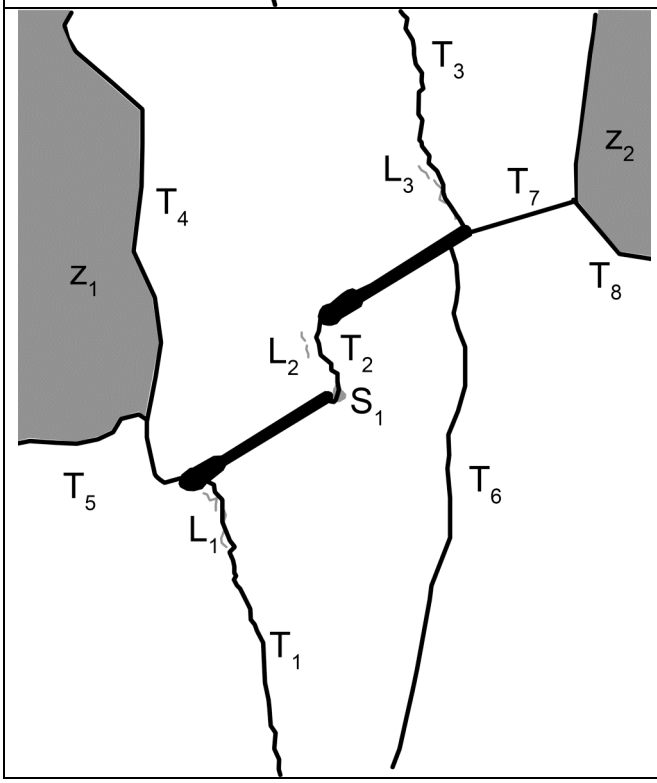	**Time:** 15m41.814s **σ:** 83.2860 MPa Specimen failure occurs when several tensile cracks appear (T_4 through T_8) along with two large zones of crushed grains (z_1 and z_2).

Granite a-45-60 A (20080420)

Summary

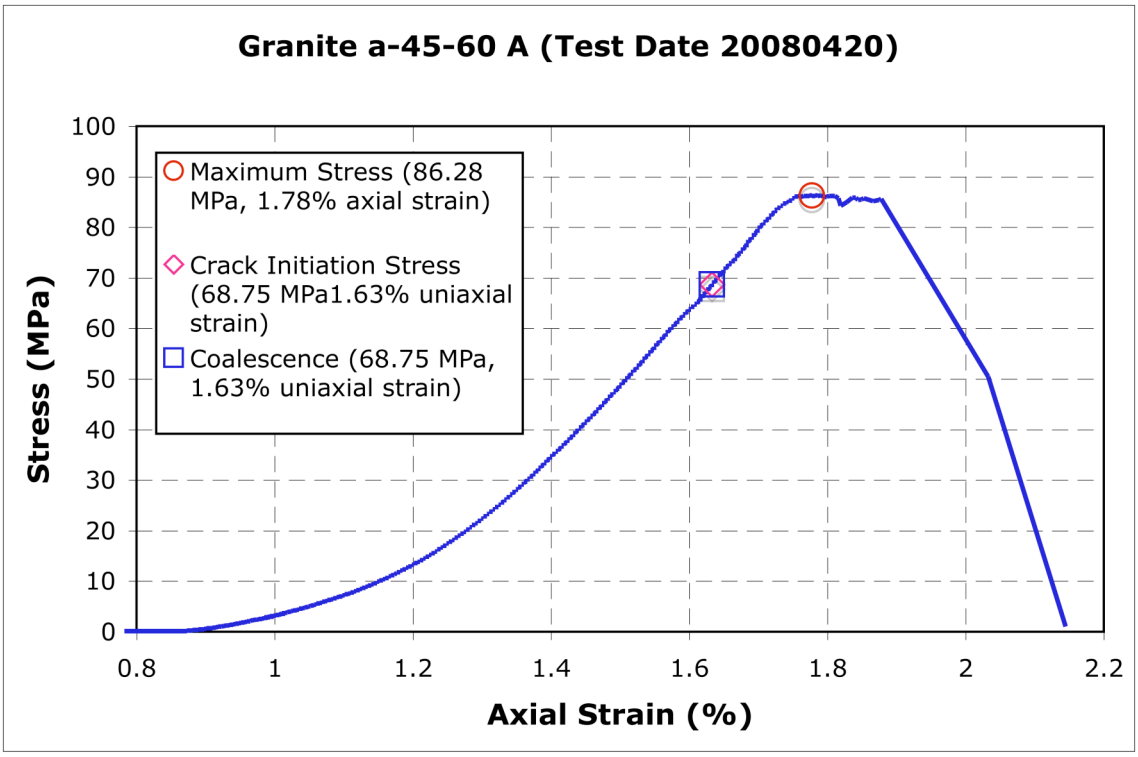

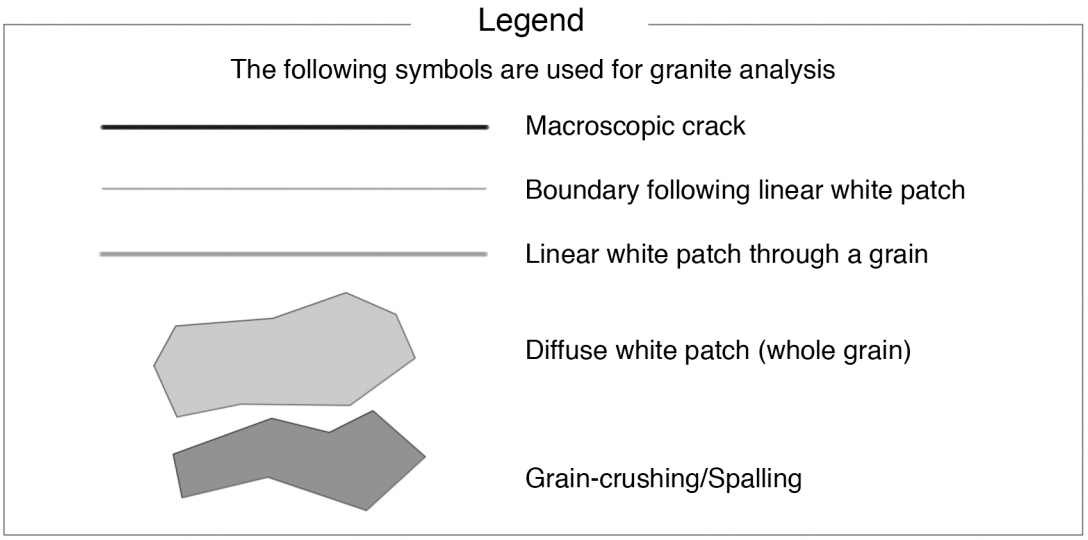

Category 6 Coalescence

Images captured from high-speed video unless otherwise noted

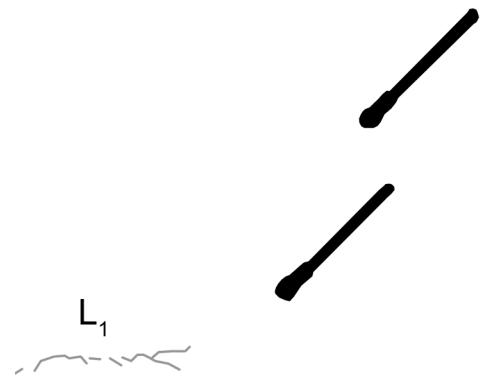	**Time:** ~4m14s **σ:** ~22.2 MPa Still image captured before high-speed recording with high-speed camera. Linear white patch L_1 enters the camera's field of view inclined horizontally. It is composed solely of boundary-following linear white patches.
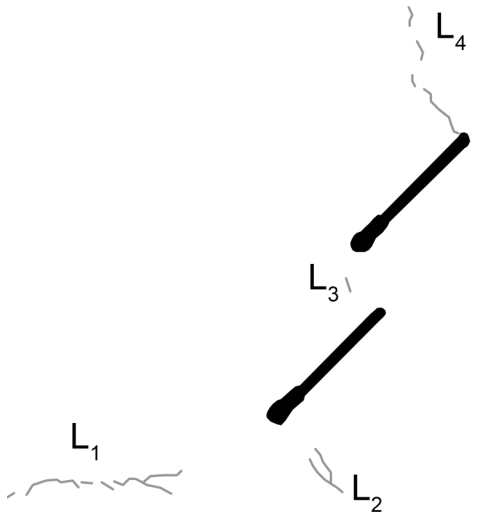	**Time:** ~11m14s **σ:** 57.7 MPa Still image captured before high-speed recording with high-speed camera. Linear white patches L_2, L_3, and L_4 appear, none of which have a horizontal alignment like L_1. All three are composed of boundary-following linear white patches.

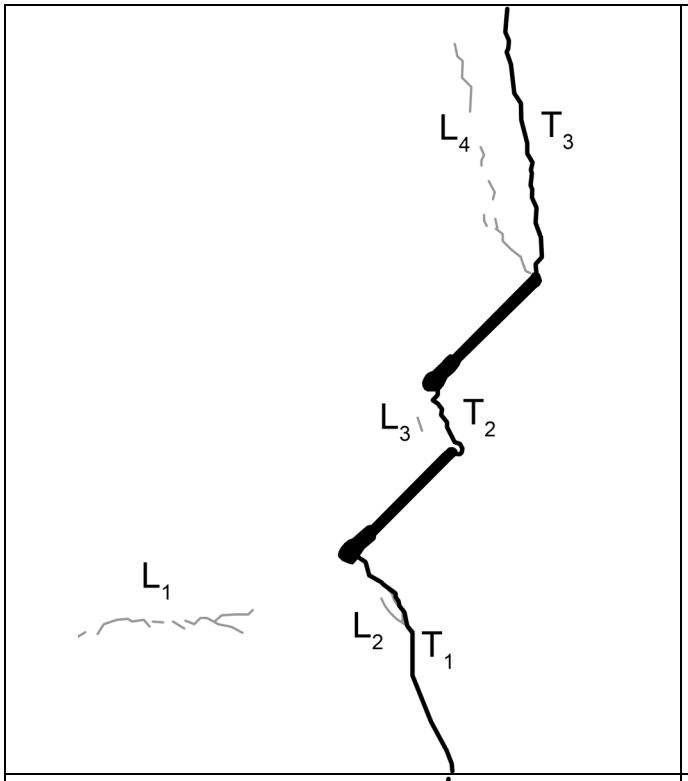	**Time:** ~13m25s **σ:** ~68.7 MPa Still image captured before high-speed recording with high-speed camera. Tensile wing cracks T_1, T_2 and T_3 appear. T_2 causes direct coalescence of the specimen (category six) as well. Order of the three tensile cracks is not possible because the image was not captured from the high-speed video. All three cracks did appear, however, immediately after an audible sound. Linear white patch L_4 extends as well.
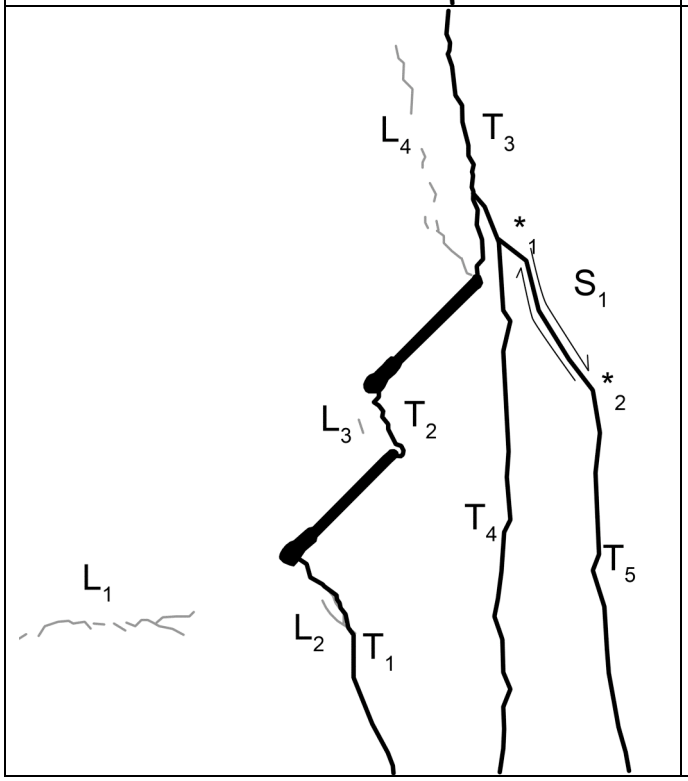	**Time:** 16m52.344s **σ:** 88.2791 MPa Specimen failure occurs. First, tensile crack T_4 appears and extends downward from T_3. Next, shear crack S_1 appears and extends from T_4 (at the point labeled '$*_1$') down to the point labeled '$*_2$' (shearing in the sense indicated) before transitioning into tensile crack T_5.

Granite a-45-60 B (20080301)

Summary

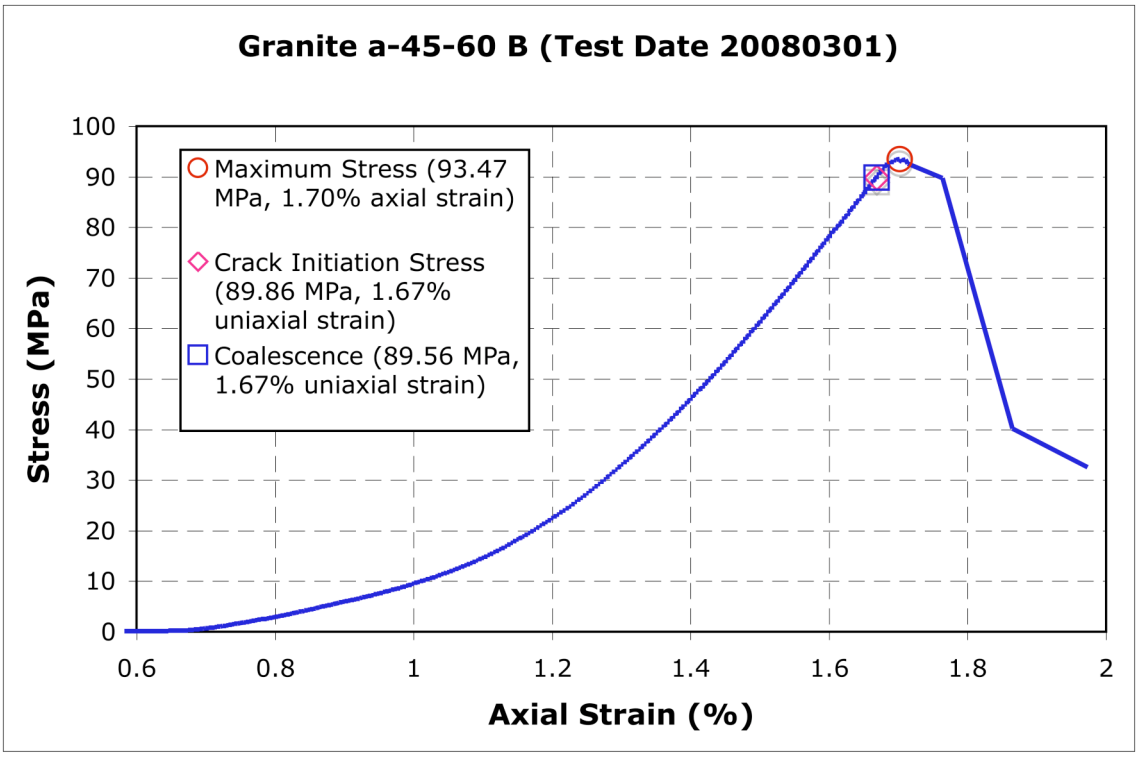

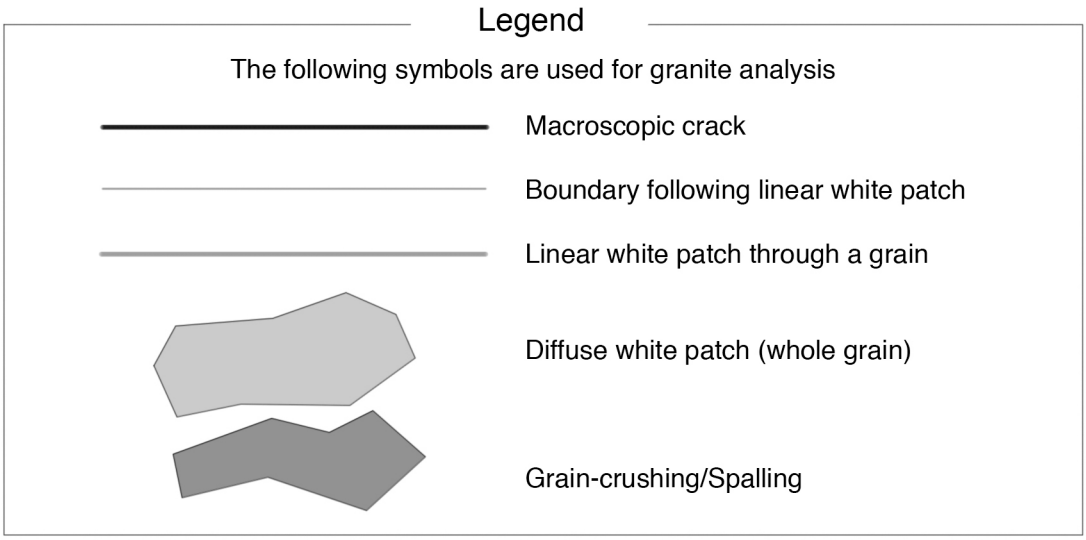

Category 6 Coalescence

Images captured from high-speed video unless otherwise noted

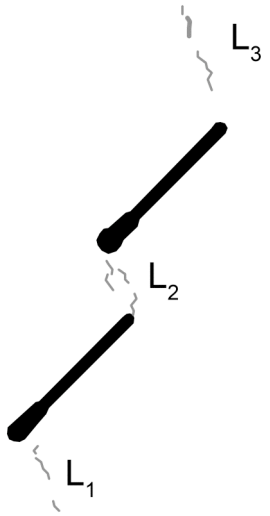	**Time:** ~8m38s **σ:** ~46.1 MPa Still image captured before high-speed recording with high-speed camera. Linear white patches L_1, L_2, and L_3 appear. All contain boundary-following linear features while L_3 also includes a through-going linear white patch.
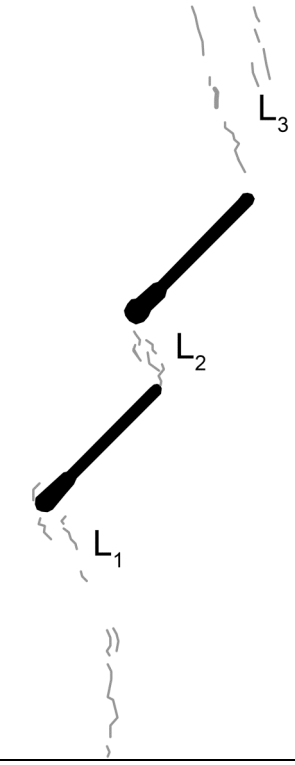	**Time:** ~13m0s **σ:** ~69.1 MPa Still image captured before high-speed recording with high-speed camera. All three linear white patches extend and expand with boundary-following linear white patches.

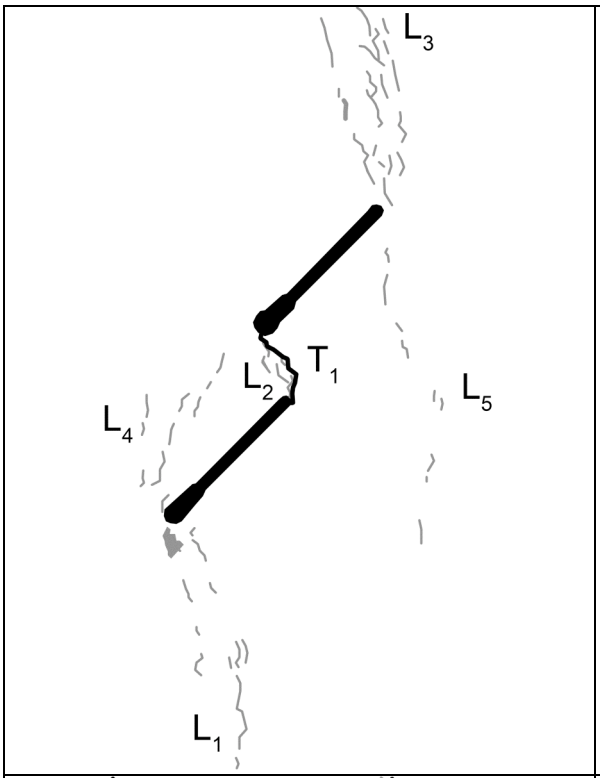	**Time:** ~16m55s **σ:** 89.9 MPa Still image captured before high-speed recording with high-speed camera. Specimen coalesces with a tensile crack (labeled) appearing between the two inner flaw tips. Coalescence is direct (category six). L_1 and L_3 both extend and expand with more boundary-following linear white patches (L_1 also includes a patch of lightened grains). Two new linear white patches also appear: L_4 and L_5. L_4 appears above the outer tip of the left flaw and bends toward the inner tip of the right flaw. L_5 appears below the outer tip of the right flaw.
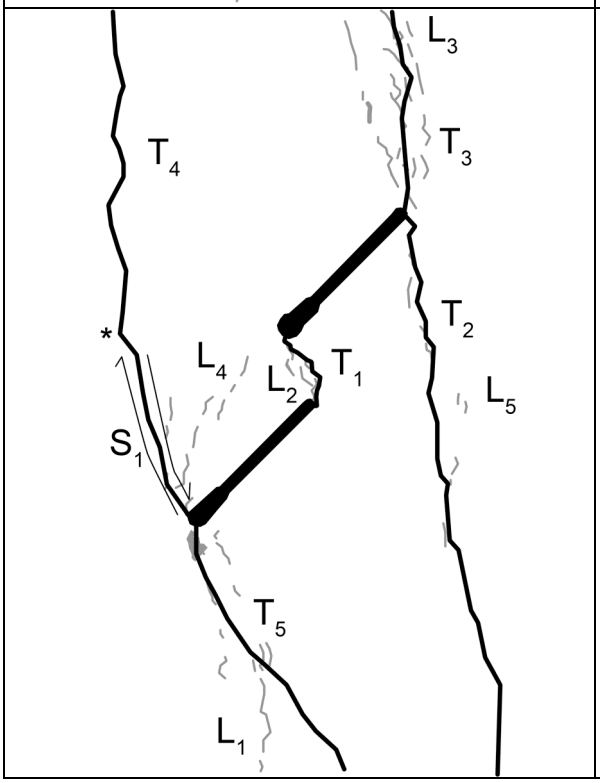	**Time:** 17m36.654s **σ:** 93.4717 MPa Tensile wing cracks T_2 and T_3 appear simultaneously and the specimen fails as the unit to the right of those wing cracks falls off the specimen. As that unit falls, wing cracks T_5 and S_1 (shearing in the sense indicated) appear. S_1 transitions into a tensile crack (labeled T_4) at the point indicated by the '*'.

Gr a-60-60 A (20080301)

Summary

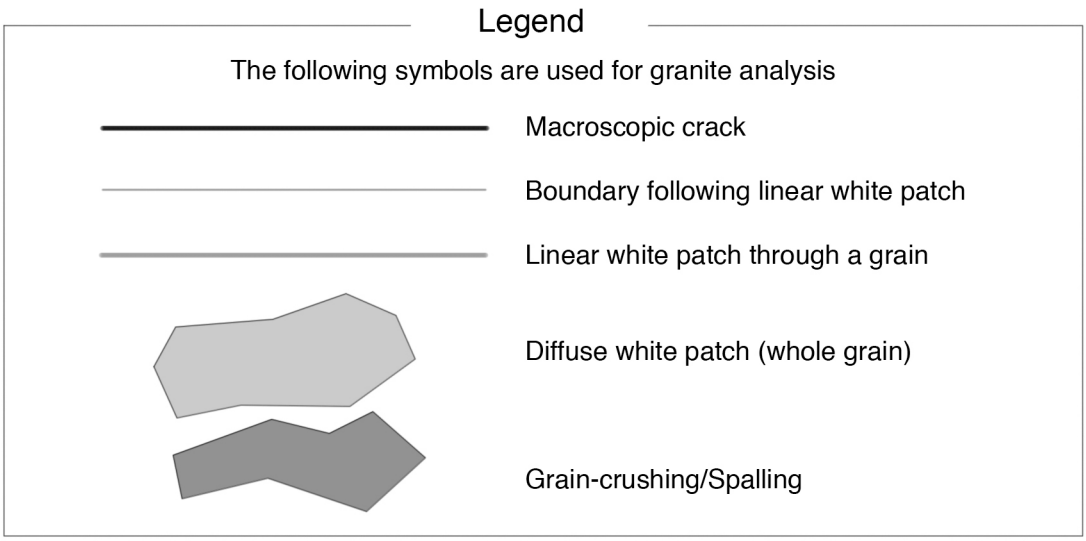

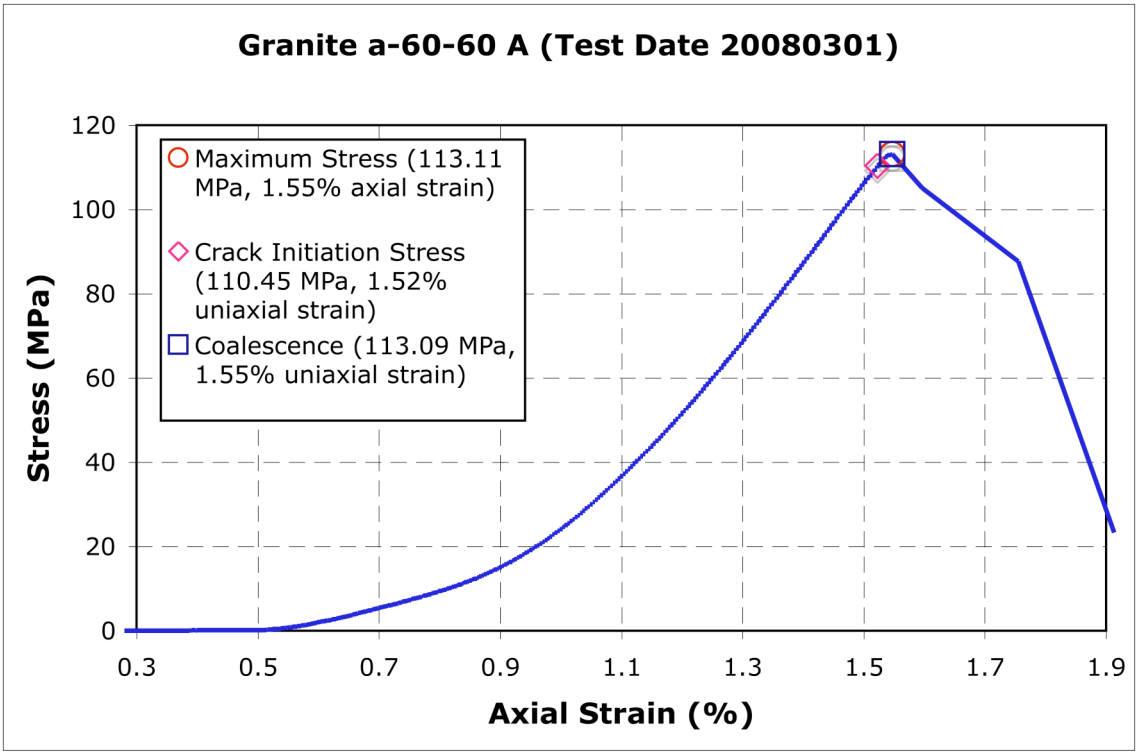

Category 6 Coalescence

Images captured from high-speed video unless otherwise noted

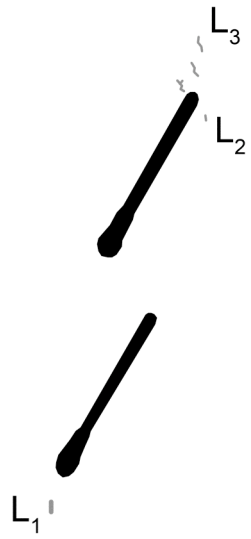	**Time:** ~8m29s **σ:** ~45.1 MPa Still image captured before high-speed recording with high-speed camera. Linear white patches L_1, L_2, and L_3 all appear. L_1 is a single through-going linear white patch. L_2 and L_3 are composed solely of boundary-following linear features.
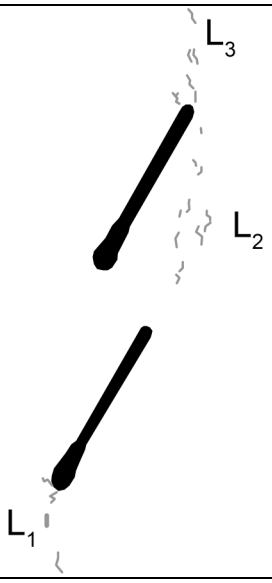	**Time:** ~15m03s **σ:** ~78.9 MPa Still image captured before high-speed recording with high-speed camera. L_1 through L_3 all extend with boundary-following linear white features. Note how L_2 appears to be extending in the direction of the left flaw's inner tip.

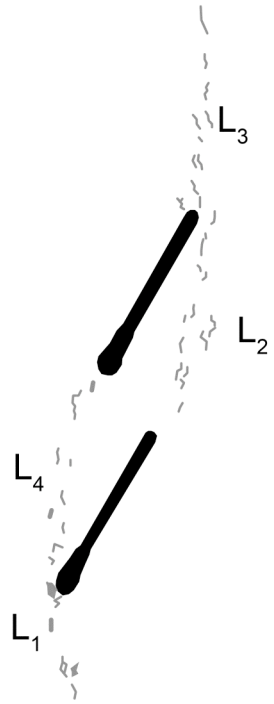	**Time:** ~19m25s **σ:** ~101.4 MPa Still image captured before high-speed recording with high-speed camera. Two different patches of grains lighten within L_1. L_2 and L_3 both extend with boundary-following linear features. Linear white patch L_4 also appears between the inner tip of the right flaw and the outer tip of the left flaw. It is composed of both boundary-following and through-going linear white patches.
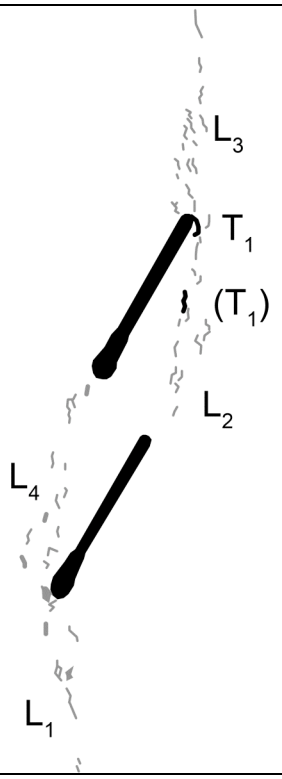	**Time:** ~21m10s **σ:** ~110.5 MPa Still image captured before high-speed recording with high-speed camera. Tensile wing crack T_1 appears as does a small tensile crack just below it, labeled (T_1), in the L_2 region. L_1, L_3, and L_4 all have more linear white patches appear (mostly boundary-following, although a through-going feature does appear in L_4).

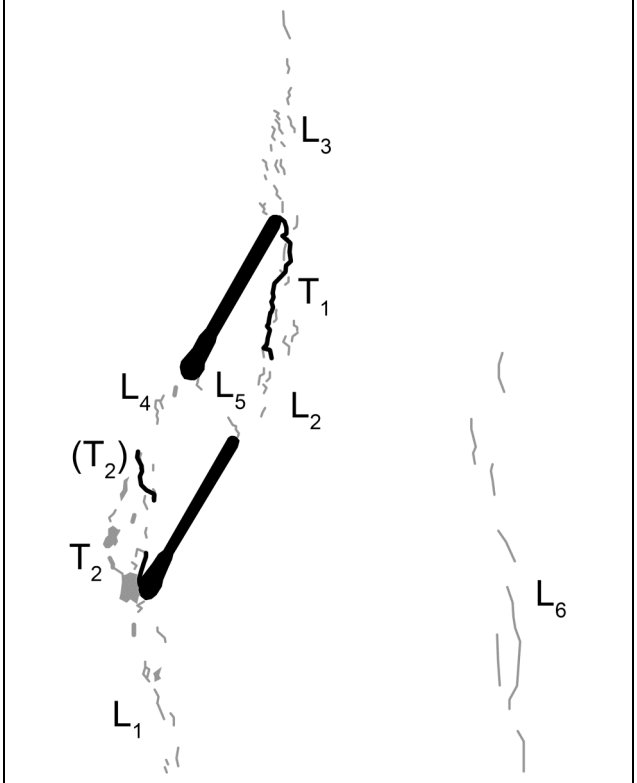	**Time:** 0.719s before failure **σ:** 113.00 MPa First frame of high-speed video. L_1 and L_4 both expand with more boundary-following linear white patches. L_4 also includes several lightened grains as well. Tensile wing crack T_2 appears above the outer tip of the left flaw. Within the L_4 region, another tensile crack appears, labeled (T_2). Boundary-following linear white patches appear on both inner flaw tips and reach into the bridge area. This pair of linear white patches is labeled L_5. A series of long, boundary-following linear white patches also appears on the right side of the camera's field of view (labeled L_6).
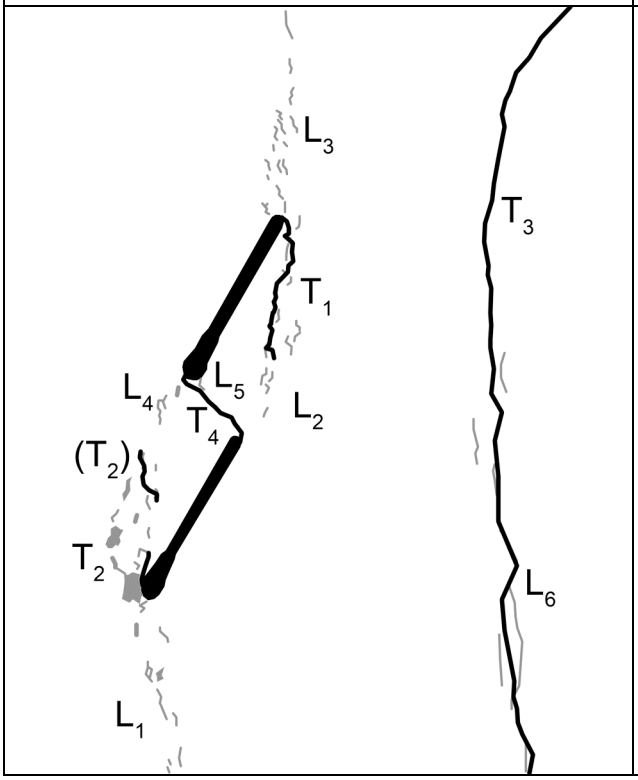	**Time:** 0.0712s before failure **σ:** 113.09 MPa A vertical tensile crack (labeled T_3) appears on the right side of the camera's field of view through the L_6 region. Sample then coalesces directly (category six) with a tensile crack (labeled T_4) connecting the inner flaw tips. T_3 appears immediately before T_4.

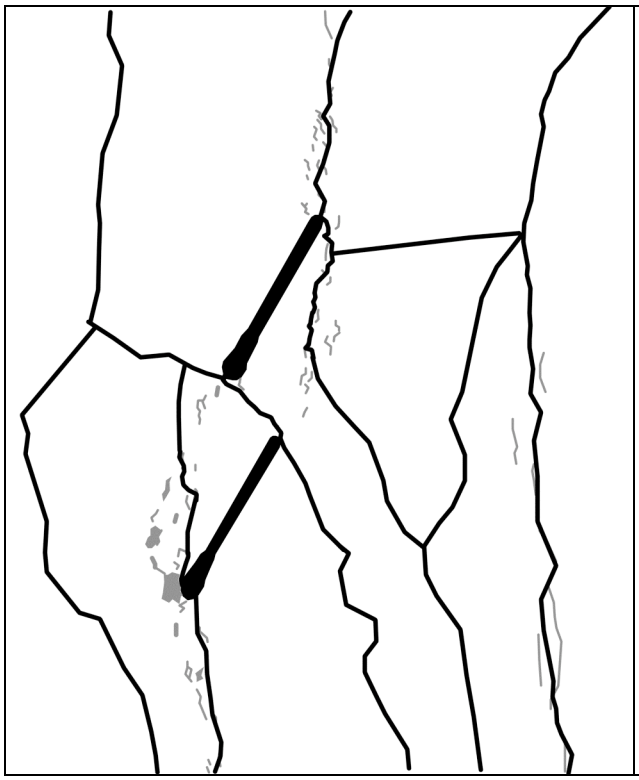

Time: 21m40.470s
σ: 113.1128 MPa

Sample failure occurs with the sudden appearance of several tensile cracks.

Gr a-60-60 B (20080420)

Summary

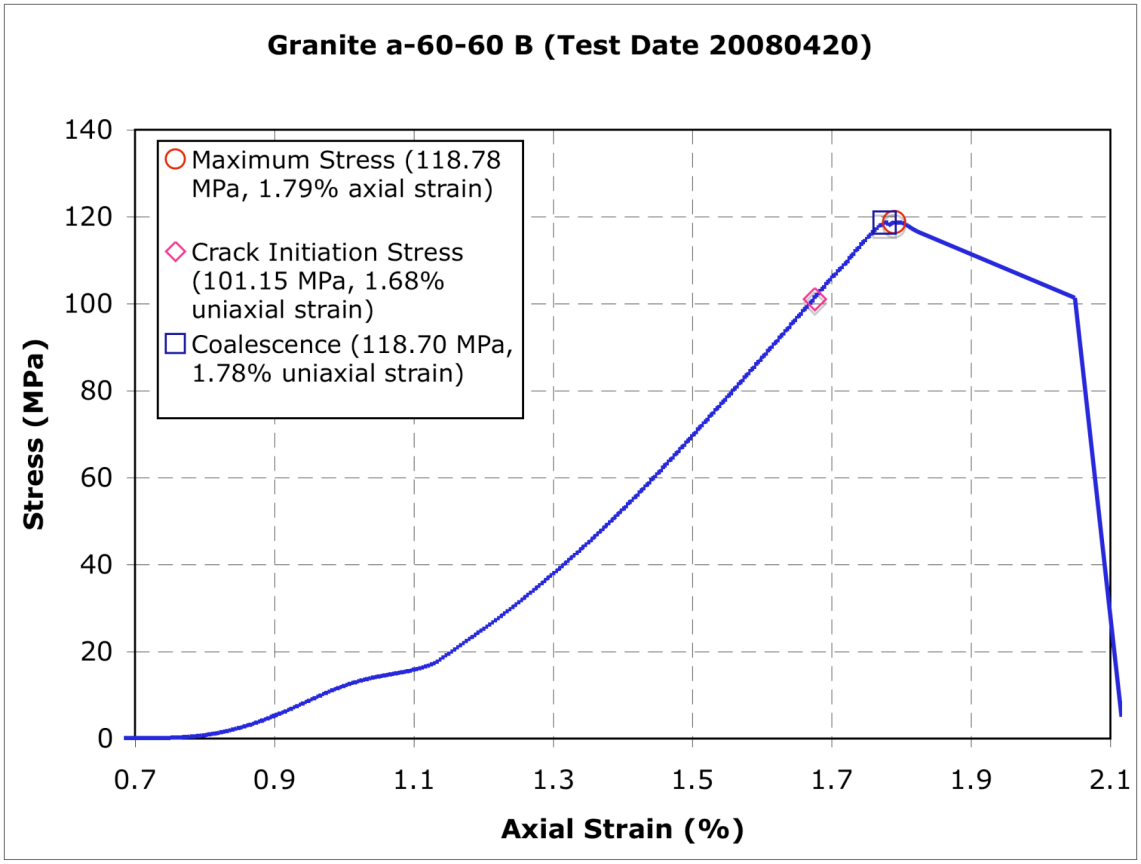

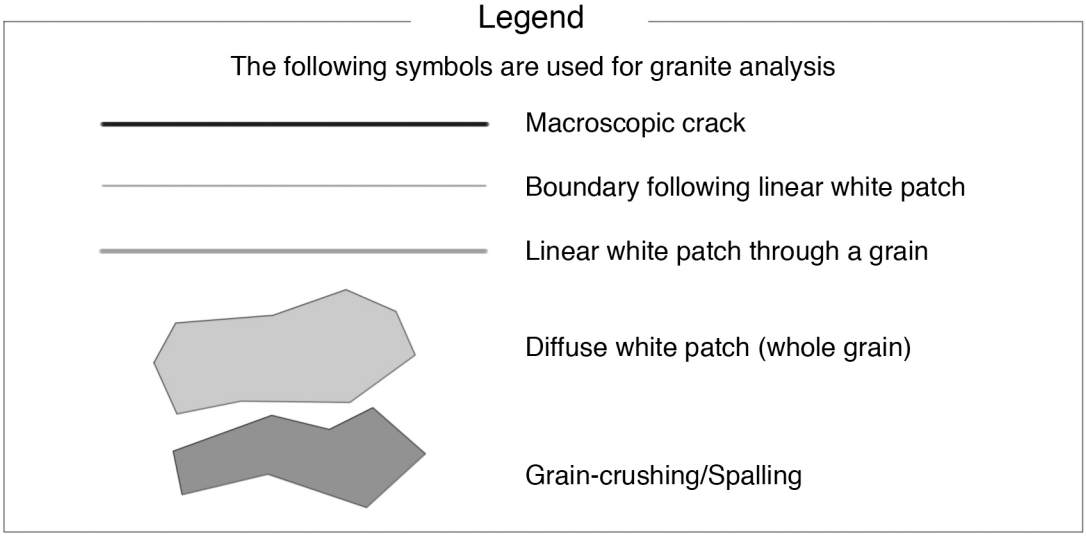

Category 6 Coalescence

Images captured from high-speed video unless otherwise noted.

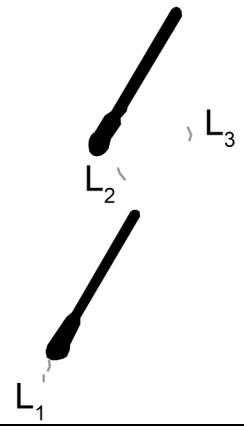	**Time:** ~10m43.8 **σ:** ~55.0 MPa Still image captured before high-speed recording with high-speed camera. Linear white patches L_1, L_2, and L_3 appear. All three are composed of boundary-following linear white patches.
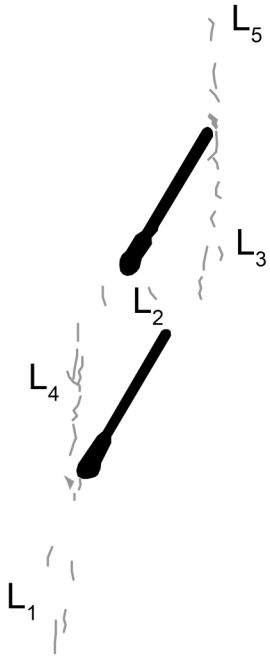	**Time:** ~17m16.4s **σ:** ~88.0 MPa Still image captured before high-speed recording with high-speed camera. L_1 and L_3 both extend with boundary-following white patches. L_1 also includes a patch of lightened grains. Linear white patches L_4 and L_5 appear above the outer flaw tips of the left and right flaws, respectively. Both have boundary-following linear features while L_5 also includes a patch of lightened grains.

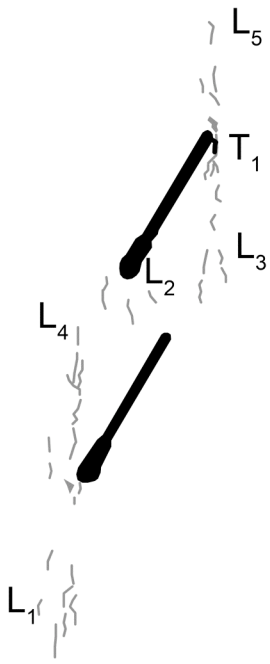	**Time:** ~19m53.0s **σ:** ~101.2 MPa Still image captured before high-speed recording with high-speed camera. All five linear white patches expand with boundary-following linear white patches. Tensile wing crack T_1 appears below the right flaw's outer tip.
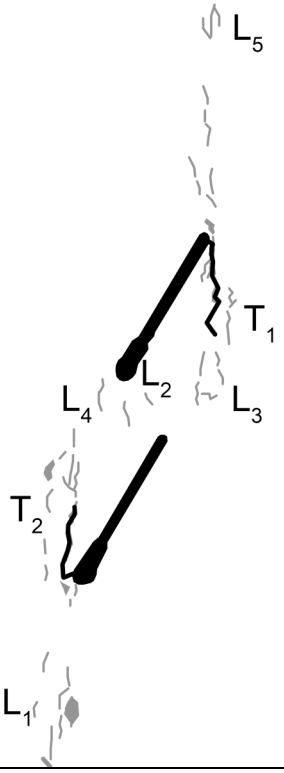	**Time:** ~21m13.1s **σ:** ~107.9 MPa Still image captured before high-speed recording with high-speed camera. Tensile wing crack T_1 extends downward while tensile wing crack T_2 appears above the outer tip of the left flaw. All the linear white patches except L_2 expand as well. A through-going feature appears in L_1 and lightened grains appear in the L_1 and L_4 regions as well.

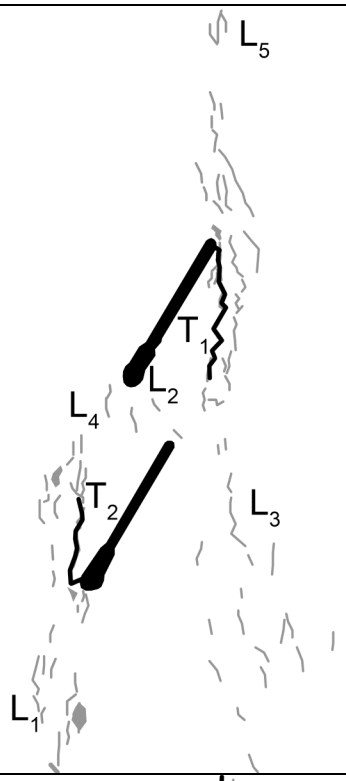	**Time:** ~22m29.7s **σ:** ~114.4 MPa Still image captured before high-speed recording with high-speed camera. All five linear white patches expand with boundary-following linear white patches. T_1 and T_2 also extend.
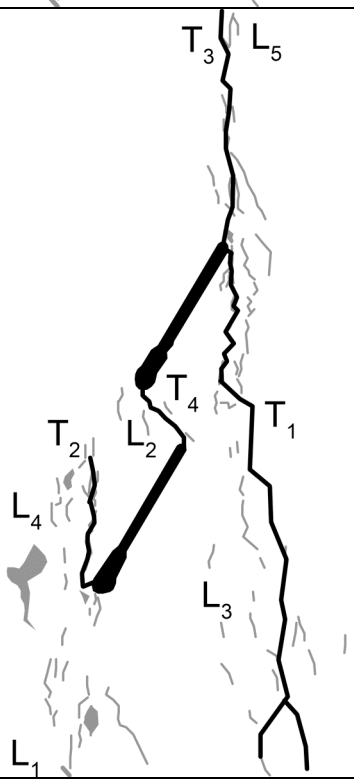	**Time:** ~23m21.8s **σ:** ~118.7 MPa Still image captured before high-speed recording with high-speed camera. Tensile wing cracks T_1 and T_2 extend. Tensile wing crack T_3 appears above the right flaw's outer tip and extends upward. Tensile crack T_4 appears and causes sample coalescence. Coalescence is direct (category six). The order of these three steps is unknown as the image was taken from an image before the high-speed recording started. A patch of grains lighten in the L_4 region near the left flaw's outer tip.

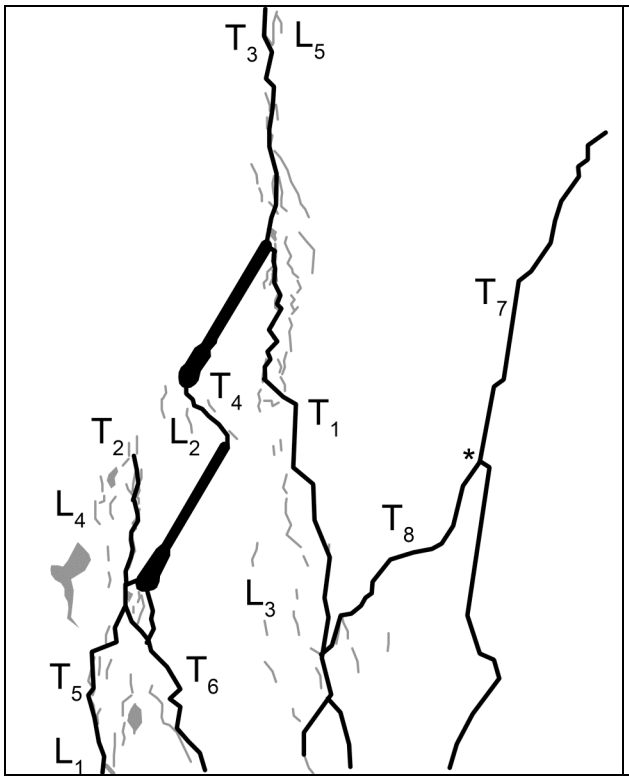

Time: 23m22.404s
σ: 118.7806 MPa

Sample fails with the appearance of several tensile cracks. T_5 and T_6 appear below the outer tip of the left flaw. A vertical tensile crack then appears on the ride side of the sample (labeled as T_7). T_7 is then connected to T_1 by tensile crack T_8.

Granite a-75-60 A (20080301)

Summary

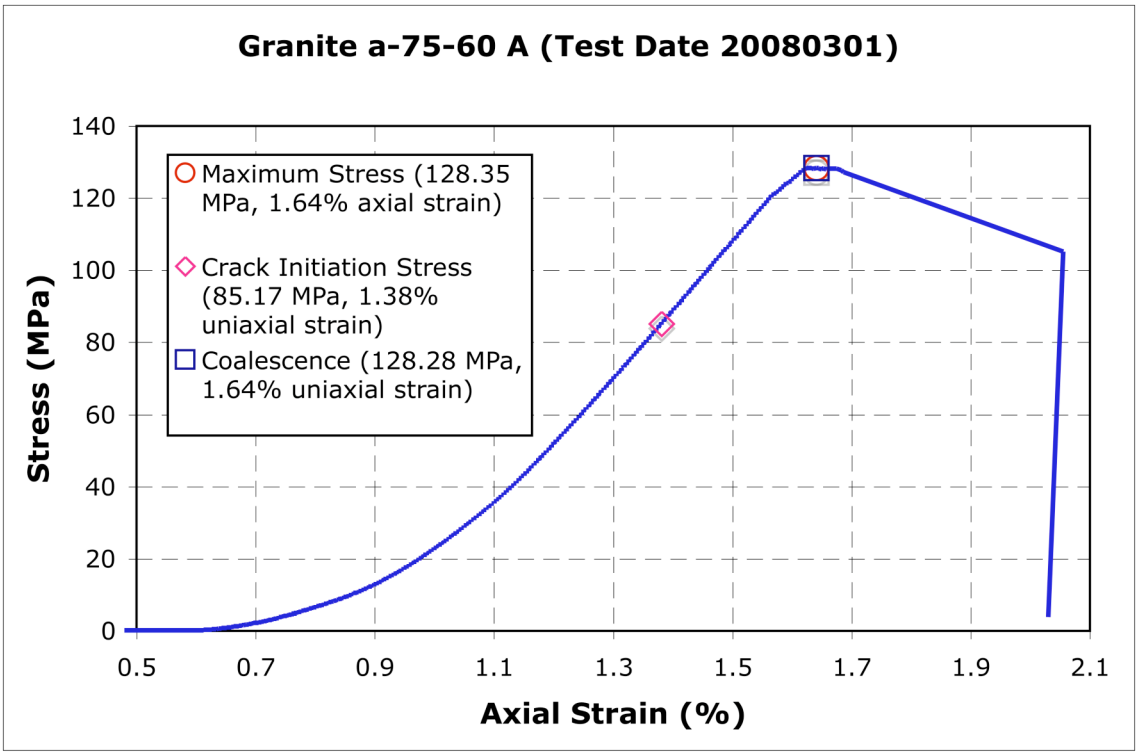

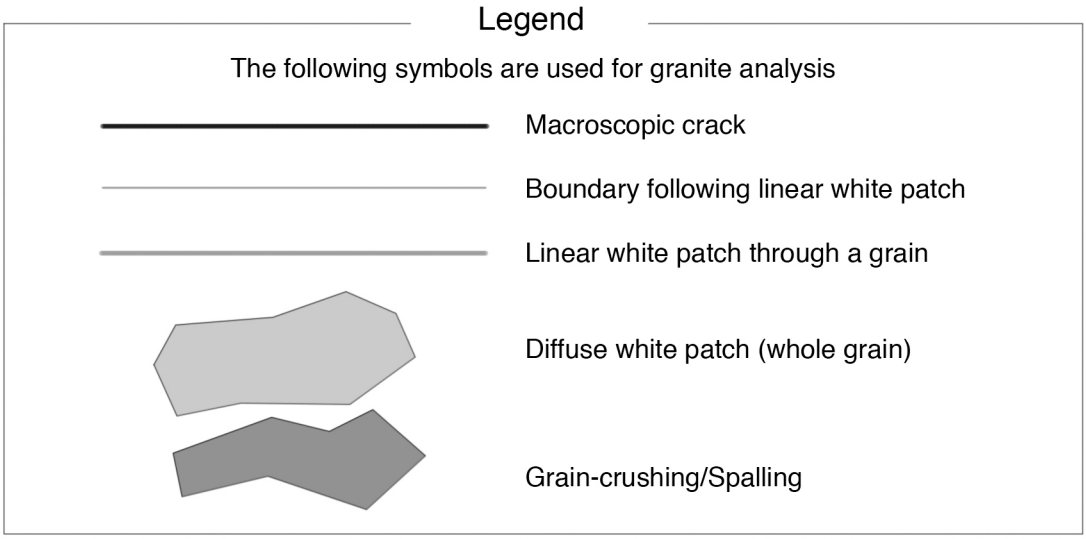

Category 7 Coalescence

Images captured from high-speed video unless otherwise noted.

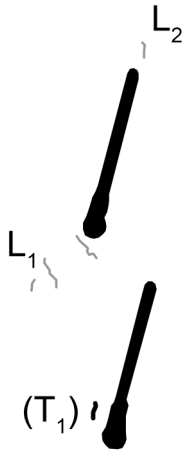	**Time:** ~17m11.1s **σ:** ~ 85.2 MPa Still image captured before high-speed recording with high-speed camera. Linear white patches L_1 and L_2 appear, composed solely of boundary-following linear white patches. The linear features in L_1 are oriented less steeply than normal. A short tensile crack (labeled as T_1) also appears between two grains above the left flaw tip.
	**Time:** ~21m32.7s **σ:** ~ 106.5 MPa Still image captured before high-speed recording with high-speed camera. L_1 and L_2 both extend. L_1 now includes a lightened grain as well as a through-going linear feature. Note that the white patches appear to be becoming more steeply inclined the further from the right flaw's inner tip they are. L_2 is still composed of boundary-following linear white patches only. A third linear white patch, L_3, appears parallel to T_1.
	**Time:** ~22.51.4s **σ:** ~112.8 MPa Still image captured before high-speed recording with high-speed camera. L_1 extends closer to the left flaw's outer tip. Linear white patch L_4 appears below the left flaw's outer tip and is composed of both through-going and boundary-following features.

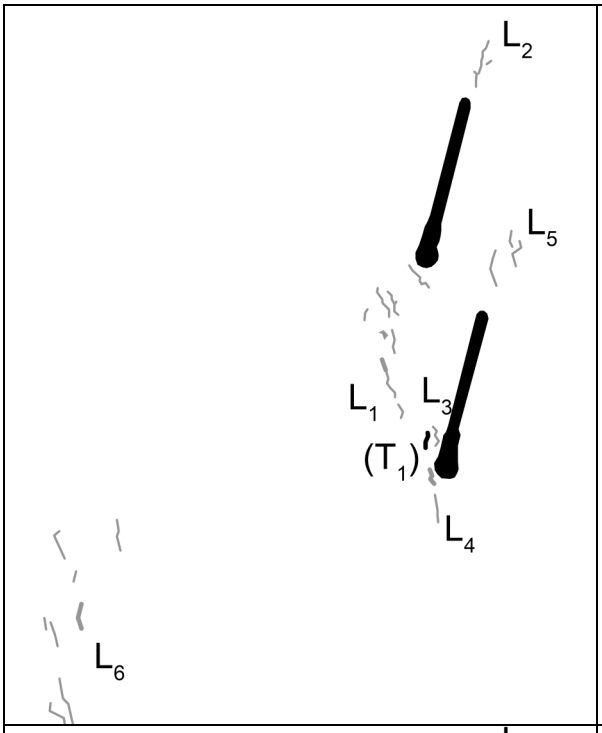	**Time:** ~24m09.8s **σ:** ~119.2 MPa Still image captured before high-speed recording with high-speed camera. L_5 appears above the left flaw's inner tip and is composed solely of boundary-following linear white patches. A group of linear white patches appear in a region in the lower left of the camera's field of view. It is labeled L_6 and has mostly boundary-following linear white patches, although there is one through-going linear feature.
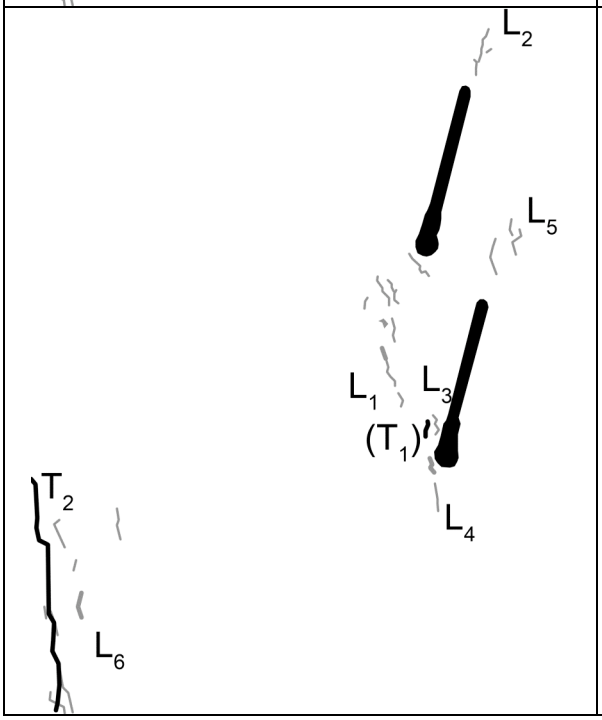	**Time:** ~24m35.5s **σ:** ~121.4 MPa Still image captured before high-speed recording with high-speed camera. A vertical tensile crack T_2 appears in the L_6 region.

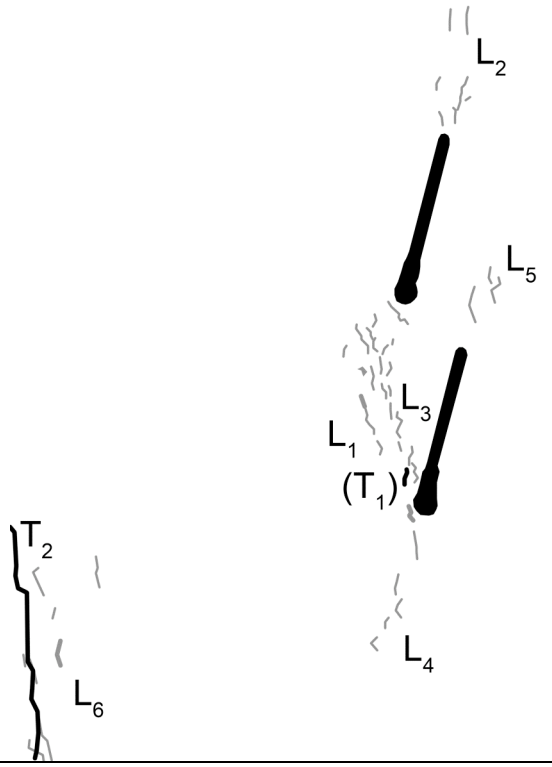	**Time:** ~25m01.9s **σ:** ~123.5 MPa Still image captured before high-speed recording with high-speed camera. L_2 and L_4 extend away from their respective outer flaw tips. L_3 extends toward the right flaw's inner tip and appears to connect with L_1. All white patch extensions are boundary-following linear features.
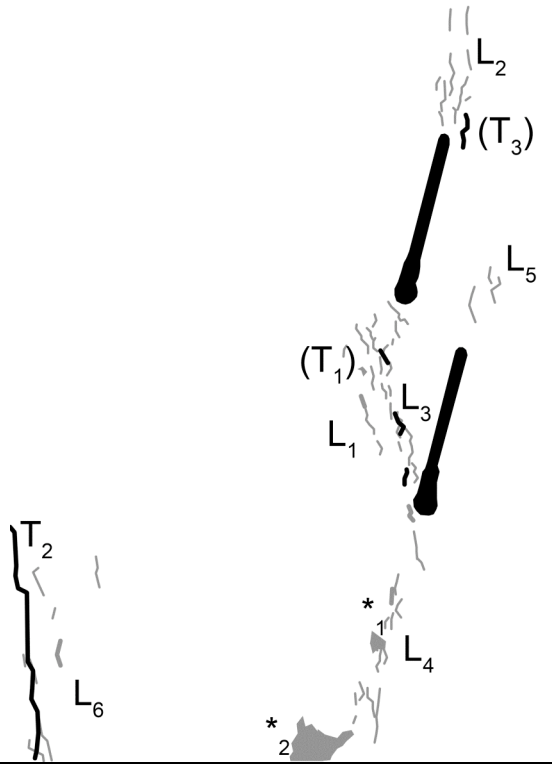	**Time:** ~25m54.6s **σ:** ~127.7 MPa Still image captured before high-speed recording with high-speed camera. L_2 and L_4 extend away from their respective outer flaw tips with boundary-following linear white patches. L_4 also includes a through-going linear white patch and two zones of lightened grains. '$*_1$' indicates the smaller zone of lightened grains as well as the through-going feature. '$*_2$' indicates the larger zone of lightened grains. More small tensile cracks form in the L_1/L_3 region, expanding (T_1). (T_3) also appears near the outer tip of the right flaw.

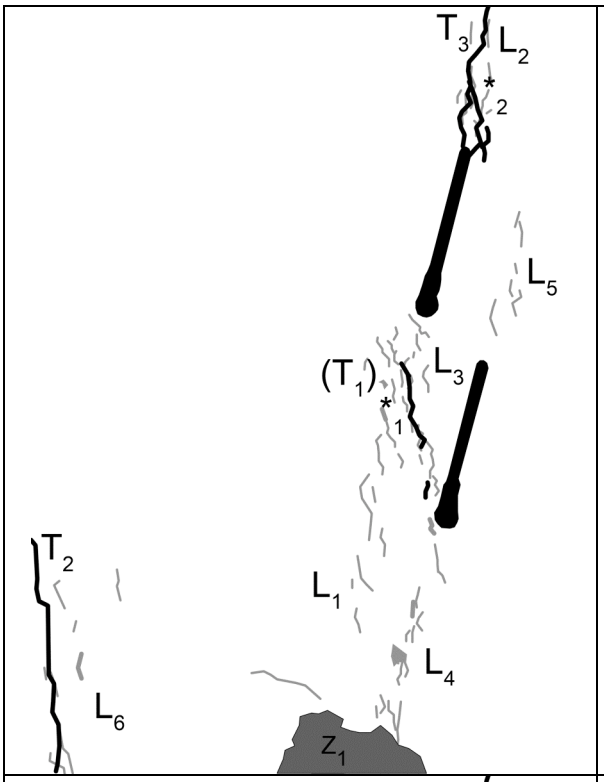	**Time:** 0.7834s before failure **σ:** 128.30 MPa First frame of high-speed video. The group of lightened grains indicated by '$*_2$' in the last image starts to crush and is labeled z_1. A horizontal linear white patch (boundary-following) appears just above z_1. L_1 also appears to extend down toward z_1. Two of the tensile cracks in (T_1) extend and link (indicated with the '$*_1$'). (T_3) extends and connects with the outer tip of the right flaw, becoming tensile wing crack T_3. T_3 attaches to the flaw tip at two points and then becomes one crack at the point indicated with the '$*_2$'
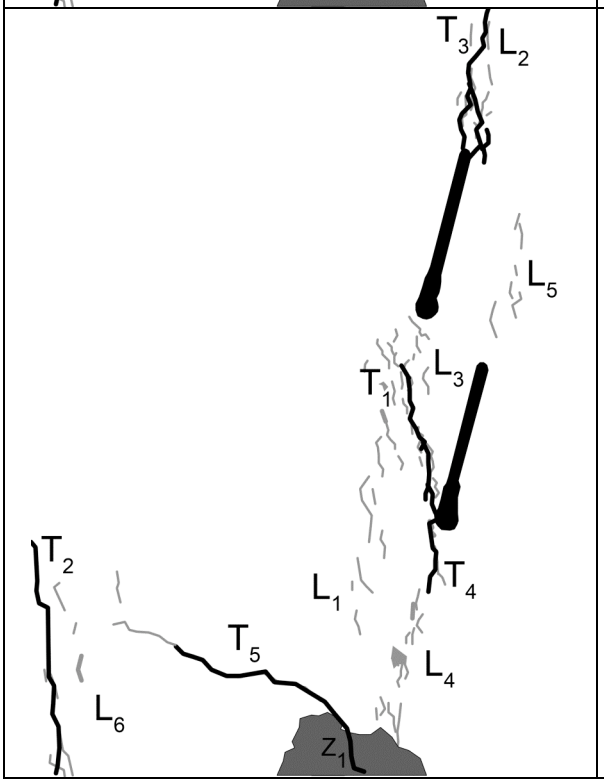	**Time:** 0.6426s before failure **σ:** 128.29 MPa The tensile cracks in (T_1) extend and link with one another as well as the outer tip of the left flaw and the new wing crack is labeled T_1. Another tensile wing crack (labeled T_4) extends below the outer tip of the left flaw. A tensile crack (labeled T_5) appears in z_1 and turns to have a more horizontal orientation and extends toward T_2. A boundary-following linear white patch appears beyond T_5 extending toward T_2.

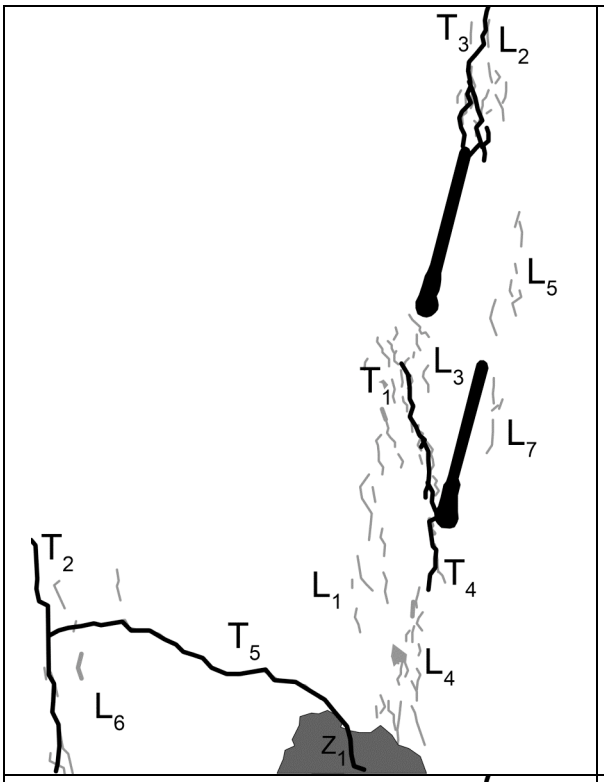	**Time:** 0.3026s before failure **σ:** 128.30 MPa L_1, L_2, and L_4 all extend with boundary-following linear white patches. Linear white patch L_7 appears below the inner tip of the left flaw and is composed solely of boundary-following linear features. T_5 extends and connects with T_2.
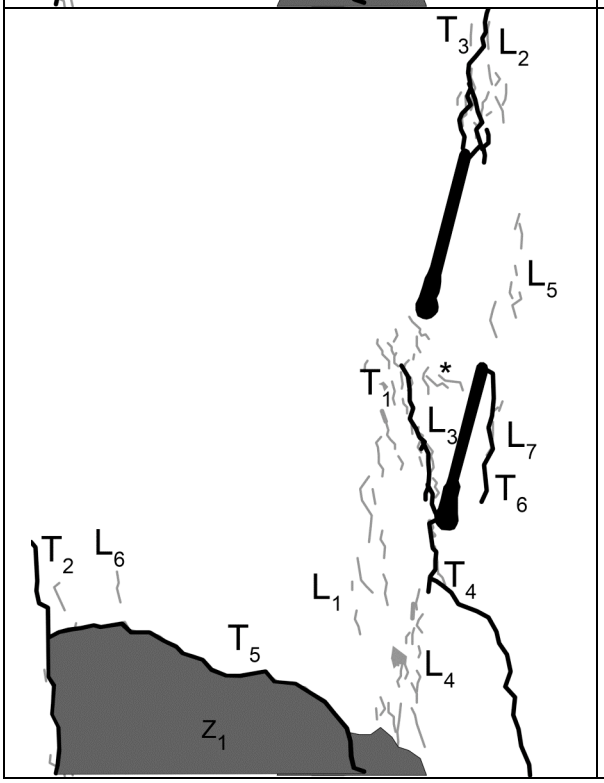	**Time:** 0.0022s before failure **σ:** 128.28 MPa Region z_1 expands and fills the region enclosed by T_2 and T_5 when more grains are crushed and ejected. T_4 extends downward and out of the camera's field of view. Another tensile wing crack (labeled as T_6) appears below the inner tip of the left flaw. A horizontal boundary-following linear white patch appears to connect the left flaw with L_3.

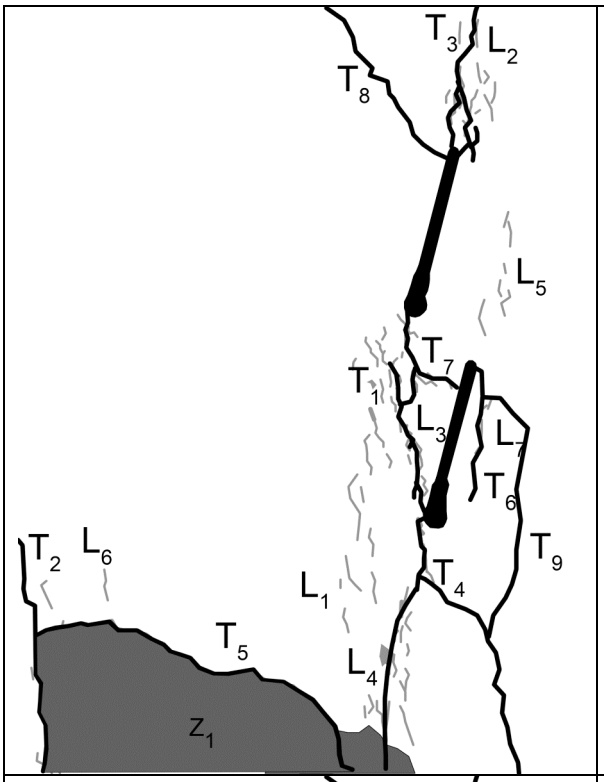	**Time:** 0.002s before failure **σ:** 128.28 MPa Specimen coalescence occurs with the formation of tensile wing crack T_7 which appears to extend from the left flaw – following the horizontal linear white patch mentioned previously – and then connect to the inner tip of the right flaw. T_1 branches and also connects to T_7. Tensile wing crack T_8 appears above the outer tip of the right flaw. Tensile crack T_9 connects T_6 and T_4 (which also extends downward through z_1.
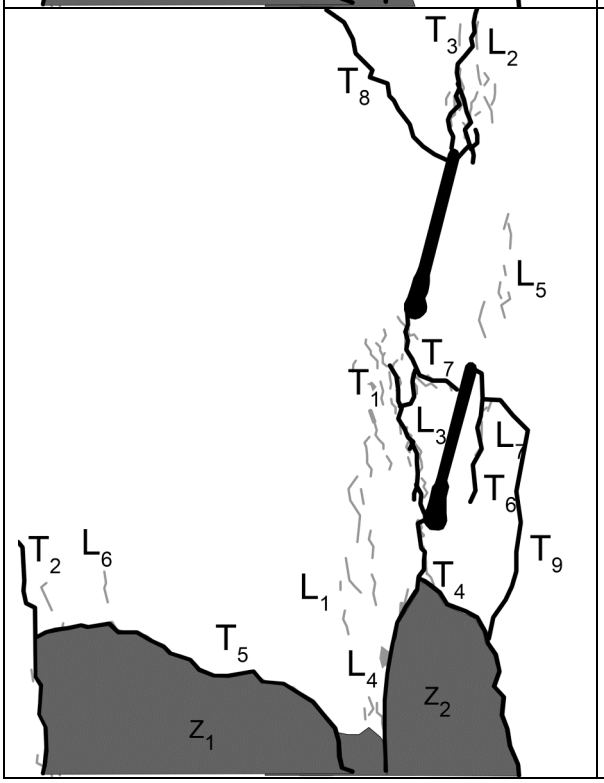	**Time:** 26m02.628s **σ:** 128.3510 MPa Specimen failure occurs with further bursting in the z_1 region as well as the region labeled as z_2.

Gr a-75-60 B

Summary

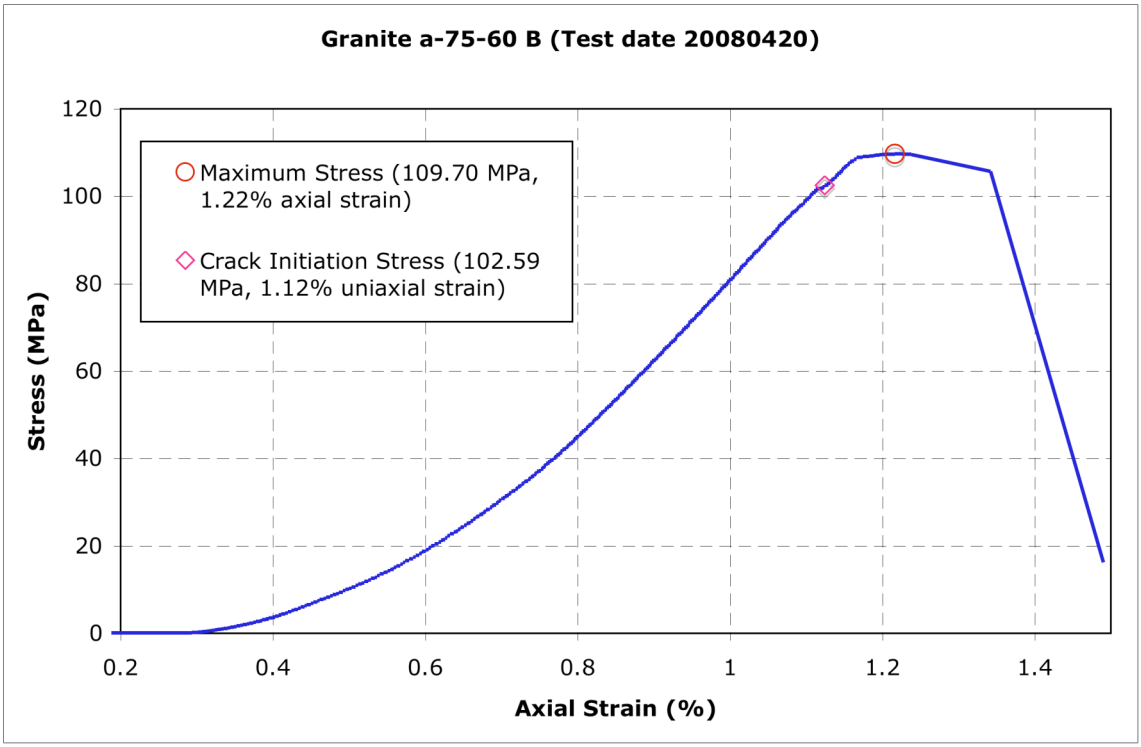

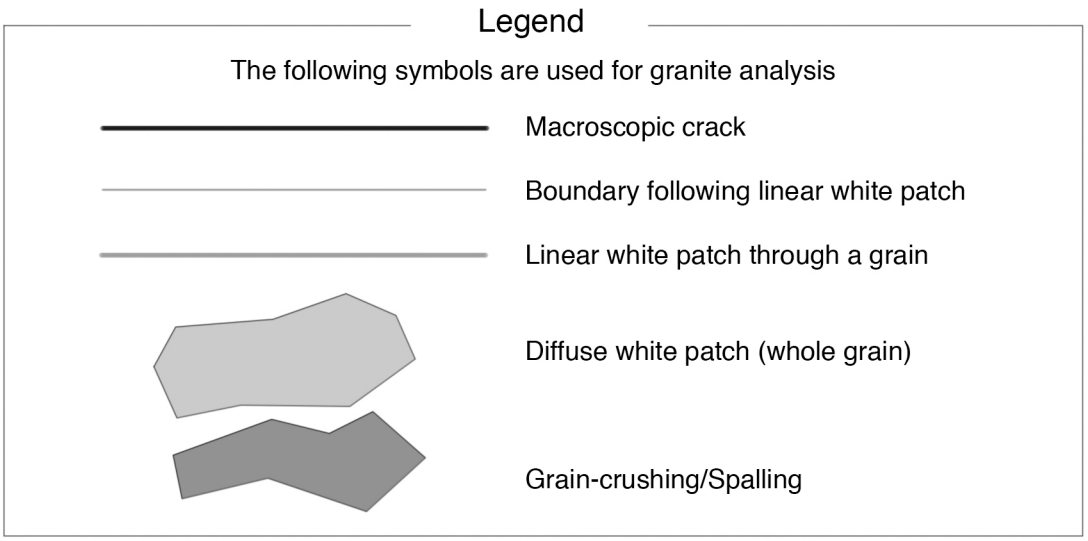

Category 1 Coalescence

Images taken from high-speed video unless otherwise noted

	**Time:** ~8m10s **σ:** ~ 43.4 MPa Still image captured before high-speed recording with high-speed camera. Linear white patch L_1 appears. It is a boundary-following white patch.
	**Time:** ~14m43s **σ:** ~75.9 MPa Still image captured before high-speed recording with high-speed camera. L_1 extends upward and transitions to a through-going linear white patch. Linear white patches L_2 and L_3 appear on the outer tips of the left and right flaws, respectively.
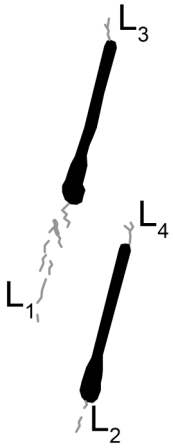	**Time:** ~19m04s **σ:** ~97.6 MPa Still image captured before high-speed recording with high-speed camera. L_1, L_2, and L_3 all extend with boundary-following linear features. Linear white patch L_4 appears above the left flaw's inner tip. It is composed solely of boundary-following linear white patches.

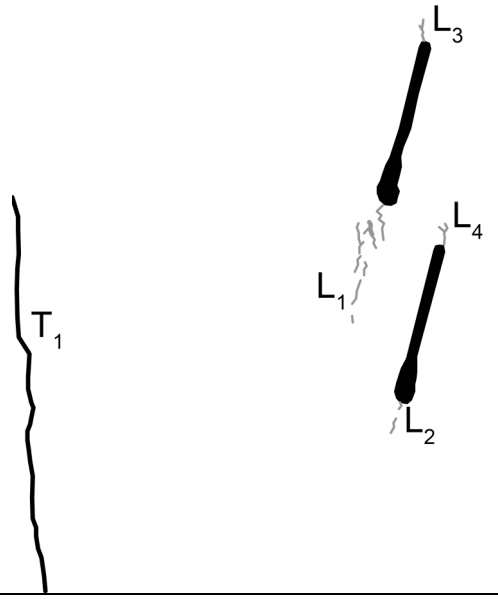	**Time:** ~20m04s **σ:** ~102.6 MPa Still image captured before high-speed recording with high-speed camera. Vertical tensile crack T_1 forms on the left side of the camera's field of view. L_1 expands slightly with boundary-following linear white patches.
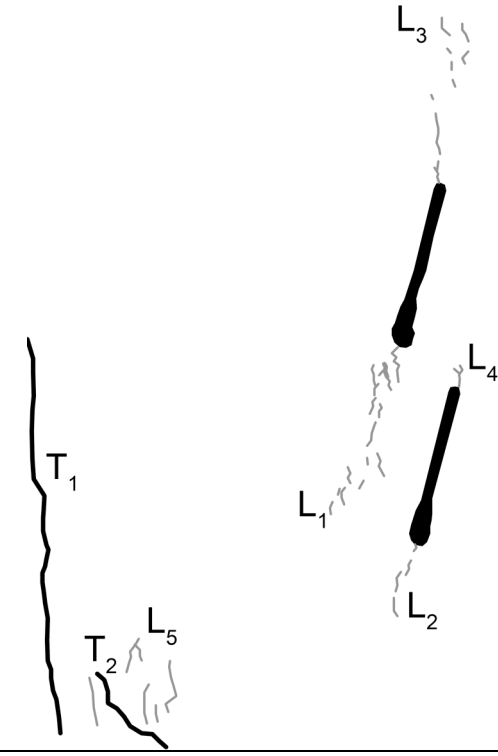	**Time:** ~21m15s **σ:** ~108.4 MPa Still image captured before high-speed recording with high-speed camera. Linear white patches L_1, L_2 and L_3 all extend away from their respective flaw tips with boundary-following linear white patches. A second tensile crack (labeled T_2) appears near T_1 along with some boundary-following linear white patches (labeled L_5).

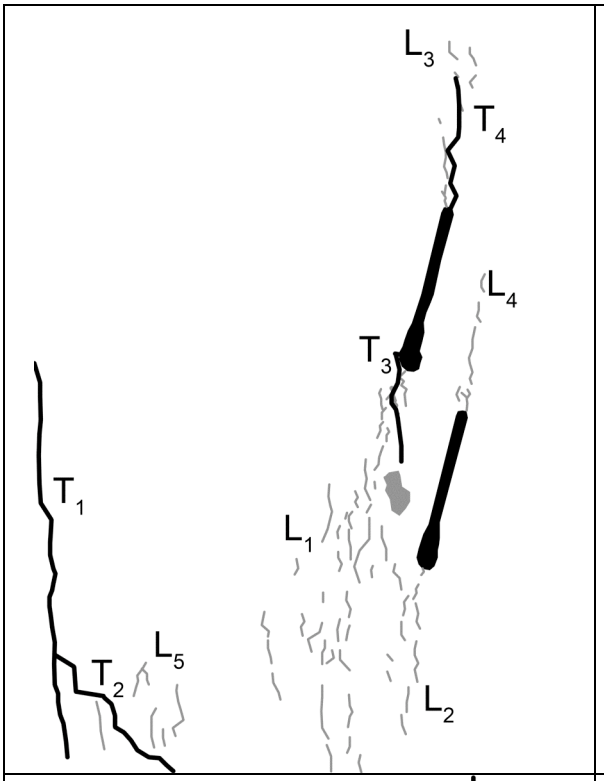	**Time:** 0.4458s before failure **σ:** 109.67 MPa First frame of high-speed video. Tensile wing cracks T_3 and T_4 appear along with extensive white patching. L_1, L_2, and L_4 all extend with boundary-following linear features. L_1 also includes one group of lightened grains. L_1 appears to join with L_2 as well. Tensile crack T_2 extends to link with T_1.
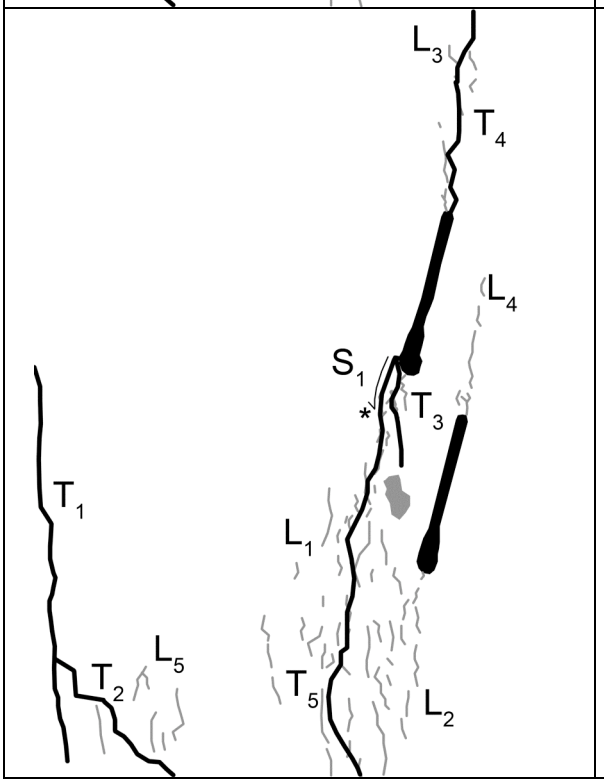	**Time:** 0.006s before failure **σ:** 109.70 MPa A new wing crack appears below the inner tip of the right flaw. The crack initiates as a shear crack (labeled as S_1 and shearing in the sense indicated) and then transitions to tensile crack T_5 at the point indicated by the "*". The crack forms within one high-speed frame, so it is impossible to tell if formation of S_1 and T_5 is simultaneous or in sequence. In the same frame, T_4 extends out of the camera's field of view.

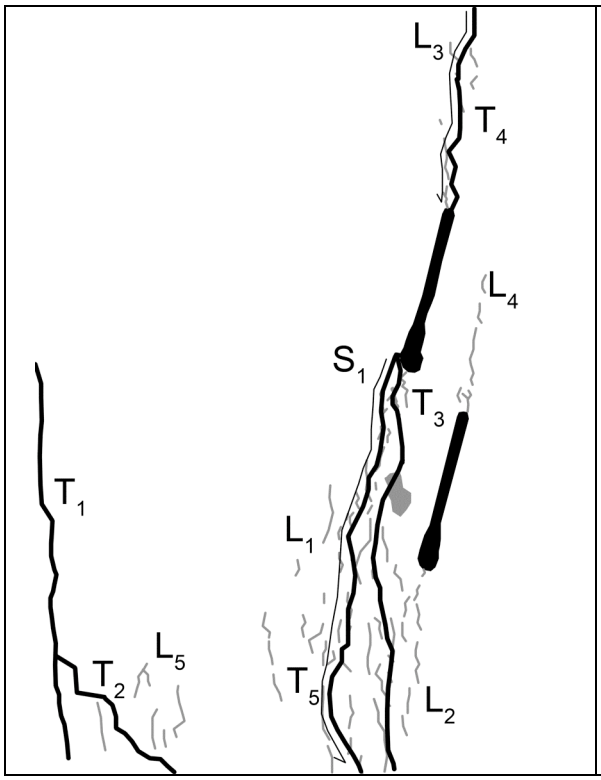

Time: 21m30.06s
σ: 109.7011 MPa

Specimen failure occurs with the extension of tensile crack T_3 and sliding along T_4, S_1 and T_5 (as shown).

APPENDIX K – Brush Platen Tests on Specimens with L = a

The following detailed analyses are for specimens with L = a (see Section 3.2 for an explanation of flaw geometry) tested as described in Chapter 3. Brush platens (see Section 3.4.2 for a description of platens) were used in all cases. This is different from the normal boundary conditions for specimens with this ligament length (see Section 3.2). For an overall summary of the results of these experiments, see Section 4.5.

Granite a-0-0 A (20080229)

Summary

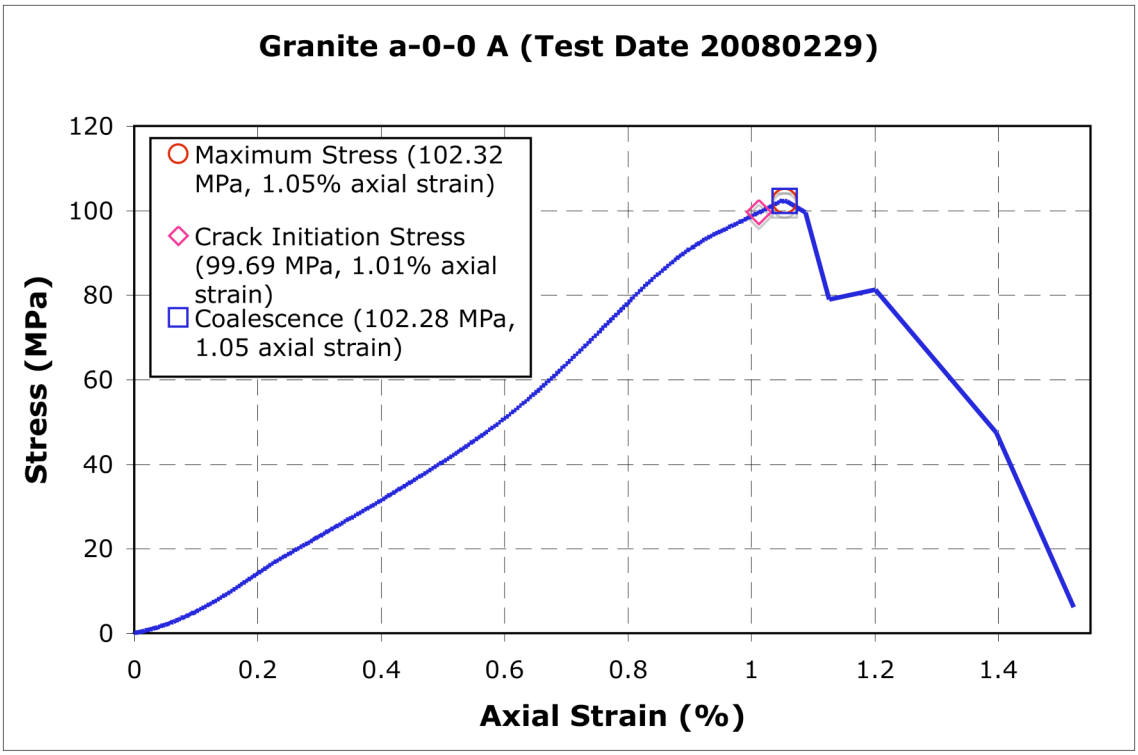

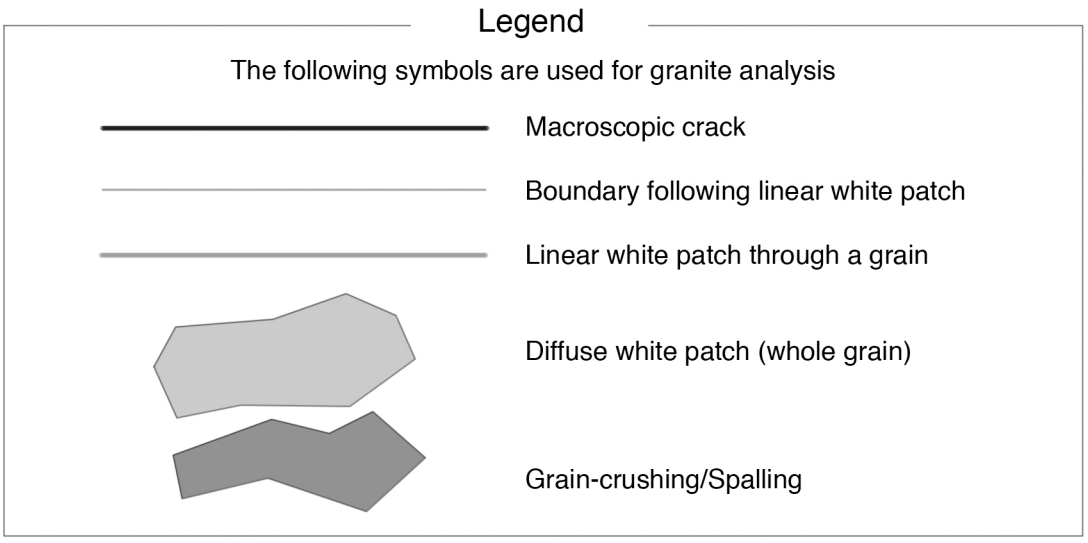

Category 2* Coalescence
Images captured from high-speed video unless otherwise noted
Brush platens used!

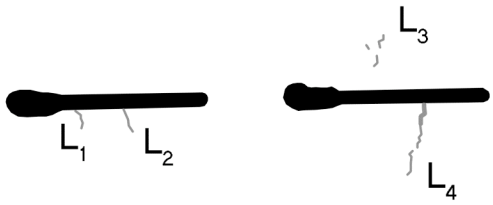	**Time:** ~12m17s **σ:** ~64.9 MPa Still image captured before high-speed recording with high-speed camera. Linear white patches L_1 through L_4 appear. L_1 and L_2 are on the lower edge of the left flaw while L_3 and L_4 are above and below, respectively, the right flaw. L_1 through L_3 are made up of boundary-following linear features while L_4 is composed of both boundary-following and through-going features.
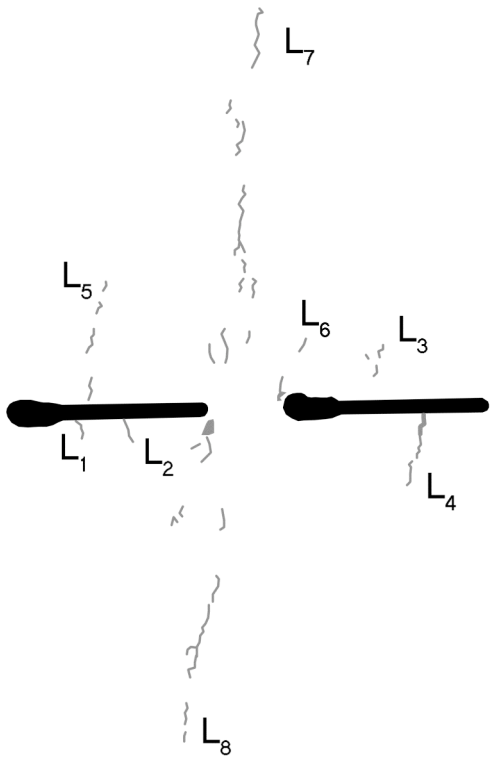	**Time:** ~18m50s **σ:** ~97.3 MPa Still image captured before high-speed recording with high-speed camera. Linear white patches L_5 through L_8 appear. L_5 is located above the middle of the left flaw and is composed solely of boundary-following features. L_6 appears above the right flaw's inner tip. It has both boundary-following linear features as well as a small group of lightened grains. L_7 and L_8 begin to appear from outside the camera's field of view into the bridge area. L_7 only has boundary-following linear features while L_8 also includes a patch of lightened grains. L_8 also seems to curve toward the inner tip of the left flaw.

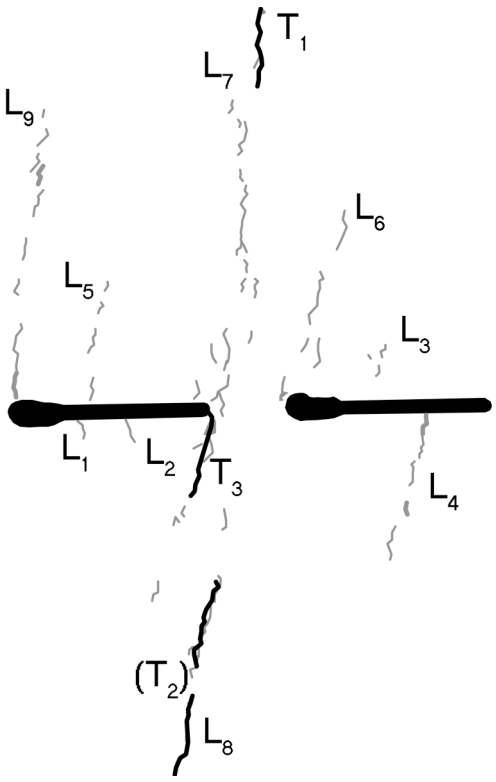

Time: ~19m19s
σ: ~99.7 MPa

Still image captured before high-speed recording with high-speed camera.

Crack initiation occurs with the appearance of tensile crack T_1, tensile crack group (T_2), and tensile wing crack T_3. T_1 and (T_2) extend into the camera's field of view toward the bridge zone. T_3 appears below the left flaw's inner tip.

In addition to tensile crack formation, Linear white patches L_4, L_6, L_7 and L_8 all grow. L_4 extends with both through-going and boundary-following linear features. L_6, L_7, and L_8 all extend with only boundary-following features. L_7 extends toward the left flaw's inner tip.

Finally, Linear white patch L_9 appears above the left flaw's outer tip. It is composed of both types of linear features, although predominantly boundary-following.

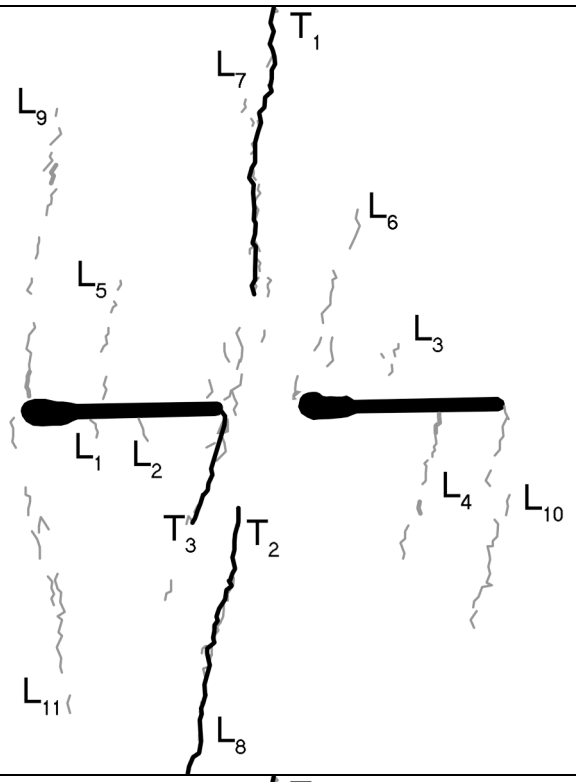	**Time:** 0.7922s before failure First frame of high-speed video. The tensile cracks with (T_2) extend and connect to form tensile crack T_2. T_1 also extends downward toward the bridge area. Linear white patches L_{10} and L_{11} appear. Both contain only boundary-following features. L_{10} is located below the left flaw's outer tip while L_{11} is below the right flaw's outer tip.
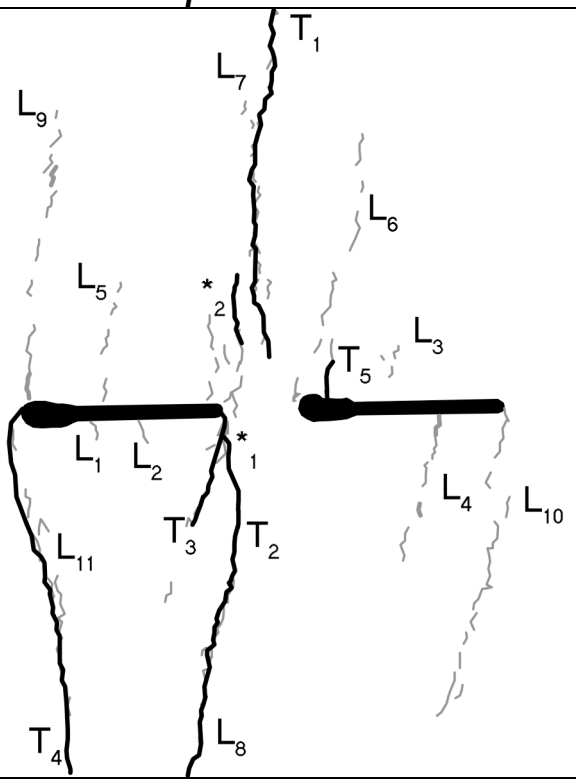	**Time:** 0.0818s before failure Tensile wing crack T_4 appears below the left flaw's outer tip. T_2 extends upward and connects with T_3 at the point labeled '$*_1$'. T_1 extends down further toward the bridge area. A second tensile crack (labeled '$*_2$') appears parallel to T_1 along with more boundary-following linear white patches near the left flaw's inner tip.

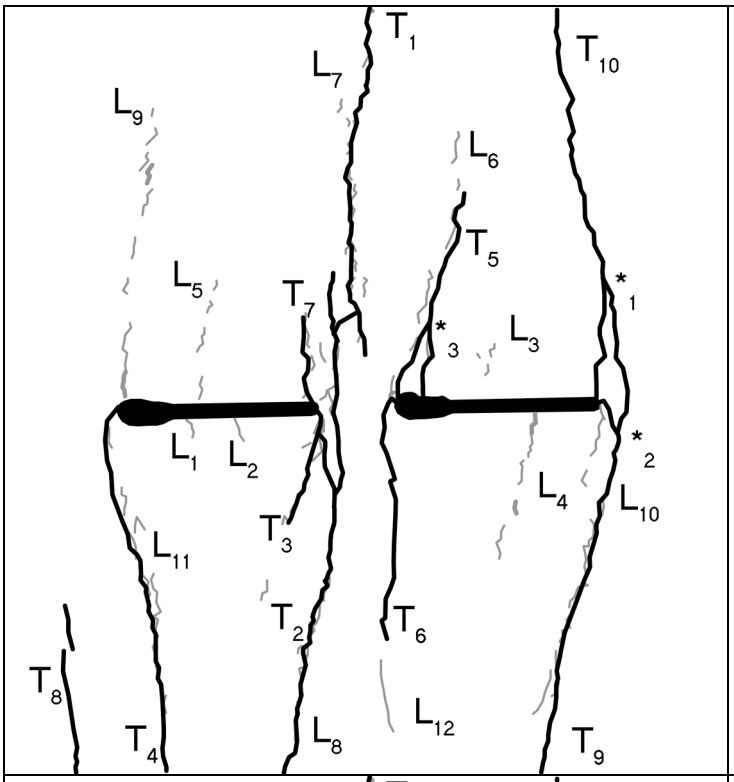	**Time:** 0.078s before failure Several events take place within one frame of high-speed recording. Tensile cracks T_8 through T_{10} appear. T_8 is parallel and adjacent to T_4. T_9 and T_{10} are attached below and above, respectively, the right flaw's outer tip. Both of these tensile cracks also are connected by a tensile crack (attaching at points '$*_1$' and '$*_2$'). T_5 also branches (at point '$*_3$') and connects to its flaw tip. T_1 extends downward and connects with T_2 just below the left flaw's inner tip.
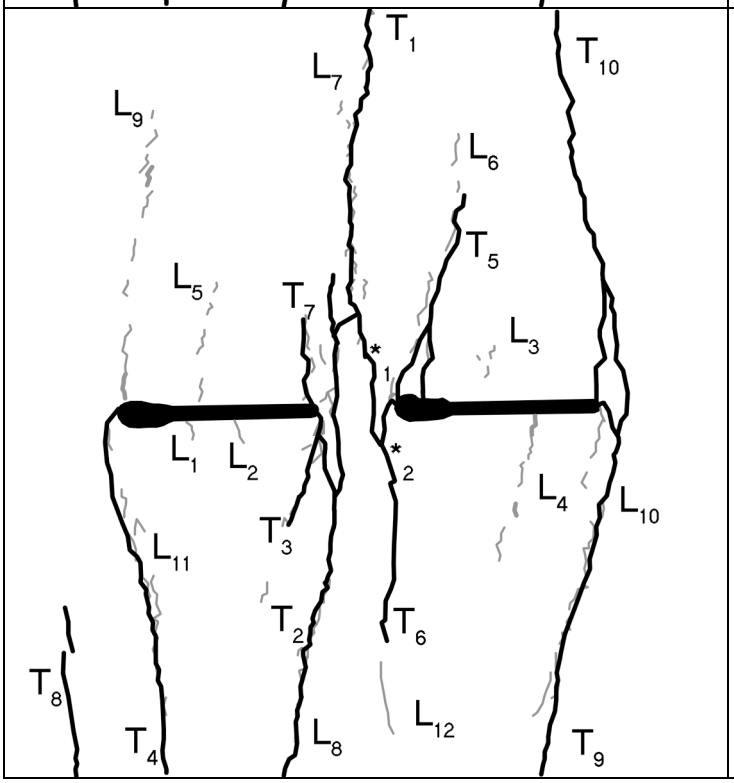	**Time:** 0.012s before failure Sample coalescence occurs when T_1 extends down (from the point labeled '$*_1$') and connects with T_6 at the point labeled '$*_2$'. Category 2* (indirect) coalescence.

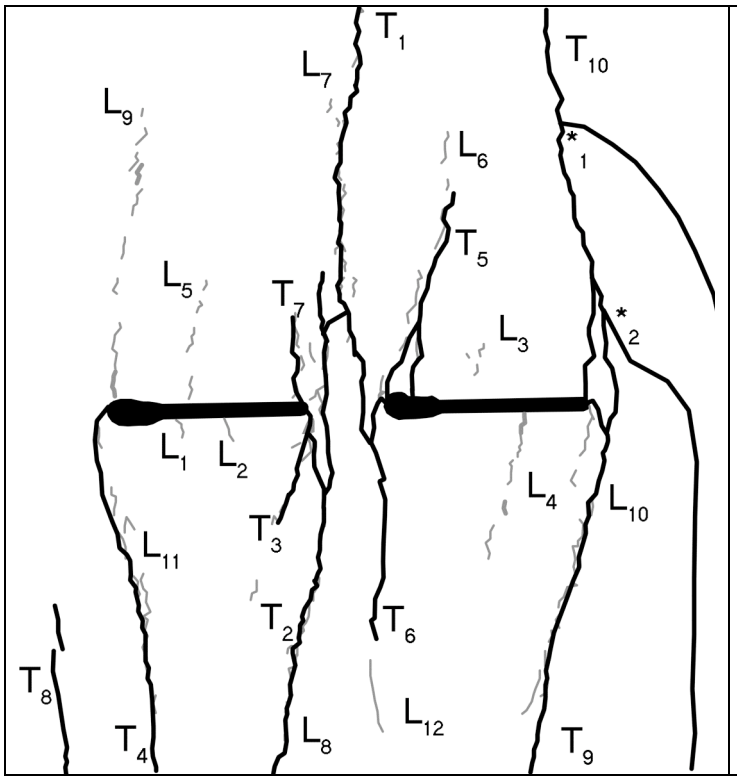

Time: 19m49.908s
σ: 102.3178 MPa

The sample fails when tensile cracks branch off of T_{10} at points labeled $*_1$ and $*_2$.

Granite a-0-60 A (20071206)

Summary

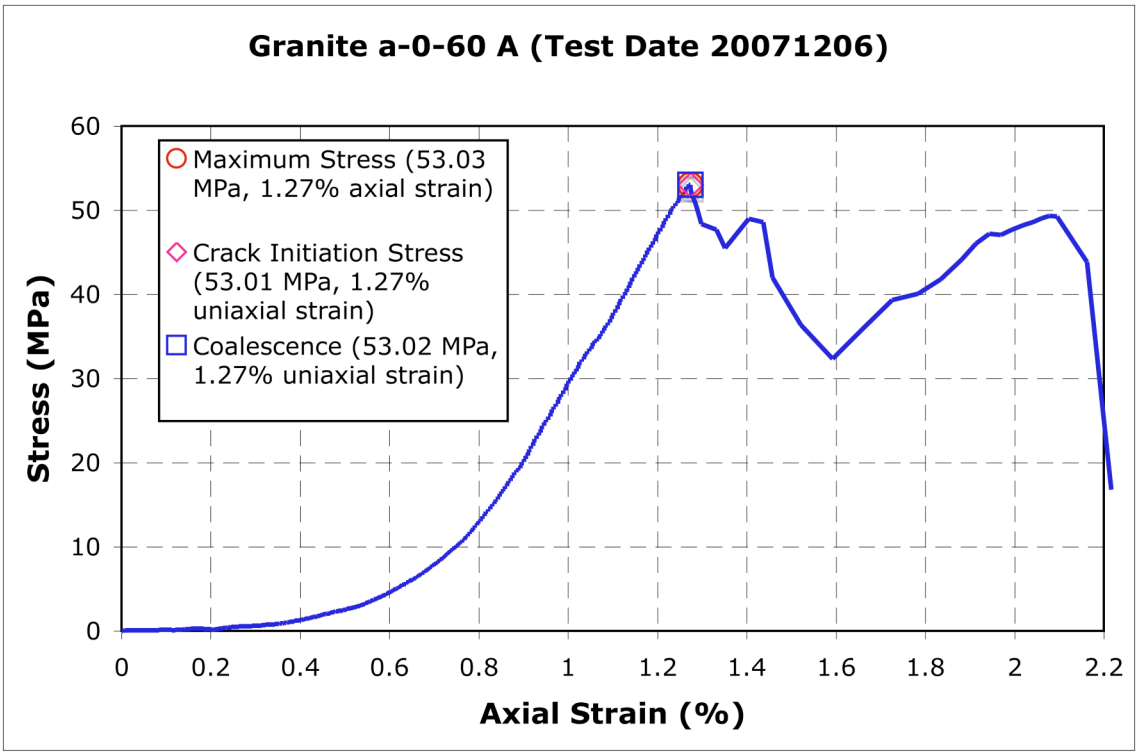

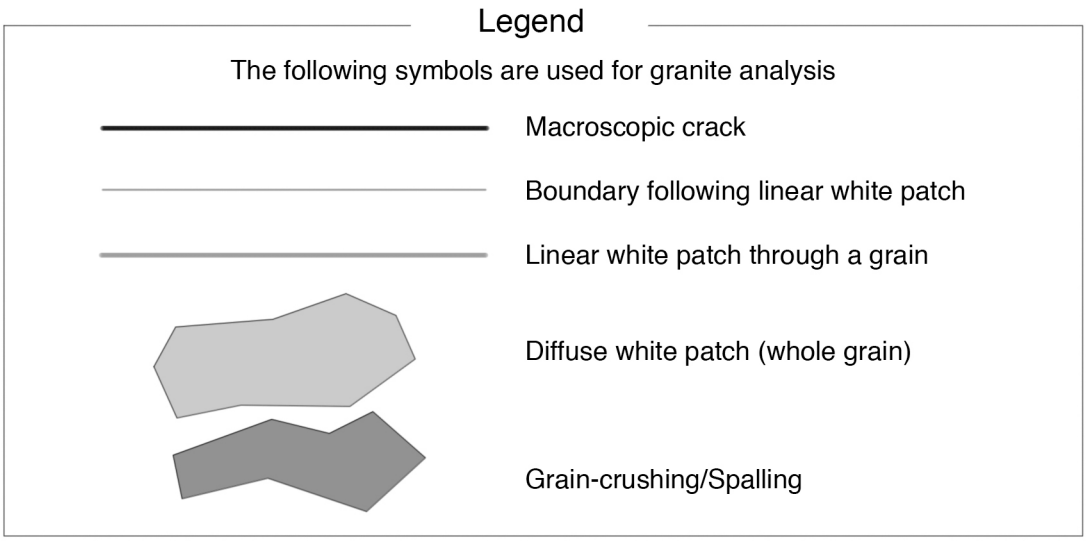

Category 2 Coalescence

Images taken from high-speed video unless otherwise noted

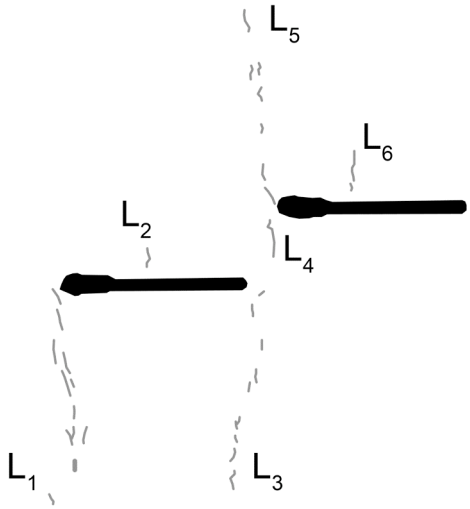	**Time:** ~9m53s **σ:** ~52.7 MPa Still image captured before high-speed recording with high-speed camera. Linear white patches L_1 through L_6 appear. All but L_1 are composed solely of boundary-following linear white patches while L_1 also includes a through-going linear white patch. L_4 is in the bridge zone.
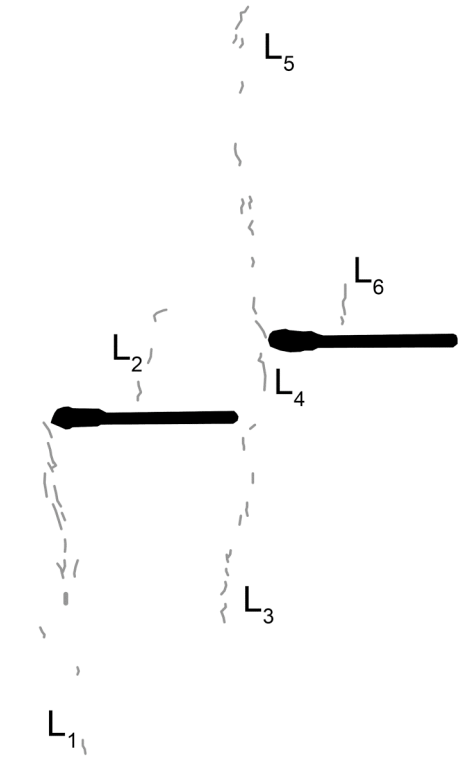	**Time**: 0.2088s before failure First frame of high-speed video analyzed. L_1, L_2, and L_5 all extend with boundary-following linear white patches.

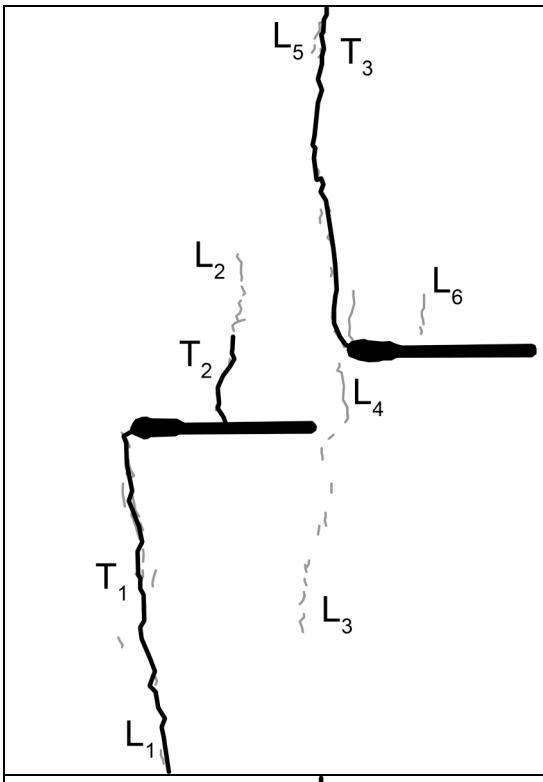	**Time:** 0.1228s before failure Tensile wing cracks T_1 and T_2 appear below and above the left tips of the left and right flaws, respectively. Tensile crack T_2 appears in the L_2 region. Linear white patch L_2 also extends upward.
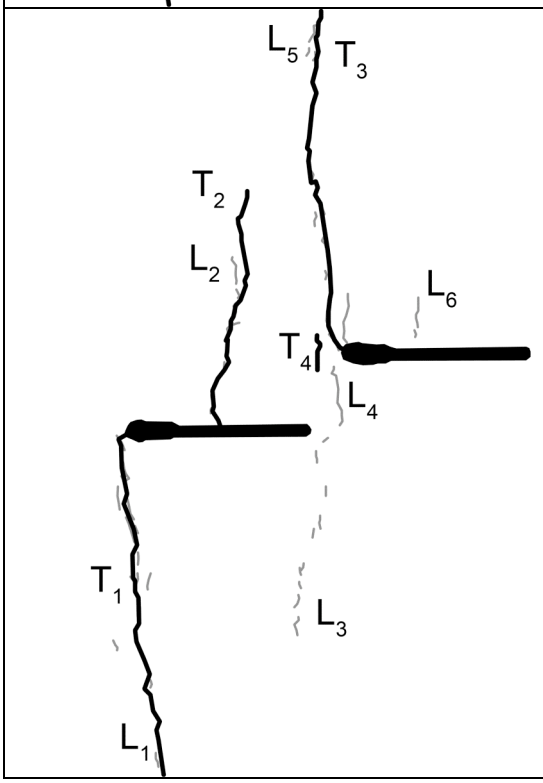	**Time:** 0.0954s before failure Tensile crack T_4 appears in the bridge area close to the inner tip of the right flaw. Tensile wing crack T_2 extends upward.

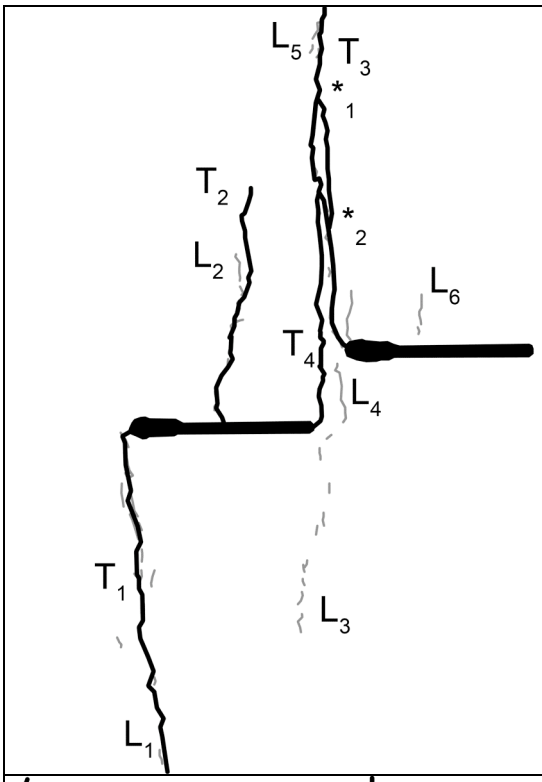	**Time:** 0.0614s before failure Specimen coalescence occurs when T_4 extends in both directions and connects the inner tip of the left flaw with T_3. Coalescence is indirect (category 2). T_3 also has a tensile crack branch off and reconnect at the points labeled '$*_1$' and '$*_2$'.
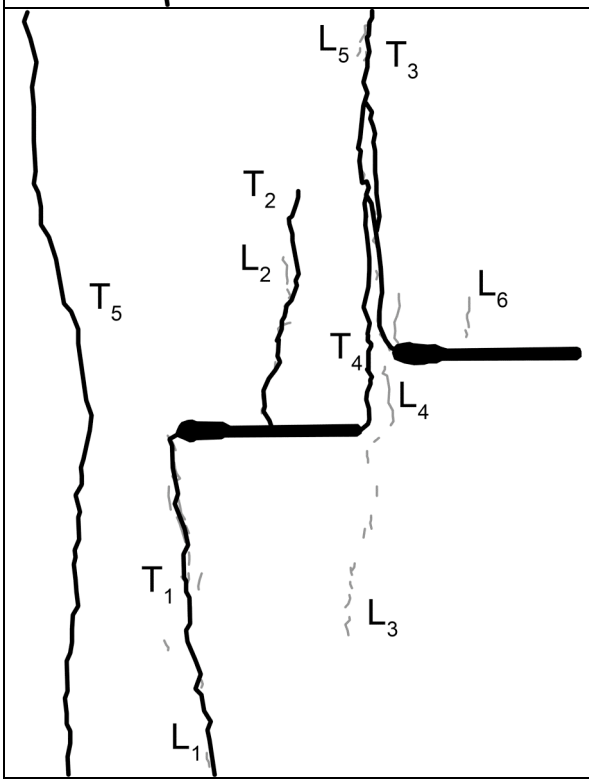	**Time:** 9m56.814s **σ:** 53.0319 MPa Sample failure occurs when vertical tensile crack T_5 appears.

APPENDIX L – Designs for Water Pressure Plates

Figures K.1, K.2, K.3, and K.4 provide schematics for pressure plates used in the experiments with pressurized flaws. Drawings were made in AutoCAD.

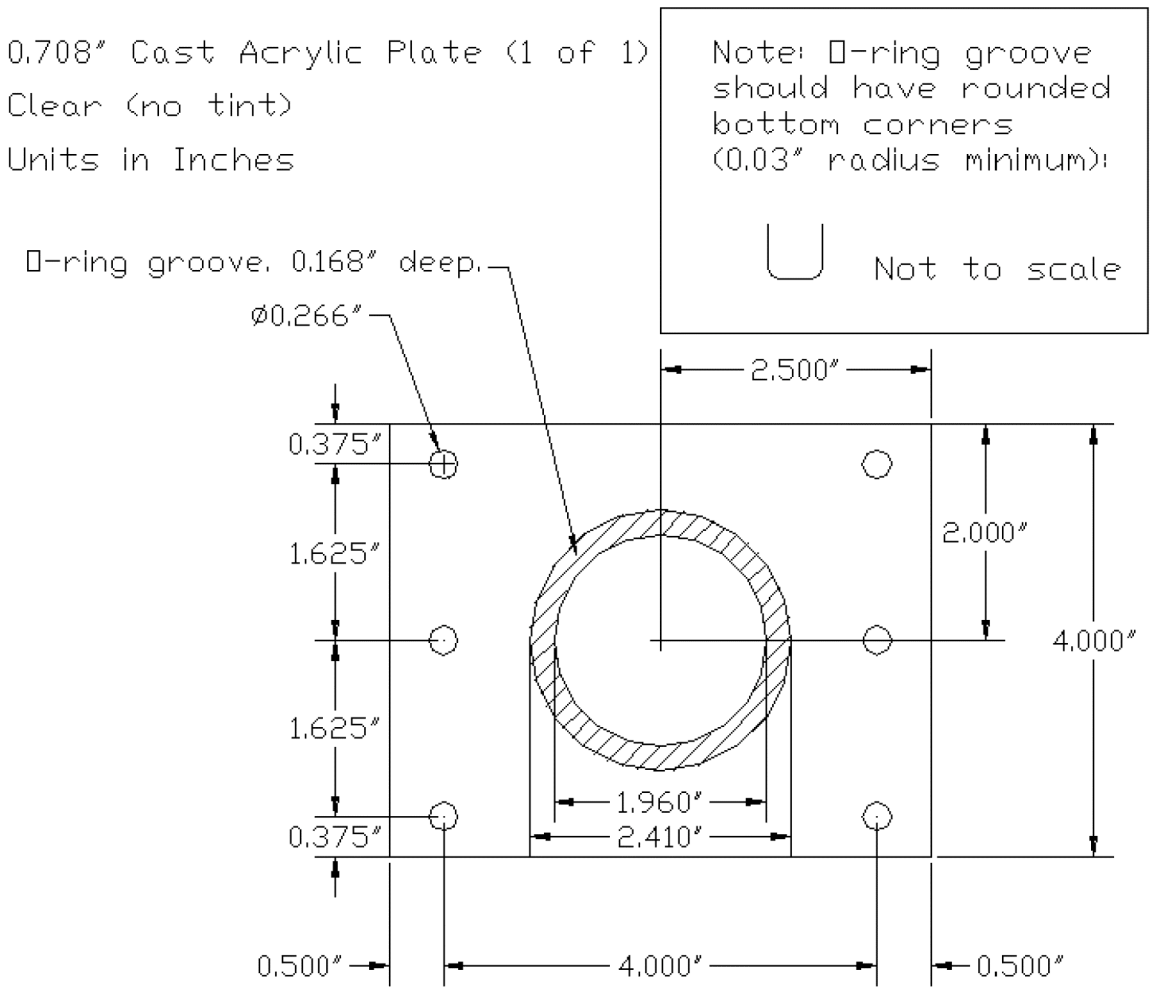

Figure K.1 – Front pressure plate plan view.

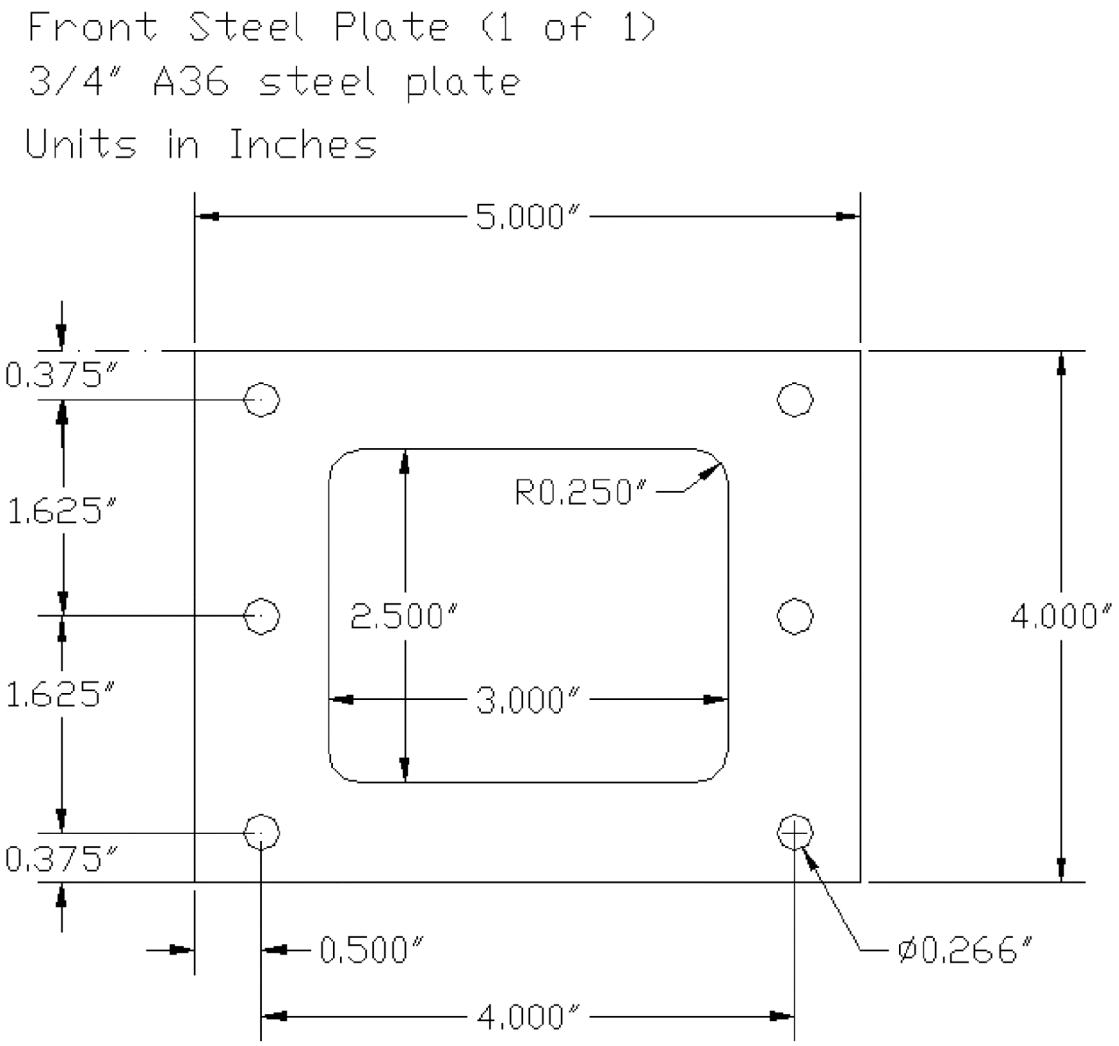

Figure K.2 – Front frame plan view.

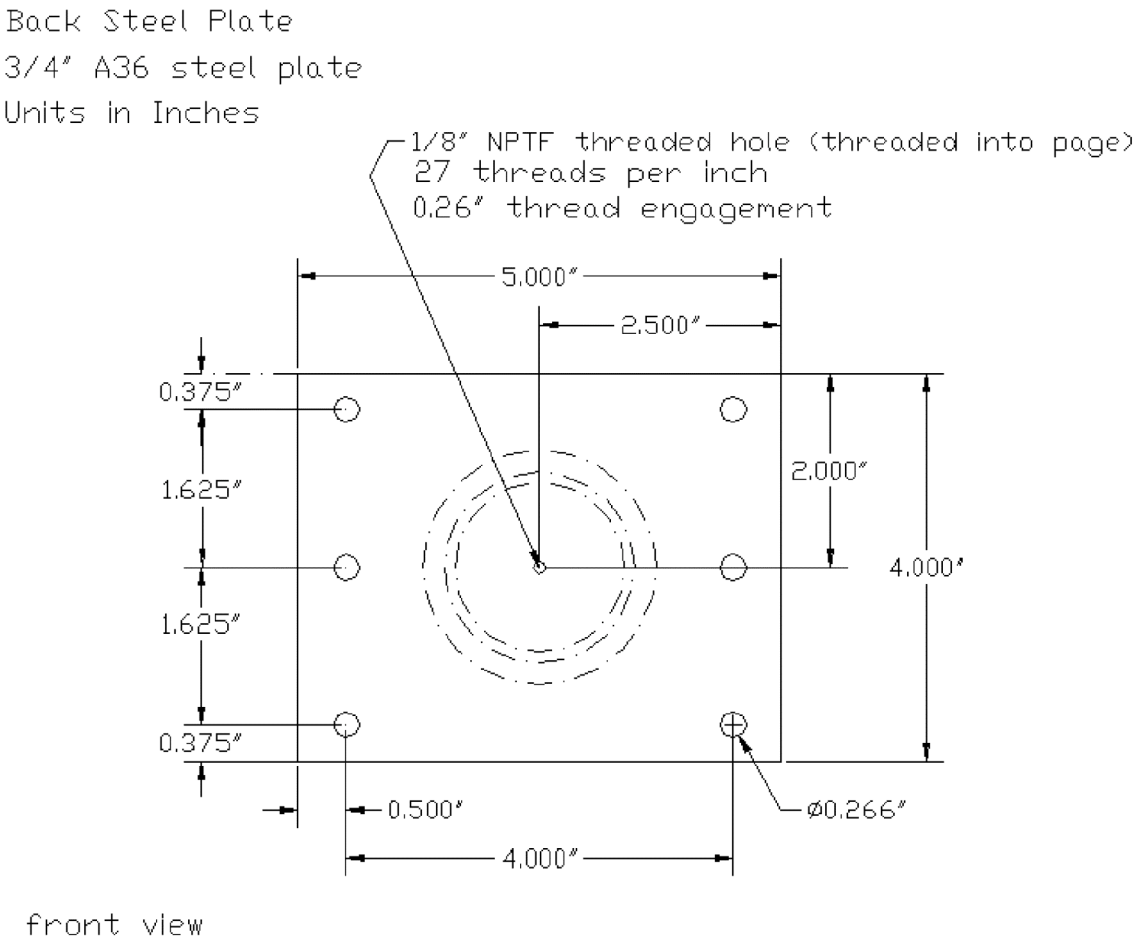

Figure K.3 – Back pressure plate plan view.

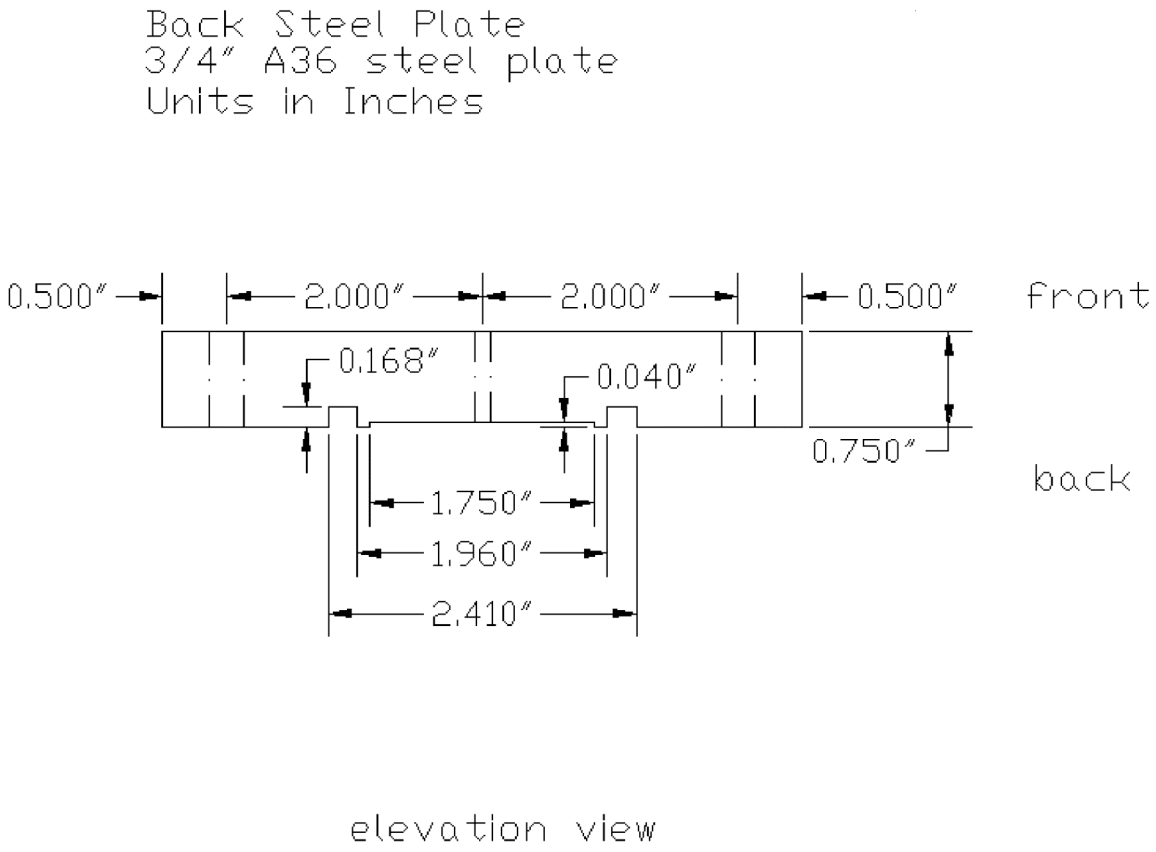

Figure K.4 – Back pressure plate elevation view.

APPENDIX M – Pressure Transducer Calibration and Specifications

M.1 Calibration

An Omega 1000 psi pressure transducer (PX102 – 1KSV) was used to monitor and record the water pressure in the flaws. Calibration was performed to relate pressure with voltage output by the transducer. A series of known oil pressures was applied, removed, and re-applied. The transducer was loaded and unloaded to check for hysteresis. A linear regression line was applied and the slope of this line is called the transducer calibration factor. Both the data and line fit to the data are shown in Figure L.1. As can be seen in Figure L.1, the fit of the regression line is very good ($R^2 = 0.99999$), so the slope was used as the calibration factor in the water pressure tests.

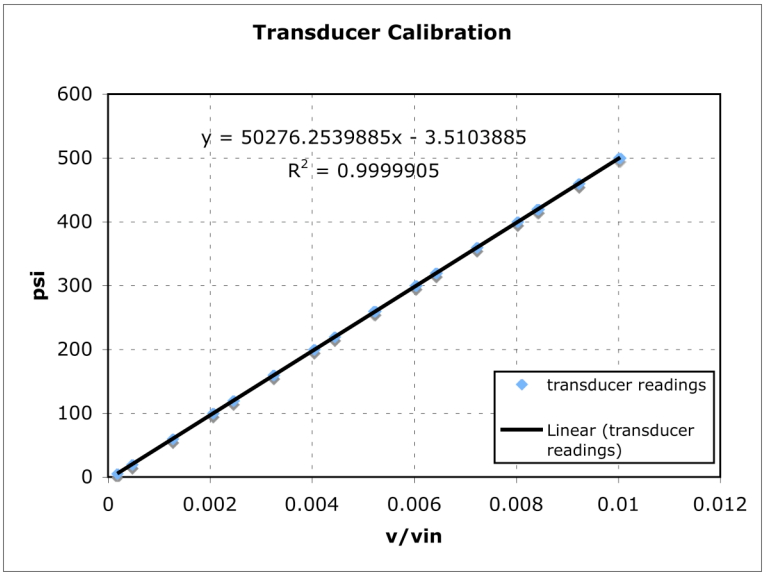

Figure L.1 – Transducer calibration data and linear regression for the data.

M.2 Specifications

Figure L.2 is the company provided technical specifications for the Omega PX102 series of transducers.

FLUSH DIAPHRAGM MILLIVOLT OUTPUT PRESSURE TRANSDUCER

PX102 Series
0-6 to 0-5000 psi
0-0.4 to 0-1345 bar

Starts at $480

MADE IN USA

SPECIFICATIONS

Excitation: 5 Vdc 35 mA (6 Vdc max)
Output: 0 to 100 mV ±1%
Input Impedance: 150 ± 50 Ω
Output Impedance: 115 ± 25 Ω
Insulation Resistance: 20 MΩ at 50 Vdc
Accuracy: 100 to 5000 psi = 0.25% BFSL, all other ranges = 0.5% BFSL
Zero Balance: ±5 mV
Operating Temperature Range: -51 to 93°C (-60 to 200°F)
Compensated Temperature Range: -1 to 71°C (30 to 160°F)
Thermal Zero Effect: ±0.1% rdg/°C (±0.05% rdg/°F)
Thermal Sensitivity Effect: ±0.02%/°C (±0.01% rdg/°F)
Proof Pressure: 2x full scale
Burst Pressure: 5x full scale minimum
Fatigue: >160 million cycles
Gages: Semiconductors on bending beam
Body/Diaphragm Material:
316 L SS: ≤50 psi
-15-5 PH SS: >50 psi
Pressure Port: Flush
Electrical Connection: 1 m (36"); shielded PVC cable, 4 leads
Weight: 57 g (2 oz)

Units 100 psi and above have cases sealed from the surrounding atmosphere, providing maximum reliability in humid or corrosive environment (psis). Ranges below 100 psi are vented to the atmosphere and read gage pressure (psig).

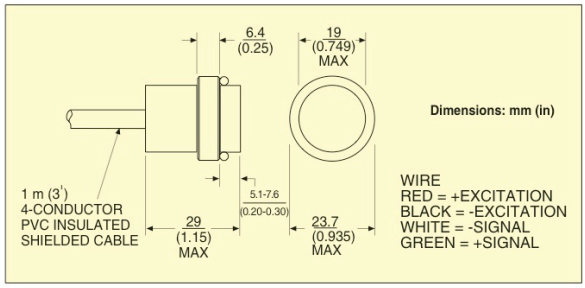

MOST POPULAR MODELS HIGHLIGHTED!

To Order *(Specify Model Number)*

RANGE		MODEL NO.	PRICE	COMPATIBLE METERS*
0 to 6 psig	0 to 0.41 bar	**PX102-006GV**	**$495**	DP25B-S, DP41-S
0 to 25 psig	0 to 1.72 bar	**PX102-025GV**	**495**	DP25B-S, DP41-S
0 to 50 psig	0 to 3.4 bar	**PX102-050GV**	**495**	DP25B-S, DP41-S
0 to 100 psis	0 to 6.9 bar	**PX102-100SV**	**480**	DP25B-S, DP41-S
0 to 200 psis	0 to 13.8 bar	**PX102-200SV**	**480**	DP25B-S, DP41-S
0 to 500 psis	0 to 34.5 bar	**PX102-500SV**	**480**	DP25B-S, DP41-S
0 to 1000 psis	0 to 68.9 bar	**PX102-1KSV**	**480**	DP25B-S, DP41-S
0 to 3000 psis	0 to 207 bar	**PX102-3KSV**	**480**	DP25B-S, DP41-S

Comes with complete operator's manual.
** See section D for compatible meters.*
Ordering Examples: PX102-006GV,** 0 to 6 psig pressure transducer, **$495.
AD-1SS,** adaptor to mount in a ¼ NPT fitting, **$125.

ACCESSORY

MODEL NO.	PRICE	DESCRIPTION
EE-2530	**$195**	Reference Book: Handbook of Systems Engineering

B-43

Figure L.2 – Technical specifications for the PX102 series of Omega transducers. The transducer used in this study was the PX102-1KSV.

APPENDIX N – Flaws with Water Pressure

The following detailed analyses are for specimens tested with water pressurized flaws, as described in Chapter 5. Only one geometry was used, with ligament length L = a, flaw inclination angle $\beta = 60°$, and bridging angle $\alpha = 60°$ (see Section 3.2 for an explanation of flaw geometry). Solid platens (see Section 3.4.2 for a description of platens) were used in all cases. Flaw pressure was set at 0, 100, 200, or 400 psi and the loading profile (see Section 5.3.6 for a description of loading profiles) was either fast or slow. For an overall summary of the results of these experiments, see Chapter 6).

Gr a-60-60 I (0 psi, slow loading)

Summary

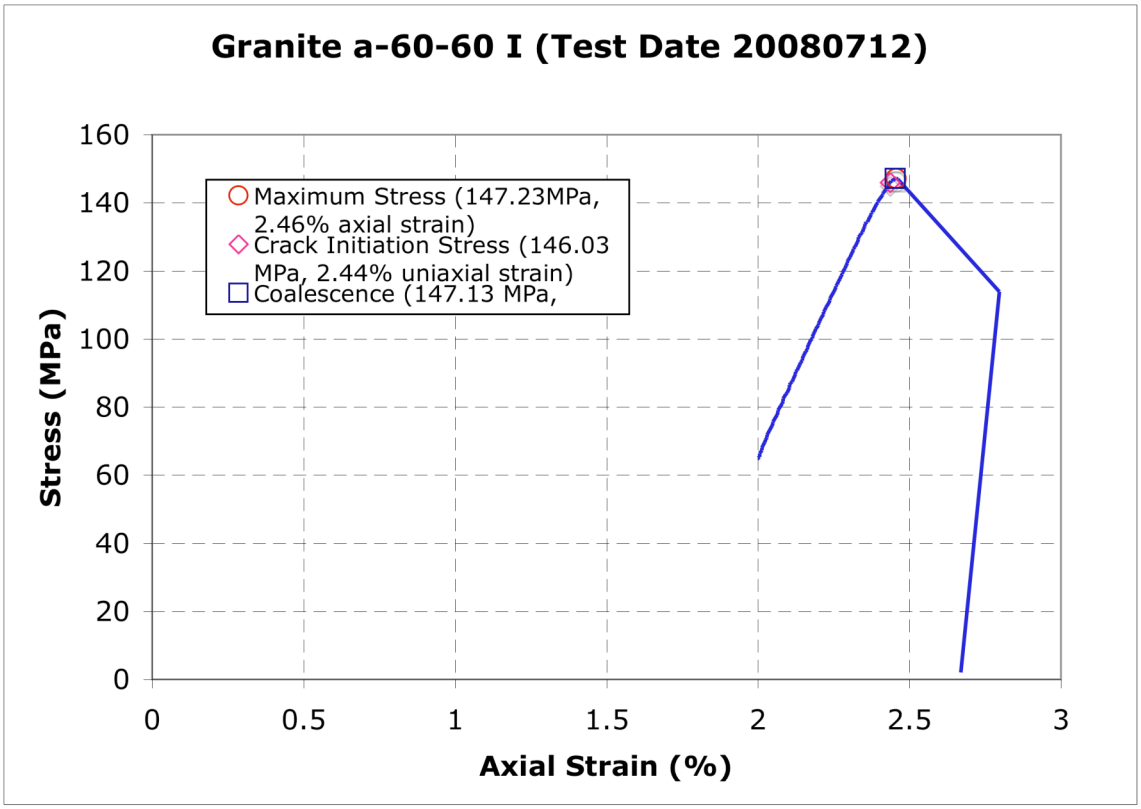

Pressure: 0 psi
Loading profile: fast
Coalescence category 4

During testing of Gr a-60-60 I, the loading machine froze during the test and had to be restarted. The specimen had not yet failed and no crack initiation had been observed. The stress-strain data from the initial loading, however, was lost. Therefore, the stress-strain curve above starts at a higher load and displacement. All three of the normally noted points were still captured with the high-speed camera. Specimen failure time, obviously, is based on the start of the second loading.

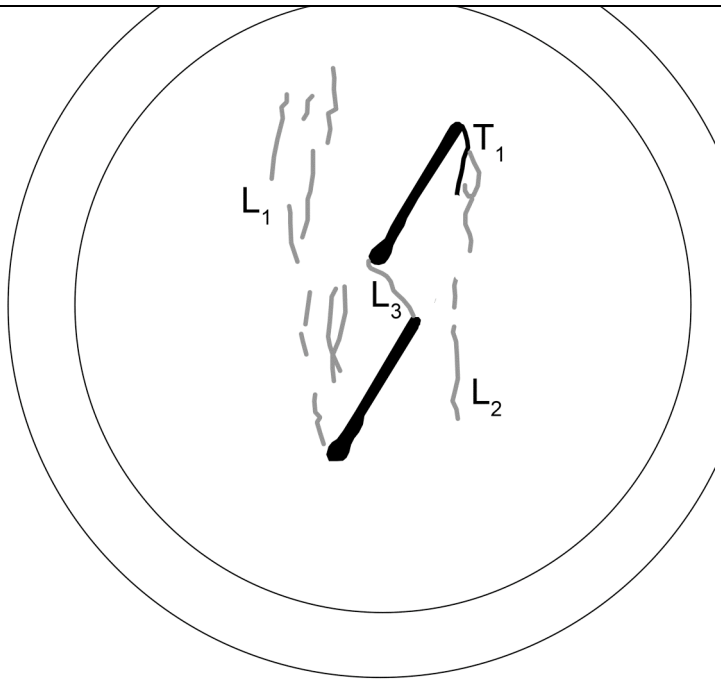	**Time:** 1.1003s before failure **σ:** 146.03 MPa First frame of high-speed video. Tensile wing crack T_1 is already present below the right flaw's outer tip. Linear white patches L_1, L_2, and L_3 are also present. These white patch locations are approximate and not all-inclusive. Only obvious white patches were found because no previous image exists for comparison.
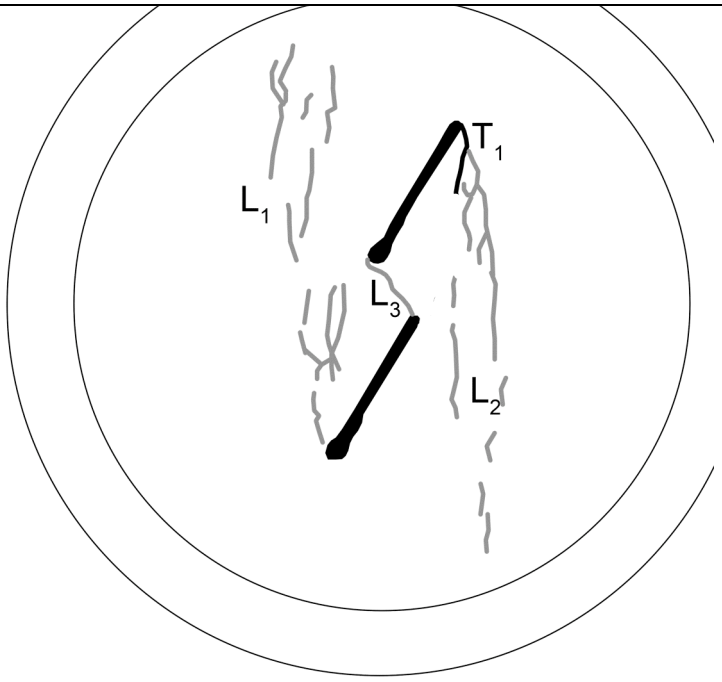	**Time:** 0.6593s before failure **σ:** 146.54 MPa Linear white patches L_1 and L_2 both extend away from their respective flaw tips.

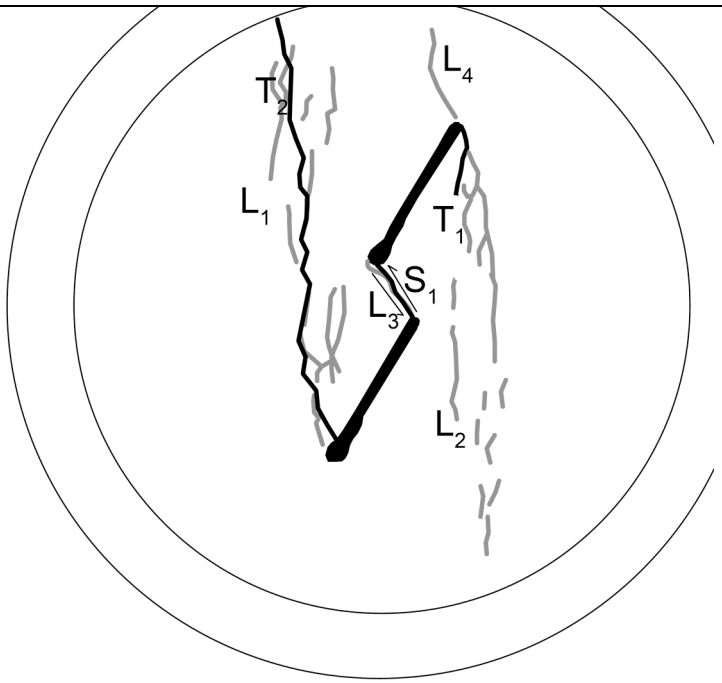	**Time:** 0.1593s before failure **σ:** 147.23 MPa Tensile wing crack T_2 appears above the left flaw's outer tip. Immediately after T_2 appears, direct sample coalescence occurs (category 4) when shear crack S_1 links the two inner flaw tips along the linear white patch L_3. The crack shears in the sense indicated. Linear white patch L_4 appears above the right flaw's outer tip.
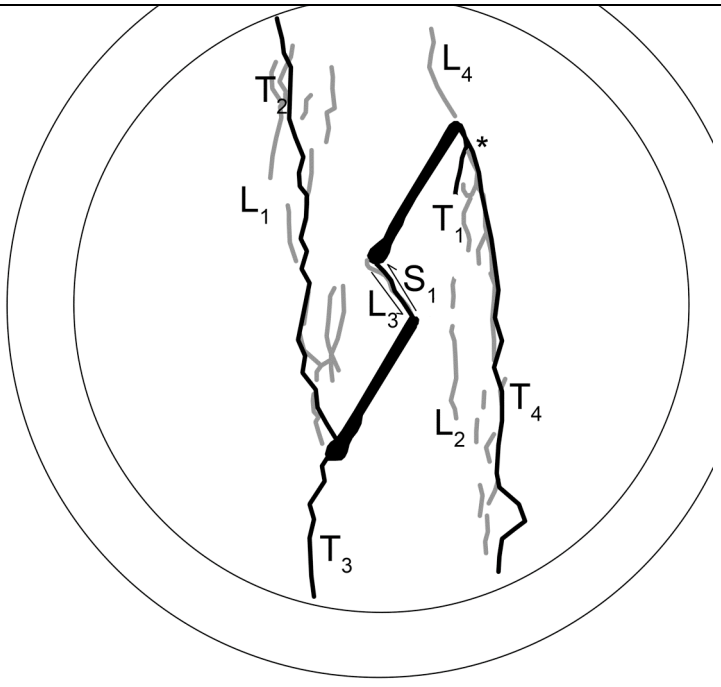	**Time:** 33.498s **σ:** 147.2289 MPa Specimen failure occurs after the appearance of tensile crack T_3 below the left flaw's outer tip followed immediately by the appearance of tensile crack T_4 branching off of T_1 at the point labeled "*".

Gr a-60-60 G (100 psi, fast loading)

Summary

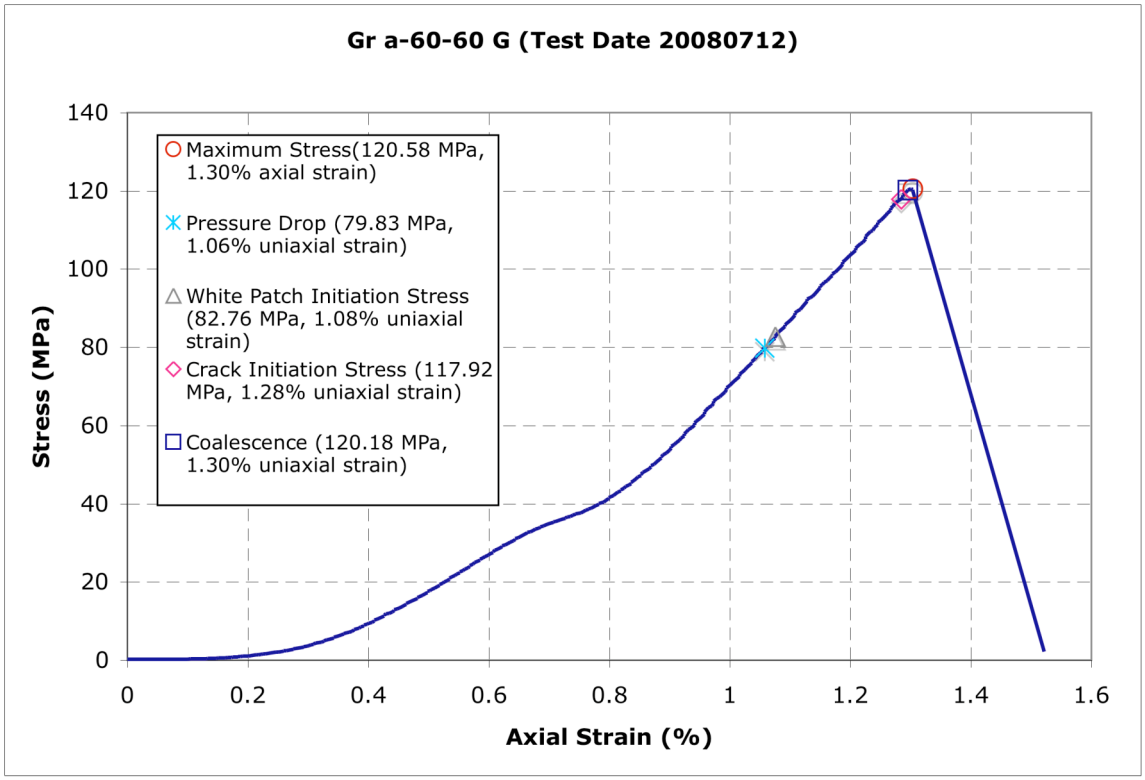

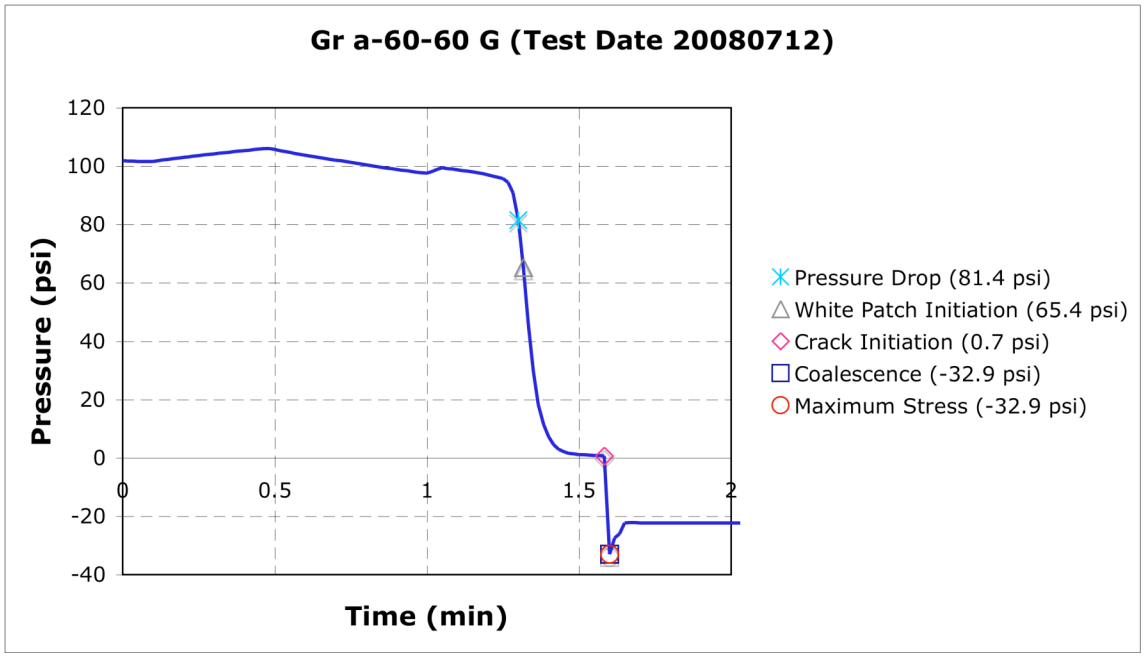

Pressure: 100 psi
Loading profile: fast
Category 5 Coalescence

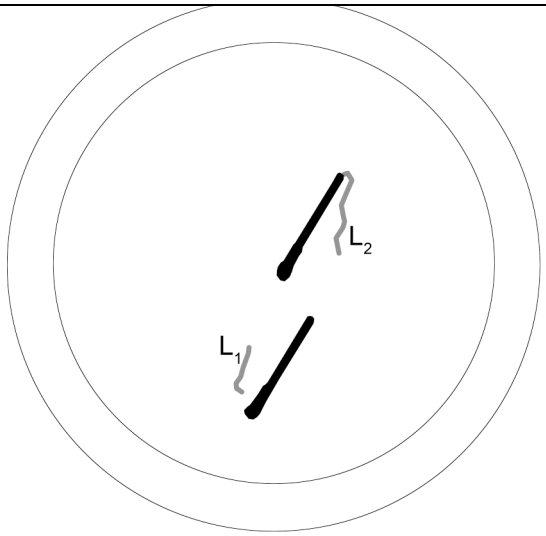	**Time:** ~1m19s **σ:** ~79.8 MPa Still image captured before high-speed recording with high-speed camera. White patches L_1 and L_2 appear on the left and right flaws' outer tips, respectively. L_1 does not appear attached to the left flaw's outer tip.
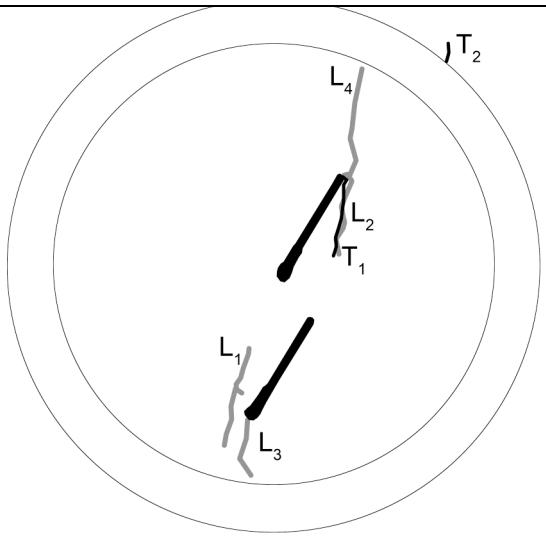	**Time:** 1.1045s before failure **σ:** 117.9172 MPa First high-speed image. Tensile wing crack T_1 appears below the outer tip of the right flaw. L_1 extends downward. White patches L_3 and L_4 appear, both extending to the O-ring. A small tensile crack appears outside the O-ring (labeled T_2).

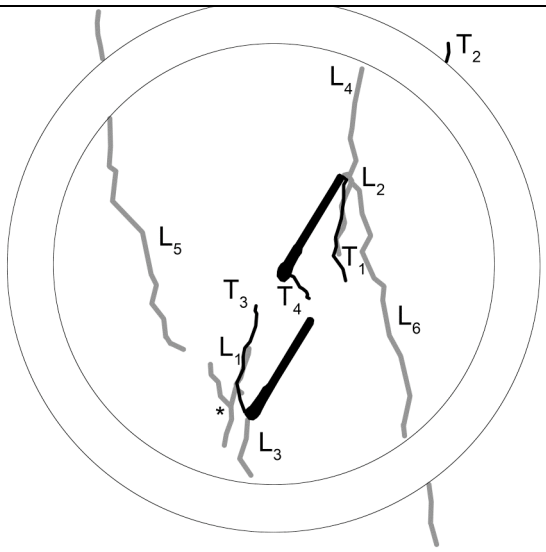	**Time:** 0.1635s before failure **σ:** 119.6258 MPa Tensile wing crack T_3 appears in the L_1 region. Tensile wing crack T_4 appears below the right flaw's inner tip and extends toward the left flaw's inner tip. White patch L_1 branches as the point indicated by the "*". White patch L_5 appears slightly beyond this branch and extends beyond the O-ring. Similarly, white patch L_6 branches off of L_2 and extends beyond the O-ring.
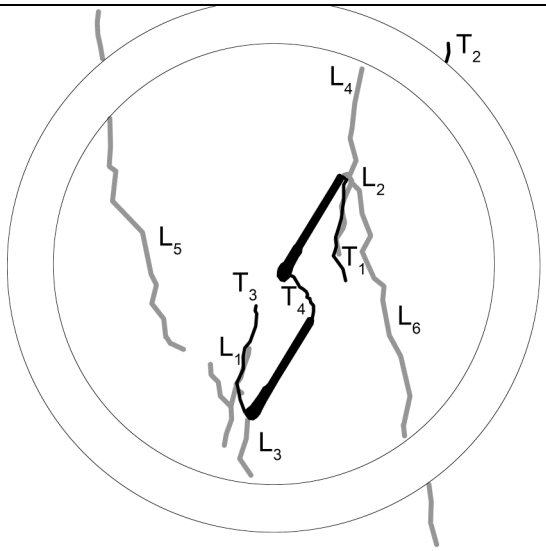	**Time:** 0.0045s before failure **σ:** 120.1817 MPa Flaws coalesce when T_4 connects with the inner tip of the left flaw.

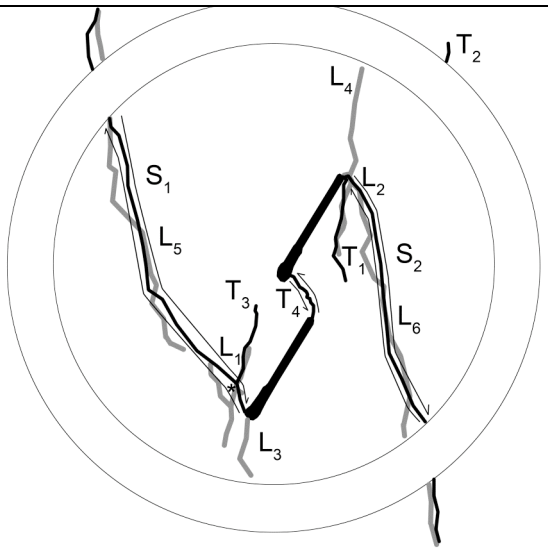

Time: 1m35.502s
σ: 120.5769 MPa

Specimen failure occurs with the appearance of shear cracks S_1 and then S_2 (both shear in the sense indicated). Both shear cracks also seem to extend beyond the O-ring, although their nature is indeterminable because of shadows cast by the window frame. S_1 branches off of T_2 at the point indicated by the asterisk. The short section of T_2 between the left flaw's outer tip and the "*" slides in the sense indicated. Sliding also occurs along T_4.

Gr a-60-60 C (100 psi, slow loading)

Summary

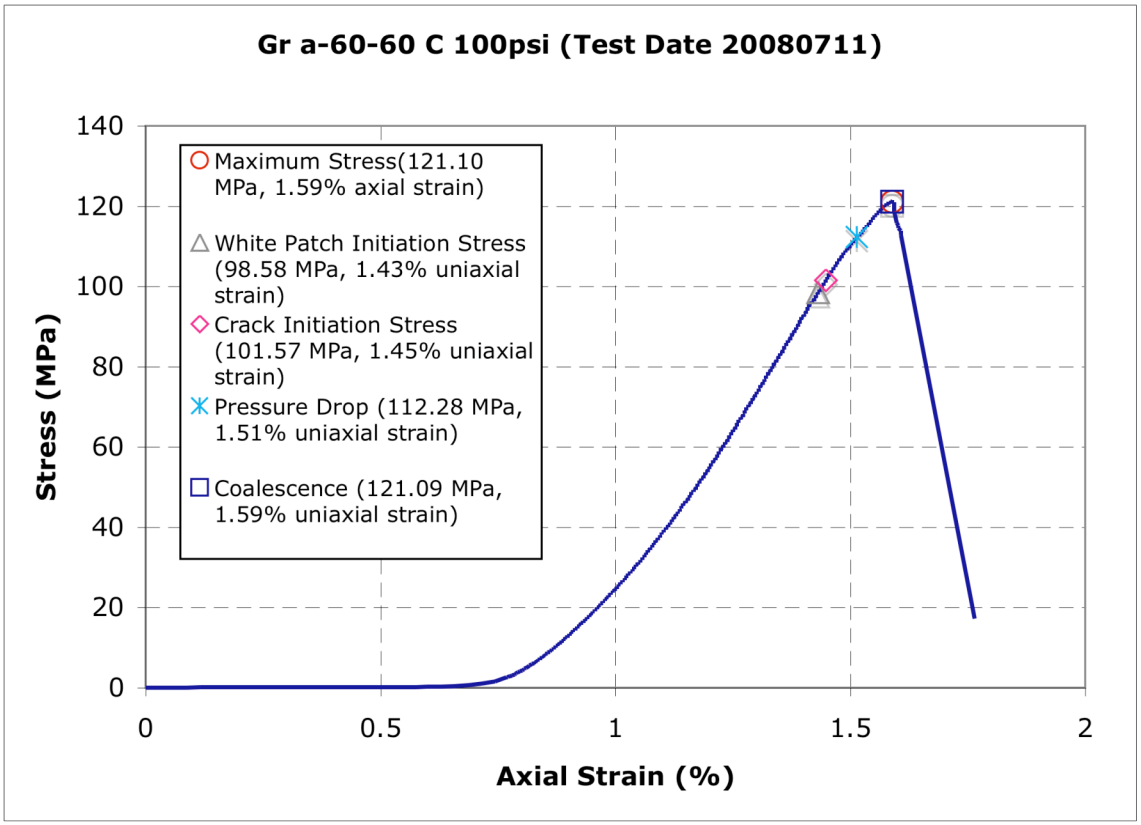

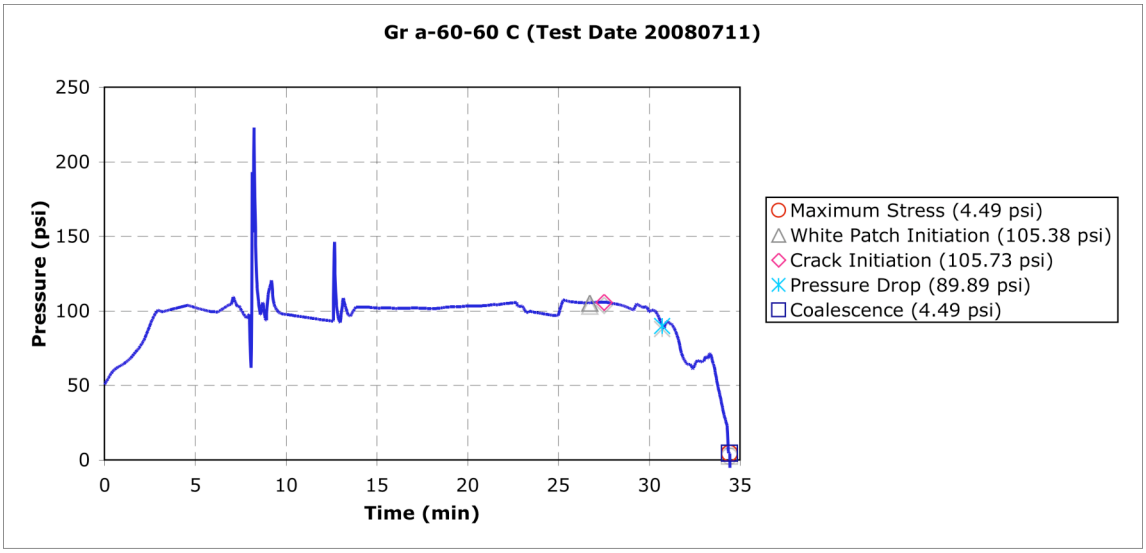

Pressure: 100 psi
Loading profile: slow
Coalescence category 4

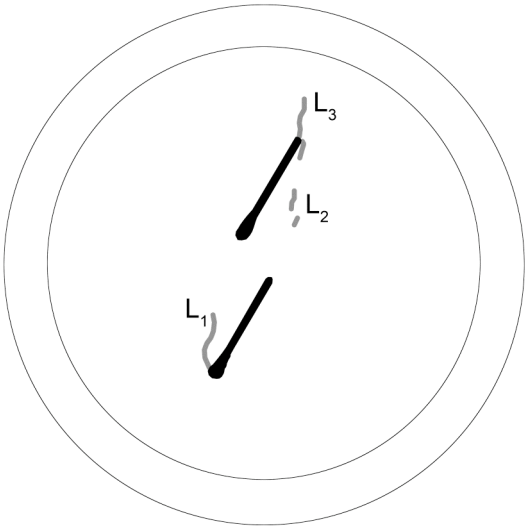	**Time:** ~19m52s **σ:** ~98.6 MPa Still image captured before recording with high-speed camera. White patches L_1, L_2, and L_3 appear. L_2 does not appear to be continuous.
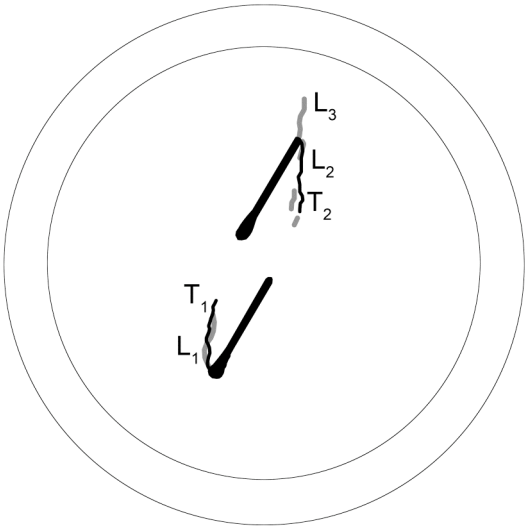	**Time:** ~20m38s **σ:** ~101.6 MPa Still image captured before recording with high-speed camera. Tensile wing cracks T_1 and T_2 appear in the L_1 and L_2 regions, respectively.

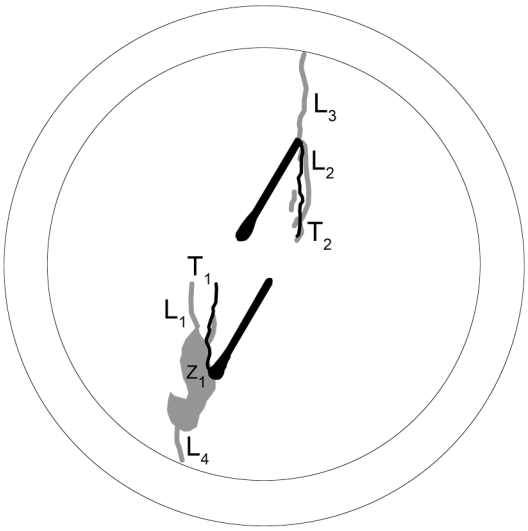	**Time:** ~25m30s **σ:** ~116.9 MPa Still image captured before recording with high-speed camera. Tensile cracks T_1 and T_2 appear to lengthen. All three white patches appear to extend, with L_3 reaching the O-ring. A zone of grains lightens near the left flaw's outer tip and is labeled z_1. A white patch (labeled L_4) appears below the zone of lightened grains and extends down to the O-ring.
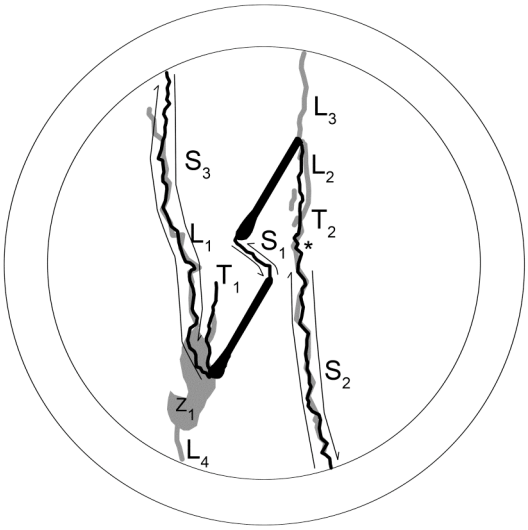	**Time:** 0.167s before failure **σ:** 121.0932 MPa Specimen coalescence occurs with the appearance of shear crack S_1, shearing in the sense indicated. Shear cracks S_2 and S_3 appear and shear as indicated coincident with coalescence. Tensile crack T_2 transitions to a shear mode at the point labeled "*". White patches L_1 and L_2 appear to extend along with crack formation. Because this is the first frame of the high-speed recording, sample coalescence is not captured exactly. Therefore, coalescence caused by a tensile crack cannot be ruled out. Shear nature is attributed to the coalescing crack in this case due to flakes of material falling from the crack and relative motion between the two sides of the crack.

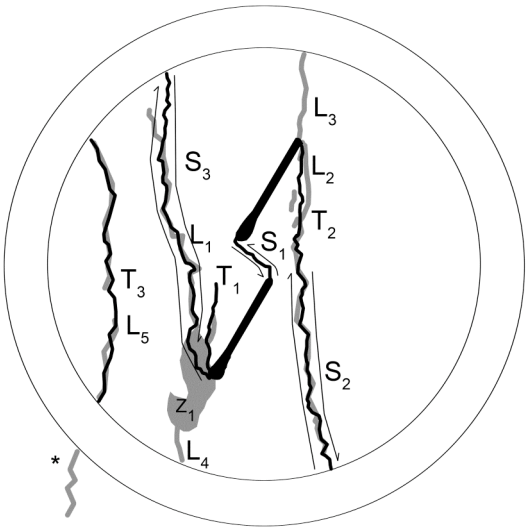	**Time:** 0.0033s before failure **σ:** 121.097 MPa Tensile crack T_3 appears to the left of both flaws. White patch L_5 appears along most of the length of T_3. Of note is the appearance of L_5 on the other side of the O-ring (labeled "*").
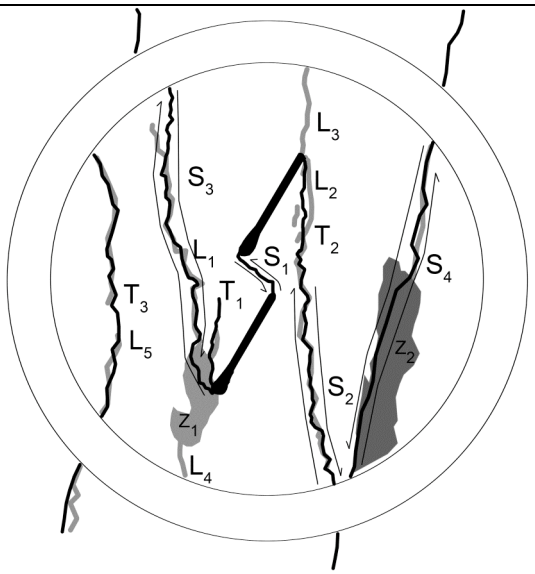	**Time:** 27m33.576s **σ:** 121.1000 MPa Specimen failure occurs with the appearance of shear crack S_4 (shearing in the sense indicated) and a patch of associated spalling (labeled z_2). Note some crack traces continue outside of the O-ring. The nature of these cracks is unknown because they are shadows caused by the window frame.

Gr a-60-60 H (200 psi, fast loading)

Summary

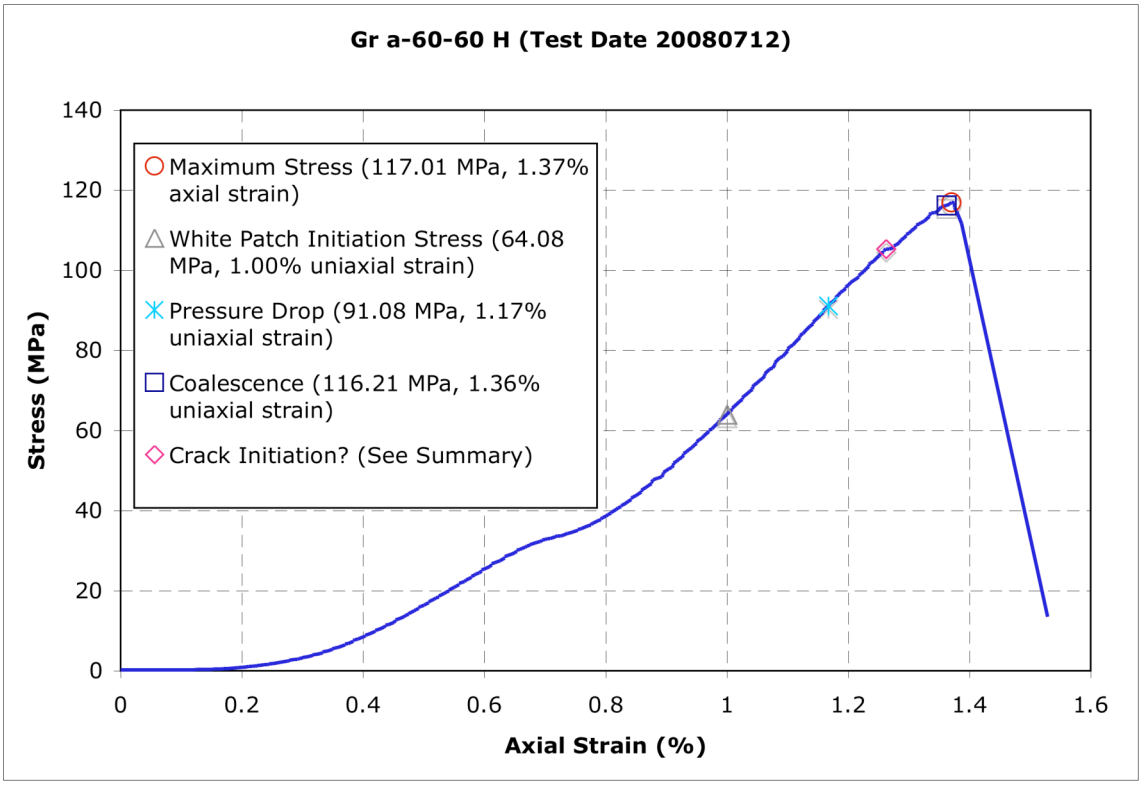

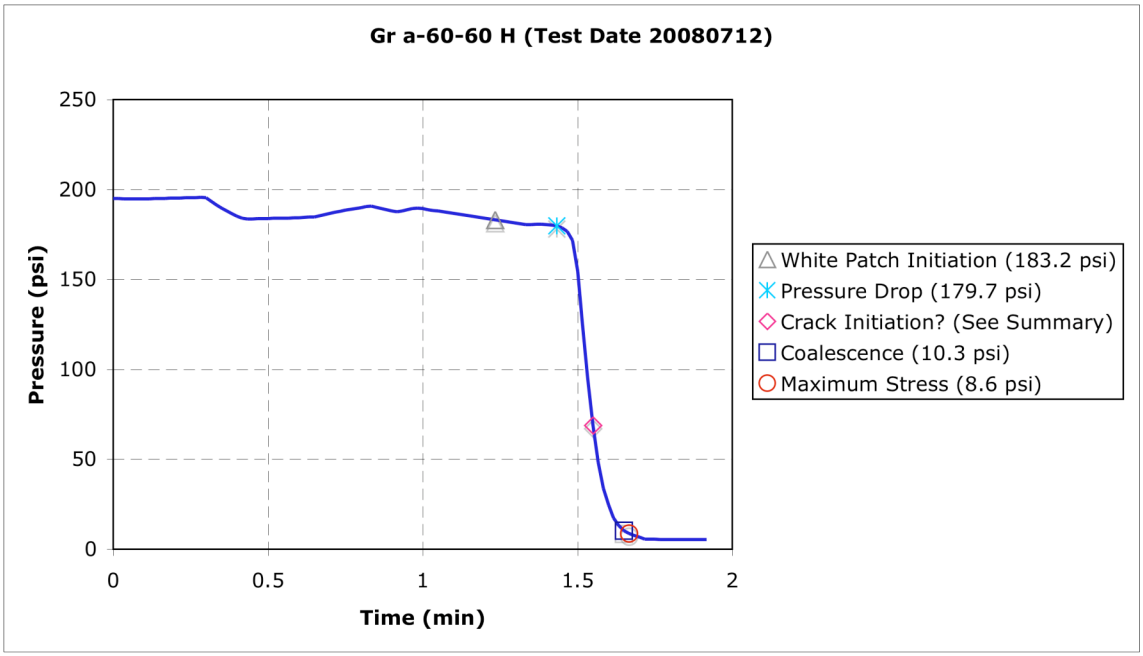

Pressure: 200 psi
Loading profile: fast
Category 8 Coalescence

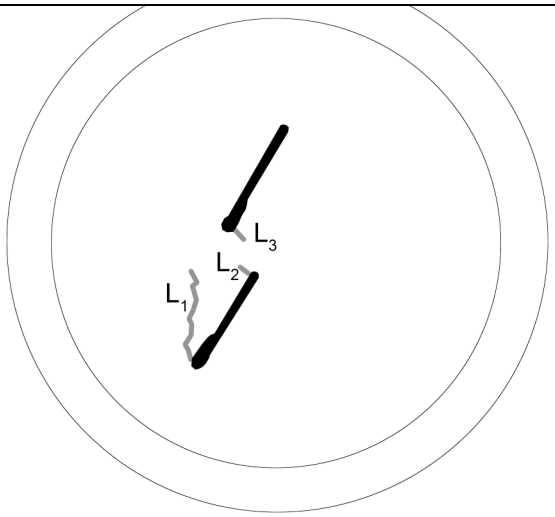	**Time:** ~1m14s **σ:** ~64.1 MPa Still image captured before high-speed recording with high-speed camera. White patches L_1, L_2, and L_3 appear.
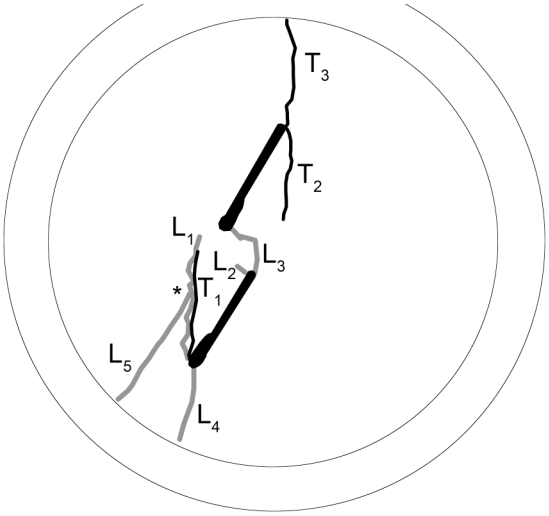	**Time:** 1.0745s before failure **σ:** 115.88 MPa First image of high-speed video. Tensile wing cracks T_1, T_2, and T_3 have already appeared. T_3 extends to the O-ring. L_1 and L_3 both extend, with L_3 connecting with the inner tip of the left flaw. L_4 appears below the left flaw's outer tip and L_5 branches off of L_1 (at the point labeled "*") and extends to the O-ring. Crack initiation stress is not determinable with any reasonable accuracy. It occurs at a point between this image and white patch initiation in the preceding image. There is a noticeable "kink" in the stress-strain curve that may correspond to crack initiation after the pressure drop.

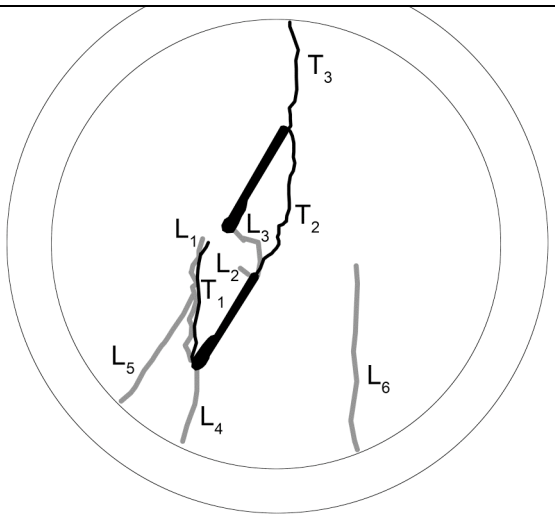	**Time:** 0.3835s before failure **σ:** 116.21 MPa Both T_1 and T_2 extend. T_2, however, also connects with the inner tip of the left flaw, causing crack coalescence. White patch L_6 appears and extends upward from the O-ring.
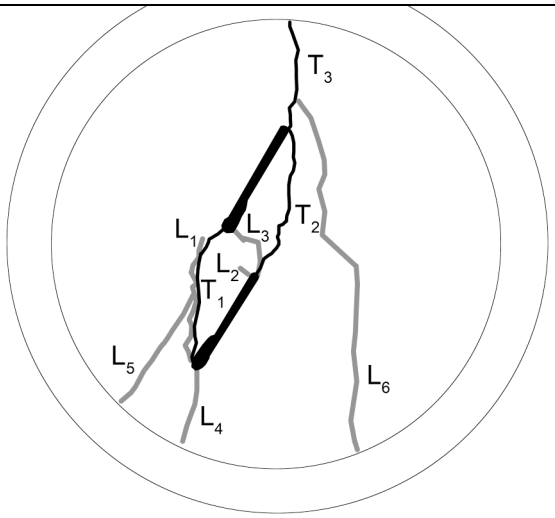	**Time:** 0.1335s before failure **σ:** 116.59 MPa T_1 extends and connects with the inner tip of the right flaw. L_6 also extends upward and connects with T_3.

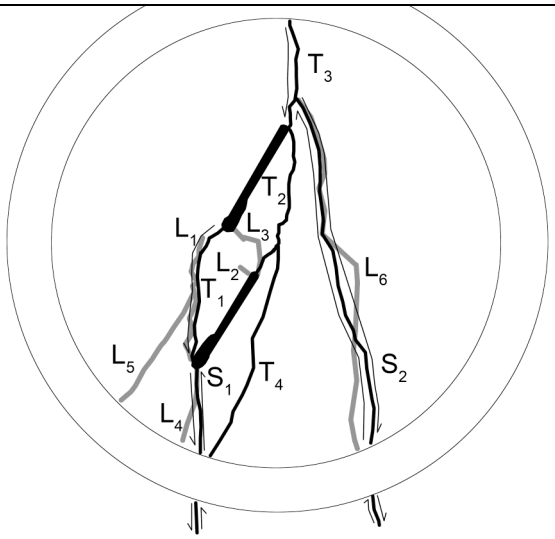

Time: 1m40.752s
σ: 117.0057 MPa

Specimen failure occurs after tensile crack T_4 appears followed by the appearance of shear cracks S_1 and S_2 (shearing in the sense indicated). Both shear cracks continue outside the O-ring. The left side of the specimen slides along T_1 and T_3 as shown as well.

Gr a-60-60 F (200 psi, slow loading)

Summary

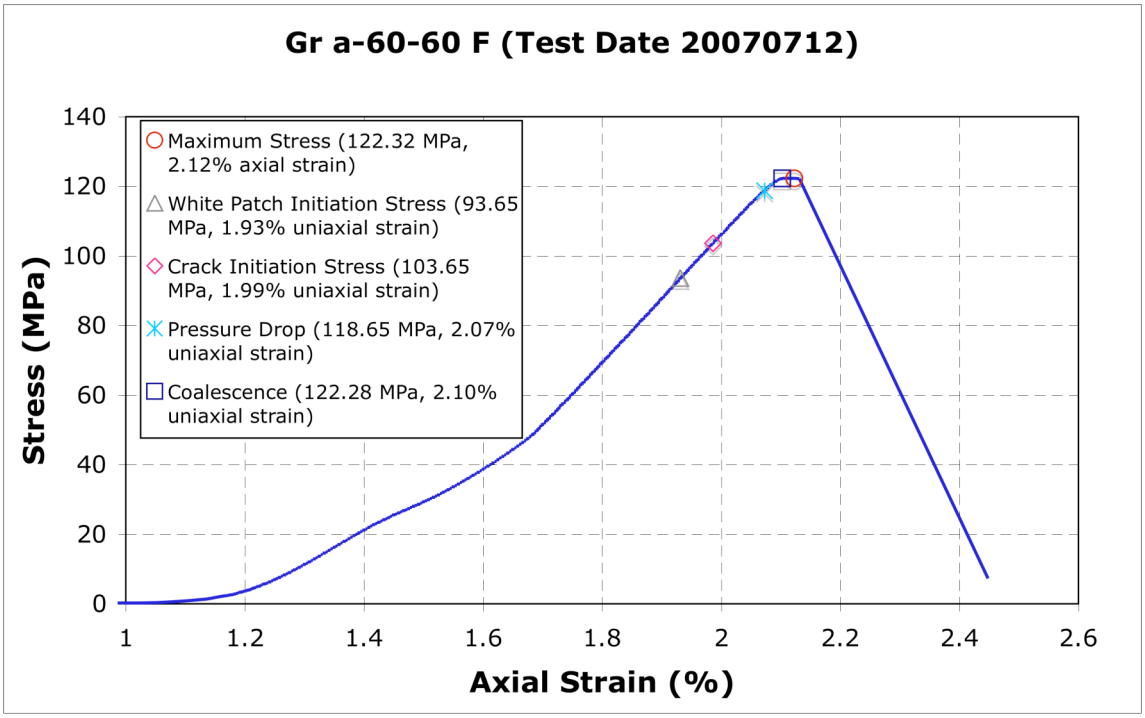

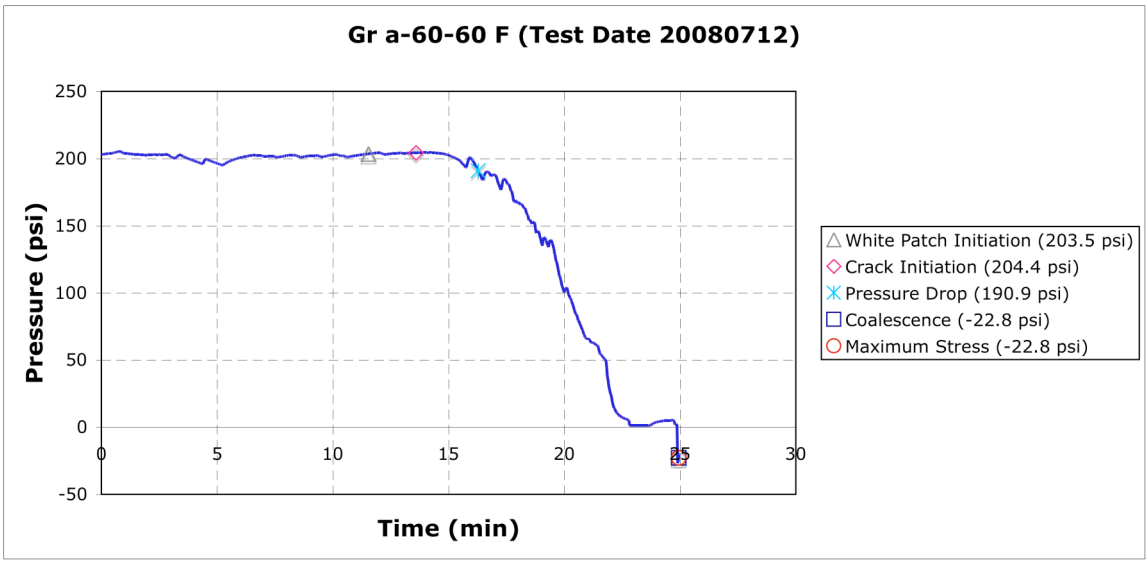

Pressure: 200 psi
Loading profile: slow
Category 4 Coalescence

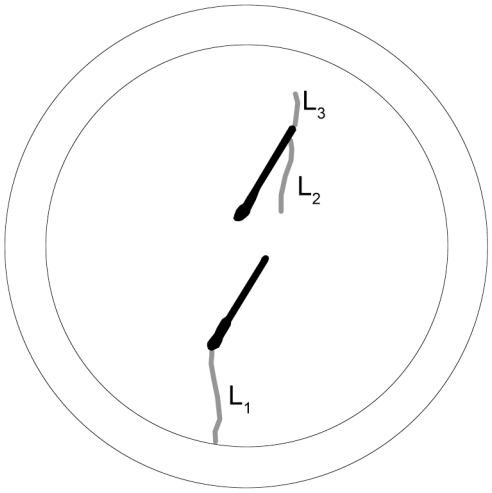	**Time:** ~19m04s **σ:** ~93.7 MPa Still image captured before high-speed recording with high-speed camera. White patches L_1, L_2, and L_3 appear. L_1 extends to the O-ring.
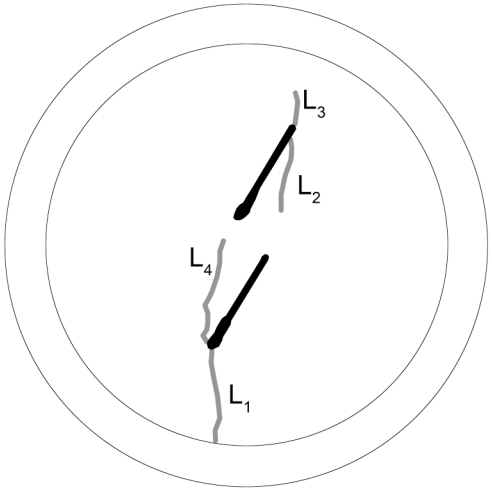	**Time:** ~19m57s **σ:** ~97.9 MPa Still image captured before high-speed recording with high-speed camera. White patch L_4 appears above the outer tip of the left flaw.

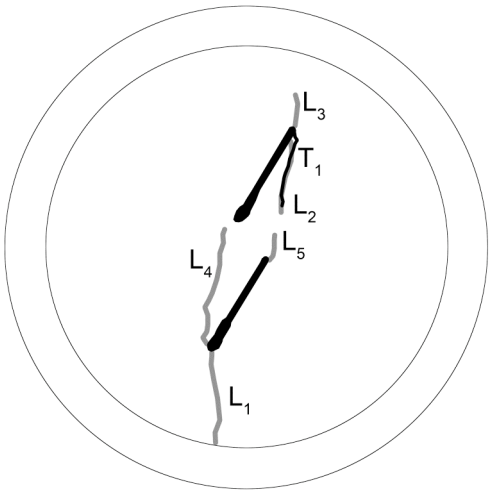	**Time:** ~21m07s **σ:** ~103.7 MPa Still image captured before high-speed recording with high-speed camera. Linear white patch L_5 appears on the inner tip of the left flaw. L_4 extends slightly. Tensile wing crack T_1 appears below the outer tip of the right flaw. It appears to follow L_2 very closely.
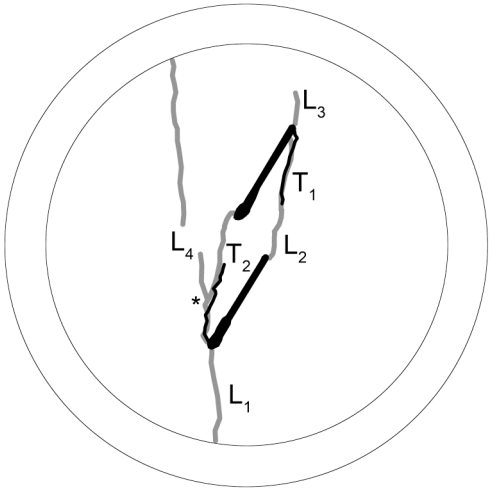	**Time:** ~23m07s **σ:** ~113.4 MPa Still image captured before high-speed recording with high-speed camera. L_4 branches at the point indicated by the "*" and one branch extends to the inner tip of the right flaw while the other branch (with a short gap) extends to the O-ring. Tensile wing crack T_2 appears above the outer tip of the left flaw and follows the original trace of L_4. L_5 and L_2 lengthen and connect (the resulting white patch is labeled as L_2).

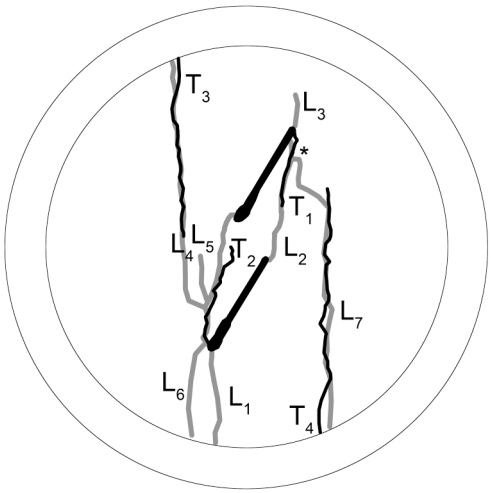	**Time:** 1.461s before failure **σ:** 122.23 MPa First high-speed image Linear white patches L_5, L_6, and L_7 appear followed by tensile cracks T_3 and T_4. L_7 attaches to L_2 at the point indicated by the "*". The tensile cracks extend from the O-ring boundary toward the outer flaw tips. They extend through L_4 and L_7, respectively.
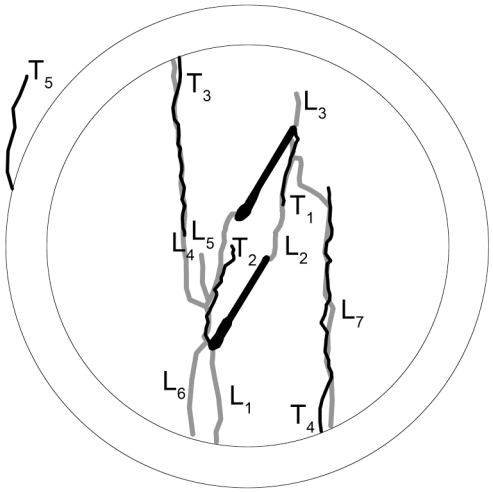	**Time:** 0.5397s before failure **σ:** 122.29 MPa Tensile crack T_5 appears outside the O-ring.

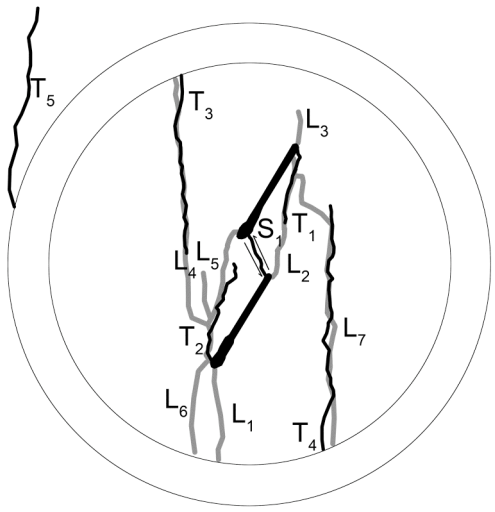	**Time:** 0.13s before failure **σ:** 122.28 MPa Flaws coalesce with the appearance of shear crack S_1 connecting the two inner flaw tips (shearing in the sense indicated). Tensile crack T_5 extends.
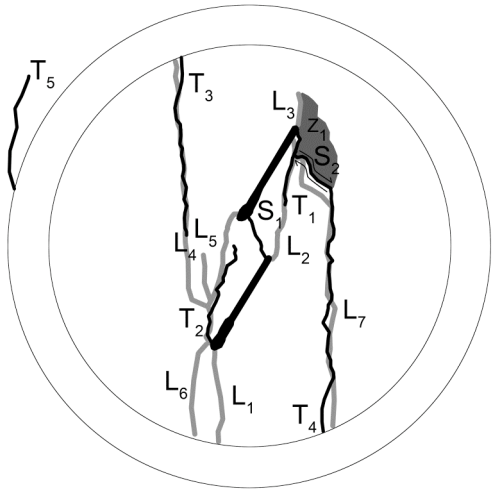	**Time:** 0.1063 s before failure **σ:** 122.28 MPa A zone of spalling (labeled z_1) appears and a shear crack (labeled S_2) appears connecting T_1 and T_4, shearing in the sense indicated.

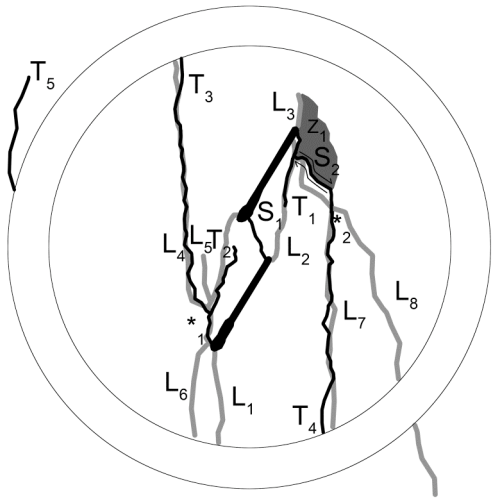	**Time:** 0.0013s before failure **σ:** 122.32 MPa Tensile crack T_3 extends downward and connects with T_2 at the point labeled "$*_1$". A white patch (labeled L_8) braches off of L_7 at the point labeled "$*_2$" and extends to the O-ring and continues on the other side.
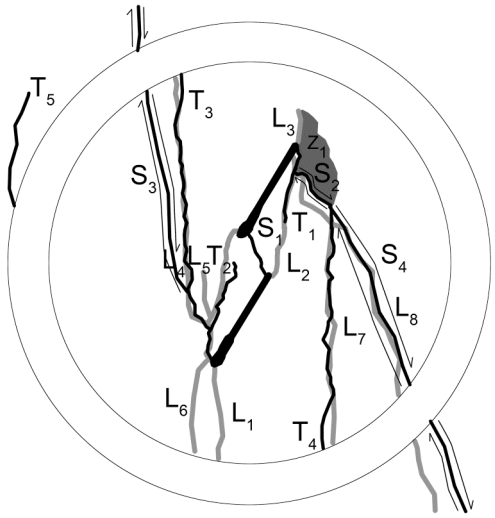	**Time:** 24m 56.172s **σ:** 122.3159 MPa Specimen failure occurs when shear cracks S_3 and S_4 appear and connect with T_3 and T_4, respectively.

Gr a-60-60 D (400 psi, slow)

Summary

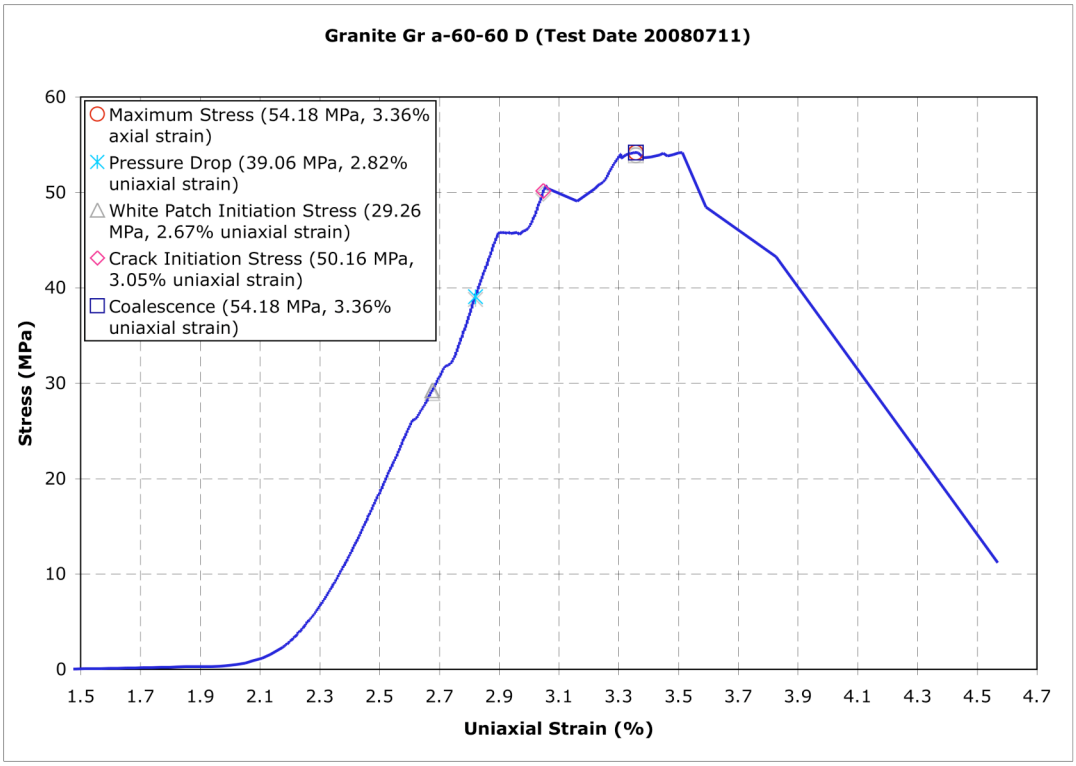

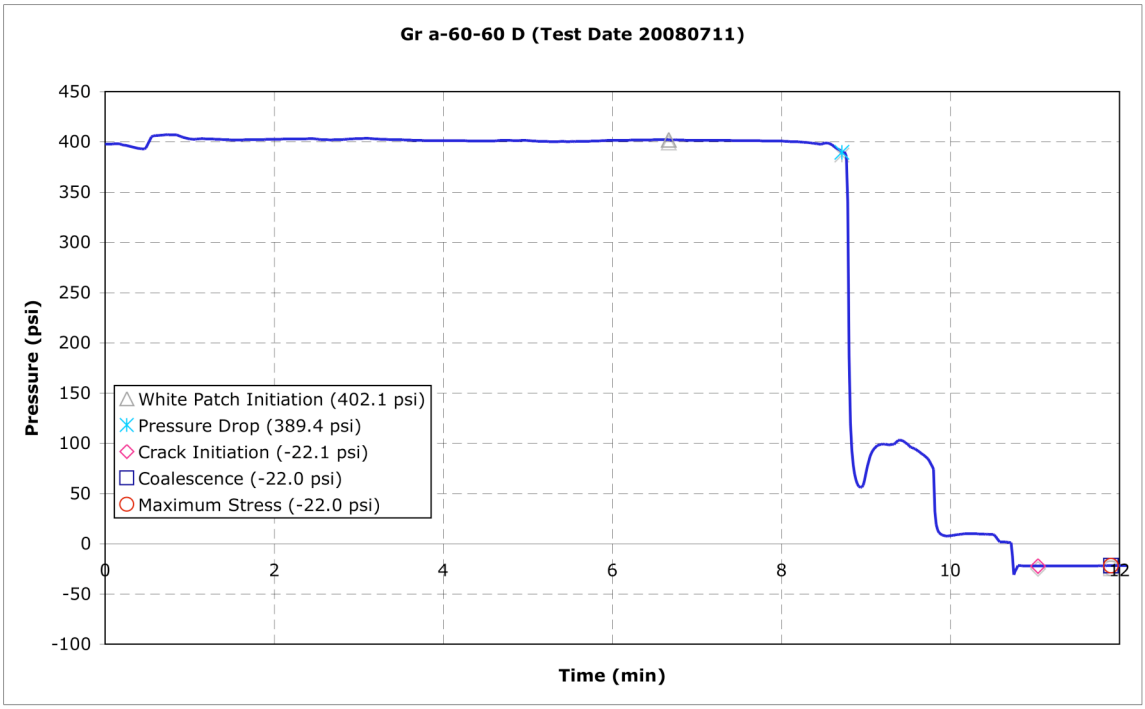

Pressure: 400 psi
Loading profile: slow
Coalescence category 6

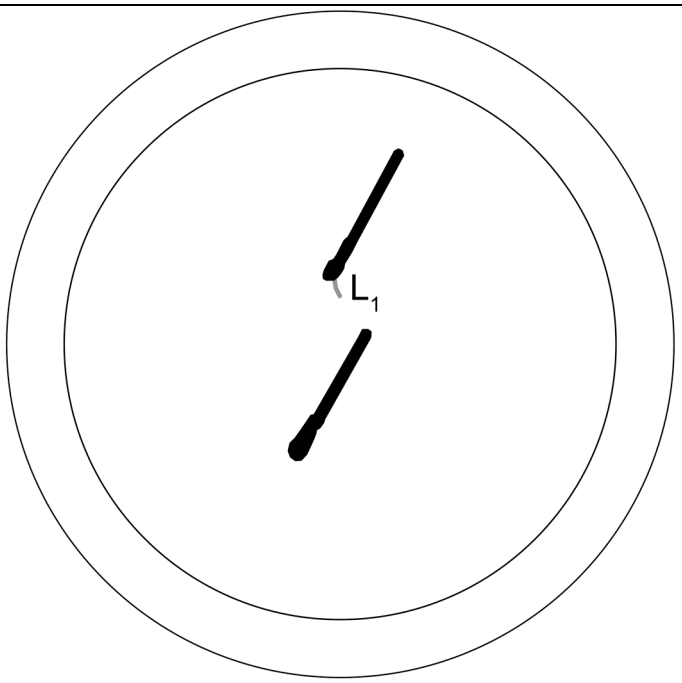	**Time:** ~6m40s **σ:** ~29.3 MPa White patch L_1 appears below the right flaw's inner tip and extends into the bridging zone.
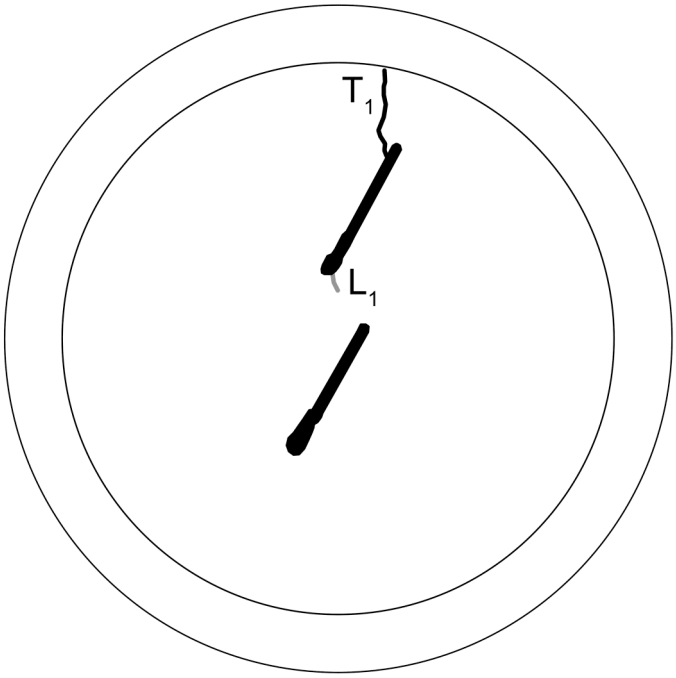	**Time:** ~11m02s **σ:** ~50.2 MPa Tensile wing crack T_1 appears above the right flaw's outer tip and extends to the O-ring.

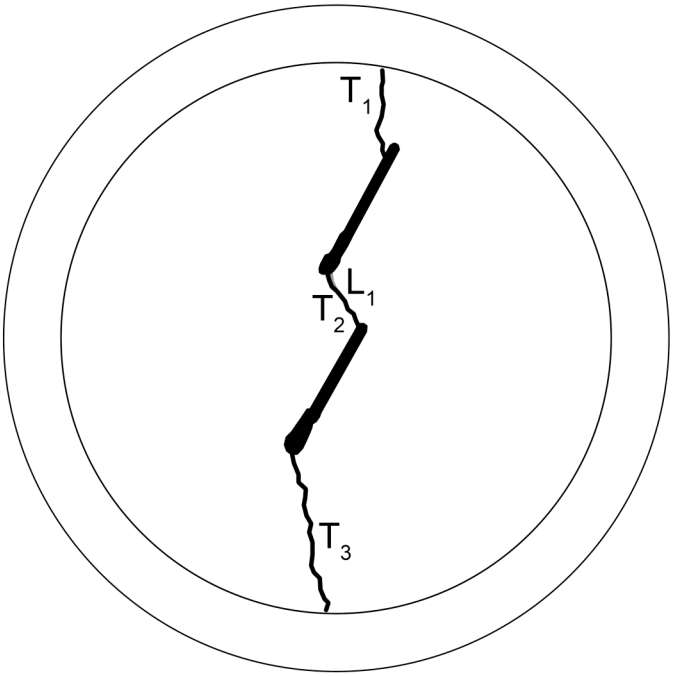	**Time:** 11m53.442s **σ:** 54.1776 MPa Tensile wing cracks T_2 and T_3 suddenly appear. Direct coalescence (category 6) results from T_2 connecting the two inner flaw tips. Specimen also fails with the appearance of these two additional tensile cracks.